VILNIUS UNIVERSITY
CENTER FOR PHYSICAL SCIENCES AND TECHNOLOGY

Jonas
KAUSTEKLIS

Vibrational spectroscopy of innovative functional materials: aggregates, conformational and dynamic processes

DOCTORAL DISSERTATION

Natural Sciences,
Physics N 002

VILNIUS 2019

This dissertation was written between 2014 and 2018 in Vilnius University
The research was supported by Research Council of Lithuania.

Academic supervisor:
Assoc. Prof. Dr. Valdemaras Aleksa (Vilnius University, Natural sciences, Physics – N 002)

This doctoral dissertation will be defended in a public meeting of the Dissertation Defence Panel:
Chairman – Prof. Habil. Dr. Gintaras Valušis (Vilnius University, Natural sciences, Physics – N 002).
Members:
Prof. Habil. Dr. Vidmantas Gulbinas (Vilnius University, Natural sciences, Physics – N 002).
Prof. Dr. Liutauras Marcinauskas (Kaunas University of Technology, Natural sciences, Physics – N 002).
Prof. Habil. Dr. Gediminas Niaura (Vilnius University, Natural sciences, Physics – N 002).
Prof. Habil. Dr. Sigitas Tumkevičius (Vilnius University, Natural sciences, Chemistry – N 003).

The dissertation shall be defended at a public meeting of the Dissertation Defence Panel at 13:00 on 23 September 2019 in Room/meeting room D401 of the Centre for Physical Sciences and Technology

Address: Saulėtekio av. 3, LT-10257 Vilnius, Lithuania
Tel. +370 5 264 8884; e-mail office@ftmc.lt.

The text of this dissertation can be accessed at the libraries of Vilnius University and Center for Physical Sciences and Technology as well as on the website of Vilnius University: www.vu.lt/lt/naujienos/ivykiu-kalendorius

VILNIAUS UNIVERSITETAS
FIZINIŲ IR TECHNOLOGIJOS MOKSLŲ CENTRAS

Jonas
KAUSTEKLIS

Inovatyviųjų funkcinių medžiagų agregatų, konformacinių ir dinaminių vyksmų virpesinė spektrometrija

DAKTARO DISERTACIJA

Gamtos mokslai,
Fizika N 002

VILNIUS 2019

Disertacija rengta 2014–2018 metais Vilniaus universitete.
Mokslinius tyrimus rėmė Lietuvos mokslo taryba.

Mokslinis vadovas:
Doc. dr. Valdemaras Aleksa (Vilniaus universitetas, gamtos mokslai, fizika – N 002).

Gynimo taryba:
Pirmininkas – **Prof. habil. dr. Gintaras Valušis** (Vilniaus universitetas, gamtos mokslai, fizika – N 002).
Nariai:
Prof. habil. dr. Vidmantas Gulbinas (Vilniaus universitetas, gamtos mokslai, fizika – N 002),
Prof. dr. Liutauras Marcinauskas (Kauno technologijos universitetas, gamtos mokslai, fizika – N 002),
Prof. habil. dr. Gediminas Niaura (Vilniaus universitetas, gamtos mokslai, fizika – N 002),
Prof. habil. dr. Sigitas Tumkevičius (Vilniaus universitetas, gamtos mokslai, chemija – N 003).

Disertacija ginama viešame Gynimo tarybos posėdyje 2019 m. rugsėjo mėn. 23 d. 13:00 val. Nacionalinio Fizinių ir Technologijos mokslų centro D401 posėdžių salėje / auditorijoje.

Adresas: Saulėtekio al. 3, LT-10257 Vilnius, Lietuva, tel. +370 5 264 8884; el. Paštas: office@ftmc.lt.

Disertaciją galima peržiūrėti Vilniaus universiteto, Fizinių ir technologijos mokslų centro bibliotekose ir VU interneto svetainėje adresu: https://www.vu.lt/naujienos/ivykiu-kalendorius

TABLE OF CONTENTS

ABBREVIATIONS

ACP – amorphous calcium phosphate
AIM – Atoms In Molecules calculations
CaP – calcium phosphate
CaHAp – calcium hydroxyapatite
D_2O – heavy water
DFT – density functional theory
DSC – differential scanning calorimetry
EDX – energy-dispersive X-ray analysis
EG – ethylene glycol
FTIR – Fourier transform infrared spectroscopy
FWHM – full width at half maximum
GL – glycerol
H_2O – water
HAp – hydroxyapatite
IL – ionic liquid
LC – liquid crystalline
MCT – mercury cadmium telluride
NBO – Natural Bond Orbital calculations
Nd:YAG – neodymium-doped yttrium aluminum garnet
NMR – nuclear magnetic resonance
NS – neutron scattering
PCA – principal component analysis
SANS – small-angle neutron scattering
SAXS – small-angle X-ray scattering
TA – tartaric acid
SEM – scanning electron microscopy
X_{H2O_MASS} – water mass fraction in the mixtures with ionic liquid
X_{D2O_MOL} – water molar fraction in the mixtures with ionic liquid
XRD – X-ray diffraction
2DCOS – two-dimensional correlation spectroscopy

LIST OF SAMPLES

$[C_4mim]I$ – 1-butyl-3-methylimidazolium iodide
$[C_4mim]Br$ – 1-butyl-3-methylimidazolium bromide
$[C_4mim]Cl$ – 1-butyl-3-methylimidazolium chloride
$[C_4mim]NO_3$ – 1-butyl-3-methylimidazolium nitrate
$[C_4mim]BF_4$ – 1-butyl-3-methylimidazolium tetrafluoroborate
$[C_4mim]OTf$ – 1-butyl-3-methylimidazolium triflate
$[C_{10}mim]Br$ – 1-decyl-3-methylimidazolium bromide
$[C_{10}mim]Cl$ – 1-decyl -3-methylimidazolium chloride
EDTA-CaHAp – 1,2-ethylendiaminetetraacetic acid calcium hydroxyapatite
TA-CaHAp – tartaric acid calcium hydroxyapatite
EG-CaHAp – ethylene glycol calcium hydroxyapatite
GL-CaHAp – glycerol calcium hydroxyapatite
CA-CaHAp – commercially available calcium hydroxyapatite
ACP-GL-CaHAp – amorphous calcium phosphate phase-based hydroxyapatite

1. INTRODUCTION

Innovative functional materials are generally characterized as the group of materials which possess the particular native properties, unique structure and functions of their own. Preservation of physical and chemical properties, structure and functions of prepared materials are the most important tasks for researchers in the field of applied sciences. Furthermore, the necessity of rapid, reliable, handy tool to characterize functional materials and their properties is essential for the materials industry.

Currently, different functional materials with many physico-chemical behavior features and compositions are known. Ionic liquids (ILs), as well as calcium phosphates (CaPs), are very well known for their application in medicine and pharmaceuticals [1–3]. While ILs are widely used for drug delivery, synthesis and biomedical analytics [3–6], the CaP‘s applications are more based on human treatment: diseases and injuries [7], CaP pastes, coatings and artificial bone implants [8–14]. Moreover, the opportunity for structure tuning increases the scope of applications for both mentioned materials. Recently, different routes for CaP materials synthesis were tried to increase the osteoinductivity – the ability to absorb guest implants, which depends on the organization of pores, cavities and surfaces [15–17]. The surface area is a comparable parameter for different types of CaP complexes analysis. CaP prepared with clustered amorphous calcium phosphate phase (ACP) will have a smaller surface area than CaP with nano- or mesophases. On the other hand, ionic liquids give the almost infinite number of functional materials with specific properties determined by various combinations of anions and cations [18,19]. Wide liquid range, high ionic conductivity, negligible vapor pressure, high electrochemical and thermal stability and significant ability to solubilize organic, inorganic or polymeric materials are mainly caused by dipolar, electron pair donor-acceptor, Coulombic interactions and hydrogen bond formation in ILs [20,21]. Highly attracted properties empowered possibilities to use ionic liquids as functional materials and engaged researchers for both experimental and theoretical studies [22–25].

Finally, the applicability of CaPs and ILs depends on the contaminants and their impact on the structure and properties. Water – one of the natural impurities, found in both: ILs and CaPs. It could be absorbed from the atmosphere or left after chemical synthesis [19]. It was found that a small amount of water can dramatically change the diffusion coefficients [26], polarity [27], viscosity [28] and surface tension [29] of ILs. Several studies employed the new strategy, emerged of mixing ILs with compounds, which

previously used to be impurities. Depending on the purpose ILs are mixed with organic compounds, other ILs, and water [30,31]. It was noted that a better understanding of interactions among ILs and water molecules is needed, as well as the structure, of various mixtures at different concentrations of constituents. The increase of the ion diffusion coefficient was observed due to viscosity decrease and arose from the suppression of the electrostatic interactions between ions, when water was incorporated into ILs [31]. Several thorough studies of different structures formed in water and ILs mixtures reported the dependency of anion, cation combination and water concentration [32–36]. The research of self aggregation, conformational and dynamic processes in neat ILs and their mixtures with water were directly connected with changes in physical and chemical properties. The states of water molecules formed in CaPs are useful for the analysis of different chemical synthesis routes used to increase osteoinductivity [37]. However, despite the use of ionic liquids and calcium phosphates for different applications, there have not been enough investigations to allow a complete understanding of their behavior and structures in mixtures with water.

Various methods are available in scope to study the structure of CaP's, ILs and ILs–water mixtures [22,38–44]. Frequently, comprehensive functional materials analysis is performed using small-angle X-ray scattering (SAXS), small-angle neutron scattering (SANS), differential scanning calorimetry (DSC), nuclear magnetic resonance (NMR) and vibrational spectroscopy techniques [45–49]. Nevertheless, vibrational spectroscopy is the method of choice to get rapid, reliable and handy information on chemical composition, mollecular structure and intermolecular interactions. Raman and Fourier Transform Infrared spectroscopy (FTIR) as complementary methods are already used together with NMR, SANS and SAXS techniques to provide a remarkably detailed picture of investigated functional materials [33,41,50,51]. The main attention in thesis is pointed to the analysis of specific functional materials and according processes which were never been investigated utilizing vibrational spectroscopy.

1.1. Goal and tasks of the work

In the view of problems discussed above, the **main goal of thesis** was to study the states of water in both, aqueous ionic liquids mixtures and newly synthesized calcium hydroxyapatites, as well as analyze the dynamic processes and conformational equilibrium in these functional materials using the vibrational spectroscopy.

The work was focused to the investigation of spectral parameters eligible for the structural changes or phase transitions identification in the functional materials mixtures with water or heavy water. To achieve this goal, the following **tasks were formulated**:

- Analyze the formation of meso-phases in 1-decyl-3-methylimidazolium bromide and 1-decyl-3-methylimidazolium chloride aqueous mixtures using Raman spectroscopy.
- Investigate the states of water in newly synthesized calcium hydroxyapatites using vibrational spectroscopy techniques.
- Analyze the states of water formation in short chain ionic liquids and apply vibrational spectroscopy techniques for comprehensive analysis of water influence to the structural changes in aqueous mixtures of ionic liquids.
- Investigate the properties of ionic liquids, which influence the hydrogen-deuterium exchange in ionic liquids mixtures with D_2O utilizing Raman spectroscopy.

1.2. Statements of the doctoral thesis

1. Vibrational spectroscopy is a reliable and handy tool to rapidly determine the differences of IL meso-phases between liquid and liquid crystalline (LC) ionogel phase states. Complex exploitation of obtained Raman data together with NMR data provides new valuable information about processes of LC ionogel phase formation and role of different states of water molecules in these systems.

2. Vibrational spectroscopy very well discriminates the differences in surface and bulk species of H_2O states in the sol-gel derived nano-structured complex CaHAps.

3. Vibrational spectroscopy can be used to determine the different states of water in ionic liquid and water mixtures. Spectral evidence was found to determine specific water structures called “water pockets “.

4. The conformational dynamics and H/D exchage in different IL–water mixtures can be monitored using vibrational spectroscopy methods.

1.3. Scientific novelty

1. For the first time, boundaries of Liquid Crystalline ionogel phase and confined water formation in ionic liquid–water mixtures, were revealed by discontinuous changes of Raman spectral parameters.

2. The degree of molecular freedom due to the order−disorder effects was noticed as a crucial effect to the H/D exchange reaction for short ([C_4mim]) and long chain ([C_{10}mim]) ionic liquids. The results of Raman spectroscopy showed that degree of heterogeneity in ionic liquid–water mixtures is not influenced by the anion type.

3. For the first time, in the nano-structured CaHAps derived using sol-gel method with various complexing agents, the different organisation of structural hydroxyl groups was shown.

4. The results obtained by Raman spectroscopy showed that conformational changes and H/D exchange processes in both, long chain and short chain imidazolium-based ILs are not simultaneous phenomena.

5. DFT calculations of vibrational spectra of [C_4mim]NO_3 and [C_4mim]OTf using wide range of basis sets were performed for the first time and the vibrational bands of these compounds were assigned.

6. The precise assignment of Raman stretching OH and OD bands of IL–water mixtures at different H_2O/D_2O content was made using low temperature and polarized Raman measurements.

1.4. Publications included in the thesis

1. **J. Kausteklis**, V. Aleksa, M. A. Iramain and S. A. Brandan, *DFT and Vibrational Spectroscopy study of 1-butyl-3-metylimidazolium trifluoromethanesulfonate*, J. Mol. Struct., vol. 1175, pp. 663–676, 2019.

2. **J. Kausteklis**, M. Talaikis, V. Aleksa and V. Balevičius, *Raman spectroscopy study of water confinement in ionic liquid 1-butyl-3-methylimidzolium nitrate*, J. Mol. Liq., vol. 271, pp. 747–755, 2018.

3. **J. Kausteklis**, V. Aleksa, M. A. Iramain and S. A. Brandan, *Effect of cation-anion interactions on the structural and vibrational properties of 1-butyl-3-methylimidazolium nitrate ionic liquid*, J. Mol. Struct., vol. 1164, pp. 563–576, 2018.

4. **J. Kausteklis**, V. Balevičius and V. Aleksa, *Two-dimensional Raman spectroscopy study of ionogel phase formation in long-chain ionic liquid/water systems*, J. Raman Spectrosc., vol. 48, no. 1, pp. 126–131, 2017.

5. K. Kristinaitytė, L. Dagys, **J. Kausteklis**, V. Klimavičius, I. Doroshenko, V. Pogorelov, N. R. Valevičienė and V. Balevičius, *NMR and FTIR studies of clustering of water molecules: From low-temperature matrices to nano-structured materials used in innovative medicine*, J. Mol. Liq., vol. 235, pp. 1–6, 2017.

6. S. Kareiva, V. Klimavičius, A. Momot, **J. Kausteklis**, A Prichodko, L. Dagys, F. Ivanauskas, S. Sakirzanovas, V. Balevičius and A. Kareiva, *Sol-gel synthesis, phase composition, morphological and structural characterization of $Ca_{10}(PO_4)_6(OH)_2$: XRD, FTIR, SEM, 3D SEM and solid-state NMR studies*, J. Mol. Struct., vol. 1119, pp. 1–11, 2016.

7. V. Klimavičius, Z. Gdaniec, **J. Kausteklis**, V. Aleksa, K. Aidas and V. Balevičius, *NMR and Raman spectroscopy monitoring of proton/deuteron exchange in aqueous solutions of ionic liquids forming hydrogen bond: A Role of anions, self-aggregation and mesophase formation*, J. Phys. Chem. B, vol. 117, no. 35, pp. 10211–10220, 2013.

8. V. Aleksa, **J. Kausteklis**, V. Klimavicius, Z. Gdaniec and V. Balevičius, *Raman and NMR spectroscopy study of liquid crystalline ionogel phase in ionic liquid/H_2O mixtures: The states of water*, J. Mol. Struct., vol. 993, no. 1–3, pp. 91–96, 2011.

1.5. Other publications by author

1. L. Dagys, V. Klimavičius, **J. Kausteklis**, A. Chodosovskaja, V. Aleksa and A. Kareiva, *Solid-State 1H and 31P NMR and FTIR Spectroscopy Study Of Static And Dynamic Structures In Sol-Gel Derived Calcium Hydroxyapatites*, Lith. J. Phys., vol. 55, no. 1, pp. 1–9, 2015.

2. **J. Kausteklis**, P. Cevc, D. Arčon, L. Nasi, D. Pontiroli, M. Mazzani and M. Riccò, *Electron paramagnetic resonance study of nanostructured graphite*, Phys. Rev. B – Condens. Matter Mater. Phys., vol. 84, no. 12, 2011.

1.6. Presentations in Conferences

1. **J. Kausteklis**, R. Platakytė, E. Zacharovas, V. Aleksa, *Conformational Equilibrium of Imidazolium-Based Ionic Liquids, Effect of Water, Temperature and Counter Anions*, EUCMOS-2018 "34th European Congress on Molecular Spectroscopy" 2018, Coimbra, Portugal.

2. **J. Kausteklis**, V. Aleksa, V. Jočys, V. Balevičius, *Water Pockets in Ionic Liquid: the Role of Hydrogen Bonding*, HBOND-2017 „Horizons in Hydrogen Bond Research", 2017, Jyväskylä, Finland.

3. **J. Kausteklis**, V. Jočys, V. Aleksa, V. Balevičius, V*ibrational Spectroscopy of Water Pockets in Ionic Liquids*, „II International Workshop Water & Other Partially Ordered Liquids", 2017, Kyiv, Ukraine.

4. V. Aleksa, **J. Kausteklis**,V. Balevičius, *2D COR Raman Study of Lyotropic Phases in Ionic Liquid/Water Solutions*, „II International Workshop Water & Other Partially Ordered Liquids", 2017, Kyiv, Ukraine.

5. A. Žalga, P. Normantas, M. Smolianskis, A. Naruševičiūtė, L. Jočionis, E. Zacharovas, **J. Kausteklis**, V. Aleksa, *Struktūrinių pokyčių lantano molibdato vandeniniuose mišiniuose tyrimas naudojant Ramano spektroskopijos metodą*, „42-oji Lietuvos nacionalinė fizikos konferencija", 2017, Vilnius, Lithuania.

6. K. Kristinaitytė, L. Dagys, **J. Kausteklis**, V. Klimavičius, I. Doroshenko, V. Pogorelov, N.R. Valevičienė, V. Balevičius, *BMR and FTIR studies of clustering of water molecules: from low-temperature matrices to nano-structured materials used in innovative medicine*, PLMMP-2016 "Physics of liquid matter: Modern Problems", 2016, Kyiv, Ukraine.

7. **J. Kausteklis**, V. Jočys, V. Aleksa, V. Balevičius, *Determination of liquid crystalline ionogel phase borders in [C_{10}mim]Cl,Br]/H2O mixtures using Raman spectroscopy*, PLMMP-2016 "Physics of liquid matter: Modern Problems", 2016, Kyiv, Ukraine.

8. **J. Kausteklis**, V. Jočys, V. Aleksa, V. Balevičius, *Raman study of water confined in ionic liquids*, EUCMOS-2016 „33rd European Congress on Molecular Spectroscopy“, 2016, Szeged, Hungary.

9. **J. Kausteklis**, V. Klimavičius, S. Kareiva, V. Aleksa, A. Kareiva, V. Balevičius, *FTIR and NMR spectroscopy of sol-gel derived calcium hydroxyapatites: correlation of experimental data and the size profiles of sub-nano spin clusters*, FM&NT-2015 „Functional Materials and Nanotechnologies“, 2015, Vilnius, Lithuania.

10. **J. Kausteklis**, V. Aleksa, V. Balevičius, *Two-Dimensional Raman Correlation Spectroscopy Study of Aggregation Process in Ionic Liquid Systems*, ICAVS 8 „International Conference on Advanced Vibrational Spectroscopy“, 2015, Viena, Austria.

11. V. Jočys, **J. Kausteklis**, J. Girskis, V. Aleksa, Dinaminių procesų joniniuose skysčiuose $[C_4mim]^+[X]^-$ (X=I, Br, Cl) tyrimas naudojant Ramano ir 2D koreliacinės spektrometrijos metodus. LNFK „41-oji Lietuvos nacionalinė fizikos konferencija“, 2015, Vilnius, Lietuva.

12. E. Zacharovas, A. Naruševičiūtė, L. Jočionis, **J. Kausteklis**, V. Aleksa, *FT-Raman spectroscopic study of water influence on conformational equilibrium in ionic liquids and water mixtures*, Open Readings 2018, 2018, Vilnius Lithuania.

13. V. Jočys, **J. Kausteklis**, A. Gruodis, V. Aleksa, *Acetonitrile associated with the ionic liquid containing imidazolium ring: equilibrium geometry and vibrational relaxation*, The 13^{th} international scientific conference Information technologies and management 2015, Riga, Latvia.

1.7. Authors contribution

The aqueous sol-gel synthesis using different complexing agents were performed in the Department of the Inorganic Chemistry, Vilnius University (Head. Prof. Habil. Dr. Aivaras Kareiva). The majority of the Raman and FTIR experimental work presented in the thesis was done by the Author. Part of the Raman experimental work published in the above mentioned publications was carried out by Dr. Ieva Matulaitienė, Martynas Velička an Martynas Talaikis. Theoretical calculations by quantum chemistry methods were performed by Prof. Dr. Silvia Brandan and Dr. Kęstutis Aidas. Other experimental work published in the publications was done by the co-authors Prof. Habil Dr. V. Balevičius, Dr. V. Klimavičius, Dr. I. Doroshenko, K. Kristinaitytė and L. Dagys. The data analysis and above publications preparation were a teamwork of all authors.

2. OVERVIEW

2.1. Various states of water in functional materials

Water appears to be a small and apparently simple molecule, which could be found everywhere around. We live on the blue planet which has about 70% of the surface covered with water and about 60% of human body consists of water too. Despite many studies water still presents the tremendous scientific challenges which are investigated in each of its phases [52]. The reason for interest arises from unusual properties of water, which could be also called anomalous [53].

Most liquids show the linear increase of the density with decreasing the temperature, while water has the maximum of density at 277 K. High heat capacity (4.18 $J \cdot K^{-1} \cdot g^{-1}$) gives the possibility to transfer enormous amount of energy [54]. High-temperature boiling and melting points exclude water from similar compounds such H_2Se, H_2Te, H_2Po, CH_4, SiH_4, GeH_4. Moreover, higher surface tension value is one more unusual property of water comparing to other mentioned liquids. All these properties could be explained by hydrogen bonding, classical electrostatic interactions between water molecules. Rearrangements of water molecules into chains and rings could strengthen the hydrogen bonding, thus the cooperativity is created. If the water molecules structures are formed from an odd number of water molecules than we have anti cooperativity [54].

H-bond is strong enough to give the structure, but weak enough to give flexibility. Lots of techniques which could be used to investigate how water molecules are arranged, was applied as a tool to investigate the mixtures with water [55]. As the water alone makes so many attractions, in the compound with functional materials it gives both: enormous possibilities to apply new compounds and capabilities to use already known water phenomena to investigate newly synthesized materials.

2.1.1. Ionic liquids

Ionic liquids (ILs) could be considered being one of the most successful breakthroughs creating “smart” materials and multifunctional compositions. ILs possess many attractive features important for the applications in high technologies, including various artificial sensors for new generation electrochemistry, membranes, fuel cells and batteries [56–58].

As ionic liquids are solely composed of ions rather than neutral molecules, varying different combinations of anionic and cationic subsystems, the physical and chemical properties can be tuned. Since the number of such

combinations is practically uncountable, the possibility to control various molecular processes in IL media makes these systems very attractive for fundamental and technological research. Wide liquid-phase temperature range (200 to 730 K), high ionic conductivity over these temperatures, negligible vapor pressure, high electrochemical and thermal stability and significant ability to solubilize organic, inorganic or polymeric materials are mainly caused by dipolar, electron pair donor-acceptor, Coulombic interactions and hydrogen bond formation. These properties empower possibilities to use ionic liquids as functionalized materials which engage researchers for theoretical and experimental studies [22–25].

Ionic liquids and numerous mixtures containing ILs, especially with water as one of the components, fall into the class of the systems earlier called "complex fluids" [57], which nowadays are so-called "functional materials" [59]. The most important properties of ILs are defined by the presence of a mesoscopic length scale structures (H-bond networks, micelle-like, and bi-continuous morphologies) [20,26]. Furthermore, numerous works on the IL systems revealed the presence of nanoscale organization effects and the appearance of micro-heterogeneous phases [31,56,60]. Vibrational and other spectroscopies are usually used to identify the differences between miscellaneous ionic liquid phases. Transitions between various phases formed in long chain ionic liquid and water mixtures were not yet deeply investigated under the light of vibrational spectroscopy. Summarizing, ionic liquids could be called structured solvents, from supramolecular to mesoscopic length scales.

Hydrogen bonding with cooperativity and anti cooperativity effects plays a crucial role in miscellaneous phases formation [61]. Many different types of H-bond may limit cooperative effects which are maximized when the H-bonds are all of the same type [62]. Strong and directional H-bonds formed between cations and anions destroy the charge symmetry and thus can fluidize ionic liquids. Asymmetric H-bonds introduce "defects" into the Coulomb network of ILs and intensifies the dynamics of the cations and anions, resulting a significant decrease in melting points and viscosity [63]. Hence, some important macroscopic properties of ILs can be tuned by adjusting the ratio between Coulomb- and the H-bond contributions, even the latter being energetically less significant. Vibrational spectroscopy experiments revealed the possibility to capture the variation of strong, localized, and directional hydrogen bonds in ionic liquids [63,64].

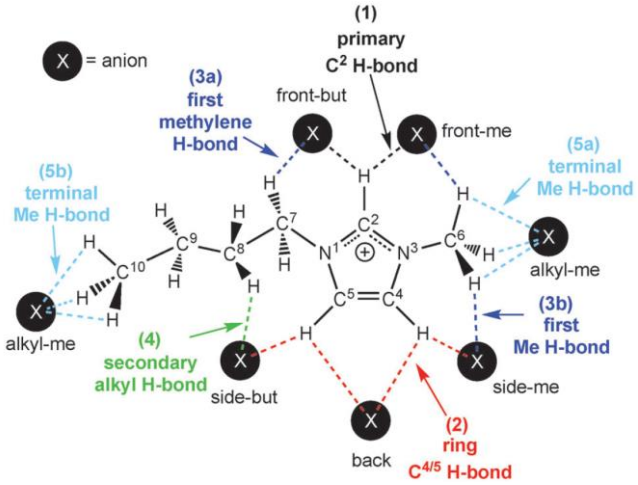

Figure 2.1.1. Imidazolium cation and possible association sites for the anion (black circles marked "X"). Different types of H-bond are color coded, numbered, and named in the picture. Primary H-Bond (1), (2), (3a), (3b). Secondary H-bond (4) and terminal-methyl H-bond (5a), (5b). Adapted from Ref. [62]. Different types of H-bond were depicted in Figure 2.1.1. and listed in Table 2.1.1.

Table 2.1.1. Different types of possible H-bond association sites with cation

H-bond in figure 2.1.1.	H-bond type	Description
(1)	Primary	with C(2)-H of the ring (black)
(2)	Primary	with C(4)-H and C(5)-H at the rear of the ring (red)
(3a)	Primary	with first methylene (3a) or with first methyl (3b) with the C(7)-H or C(6)-H groups on the alkyl chains (dark blue)
(3b)	Primary	
(4)	Secondary	with the later CH_2 groups on the alkyl chain (green)
(5a)	Terminal-methyl	with the terminal methyl groups on the alkyl chains C(6)-H (5a) or C(10)-H (5b) (light blue)
(5b)	Terminal-methyl	

Some of ILs can be conceptualized as ionic pair systems $A^{-}\cdots H^{+}B$ created by very "deep" proton transfer from the acid (A) to the defined base (B). These

ionic pairs are kind of “inverted” in respect of the traditional ones that appear in numerous H-bond systems with proton transfer. Such ILs structures can be thought as the “ground state” that can be disturbed by various external stimuli (temperature, media effects, etc.) reversing the proton migration toward the anion and maybe even culminating with the return of the system to the neutral H bond $A^{-}H\cdots B$. If this succeeded, the novel sort of phase transitions could be expected that would create the hybrid state of matter with the properties that occupy an intermediate place between ionic and nonionic liquids. IL ion-pairs, which can take on a wide range of structures and energy, can be observed by the research of conformational equilibrium [65–67]. Imidazolium ring based ILs exhibit “top” and “bottom” conformers where the anion sits above or below the imidazolium ring or C(2)–H bond. Smaller anions tend to position above or below the C(2)–H bond, while larger anions position exceptionally over the cations ring [62]. The possibility of forming hydrogen bonds can divide the imidazolium-based cations into hydrophilic (imidazolium “head” group) and hydrophobic (alkyl chain) segments Figures 2.1.1. and 2.1.2. For cations with intermediate alkyl chain length (typically butyl chain), alkyl–alkyl interactions play more dominant role. Differently for cations with long alkyl chains (typically decyl or longer), the π–π stacking of the cation “head” groups is facilitated due to inter-digitation and becomes relevant for liquid crystals formation [68]. The equilibrium of conformations is as stable as the lowest energy of H-bond structures and thus are very important for ILs description. The stability of conformers are also increased by the H-bonding between anion and the alkyl chains [68]. However, the dynamics of conformational equilibrium indicates the alterations of local environment in neat ionic liquids and their mixtures with water. As conformational space was not fully explored for our investigated ILs, the advantage was taken to perform deeper H-bonded network analysis in neat ILs and their aqueous mixtures.

As mentioned earlier, all processes which taking place in ILs on a molecular level are not completely understood. The variety of interactions between anions and cations constitute one of the main challenges in fundamental research [18,19]. Contamination in ionic liquids destroys their valuable properties and the purity of functional materials becomes significant research of “pure” ILs. The presence of water in ILs strongly affects their physical and chemical properties, aggregation, phase behavior and structural changes [69–72]. Even small amount of water can dramatically change the diffusion coefficients [26], polarity [27], viscosity [28] and surface tension [29]. The water can be added deliberately by mixing with ILs or it can present as contaminant from air [19,73]. Depending on the purpose, the number of

studies employed the new strategy emerged mixing ILs with compounds previously used to be impurities [30,31]: e.g. organic compounds [27,28], other ILs [74] and water [31,32].

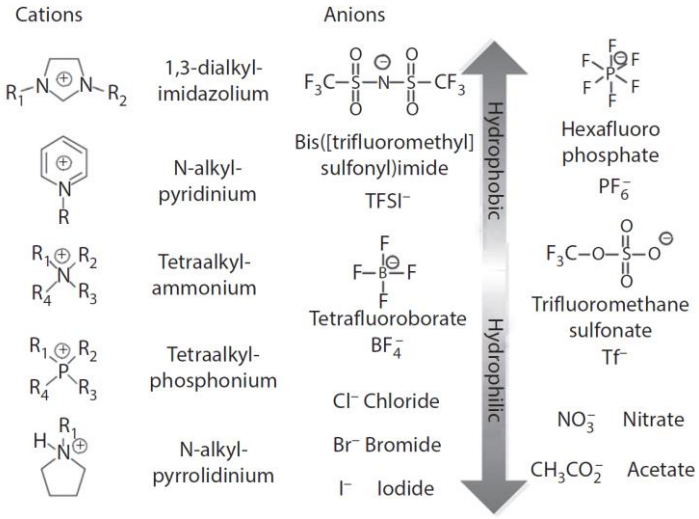

Figure 2.1.2. Examples of cations and anions used in the formation of ILs, together with changes in hydrophilic–hydrophobic properties associated with anion type. Adapted from Ref. [75].

However, better perception of ILs and water interactions, as well as the structure of mixtures at different concentrations of constituents is needed to devise methods for broader ILs application in combination with water.

Both, intramolecular and intermolecular H-bond formation are strongly dependent on the anion hydrophobicity. In Figure 2.1.2. various examples of different cations and anions used to form ILs are depicted, together with changes in hydrophilic and hydrophobic properties associated to anion type. In many of ILs the anions are the conjugate bases of various acids, in certain cases, strong and very strong, as for example, halogenides (Cl^-, Br^-), trifluoroacetate ($CF3COO^-$), triflate ($CF3SO3^-$) and others. With water incorporation into ionic liquids, the increase of ions diffusion coefficient was observed. At the same time the decrease in the mixture viscosity was reported and explained by the electrostatic interactions which arose from ion suppression [31]. The variety of different structures of water and ILs mixtures were reported to be dependent on anion and cation combination and the water concentration too [32–36].

Structure of ILs can be tailored for specific applications. During the experiments with ILs–water mixtures variety well known phenomena in phase behavior and aggregation (micellization) processes were encountered. In mixtures with water some of imidazolium-based room temperature ionic liquids with long alkyl chains (typically octyl or longer [$C_n$mim]X (n=8-18, X-anion) can form various liquid crystalline (LC) ionogel phases [71,76–79]. These phases exist at room temperature over the wide range of water concentration in ILs ($0.05<X_{H2O\_MASS}<0.4$). When the small water content ($0.1<X_{H2O\_MASS}$) added to [C_{10}mim]Cl and [C_{10}mim]Br, water molecules tend to interact with anions, rather than self-aggregate and complexes anion···H–O–H···anion with symmetrical H-bond between anions and water molecules were formed [73]. The formation of such network apparently serves to enhance the segregation of the hydrophilic and hydrophobic segments of the [$C_{10}mim^+$], thereby leading to the regions of confined water and, ultimately, to the onset of gel formation [71]. Further addition of water caused ionic liquid–water system conversion from liquid to the gel phase. Gelation is unlikely raised from two-dimensional alkyl chain packing effect [71]. Various phase formation models and structures of imidazolium-based ILs with long alkyl chains and water were discussed [77,80]. The complex-shaped ^{81}Br NMR signal as well as several new ^{1}H peaks were observed in NMR spectra of these mixtures too [81]. The reported origin of the peaks could be the result of H_2O molecules trapped in inhomogeneous regions of the sample or due to the appearance of non-equivalent water sites in LC ionogel. The exchange between those sites were reported being highly restricted or even frozen. The simultaneous appearance of a smectic liquid-crystalline phase indicated H-bonds formation near hydrophilic ILs cation part called „heads“. The small gap between imidazolium rings is mediated by a channel of water and provides enhanced ordering of the parallel molecular layers [71,82]. Previous NMR, quantum chemistry calculations and vibrational spectroscopy studies claimed that the most pronounced dependence of chemical shift on amount of water was observed for H-bonded C(2)–H···Br bridge proton while the weakest effect was detected for the terminal methyl group, C(16)–H_3 [81,83]. Various H-bond interactions effects made ionogel as material and have attracted considerable attention in the areas of biomaterials, electro-optics and as templates for the preparation of mesoporous materials and ordered thin films [84]. In certain cases, ionogel can be considered to behave as “smart” material, which possess an intrinsic ability to sense and definitely to respond to various external stimuli in a predictable way [80]. The investigation of ionogel also offered the potential to create a periodic array of the nanoparticles [85].

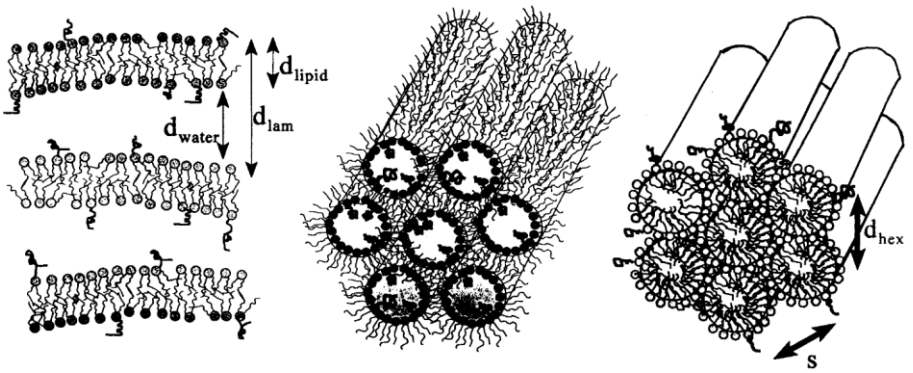

Figure 2.1.3. Schematic illustrating topology of polymer-grafted membrane lipid mesophase: (LEFT) type α-lamellar phase, $L_{\alpha g}$; (MIDDLE) inverted hexagonal phase, H_{11}; (RIGHT) normal hexagonal phase, H_1. Adapted from Ref. [77].

Various ILs carry different properties depending on cation chain length, therefore, their structures with water are differently formed. In case of $[C_{12}mim]Br$ LC phases were determined precisely, being lamellar (L_a) and hexagonal (H_1) [39,80,86]. For the $[C_{10}mim]Br$ and $[C_{10}mim]Cl$, it was identified as highly viscous, nanostructured, lamellar gel phase, called an "ionogel" [71,78,87]. Moreover, depending on the temperature and sample composition, the regions of various coexisting phases were measured on the phase diagram and the model that gels are created by non covalent interactions among the constituent molecules was suggested [80,88]. In Figure 2.1.3. polymer grafted membrane lipid mesophases equivalent to ones formed in ILs and H_2O mixtures were depicted. On the left side alfa lamellar ($L_{\alpha g}$), on the right side hexagonal (H_1) and in the middle, inverted hexagonal (H_{11}) phases schematic illustrations can be found.

Another fascinating water clusterization process called „water pockets" formation in short chain (typically butyl chain) ionic liquid $[C_4mim]NO_3$ and D_2O mixtures recently was observed applying small-angle X-ray scattering (SAXS), small-angle neutron scattering (SANS) and differential scanning calorimetry (DSC) techniques [45–47]. In the $[C_4mim]NO_3$–H_2O system anomalous freezing occurred discretely for a wide range of water concentrations ($0.7<X_{D2O\_MOL}<0.9$). The molecular dynamics (MD) simulations demonstrated water confinement in the 1-octyl-3-methylimidazolium nitrate ($[C_8mim]NO_3$) mixtures with different concentrations of water [22]. Confined water existence in the boundary between the polar and non-polar nanodomains was found and depicted in

Figure 2.1.4. Part 3 and Part 4 and Figure 2.1.5. Another research based on MD simulations identified four concentration ranges in hydrophilic ILs and water systems where four distinct structures were presented: isolated water molecules (X_{H2O_MOL}<0.5); chain-like water aggregates (0.5<X_{H2O_MOL}<0.8); bicontinuous system (earlier mentioned as mesophases) (0.8<X_{H2O_MOL}<0.95); and isolated ions or small ion clusters, respectively (X_{H2O_MOL} > 0.95) [89].

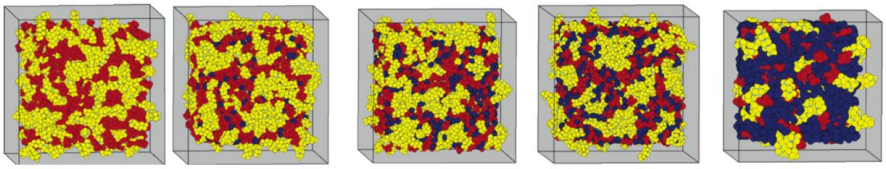

Fig 2.1.4. Snapshots of six selected simulation cells, taken from the MD trajectory data. The polar groups, non polar groups and water are colored red, yellow and dark blue, respectively. (a) Dry IL sample, (c) X_{H2O_MOL}=0.5, (d) X_{H2O_MOL}=0.75, (e) X_{H2O_MOL}=0.8, (f) X_{H2O_MOL}=0.95. Adapted from Ref. [22].

All previously mentioned ILs fall under the well-established category of aprotic ionic liquids (APILs) and together with protic ionic liquids (PILs) are two broad categories used for general classification of ILs. PILs mixtures with different molecular solvents were widely investigated in previous studies. These studies covered the properties of transport and volumetric analysis, heat capacity, viscosity and refractive index, together with water effects to the local structure and phase behavior [90–94]. In the case of PILs, differently to APILs, the anion does not play critical role in interactions, while the main attention is focused on interactions near cation and water. For PILs the polar groups of –NH and hydrophobic anions (i.e. bis(trifluoromethane-sulfonyl)imide) make the reversed scheme of interactions [93] comparing to APILs widely investigated in this work. As depicted in Figure 2.1.1. water molecules have the highest probability to interact with the anions, the cation is less interesting. The applicability of [C_4mim]NO_3 ionic liquid as solvent for proteins [94,95], tool for water removal from the protein surface [96] and advanced lubricant fluid [97] is derived by different capabilities of NO_3^- anion interactions with different materials. Moreover, the evidences for “water pockets“ already were studied on short chain cation IL–D_2O systems based on n,n-diethyl-n-methyl-n-2-methoxyethylammonium tetrafluoroborate and 1-butyl-3-methylimidazolium nitrate [46].

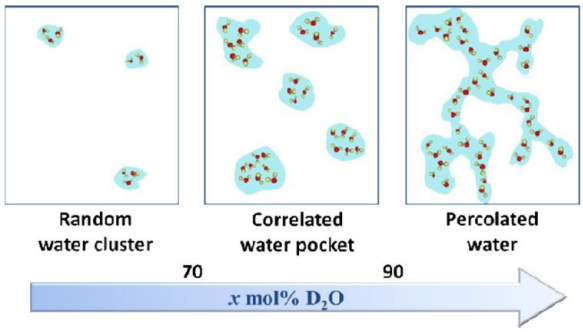

Figure 2.1.5. Schematic illustrations for three different liquid states in the $[C_4mim]NO_3$–H_2O mixtures. Below X_{H2O_MOL}<0.7, isolated water cluster cannot disturb the $[C_4mim]NO_3$ crystallization. Water percolation at water-rich region (0.94<X_{H2O_MOL}) promotes crystal nucleation of ice. Discrete appearance of amorphous (0.7<X_{H2O_MOL}<0.94) could be caused by correlated "water pocket" (0.7< X_{H2O_MOL}<0.9). Adapted from Ref. [47].

H-bonding causes one more intriguing phenomenon involving ILs and D_2O mixtures. The exchange of proton/deuteron (H/D) could determine the possible pathways of isotopic H/D exchange and provide beneficial way to investigate functional materials [98]. H/D exchange reaction and its kinetics could provide extremely valuable information on the picture of H-bond in ILs including the large amplitude proton motion and thus evaluating the chances to provoke the reverse proton migration by proper physically realizable stimuli (Figure 2.1.6.). In the short chain and halogen anion based ILs the H/D exchange reaction rate could sensitively reflect how strongly water is solvated by the small ionic liquid anions via the hydrogen bonding [99]**.** By The cation−anion interactions and various aspects of H/D exchange reactions in some imidazolium-based ILs was studied by means of X-ray photoelectron, NMR and Raman spectroscopy techniques [33,99–102].

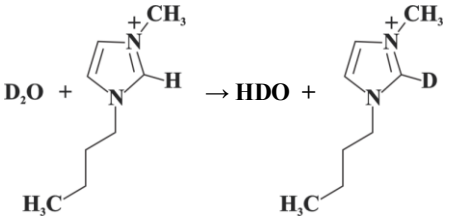

Figure 2.1.6. H/D exchange reaction scheme for $[C_4mim]^+$ cation.

Several significant findings were listed. The charge transfer was found being not related to H-bonding, however, both H-bonding and charge transfer were seen to be enhanced for small and more strongly coordinating anions. Moreover, the relation between the slowdown of rotational dynamics and the H/D exchange deactivation was deduced. Furthermore, the complex dependency of the H/D exchange rates on ILs concentration in water was observed. At very low ILs concentration in D_2O, anomalous dynamics of ions were revealed. Finally, the conformational changes in ILs were induced by H/D exchange which was affected by critical aggregation of ILs [99–101]. The H/D exchange process was not yet studied in some of investigated ILs and the impact of anions or cation chain length is obscure.

2.1.2. Calcium phosphates

Another functional material where H-bonding plays significant role is calcium hydroxyapatites (Ca10(PO4)6(OH)2) (CaHAp). CaHAps are the ones of calcium phosphate-based materials which makes up most of the inorganic components for human bones and teeth. Likewise, CaHAps are widely used in implantology, orthopedic and periodontal surgery [8–11]. The specific chemical, structural and morphological properties of CaHAps are highly sensitive to the changes in chemical composition and processing conditions [12–14]. Calcium hydroxyapatite could be called the most stable form of calcium phosphates and it was used to study the properties of antiresorptive agents for the prevention and treatment of bone diseases [7]. Although CaHAps were used as an artificial bone substitute in clinics. It was also reported that cell attachment, proliferation and differentiation behavior are regulated on the crystallinity [103–107]. Many applications of CaHAp's are based on the osteoinductivity – the ability to absorb guest implants, which depends on the organization of pores, cavities and surfaces [15–17].

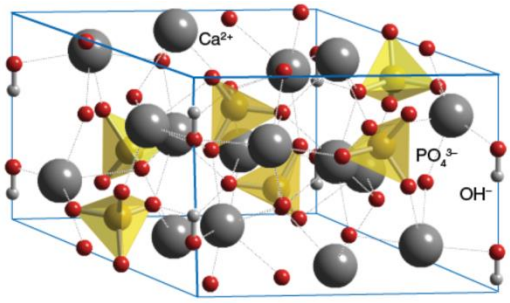

Figure 2.1.7. Hydroxyapatite structure. Adapted from Ref. [108].

Stoichiometric OH groups are not only ones founded in CaHAps. Adsorbed water and surface modes could be found in these materials too. Human bone apatite was found being not highly crystalline hydroxyapatite. From the experiments with hydrated bone samples the diminish of osteoinductivity during the 6 months period were registered when the samples were stored at ambient conditions [109]. To detect the impurities in newly synthesized CaHAp samples handy tools like vibrational or NMR spectroscopy are usually applied [44,110,111].

2.2. Spectroscopic methods used to characterize functional materials

Many spectroscopic techniques were sooner or later applied for the investigation of ionic liquids and calcium hydroxyapatites. Depending on the aim of research various techniques such as DFT, DSC, EDX, FTIR, Raman, NMR, PCA, SANS, SAXS, SEM and 2DCOS were used. The combination of theoretical calculations together with vibrational spectroscopy and mathematical spectra processing methods revealed the fast and reliable way to obtain the scientific information about functional materials.

2.2.1. Theoretical investigation

Functional materials have different possible ways to interact with environment and many ways to damage their structure by impurities. Cation-anion interactions present in the ionic liquids are of great interest in diverse fields such as preparation of nanoparticles, intramolecular interactions and charge transfer between anion and cation. Vibrational spectroscopy is useful to identify various species in composite materials and systems, which could be combined of different ionic liquids. The theoretical calculations are of great aid when structures of ionic liquids are unknown, because the specific vibrational bands are not assigned to molecular vibrations. Recently structural and vibrational characterizations on short chain based ILs $[C_4mim]NO_3$ and $[C_4mim]OTf$ were performed combining the experimental Raman data with density functional theory (DFT) calculations [112,113]. Hence, to achieve the complete vibrational assignments it is necessary to perform a deep structural investigation in order to know the most stable structures. Besides, to know the coordination mode of anion which plays an important role in the stability of the ionic liquid structure.

As mentioned in the previous section about the H-bond, one of the first calculation tasks for ILs is to find the most stable cation conformers. Moreover, the atomic charges and molecular electrostatic potentials as well as stabilization energies could be calculated. Furthermore, the bond orders and topological properties should be computed by using Natural Bond Orbital (NBO) and Atoms In Molecules (AIM) calculations and the hybrid B3LYP level of theory with different basis sets. And finally, the force fields, force constants and complete vibrational assignments could be calculated using internal coordinates and the scaled quantum mechanical force field approach.

Another way of theoretical modeling would be to calculate the dynamics of materials under the external change, e.g. dilution with water. In this case the possibility to form different intermolecular or intramolecular structures

should be counted. Huge variety of H-bond should be considered as well as the number of molecules, which interreact between each other, to have the proper results giving the easier experimental data interpretation. The highest value of theoretical models is provided only when theory is applied along with experimental data and *vice versa*.

2.2.2. Vibrational spectroscopy

The vibrational spectroscopy (FTIR, Raman) is particularly powerful method studying the states of water in the IL–water compositions [24,72,73,114]. Perhaps the most information could be found from the vibrational modes that are coupled with H-bonding vibrations of water molecules. Anion and cation vibrations are useful to study the interactions between ILs and other materials and at the same time pointing to the direct IL place where those interactions tend to happen. Unfortunately, in the case of the broad vibrational contours when the distances between the maxima of the sub-bands are much smaller then their widths, the additional methods for the mathematical spectra processing should be used. The separation of such strongly overlapped bands can not be correctly done using the standard treatments, such as the second derivative or Fourier deconvolution [115]. The analysis of vibrational spectra is based on the monitoring of various Raman and IR band parameters. The band shift, the ratio of integral intensities of couple vibrational bands and the change in bands FWHM usually are utilized analyzing the functional materials. The conformational equilibrium and orientation of $[C_4mim]^+$ cation with respect to the counter anion was investigated from Raman spectra [116].

For the CaPs, vibrational spectroscopy is also an effective tool to estimate the degree of crystallinity, content of doped ions, bulk vs. surface effects [103–107].

2.2.3. Mathematical processing of spectra

As well as vibrational spectroscopy and theoretical computational methods, mathematical processing of spectra provide supplementary data which can be used as the material to prove, or deny hypothesis raised from experimental data. The principal components analysis (PCA) and two-dimensional correlation (2DCOS) analysis were the main methods used in this work. The PCA [115,117,118] and 2DCOS [119,120], can give considerable enhancement in the resolution and thus, they can be effective tools solving this problem. It has been already demonstrated on NIR spectra of water [115,117] and on FTIR spectra of IL–water and IL–alcohol systems [121].

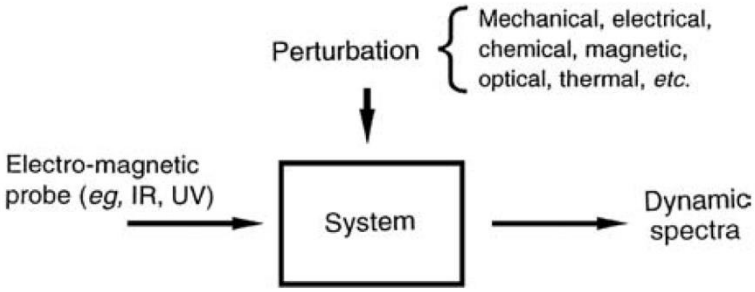

Figure 2.2.1. General scheme to obtain perturbation-based (solvent concentration in mixture) 2D correlation spectra. Adapted from Ref. [122].

The dynamic spectra for the 2D correlation analysis are constructed from the spectral intensity variation upon external perturbation [119,120] (Fig 2.2.1). Many reasonable measures of a physical quantity, such as temperature, mechanical deformation, or concentration could be used as an external stimulus. Water concentration (X_{H2O_MOL}) in IL–H_2O mixture can be used as the external variable continuous perturbation of the Raman spectra. The Raman spectra (raw spectra, or spectrum vectors) $I(\omega, X_J)$, J=1,..., M of IL–H_2O mixtures was measured due to water content increase in the mixture. The total numbers of spectra are noted by "M". The spectra are normalized to the Raman band which has the highest intensity and constant wavenumber during measurements. The dynamic spectra $I_D(\omega, X_J)$ are constructed from the spectrum vectors $I(\omega, X_J)$ subtracting the reference spectrum which is the average of all registered spectra, although other forms may be chosen [120]. This selection is somewhat arbitrary. However, the results of 2D correlation analysis could be weakly influenced by the choice of the reference. Therefore, the zero-Raman intensity (after baseline correction) could be used as the reference as well. The experimental data using the 2DCOS and the PCA are processed and realized in following steps. The data matrix **D** are composed placing the spectra $I_D(\omega, X_J)$ ($I(\omega, X_J)$) in M rows. The corresponding covariance matrix are obtained when multiplied **D** by its transpose $\mathbf{D}^T$:

$$\mathbf{Z}=\mathbf{D}^T\mathbf{D}. \quad (1)$$

In this case, i.e. the so-called variable-variable approach [117], the covariance matrix was coincident with the synchronous correlation spectrum used in the traditional Noda formalism of 2DCOS [120]: $\Phi \sim \mathbf{Z}$, whereas the asynchronous correlation spectrum Ψ was calculated as

$$\Psi \sim \mathbf{D}^T\mathbf{H}\mathbf{D}, \quad (2)$$

where **H** is the Hilbert transform matrix:

$$H_{jk} = \begin{cases} 0 & j = k \\ \frac{1}{\pi(k-j)} & j \neq k \end{cases}, \quad (3)$$

In the next steps the loads ($\mathbf{p_i}$) vectors are obtained when solved

$$\mathbf{Zp_i} = \lambda_i \boldsymbol{p_i}, \quad (4)$$

where λ_i is the eigenvalue associated with the eigenvector $\boldsymbol{p_i}$ [118]. The score vectors ($\boldsymbol{t_i}$) were calculated as

$$\boldsymbol{t_i} = \mathbf{D}\boldsymbol{p_i}. \quad (5)$$

The number of the statistically significant principal components can be evaluated using the argument of the physical changes vs. nondeterministic variation proposed in [115]. In the analysis of loadings plots of principal components (PCs) should be noted that loadings contain information on how the variables (Raman intensity) relate to each other. Thus, Raman spectra intensities stemmed from molecules vibrations responding in specific way on applied perturbation should be related by loadings. Loadings plotted against frequencies have spectrum fashion but do not present properties of real spectrum, and therefore are called as abstract spectra. Nevertheless, loadings can be very beneficial in interpretation of puzzling spectral variations and in detection of minute absorption changes hardly detected in raw spectra.

As well-known from the 2DCOS theory the *cross-peaks* are the consequence of simultaneous changes in different spectral regions [123]. But changes in *cross-peaks* could be also used to identify the spectrum band overlapping (Figure 2.2.2) or shifting in position (Figure 2.2.3). The simultaneous shift of Raman bands and intensity change was simulated for 2D spectra too (Figure 2.2.4) as well as line broadening (Figure 2.2.4). These modeled examples were used during the studies of our obtained Raman spectral data.

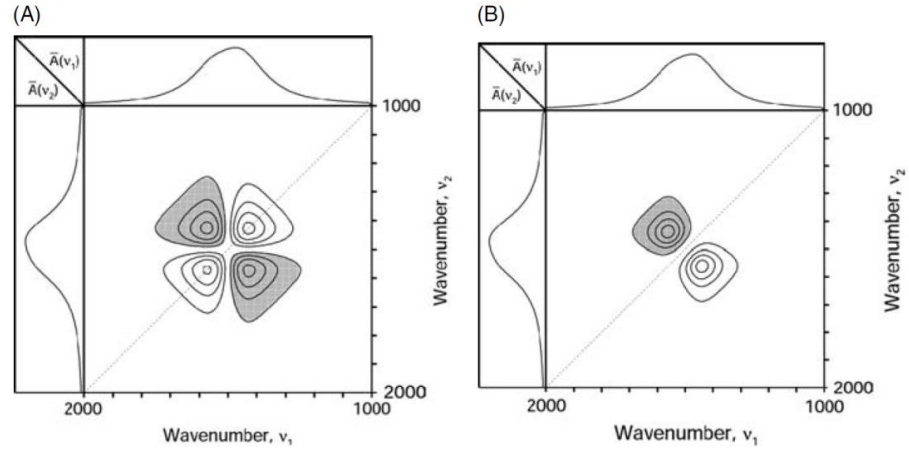

Figure 2.2.2. Synchronous (A) and asynchronous (B) 2D correlation spectrum showing the two overlapped bands changing intensity in opposite directions. Adapted from Ref. [123].

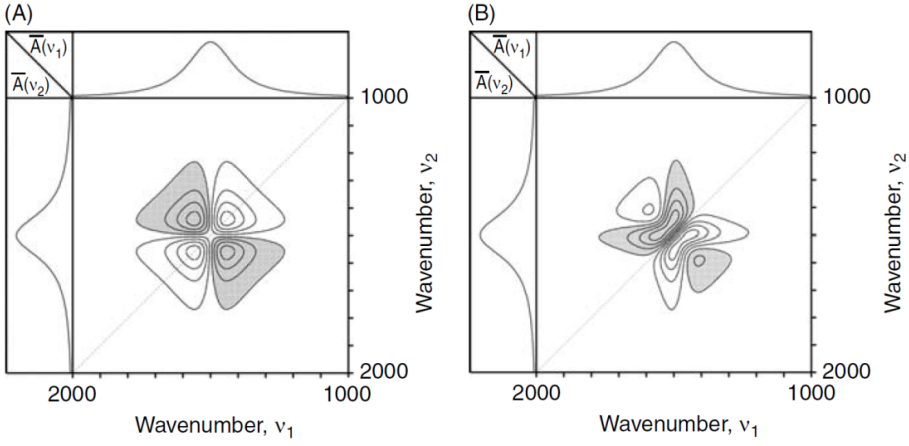

Figure 2.2.3. Synchronous (A) and asynchronous (B) 2D correlation spectrum showing the result of single band shifting in position from a lower to a higher wavenumbers. Adapted from Ref. [123].

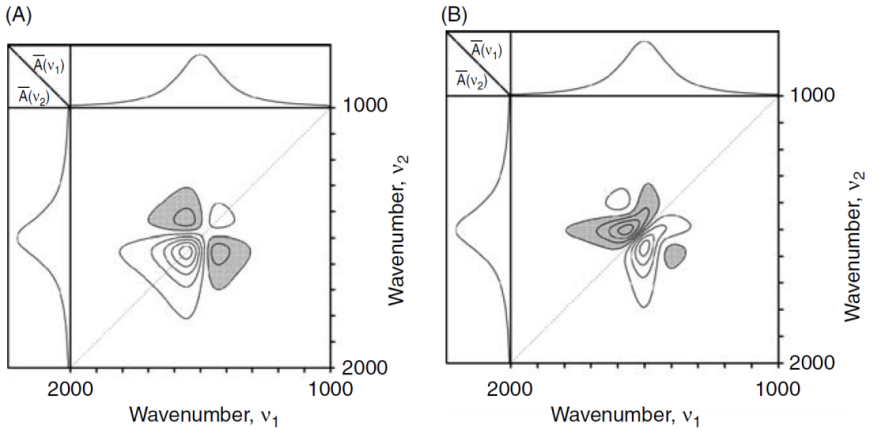

Figure 2.2.4. Synchronous (A) and asynchronous (B) 2D correlation spectrum showing the results of a single band simultaneously shifting in position from a lower to a higher wavenumbers and the increase in intensity. Adapted from Ref. [123].

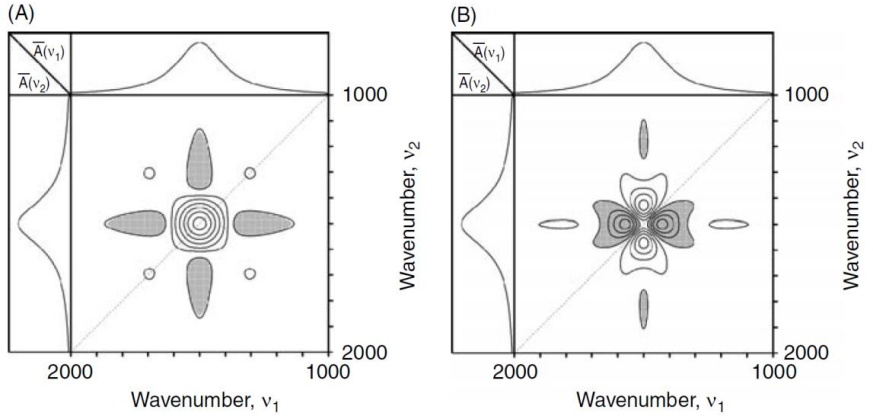

Figure 2.2.5. Synchronous (A) and asynchronous (B) 2D correlation spectrum showing the result of single band line broadening. Adapted from Ref. [123].

3. EXPERIMENTAL RESULTS

3.1. Materials

For easier classification purposes, innovative functional materials studied in this work were divided into three groups: long chain ionic liquids, short chain ionic liquids and calcium hydroxyapatites. Materials in both ionic liquid groups were ordered from *Merck KgaA Darmstadt, Sigma-Aldrich, Inc. And Ionic Liquids Technologies GmbH* (98%). The structures, as well as the atom numbering, of long chain ILs (based on 1-decyl-3-methyl-imidazolium cation $[C_{10}mim]^-$) and short chain ILs (based on 1-butyl-3-methyl-imidazolium cation $[C_4mim]^-$), are depicted in Figure 3.1.1.

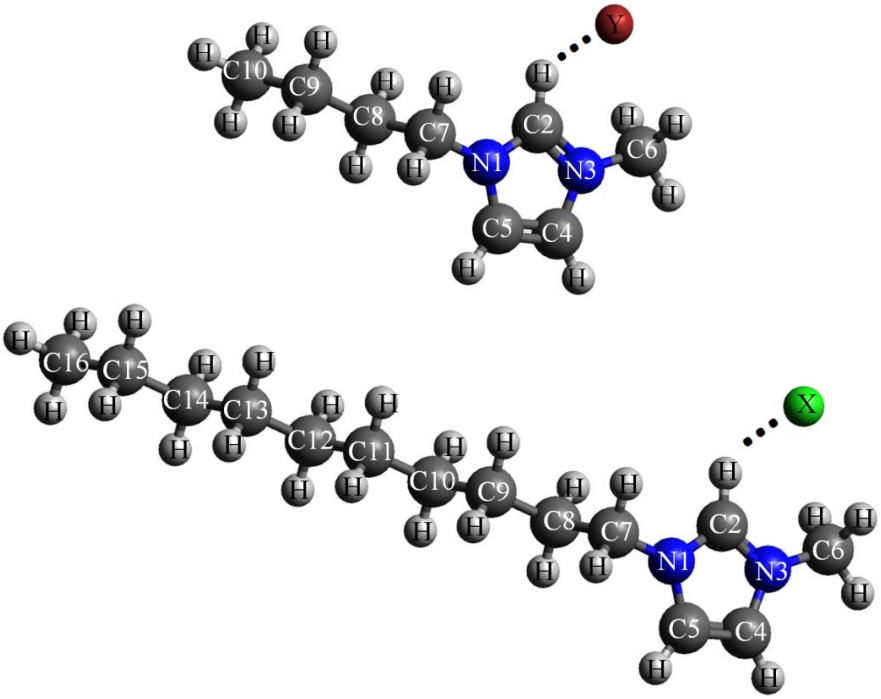

Figure 3.1.1. The structure and the atom numbering of the ionic liquids investigated in this work. Lower part of the figure depicts $[C_{10}mim]X$, where anion X=Cl, Br. Upper part represents $[C_4mim]Y$, where anion Y=I, Br, Cl, NO_3, BF_4, OTf (optimized by DFT at B3LYP/6-31++G**, in vacuo [81,113]).

The anions were differently selected for both groups of ILs. To study long alkyl chain effects to the possible structures in ILs and water mixtures only spherical chloride and bromide anions were chosen for $[C_{10}mim]^+$ cation based ILs. To reveal the H-bond effects for the $[C_4mim]^+$ cation based ILs, iodide, bromide, chloride, tetrafluoroborate, nitrate and *trifluoromethanesulfonate*

anions with different physical properties were chosen. Physicochemical characteristics of investigated ionic liquids are listed in Table 3.1.1.

Table 3.1.1. Physicochemical characteristics of investigated ionic liquids

Reference	Ionic liquid	Chemical formula	Molar mass, $g \cdot mol^{-1}$	Melting point, K	Decomposition temp, K	Density $g \cdot cm^{-3}$ (293 K)	Viscosity $mm^2 \cdot s^{-1}$ (293 K)
[124]	[C_{10}mim]Br	$C_{14}H_{27}BrN_2$	303.3	347	583	1.13	7893
[125]	[C_{10}mim]Cl	$C_{14}H_{27}ClN_2$	258.8	311	468	0.99	8570
[126]	[C_4mim]I	$C_8H_{15}IN_2$	266.1	203	596	1.49	1110
[126], [127]	[C_4mim]Br	$C_8H_{15}BrN_2$	219.1	351	546	1.29	310
[128], [129]	[C_4mim]Cl	$C_8H_{15}ClN_2$	174.6	347	537	1.05	671
[130], [131]	[C_4mim]NO_3	$C_8H_{15}BrN_2$	201.2	323	373	1.39	266
[132]	[C_4mim]BF_4	$C_8H_{15}BF_4N_2$	226.0	<293	372	1.31	104
Iolitec	[C_4mim]OTf	$C_9H_{15}F_3N_2O_3S$	288.3	289	523	1.30	80
	Water	H_2O	18	273	373	1.00	1

There are two main methods to remove water and organic solvents from ILs after synthesis: (1) sweeping solvents with nitrogen, (2) heating ILs under vacuum. Nitrogen usage was tested, but not chosen because of high viscosity of the samples. The traditional method to heat ILs under vacuum was used in this work. The reduction of water commonly needs 12 to 48 hours under pressures of 133 to 665 Pa heating the sample at 333 to 393 K [133]. As well as benefits, this method for ILs purification has some disadvantages such as long duration and possible decomposition of ILs. To avoid decomposition samples were dried under vacuum at 353K for 24 hours using sample vacuuming system built in the lab (Figure 3.1.2.). Decomposition temperature of samples was not reached in the ceramic oven (part 4) because it was maintained using temperature controller unit (±1K) (part 1) (Build in Vilnius University) and thermocouple (part 3) (*copper*-constantan). During the water removal process cuvette with sample was connected to a rotational pump (part 2) (*ILMVAC GmbH*, Rotary Vane Pump PK 2 DC, 10^{-2} mbar) via tube and placed into ceramic oven (part 4) which was heated by wire (part 5). Water (H_2O) used in experiments was freshly distilled while heavy water (D_2O) was

ordered from *Sigma-Aldrich* (≥99.9 atom % D). The samples of IL–H_2O and IL–D_2O mixtures were prepared by weighting (±0.1 mg) the components. Homogeneously mixed samples were left for 30 minutes at 298 K to reach equilibrium before measurements. In the cases when the extremely viscous gel was formed in long-chain ILs– H_2O mixtures, samples were left at 298 K for several hours.

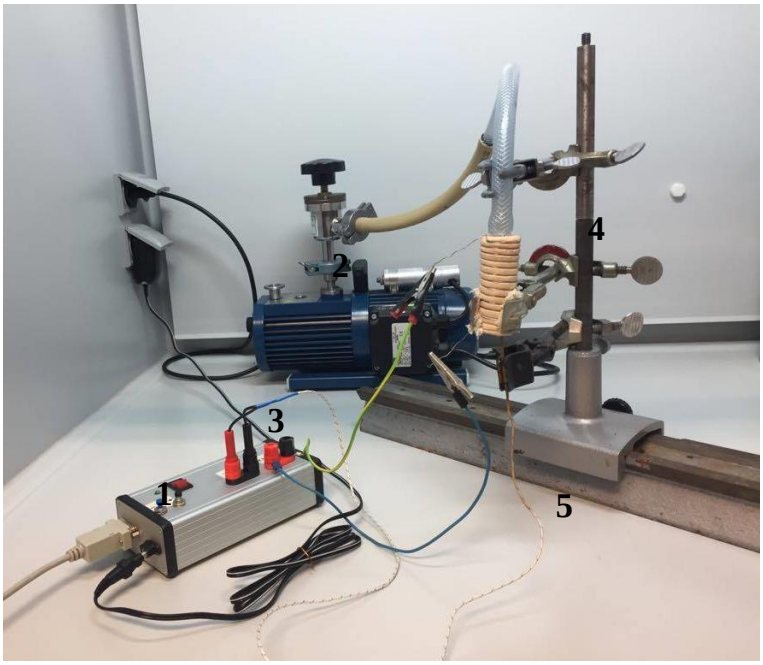

Figure 3.1.2. The system for sample vacuuming. 1 – temperature controller unit, 2 – *ATB* vacuum pump, 3 – thermocouple, 4 – ceramic oven, 5 – heating wire.

The group of calcium hydroxyapatites $Ca_{10}(PO_4)_6(OH)_2$ (CaHAp) samples were prepared by Prof. Habil. Dr. Aivaras Kareiva group in Vilnius University, Chemistry and Geosciences faculty, Department of Inorganic Chemistry. In the aqueous sol-gel synthesis route (more details in reference [50]), calcium acetate monohydrate, $Ca(CH_3COO)_2 \cdot H_2O$ and ammonium-hydrogen phosphate, $(NH_4)_2HPO_4$, were selected as Ca and P sources, respectively, in Ca/P molar ratio 1.67. To prepare nanostructured CaHAps the different complexing agents tartaric acid (TA) ($C_4H_6O_6$), 1,2-ethylendiaminetetraacetic acid (EDTA) ($C_{10}N_2H_{16}O_8$), glycerol (GL) ($C_3H_8O_3$) and ethylene glycol (EG) ($C_2H_6O_2$) were used. Depending on the complexing agent used in the aqueous synthesis route, the prepared calcium hydroxyapatites will be further called TA-CaHAp, EDTA-CaHAp, GL-CaHAp and EG-CaHap. For comparison, the commercially available

nanostructured CaHAp (CA-CaHAp) from *Sigma Aldrich* (99.999%, synthetic from metal basis) was also investigated. The last CaHAp, prepared by the same chemist group, was the calcium phosphate containing amorphous phase (ACP). The synthesized compound will be named ACP-GL-CaHAp because the glycerol (GL) ($C_3H_8O_3$) as a complexing agent was used in synthesis route (more details in reference [134]). Above mentioned, CaP based materials were characterized by scanning electron microscopy (SEM) and energy-dispersive X-ray analysis (EDX) using a *Helios NanoLab 650* scanning electron microscope coupled with energy-dispersive X-ray spectrometry system [50]. The corresponding EM micrographs and XRD patterns could be found in the appendix.

3.2. Experimental equipment and setup

All Raman and IR spectra measurements were performed in Vilnius University laboratories. Various Raman spectrometers with different excitation wavelengths were used for experiments. Ability to adjust the excitation wavelength let us precisely investigate both "Fingerprint" (100-1500 cm^{-1}) and "H-stretch" (2500-3900) cm^{-1} Raman spectral regions. All spectrometers used for experiments and their setups are listed in the Table 3.2.1.

Bruker MultiRAM FT-Raman was the main Raman spectrometer for routine ILs–H_2O mixtures and differently synthesized CaHAps measuremetns. The focus of laser beam was controlled by motorized xyz-sample stage. The signal was created using the high-sensitivity liquid nitrogen cooled germanium and InGaAs detectors. The 1064 nm wavelength beam of the pulsed Nd:YAG laser (500 mW) and the 785 nm wavelength beam of the Si diode (300 mW) as the excitation sources using the 180° scattering geometry and 3mm aperture was employed for experiments. Seeking to avoid thermal and decomposition effects, before experiments, all samples were measured using several laser power values (1 mW, 5 mW, 10 mW, 50 mW, 100 mW, 200 mW, 300 mW, 400 mW, 500 mW). The resolution of the spectrometer was set to the 2 cm^{-1}. Average of 400 Raman spectra was recorded to get better signal to noise ratio at spectral range 70-4000 cm^{-1}. All experiments we repeated at least two in some cases three and four times. Resonance Raman scattering was not registered during our experiments. To avoid the background from cuvette glass, samples were prepared and measured in silica cells. Different laser excitation was used for the research of OH and OD vibrations. The Raman spectra of neat ionic liquids were obtained with low background level, which showed that no local sample heating effects

occurred during experiments. Relatively low background and good signal to noise ratio of Raman spectra let us obtain both qualitative and quantitative information only with minimal normalization and linear baseline subtraction functions during spectra processing.

Table 3.2.1. Characteristics of Raman spectrometers

Spectrometer	Excitation parameters			Signal detector	Raman scattering geometry
	Source	Wavelenght, nm	Power, mW		
Bruker MultiRAM FT-Raman	Nd:YAG	1064	500	Germanium	180º
	Si diode	785	300	InGaAs	180º
Renishaw Raman spectrometer / microscope	DPSS laser	532	87	CCD	180º
	He-Ne	633	15	CCD	180º
	LED	785	161	CCD	180º
DFS-12	Ar^+ ion	514	200	FEU-79	90º
	MGL-H	532	1000	FEU-79	90º
RamanFlex 400 *PerkinElmer* Inc.	Si diode	785	30	CCD	180º

The FT-Raman spectrometer control and experimental data digital processing were performed using the *OPUS 7.0* and the *Microcal Origin 8*.0 software program packages. Principal component analysis (PCA) and 2D Raman correlation analysis (2DCOS) was carried out using the *MathCAD 14* package. The program for mathematical spectral processing was written in the Laboratory of Raman spectroscopy at Vilnius University.

Other spectrometers were used for to obtain Raman spectra at different temperatures and polarizations. *Renishaw* Raman spectrometer was used for low temperature measurements and polarized spectra measurements. Mostly spectra were registered with setup 532 nm, G1800, lens 50xLWD, 20 s, 100-4000 cm^{-1}, 10% of power (5.5 mW at sample). Raman frequencies were calibrated using the polystyrene standard (ASTM E 1840) spectrum. For measurements with Raman microscope it is essential to have calculated laser power near sample, otherwise heating or photo decomposition could occur. If local heating effects appear for the liquid samples during Raman experiments,

they could be reduced not only by changing the power of excitation source, but also by using large cylindrical cells [135].

Cooling rate of 3 K/min was used for the measurements of $[C_4mim]NO_3$–D_2O at low temperatures. $[C_4mim]NO_3$ Raman bands at low 153 K was not investigated, only D_2O bands was analyzed. Crystallization of the confined water pocket was not induced even the outer IL was crystallized [136].

Primary Raman spectra for long chain based ILs investigation were recorded using a DFS-12 double-grating spectrometer with a slit width of 0.08 mm. This value of the slit width was found to be optimal and let us obtain good signal to noise ratio of Raman spectra. Namely, a recording of the weakest Raman bands was still possible at this setting. On the other hand, investigated OH bands are very broad (FWHM 50-150 cm^{-1}) and the instrumental broadening of the observed Raman band width could be neglected. The excitation source was an argon-ion laser (*Stabilite*, *SpectraPhysics*) operating at 514.5 nm (120 mW). All measurements were carried out at the 90^o scattering geometry. Raman frequencies was calibrated using real-time calibration with a neon emission line. The detection part of the instrument consists of photomultiplier and a photon-counting system on line with a standard computer.

Phase transformations, composition and structural changes in the polycrystalline samples were studied by Fourier Transform Infrared spectroscopy (FTIR spectroscopy). Measurements were performed at 298 K on a *Bruker* Vertex 70 spectrometer. ACP-GL-CaHAp and nano-structured CaHAps (synthesized and commercially available) (each in amount of ca 2 mg) were mixed in the ratio of 1:100 with KBr powder and pressed into a pellet using 10 tons pressing of a manually operated *Specac* hydraulic press. FTIR transmission measurements were acquired with 2 cm^{-1} spectral resolution using a globar light source and liquid nitrogen cooled mercury cadmium telluride (MCT) detector. Total 128 interferograms were averaged and transformed into the spectrum applying the *Blackman–Harris* 3-term apodization function and the *zero*-filling factor of 2. All pellet measurements were performed 3 to 5 times with aperture 2mm, rotating the sample pellets around the central axis.

3.3. Conformational equilibrium and dynamic processes in ionic liquid–water mixtures

A variety of molecular conformations due to external perturbations is the key to understand the stability of pure ionic liquids and IL–water mixtures. Molecular orientational order, which depends on the conformational equilibrium, directly contributes to the molecular packing effects. Studies of the conformational equilibrium in ILs are useful to clarify the relationship between the molecular conformations and the phase transition behavior in ILs [137,138]. The formation of molecular structures in the ILs with different alkyl chain length cations and distinct types (spherical, halogen) anions will be discussed in this section when varying water concentration in the mixtures of IL–water.

3.3.1. Conformational equilibrium in neat ionic liquids and their aqueous mixtures

Prior to the conformational equilibrium investigation in the IL–water mixtures, the structural and vibrational characterizations for the 1-butyl-3-methylimidazolium trifluoromethanesulfonate ([C_4mim]OTf) and 1-butyl-3-methylimidazolium nitrate ([C_4mim]NO_3) ionic liquids were performed combining the experimental Raman spectroscopy and density functional theory (DFT) calculations based on the hybrid B3LYP/6-311++G** level of theory [112,139]. The necessity to have these calculations raised because no Raman spectral band assignments were found in the literature for [C_4mim]OTf and [C_4mim]NO_3. Moreover, anion effect for [C_4mim]OTf conformational equilibrium was not investigated before.

The $[OTf]^-$ anion is linked to $[C_4mim]^+$ cation by a bidentate coordination by means of two different S–O···H hydrogen bonds. Strong increase in the dipole moment value was observed when the $[OTf]^-$ anion was incorporated to $[C_4mim]^+$ cation. NBO and AIM calculations suggested high stability of [C_4mim]OTf and it was evidenced by the high dipole moment value, three intramolecular H-bonds and two halogen-bonds interactions [112]. For the proposed structures, very good correlations between the predicted IR and Raman spectra as well as experimentally obtained spectra were observed. The high stability of ionic liquid as supported by NBO, AIM and bond orders calculations [112]. The different Mulliken charges calculated for the O atoms that forming the H-bonds support the asymmetric bidentate coordination of $[OTf]^-$ anion with the $[C_4mim]^+$ cation. Comparing with [C_4mim]NO_3 ionic liquid, the $[OTf]^-$ anion increases the reactivity for [C_4mim]OTf. In addition,

the $[OTf]^-$ anion drastically reduced the electrophilicity and nucleophilicity indexes of cation evidencing the strong influence of anion on the properties of cation. The vibrational analysis has revealed shifting towards lower wavenumbers due probability for the asymmetry of S=O···H bonds. The complete vibrational assignments were performed for $[C_4mim]OTf$ and $[C_4mim]NO_3$ IL's as well as the harmonic scaled force constants were reported at the same level of theory.

Conformational equilibrium of the $[C_4mim]^+$ cation was investigated monitoring the combination of imidazolium ring deformation and the CH_2 rocking bands [140]. Two Raman bands of different neat ionic liquids were many times investigated and reported as *gauche-trans (gauche)* at lower frequency (601 cm^{-1}) and *trans-trans (trans)* (624 cm^{-1}) conformers.

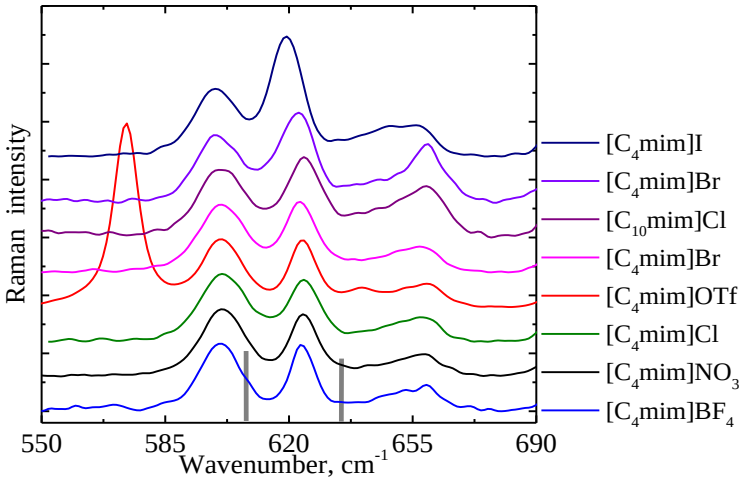

Figure 3.3.1. Raman spectra of neat $[C_4mim]OTf$ (red) and $[C_4mim]NO_3$ (black) ionic liquids in conformational spectral region between 540 and 680 cm^{-1} [141]. Grey vertical bars depict the DFT calculations result for Raman bands assigned to *gauche* and *trans* conformers vibrations. For comparison other short chain ILs spectra at the same region were depicted.

The integral intensity ratio between the Raman band at 601 cm^{-1} and the Raman band at 624 cm^{-1} was proportional to the *gauche/trans* population ratio (I_{gauche}/I_{trans}) in ionic liquid. In Figure 3.3.1. Raman spectra of pure IL $[C_4mim]OTf$ (red) and $[C_4mim]NO_3$ (black) in the 540-680 cm^{-1} spectral region are depicted together with other $[C_4mim]^+$ anion based ILs investigated in these thesis. The positions and intensities of the observed Raman bands well correlated with the relevant parameters of two $[C_4mim]^+$ conformers calculated by DFT. Calculated Raman bands depicted by grey bars in Figure

3.3.1. where the at ~ 609 cm^{-1} and ~ 634 cm^{-1} indicated the *gauche* and *trans* conformers by the rotations around C(7)–C(8) and C(8)–C(9) bonds [112,139]. The presence of both bands indicated that ILs based on $[C_4mim]^+$ cation exist as a mixed state of cation conformers regardless of the anion type. According to the integral intensity ratio of two bands in Figure 3.3.1., the preference of the *trans* conformation was found in $[C_4mim]OTf$ versus $[C_4mim]NO_3$. The explanation of this result could fall under the term of anion hydrophobicity. Usually ILs tend to interact with other materials via anion and form H-bond based network. Previous studies showed that the I_{gauche}/I_{trans} ratio increased when the water was added to neat ionic liquid $BmimNO_3$ and could help to determine water packing processes in ILs [102]. $[C_4mim]NO_3$ has more hydrophobic anion than $[C_4mim]OTf$ has and because of that more water from the atmosphere was absorbed and more packed structures of $[C_4mim]NO_3$ were found.

The anion type influence to the conformational equilibrium was investigated in the set of neat ionic liquids. In the Figure 3.3.2. the I_{gauche}/I_{trans} ratio of neat ionic liquids $[C_4mim]X$, X=I, Br, Cl, BF_4, OTf, NO_3 versus anion ionic radius is depicted. The preference of the *trans* conformation was listed in the following order: $I^- > Br^- > Cl^- > OTf^- > NO_3^- > BF_4^-$. The conformation preferences for ILs with halide anions (I^-, Br^-, Cl^-,) agreed with the previous report, which proposed the stronger electrostatic field by smaller halide anions imposes the *gauche* conformation [142]. However, non-spherical and halide anions did not order well together in the distribution of ionic radius versus *gauche*/*trans* conformers ratio. The anion hydrophobicity was used to explain the order of anions determined in our experiments [143]. The I_{gauche}/I_{trans} ratio for the most hydrophilic anion I^- was 0.8 and for the most hydrophobic anion BF_4^- was 1.9.

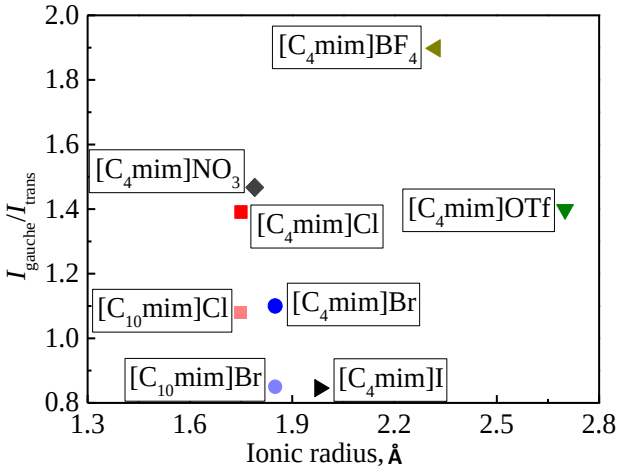

Figure 3.3.2: I_{gauche}/I_{trans} ratio dependence of the $[C_4mim]^+$ cation versus ionic radius of different anions.

As well as anion hydrophobicity the cation chain length also plays important role in conformational equilibrium. I_{gauche}/I_{trans} ratio for neat ILs [C4mim]Cl, C4mim]Br was compared to long chain ionic liquids [C10mim]Cl, [C10mim]Br I_{gauche}/I_{trans} conformers ratio. [C10mim]Cl showed 1.08 and [C10mim]Br 0.85 while [C4mim]Cl showed 1.4 and [C4mim]Br 1.1, respectively. The preference of the *trans* conformation in ILs with longer cation chain depicts the different lower mobility and more structured behavior of long chain ILs.

Furthermore the temperature impact was registered for conformational equilibrium (I_{gauche}/I_{trans} ratio) in [C4mim][OTf] and depicted in Figure 3.3.3. Below room temperature the huge increase in I_{gauche}/I_{trans} ratio was noticed. At temperature 305 K 1.5 times more ionic liquid cations oriented in *gauche* form than *trans* was registered, while at 200 K this ratio increased to 8.8. The insert in Figure 3.3.3. shows the Raman spectra at described temperatures.

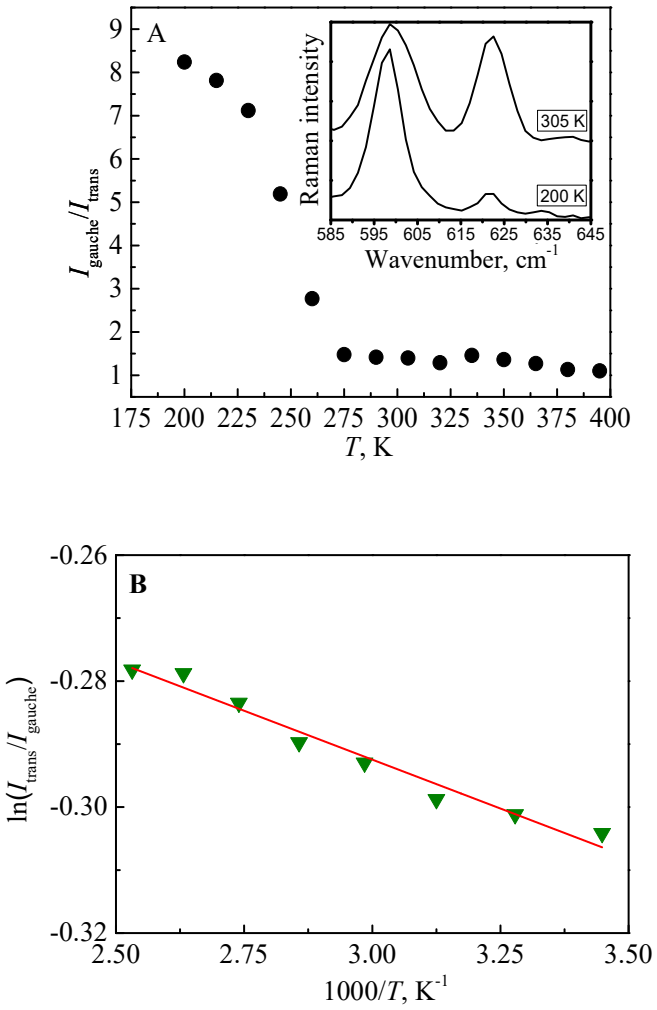

Figure 3.3.3. Temperature dependence of the I_{gauche}/I_{trans} ratio in full temperature range for pure [C$_4$mim]OTf. A: linear dependence. B: logarithmic dependence.

The decrease of anion mobility and packaging peculiarities with the decrease of temperature could be explained by these results. Moreover, the temperature dependence of conformational equilibrium could be used to investigate the difference in the partial molar enthalpy of the *trans* and *gauche* conformers ($\Delta H_{trans \rightarrow gauche}$) Fig. 3.3.3. B. As mentioned before the Raman intensity of the *trans* conformer increases as the temperature was increased for [C$_4$mim]OTf. Summing up the ratio of the Raman scattering cross-sections

between the *trans (A)* and *gauche (B)* conformers is independent of temperature. $\Delta H_{trans \rightarrow gauche}$ is given by (1) [116]

$$\Delta H^{A \rightarrow B} = -R\left\{\frac{\partial \ln(I_B/I_A)}{\partial(1/T)}\right\}_p. \qquad (1)$$

In this equation, *R*, *T* and *p* are the gas constant, temperature and pressure, respectively. I_A and I_B indicate the relative Raman intensity of conformers A and B, respectively and "A" and "B" correspond to the conformers of the $[C_4mim]^+$ cation [116]. From the slope of the line in Figure 3.3.3 B it was calculated that $\Delta H_{trans \rightarrow gauche}$ for [C_4mim][OTf] is -0.5 ± 0.2 kJ·mol^{-1}. While the values -1.1 ± 0.2 kJ·mol^{-1} for [C_4mim]NO_3, -1.5 ± 0.4 kJ·mol^{-1} for [C_4mim]SCN, -0.9 ± 0.1 kJ·mol^{-1} for [C_4mim]CH_3COO and -1.0 ± 0.1 kJ·mol^{-1} for [C_4mim]BF_4, respectively [116], was measured for other ILs. Considering the standard error, the value of $\Delta H_{trans \rightarrow gauche}$ in [C_4mim]OTf is close to the value in other ILs, which approximately are -1.0 kJ·mol^{-1} and are independent of the anionic species [137,142].

Based on relationship $\Delta G = \Delta H - T\Delta S$, our results agree to the consideration that entropy drives the thermodynamic stability of the conformational equilibrium for $[C_4mim]^+$ anion in $[C_4mim]^+$ based ILs with non-spherical anions [116].

Table 3.3.1. Calculated $\Delta H_{trans \rightarrow gauche}$ comparison for different ILs.

Ionic liquid	$\Delta H_{trans \rightarrow gauche}$	Refference
[C_4mim]OTf	-0.5 ± 0.2 kJ·mol^{-1}	This experiment
[C_4mim]NO_3	-1.1 ± 0.2 kJ·mol^{-1}	[116]
[C_4mim]SCN	-1.5 ± 0.4 kJ·mol^{-1}	[116]
[C_4mim]CH_3COO	-0.9 ± 0.1 kJ·mol^{-1}	[116]
[C_4mim]BF_4	-1.0 ± 0.1 kJ·mol^{-1}	[116]

The equilibrium of ionic liquid cation conformations (I_{gauche}/I_{trans}) in ILs and H_2O mixtures were also investigated at different water content values in the mixtures. Concentration dependences of I_{gauche}/I_{trans} ratio obtained for different ILs: [C_4mim]X (X= I^-; Br^-; Cl^-; OTf^-; NO_3^-; BF_4^-) and [C_{10}mim]Y (Y=Br^-; Cl^-) at various H_2O content in mixtures were depicted in Figure 3.3.4.

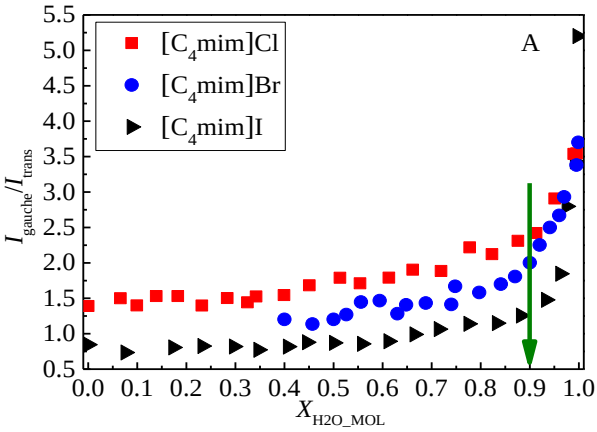
[C4mim]Cl
[C4mim]Br
[C4mim]I
A
Igauche/Itrans
XH2O_MOL

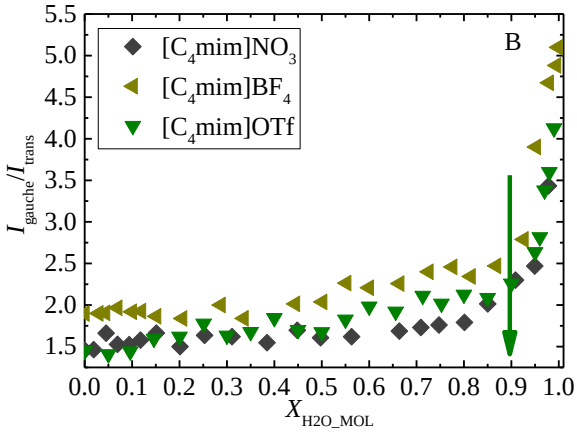
[C4mim]NO3
[C4mim]BF4
[C4mim]OTf
B
Igauche/Itrans
XH2O_MOL

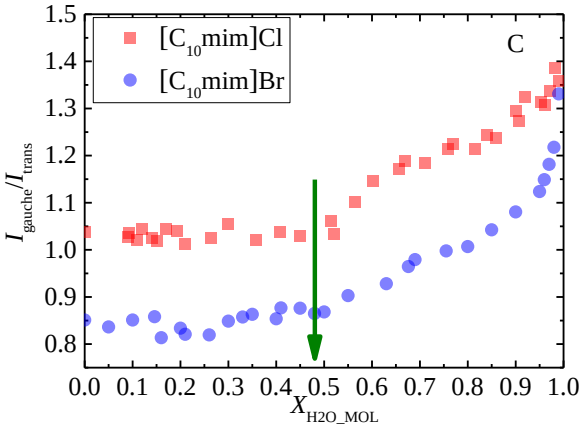
[C10mim]Cl
[C10mim]Br
C
Igauche/Itrans
XH2O_MOL

Figure 3.3.4. I_{gauche}/I_{trans} ratio between the *gauche* and *trans* Raman bands for all investigated ionic liquids plotted as a function of the H_2O molar fraction in the mixtures. Crossover points marked by red arrows correspond to the boarders of different water or ionic liquid structures formation. Part A: isolated ions or small ion clusters are formed above crossover point. Part B: small water clusters are destroyed, and bulk water is formed above crossover point. Part C: the liquid crystalline ionogel phase starts forming above the crossover point.

The distinct behavior for different ILs–H_2O mixtures was found for I_{gauche}/I_{trans} ratio. The discontinuities in concentration dependencies of I_{gauche}/I_{trans} ratio can be associated with the variation of H-bond interactions between ILs and H_2O molecules as well as the formation of different structures based on water molecules. For [C_{10}mim]Cl and [C_{10}mim]Br ILs discontinuities were found at X_{H2O_MOL}=0.45±0.05 (Figure 3.3.4. part C). This value very well correlates with LC ionogel phase formation beginning identified at X_{H2O_MASS}=0.03±0.005 (more details in 3.4. section). The increase of I_{gauche}/I_{trans} ratio began at crossover point and indicated that *gauche* conformation is more convenient due to LC ionogel phase formation in long chain ILs. Similarly to the long chain ILs, discontinuities in I_{gauche}/I_{trans} ratio for short chain ionic liquids (Figure 3.3.4. part A and B) showed the change of I_{gauche}/I_{trans} ratio due to the increase of water content in the mixtures. Differently from long chain ILs, the crossover point was registered at higher concentrations of water X_{H2O_MOL}=0.9±0.05. All possible phase formation effects were analyzed in the 3.3.3 and 3.4.1 paragraphs of this and following sections. The main idea how to explain those changes came from theoretical modelling presented in Ref. [69] which revealed that the mesophases and shapes depend on the counter ion type and alkyl chain length but also on the number of molecules that are involved in the modeling. Water molecules can be trapped in different environments and dictate the shape and size of the aggregates and its behavior [69].

3.3.2. Proton/Deuteron exchange in IL–D_2O mixtures

In this paragraph the anion, self-aggregation and mesophase effects on the H/D exchange in [C_{10}mim]Br–D_2O and [C_{10}mim]Cl–D_2O mixtures were studied by means of the Raman spectroscopy. The dependency between conformational changes and H/D exchange in imidazolium-based ILs with both shorter and longer alkyl chains additionally was investigated using Raman spectroscopy together with NMR and theoretical calculations.

As one of mesophases in long chain ILs LC ionogel will be discussed in the 3.4. part of the thesis. At further dilution with water, after the LC ionogel formation at X_{H2O_MASS}>0.4 (X_{H2O_MOL}>0.92) the LC ionogel mesophases disappeared and the viscosity of the mixtures dropped drastically. This highly diluted state of IL–H_2O mixture (0.92<X_{H2O_MOL}<0.98) was called as the aqueous solution [71]. The coexisting liquid and solid phases can appear only below 290 K [144]. It is obvious that the rates of H/D exchange process in such ILs can be crucially influenced by the phase behavior when different molecular sites and peculiar environments in the microscopic or mesoscopic scales appear. For example, the imidazolium groups can get blocked inside of inverted hexagonal structures, if such formed, or the formation of the regions with confined water (D_2O as deuteron donor) is enhanced due to the interplay between hydrophilic and hydrophobic segments, as well as the formation of the layered structures in the case of the lamellar phase [80]. In order to segregate the pure H-bond-driven contribution to the H/D exchange from possible phase/environmental effects, the composition of the samples should be chosen to have the systems are in the identical states. The aqueous solution phase (i.e., the one that is by many physical features very close to the "classical" electrolyte (water + salt) system) would be most suitable. Therefore, full range of concentration of [C_{10}mim]Br and [C_{10}mim]Cl in H_2O was investigated. Previously analyzed imidazolium ring C(n)−H Raman band shifts and different water clusters organization was used to provide useful information when predicting the structures of hydrogen bonded aggregates and changes in structure for other ILs [24,32,33,69].

In order to check the influence of the LC ionogel phase formation on the H/D exchange rate another two samples of IL–D_2O mixtures with X_{D2O_MOL}=0.99 and X_{D2O_MOL}=0.6 were prepared and investigated. The samples with anisotropic gel (X_{D2O_MOL}=0.6) were studied by 1H NMR spectroscopy and was not observer any changes in intensity of C(2)−H proton during 48 days of observation from the sample preparation. Thus, was stated that this reaction does not run in the LC ionogel phase. Comparing result of C(16)−H_3 1H integrals resonance was indicated that in imidazolium ring only

C(2)–H proton was involved in the H/D exchange under the present experimental conditions [33].

The sample concentration of X_{D2O_MOL}=0.99 in IL–D_2O mixtures was high enough to carry out the registration of Raman spectra at the same conditions as it was set in NMR studies. The Raman studies are important in trying to reveal the possibility of anomalous conformational changes around the C(7)–C(8) bond (Figure 3.1.1.) that seem to be coupled with H-bonding and H/D exchange processes [100,140]. The most comprehensive information concerning the H/D exchange should be obtained due to analysis of C(2)–H imidazolium stretching vibration ν(C(2)–H) Raman band. However, this band is strongly overlapped with other C–H bands in the spectral range 2900–3100 cm^{-1}. Therefore, the H/D exchange was monitored using the time evolution of the Raman bands assigned to the combination of the in-plane ring deformation and CH_3(N) deformation at 1010 and 1024 cm^{-1} (Figure 3.3.5.), [100,140].

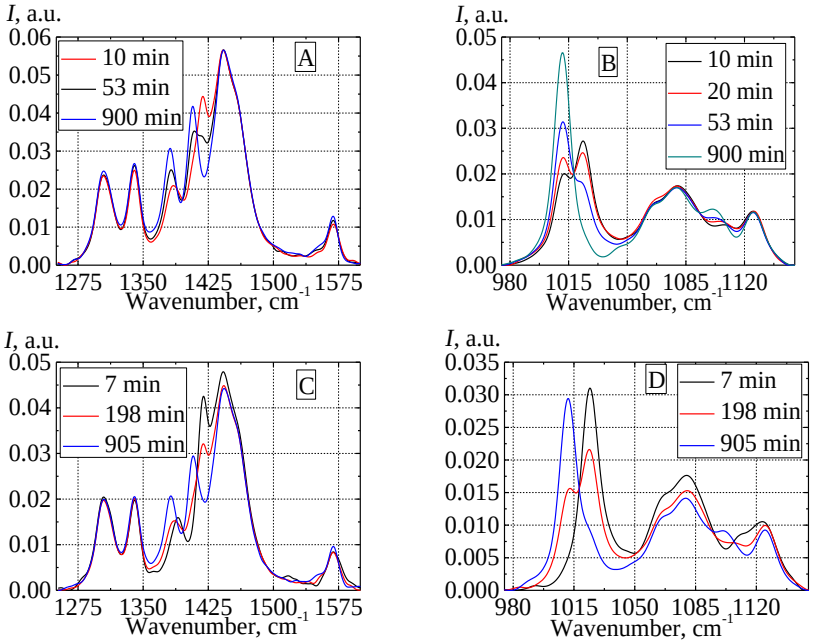

Figure 3.3.5. Monitoring the H/D exchange on Raman bands at 1010 and 1024 cm^{-1} (B, D) and 1406 and 1417 cm^{-1} (A, C) of [C_{10}mim]Br–H_2O (A, B) and [C_{10}mim]Br–H_2O (C, D) at different time from the mixture preparation.

These bands were successfully exploited for the same purpose in Raman studies of [C_4mim]BF_4–D_2O mixtures [100]. The time dependency of their integral intensities (Figure 3.3.6.) indicated crucial influence of Br^- and Cl^- anions to much faster H/D exchange in [C_{10}mim]Br–D_2O than [C_{10}mim]Cl–

D_2O mixtures. 200±2 minutes was required to reach the apparent reaction saturation for [C_{10}mim]Br–D_2O mixtures (Figure 3.3.6. A, B), whereas no features reaching this were seen for [C_{10}mim]Cl–D_2O (Figure 3.3.6. C, F) even after 1000 minutes of sample preparation. The results of H/D exchange dynamics obtained in long chain ILs and D_2O mixture by Raman spectroscopy were supported by the NMR dynamics results measured in IL–D_2O mixtures[33].

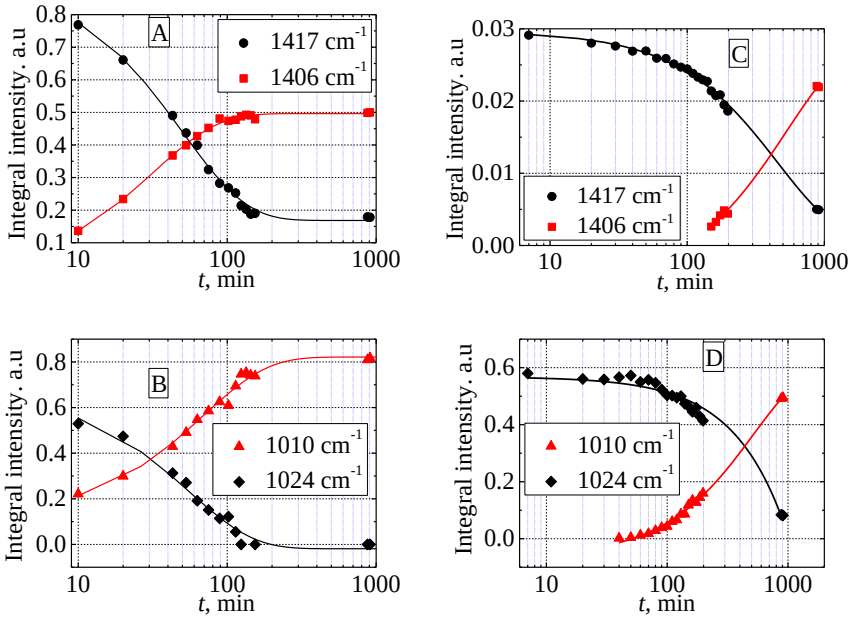

Figure 3.3.6. H/D exchange dynamics in [C_{10}mim]Br–D_2O (A, B) and [C_{10}mim]Cl–D_2O (C, D) mixtures.

To check the dynamics of H/D exchange for the different ILs with non-spherical anions and shorter alkyl chain the same experiment was repeated for [C_4mim]NO_3 and [C_4mim]OTf mixtures with D_2O. Different D_2O concentrations X_{D2O_MOL}=0.99 and X_{D2O_MOL}=0.4 in IL–D_2O mixtures were specifically chosen to avoid mesophases ("water pockets") formation in IL–water mixtures. Surprisingly, no changes were registered for Raman vibrational bands previously investigated in [C_{10}mim]Br–D_2O and [C_{10}mim]Cl–D_2O even after 58 days of mixtures preparation. Thus, for the first time it was stated that H/D reaction does not run in [C_4mim]OTf and [C_4mim]NO_3 ILs. The similar result for [C_4mim]BF_4 was obtained applying IR and NMR spectroscopies [145]. Moreover, experimental results discussed in paragraph 3.3.3. Figure 3.3.15. can be considered in the "light" of H/D exchange process too. The I_{gauche}/I_{trans} ratio dependency of water concentration

in $[C_4mim]NO_3$–H_2O and $[C_4mim]NO_3$–D_2O mixtures were found to be resembling. These results let us approve one more way how H/D exchange can be checked for the specific IL. Moreover, obtained results agree with hypothesis on external base necessity for H/D exchange to occur in ILs with coordinated and non-basic anion such as tetrafluoroborate BF_4 [146] and NO_3.

The spectral region around ~600 cm^{-1} (Figure 3.3.7.) as discussed in the paragraph 3.3.1., attained special consideration of the Raman bands at 600 and 620 cm^{-1} sensitive to the conformational changes in hydrocarbon chains attached to the imidazolium cation [100,114,140,147]. Earlier in the thesis it was deduced that conformational equilibrium in ILs depends on the type of the anion. The significant redistribution of the integral intensities at 602 and 625 cm^{-1} was clearly seen in the Raman spectra for both studied IL–D_2O mixtures at different time after sample preparation (Figure 3.3.7.). However, in the present case of $[C_{10}mim]^+$ it is hardly credible to attribute this evolution being a completely conformational effect. Indeed, the Raman experiments carried out varying the temperature in the wide range on the neat $[C_{10}mim]Br$ and revealed the conformational composition was hardly changeable even passing through the melting and at further cooling up to 49 K (Figure 3.3.8.). This behavior was completely different in the case of $[C_4mim]Cl$ observed at the melting point and thermal equilibration at 345 K [140].

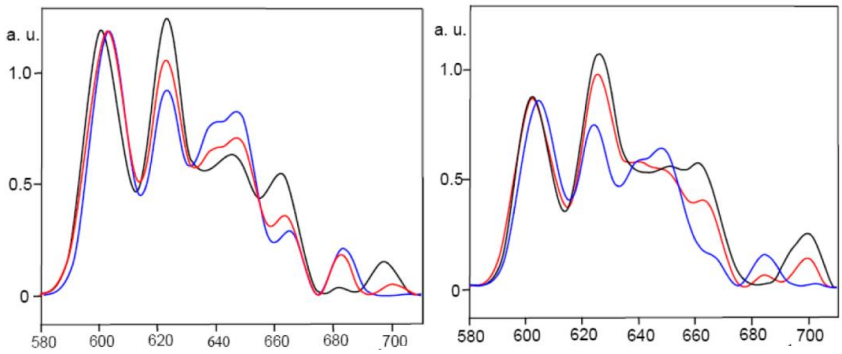

Figure 3.3.7. Time dependencies of Raman spectra in the range 600−700 cm^{-1} of $[C_{10}mim]Br$ (left; at 10 min (black), 60 min (red), 150 min (blue) after the sample prepared) and $[C_{10}mim]Cl$ (right; at 20 min (black), 220 min (red) and 900 min (blue)) in D_2O mixtures (X_{D2O_MOL}=0.99) at T=296 K.

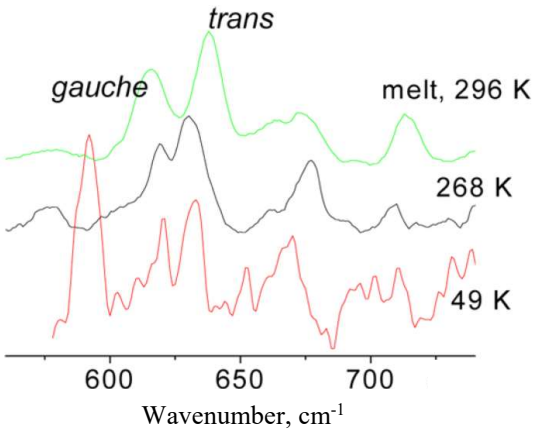

Figure 3.3.8. Raman spectra of [C_{10}mim]Br in the range 600−800 cm^{-1} in the liquid (296 K) and crystalline (268 and 49 K) phases.

The complex redistribution of several Raman intensities (Figure 3.3.7.) was due to the changes in positions of some strongly overlapping bands in this spectral region upon H/D exchange at C(2) site rather than changes in conformational equilibrium.

On the other hand, anions and aggregation effects play crucial role in IL aqueous solutions. The anions interact with cations via H-bonds and bind the water molecules in their solvation shells. The anions in highly diluted aqueous solutions are solvated and therefore, their role in H-bonding is significantly reduced. Moreover, the H/D exchange was coupled with the rotational dynamics of water molecules [99]. The interaction with anions hinders the rotational motion of D_2O molecules in the solvation shell and becomes the stronger the smaller is the size of the anion. The rotational "freezing" of D_2O molecules could hinder the supply of deuterons to the site of exchange. This occurred in [C_4mim]NO_3 and [C_4mim]OTf mixtures with D_2O because of the non-spherical anions probability to form more H-bonds with D_2O molecules than spherical anions could do. Solvated non-spherical anions were distracted from cation and was found in the position above the ring plane of the imidazolium cation. This specific interaction caused the absence of H/D exchange for non-spherical anion based ILs.

In the LC ionogel phase the strong anion−cation interaction impedes the H/D exchange process too. This factor was considered as additional contribution to the slowdown of rotational dynamics discussed just above. The kinetics of H/D exchange drastically changed in the samples of X_{D2O_MOL}=0.99 (Figure 3.3.6.). This process, depending on the anions, was very significantly damped ([C_{10}mim]Cl) or stimulated ([C_{10}mim]Br). Unfortunately, it is

virtually unknown how certain inherent properties of ILs influence the self-aggregation and phase behavior of IL–water mixtures.

Higher degree of molecular freedom due to the order−disorder effects could be summarized as a crucial role in the H/D exchange reaction in the studied mixtures. The presented experimental results are expected to be useful for the molecular design of ionic liquids and the modeling of micellar structures in aqueous solutions. The conformational changes that was coupled with the H/D exchange, as it was observed in reference [100], did not occur neither in the studied $[C_4mim]NO_3$–D_2O. $[C_4mim]OTf$–D_2O, nor in $[C_{10}mim]Br$–D_2O and $[C_{10}mim]Cl$–D_2O mixtures. The changes revealed in ^{13}C NMR spectra for the similar experiment was caused by the secondary isotope effects on chemical shifts not being the signal shifts due to the conformational [33]. Summarizing our Raman and NMR results we can clearly state that the conformational equilibrium and the H/D exchange are separate processes not coupled with each other.

3.3.3. Water confinement in 1-butyl-3-methylimidzolium nitrate

In this paragraph the utilization of Raman spectroscopy for water clusterization process „water pockets“ in the 1-butyl-3-methyl-imidazolium nitrate ([C_4mim]NO_3) was investigated.

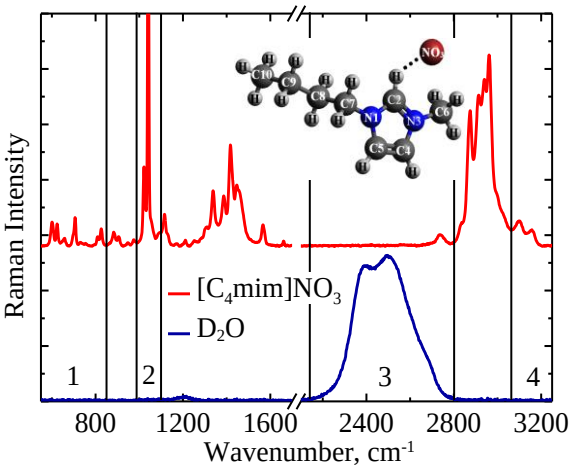

Figure 3.3.9. Raman spectra of neat [C_4mim]NO_3 (upper) and neat D_2O (lower) distributed in four spectral regions sensitive to added D_2O. Insert shows the Structure of [C_4mim]NO_3.

Water clusters sized 2-3 nm and called “Water pockets” was observed in 2014 by bead modeling referring to the observed small-angle X-ray scattering (SAXS) and small-angle neutron scattering (SANS) data [46]. The formation of „water pockets“ in [C_4mim]NO_3–H_2O mixtures recently was observed applying not only SAXS and SANS, but also differential scanning calorimetry (DSC) techniques [45–47]. In the mixtures of [C_4mim]NO_3–D_2O, anomalous freezing occurred discretely for a wide range of water concentrations ($0.7<X_{D2O\_MOL}<0.94$). The simulations of molecular dynamics (MD) demonstrated the formation of water confinement, comparable to „water pockets“ in 1-octyl-3-methylimidazolium nitrate ([C_8mim]NO_3) mixtures at various H_2O concentrations [22]. It was found that in the boundary between the polar and non-polar nanodomains the confined water could exist. This confinement could be compared with chopped “water channels” which appear between hexagonal phases of cations due to LC ionogel phase formation in long chain ILs. Another MD simulation study identified four concentration ranges in hydrophilic ILs–H_2O mixtures and presented four distinct structural models for description: 1) isolated water molecules ($X_{H2O\_MOL}<0.5$); 2) chain-

like water aggregates ($0.5<X_{H2O\_MOL}<0.8$); 3) bicontinuous system ($0.8<X_{H2O\_MOL}<0.95$); 4) isolated ions or small ion clusters, respectively ($X_{H2O\_MOL} > 0.95$) [89]. It was noted that the simulated "water pockets" depends on both temperature and water concentration. These H-bond based clusters could be called one of mesophases in ILs and was never investigated using vibrational spectroscopy.

In our experiments the changes of Raman spectra were observed in four different spectral regions due to continuous increase of heavy water content in IL–D_2O mixtures. It was found that parameters of Raman spectral bands were sensitive to the added D_2O content. The extent of „water pockets" formation was determined from the discontinuities found in the concentration dependencies of monitored Raman bands shifts and integral intensities. The blue shift of symmetric NO_3^- stretching mode at 1041 cm^{-1} and imidazolium ring stretching mode at 2nd carbon position C(2)–H at 3100 cm^{-1} was found even with a small water content addition in the mixture. The same behavior was found analyzing the Raman band at 706 cm^{-1} assigned to NO_3^- bending mode. Moreover, integral intensity ratio of two Raman bands at 600 and 625 cm^{-1} assigned to *gauche* and *trans* forms of the butyl chain was also found to be dependent of D_2O content in the mixture. The distribution among relative integrated intensities of Raman bands assigned to different water clusters vibrations was also sensitive to the D_2O content in the mixture. Overall, the beginning (i.e. lower boarder) of „water pockets" formation (X_{D2O_MOL}=0.6) in $[C_4mim]NO_3$ was determined by the discontinuous spectral changes observed for NO_3^- stretching mode and different water cluster vibrations. The end (i.e. upper boarder) of "water pocket" formation (X_{D2O_MOL}=0.86) was found from discontinuities in concentration dependencies of imidazolium ring stretching mode and different water clusters vibrations. The conformational changes were also observed, and appeared at D_2O concentration, corresponding to the upper boarder of "water pockets" formation.

Raman spectra of the neat $[C_4mim]NO_3$ and neat D_2O in the whole spectral region between 550 and 3300 cm^{-1} was depicted in Figure 3.3.9. There are four regions marked in the spectra which were found being sensitive to added D_2O. The assignments of studied $[C_4mim]NO_3$ Raman bands was well investigated by us and other scientists analyzing the ILs with the comparable structure (anion or cation) resemble the investigated ILs [65,72,116,139,140,147,153–155]. In the Region 1 (550 – 800 cm^{-1}) two peaks at 600 and 625 cm^{-1} assigned to vibration bands of the IL molecules organized in *gauche* and *trans* forms around C(7)-C(8) butyl chain and one more peak at 706 cm^{-1} assigned to the IL anion NO_3^- bending mode were distributed.

Table 3.3.2. The assignment of Raman vibrational modes used to study the formation of "water pockets"

Vibrations assignments	Waven umber, cm^{-1}	Ref.	Band assignment
Imidazolium ring deformations and CH_2 rocking vibrations assigned to *gauche* conformers	600	[140,141]	ν(*gauche*)
Imidazolium ring deformations and CH_2 rocking vibrations assigned to *trans* conformers	625	[140,141]	ν(*trans*)
NO_3^- in-plane bending vibrations	706	[116]	$\nu_4(NO_3^-)$
NO_3^- symmetric stretching vibrations	1041	[116]	$\nu_1(NO_3^-)$
OD stretching vibrations of very strong hydrogen bonded water band in quenched mixtures (VSHB)	2260	[148]	ν(VSHB)
OD stretching vibrations of water molecules within the different kinds of tetrahedral H-bonded network (SHB)	2400	[72,148,149]	ν(SSHB)
OD stretching vibrations of water molecules within highly asymmetric single donor (SD) hydrogen bonding configuration or distorted tetrahedral H-bonded network (MHB)	2525	[116,148, 149]	ν(MHB)
OD groups or free water molecules without any hydrogen bonded groups.	2643	[148,149]	ν(WHB)
Imidazolium ring C(2)–H stretching vibrations	3100	[145,150 –152]	ν(C(2)-H)
Imidazolium ring C(4,5)–H asymmetric stretching vibrations	3152	[145,150 –152]	ν(C(4,5)– H_asym)
Imidazolium ring C(4,5)–H symmetric stretching vibrations	3164	[145,150 –152]	ν(C(4,5)–H_sym)

Region 2 represented the Raman spectrum between 1000 and 1100 cm^{-1} where the band at 1041 cm^{-1} was assigned to IL anion NO_3^- stretching vibration mode. Raman vibration bands found in the Region 4 (3100 – 3200 cm^{-1}) were assigned to imidazolium ring stretching modes at the 2nd carbon position C(2)–H (3100 cm^{-1}) and at 4th 5th carbon positions C(4,5)–H symmetric and asymmetric stretching modes (3164 and 3152 cm^{-1}). The Raman spectra in the Region 3 (2000 – 2800 cm^{-1}) represented heavy water molecules vibrations, while the 1st, 2nd and 4th regions belong to the vibrations of anion and cation. Region 3 was divided in to two main bands which were assigned to the vibrations of water molecules organized in network with tetrahedral structure (network water (NW) 2420 cm^{-1}) and water molecules that are involved in a distorted network but do not form all four H-bonds with the neighboring water molecules (intermediate water (IW) 2540 cm^{-1}). More Raman bands could be found at the shoulders of spectral bands which will be discussed later. The vibrational assignments of water and IL bands are listed in the table 3.3.2.

C–H stretching vibrational modes of the imidazolium ring (Region 4)

As it was mentioned before, the most of research in IL–H2O or IL–other solvent mixtures were focused to imidazolium ring C–H stretching region [32,34,35,156,157]. The theoretical and experimental data represented the Raman region above 3100 cm−1 as the one, very sensitive to the interactions involving the imidazolium ring vibrations C(n)–H of the [C4mim]+ cation based ILs [145,150–152]. H-bond formation in [C4mim]NO3 was not an exception. Raman spectra of [C4mim]NO3–D2O mixtures at various heavy water contents in Region 4 and spectra deconvolution into three components using Voigt functions were showed in Figure 3.3.10 parts A and B. It is worth to mention that the main part of fitted curves was consisted of Gaussian shape. Based on the previous vibrational spectroscopy studies the main peaks were assigned to the vibrations of C(2)–H, C(4,5)–H asymmetric and C(4,5)–H symmetric stretching modes. In the spectrum of neat [C4mim]NO3 (XD2O_MOL=0) bands were distributed at 3100 cm-1, 3152 cm-1, 3164 cm-1, which revealed the stronger H-bond of C(2)–H…NO3 than C(4)–H…NO3 or C(5)–H…NO3. As depicted in Figure 3.3.10. part C, the positions of investigated Raman vibrational modes were slightly blue shifted when D2O was added to pure [C4mim]NO3. This blue shift indicated that added water induced the weakening of interactions between anions and cations involving their hydrogen atoms and their direct environment and was supported by previous studies [158].

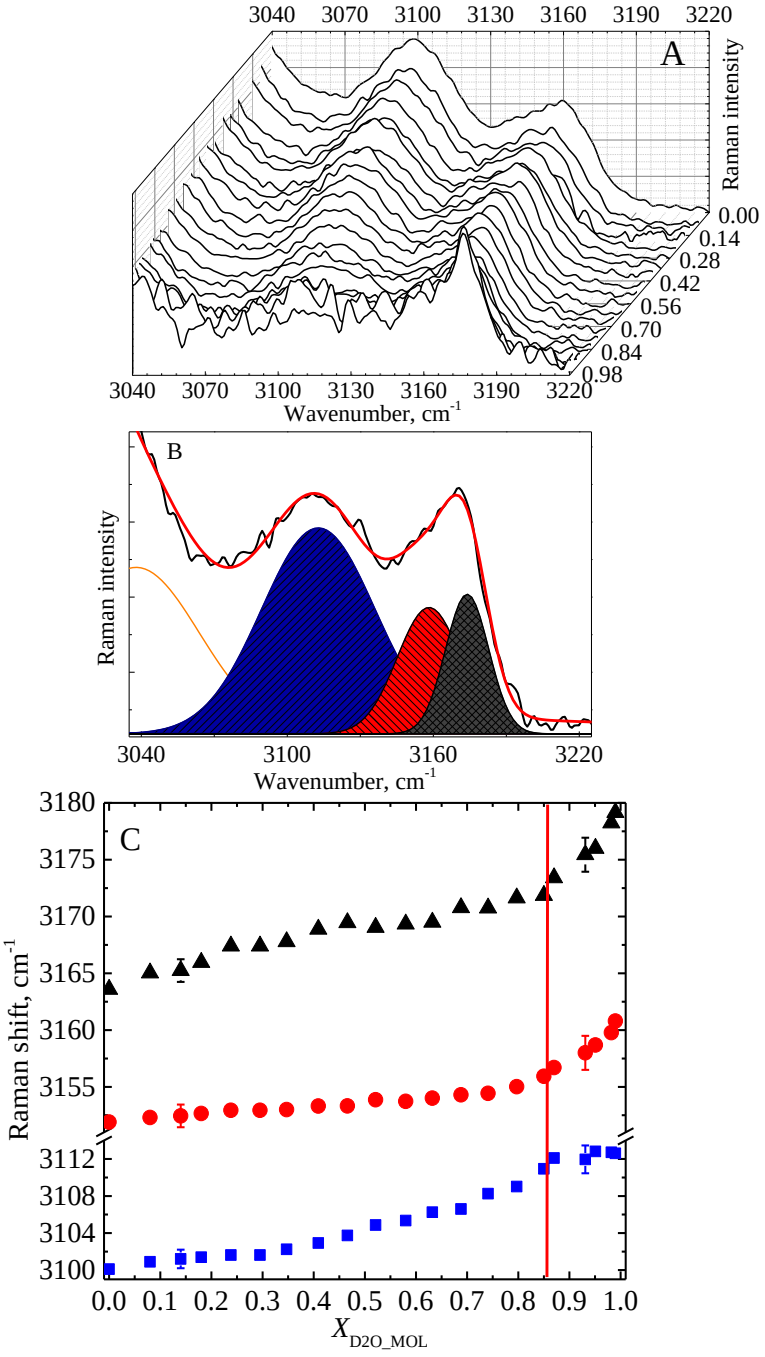

Figure 3.3.10. A: Raman spectra of $[C_4mim]NO_3$–D_2O mixtures at different water concentrations in spectral Region 4. B: Raman spectrum of $[C_4mim]NO_3$–D_2O mixture at X_{D2O_MOL}=0.87 (black line), relative fit (red line) and deconvolution in to three bands (colored blue, red and black). C: The

distribution of C(2)–H (blue squares), C(4,5)–H asymmetric (red circles) and C(4,5)–H symmetric (black triangles) stretching Raman band shift plotted as a function of the D_2O molar fraction in the mixtures. Crossover point marked by red line corresponds to the upper boarder of "water pocket" formation.

The H-bond formed between the water molecules and anions distracted the H-bond between anions and cations. This result was supported by previous studies which claimed that solvation of organic compounds in imidazolium based ILs occur only with the anion [159].

However, the most controversial part found in experimental results was related to the discontinuous and not equal distribution of the Raman shifts. The C(2)–H band totally shifted 13 cm^{-1} (from 3100 to 3113 cm^{-1}). The C(4,5)–H asymmetric band totally shifted 9 cm^{-1} (from 3152 cm^{-1} to 3161 cm^{-1}) and C(4,5)–H symmetric band totally shifted 15 cm^{-1} (from 3164 cm^{-1} to 3179 cm^{-1}). The C(2)–H band shift was found to be discontinuous with cross over point at X_{D2O_MOL}=0.86, reaching its maximum and remain constant despite further addition of D_2O. The distribution of other two band shifts was like the previous one and the cross over points were found at X_{D2O_MOL}=0.86. Differently from the C(2)–H vibrations, which showed all blue shift before the crossover point, the C(4,5)–H asymmetric and the C(4,5)–H symmetric bands was shifted by the half of total shift counted in inverse centimeters before reaching the crossover point value. The total shifts of the C(2)–H and C(4,5)–H vibration bands were comparable and indicated that anions in $[C_4mim]NO_3$–D_2O mixtures were distracted from all three imidazolium protons equally compared whole concentration range of D_2O results. The different blue shifts of vibrational modes before the crossover point at X_{D2O_MOL}=0.86 suggested the model where the anions located near imidazolium ring 2nd carbon position was distracted from cation at lower D_2O concentrations than anions near the 4th and 5th carbon positions of imidazolium ring.

NO_3 stretching modes of the IL anion (Region 2).

Well known interactions and formation of distinct aggregates between water molecules and anions are based on the formation of H-bond. At low water concentrations in the mixtures *anion···water···anion* [160] and at higher water concentrations *water···anion···water* aggregates are formed [89].

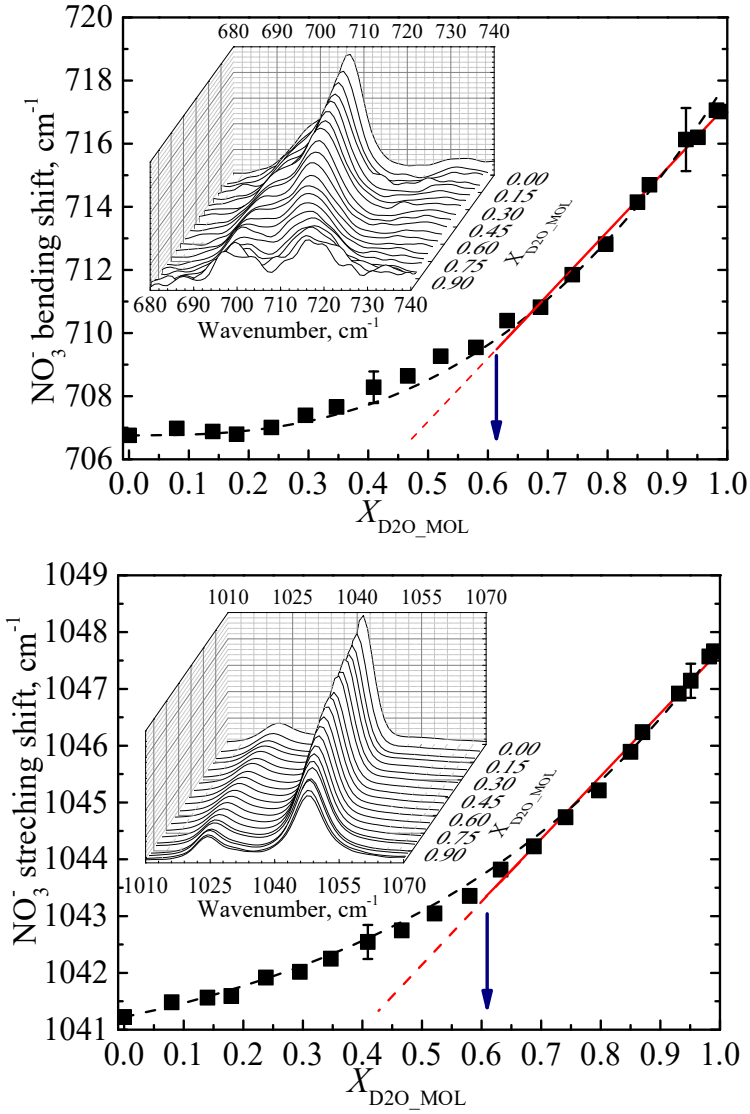

Figure 3.3.11. The Raman shift of NO_3^- symmetric stretching $\nu_1(NO_3^-)$(lower) and bending $\nu_4(NO_3^-)$ (upper) modes plotted as a function of the D_2O molar fraction in the mixtures. In both pictures the crossover points were marked as blue arrows and correspond to the lower boarder of "water pocket" formation. The Raman spectra of $[C_4mim]NO_3$–D_2O mixtures at different water concentrations in spectral Region 2 are depicted in the insets.

The evolution of NO_3^- symmetric stretching (at 1041 cm^{-1}) ($\nu_1(NO_3^-)$) and bending (in-plane deformation mode) (at 706 cm^{-1}) ($\nu_4(NO_3^-)$) vibration modes spectral parameters is depicted in Figure 3.3.11. parts A and B. The blue shift from 1041.2 cm^{-1} to 1047.7 cm^{-1} totally, (6.5 cm^{-1}) and line FWHM

broadening by 2.5 cm^{-1} was registered to the most intensive Raman spectral band $v_1(NO_3^-)$. Larger blue shift from 707 cm^{-1} to 717cm^{-1} (totally 10 cm^{-1}) and line FWHM broadening by 11 cm^{-1} was registered to the Raman spectral band $v_4(NO_3^-)$. The blue shifts were clearly attributed to the screening and weakening of the interactions between cation $[C_4mim]^+$ and anion NO_3^- but at the same time the line broadening suggested that simultaneously complexes *anion···water* $[NO_3 \cdot D_2O]^-$ and *water···anion···water* $[NO_3 \cdot (D_2O)_2]^-$ were formed [72,114,161–164]. The crossover point at X_{D2O_MOL}=0.61 was less obvious than the one registered in C–H analysis. To check the presence of crossover point the additional attempts to fit the experimental data were performed. Within the limits of experimental error Figure 3.3.11. upper and lower parts were fitted with curve similar to non-ideal behavior. Figure 3.3.11. upper with Allometric function $y=a+b^{x\wedge c}$ and 3.3.11. lower with Exponential growth function $y=a+b^x$. Both fitted curves and their parameters did not provide any valuable interpretation for fitting results. To make sure the formation "water pockets" is registered, the combination of vibrational spectroscopy and simple theoretical model was used. At the crossover point concentration, the ratio of IL and D_2O molecules are 4 to 6. Hydrophilic and non-spherical anion NO_3^- could totally can form 3 H-bonds. If one H-bond is formed with cation than another two could be either intermolecular ones and formed with D_2O molecules or intramolecular one with other cations. In this situation six D_2O molecules can form up to 24 H-bonds (up to 4 H-bonds for each D_2O) and four NO_3^- anions could be involved in to 8 H-bonds formation. Counting the probable H-bonds in the mixture there is high possibility to have the intermolecular D_2O–D_2O interactions at X_{D2O_MOL}=0.61. At this concentration all possible H-bonds of anion were occupied by water molecules and the formation of distorted solvation shell structures "water pockets" were started. For the micro hydrated NO_3^- anions the onset of extensive water-water hydrogen bonding was observed with four water molecules and persisted in the larger clusters [165]. Discontinuities in concentration dependencies of Raman bands blue shift could be associated with "water pockets" formation boarders. Lower boarder was indicated in spectral Region 2 and upper boarder in spectral Region 4.

Heavy water OD stretching vibration modes (Region 3)

From the Figure 3.3.12 it is clearly seen that the Raman line shape in Region 3 is multi-structured [53,82,166].

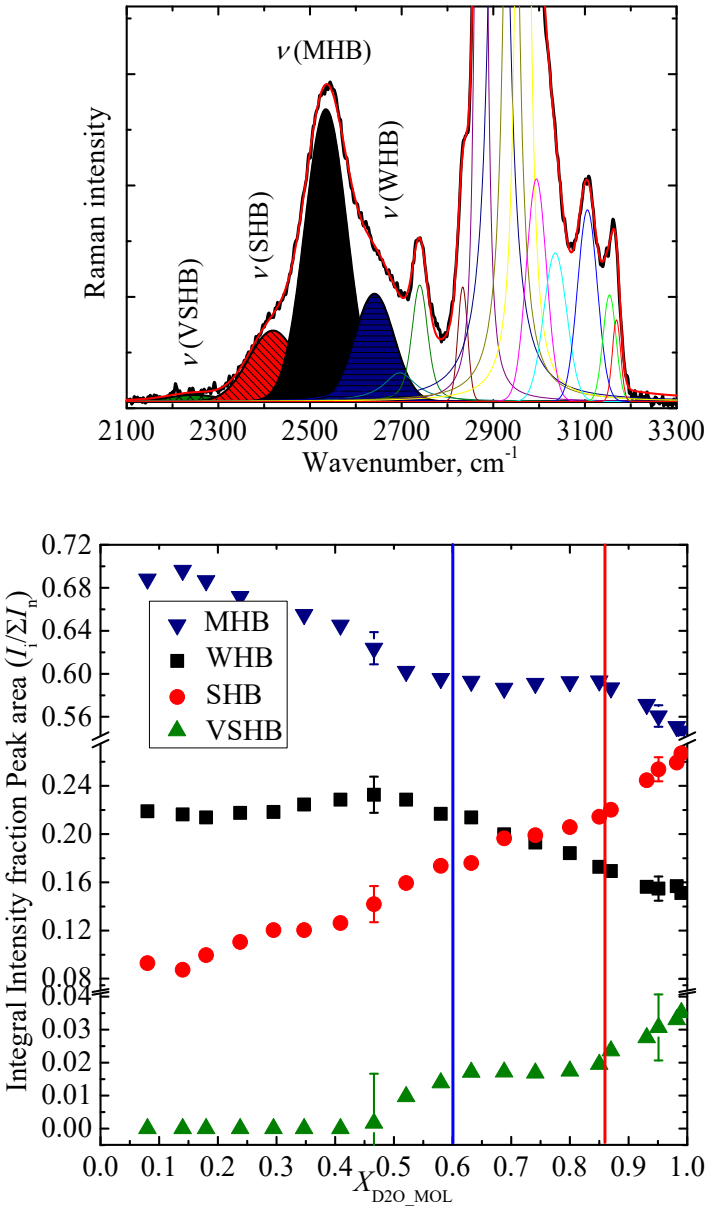

Figure 3.3.12. A: Black line – Raman spectrum of $[C_4mim]NO_3$–D_2O mixture at X_{D2O_MOL}=0.87. Red line – relative fit and spectral Region 3 deconvolution to four OD bands listed in Table 3.3.2. B: Integral intensity ratio between Raman bands assigned to water molecules organized in all types of clusters and the total self-aggregated water plotted against molar water content X_{D2O_MOL}. Crossover points marked by blue and red lines correspond to the lower and upper boarders of "water pocket" formation.

The distribution of Raman bans assigned to the vibrations of heavy water molecules may be related to the various structures of the surrounding environment in IL–D_2O mixtures. Higher red shift of OD stretching mode represents stronger intermolecular network formed from water molecules interacting with H-bonds. Of course, the accurate assignment of water and heavy water vibrational modes remains an actual topic as various ILs–D_2O mixtures shows different Raman bands distribution in spectral Region 3. Raman spectral band assignments were made from the previous works Raman and IR spectra analysis [98,149,167–170].

The first insight to the Raman spectra in D_2O shows three typical bands centered at around 2400 cm^{-1}, 2525 cm^{-1} and 2643 cm^{-1} which could be assigned to the different local hydrogen bonding (HB) environments. The band at lowest frequency (ν2400) was assigned to the OD stretching vibrations of water molecules within the different kinds of tetrahedral H-bonded network, the similar OH stretching band was called network water [NW] [72]. In explanation of our results it was called (i) strongly hydrogen bonded water band (νSHB) [148]. In quenched samples this band showed the highest symmetry of all OD stretching vibration bands (see Figure 3.3.14) and was assigned to the highest order of water structure. Another Raman band (ν2525) was assigned to the OD stretching vibrations of water molecules within highly asymmetric single donor (SD) hydrogen bonding configuration or distorted tetrahedral H-bonded network (in the similarity with OH band called intermediate water [IW]). In our experiment it was called (ii) medium hydrogen bonded water band (νMHB) [148]. And finally the highest frequency band (ν2643) could be assigned to the vibrations of free OD groups or free water molecules without any hydrogen bonded groups. These molecules are close to ones found in the vapor phase (in the similarity with OH band called multimer water [MW]). In our experiment it was called (iii) weakly hydrogen bonded water band (νWHB) [148]. The similar OH stretching bands assignment was found analyzing the dependence of water dynamics upon confinement size using IR spectroscopy of micellar solutions [149]. One more OD stretching band at the low frequency shoulder at 2260 cm^{-1} was reported as very strong hydrogen bonded water (VSHB) [148] in quenched mixtures. To verify the assignment of this band the low temperature measurements were performed and will be discussed later.

The integral intensities of all Raman O–D stretching bands were processed and the changes in relative integral intensities were identified in Figure 3.3.12. part B. It was noted that all previously mentioned structures of water molecules should be found in confinement called “water pocket” which was

formed in the system $[C_4mim]NO_3$–D_2O water rich regions ($0.7<X_{D2O\_MOL}<0.94$) [46,171].

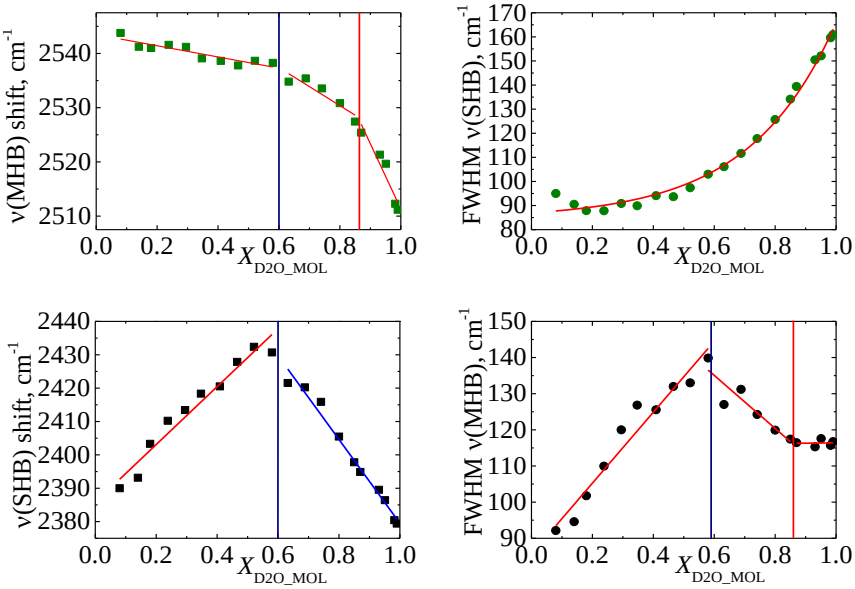

Figure 3.3.13. The Raman shift of *v*MHB (upper left) and *v*SHB (lower left) plotted as a function of the D_2O molar fraction in the $[C_4mim]NO_3$–D_2O mixtures. The FWHM for Raman bands *v*MHB (upper right) and *v*SHB (lower right) plotted as a function of the D_2O molar fraction in the $[C_4mim]NO_3$–D_2O mixtures. Crossover points in all cases marked by blue and red lines correspond to the lower and upper boarders of "water pocket" formation.

To understand the dynamics of water molecule structures formed in the "water pocket" two lines marking the discontinuities of most intensive band *v*MHB relative integral intensity change was added. The boarders of "water pocket" formation were set in figure 3.3.12. part B. The lower boarder at $X_{D2O\_MOL}=0.6$ was depicted as the blue and upper one at $X_{D2O\_MOL}=0.86$ as the red lines. The stable relative integral intensity of *v*MHB band in this concentration region proposed that amount of water molecules involved in distorted water network with anions did not change in "water pocket". To identifying fingerprints of "water pocket" formation other bands OD stretching bands behavior should be analyzed as primary processes. Discontinuities in concentration dependencies of OD stretching bands relative integral intensities could indicate the dynamic processes in the water confinements called "water pockets". The *v*MHB and *v*VSHB bands relative integral intensities did not change in the region where water was confined, but the clear decrease in integral intensity was registered of the band *v*WHB while

at the concentration region *v*SHB band integral intensity increased. This outcome was considered as a regroup of sporadic water molecules from the isolated ones to highly ordered water structures and well fitted with model suggested by MD simulations [22]. The "water pocket" formation boarders identified on *v*MHB band relative integral intensity change could be used as spectral evidences of water confinements in IL.

It was also noted that all three bands *v*SHB, *v*MHB and *v*WHB had a different concentration dependencies of Raman shift during the $[C_4mim]NO_3$ dilution with D_2O. The *v*WHB band Raman shift was constant 2643±3 cm^{-1} and did not change much in whole concentration range. The different situation with *v*MHB and *v*SHB was found and depicted in Figure 3.3.13. The *v*MHB band totally blue shifted by 32 cm^{-1} from 2544 to 2511 cm^{-1} and this shift as well as the relative integral intensity distribution of O–D stretching band was discontinuous. Two discontinuities, at the same concentrations as previously, were identified monitoring the Raman band assigned to different water clusters shifts. The extent of "water pocket" formation was also set in Figure 3.3.13. adding boarders as a line at X_{D2O_MOL}=0.6 (lower, blue line) and at X_{D2O_MOL}=0.86 (upper, red line). The distribution of *v*SHB band parameters was slightly different from *v*MHB and *v*SHB. The band totally was red shifted only by 10 cm^{-1} from 2390 to 2380 cm^{-1}. But the distinct crossover point in a band shift at X_{D2O_MOL}=0.6 was registered. At the water concentration range $0<X_{D2O\_MOL}<0.6$ the band blue shifted by 42 cm^{-1} from 2390 to 2432 cm^{-1} and at the water concentration range $0.6<X_{D2O\_MOL}<0.999$ the red shift from 2432 to 2380 by 48 cm^{-1} was found (Figure 3.3.13. lower part left). As a comparison the constant relative integral intensity increase of *v*SHB was registered in all mixture concentrations. Multiple water molecules interactions with IL and other water molecules were indicated at different concentrations in mixtures. The blue shift in mixtures when water concentration was increased from X_{D2O_MOL}=0 to X_{D2O_MOL}=0.6 represented the destruction of highly ordered water structures. Water···water aggregates was changed by the anion···water···anion complexes. Different view was found for the system when water concentration was increased from X_{D2O_MOL}=0.6 to X_{D2O_MOL}=0.999. The red shift showed the increase of H-bond strength. Stronger H-bond was associated with closer water···water interactions in pockets when the intermolecular interaction changed from anion···water···anion to water···anion···water. Moreover, the same discontinuities in concentration dependencies were registered for the Raman band parameter FWHM (see in Figure 3.3.13. lower part right). The increase in FWHM from 90 to 115 cm^{-1} with crossover point 140 cm^{-1} at 0.6 molar D_2O fraction was registered and supported our previous results.

One more band for OD stretching fit was found when the low temperature Raman experiment with different laser polarization was performed for various $[C_4mim]NO_3$–D_2O concentrations and neat D_2O. The low frequency (at around 2250 cm^{-1}) shoulder was reported as VSHB [172] which was hardly seen in Raman spectra at room temperature of $[C_4mim]$–D_2O mixtures without formed "water pocket". During the fitting this band was involved to our procedure, but the relative integral intensity of this band was only up to 0.035 counting to all OD stretching bands and deeper analysis of this band was not performed. Worth to mention, that VSHB band was totally depolarized at low temperature measurements see the band at around 2260 cm^{-1} in Figure 3.3.14. Furthermore, both VSHB and SHB bands were not found bellow "water pocket" concentration boarder at X_{D2O_MOL}=0.48 (red line) see Figure 3.3.14 vibrational bands at 2300 and 2260 cm^{-1}.

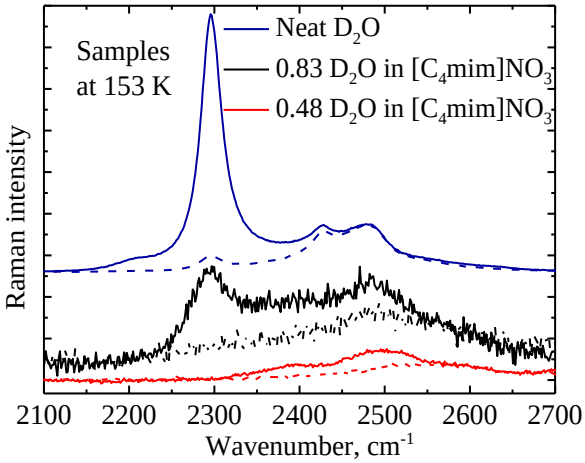

Figure 3.3.14. Raman spectra of $[C_4mim]NO_3$–D_2O mixtures at different D_2O molar ratio registered with different polarization at 153K. Sloid line spectra VV and dash lined spectra VH polarization. From the top to the bottom X_{D2O_MOL}=1 (neat D_2O blue), X_{D2O_MOL}=0.83 (black) and X_{D2O_MOL}=0.43 (red).

Conformational equilibrium changes (Region 1)

Conformational equilibrium of the $[C_4mim]^+$ cation (Figure 3.3.15.) was investigated monitoring the combination of the ring deformation and the CH_2 rocking bands [140] in the same way as in the paragraph 3.3.1. Two Raman bands assigned to the vibrations of *gauche* at lower frequency (601 cm^{-1}) and *trans* (624 cm^{-1}) conformers were investigated considering the relative integral intensity ratio of these Raman bands. The discontinuous change in

I_{gauche}/I_{trans} ratio with addition of water in IL–H_2O mixtures was discussed in paragraph 3.3.1. For the current experiment the anomalous conformational changes were obtained in [C_4mim]NO_3–D_2O mixtures too. Similar concentration dependencies of I_{gauche}/I_{trans} ratio and discontinuities with crossover point at X_{D2O_MOL}=0.84 was noticed in [C_4mim]NO_3–D_2O and [C_4mim]NO_3–H_2O mixtures. The constant I_{gauche}/I_{trans} ratio at low water concentrations X_{D2O_MOL}<0.84 confirmed the hypothesis that water molecules do not interact with cation tails at low water concentrations and the I_{gauche}/I_{trans} ratio could not show the beginning of "water pocket" formation. Differently, for higher water concentrations, when the crossover point at approximate X_{D2O_MOL}=0.84 was passed, the increase of I_{gauche}/I_{trans} ratio from 1.6 to 3.5 was registered. At these concentrations IL molecules were losing the molecular packing, because of IL solvation with the localized water ponds "water pockets".

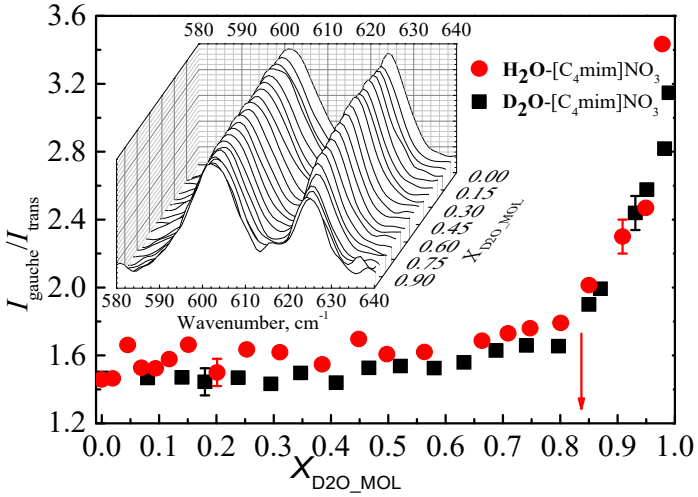

Figure 3.3.15. Area ratio between the *gauche* and *trans* peaks with of [C_4mim]NO_3–H_2O (red dots) and [C_4mim]NO_3–D_2O (black squares) plotted as a function of the D_2O molar fraction in the mixtures. In the inset Raman spectra of [C_4mim]NO_3–D_2O mixtures at different water concentrations in spectral Region 1. Crossover point marked by red arrow corresponds to the upper boarder of "water pocket" formation.

The upper boarder of "water pocket" formation could be determined. The increase of "water pockets" size caused the merge of them and bulk water formation in whole sample. Our assumption very well agree with similar behavior earlier reported for [C_8mim]NO_3–H_2O samples [22].

Summarizing, the water clusterization process „water pockets“ was observed using Raman spectroscopy. Some of Raman band parameters were changing with added D_2O in ionic liquid $[C_4mim]NO_3$ and D_2O mixtures. Discontinuities in concentration dependences of these parameters were found and let to determine the beginning and the end of the “water pocket” formation. The extent of “water pocket” formation was measured to be at 0.6÷0.86 D_2O molar fraction. This result well correlated to the values found using other (SANS, SAXS and DSC) methods at 0.7÷0.95 D_2O molar ratio. The extent of “water pocket” remained the same, only the constant shift to lower concentrations region was registered in our experiment. This shift could be explained as a result of various delays (SANS, SAXS, DSC and Raman) in dynamic response detection.

The Raman shifts, relative integral intensities and FWHM were found to be sensitive to added D_2O content. Discontinuities in concentration dependences of vibrational band parameters were found for NO_3^- stretching, NO_3^- bending and different water clusters OD stretching modes. These discontinuities were considered as the indication of the “water pocket” formation beginning (lower boarder). Furthermore, discontinuous concentration dependences of previously mentioned vibrational band parameters was found for imidazolium ring stretching modes at C(2)–H, C(4,5)–H asymmetric and C(4,5)–H symmetric stretching vibration modes as well as different water clusters OD stretching modes parameters. Also, the changes of integral intensities ratio of Raman vibration bands corresponding to *gauche* and *trans* conformers was registered in the same concentration region. All these discontinuities in concentration dependences were indicated as the “water pocket” formation end (upper boarder).

The change in Raman spectral parameters which could prove the deuteration in $[C_4mim]NO_3$–D_2O mixtures was not found. Imidazolium ring stretching mode C(2)–H behavior was monitored at different D_2O concentrations in mixtures and C(2)-D vibration formations was not happening. Other suggested method to check for the H/D exchange was monitoring the integral intensities ratio of Raman bands corresponding to vibrations of *gauche* and *trans* conformers. Using this method, we found that distribution *gauche* and *trans* bands ratio is the same in $[C_4mim]NO_3$–D_2O mixtures and $[C_4mim]NO_3$–H_2O mixtures. This could prove that deuteration is not happening in $[C_4mim]NO_3$ and D_2O mixtures.

Low temperature and different polarization measurements of $[C_4mim]NO_3$–D_2O Raman spectra at different D_2O content let to ascertain the precise OD stretching band assignment to the very strong, strong, medium and weakly hydrogen bonded water Raman bands[47].

3.3.4. Summary of 3.3.

The *gauche* (GT) conformer preference was determined for a short chain ionic liquids ($[C_4mim]^+$) in conformational equilibrium. The impact of anion radius as well as the anion hydrophobicity to conformations was found for spherical and non-spherical anions based ionic liquids. The lower anion hydrophobicity, the greater preference for *trans* conformers was determined and anions were aligned in following order: I^-> Br^-> Cl^-> OTf^-> NO_3^-> BF_4^- . It was determined that water also changes the ionic liquids conformational equilibrium.

The lower boarder of „water pockets“ formation process at X_{H2O_MOL}=0.60±0.04 in $[C_4mim]NO_3$–D_2O mixtures was determined by the discontinuous spectral changes observed for NO_3^- stretching and bending modes as well as for different water clusters vibrations.

The upper boarder of “water pockets” formation process X_{H2O_MOL}=0.86±0.04 was found from discontinuities in concentration dependencies of imidazolium ring stretching mode and different water clusters vibrations. The conformational equilibrium ratio I_{gauche}/I_{trans} increase was observed at the same D_2O concentration which was assigned to the upper boarder of “water pockets” formation.

The dynamics of H/D exchange in IL–D_2O mixtures was studied using Raman spectroscopy and investigating bands assigned to the imidazolium ring vibrations involving C(2)–H stretching mode. It was determined, that H/D exchange reaction is influenced by anion type, sample purity and temperature as well as water aggregations and structures formed in IL–D_2O mixture. The H-bond between anions and cations are suppressed by water molecules creating H-bonded aggregates *anion···water* and *cation···water*.

In IL–D_2O mixtures anion type and cation localization have the greatest influence on H/D exchange reactions. It was found that the exchange of H/D occurs in ionic liquids composed of both long and short alkyl chains and halogen anions (I^-,Br^-, Cl^-) that form hydrogen bonds on the imidazolium ring plane. In ionic liquids composed of non-spherical anions (OTf^-; NO_3^-; BF_4^-) and short alkyl chains H/D exchange was not set. The concept of simultaneous conformational changes and H/D exchange processes in both long chain ($[C_{10}mim]$) and chort chain ($[C_4mim]$) imidazolium-based ILs was not approved

3.4. Liquid Crystalline ionogel phase formation in long chain ionic liquids and water mixtures

Previous section was finished analyzing the formation of water confinement in short chain cation-based [C_4mim]NO_3–D_2O mixtures and how Raman spectroscopy could help us identify "water pocket" formation. In this section long chain cation based ILs [C_{10}mim]Cl and [C_{10}mim]Br and their mixtures with water was analyzed to obtain boundaries of Liquid Crystalline ionogel phase formation by discontinuous changes of Raman spectral parameters. No application of vibrational spectroscopy was utilized for such cases before, while NMR, SANS and SAXS techniques continuously improve their methodology for phase formation separation. The lack of systematic investigations using Raman and IR experiments in this field could be related to the experimental difficulties while preparing and registering spectra of complex mixtures with separate phases.

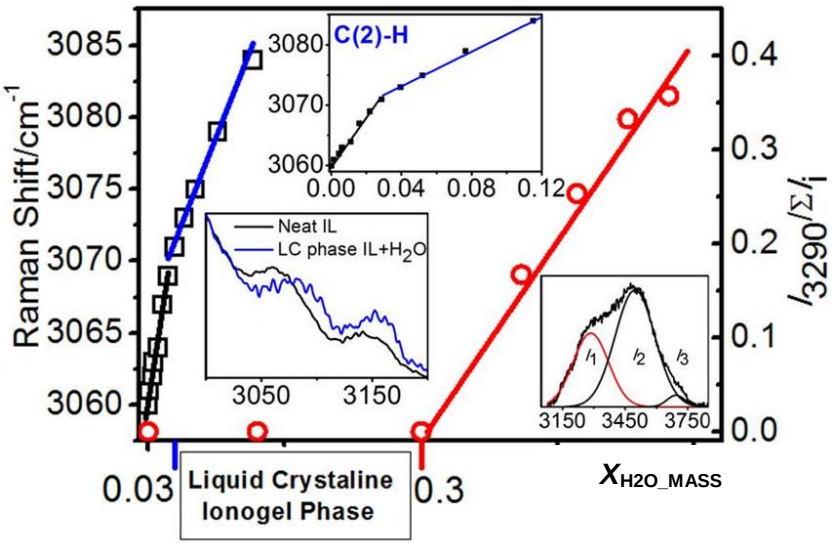

Figure 3.4.1. The extent of LC ionogel phase formation. Boundaries were discovered using Raman spectroscopy. The lower boarder fingerprint of liquid crystalline ionogel phase formation is marked blue and upper boarder is marked red lines.

In the Overview section the variety of H-bond based structures formed in IL and water mixtures were discussed. The lamellar (L_a) and the hexagonal (H_1) phases were precisely determined for [C_{12}mim]Br–H_2O mixtures [80]. For the [C_{10}mim]Br–H_2O mixtures viscous, nanostructured, lamellar gel phase was determined and called "ionogel" [71,78]. The variety of methods were

used to study liquid crystalline phases and heterogeneities formation in both neat ionic liquids and IL–H_2O mixtures [22,38–43]. As the main vibrations of IL–H_2O mixtures involved in to interactions C(2)–H, C(4)–H and C(5)–H earlier were studied for various ILs by vibrational spectroscopy techniques solving a broad variety of structuring problems [71–73,114,173]. But only our experimental results provided the combined investigation of ionogel formation related molecular vibrations of [C_{10}mim]Cl and [C_{10}mim]Br which was not investigated before.

3.4.1. LC phase effect to imidazolium ring C–H vibrations

For the [C_{10}mim]Cl and [C_{10}mim]Br in IL–H_2O mixtures the phase change from thick liquid into hardened gel was registered at about X_{H2O_MASS}=0.03±0.005. Firstly, the phase transition was noticed by eye and by the difficulties raised when mixing the samples. The exact transition boarder was determined form the Raman spectral changes of IL–H_2O mixtures. Some experimental difficulties were caused by ionogel formation and the challenge to prepare the homogenous sample, which was solved with the usage of mechanical and ultrasound mixing techniques. Ionogel was found to be stable over range the range of $0.05<X_{H2O\_\ MASS}<0.4$ for both investigated [C_{10}mim]Br–H_2O and [C_{10}mim]Cl–H_2O mixtures [36].

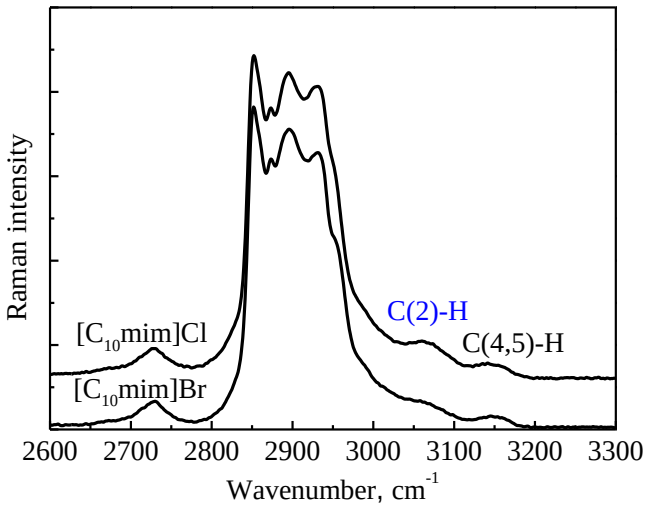

Figure 3.4.2. Raman spectra of neat [C_{10}mim]Cl and [C_{10}mim]Br ILs in C–H vibrations region.

In order to check the anion influence for the ionogel phase formation in long chain ionic liquids, IL–H_2O samples with different water content were prepared and investigated. LC ionogel phase formation and the strength of the cation-anion interactions through H-bonding was investigated monitoring the Raman shift of Raman bands assigned to the $[C_{10}mim]^+$ cation C(n)–H stretching vibrational modes at imidazolium ring carbon positions n=2, 4, 5 [93]. Raman spectra of neat $[C_{10}mim]Br$ and $[C_{10}mim]Cl$ in the spectral region 2500-3300 cm^{-1} is depicted in Figure 3.4.2.

Earlier studies resolved Raman bands structure of ILs which have similar structure properties to the $[C_{10}mim]Cl$ and $[C_{10}mim]Br$ [140,150]. It was quite common to decompose broad vibrational bands in C–H region into two components [174]. The wavenumber correlation with our experimental data was found and vibrational band assignments were made. Raman band at around 3080 cm^{-1} was assigned to the vibrational mode ν(C(2)–H) and Raman band at around 3150 cm^{-1} to the vibrational mode ν(C(4,5)–H) (details in Table 3.4.1.).

Table 3.4.1. Raman spectral bands assignments in C–H stretching region registered for ILs with different cation chain length.

Ionic liquids	$[C_6mim]Cl$	$[C_8mim]Cl$	$[C_{10}mim]Cl$	$[C_{10}mim]Br$
Band assignment	Wavenumber, cm^{-1}			
ν(C(2)–H) stretching	3062±1	3070±1	3043±1	3060±1
ν(C(4,5)–H) stretching	3142±2	3143±1	3147±1	3144±1
Reference	Experiment [140]	Experiment [150]	This experiment	This experiment

Changes in wavenumber were observed for these bands due to addition of water in IL–H_2O mixtures (Figure 3.4.3.). According to the literature, the hydrogen bond formation involving aromatic C–H on the imidazolium ring was classified as the red shift of H-bond [158,175]. The data of Raman band shift assigned to ν(C(2)–H) and ν(C(4,5)–H) imidazolium ring stretching modes at various water concentrations of IL–H_2O mixtures were depicted in Figure 3.4.4. When the water content in the mixtures were changed from X_{H2O_MASS}=0 to X_{H2O_MASS}=0.12 not the red shift, but the blue shift of corresponding Raman bands was registered. The indication of the weakening of the C–H···*anion* hydrogen bond was registered.

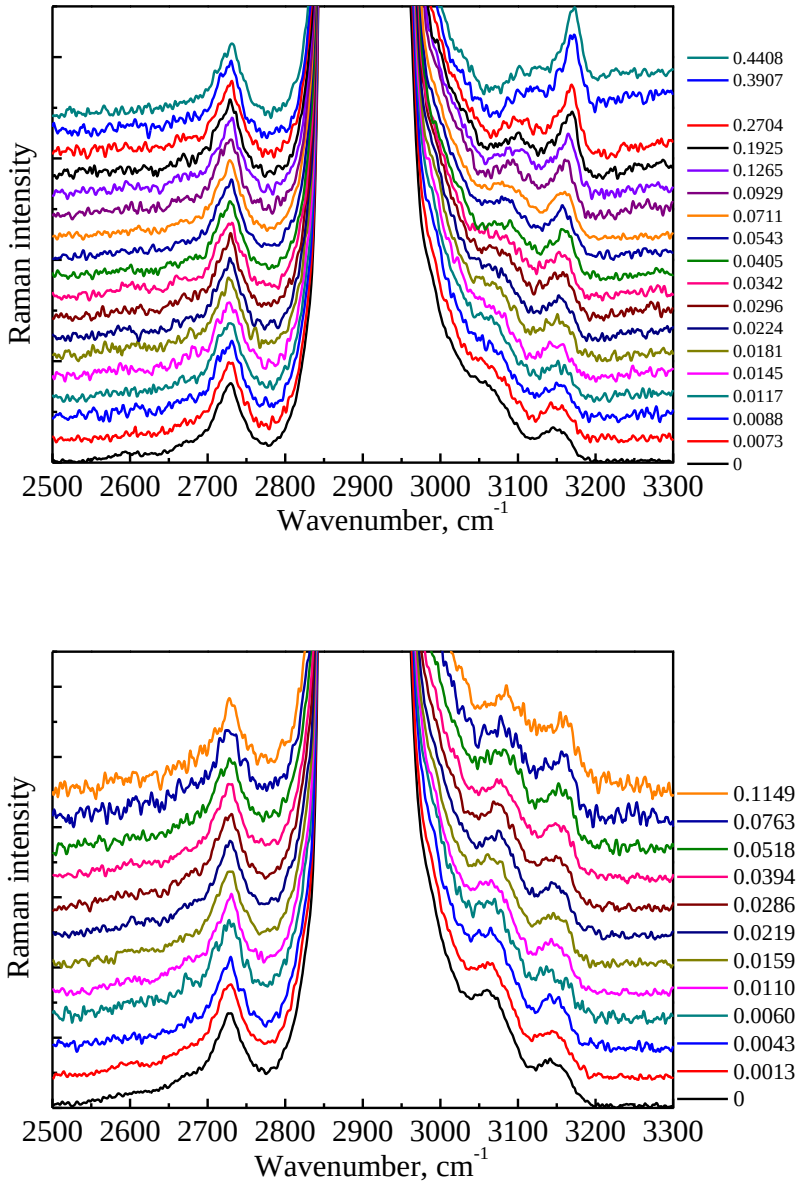

Figure 3.4.3. Raman spectra of [C_{10}mim]Cl–water (upper) and [C_{10}mim]Br–water mixtures with different water mass concentration. Water concentration values are listed in right side insert.

Regular disorganization of H-bonds was perturbed at X_{H2O_MASS}=0.03 for [C_{10}mim]Cl and X_{H2O_MASS}=0.03 for [C_{10}mim]Br (Figure 3.4.4.). The

discontinuities in concentration dependencies was explained by the change of the mobility in IL–H_2O mixtures when the mixture phase changed from thick liquid into hardened gel.

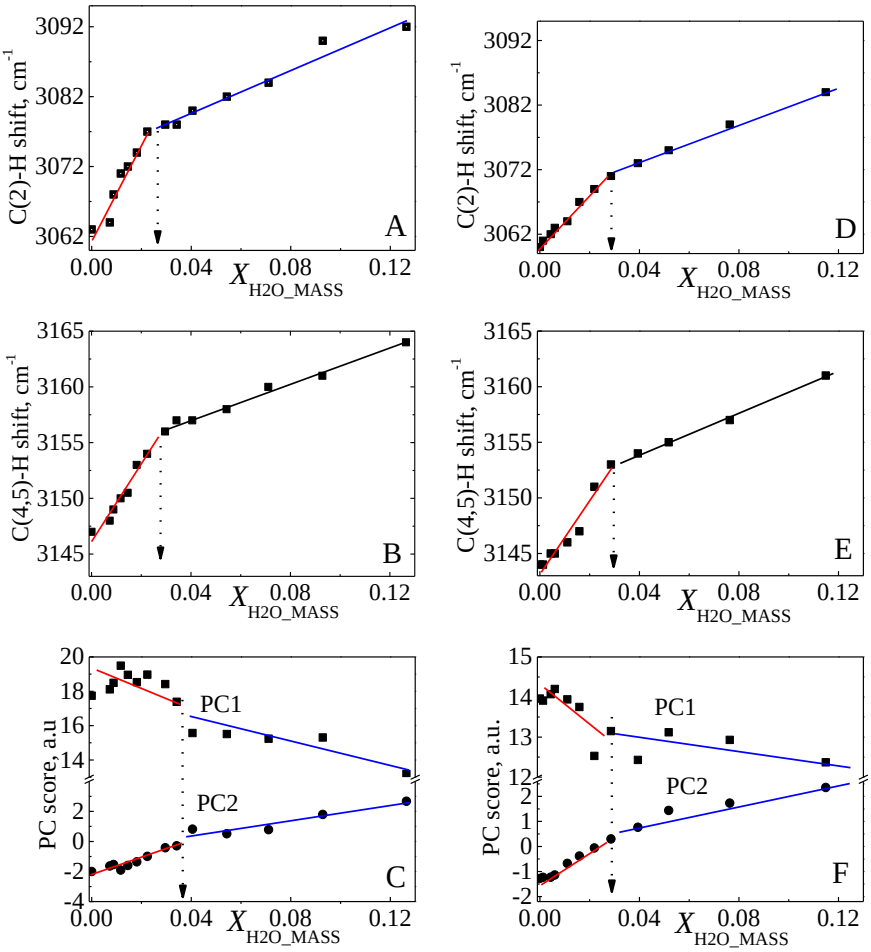

Figure 3.4.4. Determination of LC ionogel phase lower boarder formation in [C_{10}mim]Cl–H_2O (A,B,C) and [C_{10}mim]Cl–H_2O (D,E,F) mixtures. Discontinuous concentration dependencies of the Raman vibrational modes *v*(C(2)–H) (A,D) and *v*(C(4,5)–H) (B,E) shifts as well as the scores of the first and second PCs (C,F).

Our experimental results and previous studies suggested that gelation arises from diminution of hydrogen bonding between the imidazolium ring and the anion (bromide, chloride) as well as the concomitant formation of an H-bonded network comprising water molecules, anion and the imidazolium cation [36,71]. The discontinuity in concentration dependencies of Raman

blue shift at water concentration value X_{H2O_MASS}=0.03 was used as the spectral fingerprint for lower boarder of the liquid crystalline ionogel phase formation. The value btained in our experiment strongly correlates with the LC ionogel phase concentration of [C_{10}mim]Br–H_2O mixtures (X_{H2O_MASS}=0.05) detected by SAXS, DSC and polarized microscopy [71].

The different Raman shift behavior of the C(4,5)–H and the C(2)–H bands indicated that forming the liquid crystalline ionogel phase water molecules mediated hydrogen bonds with the ring protons and anions differently (more details in Table 3.4.2.). Very large blue shift of the C(2)–H band represented the higher imidazolium ring proton-water interactions as the consequence of ionic dissociation.

This can be attributed to the stronger hydrogen bond formation of the *C(2)–H···anion* than that of the *C(4,5)–H···anion*. Our results correlate with hydrogen bond network strength measurements using CARS [154]. Moreover it was found that the degree of heterogeneity for investigated systems [C_{10}mim]Cl–H_2O ir [C_{10}mim]Br–H_2O were not influenced by the anion type. Only temperature and water content was able to change the heterogeneity of mixture [80].

Table 3.4.2. Raman shift at specific X_{H2O_MASS} concentrations in IL–H_2O mixtures registered for different modes assigned to the imidazolium ring vibrations.

Water content X_{H2O_MASS}	0		0.03		0.12	
[C_{10}mim]Cl–H_2O		$\Delta\upsilon_{0\text{-}0.03}$		$\Delta\upsilon_{0.03\text{-}0.09}$		$\Delta\upsilon_{0\text{-}0.12}$
υ(C(2)–H), cm^{-1}	3062 ±1	16±2	3078 ±1	13±2	3091 ±1	29±2
υ(C(4,5)–H), cm^{-1}	3147 ±1	9±2	3156 ±1	7±2	3163 ±1	16±2
[C_{10}mim]Br–H_2O		$\Delta\upsilon_{0\text{-}0.03}$		$\Delta\upsilon_{0.06\text{-}0.09}$		$\Delta\upsilon_{0\text{-}0.12}$
υ(C(2)–H), cm^{-1}	3060 ±1	11±2	3071 ±1	13±2	3084 ±1	24±2
υ(C(4,5)–H), cm^{-1}	3144 ±1	9±2	3153 ±1	8±2	3161 ±1	17±2

The mathematical spectra analysis was also performed for the spectral results using 2DCOS and PCA methods. Mathematical analysis and fitting procedure results were compared (Figure 3.4.4).

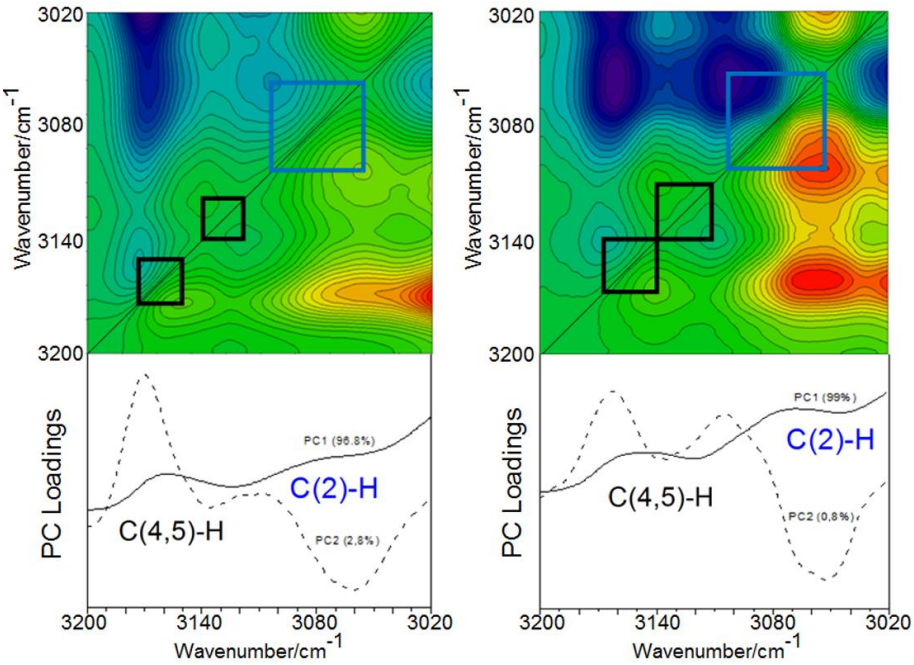

Figure 3.4.5. 2D Raman asynchronous correlation spectra in the contour plotting (up) and loadings on the first and second principal components (down); in [C_{10}mim]Cl–H_2O on the left and in [C_{10}mim]Br–H_2O on the right.

It was found that first two Principal Components practically captured the total amount of variation in the Raman spectra range of 3000-3200 cm^{-1}. [C_{10}mim]Cl ~96.8% (PC1) and ~2.8% (PC2) and for [C_{10}mim]Br ~99% (PC1) and ~0.8% (PC2) was calculated respectively (Figure 3.4.5. lower part left and right). For both studied ionic liquids the scores for the third PC (<0.1%) looked like noise and therefore PC3 was further not analyzed. The results obtained for PC1 and PC2 scores concentration dependence (Figure 3.3.4 C, F parts) strongly correlate with blue shift results of corresponding C(2)–H, C(4,5)–H Raman bands. The lower boarder of liquid crystalline ionogel formation was indicated at the same point as other studies obtained [4]. The results of 2DCOS analysis of Raman spectra of [C_{10}mim]Cl–H_2O and [C_{10}mim]Br–H_2O mixtures were shown in Figure 3.4.5 (upper part). 2DCOS Raman results very well correlated with the data obtained using standard Lorentzian band shape approach and the nonlinear curve fitting procedure. More fine structure of the bands envelope at the 3000-3200 cm^{-1} was resolved in the loadings of the principal components as well as in the asynchronous two-dimensional maps (Figure 3.4.5.). Namely, the six cross-peaks were assigned to the three Raman vibrational modes shifts during the increase of water in IL–water mixtures.

Two cross-peaks (Figure 3.4.5., square in blue) show the shift of C(2)–H stretching mode at around 3100 cm^{-1}. Other four cross-peaks (squares in black) was assigned to the symmetric and asymmetric C(4,5)–H stretching vibration modes shifts to 3140 cm^{-1} and 3173 cm^{-1} for $[C_{10}mim]Cl–H_2O$ and to 3139 cm^{-1} and 3168 cm^{-1} for $[C_{10}mim]Br–H_2O$, respectively. Summarizing PCA provided clearly expressed discontinuous concentration changes and 2DCOS analysis helped to distinguish the number of Raman band in broad region.

3.4.2. OH band structure investigation

The upper boarder of liquid crystalline ionogel phase formation was determined by the analysis of OH stretching modes assigned to different water clusters vibrations in IL–H_2O mixtures [36].

The Raman spectra of 1-decyl-3-methyl-imidazolium bromide ($[C_{10}mim]Br$) aqueous solutions were measured while continuously increasing the water content in the system from X_{H2O_MASS}=0 to X_{H2O_MASS}=0.99. Principal component (PC) and 2D Raman correlation (2DCOS) analysis was carried out, the main attention concentrating to the region of O–H stretching vibrations at 3100–3800 cm^{-1}.

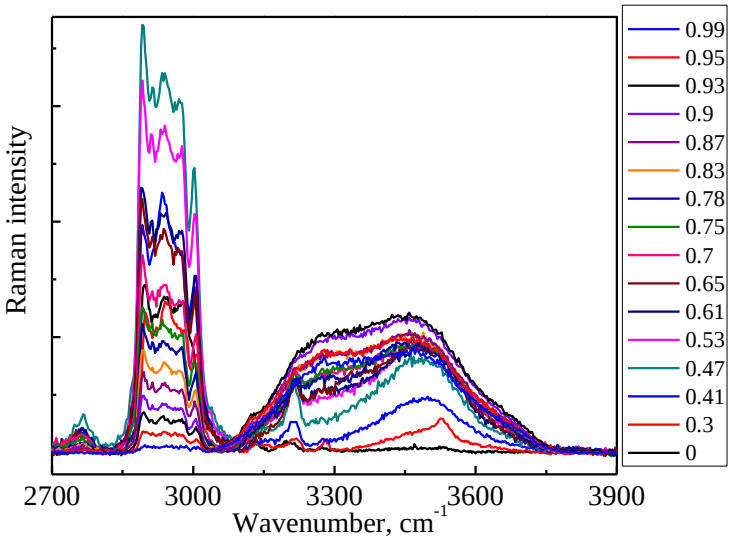

Figure 3.4.6. Raman spectra of $[C_{10}mim]Br$ aqueous solutions in the O–H and C–H stretching regions (3100-3800 and 2800-3100 cm^{-1}, respectively) with changing X_{H2O_MASS} concentration from 0.01 to 0.98.

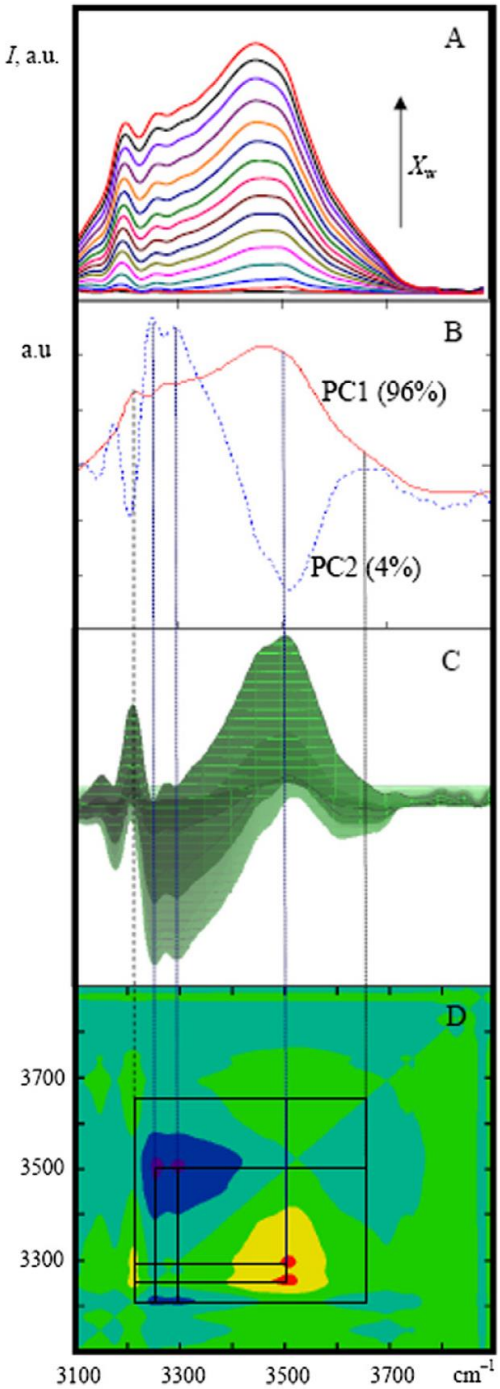

Fig. 3.4.7. Raman spectra of [C10mim][Br] aqueous solutions at different water concentrations (A); loadings on the first and second principal components (B); 2D Raman asynchronous correlation spectra in the surface (C) and contour plotting (D).

The band structure was resolved in the loadings on PC1and PC2 as well as in 2DCOS spectra. It indicates the presence in the studied system of several nonequivalent states of water. Various states of water were also revealed in the 1H NMR spectra. They were assigned to non-bonded or weakly H-bonded water molecules, those involved in the fast isotropic reorientation motion as well as in the H-bond exchange processes and finally – water in the LC ionogel structures. The borders of the liquid crystalline (LC) ionogel phase was determined using the concentration dependence of the integral intensities of Raman bands and the scores on PC1.

In the present work these techniques were applied on the Raman spectra. The dynamic spectra for 2D correlation analysis were constructed using the spectral intensity variation upon external perturbation [120,176]. As an external stimulus can be any reasonable measure of a physical quantity, such as mechanical deformation, temperature, or concentration.

The number of the statistically significant principal components was evaluated using the argument of physical changes and on deterministic variation proposed in [115]. It was found that first two PCs capture practically total amount of variation in the Raman spectra in the range of 3100-3900 cm^{-1} upon dilution, ~ 96% (PC1) and <4 % (PC2), respectively (Figure 3.4.7. A, B). The scores for the third PC (< 1 %) looked like a noise and therefore PC3 was further not analyzed. The results of 2DCOS analysis of Raman spectra of $[C_{10}mim]Br–H_2O$ mixtures was depicted in Figure 3.4.7. parts C and D. It was quite common to decompose this complex and very broad spectral contour into 3 components. According to different authors (terminologies in brackets) these Raman bands were recognized at 3220-3330 cm^{-1} (H_2O molecules involved in more regular structures of fairly unstrained H-bonds, the "ice-like" peak, "network water", SHB); 3400-3560 cm^{-1} (water molecules trapped into more irregular structures with energetically unfavorable H-bonds, the "liquid-like" peak, "intermediate water", MHB) and ~3600 cm^{-1} (H_2O monomers, non-H-bonded, weakly H-bonded OH groups or WHB). These peaks can be quite easily extracted from the νO–H contours also in the present case of $[C_{10}mim]Br–H_2O$ mixtures (Figure 3.4.6.) using standard Gaussian band shape approach and the nonlinear curve fitting procedure. However, the PCA and 2D correlation analysis allowed getting into more details. The Raman bands below ~3200 cm^{-1} are originated from the imidazolium ring C–H stretching and other νC–H modes of IL [12]. More fine structure of the band envelope at 3220-3510 cm^{-1} was resolved in the loadings of the principal components as well as in the asynchronous 2D maps (Figure 3.4.7.). Namely, the cross-peaks at 3220, 3260, 3290 3510 and 3690 cm^{-1} indicated that various

nonequivalent states of water are very likely in [C_{10}mim]Br–H_2O mixtures. These states may appear from several origins. The attribution of the bands at 3690 and 3501 cm^{-1} to non-H-bonded or weakly H-bonded OH groups and, where water molecules were found located mainly in the periphery of the polar core of the micro emulsion droplets. The broad intensive band at 3290 cm^{-1} can be attributed to the 'ice-like' or 'network water'. Two other peaks at 3220 and 3260 cm^{-1} can be assigned to water molecules very tightly bonded to IL (in previous section called VSHB). Note two nonequivalent sites (two potential minima on the energy surface) placing water surround Br^- ion in [C_{10}mim]Br was found by quantum chemistry calculations [27]. The cross correlation of these peaks in 2D Raman spectrum with that at 3690 cm^{-1}, i.e. H_2O monomers, indicates that the population of these states goes via interacting monomeric water with IL species (Figure 3D). These states should be energetically more favorable than in the regular "network water". Moreover, these peaks can be detected in the Raman spectra of [C_{10}mim]Br–water solutions at very low concentrations of water (X_{H2O_MASS}=0.01), or sometimes even in the "neat" ILs. In such cases water should be considered as a contaminant that cannot be removed from IL completely using standard drying methods. Thus the term "neat ionic liquid" looks then rather provisory and it should be used with a reservation. Some aspects of determination of the borders of LC ionogel phase using spectroscopy data should to be discussed. Thus the NMR chemical shifts of [C_{10}mim]Br are not suitable estimating the borders of the supposed mesophases [36]. The processing of Raman intensities of νO–H bands seems to be much powerful tool solving this problem. The scores on the first PC and the concentration dependence of the relative integral intensities of Raman bands of water allow to determine the borders of LC ionogel phase (Figure 3.4.8.). These quantities indeed highlight that water is getting drastic ordered in the concentration range $0.2<X_{H2O\_MASS}<0.5$. This range significantly overlapped with those [C_{10}mim]Br–H_2O mixtures ($0.05<X_{H2O\_MASS}<0.4$) where liquid crystalline behavior was detected by SAXS, DSC and polarized microscopy [71].

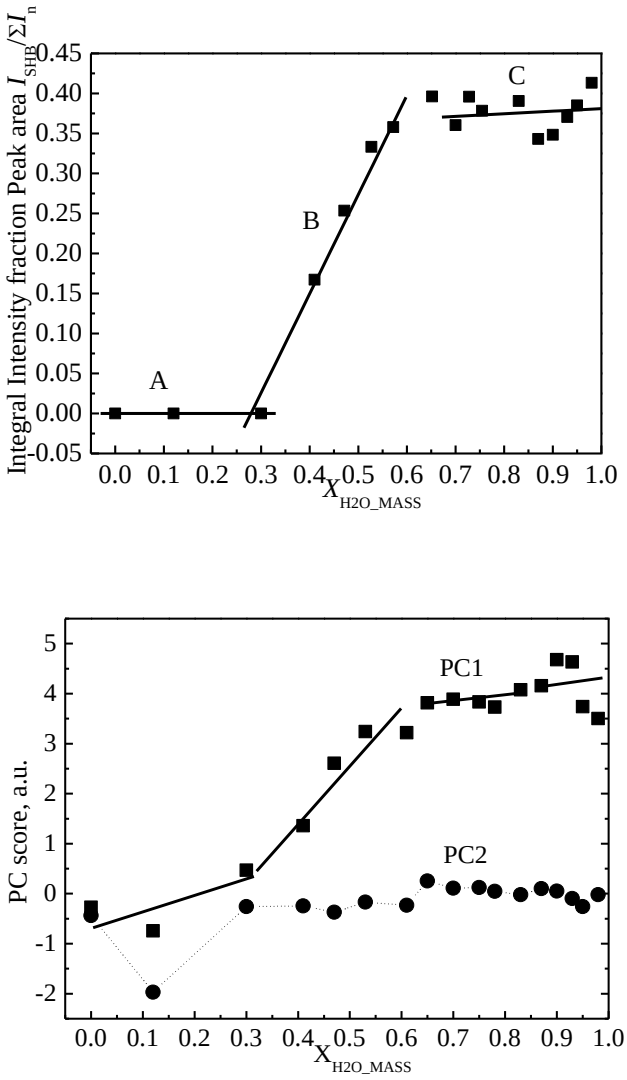

Figure 3.4.8. Determination of the borders of LC ionogel phase in $[C_{10}mim]Br–H_2O$ solution: from the concentration dependence of the integral intensity of overlapped Raman νOH bands of water (an insert) by nonlinear curve fitting (A); from the scores of the first and second PCs (B).

3.4.3. Summary of 3.4.

Raman spectra of $[C_{10}mim]Br–H_2O$ and $[C_{10}mim]Cl–H_2O$ mixtures was measured continuously increasing the water content X_{H2O_MASS} in the system (from $0<X_{H2O\_MASS}<0.99$). PCA and 2D Raman correlation analysis was carried out, the main attention concentrating to the region of C–H and O–H stretching vibrations. The presence of several nonequivalent states of water in the studied mixtures was indicated.

The discontinuous changes of the imidazolium ring Raman C–H stretching modes in the region 3000-3200 cm^{-1} and O–H stretching modes in the region 3100-3900 cm^{-1} spectral parameter shown different ionic liquid and water structural organization in IL–water mixtures. The information from these Raman spectral regions provided reliable method to determine the extent of liquid crystalline ionogel phase formation.

Discontinuous Raman shift change of imidazolium ring C–H stretching modes with crossover point at $X_{H2O\_MASS}=0.03\pm0.005$ is related to the decrease of anions mobility when LC crystalline phase is formed in $[C_{10}mim]Br–H_2O$ ir $[C_{10}mim]Cl–H_2O$ mixtures. This change was identified as a spectral evidence for the beginning (lower boarder) of LC crystalline phase formation. Anion type did not influence the onset of ionogel phase formation for both systems.

Discontinuous integral intensity changes of O–H stretching modes assigned to different clusters with crossover point at $X_{H2O\_MASS}=0.4\pm0.005$ is related to the change of interaction between IL and water molecules. The increase of vibrational band assigned to the strongly hydrogen bonded water clusters vibrations reveals the beginning of water clusters formation at the same time the end of LC ionogel phase formation.

The different imidazolium ring Raman shifts for C(2)–H, C(4)–H, C(5)–H vibrational modes and the result supports hypothesis that long chain ionic liquids and water molecules form weaker H bonds in position of C(4) and C(5) than in position C(2) with imidazolium ring. The results let to ascertain, that when water was added to ionic liquid it firstly interacts with anion forming hydrogen bonded network *anion*···H–O–H···*anion*.

3.5. Water states in mesoporous materials Hydroxyapatites

Raman results obtained in previous sections analyzing distinct water structures and mesophase formation in various IL–H_2O and IL–D_2O mixtures showed good agreement with other experimental techniques. For the solid hydroxyapatite samples the discussion in literature reveals that vibrational spectroscopy is also one of the most effective tool to estimate the degree of crystallinity, content of doped ions, bulk vs. surface effects [103–107]. This section was dedicated for the investigation of calcium hydroxyapatite samples newly synthesized via the sol-gel synthesis routes using various complexing agents.

3.5.1. Nanostructured and amorphous CaHAp's

The complementary data sets of newly synthesized materials were obtained using NMR, FTIR and Raman techniques. In this paragraph two newly synthesized CaHAp and commercially available samples were analyzed using FTIR spectroscopy. FTIR spectra were registered for the samples containing an amorphous phosphate phase (ACP-GL-CaHAp), nano-structured phosphate phase (TA-CaHAp), commercially available nano-structured hydroxyapatite (CA-CaHAp) and depicted in Figure 3.5.1.

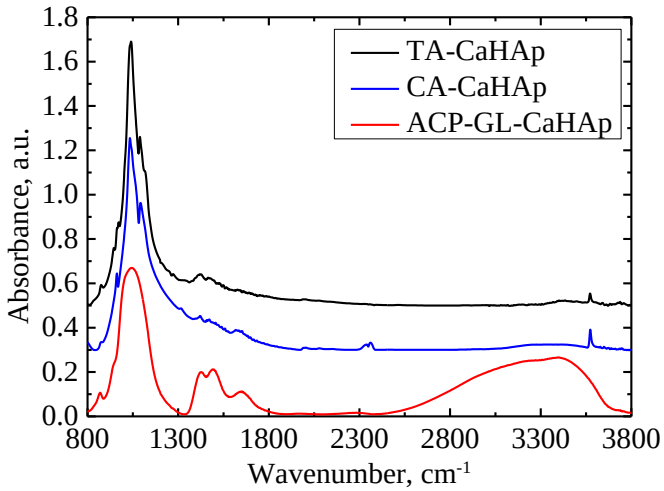

Figure 3.5.1. The comparison of FTIR spectra of calcium hydroxyapatite containing amorphous phosphate phase ACP-GL-CaHAp (red), nano-structured – TA-CaHAp(black) and commercially available hydroxyapatite CA-CaHAp (blue).

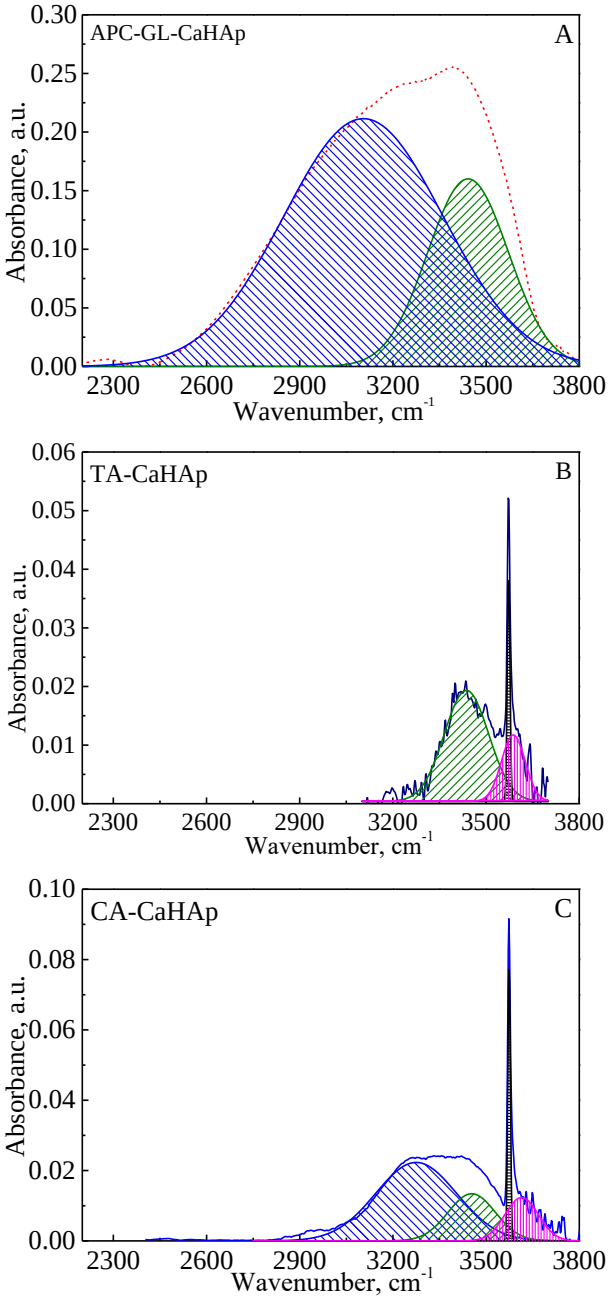

Figure 3.5.2. IR spectra of A: ACP-GL-CaHAp, B: TA-CaHAp and C: CA-CaHAp samples with the assignments of FTIR bands of different OH groups, which follows the reference [104].

Synthesis products were also characterized by scanning electron microscopy (SEM) and energy-dispersive X-ray analysis (EDX) using a

Helios NanoLab 650 scanning electron microscope coupled with an energy-dispersive X-ray spectrometry system. The XRD analysis have revealed that all CaHAps were composed of principal apatite crystalline phase. EDX study proved that additional calcium and phosphorous containing phases which are not detectable by XRD are present in the CaHAp samples (more details in appendix B, C, D) [44].

The most crucial factors that influence the fine details of structural organization in the products during the applied synthesis routes were not known. However, CaHAps was compared with respect to the presence of structural manifolds of hydroxyl groups by means FTIR spectroscopy (Figure 3.5.2.).

The relative content of –OH groups can be estimated comparing the broad FTIR peaks between 2500 and 3800 cm^{-1}. The amount of adsorbed water in both nano-structured CaHAp samples was so low that even the band of structural –OH groups was seen in the spectrum (peak at 3442 cm^{-1}, Figure 3.5.2 B and C, green contour). Similar feature was registered in the series of FTIR spectra of Mg^{2+} and CO_3^{2-} doped hydroxyapatites [104]. In the ACP-GL-CaHAp IR spectra the opposite situation was registered (Figure 3.5.2. A). The band at 3442 cm^{-1} even cannot be seen in the FTIR spectrum and thus it can be supposed that the amount of structural hydroxyl groups is practically negligible in comparison with adsorbed water, or they are even absent. Only detailed FTIR spectroscopy data confirm the presence of structural –OH groups in ACP-GL-CaHAp (Figure 3.5.2 A, green contour). The broad and complex-shaped νO–H contour at ~3200 cm^{-1} was decomposed in two strongly overlapped bands with maxima at 3442±2 cm^{-1} and 3110±4 cm^{-1}, respectively (Figure 3.5.2. A). The first one can be attributed to the stretching of structural O–H and compared with the band at 3438±2 cm^{-1} in nano structured CaHAp. The second band (3110 cm^{-1}) is originated from O–H stretching of water molecules in H-bond networks [177]. In the long chain ionic liquids and water mixtures this band was investigated as strong hydrogen bonded water molecules vibrations ν(SHB). Furthermore, the vibrational bands of OH bending mode at 1645 cm^{-1} was also present in the FTIR spectrum and its relative integral intensity was correlated with relative integral intensity of the adsorbed water ν(3110) vibrational mode. Hence the amount of adsorbed water in ACP-GL-CaHAp was high indeed. The integral intensity ratio of the FTIR bands assigned to adsorbed water (3110 cm^{-1}) and structural hydroxyl groups (3442 cm^{-1}) in ACP-GL-CaHAp was 3, in CA-CaHAp was 2.8 while in nano-structured TA-CaHAp only 0.001. Weak dependency of O–H signals relaxation time on temperature was found analyzing NMR results of

ACP-GL-CaHAp and nano-structured TA-CaHAp [110]. This observation could be compared with behavior of propanol H-bond aggregates isolated in the cavities of argon matrix [178]. Narrow FTIR spectral bands assigned to O–H vibrations showed that the molecules of adsorbed water can also be captured in certain studied porous materials. Narrow band at 3572±2 cm^{-1} was assigned to stoichiometric $O–H^-$ vibration in the cavities of CaHAp [106,179]. This band is the most intensive one in GL-CaHAp and CA-CaHAp IR spectra while in ACP-GL-CaHAp IR spectra it is negligible. The IR band at 3587 cm^{-1} was assigned for surface O–H vibrations in P–O–H groups [106,179] [180], as well as stoichiometric band it was not registered in ACP-GL-CaHAp samples. It was stated that IR bands which has higher frequency than 3450 cm^{-1} can be used as spectral fingerprints to determine the existence of nanostructures in different CaHAp samples.

3.5.2. Nanostructured CaHAp's prepared in different synthesis routes

FTIR spectroscopy was found to be is highly sensitive to the impurities and substitutions in the structure of apatite [48,181]. The FTIR spectra of CaHAp samples obtained at 1000 °C in the sol gel process using different complexing in OH stretching region agents was shown in Figure 3.5.3. The main attitude was placed to the spectra of all samples a complex band of the asymmetric stretching vibration of the phosphate group at 1000-1100 cm^{-1}. Figure AE (Appendix E) also shows well-expressed asymmetric bending modes in the region of 660-520 cm^{-1}. Moreover, the specific OH^- Vibration mode near 635-630 cm^{-1} is visible in our IR spectra. The peak intensity at 630 cm^{-1} was assigned to OH vibration, as well as the band of the stretch vibration of OH group at ~3600 cm^{-1} in CaHAp spectra, remained unchanged for all specimens. At the same time the intensity of the band at 3644 cm^{-1} assigned to $Ca(OH)_2$ decreases. Two additional peaks are expressed at 1300-1225 cm^{-1} in the IR spectra of CaHAp samples synthesized using CDTA and EDTA as complexing agents.

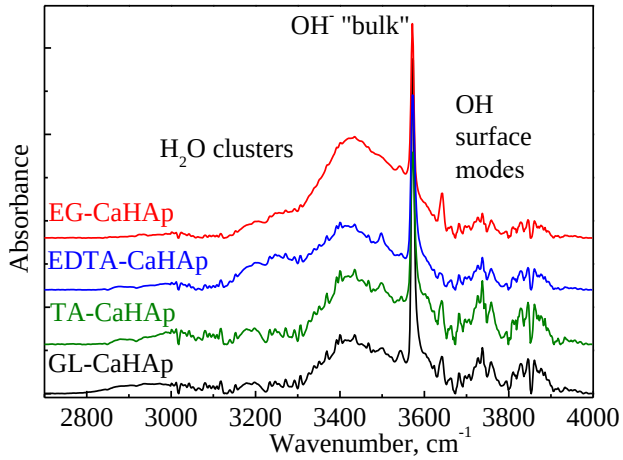

Figure 3.5.3. FTIR spectra of CaHAp synthesized using various complexing agents (detail in the Figure) in O–H stretching region. The intensities of the absorption bands are normalized; the spectra are shifted along absorbance axis for a more convenient view. For other conditions see Experimental.

Unfortunately, these absorption peaks could not be assigned for vibrations in any groups presented in apatite structure. The representative synthesized materials were analyzed more detailed respect to the presence of the structural manifolds of hydroxyl groups. The structural organization of –OH groups was found being very similar. Absorption bands could be attributed to adsorbed

water and structural hydroxyl groups (OH–) as discussed earlier. It can be concluded from FTIR spectra (Figure 3.5.3.), that for all materials the amount of structural –OH groups in is significantly higher than from adsorbed water.

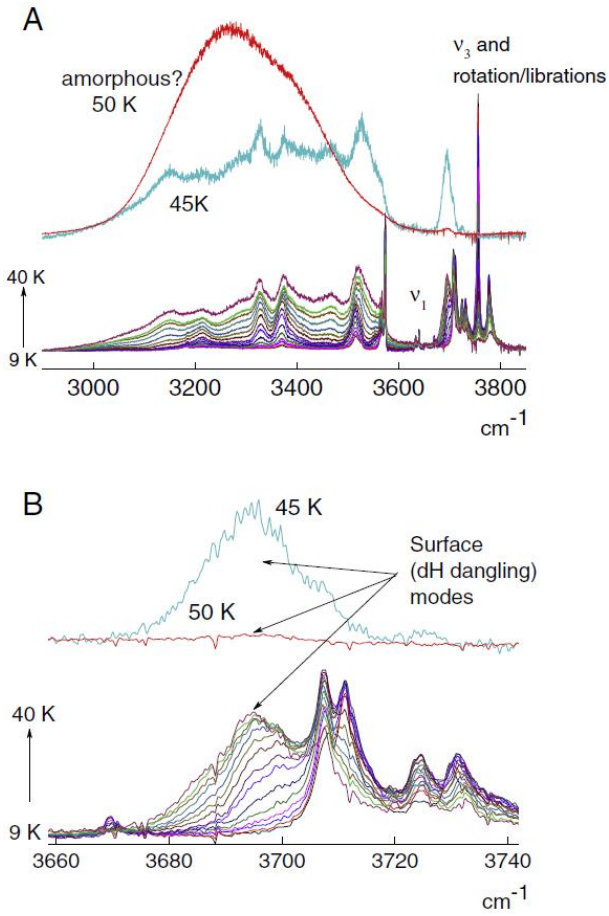

Figure 3.5.4. Part A: measured FTIR spectra of water in argon matrix in O–H stretching region over the temperature range 9–40 K (from bottom to upper, by stepping ΔT= 2 K). The base line was corrected drawing the line through the end points of this range. The spectra at 45 K and 50 K were added to support the assignment of surface (dangling) modes. Part B: the zoomed range 3660–3740 cm−1 in order better to display the peculiar thermal evolution of these modes. More comments in text. Adapted from. Kristinaitytė, Dagys, Kausteklis et all [170].

The sharp strong peak at 3570 cm^{-1} attributed to the stretching vibration of OH^- ions in the crystals (stoichiometric) [104] was clearly seen in all these spectra. Whereas the broad contour for bulk water spread (Discussed in 3.5.1.

paragraph) over ~3000-3400 cm^{-1} and that was dominant in the case of CaHAp containing amorphous phosphate phase, is practically absent in the present materials. Some bands that are seen over 3100-3600 cm^{-1} range (Figure 3.5.3.) can be recognized as those of small water clusters or surface modes which will be discussed later. To obtain detail information about water trapped in different environments firstly the water structure in argon matrix was studied using FTIR spectroscopy (Figure 3.5.4.).

Table 3.5.1. Structures of water molecules trapped in different materials

$(H_2O)n$	Argon matrix	CCl_4 [182]	Nano-structured CaHAps
	9–40 K	273–313 K	298 K
Dimerai	9–40 K	3615–3616	3526 ± 2 (a)
n = 2	3573–3573.5		3591 ± 4 (b)
	3574 [183]		3598 ± 1 (c)
Trimerai	3574.5 [184]	3535–3587	N/A
n = 3	3515–3520		
	3515 [185]		
	3516 [183,186]		
Tetramerai	3517 [184]	3395–3433	3420 ± 2 (a)
n = 4	3369–3374		3439 ± 2 (b)
	3372 [185,187]		3450 ± 2 (c)
Pentamerai	3372 [184]	N/A	N/A
n = 5	3327–3330		
	3325 [185]		
Heksamerai	3330 [187]	3221–3254	3237 ± 2 (a)
n = 6	3211–3214		– (b)
	3212 [185]		3263 ± 3 (c)
	3211 [187]		
	3327 (chair),		
n ≥ 6	3212 (cage) [177]	3043–3074	– (a)
	3100–3160		– (b)
	3144 [185]		2940 ± 10 (c)
	3140 [187]		
Paviršinės modos	3150 (prism) [177]	N/A	3642, 3737, 3866 (a)
	3695–3701		3640, 3737, 3848 (b)
	3698 [180,188]		~3651, ~3700 (c)

The obtained results were compared to the water in clusters in the CCl_4 and different CaHAp samples and vibrational assignments table with reference to other studies were created (Table 3.5.1).

The group of the bands of *ν*O–H of H-bonded clusters at 3000–3600 cm^{-1} transforms at 50 K to the broad spectral contour (Figure 3.5.4.A). The whole spectrum reminds of the profile observed for amorphous water with the characteristic dangling modes at 3720 and 3698 cm^{-1}, denoted as dH [180,189]. Theoretical calculations, supported by experimental studies, suggest that water molecules in the dH mode are bi- or tri-coordinated, presenting one free OH bond dangling at the surface [180]. Due to this similarity the band at 3695–3701 cm^{-1} was ascribed to the surface (dangling) mode. This mode can be recognized also in the FTIR spectra of water in nano-CaHAps at 3640–3651 cm^{-1}.

Another spectral features within 3700-3850 cm^{-1}, which slightly shift depending on the samples, can be assigned to the O–H stretching vibration of the P–O–H groups of surface HPO_4^{2-} and $H_2PO_4^-$ ions produced by the proton-cation of PO_4^{3-} ions [106,179]. The presence of protonated ions on the crystallite surfaces in the studied materials was confirmed by ^1H–^{31}P CP MAS kinetics experiments [50]. IR bands at ≥3800cm^{-1} that observed in the home-made CaHAps and not seen in the commercial sample, to our knowledge, were never reported in the literature. Thus, their origin must be studied in the future works. Since these peaks do not appear in CP MAS NMR spectra, most probably, they are originated from the highly mobile protons. However, their assignment presented in literature was long time controversial. Only recently in the work [190] it was shown that these peaks were originated to the structured external water molecules stacking in continuity to the columnar O–H channels in CaHAps.

Note, the H-bonded O–H stretching band in FTIR spectra was identified in many works on CaHAps and related systems [104,106,110,179]. However, this band usually is taken as the unity without getting into its shape and structure. Water clusters were revealed in nano-CaHAps in the present work for the first time. The bands of water dimmer, tetramer, hexamer and in the commercial sample maybe even n ≥ 6were resolved at 2900– 3600 cm−1 (Figure 3.5.5). They were assigned comparing with the spectra of water in argon matrix and in hydrophobic solvent (CCl_4). The size of formed cluster depends on the hydration level.

Hexamer- or even higher structures were observed only in the samples containing significant amount of adsorbed water (Figure 3.5.5 A, C). The amount of adsorbed water in the studied nano-CaHAps was probed using the intensity of the broad 1H signal at ca 5.1 ppm normalized respect to OH– peak

at ~0 ppm [170]. Thus, the NMR data perfectly correlate with those obtained by FTIR spectroscopy.

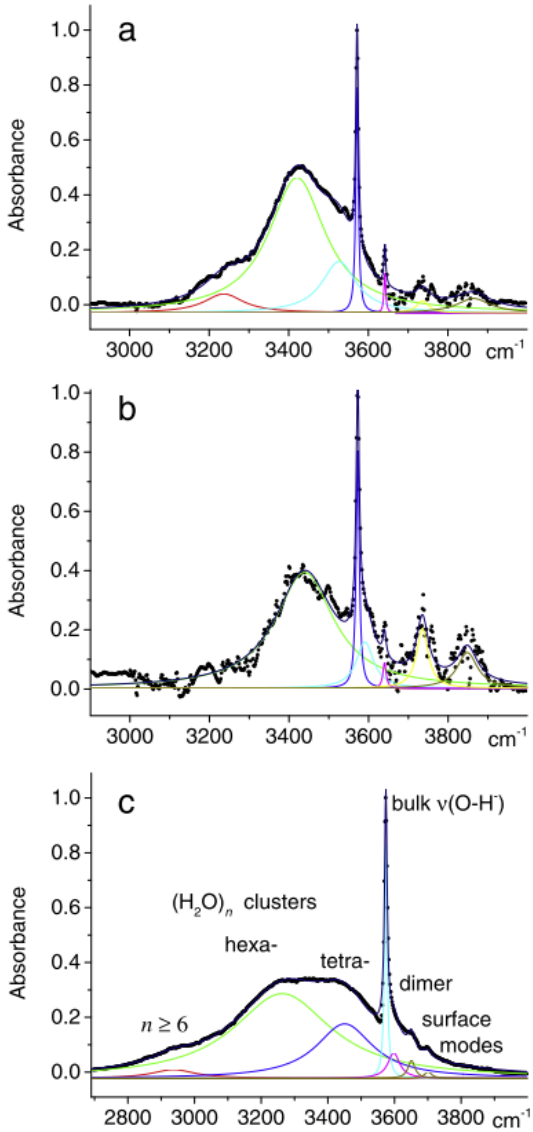

Figure 3.5.5. FTIR spectra of nano-structured CaHAs prepared via the sol-gel synthesis routes using various complexing agents: a – ethylene glycol; b – tartaric acid; c – commercial. The base line was corrected drawing the line through the end points of this range. The intensities were normalized respect to the peak of $\nu(O–H^-)$ in the bulk at 3573±1 cm^{-1}.

3.5.3. Summary of 3.5.

Nanostructured CaHAps synthesized via aqueous sol-gel route using different complexing agents, commercially available nano-structured CaHAp and CaHAp with amorphous phosphate phase were investigated using vibrational spectroscopy with respect to the structural organization of hydroxyl groups. The analysis IR absorption spectra showed the different self-organization of OH groups. Comparing ACP-CaHAp and nanostructured CaHAp, the stoichiometric OH content is significantly higher in nanostructured CaHAp than hydroxyl groups formed from adsorbed water.

Water cluster structure was revealed by FTIR spectroscopy in nano-structured CaHAps for the first time. The bands of water dimer, tetramer, hexamer and several stoichiometric O–H, surface O–H and P–O–H modes were resolved at 2900–3900 cm^{-1} and assigned under comparison of water spectra in argon matrix and in CCl_4.

The joint application of FTIR and NMR methods allowed revealing very fine details in the state of water and in the structural organization of OH groups. This could not be achieved applying these methods separately either because of difficulties assigning the observed spectral features or due to the overflow of information.

It was determined that using the IR absorption spectroscopy it is possible to evaluate the hydration of CaHAp. The degree of hydration of EG-CaHAp is 2 times higher than of TA-CaHAp. The degree of hydration of CaHAp is important for applications, which is a prerequisite for maintaining unchanged osteoinductivity.

CONCLUSIONS OF THE THESIS

1. Raman spectroscopy of long chain ionic liquids is powerful experimental technique to reveal the phase transitions in ionic liquid and water mixtures. Together with advanced spectral data processing methods 2DCOS and PCA the extent of liquid crystalline ionogel phase formation was determined. The combination of Raman spectral parameters changes in CH and OH stretching modes vibrational regions lead to determine the lower and the upper boarders of mixture phase transition.

2. Vibrational spectroscopy (Raman and IR) as a powerful experimental technique was used to analyze surface chemical species in the nano-structured sol-gel derived calcium hydroxyapatites and the calcium hydroxyapatites containing amorphous calcium phosphate phase. The precise analysis of the Raman and Infrared spectral contours allowed investigating the fine details of the structural organization of phosphate and hydroxyl groups in calcium hydroxyapatites derived via aqueous sol-gel route using different complexing agents.

3. The conformational equilibrium of short chain ionic liquids cation $[C_4mim]^+$ were investigated and anion influence to the preference of *gauche* conformation was revealed by Raman spectroscopy. The distribution by anion hydrophobicity, but not the ionic radius, let us to align the non-spherical and halide anions together by the preference of *trans* conformation in this order: $I^- > Br^- > Cl^- > OTf^- > NO_3^- > BF_4^-$. The higher preference of the *trans* conformation in ionic liquids with halide anions but longer cation chain, was influenced by lower mobility and more structured behavior.

4. As hydrophobicity plays important role in conformations preference, water for the purpose or as impurity could be used in neat ionic liquids. The dynamics of conformational equilibrium was used to monitor the effects caused by water in ionic liquids. Together with Raman spectral band parameters (shifts, relative intensity ratios and bandwidths) the conformational equilibrium was utilized to determine the boundaries of heavy water confinement in $[C_4mim]NO_3$.

5. The dynamics of H/D exchange in ionic liquid and heavy water mixtures were monitored using Raman spectroscopy. Higher degree of molecular freedom due to the order−disorder effects, anions and their aggregation play the crucial role in the H/D exchange reaction in the studied systems. The

anions interact with cations via H-bonds and bind the water molecules in their solvation shells. The overlap and the competition of these processes may cause rather complex dependency of the H/D exchange reaction rate on the sample composition and on other experimental conditions (temperature, degree of purification, etc.).

6. The anion place near cation in the IL–water mixture could be most important condition for H/D exchange to occur. In ionic liquids with halide anions (I^-;Br^-;Cl^-) which could be placed in plane with imidazolium ring H/D exchange happened in both type ionic liquids: with long chain and short chain cation. Despite the fact that for the spherical anions (OTf^-; $NO3^-$; $BF4^-$) with short chain ionic cations the conformational equilibrium is coupled with the H/D exchange the experiment was carried out for a long time using different water concentrations in the IL-water mixtures, the H/D reaction did not occur.

REFERENCES

[1] C. Rey, Calcium Phosphates for Medical Applications, Calcium Phosphates Biol. Ind. Syst. (1998) 217–251. doi:10.1007/978-1-4615-5517-9.

[2] P.C. Schmidt, R. Herzog, Calcium phosphates in pharmaceutical tableting - 2. Comparison of tableting properties, Pharm. World Sci. 15 (1993) 116–122. doi:10.1007/BF02113939.

[3] K.S. Egorova, E.G. Gordeev, V.P. Ananikov, Biological Activity of Ionic Liquids and Their Application in Pharmaceutics and Medicine, Chem. Rev. 117 (2017) 7132–7189. doi:10.1021/acs.chemrev.6b00562.

[4] N.L. Mai, Y. Koo, Production of Biofuels and Chemicals with Ionic Liquids, 2014. doi:10.1007/978-94-007-7711-8.

[5] D. Mecerreyes, Applications of Ionic Liquids in Polymer Science and Technology, 2015.

[6] B. Demirkurt, Y. Akdogan, Development of an Ionic Liquid Based Method for the Preparation of Albumin Nanoparticles, ChemistrySelect. 3 (2018) 9940–9945. doi:10.1002/slct.201801648.

[7] F.H. Albee, Studies in Bone Growth: Triple Calcium Phosphate As a Stimulus To Osteogenesis., Ann. Surg. 71 (1920) 32–39.

[8] C.P.A.T. Klein, K. de Groot, A.A. Drissen, H.B.M. van der Lubbe, Interaction of biodegradable β-whitlockite ceramics with bone tissue: An in vivo study, Biomaterials. 6 (1985) 189–192. doi:10.1016/0142-9612(85)90008-0.

[9] P.S. Eggli, W. Müller, R.K. Schenk, Porous hydroxyapatite and tricalcium phosphate cylinders with two different pore size ranges implanted in the cancellous bone of rabbits. A comparative histomorphometric and histologic study of bony ingrowth and implant substitution., Clin. Orthop. Relat. Res. (1988) 127–38. http://www.ncbi.nlm.nih.gov/pubmed/2838207.

[10] F. Barrere, M.M.E. Snel, C.A. Van Blitterswijk, K. De Groot, P. Layrolle, Nano-scale study of the nucleation and growth of calcium phosphate coating on titanium implants, Biomaterials. 25 (2004) 2901–2910. doi:10.1016/j.biomaterials.2003.09.063.

[11] D. Apelt, F. Theiss, A.O. El-Warrak, K. Zlinszky, R. Bettschart-Wolfisberger, M. Bohner, S. Matter, J.A. Auer, B. Von Rechenberg, In vivo behavior of three different injectable hydraulic calcium phosphate cements, Biomaterials. 25 (2004) 1439–1451. doi:10.1016/j.biomaterials.2003.08.073.

[12] M. Bohner, H. Tiainen, P. Michel, N. Döbelin, Design of an inorganic dual-paste apatite cement using cation exchange, J. Mater. Sci. Mater. Med. 26 (2015) 1–13. doi:10.1007/s10856-015-5400-z.

[13] H. Seitz, W. Rieder, S. Irsen, B. Leukers, C. Tille, Three-dimensional printing of porous ceramic scaffolds for bone tissue engineering, J.

Biomed. Mater. Res. - Part B Appl. Biomater. 74 (2005) 782–788. doi:10.1002/jbm.b.30291.
[14] R.A. Levy, T.M.G. Chu, J.W. Halloran, S.E. Feinberg, S. Hollister, CT-generated porous hydroxyapatite orbital floor prosthesis as a prototype bioimplant, Am. J. Neuroradiol. 18 (1997) 1522–1525.
[15] H. Yuan, H. Fernandes, P. Habibovic, J. de Boer, A.M.C. Barradas, A. de Ruiter, W.R. Walsh, C.A. van Blitterswijk, J.D. de Bruijn, Osteoinductive ceramics as a synthetic alternative to autologous bone grafting, Proc. Natl. Acad. Sci. 107 (2010) 13614–13619. doi:10.1073/pnas.1003600107.
[16] N. Groen, N. Tahmasebi, F. Shimizu, Y. Sano, T. Kanda, D. Barbieri, H. Yuan, P. Habibovic, C.A. van Blitterswijk, J. de Boer, Exploring the Material-Induced Transcriptional Landscape of Osteoblasts on Bone Graft Materials, Adv. Healthc. Mater. 4 (2015) 1691–1700. doi:10.1002/adhm.201500171.
[17] H. Lapczyna, L. Galea, S. Wüst, M. Bohner, S. Jerban, A. Sweedy, N. Doebelin, N. van Garderen, S. Hofmann, G. Baroud, R. Müller, B. von Rechenberg, Effect of Grain Size and Microporosity on the in vivo Behavior of beta-Tricalcium Phosphate Scaffolds, Eur. Cells Mater. 28 (2014) 299–319.
[18] T. Welton, Room-Temperature Ionic Liquids. Solvents for Synthesis and Catalysis, Chem. Rev. 99 (1999) 2071–2084. doi:10.1021/cr980032t.
[19] J. Dupont, R.F. De Souza, P.A.Z. Suarez, Ionic liquid (molten salt) phase organometallic catalysis, Chem. Rev. 102 (2002) 3667–3692. doi:10.1021/cr010338r.
[20] R. Hayes, G.G. Warr, R. Atkin, Structure and Nanostructure in Ionic Liquids, Chem.Rev. 115 (2015) 6357 − 6426. doi:10.1021/cr500411q.
[21] C. Zhong, Y. Deng, W. Hu, J. Qiao, L. Zhang, J. Zhang, A review of electrolyte materials and compositions for electrochemical supercapacitors, Chem. Soc. Rev. 44 (2015) 7484–7539. doi:10.1039/c5cs00303b.
[22] W. Jiang, Y. Wang, G.A. Voth, Molecular dynamics simulation of nanostructural organization in ionic liquid/water mixtures, J. Phys. Chem. B. 111 (2007) 4812–4818. doi:10.1021/jp0671421.
[23] K. Dong, S. Zhang, J. Wang, Understanding the hydrogen bonds in ionic liquids and their roles in properties and reactions, Chem. Commun. 52 (2016) 6744–6764. doi:10.1039/C5CC10120D.
[24] Y. Zhao, S. Gao, J. Wang, J. Tang, Aggregation of Ionic Liquids [Cnmim]Br (n = 4, 6, 8, 10, 12) in D2O: A NMR Study, J. Phys. Chem. B. 112 (2008) 2031–2039. doi:10.1021/jp076467e.
[25] M.N. Garaga, M. Nayeri, A. Martinelli, Effect of the alkyl chain length in 1-alkyl-3-methylimidazolium ionic liquids on inter-molecular interactions and rotational dynamics, J. Mol. Liq. 210 (2015) 1–9. doi:10.1016/j.molliq.2015.06.055.

[26] J.D. Wadhawan, R.G. Compton, F. Marken, P. a Z. Suarez, C.S. Consorti, F. De Souza, Water-Induced Accelerated Ion Diffusion: Voltammetric Studies in [BMIM][BF4], R. Soc. Chem. 24 (2000) 1009–1015. doi:10.1039/b007172m.

[27] K.A. Fletcher, S. Pandey, Solvatochromic Probe Behavior within Ternary Room-Temperature Ionic Liquid 1-Butyl-3-methylimidazolium Hexafluorophosphate + Ethanol + Water Solutions, J. Phys. Chem. B. 107 (2003) 13532–13539. doi:10.1021/jp0276754.

[28] K.R. Seddon, A. Stark, M.-J. Torres, Influence of chloride, water, and organic solvents on the physical properties of ionic liquids*, Pure Appl. Chem. 72 (2000) 2275–2287. doi:10.1351/pac200072122275.

[29] M.G. Freire, P.J. Carvalho, A.M. Fernandes, I.M. Marrucho, A.J. Queimada, J.A.P. Coutinho, Surface tensions of imidazolium based ionic liquids: Anion, cation, temperature and water effect, J. Colloid Interface Sci. 314 (2007) 621–630. doi:10.1016/j.jcis.2007.06.003.

[30] M. Filice, O. Romero, O. Abian, B. de las Rivas, J.M. Palomo, Low ionic liquid concentration in water: a green and simple approach to improve activity and selectivity of lipases, RSC Adv. 4 (2014) 49115–49122. doi:10.1039/C4RA07625G.

[31] Y. Kohno, H. Ohno, Ionic liquid/water mixtures: from hostility to conciliation, Chem. Commun. 48 (2012) 7119. doi:10.1039/c2cc31638b.

[32] J. Kausteklis, V. Balevičius, V. Aleksa, Two-dimensional Raman spectroscopy study of ionogel phase formation in long-chain ionic liquid/water systems, J. Raman Spectrosc. 48 (2017) 126–131. doi:10.1002/jrs.4983.

[33] V. Klimavicius, Z. Gdaniec, J. Kausteklis, V. Aleksa, K. Aidas, V. Balevicius, NMR and Raman spectroscopy monitoring of proton/deuteron exchange in aqueous solutions of ionic liquids forming hydrogen bond: A Role of anions, self-aggregation, and mesophase formation, J. Phys. Chem. B. 117 (2013) 10211–10220. doi:10.1021/jp4021245.

[34] B.A. Marekha, M. Bria, M. Moreau, I. De Waele, F.A. Miannay, Y. Smortsova, T. Takamuku, O.N. Kalugin, M. Kiselev, A. Idrissi, Intermolecular interactions in mixtures of 1-n-butyl-3-methylimidazolium acetate and water: Insights from IR, Raman, NMR spectroscopy and quantum chemistry calculations, J. Mol. Liq. 210 (2015) 227–237. doi:10.1016/j.molliq.2015.05.015.

[35] T. Takamuku, H. Hoke, A. Idrissi, B.A. Marekha, M. Moreau, Y. Honda, T. Umecky, T. Shimomura, Microscopic interactions of the imidazolium-based ionic liquid with molecular liquids depending on their electron-donicity, Phys. Chem. Chem. Phys. 16 (2014) 23627–23638. doi:10.1039/C4CP03565H.

[36] V. Aleksa, J. Kausteklis, V. Klimavicius, Z. Gdaniec, V. Balevicius,

Raman and NMR spectroscopy study of liquid crystalline ionogel phase in ionic liquid/H2O mixtures: The states of water, J. Mol. Struct. 993 (2011) 91–96. doi:10.1016/j.molstruc.2010.12.060.

[37] J.C. Elliott, D.W. Holcomb, R.A. Young, Infrared determination of the degree of substitution of hydroxyl by carbonate ions in human dental enamel, Calcif. Tissue Int. 37 (1985) 372–375. doi:10.1007/BF02553704.

[38] G. Zhang, X. Chen, Y. Xie, Y. Zhao, H. Qiu, Lyotropic liquid crystalline phases in a ternary system of 1-hexadecyl-3-methylimidazolium chloride/1-decanol/water, J. Colloid Interface Sci. 315 (2007) 601–606. doi:10.1016/j.jcis.2007.07.012.

[39] X.W. Li, J. Zhang, B. Dong, L.Q. Zheng, C.H. Tung, Characterization of lyotropic liquid crystals formed in the mixtures of 1-alkyl-3-methylimidazolium bromide/p-xylene/water, Colloids Surfaces A Physicochem. Eng. Asp. 335 (2009) 80–87. doi:10.1016/j.colsurfa.2008.10.031.

[40] A.M. Moschovi, S. Ntais, V. Dracopoulos, V. Nikolakis, Vibrational spectroscopic study of the protic ionic liquid 1-H-3-methylimidazolium bis(trifluoromethanesulfonyl)imide, Vib. Spectrosc. 63 (2012) 350–359. doi:10.1016/j.vibspec.2012.08.006.

[41] S. Chen, S. Zhang, X. Liu, J. Wang, J. Wang, K. Dong, J. Sun, B. Xu, Ionic liquid clusters: structure, formation mechanism, and effect on the behavior of ionic liquids., Phys. Chem. Chem. Phys. 16 (2014) 5893–5906. doi:10.1039/c3cp53116c.

[42] H. Weingärtner, C. Cabrele, C. Herrmann, How ionic liquids can help to stabilize native proteins., Phys. Chem. Chem. Phys. 14 (2012) 415–26. doi:10.1039/c1cp21947b.

[43] Y. Ji, R. Shi, Y. Wang, G. Saielli, Effect of the chain length on the structure of ionic liquids: from spatial heterogeneity to ionic liquid crystals., J. Phys. Chem. B. 117 (2013) 1104–9. doi:10.1021/jp310231f.

[44] S. Kareiva, V. Klimavicius, A. Momot, J. Kausteklis, A. Prichodko, L. Dagys, F. Ivanauskas, S. Sakirzanovas, V. Balevicius, A. Kareiva, Sol-gel synthesis, phase composition, morphological and structural characterization of Ca<inf>10</inf>(PO<inf>4</inf>)<inf>6</inf>(OH)<inf>2</inf>: XRD, FTIR, SEM, 3D SEM and solid-state NMR studies, J. Mol. Struct. 1119 (2016). doi:10.1016/j.molstruc.2016.04.046.

[45] K. Saihara, Y. Yoshimura, S. Ohta, A. Shimizu, Properties of Water Confined in Ionic Liquids, Sci. Rep. 5 (2015) 10619. doi:10.1038/srep10619.

[46] H. Abe, T. Takekiyo, M. Shigemi, Y. Yoshimura, S. Tsuge, T. Hanasaki, K. Ohishi, S. Takata, J. Suzuki, Direct Evidence of Confined Water in Room-Temperature Ionic Liquids by Complementary Use of Small-Angle X-ray and Neutron Scattering, J. Phys. Chem. Lett. 5

(2014) 1175–1180. doi:10.1021/jz500299z.
[47] H. Abe, T. Takekiyo, Y. Yoshimura, K. Saihara, A. Shimizu, Anomalous Freezing of Nano-Confined Water in Room-Temperature Ionic Liquid 1-Butyl-3-Methylimidazolium Nitrate, ChemPhysChem. 17 (2016) 1136–1142. doi:10.1002/cphc.201501199.
[48] A. Antonakos, E. Liarokapis, T. Leventouri, Micro-Raman and FTIR studies of synthetic and natural apatites, Biomaterials. 28 (2007) 3043–3054. doi:10.1016/j.biomaterials.2007.02.028.
[49] I. Rehman, W. Bonfield, Characterization of hydroxyapatite and carbonated apatite by photo acoustic FTIR spectroscopy, J. Mater. Sci. Mater. Med. 8 (1997) 1–4. doi:10.1023/A:1018570213546.
[50] S. Kareiva, V. Klimavicius, A. Momot, J. Kausteklis, Sol e gel synthesis , phase composition , morphological and structural characterization of Ca 10 (PO 4) 6 (OH) 2 : XRD , FTIR , SEM , 3D SEM and solid-state NMR studies, J. Mol. Struct. 1119 (2016) 1–11. doi:10.1016/j.molstruc.2016.04.046.
[51] M. Nayeri, K. Nygård, M. Karlsson, M. Maréchal, M. Burghammer, M. Reynolds, A. Martinelli, The role of the ionic liquid C6C1ImTFSI in the sol-gel synthesis of silica studied using in situ SAXS and Raman spectroscopy., Phys. Chem. Chem. Phys. 17 (2015) 9841–8. doi:10.1039/c5cp00709g.
[52] G.E. Walrafen, Raman spectral studies of water structure, J. Chem. Phys. 40 (1964) 3249–3256. doi:10.1063/1.1724992.
[53] A. Nilsson, L.G.M. Pettersson, The structural origin of anomalous properties of liquid water, Nat. Commun. 6 (2015) 8998. doi:10.1038/ncomms9998.
[54] R. Ludwig, The effect of hydrogen bonding on the thermodynamic and spectroscopic properties of molecular clusters and liquids, Phys. Chem. Chem. Phys. 4 (2002) 5481–5487. doi:10.1039/b207000f.
[55] Q. Sun, Local statistical interpretation for water structure, Chem. Phys. Lett. 568–569 (2013) 90–94. doi:10.1016/j.cplett.2013.03.065.
[56] H. Ohno, Electrochemical aspects of ionic liquids, 2011.
[57] T. Fukushima, T. Aida, Ionic liquids for soft functional materials with carbon nanotubes, Chem. - A Eur. J. 13 (2007) 5048–5058. doi:10.1002/chem.200700554.
[58] M. Díaz, A. Ortiz, I. Ortiz, Progress in the use of ionic liquids as electrolyte membranes in fuel cells, J. Memb. Sci. 469 (2014) 379–396. doi:10.1016/j.memsci.2014.06.033.
[59] S. Zhang, Q. Zhang, Y. Zhang, Z. Chen, M. Watanabe, Y. Deng, Beyond solvents and electrolytes: Ionic liquids-based advanced functional materials, Prog. Mater. Sci. 77 (2016) 80–124. doi:10.1016/j.pmatsci.2015.10.001.
[60] K. Fumino, A. Wulf, R. Ludwig, The potential role of hydrogen bonding in aprotic and protic ionic liquids., Phys. Chem. Chem. Phys. 11 (2009) 8790–8794. doi:10.1039/b905634c.

[61] A. Knorr, P. Stange, K. Fumino, F. Weinhold, R. Ludwig, Spectroscopic Evidence for Clusters of Like-Charged Ions in Ionic Liquids Stabilized by Cooperative Hydrogen Bonding, (2016) 458–462. doi:10.1002/cphc.201501134.

[62] P.A. Hunt, C.R. Ashworth, R.P. Matthews, Hydrogen bonding in ionic liquids, Chem. Soc. Rev. 44 (2015) 1257–1288. doi:10.1039/C4CS00278D.

[63] K. Fumino, A. Wulf, R. Ludwig, Strong , Localized , and Directional Hydrogen Bonds Fluidize Ionic Liquids **, 2 (2008) 8731–8734. doi:10.1002/anie.200803446.

[64] G.R. Desiraju, Hydrogen bridges in crystal engineering: Interactions without borders, Acc. Chem. Res. 35 (2002) 565–573. doi:10.1021/ar010054t.

[65] N.E. Heimer, R.E. Del Sesto, Z. Meng, J.S. Wilkes, W.R. Carper, Vibrational spectra of imidazolium tetrafluoroborate ionic liquids, J. Mol. Liq. 124 (2006) 84–95. doi:10.1016/j.molliq.2005.08.004.

[66] P.A. Hunt, I.R. Gould, Structural characterization of the 1-butyl-3-methylimidazolium chloride ion pair using ab initio methods, J. Phys. Chem. A. 110 (2006) 2269–2282. doi:10.1021/jp0547865.

[67] B.A. Marekha, O.N. Kalugin, A. Idrissi, Non-covalent interactions in ionic liquid ion pairs and ion pair dimers: a quantum chemical calculation analysis, Phys. Chem. Chem. Phys. 17 (2015) 16846–16857. doi:10.1039/c5cp02197a.

[68] R.P. Matthews, T. Welton, P.A. Hunt, Competitive pi interactions and hydrogen bonding within imidazolium ionic liquids, Phys. Chem. Chem. Phys. 16 (2014) 3238–3253. doi:10.1039/c3cp54672a.

[69] T. Singh, A. Kumar, Aggregation behavior of ionic liquids in aqueous solutions: effect of alkyl chain length, cations, and anions., J. Phys. Chem. B. 111 (2007) 7843–7851. doi:10.1021/jp0726889.

[70] T. Takamuku, Y. Kyoshoin, T. Shimomura, S. Kittaka, T. Yamaguchi, Effect of water on structure of hydrophilic imidazolium-based ionic liquid, J. Phys. Chem. B. 113 (2009) 10817–10824. doi:10.1021/jp9042667.

[71] M.A. Firestone, J.A. Dzielawa, P. Zapol, L. a. Curtiss, S. Seifert, M.L. Dietz, Lyotropic Liquid-Crystalline Gel Formation in a Room-Temperature Ionic Liquid, Langmuir. 18 (2002) 7258–7260. doi:10.1021/la0259499.

[72] B. Fazio, A. Triolo, G. Di Marco, Recent Advances in linear and nonlinear Raman spectroscopy I, J. Raman Spectrosc. 39 (2008) 233–237. doi:10.1002/jrs.

[73] L. Cammarata, S.G. Kazarian, P. a. Salter, T. Welton, Molecular states of water in room temperature ionic liquidsElectronic Supplementary Information available. See http://www.rsc.org/suppdata/cp/b1/b106900d/, Phys. Chem. Chem. Phys. 3 (2001) 5192–5200. doi:10.1039/b106900d.

[74] S. Cha, D. Kim, Change of hydrogen bonding structure in ionic liquid mixtures by anion type, J. Chem. Phys. 148 (2018) 193827. doi:10.1063/1.5010067.
[75] C. Zhong, W. Hu, Electrolytes for Electrochemical Supercapacitors, Electrolytes Electrochem. Supercapacitors. (2016) 31–254. doi:10.1201/b21497-3.
[76] Y. Zhao, X. Yue, X. Wang, X. Chen, Lyotropic liquid crystalline phases with a series of N-alkyl-N-methylpiperidinium bromides and water, J. Colloid Interface Sci. 389 (2013) 199–205. doi:10.1016/j.jcis.2012.09.032.
[77] M.A. Firestone, P. Thiyagarajan, D.M. Tiede, Structure and optical properties of a thermoresponsive polymer-grafted, lipid-based complex fluid, Langmuir. 14 (1998) 4688–4698. doi:10.1021/la9805995.
[78] M. a. Firestone, P.G. Rickert, S. Seifert, M.L. Dietz, Anion effects on ionogel formation in N,N′-dialkylimidazolium-based ionic liquids, Inorganica Chim. Acta. 357 (2004) 3991–3998. doi:10.1016/j.ica.2004.06.042.
[79] M. Blesic, A. Lopes, E. Melo, Z. Petrovski, N. V. Plechkova, J.N. Canongia Lopes, K.R. Seddon, L.P.N. Rebelo, On the self-aggregation and fluorescence quenching aptitude of surfactant ionic liquids, J. Phys. Chem. B. 112 (2008) 8645–8650. doi:10.1021/jp802179j.
[80] T. Inoue, B. Dong, L.-Q. Zheng, Phase behavior of binary mixture of 1-dodecyl-3-methylimidazolium bromide and water revealed by differential scanning calorimetry and polarized optical microscopy., J. Colloid Interface Sci. 307 (2007) 578–81. doi:10.1016/j.jcis.2006.12.063.
[81] V. Balevicius, Z. Gdaniec, K. Aidas, J. Tamuliene, NMR and quantum chemistry study of mesoscopic effects in ionic liquids., J. Phys. Chem. A. 114 (2010) 5365–71. doi:10.1021/jp909293b.
[82] F. Perakis, L. De Marco, A. Shalit, F. Tang, Z.R. Kann, T.D. Kühne, R. Torre, M. Bonn, Y. Nagata, Vibrational Spectroscopy and Dynamics of Water, Chem. Rev. 116 (2016) 7590–7607. doi:10.1021/acs.chemrev.5b00640.
[83] B.A. Marekha, M. Bria, M. Moreau, I. De Waele, F.-A. Miannay, Y. Smortsova, T. Takamuku, O.N. Kalugin, M. Kiselev, A. Idrissi, Intermolecular interactions in mixtures of 1-n-butyl-3-methylimidazolium acetate and water: Insights from IR, Raman, NMR spectroscopy and quantum chemistry calculations, J. Mol. Liq. 210 (2015) 227–237. doi:10.1016/j.molliq.2015.05.015.
[84] S.A.M. Noor, P.M. Bayley, M. Forsyth, D.R. MacFarlane, Ionogels based on ionic liquids as potential highly conductive solid state electrolytes, Electrochim. Acta. 91 (2013) 219–226. doi:10.1016/j.electacta.2012.11.113.
[85] M.A. Firestone, M.A. Firestone, M.L. Dietz, S. Seifert, S. Trasobares,

D.J. Miller, N.J. Zaluzec, Ionogel-Templated Synthesis and Organization of Anisotropic Gold Nanoparticles, 60439 (2005) 754–760. doi:10.1002/smll.200500030.

[86] S. Saouane, F.P.A. Fabbiani, Structural Behavior of Long-Chain Imidazolium-Based Ionic Liquid [C $_{10}$ mim]Cl–Water Mixtures, Cryst. Growth Des. 15 (2015) 3875–3884. doi:10.1021/acs.cgd.5b00494.

[87] N. Kimizuka, T. Nakashima, Spontaneous Self-Assembly of Glycolipid Bilayer Membranes in Sugar-philic Ionic Liquids and Formation of, (2001) 6759–6761.

[88] V.H. Paschoal, L.F.O. Faria, M.C.C. Ribeiro, Vibrational Spectroscopy of Ionic Liquids, Chem. Rev. 117 (2017) 7053–7112. doi:10.1021/acs.chemrev.6b00461.

[89] C.E.S. Bernardes, M.E. Minas Da Piedade, J.N. Canongia Lopes, The structure of aqueous solutions of a hydrophilic ionic liquid: The full concentration range of 1-ethyl-3-methylimidazolium ethylsulfate and water, J. Phys. Chem. B. 115 (2011) 2067–2074. doi:10.1021/jp1113202.

[90] M. Anouti, J. Jacquemin, P. Porion, Transport properties investigation of aqueous protic ionic liquid solutions through conductivity, viscosity, and NMR self-diffusion measurements, J. Phys. Chem. B. 116 (2012) 4228–4238. doi:10.1021/jp3010844.

[91] M. Anouti, M. Caillon-Caravanier, Y. Dridi, J. Jacquemin, C. Hardacre, D. Lemordant, Liquid densities, heat capacities, refractive index and excess quantities for {protic ionic liquids + water} binary system, J. Chem. Thermodyn. 41 (2009) 799–808. doi:10.1016/j.jct.2009.01.011.

[92] M. Anouti, A. Vigeant, J. Jacquemin, C. Brigouleix, D. Lemordant, Volumetric properties, viscosity and refractive index of the protic ionic liquid, pyrrolidinium octanoate, in molecular solvents, J. Chem. Thermodyn. 42 (2010) 834–845. doi:10.1016/j.jct.2010.01.013.

[93] N. Yaghini, J. Pitawala, A. Matic, A. Martinelli, Effect of Water on the Local Structure and Phase Behavior of Imidazolium-Based Protic Ionic Liquids, J. Phys. Chem. B. 119 (2015) 1611–1622. doi:10.1021/jp510691e.

[94] O. Cabeza, L. Segade, M. Domínguez-Pérez, E. Rilo, D. Ausín, A. Martinelli, N. Yaghini, B. Gollas, M. Kriechbaum, O. Russina, A. Triolo, E. López-Lago, L.M. Varela, Mesostructure and physical properties of aqueous mixtures of the ionic liquid 1-ethyl-3-methyl imidazolium octyl sulfate doped with divalent sulfate salts in the liquid and the mesomorphic states, Phys. Chem. Chem. Phys. 20 (2018) 8724–8736. doi:10.1039/c7cp07999k.

[95] P.R. Burney, J. Pfaendtner, Structural and Dynamic Features of Candida rugosa Lipase 1 in Water, Octane, Toluene, and Ionic Liquids BMIM-PF6 and BMIM-NO3, J. Phys. Chem. B. 117 (2013) 2662−2670. doi:10.1021/jp312299d.

[96] N.M. Micaelo, C.M. Soares, Protein Structure and Dynamics in Ionic Liquids . Insights from Molecular Dynamics, J. Phys. Chem. B. (2008) 2566–2572. doi:10.1021/jp0766050.
[97] M.D. Bermúdez, A.E. Jiménez, J. Sanes, F.J. Carrión, Ionic liquids as advanced lubricant fluids, Molecules. 14 (2009) 2888–2908. doi:10.3390/molecules14082888.
[98] Q. Hu, H. Zhao, S. Ouyang, Understanding water structure from Raman spectra of isotopic substitution H2O/D2O up to 573 K, Phys. Chem. Chem. Phys. 19 (2017) 21540–21547. doi:10.1039/C7CP02065A.
[99] Y. Yasaka, C. Wakai, N. Matubayasi, M. Nakahara, Slowdown of H/D exchange reaction rate and water dynamics in ionic liquids: deactivation of solitary water solvated by small anions in 1-butyl-3-methyl- imidazolium chloride, J. Phys. Chem. A. 111 (2007) 541–543. doi:10.1021/jp0673720.
[100] N. Hatano, M. Watanabe, T. Takekiyo, H. Abe, Y. Yoshimura, Anomalous Conformational Change in 1-Butyl-3-methylimidazolium Tetrafluoroborate-D2O Mixtures, J. Phys. Chem. A. 116 (2012) 1208–1212. doi:10.1021/jp2097873.
[101] T. Cremer, C. Kolbeck, K.R.J. Lovelock, N. Paape, R. Wölfel, P.S. Schulz, P. Wasserscheid, H. Weber, J. Thar, B. Kirchner, F. Maier, H.-P. Steinrück, Towards a Molecular Understanding of Cation-Anion Interactions-Probing the Electronic Structure of Imidazolium Ionic Liquids by NMR Spectroscopy, X-ray Photoelectron Spectroscopy and Theoretical Calculations, Chem. - A Eur. J. 16 (2010) 9018–9033. doi:10.1002/chem.201001032.
[102] J. Kausteklis, M. Talaikis, V. Aleksa, V. Balevičius, Raman spectroscopy study of water confinement in ionic liquid 1-butyl-3-methylimidzolium nitrate, J. Mol. Liq. 271 (2018) 747–755. doi:10.1016/j.molliq.2018.09.060.
[103] P. Pascaud, P. Gras, Y. Coppel, C. Rey, S. Sarda, Interaction between a bisphosphonate, tiludronate, and biomimetic nanocrystalline apatites, Langmuir. 29 (2013) 2224–2232. doi:10.1021/la3046548.
[104] J. Kolmas, A. Jaklewicz, A. Zima, M. Bućko, Z. Paszkiewicz, J. Lis, A. Ślósarczyk, W. Kolodziejski, Incorporation of carbonate and magnesium ions into synthetic hydroxyapatite: The effect on physicochemical properties, J. Mol. Struct. 987 (2011) 40–50. doi:10.1016/j.molstruc.2010.11.058.
[105] J.D. Termine, A.S. Posner, Infra-red determination of the percentage of crystallinity in apatitic calcium phosphates, Nature. 211 (1966) 268–270. doi:10.1038/211268a0.
[106] T. Ishikawa, A. Teramachi, H. Tanaka, A. Yasukawa, K. Kandori, Fourier transform infrared spectroscopy study of deuteration of calcium hydroxyapatite particles, Langmuir. 16 (2000) 10221–10226. doi:10.1021/la0004855.

[107] Z.H. Cheng, A. Yasukawa, K. Kandori, T. Ishikawa, FTIR Study of Adsorption of CO 2 on Nonstoichiometric Calcium Hydroxyapatite, J.Chem.Soc ., Faraday T RansSoc. 94 (1998) 1501–1505. doi:10.1021/la980339n.
[108] A. Solhy, W. Amer, M. Karkouri, R. Tahir, A. El Bouari, A. Fihri, M. Bousmina, M. Zahouily, Bi-functional modified-phosphate catalyzed the synthesis of α-α′-(EE)-bis(benzylidene)-cycloalkanones: Microwave versus conventional-heating, J. Mol. Catal. A Chem. 336 (2011) 8–15. doi:10.1016/j.molcata.2010.11.032.
[109] Q.Q. Qiu, J. Connor, Effects of γ-irradiation, storage and hydration on osteoinductivity of DBM and DBM/AM composite, J. Biomed. Mater. Res. - Part A. 87 (2008) 373–379. doi:10.1002/jbm.a.31790.
[110] L. Dagys, V. Klimavičius, J. Kausteklis, A. Chodosovskaja, V. Aleksa, A. Kareiva, SOLID-STATE 1 H AND 31 P NMR AND FTIR SPECTROSCOPY STUDY OF STATIC AND DYNAMIC STRUCTURES IN SOL-GEL DERIVED CALCIUM HYDROXYAPATITES, 55 (2015) 1–9.
[111] K. Kristinaitytė, L. Dagys, J. Kausteklis, V. Klimavicius, I. Doroshenko, V. Pogorelov, N.R. Valevičienė, V. Balevicius, NMR and FTIR studies of clustering of water molecules: From low-temperature matrices to nano-structured materials used in innovative medicine, J. Mol. Liq. 235 (2017) 1–6. doi:10.1016/j.molliq.2016.11.076.
[112] J. Kausteklis, V. Aleksa, M.A. Iramain, S.A. Brandán, DFT and vibrational spectroscopy study of 1-butyl-3-methylimidazolium trifluoromethanesulfonate ionic liquid, J. Mol. Struct. 1175 (2019) 663–676. doi:10.1016/j.molstruc.2018.08.014.
[113] J. Kausteklis, V. Aleksa, M.A. Iramain, S.A. Brandán, Effect of cation-anion interactions on the structural and vibrational properties of 1-buthyl-3-methyl imidazolium nitrate ionic liquid, J. Mol. Struct. 1164 (2018). doi:10.1016/j.molstruc.2018.03.100.
[114] Y. Jeon, J. Sung, D. Kim, C. Seo, H. Cheong, Y. Ouchi, R. Ozawa, H.O. Hamaguchi, Structural change of 1-butyl-3-methylimidazolium tetrafluoroborate + water mixtures studied by infrared vibrational spectroscopy, J. Phys. Chem. B. 112 (2008) 923–928. doi:10.1021/jp0746650.
[115] B. Czarnik-Matusewicz, S. Pilorz, Study of the temperature-dependent near-infrared spectra of water by two-dimensional correlation spectroscopy and principal components analysis, Vib. Spectrosc. 40 (2006) 235–245. doi:10.1016/j.vibspec.2005.10.002.
[116] N. Hatano, T. Takekiyo, H. Abe, Y. Yoshimura, Effect of Counteranions on the Conformational Equilibrium of 1-Butyl-3-methylimidazolium-Based Ionic Liquids, Int. J. Spectrosc. 2011 (2011) 1–5. doi:10.1155/2011/648245.
[117] V.H. Segtnan, Š. Šašić, T. Isaksson, Y. Ozaki, Studies on the structure of water using two-dimensional near-infrared correlation spectroscopy

and principal component analysis, Anal. Chem. 73 (2001) 3153–3161. doi:10.1021/ac010102n.
[118] C. Thibault, P. Huguet, P. Sistat, G. Pourcelly, Confocal Raman micro-spectroscopy and electrochemical investigation of anion transport through ion-exchange membranes, Desalination. 149 (2002) 429–433. doi:10.1016/S0011-9164(02)00770-1.
[119] Y.O. Isao Noda, Two- Dimensional Correlation Spectroscopy, 2004.
[120] I. Noda, Determination of Two - Dimensional Correlation Spectra Using the Hilbert Transform, Appl. Spectrosc. 54 (2000) 994–999. doi:10.1366/0003702001950454.
[121] B. Dong, X. Zhao, L. Zheng, J. Zhang, N. Li, T. Inoue, Aggregation behavior of long-chain imidazolium ionic liquids in aqueous solution: Micellization and characterization of micelle microenvironment, Colloids Surfaces A Physicochem. Eng. Asp. 317 (2008) 666–672. doi:10.1016/j.colsurfa.2007.12.001.
[122] I. Noda, Generalized two-dimensional correlation method applicable to infrared, Raman, and other types of spectroscopy, Appl. Spectrosc. 47 (1993) 1329–1336. doi:10.1366/0003702934067694.
[123] I. Noda, A.E. Dowrey, C. Marcott, G.M. Story, Generalized Two-Dimensional Correlation Spectroscopy, Appl. Spectrosc. 54 (2000) 236–248. doi:10.1021/jp2043043.
[124] J. Zhu, L. Bai, B. Chen, W. Fei, Thermodynamical properties of phase change materials based on ionic liquids, Chem. Eng. J. 147 (2009) 58–62. doi:10.1016/j.cej.2008.11.016.
[125] U. Domańska, E. Bogel-Łukasik, Measurements and Correlation of the (Solid + Liquid) Equilibria of [1-Decyl-3-methylimidazolium Chloride + Alcohols (C 2 −C 12)] † , Ind. Eng. Chem. Res. 42 (2003) 6986–6992. doi:10.1021/ie030464g.
[126] L.H. Kim, Ki-Sub, Shin Bae-Kun, K. Kim, B. Shin, H. Lee, Physical and Electrochemical Properties of 1-Butyl-3-methylimidazolium Bromide, 1-Butyl-3-methylimidazolium Iodide, and 1-Butyl-3-methylimidazolium Tetrafluoroborate, Korean J. Chem. English. 21 (2004) 1010–1014. doi:10.1016/j.jpowsour.2007.10.062.
[127] P.N. Tshibangu, S.N. Ndwandwe, E.D. Dikio, Density , Viscosity and Conductivity Study of 1-Butyl-3- Methylimidazolium Bromide, Int. J. Electrochem. Sci. 6 (2011) 2201–2213.
[128] S. Fendt, S. Padmanabhan, H.W. Blanch, J.M. Prausnitz, Viscosities of acetate or chloride-based ionic liquids and some of their mixtures with water or other common solvents, J. Chem. Eng. Data. 56 (2011) 31–34. doi:10.1021/je1007235.
[129] S. a. Dharaskar, M.N. Varma, D.Z. Shende, C.K. Yoo, K.L. Wasewar, Synthesis, characterization and application of 1-butyl-3 methylimidazolium chloride as green material for extractive desulfurization of liquid fuel, Sci. World J. 2013 (2013). doi:10.1155/2013/395274.

[130] A.A. Strechan, A.G. Kabo, Y.U. Paulechka, A. V. Blokhin, G.J. Kabo, A.S. Shaplov, E.I. Lozinskaya, Thermochemical properties of 1-butyl-3-methylimidazolium nitrate, Thermochim. Acta. 474 (2008) 25–31. doi:10.1016/j.tca.2008.05.002.
[131] B. Mokhtarani, A. Sharifi, H.R. Mortaheb, M. Mirzaei, M. Mafi, F. Sadeghian, Density and viscosity of 1-butyl-3-methylimidazolium nitrate with ethanol, 1-propanol, or 1-butanol at several temperatures, J. Chem. Thermodyn. 41 (2009) 1432–1438. doi:10.1016/j.jct.2009.06.023.
[132] J. JR, S. M, Thermal Characteristics of 1-Butyl-3-Methylimimidazolium Based Oxidant Ionic Liquids, J. Chem. Eng. Process Technol. 07 (2016) 4–9. doi:10.4172/2157-7048.1000309.
[133] S. Ren, Y. Hou, W. Wu, W. Liu, Purification of Ionic Liquids : Sweeping Solvents by Nitrogen, (2010) 5074–5077.
[134] V. Klimavicius, A. Kareiva, V. Balevicius, Solid-State NMR Study of Hydroxyapatite Containing Amorphous Phosphate Phase and Nanostructured Hydroxyapatite: Cut-O ff Averaging of CP-MAS Kinetics and Size Pro fi les of Spin Clusters, (2014). doi:10.1021/jp510229f.
[135] J.M. Hollas, Modern Spectroscopy, (2004).
[136] H. Abe, T. Yamada, K. Shibata, Dynamic properties of nano-confined water in an ionic liquid, J. Mol. Liq. 264 (2018) 54–57. doi:10.1016/j.molliq.2018.05.006.
[137] Y. Jeon, J. Sung, C. Seo, H. Lim, H. Cheong, M. Kang, B. Moon, Y. Ouchi, D. Kim, Structures of ionic liquids with different anions studied by infrared vibration spectroscopy, J. Phys. Chem. B. 112 (2008) 4735–4740. doi:10.1021/jp7120752.
[138] T. Endo, T. Kato, K.I. Tozaki, K. Nishikawa, Phase behaviors of room temperature ionic liquid linked with cation conformational changes: 1-Butyl-3-methylimidazolium Hexafluorophosphate, J. Phys. Chem. B. 114 (2010) 407–411. doi:10.1021/jp909256j.
[139] J. Kausteklis, V. Aleksa, M.A. Iramain, S.A. Brandan, Effect of cation-anion interactions on the structural and vibrational properties of 1-butyl-3-metylimidazolium nitrate ionic liquid, J. Mol. Struct. 1164 (2018) 1–14. doi:10.1016/j.molstruc.2018.03.100.
[140] R.W. Berg, M. Deetlefs, K.R. Seddon, I. Shim, J.M. Thompson, Raman and ab initio studies of simple and binary 1-alkyl-3-methylimidazolium ionic liquids, J. Phys. Chem. B. 109 (2005) 19018–19025. doi:10.1021/jp050691r.
[141] R.O. H. Hamaguchi, Structure of Ionic Liquids and Ionic Liquid Compounds: Are Ionic Liquids Genuine Liquids in the Conventional Sense?, Adv. Chem. Ph. 131 (2005) 85–102.
[142] Y. Umebayashi, H. Hamano, S. Tsuzuki, J.N. Canongia Lopes, A.A.H. Pádua, Y. Kameda, S. Kohara, T. Yamaguchi, K. Fujii, S.I. Ishiguro, Dependence of the conformational isomerism in 1-n-butyl-3-

methylimidazolium ionic liquids on the nature of the halide anion, J. Phys. Chem. B. 114 (2010) 11715–11724. doi:10.1021/jp1044755.
[143] Y.-S. Ye, J. Rick, B.-J. Hwang, Ionic liquid polymer electrolytes, J. Mater. Chem. A. 1 (2013) 2719–2743. doi:10.1039/b000000x.
[144] V. Balevičius, L. Džiaugys, F. Kuliešius, A. Maršalka, ^{1}H and ^{13}C NMR study of phase transition and molecular motion in ionic liquids forming lyotropic liquid-crystalline ionogels, Lith. J. Phys. 51 (2011) 212–220. doi:10.3952/lithjphys.51309.
[145] S. Cha, M. Ao, W. Sung, B. Moon, B. Ahlström, P. Johansson, Y. Ouchi, D. Kim, Structures of ionic liquid-water mixtures investigated by IR and NMR spectroscopy, Phys. Chem. Chem. Phys. 16 (2014) 9591–601. doi:10.1039/c4cp00589a.
[146] S. Sowmiah, V. Srinivasadesikan, M.C. Tseng, Y.H. Chu, On the chemical stabilities of ionic liquids, Molecules. 14 (2009) 3780–3813. doi:10.3390/molecules14093780.
[147] R.W. Berg, Raman spectroscopy and ab-initio model calculations on ionic liquids, Monatsh. Chem. 138 (2007) 1045–1075. doi:10.1007/s00706-007-0760-9.
[148] T. Takekiyo, K. Yamazaki, E. Yamaguchi, H. Abe, Y. Yoshimura, High ionic liquid concentration-induced structural change of protein in aqueous solution: A case study of lysozyme, J. Phys. Chem. B. 116 (2012) 11092–11097. doi:10.1021/jp3057064.
[149] J.-B. Brubach, A. Mermet, A. Filabozzi, A. Gerschel, D. Lairez, M.P. Krafft, P. Roy, Dependence of Water Dynamics upon Confinement Size, J. Phys. Chem. B. 105 (2001) 430–435. doi:10.1021/jp002983s.
[150] T. Singh, A. Kumar, Cation-anion-water interactions in aqueous mixtures of imidazolium based ionic liquids, Vib. Spectrosc. 55 (2011) 119–125. doi:10.1016/j.vibspec.2010.09.009.
[151] Y. Xu, Y. Gao, L. Zhang, J. Yao, C. Wang, H. Li, Microscopic structures of ionic liquids 1-ethyl-3-methylimidazolium tetrafluoroborate in water probed by the relative chemical shift, Sci. China Chem. 53 (2010) 1561–1565. doi:10.1007/s11426-010-3198-6.
[152] Y. Chen, Y. Cao, X. Sun, T. Mu, Hydrogen bonding interaction between acetate-based ionic liquid 1-ethyl-3-methylimidazolium acetate and common solvents, J. Mol. Liq. 190 (2014) 151–158. doi:10.1016/j.molliq.2013.11.010.
[153] E. Bodo, S. Mangialardo, F. Capitani, L. Gontrani, F. Leonelli, P. Postorino, Interaction of a long alkyl chain protic ionic liquid and water, J. Chem. Phys. 140 (2014) 204503. doi:10.1063/1.4876036.
[154] C. Roth, S. Chatzipapadopoulos, D. Kerlé, F. Friedriszik, M. Lütgens, S. Lochbrunner, O. Kühn, R. Ludwig, Hydrogen bonding in ionic liquids probed by linear and nonlinear vibrational spectroscopy, New J. Phys. 14 (2012) 105026. doi:10.1088/1367-2630/14/10/105026.
[155] M.C.C. Ribeiro, High Viscosity of Imidazolium Ionic Liquids with the Hydrogen Sulfate Anion: A Raman Spectroscopy Study, J. Phys.

Chem. B. 116 (2012) 7281–7290. doi:Doi 10.1021/Jp302091d1.
[156] K.-L. Han, G.-J. Zhao, Hydrogen bonding and transfer in the excited state, 2011.
[157] M. Moreno, F. Castiglione, A. Mele, C. Pasqui, G. Raos, Interaction of water with the model ionic liquid [bmim][BF4]: molecular dynamics simulations and comparison with NMR data, J. Phys. Chem. B. 112 (2008) 7826–7836. doi:10.1021/jp800383g.
[158] J. Joseph, E.D. Jemmis, Red-, blue-, or no-shift in hydrogen bonds: A unified explanation, J. Am. Chem. Soc. 129 (2007) 4620–4632. doi:10.1021/ja067545z.
[159] C.G. Hanke, N.A. Atamas, R.M. Lynden-Bell, Solvation of small molecules in imidazolium ionic liquids: a simulation study, Green Chem. 4 (2002) 107–111. doi:10.1039/b109179b.
[160] O. Russina, A. Triolo, L. Gontrani, R. Caminiti, D. Xiao, L.G. Hines Jr, R.A. Bartsch, E.L. Quitevis, N. Pleckhova, K.R. Seddon, Morphology and intermolecular dynamics of 1-alkyl-3-methylimidazolium bis{(trifluoromethane)sulfonyl}amide ionic liquids: structural and dynamic evidence of nanoscale segregation, J. Phys. Condens. Matter. 21 (2009) 424121. doi:10.1088/0953-8984/21/42/424121.
[161] F.W.B. Einstein, D.G. Tuck, A Refinement of the Crystal Structure of NH4NO3.2HNO3, Acta Cryst. B26 (1970) 1117–1120. doi:10.1107/S0567740869003323.
[162] K. Kaneko, Y. Yoshimura, A. Shimizu, Water concentration dependence of the refractive index of various ionic liquid-water mixtures, J. Mol. Liq. 250 (2018) 283–286. doi:10.1016/j.molliq.2017.12.009.
[163] S. Mangialardo, L. Baldassarre, E. Bodo, P. Postorino, The Structure of Ionic Liquids, 2014. doi:10.1007/978-3-319-01698-6.
[164] M.R. Waterland, D. Stockwell, A.M. Kelley, Symmetry breaking effects in NO3-: Raman spectra of nitrate salts and ab initio resonance Raman spectra of nitrate-water complexes, J. Chem. Phys. 114 (2001) 6249–6258. doi:10.1063/1.1355657.
[165] D.J. Goebbert, E. Garand, T. Wende, R. Bergmann, G. Meijer, K.R. Asmis, D.M. Neumark, Infrared spectroscopy of the microhydrated nitrate ions $NO_3^-\cdot(H2O)_{(1-6)}$., J. Phys. Chem. A. 113 (2009) 7584–92. doi:10.1021/jp9017103.
[166] C. Choe, J. Lademann, M.E. Darvin, Depth profiles of hydrogen bound water molecule types and their relation to lipid and protein interaction in the human stratum corneum in vivo, Analyst. 141 (2016) 6329–6337. doi:10.1039/C6AN01717G.
[167] C. Boissière, J.B. Brubach, A. Mermet, G. Marzi De, C. Bourgaux, E. Prouzet, P. Roy, Water confined in lamellar structures of AOT surfactants: An infrared investigation, J. Phys. Chem. B. 106 (2002) 1032–1035. doi:10.1021/jp012724i.

[168] A. V. Frontzek, L. Paccou, Y. Guinet, A. Hédoux, Study of the phase transition in lysozyme crystals by Raman spectroscopy, Biochim. Biophys. Acta - Gen. Subj. 1860 (2016) 412–423. doi:10.1016/j.bbagen.2015.10.020.
[169] A. Lerbret, P. Bordat, F. Affouard, Y. Guinet, A. Hédoux, L. Paccou, D. Prévost, M. Descamps, Influence of homologous disaccharides on the hydrogen-bond network of water: Complementary Raman scattering experiments and molecular dynamics simulations, Carbohydr. Res. 340 (2005) 881–887. doi:10.1016/j.carres.2005.01.036.
[170] K. Kristinaitytė, L. Dagys, J. Kausteklis, V. Klimavicius, I. Doroshenko, V. Pogorelov, N.R. Valevičienė, V. Balevicius, NMR and FTIR studies of clustering of water molecules: From low-temperature matrices to nano-structured materials used in innovative medicine, J. Mol. Liq. 235 (2017). doi:10.1016/j.molliq.2016.11.076.
[171] H. Abe, T. Takekiyo, M. Aono, H. Kishimura, Y. Yoshimura, N. Hamaya, Polymorphs in room-temperature ionic liquids: Hierarchical structure, confined water and pressure-induced frustration, J. Mol. Liq. 210 (2015) 200–214. doi:10.1016/j.molliq.2015.05.057.
[172] Y. Yoshimura, T. Takekiyo, C. Okamoto, N. Hatano, H. Abe, Switching of hydrogen bonds of water in ionic liquid, 1-butyl-3-methylimidazolium tetrafluoroborate, J. Raman Spectrosc. 44 (2013) 475–480. doi:10.1002/jrs.4197.
[173] X. Shen, Q. Chen, J. Zhang, P. Fu, Supramolecular Structures in the Presence of Ionic Liquids, Supramol. Struct. Presence Ion. Liq. Theory, Prop. New Approaches. (2011) 427–482.
[174] O. Russina, B. Fazio, G. Di Marco, R. Caminiti, The Structure of Ionic Liquids, (2014). doi:10.1007/978-3-319-01698-6.
[175] Q.G. Zhang, N.N. Wang, S.L. Wang, Z.W. Yu, Hydrogen bonding behaviors of binary systems containing the ionic liquid 1-butyl-3-methylimidazolium trifluoroacetate and water/methanol, J. Phys. Chem. B. 115 (2011) 11127–11136. doi:10.1021/jp204305g.
[176] L. Zhang, Z. Xu, Y. Wang, H. Li, Prediction of the solvation and structural properties of ionic liquids in water by two-dimensional correlation spectroscopy, J. Phys. Chem. B. 112 (2008) 6411–6419. doi:10.1021/jp8001349.
[177] K. Ohno, M. Okimura, N. Akai, Y. Katsumoto, The effect of cooperative hydrogen bonding on the OH stretching-band shift for water clusters studied by matrix-isolation infrared spectroscopy and density functional theory, Phys. Chem. Chem. Phys. 7 (2005) 3005–3014. doi:10.1039/b506641g.
[178] I. Doroshenko, V. Balevicius, G. Pitsevich, K. Aidas, V. Sablinskas, V. Pogorelov, FTIR/PCA study of propanol in argon matrix: The initial stage of clustering and conformational transitions, Low Temp. Phys. 40 (2014) 1077–1082. doi:10.1063/1.4902228.

[179] S. Diallo-Garcia, M. Ben Osman, J.M. Krafft, S. Boujday, C. Guylène, Discrimination of infrared fingerprints of bulk and surface POH and OH of hydroxyapatites, Catal. Today. 226 (2014) 81–88. doi:10.1016/j.cattod.2013.11.041.
[180] J.A. Noble, C. Martin, H.J. Fraser, P. Roubin, S. Coussan, IR selective irradiations of amorphous solid water dangling modes: Irradiation vs annealing effects, J. Phys. Chem. C. 118 (2014) 20488–20495. doi:10.1021/jp506943k.
[181] E. Garskaite, K.A. Gross, S.W. Yang, T.C.K. Yang, J.C. Yang, A. Kareiva, Effect of processing conditions on the crystallinity and structure of carbonated calcium hydroxyapatite (CHAp), CrystEngComm. 16 (2014) 3950–3959. doi:10.1039/c4ce00119b.
[182] T. Köddermann, F. Schulte, M. Huelsekopf, R. Ludwig, Formation of Water Clusters in a Hydrophobic Solvent, Angew. Chemie - Int. Ed. 42 (2003) 4904–4908. doi:10.1002/anie.200351438.
[183] R.M. Bentwood, A.J. Barnes, W.J. Orville-Thomas, Studies of intermolecular interactions by matrix isolation vibrational spectroscopy and normal coordinate analysis. Self-association of hydrogen cyanide, J. Mol. Spectrosc. 84 (1980) 391–404. doi:10.1016/0022-2852(78)90042-5.
[184] G.P. Ayers, A.D.E. Pullin, The i.r. spectra of matrix isolated water species-I. Assignment of bands to (H2O)2, (D2O)2 and HDO dimer species in argon matrices., Spectrochim. Acta Part A Mol. Spectrosc. 32 (1976) 1629–1639. doi:10.1016/0584-8539(76)80265-6.
[185] S. Coussan, P. Roubin, J.P. Perchard, Infrared induced isomerizations of water polymers trapped in nitrogen matrix, Chem. Phys. 324 (2006) 527–540. doi:10.1016/j.chemphys.2005.11.017.
[186] A. Engdahl, B. Nelander, On the structure of the water trimer. a matrix isolation study, J. Chem. Phys. 86 (1987) 4831–4837. doi:10.1063/1.452676.
[187] J. Ceponkus, P. Uvdal, B. Nelander, Water tetramer, pentamer, and hexamer in inert matrices, J. Phys. Chem. A. 116 (2012) 4842–4850. doi:10.1021/jp301521b.
[188] J.A. Noble, C. Martin, H.J. Fraser, P. Roubin, S. Coussan, Unveiling the surface structure of amorphous solid water via selective infrared irradiation of OH stretching modes, J. Phys. Chem. Lett. 5 (2014) 826–829. doi:10.1021/jz5000066.
[189] S. Coussan, P. Roubin, J.A. Noble, Inhomogeneity of the amorphous solid water dangling bonds, Phys. Chem. Chem. Phys. 17 (2015) 9429–9435. doi:10.1039/c5cp00662g.
[190] M. Ben Osman, S. Diallo-Garcia, V. Herledan, D. Brouri, T. Yoshioka, J. Kubo, Y. Millot, G. Costentin, Discrimination of Surface and Bulk Structure of Crystalline Hydroxyapatite Nanoparticles by NMR, J. Phys. Chem. C. 119 (2015) 23008–23020. doi:10.1021/acs.jpcc.5b08732.

[191] V. Balevicius, Z. Gdaniec, K. Aidas, NMR and DFT study on media effects on proton transfer in hydrogen bonding: concept of molecular probe with an application to ionic and super-polar liquids., Phys. Chem. Chem. Phys. 11 (2009) 8592–8600. doi:10.1039/b819666d.

APENDIXES

Appendix A

COMPUTATIONAL DETAILS

Electronic structure calculations were conducted using Gaussian09 program.18 Equilibrium geometries and harmonic vibrational frequencies as well as Raman activities of the 1- butyl-3-methyl-imidazolium cation isotopologues are based on the calculations using the B3LYP exchange-correlation func- tional19 and the 6-311++G** basis set.20 Bulk solvent effects are accounted for by using a polarizable continuum model (PCM).21 Default settings of PCM were utilized apart from parameters ofac and rmim, which were assigned values of 0.8 and 0.5, respectively. Anharmonic analysis was performed at the B3LYP/6-31G* level in vacuo using second order perturbative approach22 implemented in Gaussian09. 1H and 13C magnetic shielding tensors were calculated at the level of PBE0/6-311+ +G(2d,2p)/PCM. CALCULATIONS More details concerning this choice are given in ref [191].

Appendix B

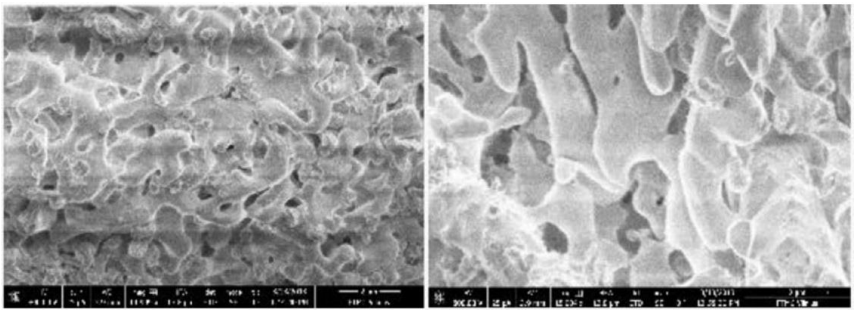

EDTA

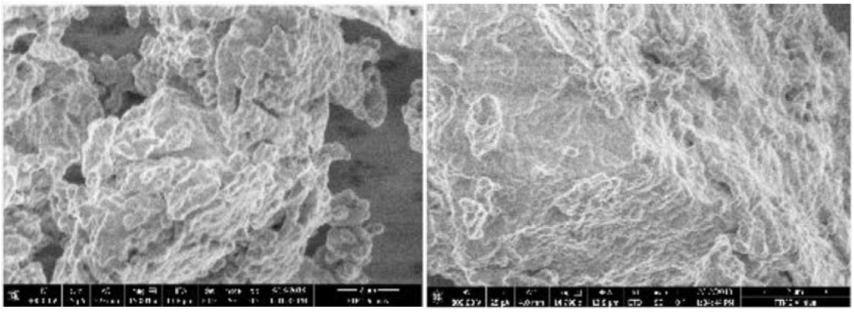

TA

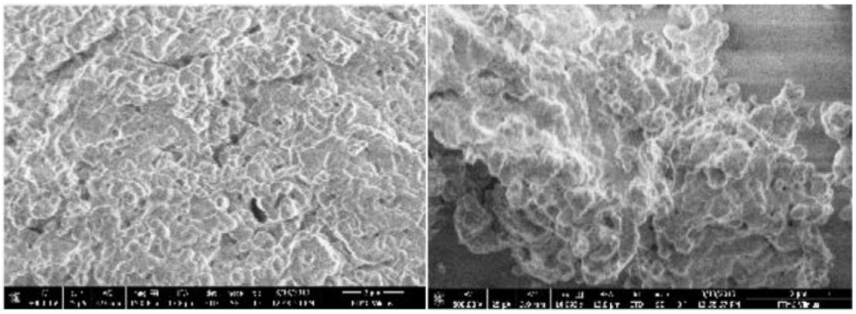

EG

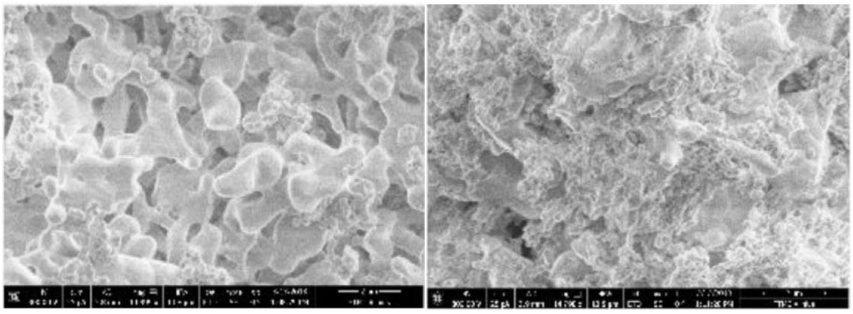

GL

Fig AB. SEM micrographs of CaHAp samples synthesized at 1000 ºC from the gels prepared with (from top): EDTA, TA, EG and GL. The molar ratio of complexing agent and Ca was 2 (left) or 1 (Right). Adapted from [44].

Appendix C

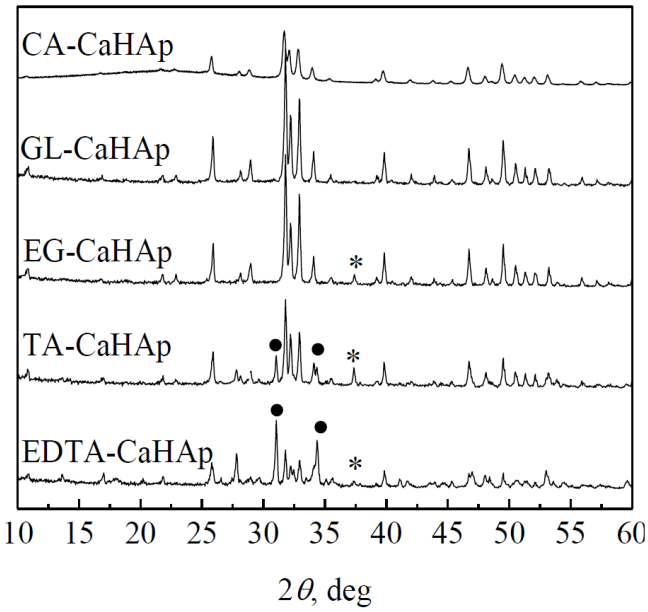

Figure AC. XRD patterns of CA/GL/EG/TA/EDTA-CaHAps. Impurity phases: Ca3(PO4) - *, CaO - ●. Adapted from [44].

Appendix D

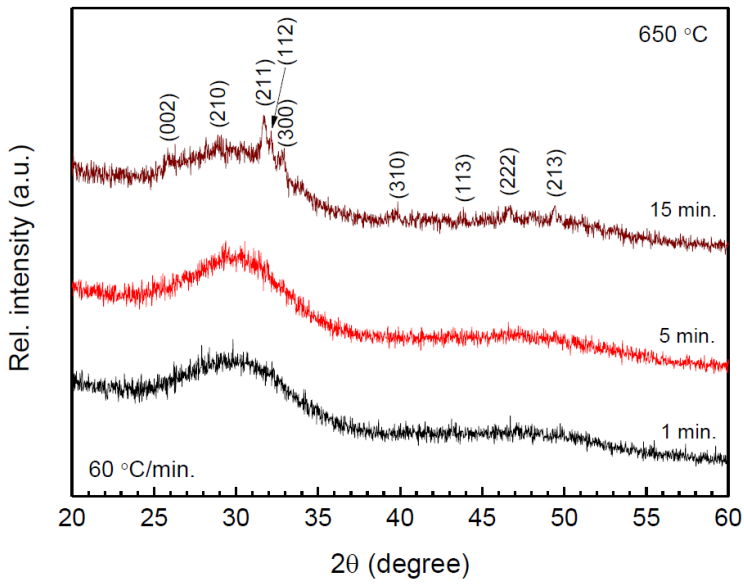

Figure AD. XRD patterns of ACP-GL-CaHAp depending on the sintering time at 650˚C. Adapted from [44].

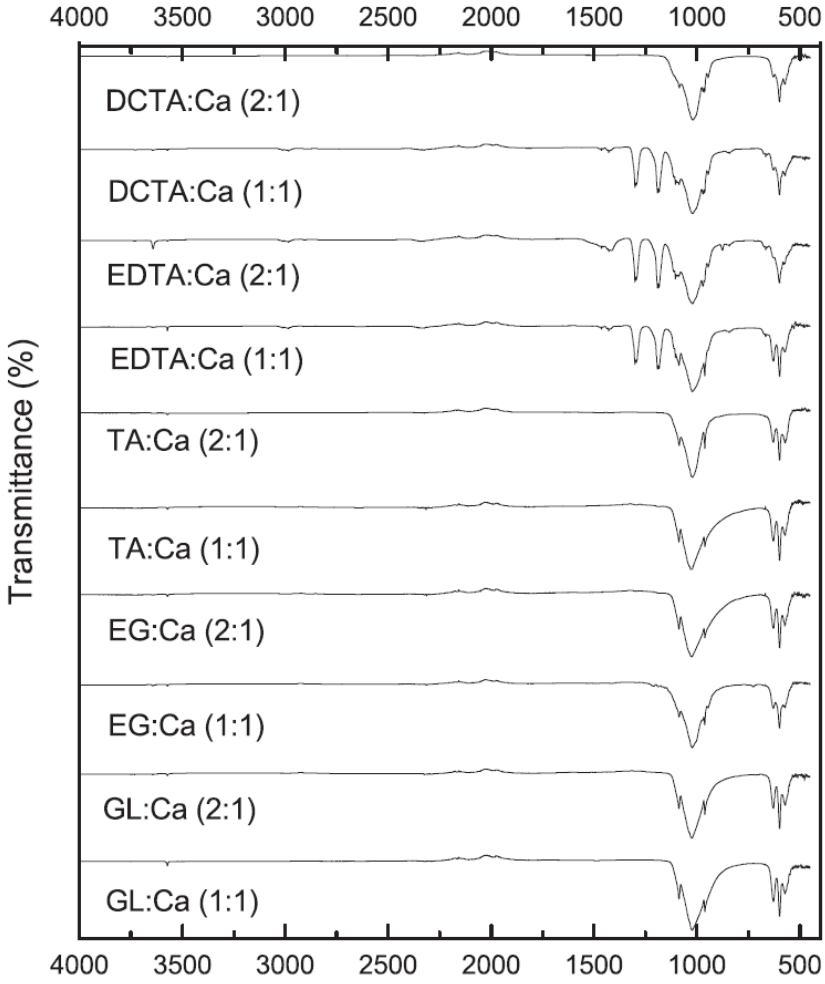

Figure AE. FTIR spectra of CaHAp samples synthesized at 1000 ^{o}C using different complexing agents in the sol-gel processing: DCTA, EDTA, TA, EG and GL. The molar ratio of complexing agent and Ca was 2 or 1 a. Adapted from [44].

SANTRAUKA

Inovatyviųjų technologijų vystymui ypač reikalingos funkcinės medžiagos, kurios dažniausiai apibūdinamos kaip turinčios ypatingas fizikines ir chemines savybes bei unikalią struktūrą, suteikiančią galimybę medžiagą panaudoti tam tikrai funkcijai atlikti. Viena aktualių mokslinių užduočių – funkcinių medžiagų fizikinių ir cheminių savybių bei struktūrų išsaugojimas įvairiose aplinkose veikiant skirtingoms aplinkos sąlygoms. Sumanios funkcinės medžiagos gali prisitaikyti prie kintančių aplinkos sąlygų ir pakeisti savo struktūrą ar elgseną. Todėl pramonės reikmėms yra būtini metodai, kuriuos taikant būtų galima greitai ir patikimai apibūdinti funkcinių medžiagų sandarą, jų savybes ir sąveikas su kitomis medžiagomis. Neaprėpiamos funkcinių medžiagų panaudojimo sritys pramonėje verčia ieškoti efektyvesnių bei ekonomiškesnių sintezės būdų, kuriems būtini ir fundamentiniai medžiagų tyrimai. Joniniai skysčiai (*angl.* Ionic liquids, IL) ir kalcio fosfatai (CaP) – gerai žinomos funkcinės medžiagos, kurios plačiai pritaikomos tiek medicinoje, tiek farmacijoje [1–3]. Joniniai skysčiai yra plačiai naudojami vaistų pernašai organizme, cheminei sintezei ir biomedicinos tyrimų srityje [3–5]. Kalcio fosfatai taikomi žmogaus ligų ir traumų gydymui [7,11], pastoms, dangoms ir dirbtinių kaulų implantams gaminti [8–14]. Galimybė modifikuoti joninių skysčių ir CaP struktūras pagal poreikius padidina jų pritaikomumą ir išplečia panaudojimo galimybes. Osteoinduktyvumas – medžiagos savybė lemianti svetimkūnio/implanto atmetimą žmogaus organizme. Implanto paviršiuje vyksta aplinkinių audinių ląstelių diferenciacija ir vertimas į osteoblastus, kurie priklauso nuo CaP esančių porų, ertmių ir CaP paviršių struktūros [15–17].

Lyginant skirtingais cheminės sintezės metodais pagamintų CaP paviršiaus plotų dydžius galima nustatyti įvairių CaP kompleksų egzistavimą. Kuo medžiaga nano-struktūriškesnė, tuo jos paviršiaus sąveikos plotas didesnis. CaP dangų, paruoštų naudojant klasterizuotą amorfinę kalcio fosfato fazę (*angl.* Amorphous calcium phosphate, ACP), paviršiaus plotas yra mažesnis nei CaP su nano- arba mezofazėmis. Nano- ir mezofazės formuojasi ne tik kietuose CaP, tačiau ir skystuose joninio skysčio bei vandens mišiniuose. Joniniai skysčiai suteikia galimybę suformuoti beveik neribotą skaičių funkcinių medžiagų su specifinėmis savybėmis, gaunamomis derinant įvairias anijonų ir katijonų poras [18,19]

Skystoji fazė plačioje temperatūros srityje, didelis jonų laidumas, žemas garų slėgis, aukštas elektrocheminis ir šiluminis stabilumas bei galimybė ištirpinti organines, neorganines arba polimerines medžiagas gaunamos dėl joniniuose skysčiuose besiformuojančių dipolių, elektronų porų (donorų-

akceptorių), kuloninių sąveikų ir vandenilių ryšių [20,21]. Aukščiau paminėtos joninių skysčių savybės telkia mokslininkus tirti šias funkcines medžiagas tiek eksperimentiškai, tiek teoriškai [22–25].

Galiausiai, CaP ir IL taikymas priklauso nuo priemaišų, esančių bandinyje, ir jų poveikio medžiagos struktūrai bei savybėms. Vanduo - viena natūralių priemaišų, esančių tiek IL, tiek CaP. Jis gali būti adsorbuojamas iš atmosferos arba likti kaip priemaiša medžiagoje po cheminės sintezės [19]. Nustatyta, kad ir nedidelis vandens kiekis gali žymiai pakeisti IL difuzijos koeficientą [26], poliškumą [27], klampą [28] ir paviršiaus įtempimą [29]. Siekiant platesnio IL pritaikymo, priklausomai nuo atliekamos funkcijos, jie pradėti naudoti mišiniuose su junginiais, kurie anksčiau buvo traktuojami kaip priemaišos, t.y. organiniai tirpikliai, kiti IL ir vanduo [30,31]. Pažymėtina, kad reikalingas daug gilesnis IL ir vandens molekulių sąveikų supratimas. Mišinių struktūra esant skirtingai sudedamųjų dalių koncentracijai nėra visiškai aiški. Vandens ir IL mišiniuose susidarančios skirtingos struktūros priklauso nuo anijonų, katijonų ir vandens koncentracijos [32–36]. IL ir vandens mišiniuose jonų difuzijos koeficiento padidėjimas siejamas su klampos mažėjimu, kuris atsiranda slopinant elektrostatinę jonų sąveiką [31]. Tiek grynuose IL, tiek IL ir vandens mišiniuose, kai formuojasi agregatai, konformacinių ir dinaminių procesų tyrimas yra tiesiogiai susijęs su tiriamais IL fizikinių ir cheminių savybių pokyčiais. Vandens molekulių struktūros, susidariusios kalcio fosfatuose, yra būtinos skirtingų cheminės sintezės būdų, naudojamų osteoinduktyvumui padidinti, paieškai [37]. Nepaisant joninių skysčių ir kalcio fosfatų plataus panaudojimo skirtingoms reikmėms, yra ženklus tyrimų, kurie reikalingi norint visapusiškai suvokti šių funkcinių medžiagų pritaikymo galimybes ir struktūras, trūkumas.

IL ir vandens mišinių struktūroms tirti taikomi įvairūs fizikiniai metodai [22,38–44], tačiau dažniausiai yra naudojami mažu kampu išsklaidytos rentgeno spinduliuotės (*angl.* SAXS), neutronų sklaidos mažu kampu (*angl.* SANS), diferencinės skenavimo kalorimetrijos (*angl.* DSC), branduolių magnetinio rezonanso (*angl.* NMR) ir virpesinės spektrometrijos metodai [45–49]. Nepaisant metodų gausos, virpesinė spektrometrija yra vienas tinkamiausių būdų greitai gauti patikimą informaciją apie cheminę medžiagos sudėtį, molekulinę struktūrą ir tarpmolekulines sąveikas. Ramano sklaidos ir Furjė transformacijos infraraudonosios sugerties spektrometrijos (FTIR) metodai taip pat naudojami kartu su NMR, SANS ir SAXS metodais siekiant pateikti išsamią tiriamų funkcinių medžiagų analizę [33,41,50,51].

PAGRINDINIS DISERTACIJOS TIKSLAS IR UŽDAVINIAI

Atsižvelgiant į aukščiau aptartas problemas suformuluotas **pagrindinis šio darbo tikslas** – ištirti joninių skysčių, kalcio hidroksiapatitų bei vandeninių jų mišinių struktūras, konformacinius bei dinaminius vyksmus, taikant virpesinės spektrometrijos metodus. Darbas orientuotas į spektrinių parametrų kitimo identifikavimą vykstant struktūriniams pokyčiams ir fazių pasikeitimams funkcinėse medžiagose bei jų vandeniniuose mišiniuose.

Pagrindiniai **uždaviniai** suformuluoti šiam tikslui pasiekti:

1. Ištirti Ramano spektrometrijos metodo naudojimo galimybes joninių skysčių 1-decil-3-metilimidazolo chlorido, 1-decil-3-metilimidazolo bromido ir vandens mišiniuose besiformuojančių mezofazių analizei.
2. Išanalizuoti vandens struktūrų formavimąsi skirtingais būdais susintetintuose kalcio hidroksi apatituose, taikant virpesinės spektrometrijos metodus.
3. Išnagrinėti skirtingų vandens struktūrų joninių skysčių ir vandens mišiniuose identifikavimo galimybes ir iš Ramano sklaidos spektrų nustatyti „vandens kišenių“ formavimosi sritis 1-butil-3-metilimidazolo nitrato ir sunkiojo vandens mišiniuose.
4. Naudojant virpesinės spektrometrijos metodus ištirti vandenilio ir deuterio atomų apsikeitimo reakcijos dinamiką joninių skysčių ir sunkiojo vandens mišiniuose bei konformacinių vyksmų dinamiką joninių skysčių ir vandens mišiniuose.

GINAMIEJI TEIGINIAI

1. Virpesinė spektrometrija yra tinkamas metodas nustatyti skystosios kristalinės jonogelio fazės ir mezofazų joninių skysčių vandeniniuose mišiniuose skirtumus. Gautų Ramano sklaidos ir NMR spektrinių duomenų kompleksinis panaudojimas suteikia naujos vertingos informacijos apie LC jonogelio fazės formavimosi procesus ir skirtingų vandens molekulių spiečių vaidmenį mišiniuose.
2. Naudojant virpesinės spektrometrijos metodus galima tiksliai išskirti skirtingas vandens būsenas, esančias tiek nanostruktūrizuotų kalcio hidroksiapatitų (CaHAp) paviršiuje, tiek tūryje. Žematemperatūris FTIR sugerties spektrometrijos metodas yra ypač tinkamas skirtingų vandens molekulių spiečių nustatymui.
3. Virpesinė spektrometrija gali būti naudojama nustatant skirtingas vandens būsenas joninių skysčių ir vandens mišiniuose. Eksperimentiškai

galima nustatyti, jog 1-butil-3-metilimidazolo nitrato ir sunkiojo vandens mišiniuose formuojasi "vandens kišenės"

4. Vandenilio ir deuterio atomų apsikeitimą bei konformacinių vyksmų dinamiką joninių skysčių ir sunkiojo vandens mišiniuose galima tirti naudojant Ramano spektrometrijos metodą. Deuteravimas 1-butil-3-metilimidazolo nitrato ir sunkiojo vandens bei 1-butil-3-metilimidazolo trifluormetilsulfonato ir sunkiojo vandens mišiniuose nevyksta.

DARBO NAUJUMAS IR AKTUALUMAS

1. Pirmą kartą parodyta, kad Ramano sklaidos spektrinių parametrų pokyčiai gali būti naudojami skystosios kristalinės jonogelio fazės ir „vandens kišenių“ formavimosi sričių kambario temperatūros joninių skysčių ir vandens mišiniuose identifikavimui.

2. Nustatyta, kad didesnis molekulių laisvės laipsnis yra svarbus vandenilio ir deuterio apsikeitimo (H/D) reakcijoje. Taikant Ramano spektrometriją ištirta, kad anijono tipas nedaro įtakos joninių skysčių ir vandens mišinių heterogeniškumo laipsniui.

3. Pirmą kartą naudojant Ramano sklaidos ir infraraudonosios sugerties spektrometrijos metodus ištirti struktūriniai hidroksilo grupių skirtumai nanostruktūrizuotose kalcio hidroksiapatituose (CaHAp), susintetintuose zolių-gelių metodu naudojant skirtingus kompleksadarius.

4. Parodyta, jog skirtingą katijoną turinčių joninių skysčių (1-decil-3-metilimidazolo ir 1-butil-3-metilimidazolo) vandeniniuose mišiniuose konformaciniai pokyčiai bei vandenilio ir deuterio atomų apsikeitimas (H/D) nevyksta tuo pačiu metu.

5. Pagal teorinius skaičiavimus kvantinės chemijos metodais pirmą kartą atliktas $[C_4mim]NO_3$ ir $[C_4mim]OTf$ joninių skysčių virpesinių spektrų juostų priskyrimas.

6. Iš žemos temperatūros ir poliarizuotųjų joninių skysčių ir vandens mišinių, esant skirtingoms H_2O/D_2O koncentracijoms, Ramano sklaidos spektrų atliktas tikslus vandeniliniu ryšiu susietų vandens molekulių virpesinių OH ir OD juostų priskyrimas.

AUTORIAUS INDĖLIS

Kalcio hidroksiapatitų vandeninė zolių-gelių sintezė, naudojant skirtingus kompleksadarius, vykdyta Vilniaus universitete Chemijos fakultete Neorganinės chemijos katedroje (vadovas prof. habil. dr. Aivaras Kareiva). Didžioji dauguma eksperimentinų tyrimų, naudojant Ramano sklaidos ir

infraraudonosios sugerties spektrometrijos metodus, atlikti autoriaus. Dalį publikuotų Ramano sklaidos eksperimentinių rezultatų kartu su autoriumi užregistravo dr. Ieva Matulaitienė, dokt. Martynas Velička ir dokt. Martynas Talaikis. Molekulių teorinius skaičiavimus kvantinės chemijos metodais atliko prof. dr. Silvia Brandan ir dr. Kęstutis Aidas. Kiti publikacijose paskelbti eksperimentiniai tyrimų rezultatai gauti straipsnių bendraautorių – prof. habil dr. V. Balevičiaus, dr. V.Klimavičiaus, dr. I. Doroshenko dokt. K.Kristinaitytės ir dotkt. L. Dagio. Duomenų analizė ir publikacijų rengimas - bendras autorių komandos darbas.

DISERTACIJOS SANDARA

Disertaciją sudaro įvadas, apžvalga, eksperimentinė dalis, rezultatai, išvados, cituojamoji literatūra ir priedai. Įvade pristatoma disertacijos tema, aptariamos problematikos ir galimybės jas išspręsti. Įvade suformuluojamas ir darbo tikslas, bei jo pasiekimui iškelti uždaviniai. Įvade taip pat pristatomi ginamieji teiginiai, darbo aktualumas ir naujumas, bei su disertacija susijusių mokslinių publikacijų ir pranešimų konferencijose sąrašai. Apžvalgoje aprašoma tiriamosios medžiagos ir metodai skirti jų charakterizavimui. Eksperimentinėje dalyje detalizuojami tiriamųjų medžiagų ir taikytų eksperimentinių metodų techniniai parametrai. Rezultatų dalis išskirstyta į tris skyrius.

Pirmajame skyriuje nagrinėjami vandens struktūrų formavimosi ypatumai trumpas alkilines grandines turinčių joninių skysčių ir vandens mišiniuose bei efektai, lydintys šių struktūrų formavimąsi. Rezultatai išskirstyti į tris poskyrius. Antrajame skyriuje nagrinėjami skystosios kristalinės jonogelio fazės formavimosi ypatumai ilgas alkilines grandines turinčių joninių skysčių ir vandens mišiniuose. Rezultatai išskirstyti į du poskyrius. Trečiajame skyriuje nagrinėjamos vandens molekulių struktūros nanostruktūrizuotų kalcio hidroksiapatitų bandiniuose. Rezultatai išskirstyti į du poskyrius. Kiekvienas skyrius užbaigiamas išvadų skiltimi. Disertacijos pabaigoje pateikiamos apibendrintos išvados.

1. KONFORMACINĖ PUSIAUSVYRA IR DINAMINIAI VYKSMAI JONINIŲ SKYSČIŲ IR VANDENS MIŠINIUOSE.

Šiame skyriuje nagrinėjama grynų joninių skysčių ir vandenių IL mišinių konformacinė pusiausvyra bei jos kitimas. Aptariamas molekulių struktūrų formavimasis bandiniuose esant skirtingai vandens koncentracijai skirtingo ilgio grandinių katijonus ir sferinius bei halogeninius anijonus turinčiuose joniniuose skysčiuose.

1.1. Konformacinė pusiausvyra grynuose joniniuose skysčiuose ir jų mišiniuose su vandeniu

Konformacinė pusiausvyra grynuose joniniuose skysčiuose nagrinėjama pirmame poskyryje. Katijono $[C_4mim]^+$ konformacijos tiriamos analizuojant kombinacinius imidazolio žiedo deformacijų ir CH_2 grupių švytuoklinius virpesius [140]. Virpesinės Ramano sklaidos juostos ties 601 cm^{-1} ir 625 cm^{-1} skirtinguose joniniuose skysčiuose priskiriamos *gauche* ir *trans* konformerams susiformuojantiems alkilinei anijono grandinei pasisukus apie C(7)–C(8) jungtį [141]. Šių virpesinių juostų integrinių intensyvumų santykis I_{gauche}/I_{trans} parodo atitinkamų konformerų santykį tiriamame joniniame skystyje. Ištirtų joninių skysčių Ramano sklaidos spektrai konformacinių virpesių srityje pavaizduoti 1 pav.

.

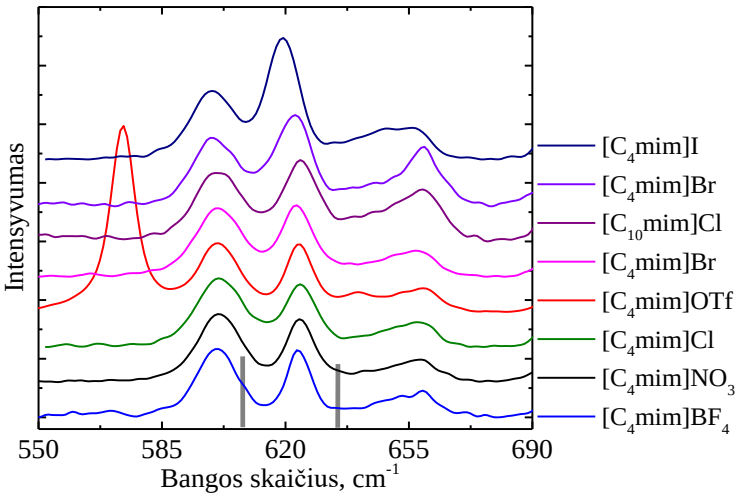

1 pav. Grynų joninių skysčių Ramano sklaidos spektrai konformacinių virpesių 550-690 cm^{-1} srityje. Pilkai pažymėti vertikalūs stulpeliai atitinka *gauche* ir *trans* konformerų virpesinių juostų bangos skaičius iš teorinių $[C_4mim]OTf$ ir $[C_4mim]NO_3$ skaičiavimų [112].

Joninių skysčių 1-butil-3-metilimidazolo trifluorometansulfonato ([C_4mim]OTf) ir 1-butil-3-metilimidazolo nitrato ([C_4mim]NO_3) Ramano sklaidos spektruose I_{gauche}/I_{trans} skaitinė vertė [C_4mim]OTf atveju yra 1,4, o [C_4mim]NO_3 atveju – 1,5. Tai rodo, kad [C_4mim]NO_3 atveju žemiausios energijos *trans* konformerų yra daugiau nei [C_4mim]OTf. Dažniausiai literatūroje minimi tokie joninių skysčių konformacijų pusiausvyrai įtaką darantys veiksniai: alkilinės grandinės ilgis, anijono skersmuo ir priemaišos bandinyje. Svarbu paminėti, kad nustatyta nevienoda [C_4mim]OTf ir [C_4mim]NO_3 joninių skysčių katijonų konformacijų pusiausvyra yra siejama su skirtingu anijonų hidrofobiškumu. Siekiant patvirtinti šį dėsningumą virpesinių Ramano sklaidos juostų I_{gauche}/I_{trans} santykis išmatuotas ir skirtingus anijonus turinčių joninių skysčių atvejais. Tyrimų rezultatai pavaizduoti 2 pav.

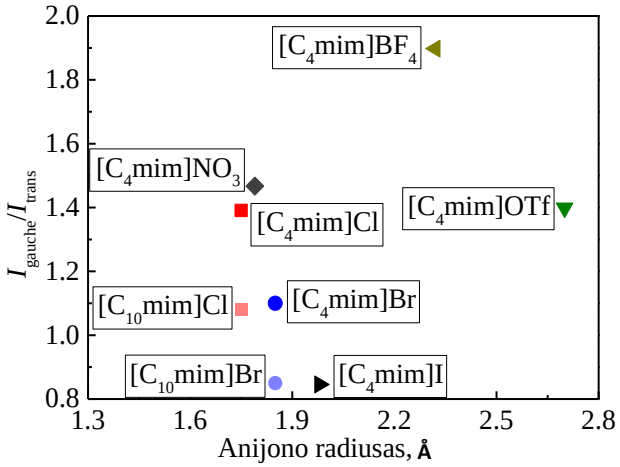

2 pav. Konformacinę pusiausvyrą atitinkančio satykio I_{gauche}/I_{trans} priklausomybė nuo anijono skersmens joniniuose skysčiuose [C_4mim][X], X=I, Br, Cl, BF_4, OTf, NO_3. Katijono grandinės ilgio įtakos palyginimo tikslu pateikti ir [C_{10}mim]Br ir [C_{10}mim]Cl tyrimų rezultatai.

Trans konformerų kiekis grynuose joniniuose skysčiuose [C_4mim]X mažėja tokia atitinkamų anijonų eilės tvarka: $X= I^- > Br^- > Cl^- > OTF^- > NO_3^- > BF_4^-$. Siekiant paaiškinti šios sekos eiliškumą remiamasi prielaida [142], kad halogenų anijonus (I^-, Br^-, Cl^-) turinčiuose joniniuose skysčiuose dėl stipresnio elektrostatinio lauko, egzistuojančio mažesnio skersmens anijonų atveju, susiformuoja daugiau *gauche* konformerų nei *trans*. Iš rezultatų, pateiktų 2 pav., matoma, kad šis modelis netinkamas nesferinių anijonų atveju (OTf^-, NO_3^-, BF_4^-). Šiuo atveju anijonų sekos eiliškumas paaiškinamas

skirtingu anijonų hidrofobiškumu [143]. I_{gauche}/I_{trans} santykio didėjimas atitinkia hidrofobiškumo augimą pagal anijono tipą.

Katijono grandinės ilgis, kaip ir anijono hidrofobiškumas, daro įtaką konformacijų pusiausvyrai IL. Palyginus grynuose IL [C_4mim]Cl ir [C_4mim]Br esančių konformerų santykį (I_{gauche}/I_{trans}) su šiuo santykiu [C_{10}mim]Cl ir [C_{10}mim]Br IL atvejais, nustatyta, kad ilgas grandines turinčiuose joniniuose skysčiuose *trans* konformerų yra 1,3 karto daugiau. Taip pat nustatyta, kad [C_{10}mim]$^+$ katijonų atveju *trans* konformerų bandinyje yra daugiau nei *gauche*, o [C_4mim]$^+$ atveju išmatuota atvirkščia proporcija. Tokie rezultatai pagrindžiami skirtingu anijonų mobilumu, kuris daro lemiamą įtaką anijonų transformavimuisi į žemesnės energijos *trans* konfomerus.

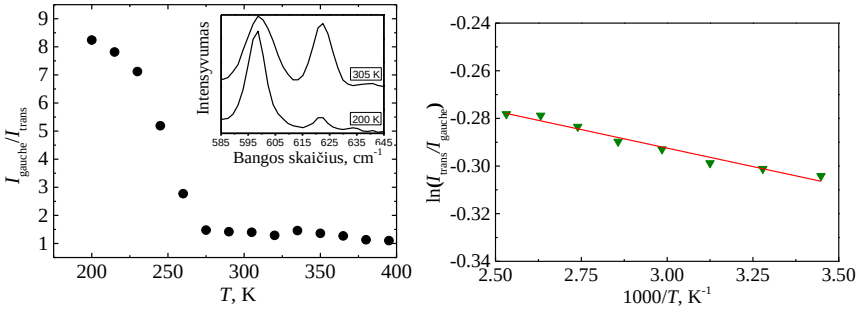

3 pav. [C_4mim]OTf Ramano sklaidos spektro *gauche* ir *trans* konformerų virpesinių juostų I_{gauche}/I_{trans} priklausomybė nuo temperatūros.

Temperatūra – vienas veiksnių, keičiančių konformacijų pusiausvyrą joniniuose skysčiuose. Ištirta I_{gauche}/I_{trans} santykio priklausomybė nuo temperatūros ir nustatytas esminis *gauche* konformerų kiekio IL padidėjimas žeminant temperatūrą nuo 275 K iki 200 K (3 pav.). Kai bandinio temperatūra yra 305 K, I_{gauche}/I_{trans}=1,5, o kai temperatūra 200 K, I_{gauche}/I_{trans}=8,8. Iš šio pokyčio nustatytas *trans* ir *gauche* konformerų entalpijų skirtumas $\Delta H_{trans\rightarrow gauche}$. Tarkime, kad *trans* (A) ir *gauche* (B) Ramano sklaidos virpesinių juostų integrinis intensyvumas nepriklauso nuo temperatūros, tada $\Delta H_{trans\rightarrow gauche}$ užrašoma (1) lygtimi [116]:

$$\Delta H^{A\rightarrow B} = -R\left\{\frac{\partial \ln(I_B/I_A)}{\partial(1/T)}\right\}_p \quad , (1)$$

čia R, T ir p yra universaliosios konstantos. I_A ir I_B yra Ramano sklaidos virpesinių juostų, priskiriamų [C_4mim]$^+$ katijono *gauche* ir *trans* virpesiams, integriniai intensyvumai [116]. Iš tiesės (3 pav., B) polinkio kampo nustatyta,

kad [C_4mim]OTf atveju skaitinė $\Delta H_{trans \rightarrow gauche}$ vertė yra −0,5±0,2 kJ/mol. Entalpijų skirtumai įvairių joninių skysčių atveju pateikti 1 lentelėje.

1 lentelė. Skirtingų joninių skysčių $\Delta H_{trans \rightarrow gauche}$ vertės.

Joninis skystis	$\Delta H_{trans \rightarrow gauche}$	Šaltinis
[C_4mim]OTf	-0.5 ± 0.2 kJ·mol^{-1}	Šis eksperimentas
[C_4mim]NO_3	-1.1 ± 0.2 kJ·mol^{-1}	[116]
[C_4mim]SCN	-1.5 ± 0.4 kJ·mol^{-1}	[116]
[C_4mim]CH_3COO	-0.9 ± 0.1 kJ·mol^{-1}	[116]
[C_4mim]BF_4	-1.0 ± 0.1 kJ·mol^{-1}	[116]

Antrame poskyryje aptariami konformacinės pusiausvyros (I_{gauche}/I_{trans}) kitimo netolydumai joninių skysčių ir vandens mišiniuose. Nustatytos vandens ir joninių skysčių [C_4mim]X (X= I^-; Br^-; Cl^-; OTf^-; NO_3^-; BF_4^-) bei [C_{10}mim]Y (Y= Br^-; Cl^-) I_{gauche}/I_{trans} priklausomybės pateiktos 4 pav. Iš rezultatų matyti kaip priemaišos (šio tyrimo atveju H_2O) keičia konformacinę pusiausvyrą. Dėl vandens sąveikų su IL molekulėmis šiose priklausomybėse nustatyti netolydumai gali būti siejami su kintančiomis IL ir H_2O sąveikomis bei skirtingų vandens molekulių struktūrų formavimusi. [C_{10}mim]Cl ir [C_{10}mim]Br atveju netolydus konformacinės pusiausvyros pasikeitimas registruojamas ties X_{H2O_MOL}=0,45±0,05. Ši vertė koreliuoja su antrajame skyriuje nagrinėjamos skystosios kristalinės (LC) jonogelio fazės formavimosi pradžia, kai X_{H2O_MASS}=0,03±0,005. Netolydumų, užregistruotų I_{gauche}/I_{trans} santykio priklausomybėse nuo vandens koncentracijos, trumpas alkilines grandines turinčių joninių skysčių atveju, priežastys nagrinėjamos antrajame ir trečiajame poskyriuose.

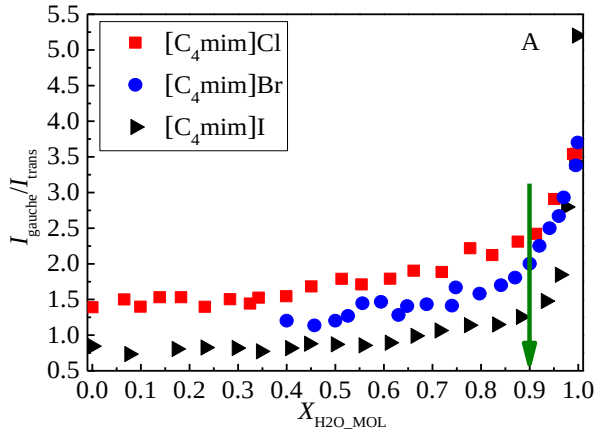
[C4mim]Cl
[C4mim]Br
[C4mim]I
A
Igauche/Itrans
XH2O_MOL

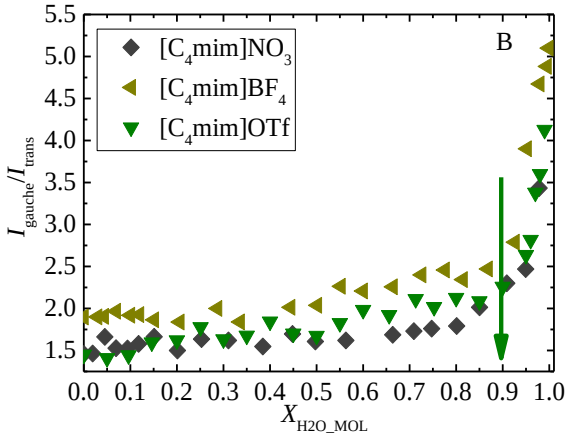
[C4mim]NO3
[C4mim]BF4
[C4mim]OTf
B
Igauche/Itrans
XH2O_MOL

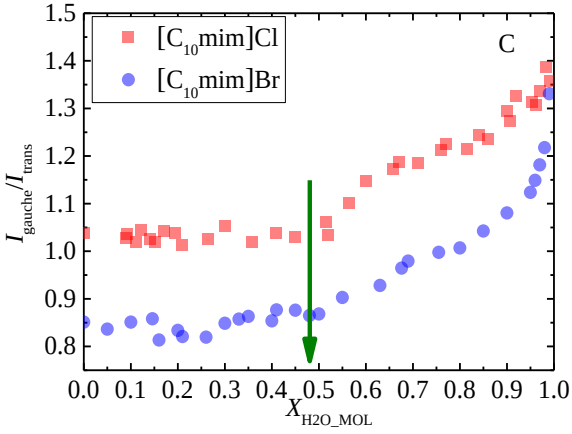
[C10mim]Cl
[C10mim]Br
C
Igauche/Itrans
XH2O_MOL

4 pav. Ramano sklaidos spektrų *gauche* ir *trans* konformerų virpesinių juostų I_{gauche}/I_{trans} priklausomybė nuo vandens koncentracijos joninių skysčių ir vandens mišiniuose. A: sferinius anijonus (I^-; Br^-; Cl^-) ir trumpas alkilinės grandines ($[C_4mim]^+$) turintys IL; B: nesferinius anijonus (OTf^-; NO_3^-; BF_4^-) ir trumpos alkilinės grandinės katijonus ($[C_4mim]^+$) turintys IL; C: sferinius anijonus (Br^-; Cl^-) ir ilgą ($[C_{10}mim]^+$) alkilinę grandinę turintys IL.

1.2. Protono ir Deuterio apsikeitimo reakcijos joninių skysčių ir sunkiojo vandens mišiniuose

Antrajame poskyryje nagrinėjama vandenilio ir deuterio apsikeitimo reakcijos dinamika joninių skysčių ir sunkiojo vandens (D_2O) mišiniuose, kai „rugštingiausias“ imidazolio žiedo vandenilio atomas pakeičiamas deuteriu (5 pav.).

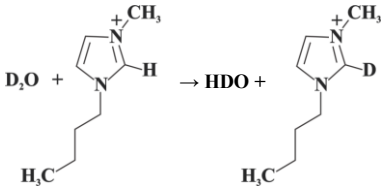

5 pav. Vandenilio ir deuterio apsikeitimo reakcijos schema $[C_4mim]^+$ katijono atveju.

Eksperimento metu bandiniai iš *X*IL_MOL=0,01 joninio skysčio ir *X*D2O_MOL=0,99 D_2O sumaišomi ir registruojamo Ramano sklaidos spektrai. Analizuojant Ramano sklaidos spektrus nustatyta, kad vykstant apsikeitimo reakcijai labiausiai kinta virpesinės juostos, priskiriamos suminiams imidzolio žiedo kvėpuojamiesiems ir CH_3(N) deformaciniams virpesiams 1000−1400 cm^{-1} srityje (toliau naudojami modų sutrumpinimai $\nu_{1010}, \nu_{1024}, \nu_{1406}, \nu_{1417}$) (6 pav.). Taip pat konformacinės pusiausvyros pokyčiai, registruojami ties 600 cm^{-1} (toliau naudojami sutrumpinimai ν_{602}, ν_{620}). Užregistruotas virpesinių juostų integrinio intensyvumo kitimas laike: ν_{1024} ir ν_{1417} mažėja ir juostos išnyksta, o virpesinių modų ν_{1010}, ν_{1406} − išauga. Pastebėta, kad išaugusių virpesinių juostų bangos skaičiaus skaitinė vertė (1010 cm^{-1} ir 1406 cm^{-1}) tiesiogiai proporcinga išnykusios virpesinės juostos bangos skaičiaus skaitinei vertei ir virpesį atitinkančių cheminių elementų molekulinės masės pokyčio santykio sandaugai. 6 pav. pateiktos virpesinių ν_{1406}, ν_{1417}, ν_{1010} ν_{1024} modų integrinių intensyvumų santykio kitimo laikinės priklausomybės.

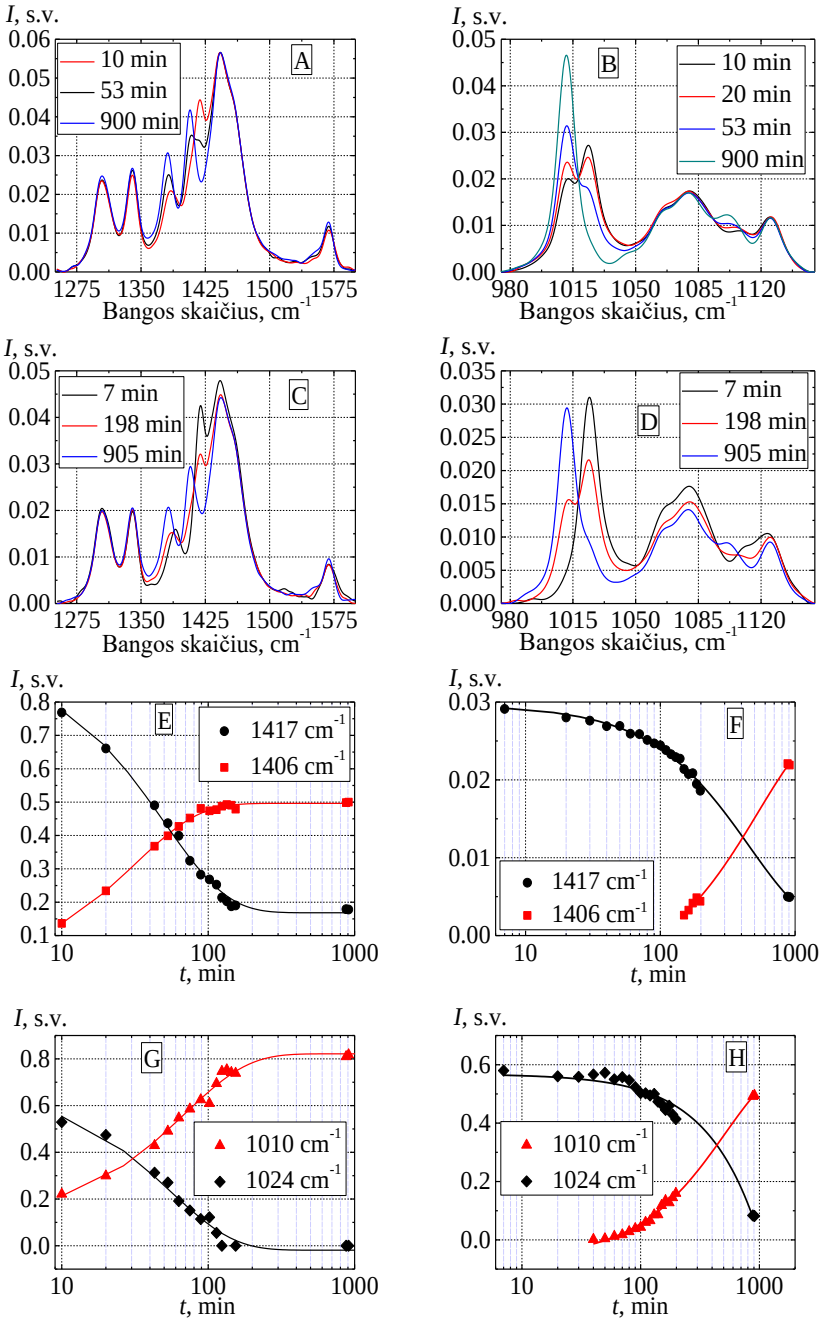

6 pav. Vandenilio ir deuterio apsikeitimo reakcijos spektriniai pokyčiai (A, B, C, D) ir dinamikos (D, E, F, G) užregistruotos joninių skysčių [C_{10}mim]Br (A, B, E, G) ir [C_{10}mim]Cl (C, D, F, H) bei D_2O mišiniuose praėjus skirtingam laikui nuo bandinio paruošimo.

Užregistruotas aukštesnio dažnio virpesinės modos pakeitimas žemesnio dažnio virpesine moda. Šie Ramano sklaidos spektrų pokyčiai siejami su deuteravimo procesu. Nustatyta, kad vandeniniame 1-decil-3-metilimidazolo bromido tirpale deutravimo procesas yra greitesnis nei 1-decil-3-metilimidazolo chlorido atveju. Bromido vandeniniame tirpale tiriamų virpesinių modų ν_{1406} ir ν_{1417} integriniai intensyvumai susilygina po 55±2 min, o sistema tampa pusiausvyra po 200 min. Chlorido atveju virpesinių ν_{1406} ir ν_{1417} modų integriniai intensyvumai spektruose susilygina po 330 min, o sistema tampa pusiausvyra po 900 min. Analogiški rezultatai gauti ir tiriant virpesinių ν_{1024} ir ν_{1010} modų integrinių intensyvumų laikines priklausomybes. Bromido atveju virpesinių modų ν_{1010} ir ν_{1024} integriniai intensyvumai susilygina po 30 min., sistema tampa pusiausvyra po 200 min. Chlorido atveju – atitinkamai, po 430 min ir 900 min. Gautieji rezultatai gerai koreliuoja su mišinių BMR matavimų rezultatais. Tokiems dinamikų skirtumams daro įtaką anijonų suformuojami vandeniliniai ryšiai su priemaišų molekulėmis. Taip pat yra nevienoda formuojamo vandenilinio ryšio tarp anijono ir vandens molekulių energija, kuri mažėja didėjant anijono molekulinei masei [28]. Vandenilio ir deuterio apsikeitimo reakcijos nagrinėtos ir ne sferinius anijonus turinčiuose joninių skysčių mišiniuose su deuteruotu vandeniu [C_4mim]OTf–D_2O ir [C_4mim]NO_3–D_2O. Spektriniai pokyčiai 1000−1400 cm^{-1} srityje neužregistruoti net po bandinio sumaišymo praėjus 60 dienų. Nustatyta, kad deuteravimo procesas šiuose mišiniuose nevyksta. Konformacinės pusiausvyros pokyčiai, registruojami ties 600 cm^{-1} ankstesniuse darbuose buvo siejami su vykstančia deuterio ir vandenilio apsikeitimo reakcija. Ištyrus [C_{10}mim]Br–D_2O, [C_{10}mim]Cl–D_2O, [C_4mim]NO_3–D_2O ir [C_4mim]OTf–D_2O mišinius nustatyta, kad H/D apsikeitimo reakcijos procesas yra nesusietas su konformacinės pusiausvyros kitimu. Konformacinės pusiausvyros kitimas laike neužregistruotas nei viename iš tirtų [C_4mim]NO_3–D_2O, [C_4mim]OTf–D_2O, [C_{10}mim]Br–D_2O ir [C_{10}mim]Cl–D_2O mišinių, nors H/D apsikeitimo reakcija vyksta [C_{10}mim]Br–D_2O ir [C_{10}mim]Cl–D_2O mišiniuose.

1.3. „Vandens kišenių“ formavimasis [C_4mim]NO_3–D_2O mišiniuose

Paskutiniajame poskyryje nagrinėjamas vandens spiečių, vadinamų „vandens kišenėmis“, formavimasis trumpą katijono alkilinę grandinę turinčio [C_4mim]NO_3 ir D_2O mišiniuose. Taip pat identifikuojami spektriniai žymenys ir jų parametrų pokyčiai, leidžiantys nustatyti vandens koncentraciją mišinyje „vandens kišenių“ susiformavimo ir suirimo atvejais. 7 pav. pavaizduoti

grynųjų $[C_4mim]NO_3$ ir D_2O Ramano sklaidos spektrai bei pažymėtos spektrinės sritys, kurių pokyčiai analizuojami.

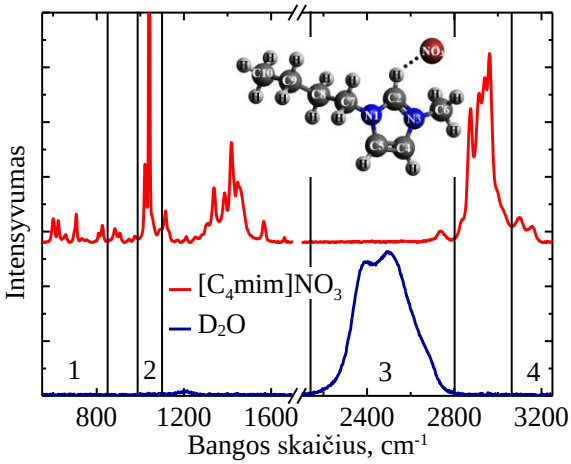

7 pav. Grynųjų medžiagų, sudarančių mišinius, Ramano sklaidos spektrai: $[C_4mim]NO_3$ (viršuje) ir D_2O (apačioje). Skaitmenimis nuo 1 iki 4 pažymėtos analizuojamos spektrinės sritys. Intarpe - $[C_4mim]NO_3$ struktūra.

Užregistruoti Ramano sklaidos spektrai, esant skirtingai D_2O koncentracijai mišiniuose, ir nustatyti ženklūs jų pokyčiai visose keturiose spektrinėse srityse. Spektrinių juostų priskyrimas atliktas naudojant teorinių molekulių skaičiavimų duomenis [112,139] ir pateiktas 2 lentelėje. Literatūroje gerai aprašytas modelis, kad žemose vandens koncentracijose (kai vandens molekulių yra mažiau nei joninio skysčio molekulių) anijonai ir vandens molekulės pirmiausia formuoja vandeniliniais ryšiais susijungusius agreagatus *anionas···vanduo···anijonas* [160].

Kai vandens molekulių kiekis mišinyje pasidaro didesnis už IL molekulių kiekį, formuojasi agregatai *vanduo···anijonas···vanduo* [89] ir atsiranda galimybė vandens molekulėms jungtis tarpusavyje ir suformuoti "vandens kišenes".

Pirmiausia ištirtas NO_3^- anijono deformacinių ($\nu_4(NO_3^-)$) ir simetrinių valentinių ($\nu_1(NO_3^-)$) virpesinių Ramano sklaidos juostų parametrų kitimas didinant sunkiojo vandens koncentraciją mišiniuose. Kartu su spektrais (intarpuose) šios priklausomybės pavaizduotos 8 pav. Mėlynasis Ramano poslinkis nuo 1041,2 cm^{-1} iki 1047,7 cm^{-1} (bangos skaičių skirtumas yra 6,5 cm^{-1}) ir $\nu_1(NO_3^-)$ virpesinės juostos išplitimas 2,5 cm^{-1}, taip pat $\nu_4(NO_3^-)$ virpesinės juostos mėlynasis Ramano poslinkis nuo 707 cm^{-1} iki 717 cm^{-1}

2 lentelė. „Vandens kišenių“ formavimosi tyrimui naudotų Ramano virpesinių modų priskyrimas.

Virpesių Priskyrimas	Virpesinių juostų bangos skaičius (cm^{-1})	Šaltinis	Virpesinė moda
Imidazolio žiedo deformaciniai ir CH_2 grupių švytuokliniai *gauche* konformerų virpesiai	600	[140,141]	ν(*gauche*)
midazolio žiedo deformaciniai ir CH_2 grupių švytuokliniai *trans* konformerų virpesiai	625	[140,141]	ν(*trans*)
NO_3^- deformaciniai virpesiai	706	[116]	$\nu_4(NO_3^-)$
NO_3^- simetriniai valentiniai virpesiai	1041	[116]	$\nu_1(NO_3^-)$
OD valentiniai vandens molekulių, suformavusių labai stipriais vandeniliniais ryšiais sujungtus spiečius (VSHB), virpesiai	2260	[148]	ν(VSHB)
OD asimetriniai valentiniai vandens molekulių, suformavusių tetraedrines struktūras (SHB), virpesiai	2400	[72,148, 149]	ν(SHB)
OD simetriniai valentiniai vandens molekulių, suformavusių suardytas tetraedrines struktūras (MHB), virpesiai	2525	[116,148,149]	ν(MHB)
OD virpesiai, priskiriami pavienėms D_2O molekulėms	2643	[148,149]	ν(WHB)
Imidazolo žiedo C(2)–H valentiniai virpesiai	3100	[145,150–152]	ν(C(2)-H)
Imidazolo žiedo C(4,5)–H asimetriniai valentiniai virpesiai	3152	[145,150–152]	ν(C(4,5)–H_asym)
Imidazolo žiedo C(4,5)–H simetriniai valentiniai virpesiai	3164	[145,150–152]	ν(C(4,5)–H_sym)

(skirtumas 10 cm^{-1}) ir juostos išplitimas 11 cm^{-1} užregistruoti sunkiojo vandens koncentraciją mišinyje pakeitus nuo X_{D2O_MOL}=0 iki X_{D2O_MOL}=0,99. Mėlynasis Ramano sklaidos juostų poslinkis parodo, kad anijonas NO_3^- yra atitraukiamas nuo katijono $[C_4mim]^+$, o virpesinių juostų išplitimą galima sieti su skirtingų agregatų *anijonas···vanduo* ir vanduo···anijonas···vanduo formavimusi tuo pačiu metu [38, 50, 53–56]. Iš 8 pav. matyti, kad vandens koncentracijai mišinyje pasiekus X_{D2O_MOL}=0,61 Ramano sklaidos juostų bangos skaičiaus kitimas tampa netolydus, t.y., toliau didinant vandens

koncentraciją, virpesinių juostų poslinkio didėjimas spartėja. Šie pokyčiai siejami su pasikeitusia sąveika tarp vandens ir joninio skysčio anijonų bei prasidedančiu "vandens kišenių" formavimusi.

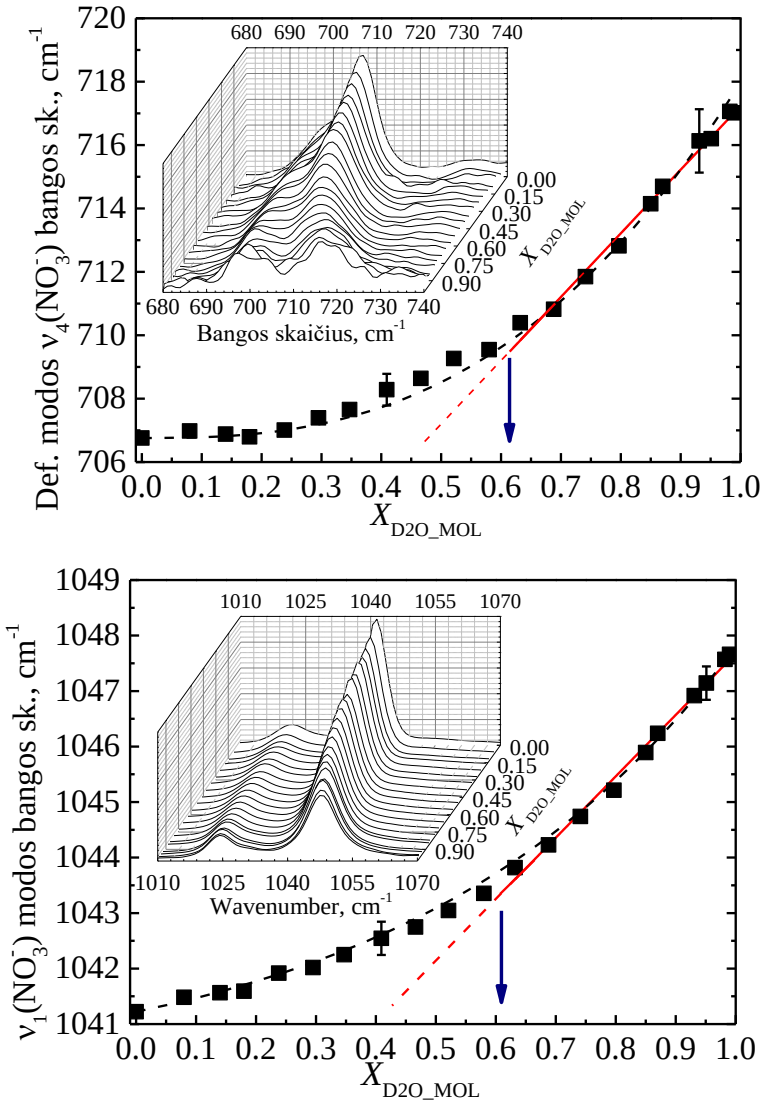

8 pav. Ramano sklaidos virpesinių juostų $\nu_4(NO_3^-)$ ir $\nu_1(NO_3^-)$ bangos skaičiaus priklausomybės nuo D_2O koncentracijos $[C_4mim]NO_3$-D_2O mišiniuose. Intarpuose pavaizduoti spektrai jonino skysčio anijono NO_3^- deformacinių (viršuje) ir valentinių (apačioje) virpesių srityse.

Bangos skaičiaus pokytis didinant D_2O koncentraciją mišiniuose taip pat ištirtas virpesinių juostų, priskiriamų imidazolo žiedo valentiniams C(n)–H virpesiams, atveju. Dėl formuojamo vandenilinio ryšio tarp anijono ir katijono šios juostos yra vienos jautriausių priemaišų įtakai joniniuose skysčiuose ir yra puikiai tinkamos identifikuoti medžiagos pasikeitimus [145,150–152,158]. Ramano virpesinių juostų bangos skaičiaus kitimas ilgas grandines turinčiuose joniniuose skysčiuose bus aptariamas antrajame santraukos skyriuje (3.4. disertacijos skyrius). Šiuo atveju Ramano sklaidos spektrai C(n)–H virpesių srityje (3040-3220 cm^{-1}), virpesinių juostų aproksimacijos ir mėlynojo poslinkio priklausomybės nuo vandens koncentracijos pavaizduotos 9 pav. A, B ir C dalyse.

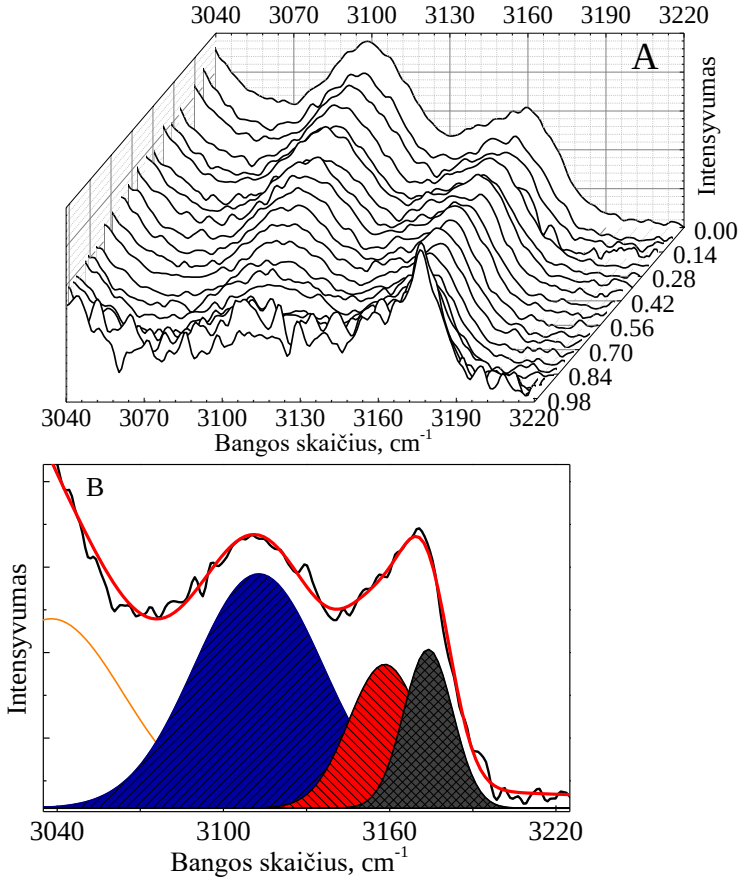

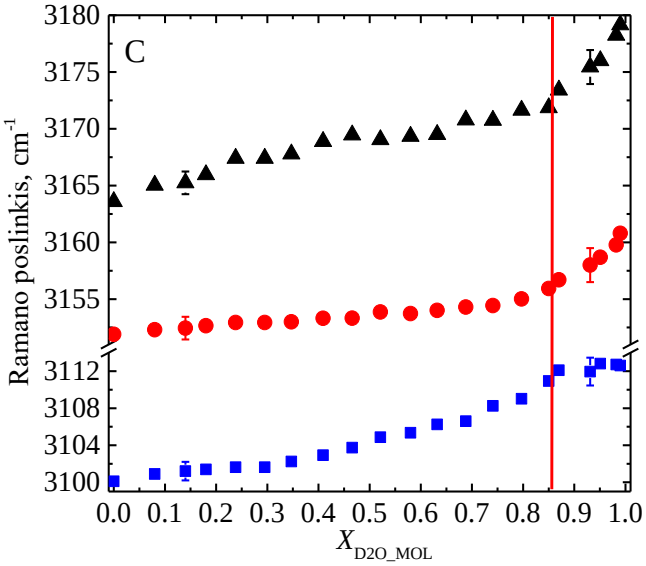

9 pav. Ramano sklaidos spektrai C(n)–H virpesių srityje 3040-3220 cm^{-1} (A), aproksimuotos virpesinės juostos (B) ir mėlynojo poslinkio priklausomybės nuo vandens koncentracijos (C).

Grynojo joninio skysčio Ramano sklaidos virpesinės modos, priskiriamos C(2)–H, C(4,5)–H asimetriniams bei C(4,5)–H simetriniams valentiniams virpesiams, yra ties 3100 cm^{-1}, 3152 cm^{-1}, 3164 cm^{-1} bangos skaičiaus vertėmis. Iš šių verčių nustatyta, kad formuojamas vandenilinis ryšys tarp C(2)–H···NO_3 yra stipresnis negu C(4,5)–H···NO_3 atveju. 9 pav. matomas mėlynasis virpesinių juostų poslinkis tik patvirtina anksčiau aptartą anijono atitraukimo nuo katijono modelį. Kaip ir aukščiau nagrinėtuose virpesių parametrų pokyčiuose, taip ir C(n)–H atveju yra nustatytas netolydus mėlynasis Ramano poslinkis. ν(C(2)–H) virpesinės modos bangos skaičius pakito 13 cm^{-1} (nuo 3100 iki 3113 cm^{-1}), ν(C(4,5)–H_asym) 9 cm^{-1} (nuo 3152 cm^{-1} iki 3161 cm^{-1}) ir ν(C(4,5)–H_sym) 15 cm^{-1} (nuo 3164 cm^{-1} iki 3179 cm^{-1}). Netolydumai tiek ν(C(2)–H)modos bangos skaičiaus kitime, tiek ν(C(4,5)–H _asym) ir ν(C(4,5)–H _sym) virpesinių modų bangos skaičiaus kitime nustatyti ties X_{D2O_MOL}=0,86. Svarbu paminėti, kad nustatytos mėlynojo Ramano poslinkio vertės yra panašios, tačiau jų pokyčio koncentracinės kreivės nėra vienodos. ν(C(2)-H) virpesinės modos visas poslinkis (100% – 13 cm^{-1}) registruojamas, kai koncentracija didėja nuo X_{D2O_MOL}=0 iki X_{D2O_MOL}=0,86, kai, tuo tarpu, ν(C(4,5)–H _asym) ir ν(C(4,5)–H_sym) virpesinių modų poslinkis šioje koncentracijų srityje sudaro tik pusę viso poslinkio (50% – 4 ir 7 cm^{-1}). Nevienodos procentinės poslinkio vertės, pasiekus X_{D2O_MOL}=0,86±0,04 koncentraciją, patvirtina ansktesnius teiginius,

kad joninio skysčio ir vandens molelulių sąveika pirmiausia vyksta su anijonu, esančiu prie "rūgštingesnio" C2 anglies atomo imidazolio žiede, o tik po to – su anijonais ties C4 ir C5. Spektrinių parametrų netolydumo taške D_2O ir IL molekulių santykis mišinyje yra 9:1. Iki pasiekiant X_{D2O_MOL}=0,86±0,04 koncentraciją mišinyje anijonai ir katijonai atskirti, ir jau yra susiformavę vandeniliniai ryšiai *vanduo···anijonas* [164], *vanduo···vanduo* ("vandens kišenė"), C(2)–H···*vanduo*. Dar padidinus koncentraciją vandeniliniai ryšiai C(2)–H···*vanduo* nebesiformuoja, registruojamas vandenilinių ryšių C(4,5)–H···*vanduo* atsiradimas, "vandens kišenių" išardymas bei vandens spiečių formavimasis.

Vandens spiečių formavimasis tirtas analizuojant OD virpesių sritį Ramano spektruose nuo 2100 cm^{-1} iki 2800 cm^{-1}. Skirtingų vandens molekulių spiečių ir pavienių vandens molekulių virpesinių juostų priskyrimai pateikti 2 lentelėje. 10 pav. viršutinėje dalyje pavaizduotas $[C_4mim]NO_3$–D_2O Ramano sklaidos spektras su aproksimuotomis sunkiojo vandens molekulių virpesinėmis juostomis, o apatinėje - šių virpesinių juostų integrinių intensyvumų santykio priklausomybė nuo D_2O koncentracijos mišinyje. Ribinės D_2O koncentracijos, kuriose mišinyje formuojasi "vandens kišenės", yra pažymėtos vertikaliomis tiesėmis: mėlyna, kai X_{D2O_MOL}=0,6 ir raudona, kai X_{D2O_MOL}=0,86, žyminčiomis "kišenių" formavimosi pradžią ir pabaigą [19, 67]. Šios ribos nustatytos pagal virpesinės modos ν(MHB) integrinio intensyvumo kitimo netolydumus. Skirtingiems vandens spiečiams priskiriamų virpesinių juostų integrinių intensyvumų kitimas "vandens kišenių" formavimosi srityje leidžia teigti, kad susiformavusiose "vandens kišenėse" aptinkama visų rūšių vandens spiečių. Svarbu paminėti, kad struktūrų, kurių virpesius atitinka ν(VSHB) ir ν(MHB), kiekis susiformavusiose "vandens kišenėse" nesikeičia, kitų struktūrų kiekis (ν(WHB)) – mažėja ir didėja ν(SHB)). Tai rodo, jog "vandens kišenėse" vyksta pavienių vandens molekulių persigrupavimas į spiečius. Šis rezultatas gerai koreliuoja su kitų autorių teoriniais skaičiavimais [22] ir ankstensiuose poskyriuose aptartu skirtingų agregatų, sudarytų iš anijonų ir vandens molekulių, formavimosi ypatumais. Iš virpesinių modų ν(SHB), ν(MHB) ir ν(WHB) spektrinių parametrų priklausomybių nuo koncentracijos nustatytas netolydus virpesinių modų bangos skaičiaus ir juostų puspločių kitimas kai vandens koncentracija viršija X_{D2O_MOL}=0,6.

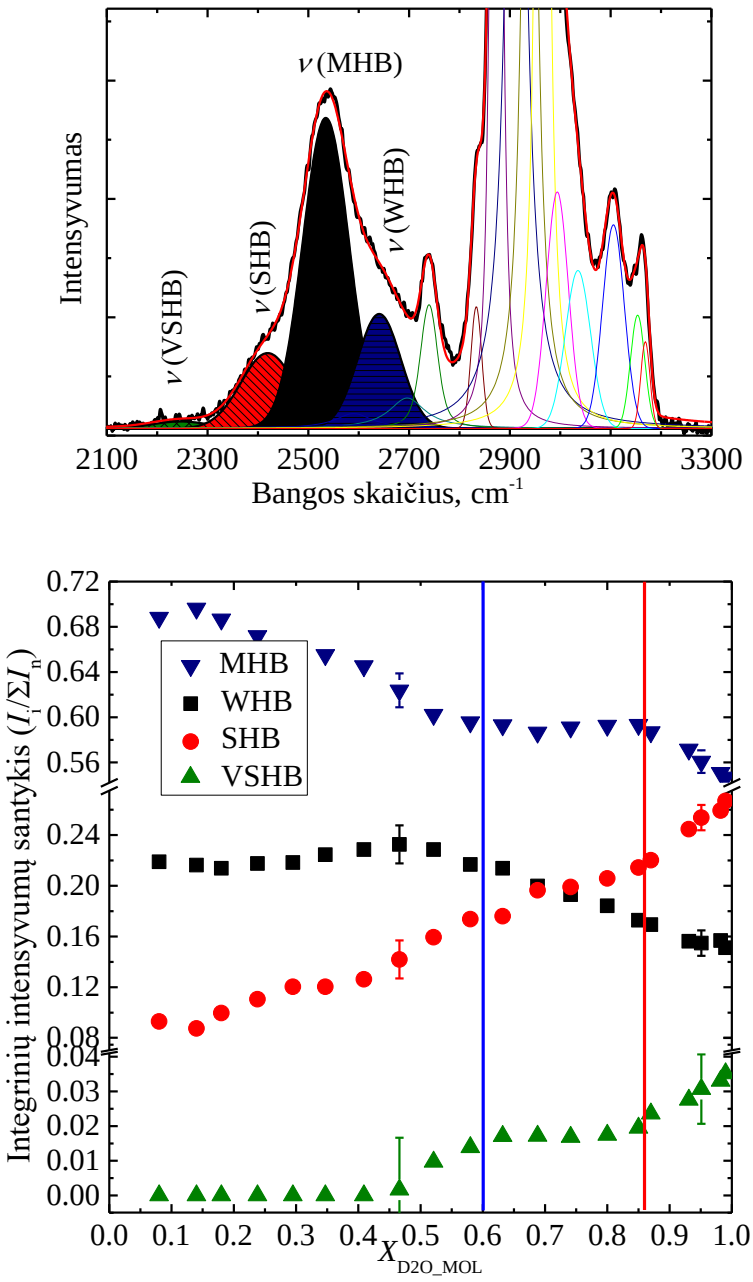

10 pav. Mišinio $[C_4mim]NO_3$-D_2O Ramano sklaidos spektras D–H virpesių srityje (X_{D2O_MOL}=0,87) ir aproksimuotos virpesinės juostos (viršuje), skirtingų vandens spiečių virpesinių juostų integrinių intensyvumų priklausomybės nuo koncentracijos (apačioje). Mėlyna vertikali tiesė žymi "vandens kišenių" formavimosi pradžią, raudona - pabaigą.

Šie spektrinių juostų parametrų pokyčiai susieti su stiprėjančiu vandeniliniu ryšiu tarp vandens molekulių, kai sąveikos tarp IL ir D_2O molekulių pasikeičia iš *anijonas···vanduo···anijonas* į *vanduo···anijonas···vanduo*. Virpesinės juostos ν(VSHB) analizei užregistruoti žematemperatūriai (153 K), poliarizuotieji grynojo $[C_4mim]NO_3$ ir skirtingų D_2O koncentracijų IL ir D_2O mišinių Ramano sklaidos spektrai. Kitų autorių eksperimentuose [172] atliktas toks pat spektrinės juostos ties 2260 cm^{-1} priskyrimas, tačiau kambario temperatūros mišinių spektruose nustatytas labai mažas jos integrinis intensyvumas, todėl šios juostos spektrinių parametrų pokyčiai nebuvo detalizuojami. Svarbu paminėti, kad žemos temperatūros (153 K) mišinių atveju, registruojama pilnai depoliarizuota virpesinė ν(VSHB) juosta (detalėsnė informacija 3 disertacijos dalyje). Tai rodo, kad šiai virpesinei modai priskiriami itin aukštos simetrijos virpesiai. Žemos temperatūros mišinių, kai X_{D2O_MOL}=0,48 (vandens kišenės nesiformuoja), Ramano sklaidos spektruose, ν(VSHB) ir ν(SHB) neregistruojamos.

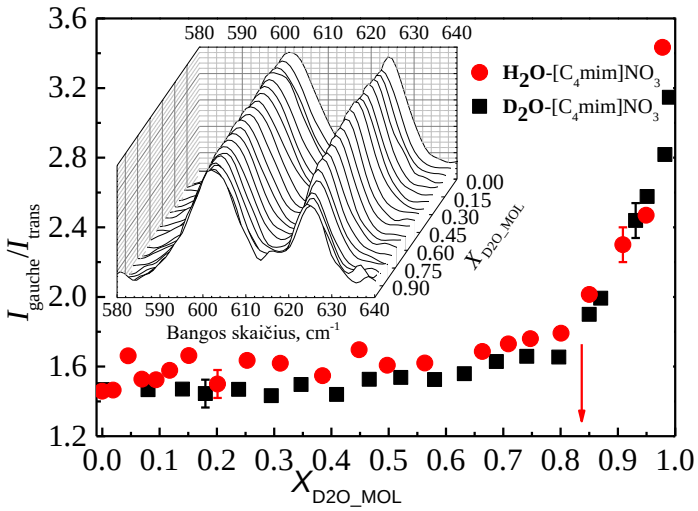

11 pav. Ramano sklaidos *gauche* ir *trans* konformerų virpesinių juostų integrinių intensyvumų santykio I_{gauche}/I_{trans} priklausomybės nuo H_2O/ D_2O koncentracijos vandeniniuose $[C_4mim]NO_3$ mišiniuose ir mišinio spektrai 580-640 cm^{-1} srityje (viršuje). Raudona vertikalia tiese pažymėta „vandens kišenių“ formavimosi pabaiga.

Svarbu paminėti, jog Ramano sklaidos juostų, priskiriamų joninio skysčio molekulių *gauche* ir *trans* konformerams, integrinių intensyvumų santykio

I_{gauche}/I_{trans} pokytis tiek IL mišinių su H_2O, tiek su D_2O atvejais sutampa. Šie rezultatai patvirtina, kad deuteravimas $[C_4mim]NO_3$–D_2O mišiniuose nevyksta. Detaliau deuteravimo procesas aptariamas antrajame šio skyriaus poskyryje. Taip pat nustatytas netolydus I_{gauche}/I_{trans} integrinių intensyvumų santykio augimas didinant D_2O koncentraciją mišinyje (11 pav.). Iki D_2O koncentracijos vertės X_{D2O_MOL}=0,86±0,04 I_{gauche}/I_{trans} santykis yra pastovus ir lygus 1,4±0,2, o esant didesnėms vandens koncentracijoms šis santykis išauga iki 3,2±0,2. Tokie pokyčiai paaiškinami aukščiau minėtu modeliu, kai anijonai yra atskiriami nuo katijonų, formuojasi dideli vandens spiečiai, ardydami susiformavusias „vandens kišenes“.

1.4. Skyriaus išvados

Nustatyta, kad konformacinėje pusiausvyroje trumpas alkilines grandines turinčių joninių skysčių atveju katijonai $[C_4mim]^+$ labiau linkę formuotis kaip *gauche* (*GT*) konformerai.

Konformacinei pusiausvyrai joniniuose skysčiuose daro įtaką ne tik katijonų, tačiau ir anijonų fizikiniai parametrai. Halogenų ir nesferiškus anijonus turinčių joninių skysčių *gauche* (*GT*) ir *trans* (*TT*) konformacijų pusiausvyrai esminę įtaką daro anijono spindulys ir hidrofobiškumas. Kuo mažesnis anijono hidrofobiškumas, tuo didesnė dalis joninių skysčių molekulių susiformuoja kaip *trans* konformerai tokia tvarka: $I^- > Br^- > Cl^- > Otf^- > NO_3^- > BF_4^-$. Nustatyta, vanduo keičia joninio skysčio konformacinę pusiausvyrą.

Vandeninių joninių skysčių $[C_4mim]NO_3$ mišinių Ramano sklaidos spektruose anijono virpesinių juostų $\nu_4(NO_3^-)$, $\nu_1(NO_3^-)$ bei skirtingiems vandens molekulių spiečiams priskiriamų virpesinių juostų bangos skaičiaus kitimo netolydumai, užregistruoti žemų D_2O koncentracijų (X_{D2O_MOL}=0,60±0,04) srityje, sietini su “vandens kišenių” formavimosi pradžia.

Aukštų D_2O koncentracijų (X_{D2O_MOL}=0,86±0,04) atveju $[C_4mim]NO_3$-D_2O mišinių spektruose taip pat nustatyti spektrinių parametrų kitimo netolydumai. *Gauche* ir *trans* konformerų virpesiams priskiriamų spektrinių juostų integrinių intensyvumų santykio kitimo, joninio skysčio imidazolo žiedo valentinius virpesius ir skirtingų vandens spiečių molekulių virpesius atitinkančių juostų spektrinių parametrų kitimo netolydumai, keičiant D_2O koncentraciją mišinyje, siejami su “vandens kišenių” formavimosi pabaiga.

Vandenilio ir deuterio apsikeitimo dinamika joninių skysčių ir sunkiojo vandens mišiniuose tirta taikant Ramano spektrometrijos metodą. Nustatyta, kad molekulių mobilumas dėl besikeičiančių tvarkos ir netvarkos parametrų bei anijonų ir vandens agregacija įtakoja H/D mainų reakcijas. Anijonai ir katijonai yra sujungti vandeniliniu ryšiu, kurį silpnina vandens molekulės pakeisdamos *anijonas···katijonas* sąveikas į *anijonas···vanduo* ir *katijonas···vanduo* sąveikas. H/D mainų reakcijos greitis priklauso nuo anijono tipo, bandinio grynumo ir temperatūros.

Anijono tipas ir katijono lokalizacija daro didžiausią įtaką H/D mainų reakcijoms joninio skysčio ir vandens mišiniuose. Nustatyta, kad H/D mainai vyksta Joniniuose skysčiuose sudarytuose tiek iš ilgų, tiek iš trumpų katijono grandinių ir halogenų anijonų (I^-, Br^-, Cl^-), kurie sudaro vandenilinius ryšius imidazolo žiedo plokštumoje. Joniniuose skysčiuose, sudarytuose iš nesferiškų anijonų (OTf^-; NO_3^-; BF_4^-) ir trumpų alkilinių grandinių, H/D mainai nevyksta.

Konformacinės pusiausvyros kitimas neturi įtakos H/D mainams, kaip buvo nustatyta ir [100] tyrime. Deuteravimas 1-butil-3-metilimidazolo nitrato ir sunkiojo vandens bei 1-butil-3-metilimidazolo trifluormetilsulfonato ir sunkiojo vandens mišiniuose nevyksta, nepriklausomai nei nuo D_2O koncentracijos, nei nuo eksperimento vykdymo trukmės.

2. SKYSTOSIOS KRISTALINĖS JONOGELIO FAZĖS FORMAVIMOSI YPATUMAI ILGAS ALKILINES GRANDINES TURINČIŲ JONINIŲ SKYSČIŲ IR VANDENS MIŠINIUOSE

Šiame skyriuje nagrinėjami ilgas alkilines grandines turinčių jonininių (IL) skysčių 1-decil-3-metilimidazolo Bromido ([C_{10}mim]Br) ir 1-decil-3-metilimidazolo Chlorido ([C_{10}mim]Cl) mišiniai su vandeniu. Joninių skysčių ir vandens mišiniai keičiant vandens masės dalį (X_{H2O_MASS}) nuo 0 iki 0,99 buvo tiriami naudojant Ramano sklaidos spektrometrijos metodą. Dėl skirtingų vandens ir joninio skysčio molekulių sąveikų keičiantis vandens koncentracijai formuojasi įvairios struktūros [69,71,76–78,80,121], kurios identifikuotos tiriant skirtingus molekulių virpesius.

2.1. Imidazolo žiedo C–H virpesinių modų tyrimas

Pirmajame poskyryje analizuojama Ramano virpesinių juostų, priskiriamų imidazolo žiedo valentiniams C(2)–H, C(4)–H ir C(5)–H virpesiams, bangos skaičiaus priklausomybė nuo vandens koncentracijos mišinyje. 12 pav. pavaizduoti grynų joninių skysčių Ramano spektrai 2600-3300 cm^{-1} srityje, kurioje stebimi spektriniai pokyčiai. Skirtingų IL–H_2O mišinių tyrimams dažnai naudojami virpesinės spektrometrijos metodai (FTIR, Raman) [72,73,114,173]. Šiuose eksperimentuose tirtų joninių skysčių virpesinių juostų priskyrimas atliktas naudojantis ankstesnių tyrimų rezultatais [140,150] (3 lentelė).

3 lentelė. Skirtingus alkilinių grandinių ilgius turinčių joninių skysčių virpesinių Ramano sklaidos juostų priskyrimas imidazolo žiedo valentiniams C–H virpesiams.

Joniniai skysčiai	[C_6mim]Cl	[C_8mim]Cl	[C_{10}mim]Cl	[C_{10}mim]Br
Virpesiai	Virpesinių juostų bangos skaičius (cm^{-1})			
v(C(2)–H) valentiniai	3062±1	3070±1	3043±1	3060±1
v(C(4,5)–H) valentiniai	3142±2	3143±1	3147±1	3144±1
Nuoroda	[140]	[150]	Šis tyrimas	Šis tyrimas

Virpesinių juostų priskiriamų imidazolo žiedo valentiniams C(2)–H, C(4)–H ir C(5)–H parametrai keičiasi pirmiausia, nes vandens molekulės pirmiausia linkusios sąveikauti su anijonu ir hidrofiline tiriamų joninių skysčių molekulių dalimi imidazolo žiede.

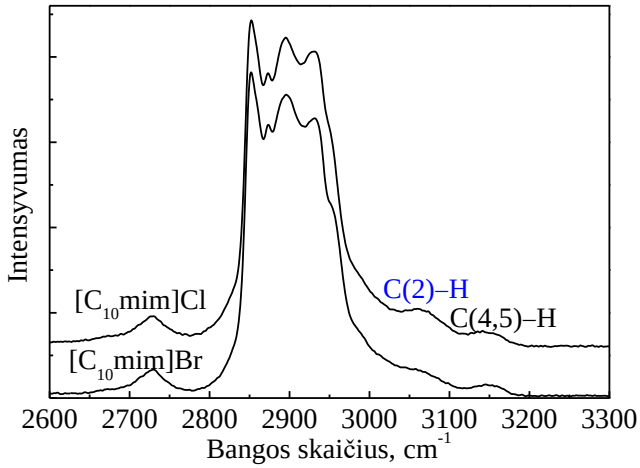

12 pav. [C_{10}mim]Cl ir [C_{10}mim]Br Ramano sklaidos spektrai C–H virpesinių juostų srityje.

Formuojantis vandeniliniams ryšiams C–H··· jungčių atveju virpesinėje spektrometrijoje dažniausiai stebime bangos skaičiaus sumažėjimą literatūroje vadinamą raudonuoju poslinkiu [158,175]. [C_{10}mim]Br ir [C_{10}mim]Cl atveju joniniame skystyje didėjant vandens koncentracijai virpesinių juostų ν(C(2)–H) ir ν(C(4,5)–H) bangos skaičius taip pat padidėja, literatūroje šis dažnio poslinkis vadinamas mėlynuoju poslinkiu (13 pav.). Šiuo atveju vyksta ne vandenilinių ryšių *C–H*··· susidarymas, o jų ardymas. Vandens molekulės, sudarydamos vandenilinius ryšius su anijonais, atitraukia juos nuo katijonų, taip silpnindamos vandenilinius ryšius tarp anijono ir katijono (*C–H*···*anijonas*). Formuojasi molekuliniai agregatai *anijonas*···*vanduo*···*anijonas*. Didinant vandens masės dalį mišiniuose X_{H2O_MASS} aptiktas netolydus šių Ramano sklaidos juostų mėlynasis poslinkis. Vandens koncentracijai mišinyje pasiekus X_{H2O_MASS}=0,03±0,001 nustatytas C–H virpesinių modų bangos skaičiaus didėjimo pasikeitimas (14 pav.). Užregistruota nuožulnesnė bangos skaičiaus priklausomybė nuo vandens masės dalies mišinyje (15 pav. A ir C mėlyna dalis, D ir F juoda dalis). Eksperimento metu nustatytos nevienodos mėlynojo poslinkio vertės mišiniuose [C_{10}mim]Cl–H_2O ir [C_{10}mim]Br–H_2O esant skirtingoms vandens koncentracijoms (4 lentelė).

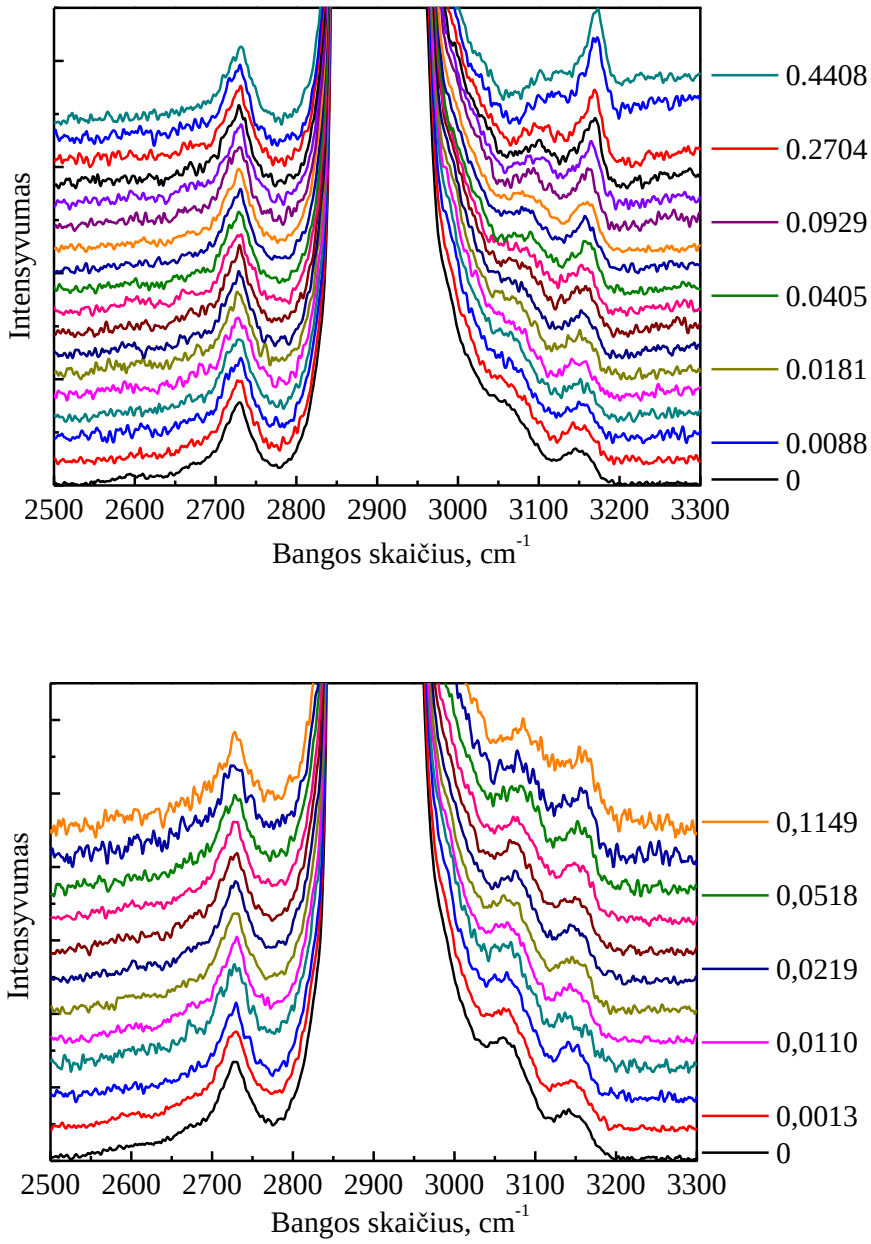

13 pav. Mišinių [C_{10}mim]Cl–H_2O (viršuje) ir [C_{10}mim]Br–H_2O (apačioje) Ramano sklaidos spektrai keičiant vandens koncentraciją.

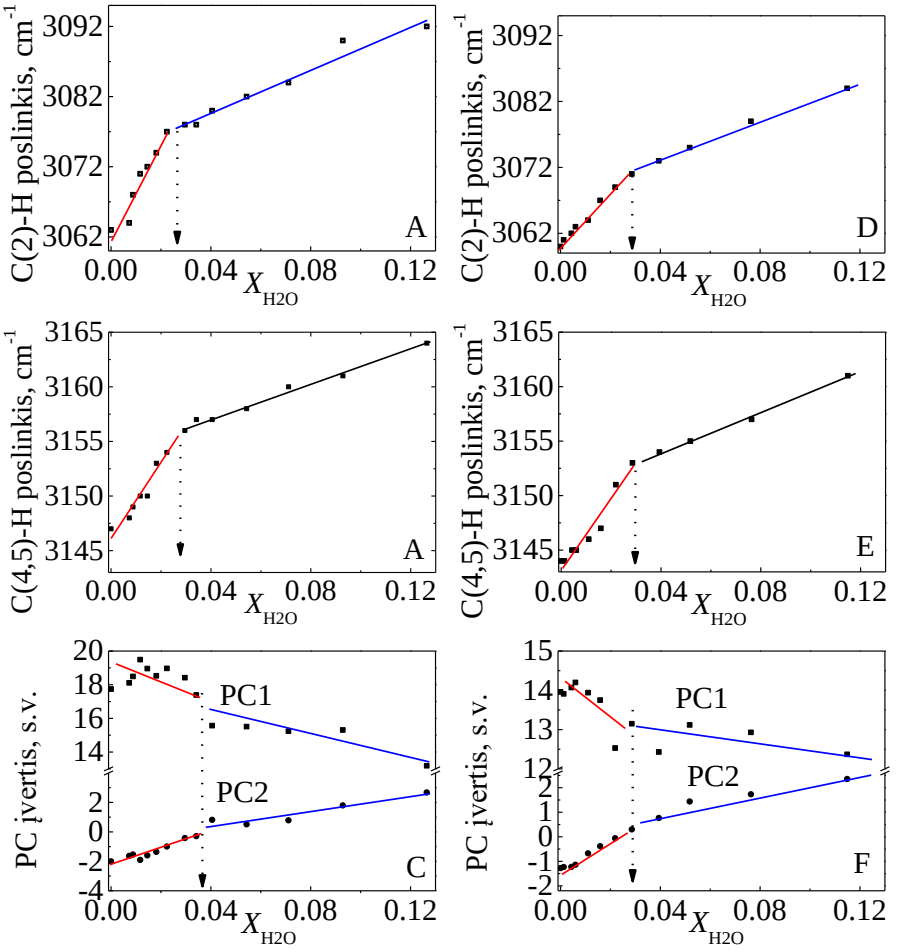

14 pav. LC jonogelio fazės formavimosi pradžios nustatymas iš PC įverčių ir C–H spektrinių juostų parametrų priklausomybių nuo vandens koncentracijos mišiniuose [C_{10}mim]Cl–H_2O (A,B,C) ir [C_{10}mim]Br–H_2O (D,E,F). Netolydžios ν(C(2)–H) virpesinių modų (A,D), ν(C(4,5)–H) virpesinių modų (B,E), bei PCA metodu gautų pirmojo ir antrojo principinių komponentų įverčio vektoriaus (C,F) priklausomybės nuo vandens koncentracijos.

Vandens koncentracijai mišiniuose pasikeitus nuo X_{H2O_MASS}=0,00 iki X_{H2O_MASS}=0,03 užregistruoti Ramano sklaidos juostų dažnių poslinkiai yra lygūs juostų dažnių poslinkių vertėms gautioms vandens koncentracijai mišiniuose pasikeitus nuo X_{H2O_MASS}=0,03 iki X_{H2O_MASS}=0,12. Pridėto vandens kiekis skiriasi tris kartus todėl vandens ir joninių skysčių molekulių sąveikos esant skirtingai vandens koncentracijai mišiniuose yra siejamos su tarpmolekulinių sąveikų pokyčiais ir joninio skysčio molekulių mobilumo sumažėjimu, kai mišinyje formuojasi LC jonogelio fazė. Lėtesnis mėlynojo

Ramano sklaidos juostų poslinkio kitimas perkopus „lūžio“ koncentraciją mišiniuose X_{H2O_MASS}=0,03 taip pat siejamas su molekulinių agregatų *vanduo···anijonas···vanduo* formavimusi. Susidarant šiems agregatams, vandens molekulės sąveikauja ne tik su anijonais tačiau ir tarpusavyje ir suformuoja vandens kanalus (*angl.* water channels), būdingus LC jonogelio fazei ilgas grandines turinčiuose joniniuose skysčiuose. Plačiau vandens molekulių tarpusavio sąveikos aptariamos antroje šio skyriaus dalyje.

4 lentelė. Virpesinių Ramano sklaidos juostų, priskiriamų imidazolo žiedo valentiniams C–H virpesiams, bangos skaičiaus kitimas ($\Delta\nu$) esant skirtingoms vandens koncentracijoms IL–H2O mišiniuose.

Vandens masės dalis mišinyje X_{H2O_MASS}	0		0,03		0,12	
[C_{10}mim]Cl–H_2O		$\Delta\nu_{0\text{-}0,03}$		$\Delta\nu_{0,03\text{-}0,09}$		$\Delta\nu_{0\text{-}0,12}$
νC(2)–H, cm^{-1}	3062±1	16±2	3078±1	13±2	3091±1	29±2
νC(4,5)–H, cm^{-1}	3147±1	9±2	3156±1	7±2	3163±1	16±2
[C_{10}mim]Br–H_2O		$\Delta\nu_{0\text{-}0,03}$		$\Delta\nu_{0,06\text{-}0,09}$		$\Delta\nu_{0\text{-}0,12}$
νC(2)–H, cm^{-1}	3060±1	11±2	3071±1	13±2	3084±1	24±2
νC(4,5)–H, cm^{-1}	3144±1	9±2	3153±1	8±2	3161±1	17±2

Palyginus virpesinių juostų poslinkius, kai vandens koncentracija mišinyje keičiama nuo X_{H2O_MASS}=0 iki X_{H2O_MASS}=0,12 , nustatyta, kad νC(2)–H ir νC(4,5)–H modų bangos skaičiaus pokytis abiejų tirtų joninių skysčių atveju yra vienodas ir anijono tipas neturi įtakos nei LC jonogelio fazės formavimuisi, nei bandinio heterogeniškumui. Tačiau νC(2)–H virpesinės juostos poslinkis yra didesnis nei νC(4,5)–H, kas leidžia patvirtinti hipotezę, kad ir ilgą grandinę turinčiuose joniniuose skysčiuose priemaišos, šiuo atveju vanduo, pirmiausia sąveikauja su „rugštingesne“ imidazolo žiedo dalimi ir prie jos prisijungusiu anijonu ties C(2) anglies pozicija. Išanalizavus juostų poslinkius slirtinguose koncentracijų rėžiuose pastebėta, kad poslinkiai beveik visais atvejais vienodi. Skiriasi tik 0-0,03 koncentracijų sritis, kurioje [C_{10}mim]Cl–H_2O mišinio Ramano spektruose vykstančių νC(2)–H virpesinių juostų poslinkis didesnis nei [C_{10}mim]Br–H_2O mišinyje. Šiuos skirtumus siejame su skirtinga priemaišų koncentracija bandiniuose, nustatyta kad gryno [C_{10}mim]Cl bandinys buvo švaresnis už [C_{10}mim]Br.

Šiame skyriuje aptariami ir matematinio Ramano sklaidos spektrų apdorojimo rezultatai. Principinių komponentų (PCA) ir 2D koreliacinės (2DCOS) analizės metodai detalizuojami disertacijos tekste. 15 pav.

pavaizduoti [C_{10}mim]Cl–H_2O ir [C_{10}mim]Br–H_2O mišinių Ramano sklaidos spektrų skaitmeninio apdorojimo rezultatai.

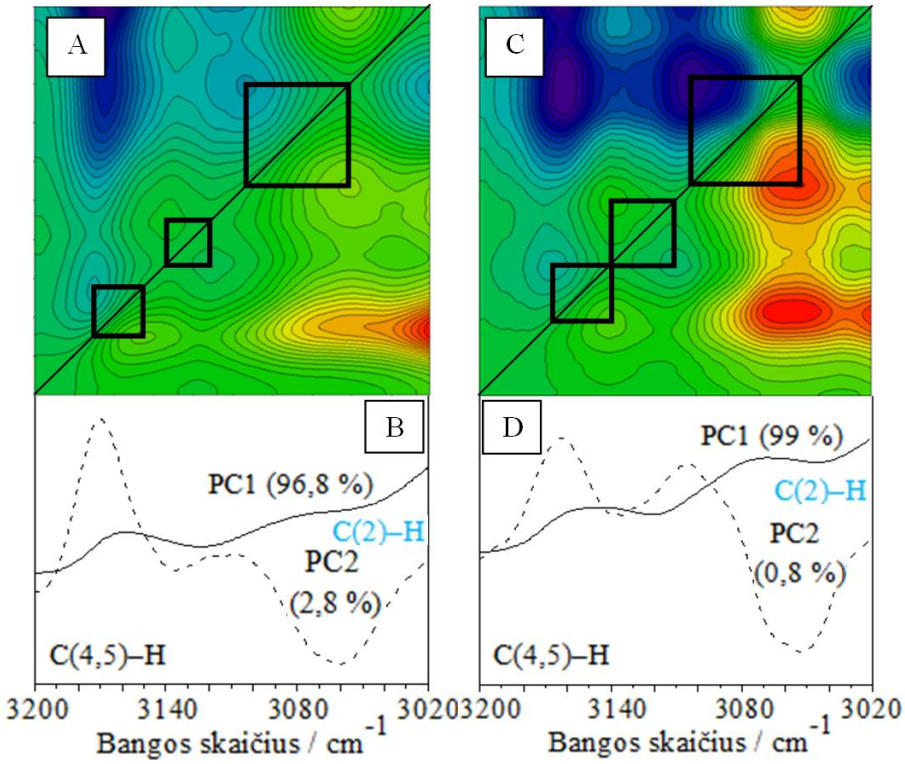

15 pav. [C_{10}mim]Cl–H_2O (A, B) ir [C_{10}mim]Br–H_2O (C, D) mišinių Ramano sklaidos spektrų skaitmeninio apdorojimo rezultatai: 2D koreliaciniai asinchroniniai Ramano spektrai viršutinėje paveikslo dalyje (A, C), apatinėje paveikslo dalyje pirmojo bei antrojo principinių komponentų įverčio vektoriai (B, D).

PCA metodu pirmojo ir antrojo principinių komponentų įverčio vektorių priklausomybės nuo vandens koncentracijos pateiktos ir 14 pav. C bei F dalyse. Vandens koncentracijai mišiniuose pasiekus X_{H2O_MASS}=0,03, tiek [C_{10}mim]Cl–H_2O (C), tiek [C_{10}mim]Br–H_2O (F) atvejais gaunami koncentracinių priklausomybių netolydumai, kurie sutampa su rezultatais gautus IL–H_2O mišinių spektrus aproksimuojant gauso kontūrais 14 pav. A, B bei D, E. [C_{10}mim]Cl–H_2O ir [C_{10}mim]Br–H_2O suskaičiuotos PC1 (96,8% ir 99%) įverčio vektoriaus vertės siejamos su nagrinėjamų Ramano šviesos sklaidos spektrų virpesinių juostų ν(C(2)-H) ir ν(C(4,5)-H) integrinių intensyvumų evoliucija, o PC2 (2,8% ir 0,8%) su virpesinių juostų dažnio

poslinkiu (15 pav. B, D). Kitų principinių komponentų nagrinėjamas neatliktas, nes visų jų suminis indėlis į spektrinius pokyčius yra tik 0,4% ir 0,2% ir todėl šiuos pokyčius priskyrėme triukšmams.

Koreliaciniais kavadratais sujungiant asinchroninio spektro *cross* smailes, nustatytas tiriamųjų virpesinių juostų poslinkis. Šie rezultatai taip pat gerai koreliuoja su virpesinių juostų aproksimavimo metodu gautomis poslinkio vertėmis. Detali *cross* smailių analizė leido nustatyti, jog užregistruotuose IL–H2O mišinių Ramano spektruose tarp 3020 ir 3200 cm^{-1} yra ne dvi, o trys virpesinės juostos. Dvi juostos registruojamos C(4,5)–H velentinių virpesių atveju ir priskiriamos simetriniams bei asimetriniams C(4,5)–H velentiniams imidazolo žiedo virpesiams.

2.2. Skirtingus vandens spiečius sudarančių vandens molekulių O–H virpesinių modų tyrimas

Antrajame poskyryje analizuojamos skirtingiems vandens molekulių spiečių virpesiams priskiriamos O-H valentinių simetrinių ir asimetrinių virpesių Ramano sklaidos juostos. Detaliai vandens molekulių sudaromi spiečiai aprašomi disertacijos tekste. Vandens molekulių spiečių O–H virpesiai Ramano spektruose registruojami 3200-3900 cm^{-1} spektrinėje srityje (16 pav.). Spiečiai pagal tarpmolekulinių vandenilinių jungčių skaičių suskirstomi į tris grupes. Stipriais vandeniliniais ryšiais surištos vandens molekulės (SHB) dar kitaip vadinamos „tinkliniu vandeniu“ [72]. Šie spiečiai sudaryti iš vandens molekulių tarpusavyje susijungusių keturiais vandeniliniais ryšiais, kurie suformuoja aukštos simetrijos tetraedrines struktūras. Virpesinė šių spiečių moda *ν*SHB priskiriama žemiausią bangos skaičių atitinkančiai Ramano sklaidos juostai ties 3250 cm^{-1}.

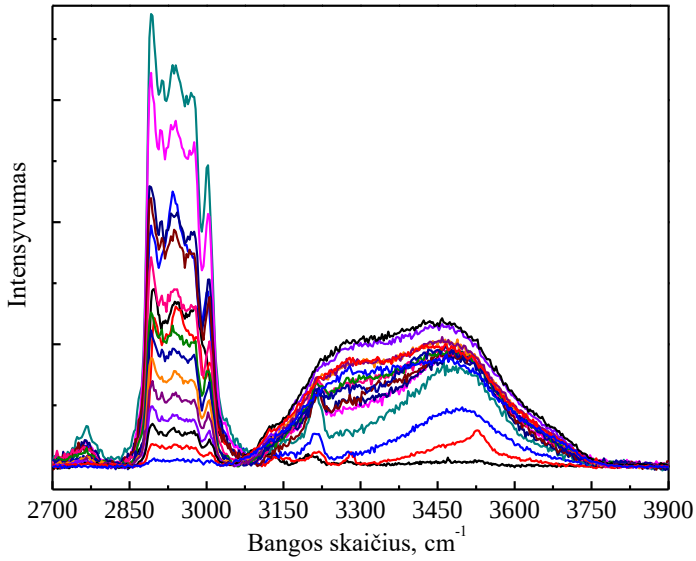

16 pav. $[C_{10}mim]Br–H_2O$ mišinių Ramano sklaidos spektrai keičiant vandens koncentraciją nuo X_{H2O_MASS}=0,0 iki X_{H2O_MASS}=0,99;

Vidutiniais stiprumo vandeniliniais ryšiais surištos vandens molekulės (MHB) [148], dar kitaip vadindamos „suardytu tinkliniu vandeniu“, suformuoja spiečius, kuriuose vandens molekulės tarpusavyje susijungusios dviem arba trim vandeniliniais ryšiais sudarydamos suardytą tetraedrinę asimetrinę struktūrą. Ramano sklaidos spektre virpesinė moda *ν*MHB atitinka juostą ties 3450 cm^{-1}. Aukščiausią bangos skaičių Ramano sklaidos spektre

atitinkanti virpesinė moda *v*WHB, ties 3650 cm^{-1} priskiriama pavienėms vandens molekulėms, kurios neformuoja vandeniliniais ryšiais sujungtų spiečių, taip pat dar vadinama multimeriniu vandeniu.

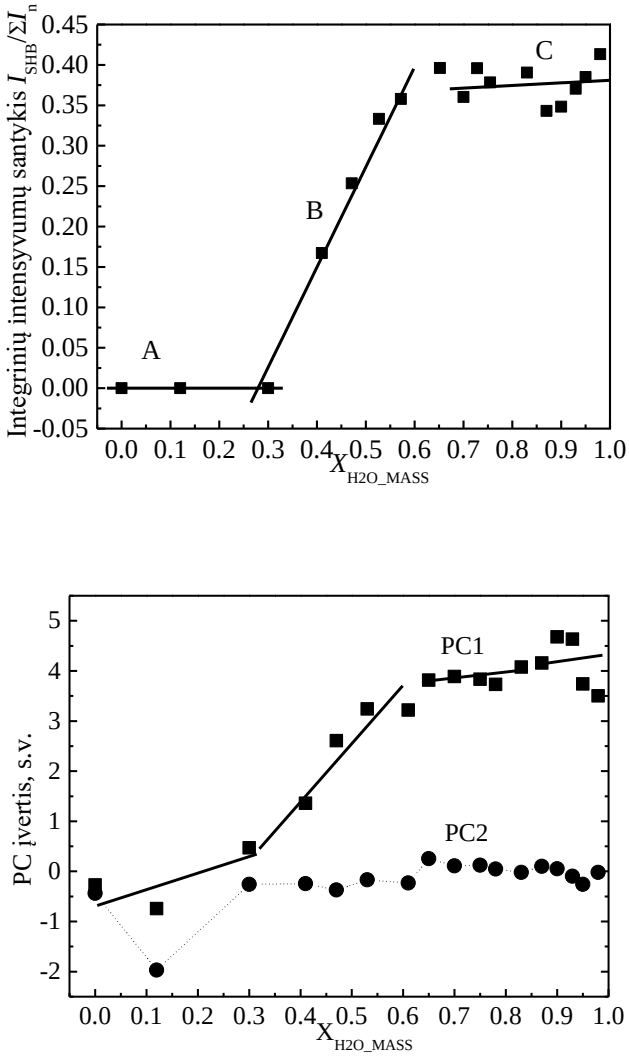

17 pav. LC jonogelio fazės formavimosi pabaigos nustatymas $[C_{10}mim]Br–H_2O$ mišiniuose iš PC įverčių ir OH virpesinių juostų parametrų priklausomybių nuo vandens koncentracijos mišiniuose.

Įvedant virpesinių juostų, priskiriamų skirtingų vandens spiečių virpesiams $[C_{10}mim]Br–H_2O$ mišiniuose, integrinių intensyvumų santykį, išreikštą $I_{SHB}/(I_{SHB}+I_{MHB}+I_{WHB})$, galime įvertinti vandens molekulių saviorganizacijos

priklausomybę nuo vandens koncentracijos mišinyje (17 pav.). Keičiant vandens masės dalį X_{H2O_MASS} mišiniuose nuo 0 iki 0,99 stebime nevienodą Ramano virpesinių juostų parametrų kitimą. Kaip aptarta pirmame poskyryje esant nedidelei vandens koncentracijai [C_{10}mim]Br–H_2O mišinyje didžioji dalis vandens molekulių labiau linkusios jungtis su anijonais (Br^- jonais) negu tarpusavyje. Šiame koncentracijų intervale vandens molekulės yra izoliuotos viena nuo kitos, suformuotų vandens spiečių nėra, susiformuoja tik agregatai, kartu ir LC jonogelio fazė (17 pav., A). Didinant vandens koncentraciją tirpale vandens molekulių sąveika su joninio skysčio anijonu keičiasi į vandens molekulių tarpusavio sąveiką. Vandens koncentracijai mišinyje pasiekus X_{H2O_MASS}=0,4±0,005 pradeda augti *ν*SHB virpesinė Ramano sklaidos juosta. H_2O molekulės jungiasi viena su kita, pradeda formuotis vandens spiečiai, agregatų formavimasis išlieka, tačiau pradedamos ardyti LC jonogelio fazės struktūros (17 pav., B). Kai vandens koncentracija tirpale X_{H2O_MASS}=0,5±0,02, *ν*SHB virpesinės juostos intensyvumo didėjimas sustoja, agregatai nebesiformuoja, visi tirpale esantys anijonai jau yra susijungę su vandens molekulėmis ir LC jonogelio fazė mišinyje galutinai suardoma. Toliau didinant vandens koncentraciją vandens spiečiai tik didėja, naujos jungtys tarp vandens molekulių ir anijonų nebesusidaro, vandens molekulės jungiasi tik tarpusavyje sudarydamos dimerus ir trimerus. (17 pav., C).

2.3. Skyriaus išvados

Iš užregistruotų [C_{10}mim]Br–H_2O ir [C_{10}mim]Cl–H_2O mišinių Ramano sklaidos spektrų virpesinių juostų parametrų pokyčių netolydumų keičiant vandens molekulių koncentraciją X_{H2O_MASS} mišinyje nuo 0 iki 0,99 nustatytos skystosios kristalinės jonogelio fazės formavimosi ribos. Jonogelio LC fazės formavimosi aptikimui pakanka stebėti valentinių virpesinių C–H ir O–H juostų, registruojamų 2700-4000 cm^{-1} srityje, spektrinių parametrų pokyčius.

Iš virpesinių juostų, priskiriamų imidazolo žiedo valentiniams C(2)–H, C(4)–H ir C(5)–H virpesiams, bangos skaičiaus priklausomybės nuo vandens koncentracijos [C_{10}mim]Br–H_2O ir [C_{10}mim]Cl–H_2O mišiniuose aptiktas netolydus mėlynasis Ramano poslinkis didinant X_{H2O_MASS}. Koncentracijai mišinyje pasiekus 0,03±0,005 H_2O sumažėja šių virpesinių modų bangos skaičiaus kitimo greitis, ir tai siejama su joninio skysčio molekulių mobilumo sumažėjimu mišinyje susiformavus skystajai kristalinei jonogelio fazei.

Nustatytas netolydus Ramano sklaidos juostų, priskiriamų skirtingiems vandens molekulių spiečių virpesiams, integrinių intensyvumų kitimas

didinant vandens koncentraciją [C_{10}mim]Br–H_2O ir [C_{10}mim]Cl–H_2O mišiniuose. Padidinus X_{H2O_MASS} mišinyje iki 0,4±0,005, virpesinių OH juostų, priskiriamų vandens spiečiams sudarytiems iš 4 ir daugiau molekulių, integrinis intensyvumas pradeda augti. Tai įvyksta dėl pasikeitusių vandens tarpmolekulinių sąveikų ir skystosios kristalinės jonogelio fazės suardymo.

Skaitmeniniais spektrų apdorojimo PCA ir 2DCOS metodais nustatytas tikslus C–H ir O–H virpesinių juostų sandų skaičius ir išanalizuoti Ramano sklaidos spektrų virpesinių juostų parametrų pokyčių netolydumai. Skystosios kristalinės jonogelio fazės formavimosi ribos, nustatytos naudojant minėtus skaitmeninius apdorojimo metodus, sutampa su ribomis, gautomis analizuojant eksperimentinius virpesinių juostų aproksimacijų parametrų pokyčius.

Nevienodas virpesinių Ramano sklaidos juostų, priskiriamų imidazolo žiedo valentiniams C(2,4,5)–H virpesiams, mėlynasis poslinkis patvirtina hipotezę, kad ilgas alkilines grandines turintys joniniai skysčiai ir vandens molekulės sudaro silpnesnes C(4)–H ir C(5)–H vandenilines jungtis nei C(2)–H atveju. Gauti rezultatai leidžia įsitikinti, kad didinant X_{H2O_MASS} joniniame skystyje vandens molekulės pirmiausia sąveikauja su anijonu ir sudaro vandeniliniu ryšiu surištus agregatus *anijonas···H–O–H···anijonas*. Taip pat nustatyta, kad anijono tipas neturi įtakos jonogelio fazės formavimosi riboms - pradžiai ir pabaigai.

3. VANDENS BŪSENOS PORĖTOSE FUNKCINĖSE MEDŽIAGOSE – KALCIO HIDROKSIAPATITUOSE

Skirtingos H_2O struktūros gali formuotis ne tik skystojoje, bet ir kietojoje terpėje. Šiame skyriuje nagrinėjamas struktūrų formavimasis kalcio hidroksiapatituose (CaHAp), susintetintuose naudojant vandeninį zolių-gelių sintezės metodą. CaHAp sintezejė panaudoti skirtingi kompleksadariai: 1,2-etilendiamintetraacetato rūgštis (EDTA), vyno rūgštis (TA), etilenglikolis (EG) ir glicerolis (GL). Glicerolis naudotas ir amorfiškai sugrupuotą fosfato fazę turinčių CaHAp sintezėje (ACP). Nanostruktūriškumo įvertinimui ištirtas ir komercinis (CA) (Sigma Aldrich; 99,999 %) CaHAp. Rezultatų aptarime naudojami medžiagų sutrumpinimai: EDTA-CaHAp, TA-CaHAp, EG-CaHAp, GL-CaHAp, ACP-GL-CaHAp, CA-CaHAp. Paruoštų bandinių tyrimui panaudotas infraraudonosios sugerties spektrometrijos metodas (FTIR), ankstesniuose tyrimuose patvirtintas kaip tinkantis OH^- jonų kristalo būsenose (*angl.* OH^- ions in the bulk [111]; ions in the crystals [50]) ir paviršiaus bei tūrinių struktūrų nustatymui CaHAp [103–107].

3.1. Nanostruktūrizuoti ir amorfiniai kalcio hidroksiapatitai

Pirmajame poskyryje nagrinėjami nanostruktūrizuotų kalcio hidroksiapatitų (TA-CaHAp), sugrupuotą amorfinę fosfato fazę turinčių kalcio hidroksiapatitų (ACP-GL-CaHAp) ir komercinių CaHAp (CA-CaHAp) skirtumai. Kambario temperatūros bandinių FTIR sugerties spektrai pavaizduoti 18 pav.

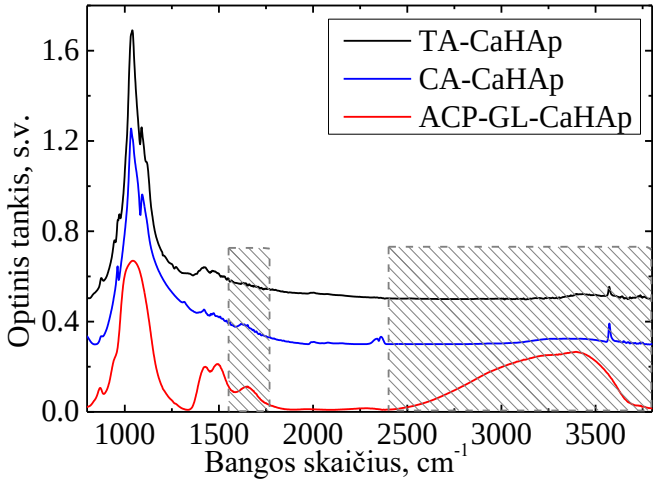

18 pav. TA-CaHAp, CA-CaHAp ir ACP-GL-CaHAp IR sugerties spektrai.

Iš spektrinių juostų, esančių tarp 2500 ir 3800 cm^{-1} (pažymėta pilkai), integrinio intensyvumo skirtumo nustatyta, kad ACP-GL-CaHAp bandiniuose adsorbuoto vandens kiekis yra 11 kartų didesnis nei TA-CaHAp ir CA-CaHAp. Atlikus detalų OH virpesinių juostų priskyrimą ir spektrinių kontūrų atskyrimo procedūrą nustatytos skirtingos OH saviorganizacijos grupės, susiformavusios tirtuose CaHAp bandiniuose (19 pav.). Struktūrizuoto vandens egzistavimą puikiai iliustruoja platus ir nevienalytis OH virpesių kontūras esantis ties 3200 cm^{-1} (19 pav., A). Remiantis literatūra [177] šią juostą galime aproksimuoti dviem persiklojančiais kontūrais ties 3442±2 cm^{-1} ir 3110±4 cm^{-1}. Virpesinė juosta ν3442 priskiriama struktūrizuoto vandens valentiniams O–H virpesiams. Ši virpesinė juosta taip pat registruojama nano struktūrizuotuose CAHAp bandinių TA-CaHAp ir CA-CaHAp spektruose ties 3438 ± 2 cm^{-1} (19 pav., B ir C). Virpesinė juosta ν3110 priskiriama vandens molekulių, susijungusių į tinklus, valentiniams O–H virpesiams [177]. Ilgas grandines turinčių joninių skysčių atveju ši virpesinė juosta atitinka νSHB juostą, priskiriamą stipriais vandeniliniais ryšiais surištų vandens molekulių virpesiams. Ties 1645 cm^{-1} registruojamos deformacinių O–H virpesių modos integrinio intesyvumo kitimas skirtinguose CaHAp koreliuoja su ν3110 virpesinės modos integrinio intensyvumo kitimu ir gali būti naudojamas kaip spektrinis žymuo tiriant vandens kiekį bandinyje. Adsorbuoto vandens kiekiui skirtinguose bandiniuose nustatyti galima palyginti ν3110 ir ν3442 virpesinių modų integrinių intensyvumų santykį (I_{3110}/I_{3442}). ACP-GL-CaHAp ir CA-CaHAp atvejais I_{3110}/I_{3442} yra beveik vienodas, atitinkamai, 3 ir 2,8, tačiau TA-CaHAp bandinio atveju šio santykio skaitinė vertė tik 0,001. Siaura virpesinė juosta ties 3572±2 cm^{-1} priskiriama $O–H^-$ virpesiams apatitų ertmėse [106,179]. Amorfinę fosfato fazę turinčių CaHAp IR sugerties sepktruose ši juosta neregistruojama, tuo tarpu nano struktūrizuotųjų CA-CaHAp ir TA-CaHAp IR sugerties spektruose ši juosta labai intensyvi. Virpesinė juosta ties 3587 cm^{-1} registruojama tiek komercinio, tiek TA kompleksadarį naudojant susintetintuose apatitų IR spektruose ir priskiriama paviršiniams valentiniams O–H virpesiams P–O–H grupėse [106,179] arba struktūriškai susietoms paviršinėms –OH modoms [180]. Visos virpesinės juostuos, kurių bangos skaičius didesnis nei 3450 cm^{-1}, gali būti naudojamos kaip spektriniai žymenys CA-CaHAp nano-struktūrų nustatymui.

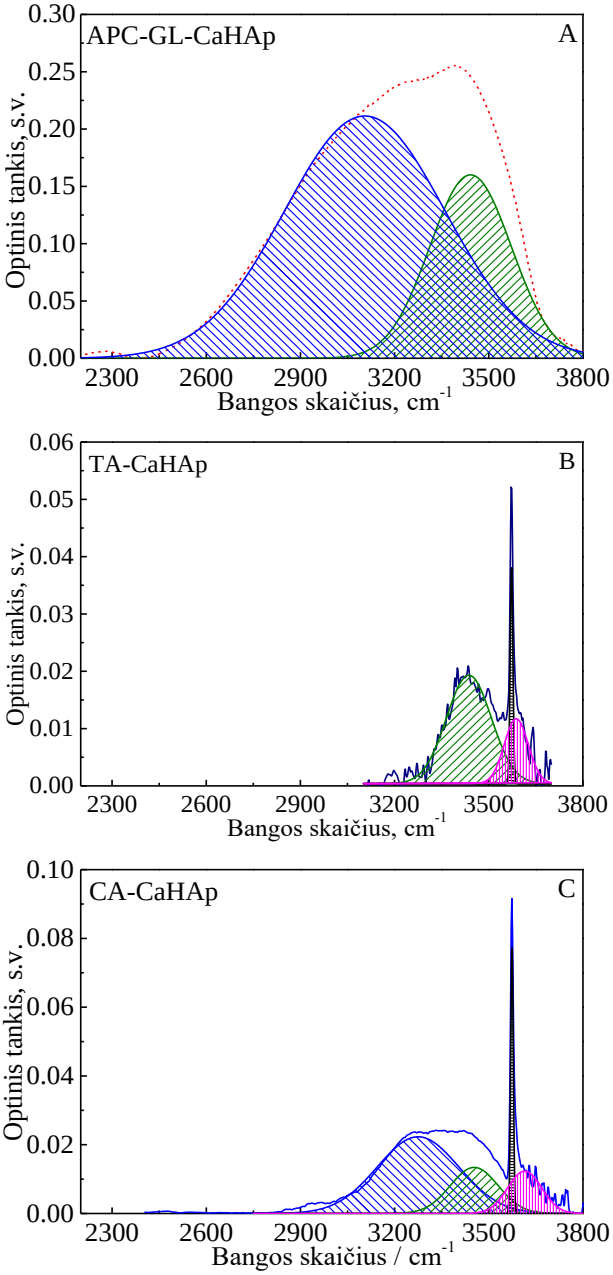

19 pav. ACP-GL-CaHAp, TA-CaHAp ir CA-CaHAp IR sugerties spektrai su aproksimuotomis virpesinėmis juostomis, priskiramomis įvairioms OH grupėms tiek CaHAp tūryje, tiek paviršiuje [104].

3.2. Kalcio hidroksiapatitai, susintetinti naudojant skirtingus kompleksadarius

Šiame poskyryje nagrinėjama cheminės sintezės metu pasirinkto kompleksadario įtaką CaHAp nanostruktūriškumui. Taip pat detaliai analizuojamos OH virpesinės struktūros kambario temperatūroje apribotos CaHAp medžiagose remiantis vandens molekulių tyrimo rezultatais gautais naudojant žematamperatūrės FTIR matricinės izoliacijos metodą. Užregistruoti susintetintų, naudojant skirtingus kompleksadarius, CaHAp kambario temperatūros bandinių IR sugerties spektrai yra pavaizduoti 20 pav.

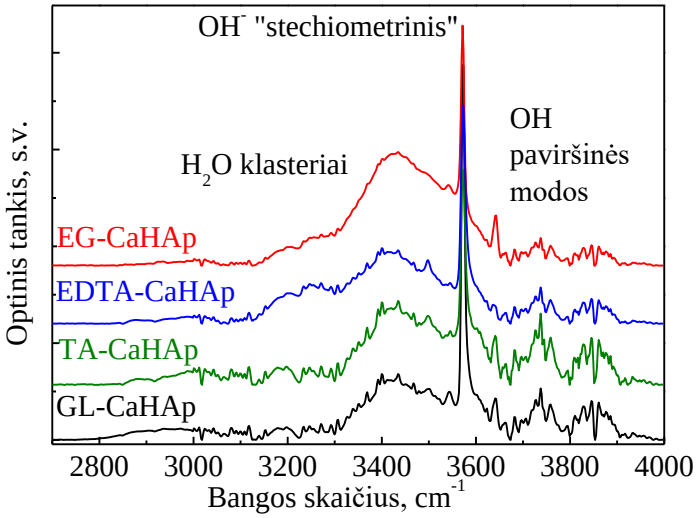

20 pav. Nano struktūrizuotų CaHAp, susintetintų naudojant skirtingus kompleksadarius, IR sugerties spektrai OH virpesių srityje 2700-4000 cm^{-1}. Pažymėtos spektrinės vandens molekulių spiečių, stechiometrinio OH ir paviršinių OH virpesių sritys.

Užregistruotą IR sugerties spektrą galima padalinti į skirtingas sritis, priskiriamas vandens molekulių spiečių, OH stechiometriniams ir paviršinių OH virpesiams, lygiai taip pat, kaip ir pirmojo poskyrio rezultatų aptarime. Šiuo atveju, bandinių IR sugerties spektrų skirtumai nėra tokie drastiški, todėl detaliai analizei reikalingi papildomi tyrimai, kuriuos atlikus, nustatomos skirtingos OH juostų struktūros. Tiksliam vandens molekulių spiečių virpesinių juostų parametrų nustatymui keičiant temperatūrą nuo T=9 K iki T=40 K argono matricoje užregistruoti bandinių žematemperatūriai IR sugerties spektrai. Eksperimentinius duomenis apdorojus 2DCOS skaitmeniniu metodu ir rezultatus palyginus su literatūroje pateikiamais

skirtingų dydžių $(H_2O)_n$ spiečiams priskiriamomis IR sugerties juostoms, sudaryta virpesių priskyrimo 3 *lentelė*.

5 lentelė. Įvairiose terpėse izoliuotų vandens molekulių spiečių ir paviršinių virpesinių O–H modų priskyrimas IR sugerties spektruose.

$(H_2O)n$	Argono matricoje	CCl_4 [182]	Nano-struktūrizuotuose CaHAps
	9–40 K	273–313 K	298 K
Dimerai	9–40 K	3615–3616	3526 ± 2 (a)
n = 2	3573–3573.5		3591 ± 4 (b)
	3574 [183]		3598 ± 1 (c)
Trimerai	3574.5 [184]	3535–3587	N/A
n = 3	3515–3520		
	3515 [185]		
	3516 [183,186]		
Tetramerai	3517 [184]	3395–3433	3420 ± 2 (a)
n = 4	3369–3374		3439 ± 2 (b)
	3372 [185,187]		3450 ± 2 (c)
Pentamerai	3372 [184]	N/A	N/A
n = 5	3327–3330		
	3325 [185]		
Heksamerai	3330 [187]	3221–3254	3237 ± 2 (a)
n = 6	3211–3214		– (b)
	3212 [185]		3263 ± 3 (c)
	3211 [187]		
	3327 (chair),		
n ≥ 6	3212 (cage) [177]	3043–3074	– (a)
	3100–3160		– (b)
	3144 [185]		2940 ± 10 (c)
	3140 [187]		
Paviršinės modos	3150 (prism) [177]	N/A	3642, 3737, 3866 (a)
	3695–3701		3640, 3737, 3848 (b)
	3698 [180,188]		~3651, ~3700 (c)

Siekiant surasti koreliaciją tarp žemose temperatūrose gautų rezultatų ir kambario temperatūroje registruojamų $(H_2O)_n$ spiečių šioje letelėje taip pat surinkti skirtingiems $(H_2O)_n$ spiečių priskiriamų virpesinių juostų dažniai gauti tiriant vandens ir hidrofobiško tirpiklio CCl_4 mišinius [182].

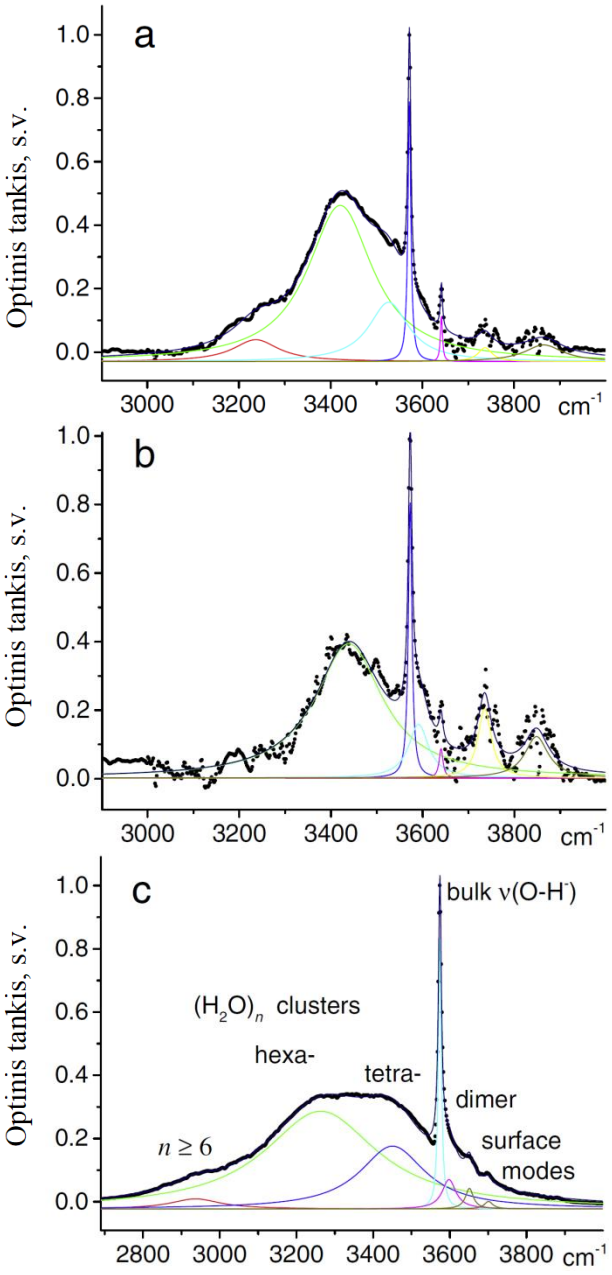

21 pav. Nanostruktūrizuotų CaHAp IR sugerties spektrai: a – EG-CaHAp, b – TA-CaHAp, c – CA-CaHAp IR sugerties spektrai su aproksimuotomis virpesinėmis juostomis, priskiramomis įvairioms OH grupėms (3 lentelė).

Eksperimentiniai EG-CaHAp, TA-CaHAp ir CA-CaHAp IR sugerties spektrai pavaizduoti 21 pav. Susintetintuose naudojant EG kompleksadarį

CaHAp formuojasi visos galimos H_2O struktūros: spektruose registruojamos heksamerų, tetramerų, dimerų ir paviršinės OH modos. TA-CaHAp bandinių atveju IR sugerties spektruose yra panašus virpesinių juostų, priskiriamų tetramerams ir dimerams, kiekis, tačiau paviršiniams OH virpesiams priskiriamų juostų integrinis intesyvumas yra tris kartus didesnis, o heksamerų virpesius atitinkančių juostų intensyvumas labai mažas, t.y., jos registruojamos triukšmo lygyje. Palyginus šių dviejų susintetintų ir komercinių CaHAp bandinių IR sugerties spektrinių juostų aproksimacijų parametrus, matomas didžiulis vandens heksamerų ir aukštenės eilės vandens molekulių spiečių skirtumas bandiniuose. Naudojant šiuos rezultatus galime nustatyti bandinių hidratacijos laipsnį. Ankstesniuose tyrimuose nustatyta, kad demineralizuotose kaulų matricose hidratavimas (*angl.* hydrating) neigiamai veikia osteoinduktyvumą bandiniuose [109].

3.3. Skyriaus išvados

Pirmą kartą ištirti struktūriniai vandens molekulių spiečių $(H_2O)_n$ grupių skirtumai nanostruktūrizuotuose kalcio hidroksiapatituose (CaHAp), susintetintuose naudojant skirtingus kompleksadarius. IR sugerties spektruose 2900-3900 cm^{-1} srityje identifikuotos vandens dimerų, tetramerų, heksamerų, paviršinių O–H ir P–O–H modos. Virpesinių juostų priskyrimas atliktas iš vandens FTIR sugerties spektrų, užregistruotų naudojant matricinės izoliacijos metodą ir iš literatūroje pateikiamų H_2O ir CCl_4 mišinių tyrimų rezultatų.

Analizuojant IR sugerties juostų, priskiriamų struktūrinio ir adsorbuoto vandens molekulių virpesiams, intensyvumų santykį I_{3110}/I_{3442} skirtingų CaHAp bandinių spektruose galima įvertinti skirtingą OH grupių saviorganizaciją. Parodyta, kad nanostruktūrizuotuose CaHA, priešingai nei ACP-CaHAp, stechiometrinių –OH dalis yra ženkliai didesnė už hidroksilo grupių, suformuotų iš adsorbuoto vandens.

Nustatyta, kad naudojant IR sugerties metodą galima įvertinti CaHAp bandinių hidratacijos laipnį. EG-CaHAp hidratacijos laipsnis yra 2 kartus didesnis nei TA-CaHAp atveju.

DISERTACIJOS IŠVADOS

1. Virpesinė spektrometrija yra tinkamas metodas nustatyti skystosios kristalinės jonogelio fazės formavimasi ilgas alkilines grandines turinčių joninių skysčių vandeniniuose mišiniuose. Kompleksinis Ramano, NMR, 2DCOS ir PCA metodų panaudojimas suteikia naujos vertingos informacijos apie skystosios kristalinės jonogelio fazės formavimosi procesus ir skirtingų vandens molekulių spiečių vaidmenį šiuose mišiniuose. Nustatyta, kad skystosios kristalinės jongelio fazės formavimosi aptikimui tinkami spektriniai žymenys yra 2700-4000 cm^{-1} srityje ir yra priskiriami valentiniams C-H ir OH grupių virpesiams.

2. Skirtingos vandens molekulių būsenos, esančios nanostruktūrizuotuose kalcio hidroksiapatituose ir amorfinę kalcio fosfato fazę turinčiuose hidroksiapatituose, ištirtos naudojant infraraudonosios sugerties spektrometrijos metodą. Naudojant žematemperatūrį FTIR sugerties metodą pirmą kartą ištirti struktūriniai hidroksilo grupių skirtumai nanostruktūrizuotuose kalcio hidroksiapatituose (CaHAp), susintetintuose naudojant skirtingus kompleksadarius.

3. Nustatyta, kad konformacinėje pusiausvyroje trumpas alkilines grandines turinčių joninių skysčių katijonai $[C_4mim]^+$ labiau linkę formuoti *gauche* konformerus. Konformerų pusiausvyrą joniniuose skysčiuose lemia ir anijonų fizikiniai parametrai. Halogenų ir nesferinius anijonus turinčių joninių skysčių konformerų *gauche* ir *trans* pusiausvyrai daro įtaką ne tik anijono spindulys, tačiau ir anijono hidrofobiškumas. Kuo mažesnis anijono hidrofobiškumas, tuo didesnė dalis joninių skyčių molekulių susiformuoja kaip *trans* konformerai tokia tvarka: $I^- > Br^- > Cl^- > OTf^- > NO_3^- > BF_4^-$, t.y. vanduo pakeičia konformacinę pusiausvyrą joniniame skystyje.

4. Vandens ir joninio skysčio $[C_4mim]NO_3$ mišinių Ramano sklaidos spektruose anijono virpesinių modų $\nu_4(NO_3^-)$, $\nu_1(NO_3^-)$ bei skirtingiems vandens molekulių spiečiams priskiriamų virpesinių modų bangos skaičiaus kitimo netolydumai, užregistruoti žemų D_2O koncentracijų srityje (X_{D2O_MOL}=0,60±0,04), sietini su "vandens kišenių" formavimosi pradžia. Aukštų D_2O koncentracijų srityje $[C_4mim]NO_3$-D_2O mišinyje (X_{D2O_MOL}=0,86±0,04) taip pat užregistruoti spektrinių parametrų kitimo netolydumai. *Gauche* ir *trans* konformerų spektrinių juostų integrinių intensyvumų santykio kitimas, joninio skysčio imidazolo žiedo valentinius virpesius ir skirtingų vandens spiečių molekulių virpesius atitinkančių juostų

spektrinių parametrų netolydumai keičiant D_2O koncentraciją mišinyje yra siejami su “vandens kišenių” formavimosi pabaiga.

5. Vandenilio ir deuterio apsikeitimo dinamika joninių skysčių ir sunkiojo vandens mišiniuose tirta naudojant Ramano spektroskopijos metodą. Nustatyta, kad molekulių mobilumas dėl besikeičiančių tvarkos ir netvarkos parametrų bei anijonų agregacijos su vandeniu įtakoja H/D mainų reakcijas. Anijonai ir katijonai, sujungti vandeniliniu ryšiu, kurį silpnina vandens molekulės pakeisdamos sąveikas *anijonas···katijonas* į sąveikas *anijonas···vanduo* ir *katijonas···vanduo*. H/D mainų reakcijos greitis priklauso nuo anijono tipo, bandinio švarumo ir temperatūros.

6. Anijono tipas ir katijono lokacija joninio skysčio ir vandens mišinyje yra svarbiausios H/D mainų reakcijos sąlygos. Joniniuose skysčiuose su halogenų anijonais (I^-, Br^-, Cl^-), kurie sudaro vandenilinius ryšius su imidazolo žiedu plokštumoje, H/D mainai vyksta abiejų tipų joniniuose skysčiuose: su ilgos ir trumpos alkilinės grandinės katijonais. Joniniuose skysčiuose, sudarytuose iš nesferinių anijonų (OTf^-; NO_3^-) ir trumpų alkilinų grandinių, H/D mainai nevyksta. Konformacinės pusiausvyros kitimas neturi įtakos H/D mainams. Deuteravimas 1-butil-3-metilimidazolo nitrato ir sunkiojo vandens bei 1-butil-3-metilimidazolo trifluormetilsulfonato ir sunkiojo vandens mišiniuose nevyksta, nepriklausomai nuo D_2O kiekio ir eksperimento vykdymo trukmės.

[1] C. Rey, Calcium Phosphates for Medical Applications, Calcium Phosphates Biol. Ind. Syst. (1998) 217–251. doi:10.1007/978-1-4615-5517-9.

[2] P.C. Schmidt, R. Herzog, Calcium phosphates in pharmaceutical tableting - 2. Comparison of tableting properties, Pharm. World Sci. 15 (1993) 116–122. doi:10.1007/BF02113939.

[3] K.S. Egorova, E.G. Gordeev, V.P. Ananikov, Biological Activity of Ionic Liquids and Their Application in Pharmaceutics and Medicine, Chem. Rev. 117 (2017) 7132–7189. doi:10.1021/acs.chemrev.6b00562.

[4] N.L. Mai, Y. Koo, Production of Biofuels and Chemicals with Ionic Liquids, 2014. doi:10.1007/978-94-007-7711-8.

[5] D. Mecerreyes, Applications of Ionic Liquids in Polymer Science and Technology, 2015.

[6] B. Demirkurt, Y. Akdogan, Development of an Ionic Liquid Based Method for the Preparation of Albumin Nanoparticles, ChemistrySelect. 3 (2018) 9940–9945. doi:10.1002/slct.201801648.

[7] F.H. Albee, Studies in Bone Growth: Triple Calcium Phosphate As a Stimulus To Osteogenesis., Ann. Surg. 71 (1920) 32–39.

[8] C.P.A.T. Klein, K. de Groot, A.A. Drissen, H.B.M. van der Lubbe, Interaction of biodegradable β-whitlockite ceramics with bone tissue: An in vivo study, Biomaterials. 6 (1985) 189–192. doi:10.1016/0142-9612(85)90008-0.

[9] P.S. Eggli, W. Müller, R.K. Schenk, Porous hydroxyapatite and tricalcium phosphate cylinders with two different pore size ranges implanted in the cancellous bone of rabbits. A comparative histomorphometric and histologic study of bony ingrowth and implant substitution., Clin. Orthop. Relat. Res. (1988) 127–38. http://www.ncbi.nlm.nih.gov/pubmed/2838207.

[10] F. Barrere, M.M.E. Snel, C.A. Van Blitterswijk, K. De Groot, P. Layrolle, Nano-scale study of the nucleation and growth of calcium phosphate coating on titanium implants, Biomaterials. 25 (2004) 2901–2910. doi:10.1016/j.biomaterials.2003.09.063.

[11] D. Apelt, F. Theiss, A.O. El-Warrak, K. Zlinszky, R. Bettschart-Wolfisberger, M. Bohner, S. Matter, J.A. Auer, B. Von Rechenberg, In vivo behavior of three different injectable hydraulic calcium phosphate cements, Biomaterials. 25 (2004) 1439–1451. doi:10.1016/j.biomaterials.2003.08.073.

[12] M. Bohner, H. Tiainen, P. Michel, N. Döbelin, Design of an inorganic dual-paste apatite cement using cation exchange, J. Mater. Sci. Mater. Med. 26 (2015) 1–13. doi:10.1007/s10856-015-5400-z.

[13] H. Seitz, W. Rieder, S. Irsen, B. Leukers, C. Tille, Three-dimensional printing of porous ceramic scaffolds for bone tissue engineering, J.

Biomed. Mater. Res. - Part B Appl. Biomater. 74 (2005) 782–788. doi:10.1002/jbm.b.30291.
[14] R.A. Levy, T.M.G. Chu, J.W. Halloran, S.E. Feinberg, S. Hollister, CT-generated porous hydroxyapatite orbital floor prosthesis as a prototype bioimplant, Am. J. Neuroradiol. 18 (1997) 1522–1525.
[15] H. Yuan, H. Fernandes, P. Habibovic, J. de Boer, A.M.C. Barradas, A. de Ruiter, W.R. Walsh, C.A. van Blitterswijk, J.D. de Bruijn, Osteoinductive ceramics as a synthetic alternative to autologous bone grafting, Proc. Natl. Acad. Sci. 107 (2010) 13614–13619. doi:10.1073/pnas.1003600107.
[16] N. Groen, N. Tahmasebi, F. Shimizu, Y. Sano, T. Kanda, D. Barbieri, H. Yuan, P. Habibovic, C.A. van Blitterswijk, J. de Boer, Exploring the Material-Induced Transcriptional Landscape of Osteoblasts on Bone Graft Materials, Adv. Healthc. Mater. 4 (2015) 1691–1700. doi:10.1002/adhm.201500171.
[17] H. Lapczyna, L. Galea, S. Wüst, M. Bohner, S. Jerban, A. Sweedy, N. Doebelin, N. van Garderen, S. Hofmann, G. Baroud, R. Müller, B. von Rechenberg, Effect of Grain Size and Microporosity on the in vivo Behavior of beta-Tricalcium Phosphate Scaffolds, Eur. Cells Mater. 28 (2014) 299–319.
[18] T. Welton, Room-Temperature Ionic Liquids. Solvents for Synthesis and Catalysis, Chem. Rev. 99 (1999) 2071–2084. doi:10.1021/cr980032t.
[19] J. Dupont, R.F. De Souza, P.A.Z. Suarez, Ionic liquid (molten salt) phase organometallic catalysis, Chem. Rev. 102 (2002) 3667–3692. doi:10.1021/cr010338r.
[20] R. Hayes, G.G. Warr, R. Atkin, Structure and Nanostructure in Ionic Liquids, Chem.Rev. 115 (2015) 6357 − 6426. doi:10.1021/cr500411q.
[21] C. Zhong, Y. Deng, W. Hu, J. Qiao, L. Zhang, J. Zhang, A review of electrolyte materials and compositions for electrochemical supercapacitors, Chem. Soc. Rev. 44 (2015) 7484–7539. doi:10.1039/c5cs00303b.
[22] W. Jiang, Y. Wang, G.A. Voth, Molecular dynamics simulation of nanostructural organization in ionic liquid/water mixtures, J. Phys. Chem. B. 111 (2007) 4812–4818. doi:10.1021/jp0671421.
[23] K. Dong, S. Zhang, J. Wang, Understanding the hydrogen bonds in ionic liquids and their roles in properties and reactions, Chem. Commun. 52 (2016) 6744–6764. doi:10.1039/C5CC10120D.
[24] Y. Zhao, S. Gao, J. Wang, J. Tang, Aggregation of Ionic Liquids [Cnmim]Br (n = 4, 6, 8, 10, 12) in D2O: A NMR Study, J. Phys. Chem. B. 112 (2008) 2031–2039. doi:10.1021/jp076467e.
[25] M.N. Garaga, M. Nayeri, A. Martinelli, Effect of the alkyl chain length in 1-alkyl-3-methylimidazolium ionic liquids on inter-molecular interactions and rotational dynamics, J. Mol. Liq. 210 (2015) 1–9. doi:10.1016/j.molliq.2015.06.055.

[26] J.D. Wadhawan, R.G. Compton, F. Marken, P. a Z. Suarez, C.S. Consorti, F. De Souza, Water-Induced Accelerated Ion Diffusion: Voltammetric Studies in [BMIM][BF4], R. Soc. Chem. 24 (2000) 1009–1015. doi:10.1039/b007172m.

[27] K.A. Fletcher, S. Pandey, Solvatochromic Probe Behavior within Ternary Room-Temperature Ionic Liquid 1-Butyl-3-methylimidazolium Hexafluorophosphate + Ethanol + Water Solutions, J. Phys. Chem. B. 107 (2003) 13532–13539. doi:10.1021/jp0276754.

[28] K.R. Seddon, A. Stark, M.-J. Torres, Influence of chloride, water, and organic solvents on the physical properties of ionic liquids*, Pure Appl. Chem. 72 (2000) 2275–2287. doi:10.1351/pac200072122275.

[29] M.G. Freire, P.J. Carvalho, A.M. Fernandes, I.M. Marrucho, A.J. Queimada, J.A.P. Coutinho, Surface tensions of imidazolium based ionic liquids: Anion, cation, temperature and water effect, J. Colloid Interface Sci. 314 (2007) 621–630. doi:10.1016/j.jcis.2007.06.003.

[30] M. Filice, O. Romero, O. Abian, B. de las Rivas, J.M. Palomo, Low ionic liquid concentration in water: a green and simple approach to improve activity and selectivity of lipases, RSC Adv. 4 (2014) 49115–49122. doi:10.1039/C4RA07625G.

[31] Y. Kohno, H. Ohno, Ionic liquid/water mixtures: from hostility to conciliation, Chem. Commun. 48 (2012) 7119. doi:10.1039/c2cc31638b.

[32] J. Kausteklis, V. Balevičius, V. Aleksa, Two-dimensional Raman spectroscopy study of ionogel phase formation in long-chain ionic liquid/water systems, J. Raman Spectrosc. 48 (2017) 126–131. doi:10.1002/jrs.4983.

[33] V. Klimavicius, Z. Gdaniec, J. Kausteklis, V. Aleksa, K. Aidas, V. Balevicius, NMR and Raman spectroscopy monitoring of proton/deuteron exchange in aqueous solutions of ionic liquids forming hydrogen bond: A Role of anions, self-aggregation, and mesophase formation, J. Phys. Chem. B. 117 (2013) 10211–10220. doi:10.1021/jp4021245.

[34] B.A. Marekha, M. Bria, M. Moreau, I. De Waele, F.A. Miannay, Y. Smortsova, T. Takamuku, O.N. Kalugin, M. Kiselev, A. Idrissi, Intermolecular interactions in mixtures of 1-n-butyl-3-methylimidazolium acetate and water: Insights from IR, Raman, NMR spectroscopy and quantum chemistry calculations, J. Mol. Liq. 210 (2015) 227–237. doi:10.1016/j.molliq.2015.05.015.

[35] T. Takamuku, H. Hoke, A. Idrissi, B.A. Marekha, M. Moreau, Y. Honda, T. Umecky, T. Shimomura, Microscopic interactions of the imidazolium-based ionic liquid with molecular liquids depending on their electron-donicity, Phys. Chem. Chem. Phys. 16 (2014) 23627–23638. doi:10.1039/C4CP03565H.

[36] V. Aleksa, J. Kausteklis, V. Klimavicius, Z. Gdaniec, V. Balevicius,

Raman and NMR spectroscopy study of liquid crystalline ionogel phase in ionic liquid/H2O mixtures: The states of water, J. Mol. Struct. 993 (2011) 91–96. doi:10.1016/j.molstruc.2010.12.060.

[37] J.C. Elliott, D.W. Holcomb, R.A. Young, Infrared determination of the degree of substitution of hydroxyl by carbonate ions in human dental enamel, Calcif. Tissue Int. 37 (1985) 372–375. doi:10.1007/BF02553704.

[38] G. Zhang, X. Chen, Y. Xie, Y. Zhao, H. Qiu, Lyotropic liquid crystalline phases in a ternary system of 1-hexadecyl-3-methylimidazolium chloride/1-decanol/water, J. Colloid Interface Sci. 315 (2007) 601–606. doi:10.1016/j.jcis.2007.07.012.

[39] X.W. Li, J. Zhang, B. Dong, L.Q. Zheng, C.H. Tung, Characterization of lyotropic liquid crystals formed in the mixtures of 1-alkyl-3-methylimidazolium bromide/p-xylene/water, Colloids Surfaces A Physicochem. Eng. Asp. 335 (2009) 80–87. doi:10.1016/j.colsurfa.2008.10.031.

[40] A.M. Moschovi, S. Ntais, V. Dracopoulos, V. Nikolakis, Vibrational spectroscopic study of the protic ionic liquid 1-H-3-methylimidazolium bis(trifluoromethanesulfonyl)imide, Vib. Spectrosc. 63 (2012) 350–359. doi:10.1016/j.vibspec.2012.08.006.

[41] S. Chen, S. Zhang, X. Liu, J. Wang, J. Wang, K. Dong, J. Sun, B. Xu, Ionic liquid clusters: structure, formation mechanism, and effect on the behavior of ionic liquids., Phys. Chem. Chem. Phys. 16 (2014) 5893–5906. doi:10.1039/c3cp53116c.

[42] H. Weingärtner, C. Cabrele, C. Herrmann, How ionic liquids can help to stabilize native proteins., Phys. Chem. Chem. Phys. 14 (2012) 415–26. doi:10.1039/c1cp21947b.

[43] Y. Ji, R. Shi, Y. Wang, G. Saielli, Effect of the chain length on the structure of ionic liquids: from spatial heterogeneity to ionic liquid crystals., J. Phys. Chem. B. 117 (2013) 1104–9. doi:10.1021/jp310231f.

[44] S. Kareiva, V. Klimavicius, A. Momot, J. Kausteklis, A. Prichodko, L. Dagys, F. Ivanauskas, S. Sakirzanovas, V. Balevicius, A. Kareiva, Sol-gel synthesis, phase composition, morphological and structural characterization of Ca<inf>10</inf>(PO<inf>4</inf>)<inf>6</inf>(OH)<inf>2</inf>: XRD, FTIR, SEM, 3D SEM and solid-state NMR studies, J. Mol. Struct. 1119 (2016). doi:10.1016/j.molstruc.2016.04.046.

[45] K. Saihara, Y. Yoshimura, S. Ohta, A. Shimizu, Properties of Water Confined in Ionic Liquids, Sci. Rep. 5 (2015) 10619. doi:10.1038/srep10619.

[46] H. Abe, T. Takekiyo, M. Shigemi, Y. Yoshimura, S. Tsuge, T. Hanasaki, K. Ohishi, S. Takata, J. Suzuki, Direct Evidence of Confined Water in Room-Temperature Ionic Liquids by Complementary Use of Small-Angle X-ray and Neutron Scattering, J. Phys. Chem. Lett. 5

(2014) 1175–1180. doi:10.1021/jz500299z.
[47] H. Abe, T. Takekiyo, Y. Yoshimura, K. Saihara, A. Shimizu, Anomalous Freezing of Nano-Confined Water in Room-Temperature Ionic Liquid 1-Butyl-3-Methylimidazolium Nitrate, ChemPhysChem. 17 (2016) 1136–1142. doi:10.1002/cphc.201501199.
[48] A. Antonakos, E. Liarokapis, T. Leventouri, Micro-Raman and FTIR studies of synthetic and natural apatites, Biomaterials. 28 (2007) 3043–3054. doi:10.1016/j.biomaterials.2007.02.028.
[49] I. Rehman, W. Bonfield, Characterization of hydroxyapatite and carbonated apatite by photo acoustic FTIR spectroscopy, J. Mater. Sci. Mater. Med. 8 (1997) 1–4. doi:10.1023/A:1018570213546.
[50] S. Kareiva, V. Klimavicius, A. Momot, J. Kausteklis, Sol e gel synthesis , phase composition , morphological and structural characterization of Ca 10 (PO 4) 6 (OH) 2 : XRD , FTIR , SEM , 3D SEM and solid-state NMR studies, J. Mol. Struct. 1119 (2016) 1–11. doi:10.1016/j.molstruc.2016.04.046.
[51] M. Nayeri, K. Nygård, M. Karlsson, M. Maréchal, M. Burghammer, M. Reynolds, A. Martinelli, The role of the ionic liquid C6C1ImTFSI in the sol-gel synthesis of silica studied using in situ SAXS and Raman spectroscopy., Phys. Chem. Chem. Phys. 17 (2015) 9841–8. doi:10.1039/c5cp00709g.
[52] G.E. Walrafen, Raman spectral studies of water structure, J. Chem. Phys. 40 (1964) 3249–3256. doi:10.1063/1.1724992.
[53] A. Nilsson, L.G.M. Pettersson, The structural origin of anomalous properties of liquid water, Nat. Commun. 6 (2015) 8998. doi:10.1038/ncomms9998.
[54] R. Ludwig, The effect of hydrogen bonding on the thermodynamic and spectroscopic properties of molecular clusters and liquids, Phys. Chem. Chem. Phys. 4 (2002) 5481–5487. doi:10.1039/b207000f.
[55] Q. Sun, Local statistical interpretation for water structure, Chem. Phys. Lett. 568–569 (2013) 90–94. doi:10.1016/j.cplett.2013.03.065.
[56] H. Ohno, Electrochemical aspects of ionic liquids, 2011.
[57] T. Fukushima, T. Aida, Ionic liquids for soft functional materials with carbon nanotubes, Chem. - A Eur. J. 13 (2007) 5048–5058. doi:10.1002/chem.200700554.
[58] M. Díaz, A. Ortiz, I. Ortiz, Progress in the use of ionic liquids as electrolyte membranes in fuel cells, J. Memb. Sci. 469 (2014) 379–396. doi:10.1016/j.memsci.2014.06.033.
[59] S. Zhang, Q. Zhang, Y. Zhang, Z. Chen, M. Watanabe, Y. Deng, Beyond solvents and electrolytes: Ionic liquids-based advanced functional materials, Prog. Mater. Sci. 77 (2016) 80–124. doi:10.1016/j.pmatsci.2015.10.001.
[60] K. Fumino, A. Wulf, R. Ludwig, The potential role of hydrogen bonding in aprotic and protic ionic liquids., Phys. Chem. Chem. Phys. 11 (2009) 8790–8794. doi:10.1039/b905634c.

[61] A. Knorr, P. Stange, K. Fumino, F. Weinhold, R. Ludwig, Spectroscopic Evidence for Clusters of Like-Charged Ions in Ionic Liquids Stabilized by Cooperative Hydrogen Bonding, (2016) 458–462. doi:10.1002/cphc.201501134.

[62] P.A. Hunt, C.R. Ashworth, R.P. Matthews, Hydrogen bonding in ionic liquids, Chem. Soc. Rev. 44 (2015) 1257–1288. doi:10.1039/C4CS00278D.

[63] K. Fumino, A. Wulf, R. Ludwig, Strong , Localized , and Directional Hydrogen Bonds Fluidize Ionic Liquids **, 2 (2008) 8731–8734. doi:10.1002/anie.200803446.

[64] G.R. Desiraju, Hydrogen bridges in crystal engineering: Interactions without borders, Acc. Chem. Res. 35 (2002) 565–573. doi:10.1021/ar010054t.

[65] N.E. Heimer, R.E. Del Sesto, Z. Meng, J.S. Wilkes, W.R. Carper, Vibrational spectra of imidazolium tetrafluoroborate ionic liquids, J. Mol. Liq. 124 (2006) 84–95. doi:10.1016/j.molliq.2005.08.004.

[66] P.A. Hunt, I.R. Gould, Structural characterization of the 1-butyl-3-methylimidazolium chloride ion pair using ab initio methods, J. Phys. Chem. A. 110 (2006) 2269–2282. doi:10.1021/jp0547865.

[67] B.A. Marekha, O.N. Kalugin, A. Idrissi, Non-covalent interactions in ionic liquid ion pairs and ion pair dimers: a quantum chemical calculation analysis, Phys. Chem. Chem. Phys. 17 (2015) 16846–16857. doi:10.1039/c5cp02197a.

[68] R.P. Matthews, T. Welton, P.A. Hunt, Competitive pi interactions and hydrogen bonding within imidazolium ionic liquids, Phys. Chem. Chem. Phys. 16 (2014) 3238–3253. doi:10.1039/c3cp54672a.

[69] T. Singh, A. Kumar, Aggregation behavior of ionic liquids in aqueous solutions: effect of alkyl chain length, cations, and anions., J. Phys. Chem. B. 111 (2007) 7843–7851. doi:10.1021/jp0726889.

[70] T. Takamuku, Y. Kyoshoin, T. Shimomura, S. Kittaka, T. Yamaguchi, Effect of water on structure of hydrophilic imidazolium-based ionic liquid, J. Phys. Chem. B. 113 (2009) 10817–10824. doi:10.1021/jp9042667.

[71] M.A. Firestone, J.A. Dzielawa, P. Zapol, L. a. Curtiss, S. Seifert, M.L. Dietz, Lyotropic Liquid-Crystalline Gel Formation in a Room-Temperature Ionic Liquid, Langmuir. 18 (2002) 7258–7260. doi:10.1021/la0259499.

[72] B. Fazio, A. Triolo, G. Di Marco, Recent Advances in linear and nonlinear Raman spectroscopy I, J. Raman Spectrosc. 39 (2008) 233–237. doi:10.1002/jrs.

[73] L. Cammarata, S.G. Kazarian, P. a. Salter, T. Welton, Molecular states of water in room temperature ionic liquidsElectronic Supplementary Information available. See http://www.rsc.org/suppdata/cp/b1/b106900d/, Phys. Chem. Chem. Phys. 3 (2001) 5192–5200. doi:10.1039/b106900d.

[74] S. Cha, D. Kim, Change of hydrogen bonding structure in ionic liquid mixtures by anion type, J. Chem. Phys. 148 (2018) 193827. doi:10.1063/1.5010067.
[75] C. Zhong, W. Hu, Electrolytes for Electrochemical Supercapacitors, Electrolytes Electrochem. Supercapacitors. (2016) 31–254. doi:10.1201/b21497-3.
[76] Y. Zhao, X. Yue, X. Wang, X. Chen, Lyotropic liquid crystalline phases with a series of N-alkyl-N-methylpiperidinium bromides and water, J. Colloid Interface Sci. 389 (2013) 199–205. doi:10.1016/j.jcis.2012.09.032.
[77] M.A. Firestone, P. Thiyagarajan, D.M. Tiede, Structure and optical properties of a thermoresponsive polymer-grafted, lipid-based complex fluid, Langmuir. 14 (1998) 4688–4698. doi:10.1021/la9805995.
[78] M. a. Firestone, P.G. Rickert, S. Seifert, M.L. Dietz, Anion effects on ionogel formation in N,N′-dialkylimidazolium-based ionic liquids, Inorganica Chim. Acta. 357 (2004) 3991–3998. doi:10.1016/j.ica.2004.06.042.
[79] M. Blesic, A. Lopes, E. Melo, Z. Petrovski, N. V. Plechkova, J.N. Canongia Lopes, K.R. Seddon, L.P.N. Rebelo, On the self-aggregation and fluorescence quenching aptitude of surfactant ionic liquids, J. Phys. Chem. B. 112 (2008) 8645–8650. doi:10.1021/jp802179j.
[80] T. Inoue, B. Dong, L.-Q. Zheng, Phase behavior of binary mixture of 1-dodecyl-3-methylimidazolium bromide and water revealed by differential scanning calorimetry and polarized optical microscopy., J. Colloid Interface Sci. 307 (2007) 578–81. doi:10.1016/j.jcis.2006.12.063.
[81] V. Balevicius, Z. Gdaniec, K. Aidas, J. Tamuliene, NMR and quantum chemistry study of mesoscopic effects in ionic liquids., J. Phys. Chem. A. 114 (2010) 5365–71. doi:10.1021/jp909293b.
[82] F. Perakis, L. De Marco, A. Shalit, F. Tang, Z.R. Kann, T.D. Kühne, R. Torre, M. Bonn, Y. Nagata, Vibrational Spectroscopy and Dynamics of Water, Chem. Rev. 116 (2016) 7590–7607. doi:10.1021/acs.chemrev.5b00640.
[83] B.A. Marekha, M. Bria, M. Moreau, I. De Waele, F.-A. Miannay, Y. Smortsova, T. Takamuku, O.N. Kalugin, M. Kiselev, A. Idrissi, Intermolecular interactions in mixtures of 1-n-butyl-3-methylimidazolium acetate and water: Insights from IR, Raman, NMR spectroscopy and quantum chemistry calculations, J. Mol. Liq. 210 (2015) 227–237. doi:10.1016/j.molliq.2015.05.015.
[84] S.A.M. Noor, P.M. Bayley, M. Forsyth, D.R. MacFarlane, Ionogels based on ionic liquids as potential highly conductive solid state electrolytes, Electrochim. Acta. 91 (2013) 219–226. doi:10.1016/j.electacta.2012.11.113.
[85] M.A. Firestone, M.A. Firestone, M.L. Dietz, S. Seifert, S. Trasobares,

D.J. Miller, N.J. Zaluzec, Ionogel-Templated Synthesis and Organization of Anisotropic Gold Nanoparticles, 60439 (2005) 754–760. doi:10.1002/smll.200500030.

[86] S. Saouane, F.P.A. Fabbiani, Structural Behavior of Long-Chain Imidazolium-Based Ionic Liquid [C $_{10}$ mim]Cl–Water Mixtures, Cryst. Growth Des. 15 (2015) 3875–3884. doi:10.1021/acs.cgd.5b00494.

[87] N. Kimizuka, T. Nakashima, Spontaneous Self-Assembly of Glycolipid Bilayer Membranes in Sugar-philic Ionic Liquids and Formation of, (2001) 6759–6761.

[88] V.H. Paschoal, L.F.O. Faria, M.C.C. Ribeiro, Vibrational Spectroscopy of Ionic Liquids, Chem. Rev. 117 (2017) 7053–7112. doi:10.1021/acs.chemrev.6b00461.

[89] C.E.S. Bernardes, M.E. Minas Da Piedade, J.N. Canongia Lopes, The structure of aqueous solutions of a hydrophilic ionic liquid: The full concentration range of 1-ethyl-3-methylimidazolium ethylsulfate and water, J. Phys. Chem. B. 115 (2011) 2067–2074. doi:10.1021/jp1113202.

[90] M. Anouti, J. Jacquemin, P. Porion, Transport properties investigation of aqueous protic ionic liquid solutions through conductivity, viscosity, and NMR self-diffusion measurements, J. Phys. Chem. B. 116 (2012) 4228–4238. doi:10.1021/jp3010844.

[91] M. Anouti, M. Caillon-Caravanier, Y. Dridi, J. Jacquemin, C. Hardacre, D. Lemordant, Liquid densities, heat capacities, refractive index and excess quantities for {protic ionic liquids + water} binary system, J. Chem. Thermodyn. 41 (2009) 799–808. doi:10.1016/j.jct.2009.01.011.

[92] M. Anouti, A. Vigeant, J. Jacquemin, C. Brigouleix, D. Lemordant, Volumetric properties, viscosity and refractive index of the protic ionic liquid, pyrrolidinium octanoate, in molecular solvents, J. Chem. Thermodyn. 42 (2010) 834–845. doi:10.1016/j.jct.2010.01.013.

[93] N. Yaghini, J. Pitawala, A. Matic, A. Martinelli, Effect of Water on the Local Structure and Phase Behavior of Imidazolium-Based Protic Ionic Liquids, J. Phys. Chem. B. 119 (2015) 1611–1622. doi:10.1021/jp510691e.

[94] O. Cabeza, L. Segade, M. Domínguez-Pérez, E. Rilo, D. Ausín, A. Martinelli, N. Yaghini, B. Gollas, M. Kriechbaum, O. Russina, A. Triolo, E. López-Lago, L.M. Varela, Mesostructure and physical properties of aqueous mixtures of the ionic liquid 1-ethyl-3-methyl imidazolium octyl sulfate doped with divalent sulfate salts in the liquid and the mesomorphic states, Phys. Chem. Chem. Phys. 20 (2018) 8724–8736. doi:10.1039/c7cp07999k.

[95] P.R. Burney, J. Pfaendtner, Structural and Dynamic Features of Candida rugosa Lipase 1 in Water, Octane, Toluene, and Ionic Liquids BMIM-PF6 and BMIM-NO3, J. Phys. Chem. B. 117 (2013) 2662−2670. doi:10.1021/jp312299d.

[96] N.M. Micaelo, C.M. Soares, Protein Structure and Dynamics in Ionic Liquids . Insights from Molecular Dynamics, J. Phys. Chem. B. (2008) 2566–2572. doi:10.1021/jp0766050.
[97] M.D. Bermúdez, A.E. Jiménez, J. Sanes, F.J. Carrión, Ionic liquids as advanced lubricant fluids, Molecules. 14 (2009) 2888–2908. doi:10.3390/molecules14082888.
[98] Q. Hu, H. Zhao, S. Ouyang, Understanding water structure from Raman spectra of isotopic substitution H2O/D2O up to 573 K, Phys. Chem. Chem. Phys. 19 (2017) 21540–21547. doi:10.1039/C7CP02065A.
[99] Y. Yasaka, C. Wakai, N. Matubayasi, M. Nakahara, Slowdown of H/D exchange reaction rate and water dynamics in ionic liquids: deactivation of solitary water solvated by small anions in 1-butyl-3-methyl- imidazolium chloride, J. Phys. Chem. A. 111 (2007) 541–543. doi:10.1021/jp0673720.
[100] N. Hatano, M. Watanabe, T. Takekiyo, H. Abe, Y. Yoshimura, Anomalous Conformational Change in 1-Butyl-3-methylimidazolium Tetrafluoroborate-D2O Mixtures, J. Phys. Chem. A. 116 (2012) 1208–1212. doi:10.1021/jp2097873.
[101] T. Cremer, C. Kolbeck, K.R.J. Lovelock, N. Paape, R. Wölfel, P.S. Schulz, P. Wasserscheid, H. Weber, J. Thar, B. Kirchner, F. Maier, H.-P. Steinrück, Towards a Molecular Understanding of Cation-Anion Interactions-Probing the Electronic Structure of Imidazolium Ionic Liquids by NMR Spectroscopy, X-ray Photoelectron Spectroscopy and Theoretical Calculations, Chem. - A Eur. J. 16 (2010) 9018–9033. doi:10.1002/chem.201001032.
[102] J. Kausteklis, M. Talaikis, V. Aleksa, V. Balevičius, Raman spectroscopy study of water confinement in ionic liquid 1-butyl-3-methylimidzolium nitrate, J. Mol. Liq. 271 (2018) 747–755. doi:10.1016/j.molliq.2018.09.060.
[103] P. Pascaud, P. Gras, Y. Coppel, C. Rey, S. Sarda, Interaction between a bisphosphonate, tiludronate, and biomimetic nanocrystalline apatites, Langmuir. 29 (2013) 2224–2232. doi:10.1021/la3046548.
[104] J. Kolmas, A. Jaklewicz, A. Zima, M. Bućko, Z. Paszkiewicz, J. Lis, A. Ślósarczyk, W. Kolodziejski, Incorporation of carbonate and magnesium ions into synthetic hydroxyapatite: The effect on physicochemical properties, J. Mol. Struct. 987 (2011) 40–50. doi:10.1016/j.molstruc.2010.11.058.
[105] J.D. Termine, A.S. Posner, Infra-red determination of the percentage of crystallinity in apatitic calcium phosphates, Nature. 211 (1966) 268–270. doi:10.1038/211268a0.
[106] T. Ishikawa, A. Teramachi, H. Tanaka, A. Yasukawa, K. Kandori, Fourier transform infrared spectroscopy study of deuteration of calcium hydroxyapatite particles, Langmuir. 16 (2000) 10221–10226. doi:10.1021/la0004855.

[107] Z.H. Cheng, A. Yasukawa, K. Kandori, T. Ishikawa, FTIR Study of Adsorption of CO 2 on Nonstoichiometric Calcium Hydroxyapatite, J.Chem.Soc ., Faraday T RansSoc. 94 (1998) 1501–1505. doi:10.1021/la980339n.
[108] A. Solhy, W. Amer, M. Karkouri, R. Tahir, A. El Bouari, A. Fihri, M. Bousmina, M. Zahouily, Bi-functional modified-phosphate catalyzed the synthesis of α-α′-(EE)-bis(benzylidene)-cycloalkanones: Microwave versus conventional-heating, J. Mol. Catal. A Chem. 336 (2011) 8–15. doi:10.1016/j.molcata.2010.11.032.
[109] Q.Q. Qiu, J. Connor, Effects of γ-irradiation, storage and hydration on osteoinductivity of DBM and DBM/AM composite, J. Biomed. Mater. Res. - Part A. 87 (2008) 373–379. doi:10.1002/jbm.a.31790.
[110] L. Dagys, V. Klimavičius, J. Kausteklis, A. Chodosovskaja, V. Aleksa, A. Kareiva, SOLID-STATE 1 H AND 31 P NMR AND FTIR SPECTROSCOPY STUDY OF STATIC AND DYNAMIC STRUCTURES IN SOL-GEL DERIVED CALCIUM HYDROXYAPATITES, 55 (2015) 1–9.
[111] K. Kristinaitytė, L. Dagys, J. Kausteklis, V. Klimavicius, I. Doroshenko, V. Pogorelov, N.R. Valevičienė, V. Balevicius, NMR and FTIR studies of clustering of water molecules: From low-temperature matrices to nano-structured materials used in innovative medicine, J. Mol. Liq. 235 (2017) 1–6. doi:10.1016/j.molliq.2016.11.076.
[112] J. Kausteklis, V. Aleksa, M.A. Iramain, S.A. Brandán, DFT and vibrational spectroscopy study of 1-butyl-3-methylimidazolium trifluoromethanesulfonate ionic liquid, J. Mol. Struct. 1175 (2019) 663–676. doi:10.1016/j.molstruc.2018.08.014.
[113] J. Kausteklis, V. Aleksa, M.A. Iramain, S.A. Brandán, Effect of cation-anion interactions on the structural and vibrational properties of 1-buthyl-3-methyl imidazolium nitrate ionic liquid, J. Mol. Struct. 1164 (2018). doi:10.1016/j.molstruc.2018.03.100.
[114] Y. Jeon, J. Sung, D. Kim, C. Seo, H. Cheong, Y. Ouchi, R. Ozawa, H.O. Hamaguchi, Structural change of 1-butyl-3-methylimidazolium tetrafluoroborate + water mixtures studied by infrared vibrational spectroscopy, J. Phys. Chem. B. 112 (2008) 923–928. doi:10.1021/jp0746650.
[115] B. Czarnik-Matusewicz, S. Pilorz, Study of the temperature-dependent near-infrared spectra of water by two-dimensional correlation spectroscopy and principal components analysis, Vib. Spectrosc. 40 (2006) 235–245. doi:10.1016/j.vibspec.2005.10.002.
[116] N. Hatano, T. Takekiyo, H. Abe, Y. Yoshimura, Effect of Counteranions on the Conformational Equilibrium of 1-Butyl-3-methylimidazolium-Based Ionic Liquids, Int. J. Spectrosc. 2011 (2011) 1–5. doi:10.1155/2011/648245.
[117] V.H. Segtnan, Š. Šašić, T. Isaksson, Y. Ozaki, Studies on the structure of water using two-dimensional near-infrared correlation spectroscopy

and principal component analysis, Anal. Chem. 73 (2001) 3153–3161. doi:10.1021/ac010102n.
[118] C. Thibault, P. Huguet, P. Sistat, G. Pourcelly, Confocal Raman micro-spectroscopy and electrochemical investigation of anion transport through ion-exchange membranes, Desalination. 149 (2002) 429–433. doi:10.1016/S0011-9164(02)00770-1.
[119] Y.O. Isao Noda, Two- Dimensional Correlation Spectroscopy, 2004.
[120] I. Noda, Determination of Two - Dimensional Correlation Spectra Using the Hilbert Transform, Appl. Spectrosc. 54 (2000) 994–999. doi:10.1366/0003702001950454.
[121] B. Dong, X. Zhao, L. Zheng, J. Zhang, N. Li, T. Inoue, Aggregation behavior of long-chain imidazolium ionic liquids in aqueous solution: Micellization and characterization of micelle microenvironment, Colloids Surfaces A Physicochem. Eng. Asp. 317 (2008) 666–672. doi:10.1016/j.colsurfa.2007.12.001.
[122] I. Noda, Generalized two-dimensional correlation method applicable to infrared, Raman, and other types of spectroscopy, Appl. Spectrosc. 47 (1993) 1329–1336. doi:10.1366/0003702934067694.
[123] I. Noda, A.E. Dowrey, C. Marcott, G.M. Story, Generalized Two-Dimensional Correlation Spectroscopy, Appl. Spectrosc. 54 (2000) 236–248. doi:10.1021/jp2043043.
[124] J. Zhu, L. Bai, B. Chen, W. Fei, Thermodynamical properties of phase change materials based on ionic liquids, Chem. Eng. J. 147 (2009) 58–62. doi:10.1016/j.cej.2008.11.016.
[125] U. Domańska, E. Bogel-Łukasik, Measurements and Correlation of the (Solid + Liquid) Equilibria of [1-Decyl-3-methylimidazolium Chloride + Alcohols (C 2 −C 12)] † , Ind. Eng. Chem. Res. 42 (2003) 6986–6992. doi:10.1021/ie030464g.
[126] L.H. Kim, Ki-Sub, Shin Bae-Kun, K. Kim, B. Shin, H. Lee, Physical and Electrochemical Properties of 1-Butyl-3-methylimidazolium Bromide, 1-Butyl-3-methylimidazolium Iodide, and 1-Butyl-3-methylimidazolium Tetrafluoroborate, Korean J. Chem. English. 21 (2004) 1010–1014. doi:10.1016/j.jpowsour.2007.10.062.
[127] P.N. Tshibangu, S.N. Ndwandwe, E.D. Dikio, Density , Viscosity and Conductivity Study of 1-Butyl-3- Methylimidazolium Bromide, Int. J. Electrochem. Sci. 6 (2011) 2201–2213.
[128] S. Fendt, S. Padmanabhan, H.W. Blanch, J.M. Prausnitz, Viscosities of acetate or chloride-based ionic liquids and some of their mixtures with water or other common solvents, J. Chem. Eng. Data. 56 (2011) 31–34. doi:10.1021/je1007235.
[129] S. a. Dharaskar, M.N. Varma, D.Z. Shende, C.K. Yoo, K.L. Wasewar, Synthesis, characterization and application of 1-butyl-3 methylimidazolium chloride as green material for extractive desulfurization of liquid fuel, Sci. World J. 2013 (2013). doi:10.1155/2013/395274.

[130] A.A. Strechan, A.G. Kabo, Y.U. Paulechka, A. V. Blokhin, G.J. Kabo, A.S. Shaplov, E.I. Lozinskaya, Thermochemical properties of 1-butyl-3-methylimidazolium nitrate, Thermochim. Acta. 474 (2008) 25–31. doi:10.1016/j.tca.2008.05.002.
[131] B. Mokhtarani, A. Sharifi, H.R. Mortaheb, M. Mirzaei, M. Mafi, F. Sadeghian, Density and viscosity of 1-butyl-3-methylimidazolium nitrate with ethanol, 1-propanol, or 1-butanol at several temperatures, J. Chem. Thermodyn. 41 (2009) 1432–1438. doi:10.1016/j.jct.2009.06.023.
[132] J. JR, S. M, Thermal Characteristics of 1-Butyl-3-Methylimimidazolium Based Oxidant Ionic Liquids, J. Chem. Eng. Process Technol. 07 (2016) 4–9. doi:10.4172/2157-7048.1000309.
[133] S. Ren, Y. Hou, W. Wu, W. Liu, Purification of Ionic Liquids : Sweeping Solvents by Nitrogen, (2010) 5074–5077.
[134] V. Klimavicius, A. Kareiva, V. Balevicius, Solid-State NMR Study of Hydroxyapatite Containing Amorphous Phosphate Phase and Nanostructured Hydroxyapatite: Cut-O ff Averaging of CP-MAS Kinetics and Size Pro fi les of Spin Clusters, (2014). doi:10.1021/jp510229f.
[135] J.M. Hollas, Modern Spectroscopy, (2004).
[136] H. Abe, T. Yamada, K. Shibata, Dynamic properties of nano-confined water in an ionic liquid, J. Mol. Liq. 264 (2018) 54–57. doi:10.1016/j.molliq.2018.05.006.
[137] Y. Jeon, J. Sung, C. Seo, H. Lim, H. Cheong, M. Kang, B. Moon, Y. Ouchi, D. Kim, Structures of ionic liquids with different anions studied by infrared vibration spectroscopy, J. Phys. Chem. B. 112 (2008) 4735–4740. doi:10.1021/jp7120752.
[138] T. Endo, T. Kato, K.I. Tozaki, K. Nishikawa, Phase behaviors of room temperature ionic liquid linked with cation conformational changes: 1-Butyl-3-methylimidazolium Hexafluorophosphate, J. Phys. Chem. B. 114 (2010) 407–411. doi:10.1021/jp909256j.
[139] J. Kausteklis, V. Aleksa, M.A. Iramain, S.A. Brandan, Effect of cation-anion interactions on the structural and vibrational properties of 1-butyl-3-metylimidazolium nitrate ionic liquid, J. Mol. Struct. 1164 (2018) 1–14. doi:10.1016/j.molstruc.2018.03.100.
[140] R.W. Berg, M. Deetlefs, K.R. Seddon, I. Shim, J.M. Thompson, Raman and ab initio studies of simple and binary 1-alkyl-3-methylimidazolium ionic liquids, J. Phys. Chem. B. 109 (2005) 19018–19025. doi:10.1021/jp050691r.
[141] R.O. H. Hamaguchi, Structure of Ionic Liquids and Ionic Liquid Compounds: Are Ionic Liquids Genuine Liquids in the Conventional Sense?, Adv. Chem. Ph. 131 (2005) 85–102.
[142] Y. Umebayashi, H. Hamano, S. Tsuzuki, J.N. Canongia Lopes, A.A.H. Pádua, Y. Kameda, S. Kohara, T. Yamaguchi, K. Fujii, S.I. Ishiguro, Dependence of the conformational isomerism in 1-n-butyl-3-

methylimidazolium ionic liquids on the nature of the halide anion, J. Phys. Chem. B. 114 (2010) 11715–11724. doi:10.1021/jp1044755.
[143] Y.-S. Ye, J. Rick, B.-J. Hwang, Ionic liquid polymer electrolytes, J. Mater. Chem. A. 1 (2013) 2719–2743. doi:10.1039/b000000x.
[144] V. Balevičius, L. Džiaugys, F. Kuliešius, A. Maršalka, ^{1}H and ^{13}C NMR study of phase transition and molecular motion in ionic liquids forming lyotropic liquid-crystalline ionogels, Lith. J. Phys. 51 (2011) 212–220. doi:10.3952/lithjphys.51309.
[145] S. Cha, M. Ao, W. Sung, B. Moon, B. Ahlström, P. Johansson, Y. Ouchi, D. Kim, Structures of ionic liquid-water mixtures investigated by IR and NMR spectroscopy, Phys. Chem. Chem. Phys. 16 (2014) 9591–601. doi:10.1039/c4cp00589a.
[146] S. Sowmiah, V. Srinivasadesikan, M.C. Tseng, Y.H. Chu, On the chemical stabilities of ionic liquids, Molecules. 14 (2009) 3780–3813. doi:10.3390/molecules14093780.
[147] R.W. Berg, Raman spectroscopy and ab-initio model calculations on ionic liquids, Monatsh. Chem. 138 (2007) 1045–1075. doi:10.1007/s00706-007-0760-9.
[148] T. Takekiyo, K. Yamazaki, E. Yamaguchi, H. Abe, Y. Yoshimura, High ionic liquid concentration-induced structural change of protein in aqueous solution: A case study of lysozyme, J. Phys. Chem. B. 116 (2012) 11092–11097. doi:10.1021/jp3057064.
[149] J.-B. Brubach, A. Mermet, A. Filabozzi, A. Gerschel, D. Lairez, M.P. Krafft, P. Roy, Dependence of Water Dynamics upon Confinement Size, J. Phys. Chem. B. 105 (2001) 430–435. doi:10.1021/jp002983s.
[150] T. Singh, A. Kumar, Cation-anion-water interactions in aqueous mixtures of imidazolium based ionic liquids, Vib. Spectrosc. 55 (2011) 119–125. doi:10.1016/j.vibspec.2010.09.009.
[151] Y. Xu, Y. Gao, L. Zhang, J. Yao, C. Wang, H. Li, Microscopic structures of ionic liquids 1-ethyl-3-methylimidazolium tetrafluoroborate in water probed by the relative chemical shift, Sci. China Chem. 53 (2010) 1561–1565. doi:10.1007/s11426-010-3198-6.
[152] Y. Chen, Y. Cao, X. Sun, T. Mu, Hydrogen bonding interaction between acetate-based ionic liquid 1-ethyl-3-methylimidazolium acetate and common solvents, J. Mol. Liq. 190 (2014) 151–158. doi:10.1016/j.molliq.2013.11.010.
[153] E. Bodo, S. Mangialardo, F. Capitani, L. Gontrani, F. Leonelli, P. Postorino, Interaction of a long alkyl chain protic ionic liquid and water, J. Chem. Phys. 140 (2014) 204503. doi:10.1063/1.4876036.
[154] C. Roth, S. Chatzipapadopoulos, D. Kerlé, F. Friedriszik, M. Lütgens, S. Lochbrunner, O. Kühn, R. Ludwig, Hydrogen bonding in ionic liquids probed by linear and nonlinear vibrational spectroscopy, New J. Phys. 14 (2012) 105026. doi:10.1088/1367-2630/14/10/105026.
[155] M.C.C. Ribeiro, High Viscosity of Imidazolium Ionic Liquids with the Hydrogen Sulfate Anion: A Raman Spectroscopy Study, J. Phys.

Chem. B. 116 (2012) 7281–7290. doi:Doi 10.1021/Jp302091d1.
[156] K.-L. Han, G.-J. Zhao, Hydrogen bonding and transfer in the excited state, 2011.
[157] M. Moreno, F. Castiglione, A. Mele, C. Pasqui, G. Raos, Interaction of water with the model ionic liquid [bmim][BF4]: molecular dynamics simulations and comparison with NMR data, J. Phys. Chem. B. 112 (2008) 7826–7836. doi:10.1021/jp800383g.
[158] J. Joseph, E.D. Jemmis, Red-, blue-, or no-shift in hydrogen bonds: A unified explanation, J. Am. Chem. Soc. 129 (2007) 4620–4632. doi:10.1021/ja067545z.
[159] C.G. Hanke, N.A. Atamas, R.M. Lynden-Bell, Solvation of small molecules in imidazolium ionic liquids: a simulation study, Green Chem. 4 (2002) 107–111. doi:10.1039/b109179b.
[160] O. Russina, A. Triolo, L. Gontrani, R. Caminiti, D. Xiao, L.G. Hines Jr, R.A. Bartsch, E.L. Quitevis, N. Pleckhova, K.R. Seddon, Morphology and intermolecular dynamics of 1-alkyl-3-methylimidazolium bis{(trifluoromethane)sulfonyl}amide ionic liquids: structural and dynamic evidence of nanoscale segregation, J. Phys. Condens. Matter. 21 (2009) 424121. doi:10.1088/0953-8984/21/42/424121.
[161] F.W.B. Einstein, D.G. Tuck, A Refinement of the Crystal Structure of NH4NO3.2HNO3, Acta Cryst. B26 (1970) 1117–1120. doi:10.1107/S0567740869003323.
[162] K. Kaneko, Y. Yoshimura, A. Shimizu, Water concentration dependence of the refractive index of various ionic liquid-water mixtures, J. Mol. Liq. 250 (2018) 283–286. doi:10.1016/j.molliq.2017.12.009.
[163] S. Mangialardo, L. Baldassarre, E. Bodo, P. Postorino, The Structure of Ionic Liquids, 2014. doi:10.1007/978-3-319-01698-6.
[164] M.R. Waterland, D. Stockwell, A.M. Kelley, Symmetry breaking effects in NO3-: Raman spectra of nitrate salts and ab initio resonance Raman spectra of nitrate-water complexes, J. Chem. Phys. 114 (2001) 6249–6258. doi:10.1063/1.1355657.
[165] D.J. Goebbert, E. Garand, T. Wende, R. Bergmann, G. Meijer, K.R. Asmis, D.M. Neumark, Infrared spectroscopy of the microhydrated nitrate ions $NO_3^-\cdot(H2O)_{(1-6)}$., J. Phys. Chem. A. 113 (2009) 7584–92. doi:10.1021/jp9017103.
[166] C. Choe, J. Lademann, M.E. Darvin, Depth profiles of hydrogen bound water molecule types and their relation to lipid and protein interaction in the human stratum corneum in vivo, Analyst. 141 (2016) 6329–6337. doi:10.1039/C6AN01717G.
[167] C. Boissière, J.B. Brubach, A. Mermet, G. Marzi De, C. Bourgaux, E. Prouzet, P. Roy, Water confined in lamellar structures of AOT surfactants: An infrared investigation, J. Phys. Chem. B. 106 (2002) 1032–1035. doi:10.1021/jp012724i.

[168] A. V. Frontzek, L. Paccou, Y. Guinet, A. Hédoux, Study of the phase transition in lysozyme crystals by Raman spectroscopy, Biochim. Biophys. Acta - Gen. Subj. 1860 (2016) 412–423. doi:10.1016/j.bbagen.2015.10.020.
[169] A. Lerbret, P. Bordat, F. Affouard, Y. Guinet, A. Hédoux, L. Paccou, D. Prévost, M. Descamps, Influence of homologous disaccharides on the hydrogen-bond network of water: Complementary Raman scattering experiments and molecular dynamics simulations, Carbohydr. Res. 340 (2005) 881–887. doi:10.1016/j.carres.2005.01.036.
[170] K. Kristinaitytė, L. Dagys, J. Kausteklis, V. Klimavicius, I. Doroshenko, V. Pogorelov, N.R. Valevičienė, V. Balevicius, NMR and FTIR studies of clustering of water molecules: From low-temperature matrices to nano-structured materials used in innovative medicine, J. Mol. Liq. 235 (2017). doi:10.1016/j.molliq.2016.11.076.
[171] H. Abe, T. Takekiyo, M. Aono, H. Kishimura, Y. Yoshimura, N. Hamaya, Polymorphs in room-temperature ionic liquids: Hierarchical structure, confined water and pressure-induced frustration, J. Mol. Liq. 210 (2015) 200–214. doi:10.1016/j.molliq.2015.05.057.
[172] Y. Yoshimura, T. Takekiyo, C. Okamoto, N. Hatano, H. Abe, Switching of hydrogen bonds of water in ionic liquid, 1-butyl-3-methylimidazolium tetrafluoroborate, J. Raman Spectrosc. 44 (2013) 475–480. doi:10.1002/jrs.4197.
[173] X. Shen, Q. Chen, J. Zhang, P. Fu, Supramolecular Structures in the Presence of Ionic Liquids, Supramol. Struct. Presence Ion. Liq. Theory, Prop. New Approaches. (2011) 427–482.
[174] O. Russina, B. Fazio, G. Di Marco, R. Caminiti, The Structure of Ionic Liquids, (2014). doi:10.1007/978-3-319-01698-6.
[175] Q.G. Zhang, N.N. Wang, S.L. Wang, Z.W. Yu, Hydrogen bonding behaviors of binary systems containing the ionic liquid 1-butyl-3-methylimidazolium trifluoroacetate and water/methanol, J. Phys. Chem. B. 115 (2011) 11127–11136. doi:10.1021/jp204305g.
[176] L. Zhang, Z. Xu, Y. Wang, H. Li, Prediction of the solvation and structural properties of ionic liquids in water by two-dimensional correlation spectroscopy, J. Phys. Chem. B. 112 (2008) 6411–6419. doi:10.1021/jp8001349.
[177] K. Ohno, M. Okimura, N. Akai, Y. Katsumoto, The effect of cooperative hydrogen bonding on the OH stretching-band shift for water clusters studied by matrix-isolation infrared spectroscopy and density functional theory, Phys. Chem. Chem. Phys. 7 (2005) 3005–3014. doi:10.1039/b506641g.
[178] I. Doroshenko, V. Balevicius, G. Pitsevich, K. Aidas, V. Sablinskas, V. Pogorelov, FTIR/PCA study of propanol in argon matrix: The initial stage of clustering and conformational transitions, Low Temp. Phys. 40 (2014) 1077–1082. doi:10.1063/1.4902228.

[179] S. Diallo-Garcia, M. Ben Osman, J.M. Krafft, S. Boujday, C. Guylène, Discrimination of infrared fingerprints of bulk and surface POH and OH of hydroxyapatites, Catal. Today. 226 (2014) 81–88. doi:10.1016/j.cattod.2013.11.041.
[180] J.A. Noble, C. Martin, H.J. Fraser, P. Roubin, S. Coussan, IR selective irradiations of amorphous solid water dangling modes: Irradiation vs annealing effects, J. Phys. Chem. C. 118 (2014) 20488–20495. doi:10.1021/jp506943k.
[181] E. Garskaite, K.A. Gross, S.W. Yang, T.C.K. Yang, J.C. Yang, A. Kareiva, Effect of processing conditions on the crystallinity and structure of carbonated calcium hydroxyapatite (CHAp), CrystEngComm. 16 (2014) 3950–3959. doi:10.1039/c4ce00119b.
[182] T. Köddermann, F. Schulte, M. Huelsekopf, R. Ludwig, Formation of Water Clusters in a Hydrophobic Solvent, Angew. Chemie - Int. Ed. 42 (2003) 4904–4908. doi:10.1002/anie.200351438.
[183] R.M. Bentwood, A.J. Barnes, W.J. Orville-Thomas, Studies of intermolecular interactions by matrix isolation vibrational spectroscopy and normal coordinate analysis. Self-association of hydrogen cyanide, J. Mol. Spectrosc. 84 (1980) 391–404. doi:10.1016/0022-2852(78)90042-5.
[184] G.P. Ayers, A.D.E. Pullin, The i.r. spectra of matrix isolated water species-I. Assignment of bands to (H2O)2, (D2O)2 and HDO dimer species in argon matrices., Spectrochim. Acta Part A Mol. Spectrosc. 32 (1976) 1629–1639. doi:10.1016/0584-8539(76)80265-6.
[185] S. Coussan, P. Roubin, J.P. Perchard, Infrared induced isomerizations of water polymers trapped in nitrogen matrix, Chem. Phys. 324 (2006) 527–540. doi:10.1016/j.chemphys.2005.11.017.
[186] A. Engdahl, B. Nelander, On the structure of the water trimer. a matrix isolation study, J. Chem. Phys. 86 (1987) 4831–4837. doi:10.1063/1.452676.
[187] J. Ceponkus, P. Uvdal, B. Nelander, Water tetramer, pentamer, and hexamer in inert matrices, J. Phys. Chem. A. 116 (2012) 4842–4850. doi:10.1021/jp301521b.
[188] J.A. Noble, C. Martin, H.J. Fraser, P. Roubin, S. Coussan, Unveiling the surface structure of amorphous solid water via selective infrared irradiation of OH stretching modes, J. Phys. Chem. Lett. 5 (2014) 826–829. doi:10.1021/jz5000066.
[189] S. Coussan, P. Roubin, J.A. Noble, Inhomogeneity of the amorphous solid water dangling bonds, Phys. Chem. Chem. Phys. 17 (2015) 9429–9435. doi:10.1039/c5cp00662g.
[190] M. Ben Osman, S. Diallo-Garcia, V. Herledan, D. Brouri, T. Yoshioka, J. Kubo, Y. Millot, G. Costentin, Discrimination of Surface and Bulk Structure of Crystalline Hydroxyapatite Nanoparticles by NMR, J. Phys. Chem. C. 119 (2015) 23008–23020. doi:10.1021/acs.jpcc.5b08732.

[191] V. Balevicius, Z. Gdaniec, K. Aidas, NMR and DFT study on media effects on proton transfer in hydrogen bonding: concept of molecular probe with an application to ionic and super-polar liquids., Phys. Chem. Chem. Phys. 11 (2009) 8592–8600. doi:10.1039/b819666d.

TRUMPOS ŽINIOS APIE DISERTANTĄ

Vardas, Pavardė: Jonas Kausteklis
Gimimo data: 1987-07-10
Gimimo vieta: Gargždai, Lietuva
Kontaktai:
mob.tel.: +37065636463
el. paštas: jonas.kausteklis@gmail.com

Išsilavinimas:
2010-2012 fizikos magistras, Vilniaus universitetas
2006-2010 elektronikos inžinerijos bakalauras, Vilniaus universitetas
1994-2006 vidurinis, Gargždų Kranto vidurinė mokykyla

Darbinė veikla:
2010-2011 Inžinierius, Vilniaus universitetas
2009-2011 Technikas, Mykolo Romerio universitetas
2011-2013 Vyr specialistas, NMA prie ŽŪM
2013- dabar IT sistemų inžinierius, Thermo Fisher Scientific Balitcs, UAB

Dalyvavimas projektuose:
2016-2018 Molekulinių ir joninių nano-spiečių liotropinių skystųjų kristalų vandens tirpaluose BMR ir virpesinė spektrometrija (TAP-LU-15-017)

Mokyklos, stažuotės:
2010 Stažuotė J. Stefan Institute, Liubliana, Slovenia.

ACKNOWLEDGEMENTS

I would mostly like to acknowledge my lovely wife Indrė and daughter Gabrielė, my parents Birutė and Jonas, and rest of my family for the patience and unprecedented support throughout the study years.

Grateful acknowledgements for the exceptional supervision are dedicated to assoc. prof. Valdemaras Aleksa for guidance, patience and support, for encouraging and, sometimes, pushing me forward trough all years spent in field of spectroscopy in Vilnius university.

A large gratitude goes to prof. Vytautas Balevičius for introduction to H-bond problems and functional materials. These thesis would not had been possible without caring support of prof. Valdas Šablinskas and assoc. prof. Justinas Čeponkus in experimental and technical subtleties.

Warm gratitude is dedicated to prof. Gediminas Niaura and his team members Ieva and Martynas for excellent help with spectroscopic measurements and analysis as well as scientific discussions.

Great appreciation is dedicated to contribution of co-authors dr. Vytautas Klimavičius, prof. Aivaras Kareiva, dr. Silvia Brandan, dr. Kęstutis Aidas, dr. I. Doroshenko, L. Dagys, K. Kristinaitytė and others. The same goes to all Institute of Chemical Physics members for atmosphere during studies and work in lab. Many thanks to Martynas, Vidita, Arūnas, Alytis, Rasa and Dovilė for they smile and help during PhD journey.

And finally, I am grateful to all my friends and colleagues, especially for those who encouraged and understood my behavior during PhD process.

LIST OF PUBLICATIONS

1. **J. Kausteklis**, V. Aleksa, M. A. Iramain and S. A. Brandan, *DFT and Vibrational Spectroscopy study of 1-butyl-3-metylimidazolium trifluoromethanesulfonate*, J. Mol. Struct., vol. 1175, pp. 663–676, 2019.

2. **J. Kausteklis**, M. Talaikis, V. Aleksa and V. Balevičius, *Raman spectroscopy study of water confinement in ionic liquid 1-butyl-3-methylimidzolium nitrate*, J. Mol. Liq., vol. 271, pp. 747–755, 2018.

3. **J. Kausteklis**, V. Aleksa, M. A. Iramain and S. A. Brandan, *Effect of cation-anion interactions on the structural and vibrational properties of 1-butyl-3-methylimidazolium nitrate ionic liquid*, J. Mol. Struct., vol. 1164, pp. 563–576, 2018.

4. **J. Kausteklis**, V. Balevičius and V. Aleksa, *Two-dimensional Raman spectroscopy study of ionogel phase formation in long-chain ionic liquid/water systems*, J. Raman Spectrosc., vol. 48, no. 1, pp. 126–131, 2017.

5. K. Kristinaitytė, L. Dagys, **J. Kausteklis**, V. Klimavičius, I. Doroshenko, V. Pogorelov, N. R. Valevičienė and V. Balevičius, *NMR and FTIR studies of clustering of water molecules: From low-temperature matrices to nano-structured materials used in innovative medicine*, J. Mol. Liq., vol. 235, pp. 1–6, 2017.

6. S. Kareiva, V. Klimavičius, A. Momot, **J. Kausteklis**, A Prichodko, L. Dagys, F. Ivanauskas, S. Sakirzanovas, V. Balevičius and A. Kareiva, *Sol-gel synthesis, phase composition, morphological and structural characterization of $Ca_{10}(PO_4)_6(OH)_2$: XRD, FTIR, SEM, 3D SEM and solid-state NMR studies*, J. Mol. Struct., vol. 1119, pp. 1–11, 2016.

7. V. Klimavičius, Z. Gdaniec, **J. Kausteklis**, V. Aleksa, K. Aidas and V. Balevičius, *NMR and Raman spectroscopy monitoring of proton/deuteron exchange in aqueous solutions of ionic liquids forming hydrogen bond: A Role of anions, self-aggregation and mesophase formation*, J. Phys. Chem. B, vol. 117, no. 35, pp. 10211–10220, 2013. NO

8. V. Aleksa, **J. Kausteklis**, V. Klimavicius, Z. Gdaniec and V. Balevičius, *Raman and NMR spectroscopy study of liquid crystalline ionogel phase in ionic liquid/H_2O mixtures: The states of water*, J. Mol. Struct., vol. 993, no. 1–3, pp. 91–96, 2011.

COPIES OF PUBLICATIONS

Journal of Molecular Structure 1175 (2019) 663–676

Contents lists available at ScienceDirect

Journal of Molecular Structure

journal homepage: http://www.elsevier.com/locate/molstruc

DFT and vibrational spectroscopy study of 1-butyl-3-methylimidazolium trifluoromethanesulfonate ionic liquid

Jonas Kausteklis [a], Valdemaras Aleksa [a], Maximiliano A. Iramain [b], Silvia Antonia Brandán [b, *]

[a] Vilnius University, Sauletekio al.9-3, LT-10222 Vilnius, Lithuania
[b] Cátedra de Química General, Instituto de Química Inorgánica, Facultad de Bioquímica. Química y Farmacia, Universidad Nacional de Tucumán, Ayacucho 471, (4000) San Miguel de Tucumán, Tucumán, Argentina

ARTICLE INFO

Article history:
Received 5 June 2018
Received in revised form
3 August 2018
Accepted 5 August 2018
Available online 10 August 2018

Keywords:
1-Butyl-3-methylimidazolium
trifluoromethanesulfonate
Vibrational spectra
Conformations
Molecular structure
Descriptor properties
DFT calculations

ABSTRACT

Structural and vibrational characterizations for the 1-butyl-3-methylimidazolium trifluoromethanesulfonate ionic liquid ([BMIM][OTF]) were performed combining the experimental Raman spectrum with density functional theory (DFT) calculations based in the hybrid B3LYP/6-311++G** level of theory. Structurally, the trifluoromethanesulfonate anion, [OTF] is linked to 1-butyl-3-methylimidazolium cation, [BMIM] by a bidentate coordination by means of two different S–*O*–-H hydrogen bonds. The [OTF] anion plays a very important role in the structure and stability of [BMIM][OTF], as observed by the strong increase in the dipole moment value when the anion is added to cation. Intramolecular H and halogen bonds evidence the high stability of ionic liquid, as supported by NBO and AIM calculations. Very good correlations were observed between the predicted infrared and Raman spectra with the corresponding experimental ones. The different Mulliken charges observed on the O atoms of O–-H bonds support the asymmetric bidentate coordination of [OTF] anion with the [BMIM] cation. The [OTF] anion increase the reactivity of [BMIM][OTF], as compared with [BMIM][NO_3]. In addition, the [OTF] anion reduces drastically the electrophilicity and nucleophilicity indexes of cation evidencing the strong influence of anion on the properties of cation. The vibrational analyses have revealed a very important shifting of one of the two antisymmetric modes of [BMIM][OTF] towards lower wavenumbers due probably to an asymmetric of S═O···H bond interaction which is no observed in the anion. The complete vibrational assignments were performed for ionic liquid, cation and anion and the harmonic scaled force constants were reported at the same level of theory.

1. Introduction

The studies of cation-anion interactions present in the ionic liquids are of great interest in diverse fields, such as in nanoparticles. In particular, the identifications of different ionic liquids by using the simple technique of vibrational spectroscopy is useful and necessary to detection of these species in different media and systems [1–3]. Currently, the ionic liquids have multiple uses, for which, their structural, electrochemical and physicochemical properties have been studied since long time and from different points of view [4–12]. On the other hand, the theoretical calculations are of great aid when the structures of these ionic liquids are unknown, as in the 1-butyl-3-methylimidazolium nitrate ionic liquid [13]. In this opportunity, an experimental and theoretical study on the 1-Butyl-3-methylimidazolium trifluoromethanesulfonate ionic liquid was performed combining the experimental FT-Raman spectrum with DFT calculations because the experimental structure for this ionic liquid, so far, was no reported. In this context and due to the extended bibliography on ionic liquids, here only some studies reported in the literature for 1-butyl-3-methylimidazolium trifluoromethanesulfonate are mentioned [1–12]. First, to perform the complete vibrational assignments it is necessary to realize a deep structural investigation in order to know the most stable structure, as in the 1-butyl-3-methylimidazolium nitrate ionic liquid case [13]. Besides, to know the coordination mode of trifluoromethanesulfonate in [BMIM][OTF] is very important because it group plays an important role in

* Corresponding author.
E-mail addresses: sbrandan@fbqf.unt.edu.ar, sbrandanbrandansa@yahoo.com.ar (S.A. Brandán).

https://doi.org/10.1016/j.molstruc.2018.08.014
0022-2860/

the stability of ionic liquid. With these purposes, the structure of 1-butyl-3-methylimidazolium trifluoromethanesulfonate, identified as [BMIM][OTF] or [BMIM][CF_3SO_3], was modelled and optimized in gas phase by using the hybrid B3LYP method with the 6-311++G** basis set [14,15]. The potential energy surfaces were studied in order to find the most stable structure and, later with this structure, the vibrational analysis was performed by using the scaled quantum mechanical force field (SQMFF) approach calculated at the same level of theory and with the Molvib program [16,17]. At this point, the experimental FT-Raman spectrum of and its experimental available infrared spectrum [1,3] were used to perform the complete vibrational assignments of all bands observed in both spectra to the vibration normal modes of [BMIM][OTF]. The harmonic force constants were obtained in gas phase at the same level of theory and, then, they were compared with other reported in the literature. NBO and AIM calculations [18,19] were also performed to explain the characteristics of the cation-anion interactions observed in the most stable structure. The differences observed between the two frontier orbitals [20,21], known as gap, were also calculated and later compared with those observed for the cationic and anionic species in order to identify the effect of these two species on the properties of [BMIM][OTF]. Here, quantum chemical global the descriptors [22–25] were also computed for [BMIM][OTF] and compared with those obtained for the cationic and anionic species with the finality of explain the differences observed between cationic and anionic species [26–29] and to know the characteristics of these interactions. Finally, the conformation equilibrium in [BMIM][OTF] was also investigated and compared with those observed for other ionic liquids and for the [BMIM] cation. The conformations of [OTF] anion are highly known and, for this reason, they were not studied in this work.

2. Experimental section

Raman spectra of 1-butyl-3-methylimidazolium trifluoromethanesulfonate, [BMIM][OTF] were recorded at room temperature with a Bruker MultiRAM FT-Raman spectrometer containing the motorized xyz-sample stage and with the high-sensitivity liquid nitrogen cooled germanium detector. The 1064 nm wavelength beam of the pulsed Nd:YAG laser (500 mW) as the excitation source using the 180° scattering geometry was employed in the experiments. Average of 400 Raman spectra was recorded to get better signal to noise ratio at spectral range 4000-70 cm^{-1} and a resolution of the spectrometer of 2 cm^{-1}. The preparation and measurements of all samples were performed in Silica cells in order to avoid the background.

3. Computational details

The structure of [BMIM][OTF] ionic liquid was not experimentally determined and, for this reason, its structure was modelled with the *GaussView* program [30] taking into account the experimental position of trifluoromethanesulfonate group in the structure reported by Ganesan et al. [9] for the ionic liquid 3,30-di-n-butyl-1,10-(1,4-phenylenedimethylene)diimidazolium bis(trifluoromethanesulfonate) where between cation and anion are clearly observed C–H···F and C–H···O hydrogen bonds. In [BMIM][OTF], the trifluoromethanesulfonate anion is linked to [BMIM] by bidentate coordination to two S–*O*···H hydrogen bonds, as observed in Fig. 1 while, in Fig. 2 are observed the theoretical structures of both cation and anion. The optimizations of all structures were carried out in gas phase by using the hybrid B3LYP/6-311++G** method and with the Gaussian 09 program Revision A.02 [30]. The potential energy surfaces (PES) for [BMIM][OTF] were studied considering variations in the dihedral N2–C10–C16–C17 and C10–C16–C17–C20 angles. In both curves only one structure with minimum energy was observed and, for these reasons, they are not presented here. For the most stable structure, natural populations analysis (NPA), Mulliken charges, molecular electrostatic potentials (MEP), bond orders and topological properties were computed by using NBO calculations and the AIM2000 program [18,19]. In the vibrational studies for [BMIM][OTF] and its anion, the normal internal coordinates were built and their corresponding harmonic force fields were computed with the SQMFF procedure [16] and the Molvib program [17]. The complete assignments of those two species were performed by using Potential Energy Distribution (PED) contributions $\geq$ 10%, the experimental FT-Raman spectrum recorded here and, with that experimental available infrared spectrum [1,3]. Here, the conformations equilibrium in [BMIM][OTF] and in [BMIM] cation were investigated by using the experimental Raman spectrum and, then, these were compared with those observed for other ionic liquids. The gap values for [BMIM][OTF] and their cationic and anionic species [20,21] together with chemical potential (μ), electronegativity (χ), global hardness (η), global softness (S), global electrophilicity index (ω) and global nucleophilicity index (E) descriptors were calculated in order to predict the reactivities and behaviours of those three species [22–29]. Later, these properties were compared with those

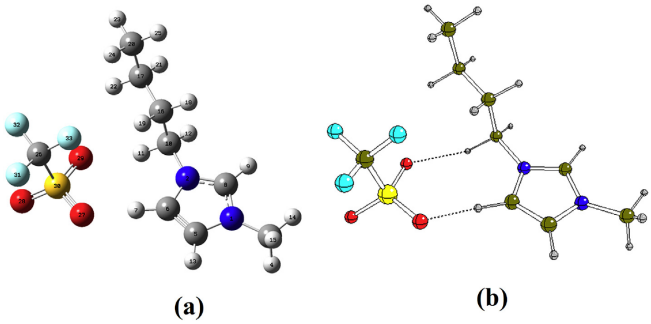

Fig. 1. a-Molecular theoretical structures of 1-buthyl-3-methyl imidazolium trifluoromethanesulfonate ionic liquid and the atoms numbering. b-The different S–*O*···H bonds are evidenced with dashes lines.

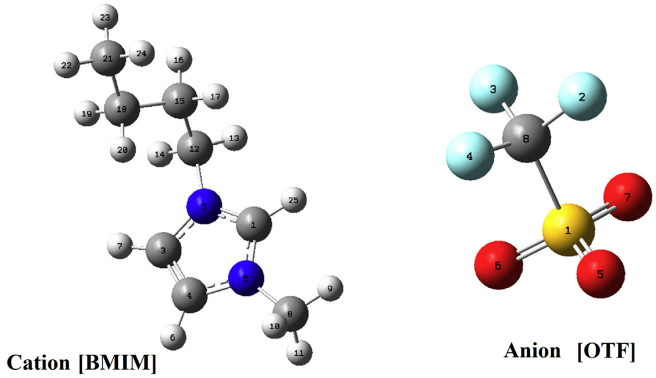

Fig. 2. Molecular theoretical structures of 1-buthyl-3-methyl imidazolium cation and trifluoromethanesulfonate anion and the atoms numbering.

Table 1
Calculated total energy (E), dipolar moment (μ) and volume for the Anionic, Cationic and 1-buthyl-3-methyl imidazolium trifluoromethanesulfonate ionic liquid in gas phase.

B3LYP/6-311++G**method			
Gas Phase			
Species	E (Hartrees)	μ (Debye)	V (Å^3)
[BMIM][OTF]	−1385.1347	19.29	274.3
[BMIM] Cation	−423.2869	4.91	188.3
[OTF] Anion	−961.7304	4.12	99.0

observed by us for 1-buthyl-3-methyl imidazolium nitrate [13] in order to examine the influence of nitrate and trifluoromethanesulfonate anions on the corresponding cations.

4. Results and discussion

4.1. Geometry study

The calculated energies, dipole moments and volume values for [BMIM][OTF] and its cation and anion species in gas phase by using B3LYP/6-311++G** level of theory are presented in Table 1. The dipole moments show low values for the two ionic species, however, the cation value increase from 4.91 D to 19.29 D when the anion is incorporated together with the cation to [BMIM][OTF]. This result obviously supports the strong influence of anion on the properties of cation. On the other hand, the volume values evidence the lower size of anion, in relation to cation, but the total volume of ionic liquid is approximately the sum of both cation and anion values (287.3 Å^3).

The calculated geometrical parameters for those three species are compared with those experimental determined by X-ray diffraction for the structure 3,3′-dimethyl-1,1'-(1,4-phenylenedimethylene)diimidazolium bis(tetrafluoroborate) by Ganesan et al. [9] by using the room means square deviation (RMSD) values and, the results are summarized in Table 2. In Fig. S1 is presented the structure of compared compound. In general, the predicted distances for the three species are overestimated when are compared with those experimental ones and, the better correlations in bond lengths are observed for the anion while reasonable correlations can be seen for cation and ionic liquid. On the other side, the bond lengths for the three species present good concordances. On the contrary, for the dihedral angles of ionic liquid and its cation poor correlations are predicted, as expected because the cation of the compared compound is very different from the cation of [BMIM][OTF]. These theoretical parameters show that the proposed structure is reasonably good to perform the vibrational study of this ionic liquid.

4.2. Charges, bond orders and molecular electrostatic potentials studies

The [OTF] anion plays a very important role in the structure and stability of [BMIM][OTF], as observed by the strong increase in the dipole moment value when the anion is incorporate to cation. For this reason, the studies of different charges, molecular electrostatic potentials and bond orders in those species are necessaries to understand what modifications undergoes the cation in [BMIM][OTF]. Thus, Mulliken and natural populations analysis (NPA) charges on all atoms for the anionic, cationic and 1-buthyl-3-methyl imidazolium trifluoromethanesulfonate in gas phase were studied by using B3LYP/6-311++G** level of theory. The results of both charges for the three species are presented in Table S1 while in Fig. S2 can be seen the variations in the Mulliken charges on all atoms. Quickly, from the comparisons between cation and ionic liquid we can observe that the Mulliken charges on practically all atoms of ionic liquid present variations, with exception of those observed on the C3, H9, C17, C20, H21 atoms. The higher modifications in the ionic liquid are observed on the N1, N2, C5, H7, C8, C10, H11, C16 and H24 atoms where the less positive value is observed on the H24 atom while the more negative values on the C5, C8 and C10 atoms. The Mulliken charges on the remaining atoms have positive values. When the charges on the atoms of anion are compared with those observed for the ionic liquid, it is observed that only the charge on the O28 atom presents less negative value on the ionic liquid than on the anion. This observation suggests bidentate coordination for the O atoms of [OTF] group because the O28 atom has a different value than the other two O atoms. When the NPA charges are compared in similar form than the Mulliken ones there are not differences among them and, for this reason, the graphic is not presented here.

The bond order, expressed as Wiberg index is a very interesting

Table 2
Comparisons of calculated geometrical parameters for the Anion, Cation and 1-buthyl-3-methyl imidazolium trifluoromethanesulfonate ionic liquid in gas phase with the experimental available obtained by X-ray diffraction for 3,3′-dimethyl-1,1'-(1,4-phenylenedimethylene)diimidazolium bis(tetrafluoroborate) [9].

B3LYP/6-311++G** method[a]				Exp[b]
Parameters	Gas phase			
	[BMIM][OTF]	[BMIM] Cation	[OTF] Anion	
Bond lengths (Å)				
C3–N1	1.462	1.470		1.476
C3–H4	1.090	1.089		0.989
C3–H14	1.088	1.088		0.989
C3–H15	1.090	1.089		
N1–C8	1.339	1.337		1.326
C8–N2	1.333	1.336		1.329
C8–H9	1.076	1.077		0.950
N2–C10	1.483	1.486		1.479
C10–H11	1.091	1.090		0.989
C10–H12	1.092	1.091		0.990
N2–C6	1.382	1.380		1.376
C6–C5	1.362	1.361		1.350
C6–H7	1.093	1.076		0.950
C5–H13	1.076	1.076		0.950
C10–C16	1.529	1.531		1.509
C16–C17	1.533	1.533		
C16–H18	1.098	1.096		
C16–H19	1.093	1.096		
C17–C20	1.530	1.531		
C17–H21	1.097	1.096		
C17–H22	1.093	1.096		
C20–H23	1.092	1.093		
C20–H24	1.093	1.091		
C20–H25	1.095	1.093		
C26–S30	1.887		1.896	1.821
C26–F31	1.339		1.351	1.320
C26–F32	1.341		1.352	1.325
C26–F33	1.356		1.351	1.331
S30–O27	1.488		1.475	1.442
S30–O28	1.460		1.475	1.437
S30–O29	1.483		1.475	1.434
RMSD[b]	**0.247**	**0.292**	**0.041**	
Bond Angles (°)				
C3–N1–C8	125.9	125.9		125.5
C3–N1–C5	125.9	125.6		126.0
N1–C8–N2	108.8	108.9		108.7
C8–N2–C10	125.4	125.3		125.5
C8–N2–C6	108.9	108.2		108.6
N2–C10–C16	112.1	113.4		110.2
N2–C6–C5	106.5	107.3		106.8
C6–C5–C1	107.5	107.0		107.3
C10–C16–C17	111.0	115.0		
C16–C17–C20	112.4	112.4		
H15–C3–H14	109.1	109.3		107.7
H15–C3–H4	109.7	110.0		
H14–C3–H4	109.2	109.4		
H15–C3–N1	109.7	109.3		109.3
H14–C3–N1	109.1	108.9		109.2
H4–C3–N1	109.8	109.5		
H9–C8–N1	125.4	125.4		125.6
H9–C8–N2	125.6	125.5		125.5
H13–C5–N1	122.0	122.1		122.5
H13–C5–C6	130.4	130.8		129.9
H7–C6–N2	122.4	122.0		125.5
H7–C6–C5	130.9	130.6		126.5
H11–C10–H12	109.5	107.5		108.1
H11–C10–N2	106.8	106.1		109.6
H11–C10–C16	109.6	111.3		109.5
H12–C10–N2	106.7	106.7		109.6
H12–C10–C16	111.6	111.2		109.6
H18–C16–H19	107.4	105.9		
H18–C16–C10	110.0	109.4		
H18–C16–C17	110.2	109.4		
H19–C16–C10	108.7	106.1		
H19–C16–C17	109.1	109.5		
H21–C17–H22	106.9	106.5		
H21–C17–C16	109.5	110.0		
H21–C17–C20	109.5	109.1		
H22–C17–C16	108.4	110.0		
H22–C17–C20	109.8	109.1		
H23–C20–H24	107.6	107.6		
H23–C20–H25	107.7	107.8		
H24–C20–H25	107.9	107.6		
F31–C26–F32	108.2		106.8	108.1
F31–C26–F33	107.5		106.8	107.8
F32–C26–F33	107.3		106.8	106.8
O27–S30–O28	115.8		115.5	114.8
O27–S30–O29	112.6		115.5	113.9
O28–S30–O29	116.5		115.5	115.5
RMSD[b]	**1.5**	**1.7**	**1.1**	
Diedral Angles (°)				
C3–N1–C8–N2	179.0	179.0		179.4
C3–N1–C5–C6	−179.1	−179.0		−179.3
N1–C8–N2–C10	177.7	178.3		−171.3
N1–C5–C6–N2	0.1	0.1		−0.2
C8–N2–C10–C16	−92.1	−82.5		91.0
C5–C6–N2–C10	−177.7	−178.4		171.6
C6–N2–C10–C16	85.0	95.5		85.0
N2–C10–C16–C17	−178.2	−64.9		
C10–C16–C17–C20	178.7	−176.9		
RMSD[b]	**149.0**	**147.7**		

[a] This work.
[b] From Ref [9].

property that predicts the characteristics or nature of the different bonds, thus, in Table S2 are summarized the bond orders (BO) for the anionic, cationic and 1-buthyl-3-methyl imidazolium trifluoromethanesulfonate in gas phase by using B3LYP/6-311++G** level of theory. Also, in this table are presented the matrix of bond orders for different interactions of the bonds hydrogen and halogen. Analyzing first, the BO values for cation and the ionic liquid it is observed variations in the BO of H7, H11, H19 and H24 atoms while when are compared the values of ionic liquid with those corresponding to anion, the higher difference and the higher value only for the O28 atom is observed. Here, newly the different values observed in the O atoms support the bidentate coordination of [OTF] group in the ionic liquid. The BO value of S30 atom is slightly higher in the anion while the BO values for F atoms are higher in the ionic liquid. Evaluating the matrix of BO, we observed a certain ionic character in the following H and halogen bonds: O29···H11, O29···H22, O27···H7, F33···H19 and F33···H24. Evidently, these interactions could support the stability of [BMIM][OTF].

Other interesting property studied for the three species in gas phase is the molecular electrostatic potential (MEP) by using B3LYP/6-311++G** level of theory because the electronic distribution in those species can be easily seen from the different colorations of their mapped surfaces which are very useful to predict reaction sites or attacks with potential electrophiles or nucleophiles. In Table S3 are presented the MEP values on all atoms of ionic liquid and its cation and anion while Fig. 3 shows the mapped MEP surfaces for the ionic liquid, cation and anion in gas phase by using B3LYP/6-311++G** level of theory. The values from Table S3 practically no present differences while important differences can be observed in their colorations. Thus, the strong red colour on all surface indicate clearly that anion is nucleophilic, as expected because it has negative charge while the contrary is observed on the cation. Therefore, all blue colours on the cation surface, with positive charge, clearly indicate its electrophilic characteristic. Now, when the mapped MEP surface for the ionic liquid is evaluated we

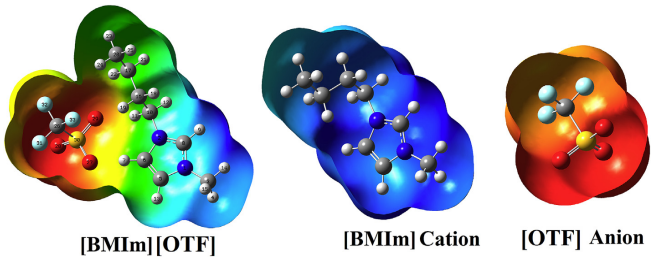

Fig. 3. Calculated electrostatic potential surfaces on the molecular surface of 1-buthyl-3-methyl imidazolium trifluoromethanesulfonate ionic liquid and its cation and anion in gas phase. Colour ranges, in au: from red −0.090 to blue +0.090. B3LYP/6-311++G** level of theory. Isodensity value of 0.005. (For interpretation of the references to colour in this figure legend, the reader is referred to the Web version of this article.)

Table 3
Main delocalization energies (in kJ/mol) for the Anionic, Cationic and 1-buthyl-3-methyl imidazolium trifluoromethanesulfonate in gas phase by using B3LYP/6-311++G** level of theory.

Delocalization	B3LYP/6-311++G**[a]		
	[BMIM][OTF]	[BMIM] Cation	[OTF] Anion
$\pi C8\text{-}N2 \rightarrow LP(1)N1$		96.39	
$\Sigma_{\pi \rightarrow LP}$		**96.39**	
$\pi N2\text{-}C8 \rightarrow \pi^*C5\text{–}C6$	70.77	70.81	
$\pi C5\text{-}C6 \rightarrow \pi^*N2\text{–}C8$	68.89	63.95	
$\Sigma_{\pi \rightarrow \pi^*}$	**139.66**	**134.76**	
$LP(2)O27 \rightarrow \sigma^*O28\text{–}S30$	65.63		
$LP(2)O27 \rightarrow \sigma^*O29\text{–}S30$	53.55		
$LP(3)O27 \rightarrow \sigma^*C26\text{–}S30$	85.56		50.03
$LP(2)O28 \rightarrow \sigma^*O27\text{–}S30$	72.44		
$LP(2)O28 \rightarrow \sigma^*O29\text{–}S30$	72.69		
$LP(3)O28 \rightarrow \sigma^*C26\text{–}S30$	107.47		50.03
$LP(3)F31 \rightarrow \sigma^*C26\text{–}F33$	51.71		
$LP(3)O29 \rightarrow \sigma^*C26\text{–}S30$			50.03
$\Sigma_{LP \rightarrow \sigma^*}$	**509.05**		**150.09**
$LP(1)N1 \rightarrow \pi^*N2\text{–}C8$	297.32	324.28	
$LP(1)N1 \rightarrow \pi^*C5\text{–}C6$	106.38	121.68	
$\Sigma_{LP \rightarrow \pi^*}$	**403.70**	**445.96**	
$\sigma^*O27\text{–}S30 \rightarrow \sigma^*O28\text{–}S30$	57.89		
$\sigma^*O29\text{–}S30 \rightarrow \sigma^*O28\text{–}S30$	71.98		
$\Sigma_{\sigma^* \rightarrow \sigma^*}$	**129.87**		
$\pi^*N2\text{–}C8 \rightarrow \pi^*C5\text{–}C6$	66.92	68.76	
$\Sigma_{\pi^* \rightarrow \pi^*}$	**66.92**	**68.76**	
ΣE_{TOTAL}	**1249.2**	**745.87**	**150.09**

[a] This work; Bold letters, different transitions.

observed the nucleophilic sites on the anion while the electrophilic sites on the ring and CH_3 groups but, on the side chain of ionic liquid a notable green colour typical of inert region is observed.

4.3. NBO and topological properties

The high dipole moment value observed for [BMIM][OTF] and the bidentate coordination that presents the [OTF] anion in the ionic liquid suggest that this ionic liquid could present a high stability and, for these reasons, NBO and AIM calculations were performed for the ionic liquid, cation and anion in gas phase by using the B3LYP/6-311++G** method. With these two studies the stability of ionic liquid can be predicted by means of the donor-acceptor energy interactions and the types of intra-molecular interactions by using the topological properties [18,19]. Thus, in Table 3 are presented the donor-acceptor energy interactions for [BMIM][OTF] and both cation and anion by using the B3LYP/6-311++G** method. Clearly, it is observed that ionic liquid present the interactions observed in the cation ($\Delta ET_{\pi \rightarrow n}$, $\Delta ET_{\pi \rightarrow \pi^*}$, $\Delta ET_{n \rightarrow \pi^*}$, $\Delta ET_{\pi^* \rightarrow \pi^*}$ interactions), in the anion ($\Delta ET_{n \rightarrow \sigma^*}$) and, also an additional formed, $\Delta ET_{\sigma^* \rightarrow \sigma^*}$ interaction while the $\Delta ET_{\pi \rightarrow n}$ interaction observed in the cation disappear in the ionic liquid. Here, the two bidentate coordination that present the [OTF] group in ionic liquid can be easily seen by the $LP(3)O27 \rightarrow \sigma^*C26\text{–}S30$ and $LP(3)O28 \rightarrow \sigma^*C26\text{–}S30$ transitions. Hence, the total energy visibly favours to ionic liquid (1249.2 kJ/mol) due to the presence of anion (509.05 kJ/mol) which give a high stability to ionic liquid by the $\Delta ET_{n \rightarrow \sigma^*}$ interaction.

The stability of [BMIM][OTF] was also analyzed by using the Bader's theory of atoms in molecules (AIM) by using the topological properties applied to the intra-molecular interactions [31]. These properties for the ionic liquid were calculated by using the AIM2000 program [19]. The computed electron density, $\rho(r)$ and the Laplacian values, $\nabla^2\rho(r)$ for ionic liquid in gas phase by using B3LYP/6-311++G** level of theory can be seen in Table 4 together

Table 4
Analysis of the Bond Critical Points (BCPs) and Ring Critical Points (RCPs) for 1-buthyl-3-methyl imidazolium trifluoromethanesulfonate in gas phase by using B3LYP/6-311++G** level of theory.

Parameter[#]	B3LYP/6-311++G**[a]									
	[BMIM][OTF]									
	RCP1	RCPN1	RCPN2	RCPN3	RCPN4	O29···H11	O27···H7	O29···H22	F33···H19	F33···H24
ρ(r)	0.0545	0.0036	0.0024	0.0050	0.0014	0.0197	0.0310	0.0059	0.0046	0.0014
$\nabla^2\rho(r)$	0.4008	0.0163	0.0112	0.0216	0.0071	0.0715	0.1106	0.0203	0.0182	0.0071
λ1	−0.0602	−0.0024	−0.0015	−0.0029	−0.0009	−0.0235	−0.0454	−0.0049	−0.0042	−0.0010
λ2	0.2148	0.0059	0.0047	0.0067	0.0003	−0.0219	−0.0427	−0.0040	−0.0041	−0.0002
λ3	0.2465	0.0128	0.0079	0.0178	0.0077	0.1170	0.1987	0.0293	0.0265	0.0083
|λ1|/λ3	0.2442	0.1875	0.1899	0.1629	0.1169	0.2008	0.2300	0.1693	0.1585	0.1205
Distances						2.091	1.861	2.705	2.686	3.249

[a] This work, parameters in atomics units, distances in Å.

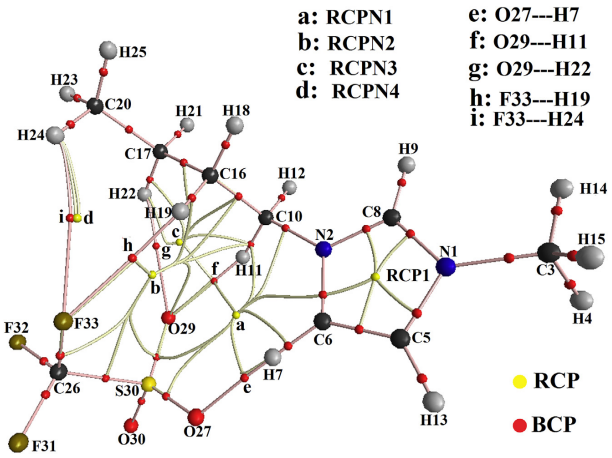

Fig. 4. Molecular graphics for 1-buthyl-3-methyl imidazolium trifluoromethanesulfonate ionic liquid in gas phase showing the geometry of all their bond critical points (BCPs) and ring critical points (RCPs) at the B3LYP/6-311++G** level of theory.

Table 5
The frontier molecular HOMO and LUMO orbitals and some descriptors for the Anionic, Cationic and 1-buthyl-3-methyl imidazolium trifluoromethanesulfonate in gas phase by using B3LYP/6-311++G** level of theory.

B3LYP/6-311++G**				
Orbital	Gas phase			
(eV)	[BMIM][OTF][a]	[BMIM][a]	[OTF][a]	[BMIM][NO_3][b]
HOMO	−6.3900	−11.7643	−2.9256	−5.5720
LUMO	−2.1690	−5.1809	3.7790	−1.3541
|GAP|	4.2211	6.5835	6.7046	4.2180
Descriptors				
(eV)	[BMIM][OTF][a]	[BMIM][a]	[OTF][a]	[BMIM][NO_3][b]
χ	−2.1105	−3.2917	−3.3523	−2.1090
μ	−4.2795	−8.4726	0.4267	−3.4630
η	2.1105	3.2917	3.3523	2.1090
S	0.2369	0.1519	0.1492	0.2371
ω	4.3387	10.9038	0.0272	2.8432
E	−9.032	−27.890	−1.430	−7.3035

χ = - [E(LUMO)- E(HOMO)]/2; μ = [E(LUMO) + E(HOMO)]/2; η = [E(LUMO) - E(HOMO)]/2.; $S = ½\eta$; $\omega = \mu^2/2\eta$ $E = \mu^4\eta$.
[a] This work.
[b] From Ref. [13].

with the eigenvalues *(λ1, λ2, λ3)* of the Hessian matrix and the $|\lambda 1|/\lambda 3$ ratio. Here, it is necessary explain that for cation and anion there are not observed interactions. For [BMIM] is observed only the RCP characteristic of ring, as was also observed in the other [BMIM][NO_3] ionic liquid [13]. In [BMIM][OTF] was observed that $\nabla^2\rho(r) > 0$ and $|\lambda 1|/\lambda 3 < 1$, where clearly there are three O29···H11, O27···H7 and O29···H22 interactions typical of H bonds and two F33···H19 and F33···H24 halogen interactions, as suggested by Bader's theory [31]. Fig. 4 shows clearly the different interactions observed by AIM analysis for [BMIM][OTF]. Note that the topological properties for the halogen bonds formed are low due to the larger distances observed among the involved F and H atoms, as compared with the H bonds. Other very important result observed in this analysis is the asymmetric bidentate coordinations observed in the O29···H11 and O27···H7 interactions because the topological properties are higher for the O27···H7 bond than the other one O29···H11 (see Fig. 1). The short distance between those two O27 and H7 atoms justify (1.861 Å) the higher properties observed for the O27···H7 interaction. Obviously, these interactions produce a high stability in this ionic liquid, as was also observed by NBO study and, besides, the bidentate coordination is confirmed by this AIM analysis.

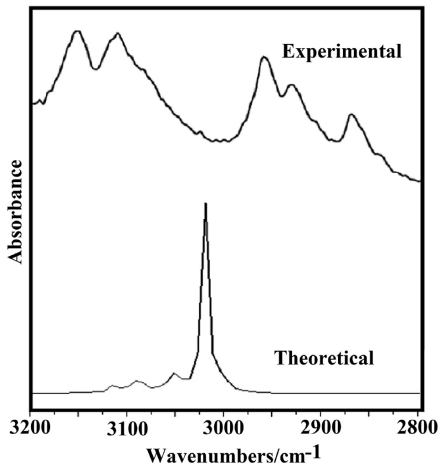

Fig. 5. Comparisons between the experimental available FTIR spectra taken from Ref. [1] in the 3200-2800 cm^{-1} region with the corresponding predicted for 1-buthyl-3-methyl imidazolium trifluoromethanesulfonate ionic liquid in the gas phase at B3LYP/6-311++G** level of theory.

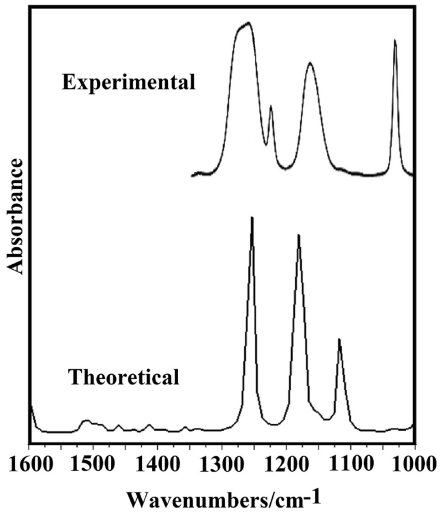

Fig. 6. Comparisons between the experimental available FTIR spectra taken from Ref. [1] in the 1600-1000 cm^{-1} region with the corresponding predicted for 1-buthyl-3-methyl imidazolium trifluoromethanesulfonate ionic liquid in the gas phase at B3LYP/6-311++G** level of theory.

4.4. Frontier orbitals and global descriptors

From the above studies is clearly evidenced the notable influence of [OTF] anion on the properties of [BMIM][OTF] and its stability, as supported by the high dipole moment value of ionic liquid and the existent bidentate coordination of anion with the cation. Then, the frontier orbitals were computed because they are useful parameters to predict the reactivities and behaviour of this ionic liquid. Hence, as suggested by Parr and Pearson [20] and Brédas [21] the gap values were calculated for [BMIM][OTF], anion and cation from the differences between the highest occupied molecular orbital (HOMO) and lowest unoccupied molecular orbital (LUMO). After that, quantum global descriptors such as, chemical potential (μ), electronegativity (χ), global hardness (η), global softness (S), global electrophilicity index (ω) and global nucleophilicity index (E) were computed for those three species [22–29]. In Table 5 are summarized the gap values and of those descriptors calculated for the three species together with the equations used. These values were compared with the reported for [BMIM][NO_3] [13]. In Fig. 10 is presented a graphic of frontier orbitals and gap values for 1-butyl-3-methylimidazolium trifluoromethanesulfonate, [BMIM] cation and [OTF] anion in gas phase by using the hybrid B3LYP/6-311++G** method. Firstly, analyzing the gap values for the three species we observed that the gap values for cation and anion are approximately similar while in the ionic liquid the value decrease drastically from 6.5835 eV in the cation up to 4.2211 eV in [BMIM][OTF]. Hence, we observed clearly that the effect of anion on cation is increase the reactivity of ionic liquid but, the reactivity of [BMIM][OTF] ionic liquid is slightly lower (4.2211 eV) than that predicted for [BMIM][NO_3] (4.2180 eV) [13]. Thus, the [NO_3] anion increases more the reactivity of cation as compared with the [OTF] anion. Now, evaluating the descriptors from Fig. S4 we observed that the electronegativity (χ), global hardness (η) and global softness (S) are similar in the three species but in the cation higher electrophilicity and nucleophilicity values are observed than the other two species. Hence, the effect of anion is to reduce the values of both properties, as evidenced by the values for [BMIM][OTF]. Then, when the descriptors of both [BMIM][OTF] and [BMIM][NO_3] ionic liquids are compared, it is clearly observed from Fig. S5, that the electronegativity (χ), global hardness (η) and global softness (S) values are similar in both species. However, higher electrophilicity and lower chemical potential and nucleophilicity are observed for [BMIM][OTF] than [BMIM][NO_3]. Hence, the influence of the [OTF] anion on

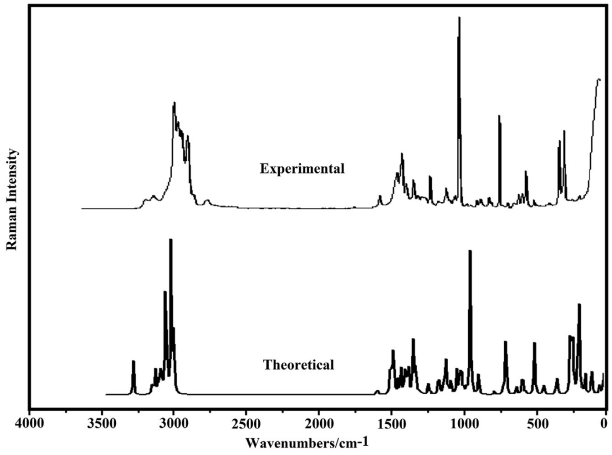

Fig. 7. Comparisons between the experimental Raman spectra with the corresponding predicted for 1-buthyl-3-methyl imidazolium trifluoromethanesulfonate ionic liquid in the gas phase at B3LYP/6-311++G** level of theory.

Table 6
Observed and calculated wavenumbers (cm^{-1}) and assignments for 1-buthyl-3-methyl imidazolium trifluoromethanesulfonate and its cation and anion in gas phase.

Experimental		[BMIM] Cation[a]		[OTF] Anion[a]		[BMIM][OTF][a]	
IR[b]	Ra[a]	SQM[c]	Assignment[a]	SQM[c]	Assignment[a]	SQM[c]	Assignment[a]
3188w	3169w	3156	ν_sC-H			3148	νC5-H13
3152s	3151w	3142	νC1-H25			3144	νC8-H9
3117sh	3114w	3139	ν_aC-H				
3110s		3033	$\nu_a CH_3$(C8)			3022	$\nu_a CH_3$(C3)
	3024sh	3018	$\nu_a CH_3$(C8)			3003	$\nu_a CH_3$(C3)
		2995	$\nu_a CH_2$(C12)			2985	$\nu_a CH_2$(C10)
		2979	$\nu_a CH_3$(C21)			2967	$\nu_a CH_3$(C20)
2963s	2968 m	2967	$\nu_a CH_3$(C21)			2959	$\nu_a CH_3$(C20)
		2951	$\nu_s CH_2$(C12)			2945	$\nu_s CH_2$(C16)
2935s	2943 m	2942	$\nu_s CH_3$(C8)			2936	$\nu_a CH_2$(C17)
2935s	2943 m	2937	$\nu_a CH_2$(C15)			2934	$\nu_s CH_3$(C3)
2935s	2917 m	2909	$\nu_a CH_2$(C18)			2923	$\nu_s CH_2$(C10)
2935s	2917 m	2907	$\nu_s CH_3$(C21)			2896	νC6-H7
2875 m	2879 m	2898	$\nu_s CH_2$(C15)			2895	$\nu_s CH_3$(C20)
2875 m	2879 m	2882	$\nu_s CH_2$(C18)			2880	$\nu_s CH_2$(C17)
2875 m	2879 m					2875	$\nu_s CH_2$(C16)
	1569w	1548	νC3-C4,νN5-C1			1554	νN2-C8,βC6-H7
		1539	νN2-C1			1542	νN1-C8
	1461w	1449	$\delta_a CH_3$(C8)			1453	δCH_2(C10)
	1448w	1445	$\delta_a CH_3$(C21)			1451	$\delta_a CH_3$(C3)
		1438	$\delta_a CH_3$(C21)			1443	$\delta_a CH_3$(C20)
	1432sh	1434	δCH_2(C12)			1437	$\delta_a CH_3$(C20)
		1429	δCH_2(C18)			1432	δCH_2(C17)
	1420 m	1422	$\delta_a CH_3$(C8)			1424	δCH_2(C16)
	1420 m	1414	δCH_2(C15)			1423	$\delta_a CH_3$(C3)
	1391w	1396	$\delta_s CH_3$(C8)			1395	$\delta_s CH_3$(C3)
	1391w	1391	νN2-C3			1390	ρCH_2(C10), νN2-C8
	1391w	1375	$wagCH_2$(C15)			1380	$wagCH_2$(C10)
		1363	$wagCH_2$(C12) $wagCH_2$(C18)			1371	$wagCH_2$(C17)
		1361	$\delta_s CH_3$(C21)			1357	νN1-C5
1334w	1341w	1354	$wagCH_2$(C12)			1349	$\delta_s CH_3$(C20)
	1313w	1316	$wagCH_2$(C18)			1317	ρCH_2(C10), βC6-H7
	1303w	1300	$wagCH_2$(C18) $wagCH_2$(C15)			1308	ρCH_2(C17)
1274s		1292	ρCH_2(C18)			1299	βC6-H7,νN1-C3
1274s	1282w	1272	βC3-H7			1284	$wagCH_2$(C16)
	1260w					1259	ρCH_2(C16)
	1226w	1235	ρCH_2(C15)				
1256s	1197w	1188	ρCH_2(C12)	1168	$\nu_a SO_3$	1206	$\nu_s SO_3$
				1168	$\nu_a SO_3$	1186	ρCH_2(C10)
1222 m				1142	$\nu_s CF_3$,$\delta_s CF_3$	1150	$\nu_s CF_3$,$\delta_s CF_3$,βC5-H13
1162s	1169w					1145	βC8-H9
1162s	1131w	1134	βC1-H25	1074	$\nu_a CF_3$	1134	$\nu_a CF_3$
				1073	$\nu_a CF_3$	1118	νC5-C6
	1118w	1118	$\rho' CH_3$(C8)			1118	$\rho' CH_3$(C3)
	1093w	1095	βC4-H6			1106	$\rho' CH_3$(C20), νC16-C17
1162s	1093w	1087	ρCH_3(C21), νC15-C18			1099	$\nu_a SO_3$
	1066w	1075	$\rho' CH_3$(C21)			1078	ρCH_3(C20)
	1057w	1069	ρCH_3(C8)				
1030s	1034vs					1069	$\nu_a CF_3$
						1068	ρCH_3(C3)
	1023s	1023	βR_2			1020	νC16-C17,νC17-C20
	1017sh	1013	βR_1,νN5-C4			1017	βR_1
		1003	νC18-C21			1003	νN2-C6,βR_2
	989vw					989	γC6-H7
	976vw					977	νC10-C16
1030s	1034vs	957	νC12-C15	938	$\nu_s SO_3$	935	$\nu_s SO_3$
	908w	908	ρCH_3(C21)			897	$\tau_w CH_2$(C10)
	886w	867	γaC-H			888	$\rho' CH_3$(C20)
	845w	842	τwCH_2(C15)				
	825vw	821	γC1-H25				
	810vw					802	γC8-H9
	757s	774	τwCH_2(C12),νC15-C18			746	γC5-H13
	757s	741	γsC-H			741	$\tau_w CH_2$(C17)
	757s			710	$\delta_s CF_3$,$\nu_s CF_3$	720	$\delta_s CF_3$,$\nu_s CF_3$
	757s					717	νN2-C10
	735w	701	τwCH_2(C18)				
	699w	668	νN5-C8			672	$\tau_w CH_2$(C16)
	653w					653	τR_1
	641w	634	τR_1				
	624w	613	τR_2			616	νN1-C3
	602w					609	τR_2
	602w			607	$\delta_s SO_3$	608	τR_2,$\delta_s SO_3$
	574w	570	νN2-C12	547	$\delta_a CF_3$	552	$\delta_a CF_3$

Table 6 (*continued*)

Experimental		[BMIM] Cation[a]		[OTF] Anion[a]		[BMIM][OTF][a]	
IR[b]	Ra[a]	SQM[c]	Assignment[a]	SQM[c]	Assignment[a]	SQM[c]	Assignment[a]
	519w			547	$\delta_a CF_3$	543	$\delta_a SO_3$
	500vw			494	$\delta_a SO_3$	496	$\delta_a SO_3$,$\delta_a CF_3$
	451vw	481	δ_C12C15C18	493	$\delta_a SO_3$	492	$\delta_a SO_3$,$\delta_a CF_3$
	432vw					426	δ_C16C17C20
							δN2C10C16
	415vw	410	βN5-C8,βN2-C12			414	βN2-C10
	349 m			327	$\rho' SO_3$	336	ρSO_3,$\rho' CF_3$
	323sh	320	δN2C12C15	327	$\rho' CF_3$,ρSO_3	329	$\rho' SO_3$
	314 m					315	νN2-C10
	282vw					281	βN1-C3
	282vw	282	δ_C15C18C21	268	νS1-C8	279	νS30-C26,$\delta_s SO_3$
	259vw	241	γN5-C8			243	γN1-C3,δ_C10C16C17
		221	τwCH_3(C21)			221	$\tau_w CH_3$(C20)
	212w	201	δ_C12C15C18,γN5-C8	191	ρCF_3	199	ρCF_3
	160sh			191	$\rho' CF_3$,ρSO_3	195	$\rho' SO_3$,$\rho' CF_3$
	160sh					194	ρSO_3,$\rho' CF_3$
	131sh	141	γN2-C12			134	νO29-H11
						111	νO27-H7
						98	τC16-C17
						84	τC10-C16
	75s	75	τC15-C18,τC12-C15			81	γN2-C10
		66	γN5-C8			65	$\tau_w CH_3$(C3)
		58	τwCH_3(C8)			57	δO27H7C6
				53	$\tau_w SO_3$	54	δ_H7O27S30
						36	$\tau_w SO_3$,$\tau_w CF_3$
						34	δO29H11C10
		19	τwC12-N2			11	δ_H11O29S30

Abbreviationsν, stretching; wag, wagging; τ, torsion; ρ, rocking; τw, twisting; δ, deformation; a, antisymmetric; s, symmetric.
[a] This work.
[b] From Ref [1,3].
[c] From scaled quantum mechanics force field B3LYP/6-311++G** method.

the ionic liquid is to reduce drastically the electrophilicity and nucleophilicity indexes of cation, as observed in Table 5.

5. Vibrational analysis

In this analysis, the theoretical structures of [BMIM][OTF] and [BMIM] were optimized with C_1 symmetries by using the B3LYP/6-311++G** method while its [OTF] anion with C_{3V} symmetry. Hence, for [BMIM][OTF] and [BMIM] are expected 93 and 69 vibration normal modes, respectively while for the anion only 18 vibration normal modes are estimated. The experimental infrared spectra for [BMIM][OTF] were taken from those available for this ionic liquid between 3200 and 2800 cm^{-1} and between 1600 and 1000 cm^{-1} regions [1,3] while the Raman spectrum was recorded by us. These spectra were compared with the corresponding predicted at the same level of theory in Figs. 5, 6 and 7, respectively. Analyzing exhaustively the IR spectra in the 3200 and 2800 cm^{-1} region we observed that there is not a very good correlation between experimental and theoretical ones, as expected because the intermolecular interactions due to the force packing were not considered in the calculations. Here, the calculations were performed for the ionic liquid isolated in the gas phase. However, the comparisons in the 1600 and 1000 cm^{-1} region (Fig. 6) show three experimental bands between 1300 and 1000 cm^{-1} that are clearly predicted by B3LYP/6-311++G** calculations (Fig. 6) evidencing a very good correlation. On the other hand, the better correlations are observed between the experimental and predicted Raman spectra from Fig. 7, especially because the calculated activities are converted to intensities by known equations [32,33]. The observed and calculated wavenumbers can be seen in Table 6 together with the corresponding assignments for [BMIM][OTF], [BMIM] cation and [OTF] anion in the gas phase by using the B3LYP/6-311++G** level of theory. The harmonic force fields in Cartesian coordinates for those three species were calculated with the SQMFF methodology [16] and the Molvib program [17] taking into account the internal coordinates. Then, in the refinement process the harmonic force fields were transformed to internal coordinates by using scale factors reported in the literature [16] in order to obtain the harmonic scaled force fields. The vibrational assignments were performed for those three species considering potential energy distribution (PED) contributions $\geq$ 10% and by comparisons with species containing similar groups [34–42]. Here, the very strong band observed in the Raman spectrum at 1034 cm^{-1}, which is predicted by B3LYP/6-311++G** calculations at 970 cm^{-1}, is easily assigned to SO_3 symmetric stretching mode. The assignments of some groups are discussed below.

5.1. Band assignments

5.1.1. CH modes

For [BMIM][OTF] and its cation are expected three C–H stretching modes, in-plane and out-of-plane deformation modes. In [BMIM][NO_3], the C–H stretching modes were assigned between 3170/3163 and 2942/2941 cm^{-1} [13] while the in-plane deformation modes are predicted between 1312 and 1307 cm^{-1} but, in the cation that modes is predicted at 1134 cm^{-1}. In this ionic liquid and its cation, the stretching modes are predicted between 3148 and 2896 cm^{-1} while the in-plane and out-of-plane deformation modes between 1554/1095 and 989/741 cm^{-1}, respectively. Hence, the IR and Raman bands between 3188 and 2935 cm^{-1} are easily associated to these stretching modes while the bands at 1317/1095 and 989/753 cm^{-1} are related to in-plane and out-of-plane deformation modes, respectively of ionic liquid and its cation. In this ionic liquid the C6–H7 stretching mode is predicted in the IR spectrum with strong intensity and, for this reason, the IR band at 2917 cm^{-1} should be assigned to that vibration mode.

Table 7
Comparisons of scaled internal force constants for 1-buthyl-3-methyl imidazolium trifluoromethanesulfonate and its cation and anion in gas phase.

B3LYP/6-311++G**Method						
Force constants	[OTF][a]	[BMIM][OTF][a]	[BMIM][a]	[BMIM][NO_3][b]		
				C1	C2	C3
f(*ν*SO_3)	7.63	7.65				
f(*ν*S-C)	2.03	2.21				
f(*ν*CF_3)	4.98	5.20				
f(*ν*C-H)		5.21	5.40	5.10	5.14	5.13
f(*ν*CH_2)		4.73	4.73	4.73	4.71	4.73
f(*ν*CH_3)		4.84	4.87	4.82	4.80	4.82
f(*ν*C-N)$_R$		6.60	6.60	6.57	6.60	6.60
f(*ν*C-N)		4.34	4.15	4.35	4.35	4.35
f(*ν*C=C)		7.47	7.60	7.60	7.60	7.60
f(*ν*C-C)		3.97	3.93	3.93	3.93	3.93
f(*δ*SO_3)	1.62	1.82				
f(*δ*CF_3)	1.54	1.23				
f(*δ*CH_2)		1.28	0.77	0.52	0.53	0.52
f(*δ*CH_3)		0.54	0.52	1.60	1.60	1.60

Units are mdyn Å^{-1} for stretching and mdyn Å rad^{-2} for angle deformations.
[a] This work.
[b] From Ref [13].

5.1.2. CH_3 modes

Here, a total of 18 vibration normal modes are expected for [BMIM][OTF] and its cation due to the presences of two CH_3 groups, as in [BMIM][NO_3] [13]. For this ionic liquid and its cation, the antisymmetric and symmetric modes are predicted between 3033 and 2895 cm^{-1}, hence, the IR and Raman bands from 3110 to 2875 cm^{-1} are assigned to those modes, as detailed in Table 6. In similar species and, in particular in [BMIM][NO_3] [13], the deformation modes are assigned between 1474 and 1366 cm^{-1} [22–26,29]. Thus, in [BMIM][OTF] and its cation the IR and Raman bands between 1461 and 1341 cm^{-1} are clearly assigned to those vibration modes, as observed in Table 6. The rocking modes in those two species are predicted between 1118 and 888 cm^{-1} and, for this reason, the bands observed in this region are assigned to those vibration modes. The twisting modes in the ionic liquid and its cation are predicted between 221 and 58 cm^{-1}, hence, these vibration modes cannot be assigned because there are not Raman bands observed in this region. Note that in the cation of [BMIm][NO_3] [13] these modes are predicted in the same region, as in similar species [22–26,29].

5.1.3. CH_2 modes

In [BMIM][NO_3], the expected antisymmetric and symmetric stretching modes for these groups were predicted between 2993 and 2872 cm^{-1} [13] while in this ionic liquid between 2995 and 2875 cm^{-1}. Accordingly, the IR and Raman bands observed in these regions can be easily assigned to those vibration modes and, of course, the symmetric modes are associated to the Raman bands of media intensities at 2943, 2917 and 2879 cm^{-1}, as detected in similar species [13,22–29]. The other vibration modes for these groups, such as deformation, wagging, rocking and twisting modes are eventually expected in different regions [13,22–29]. For instance, in [BMIM][NO_3] those modes were assigned at 1450/1417, 1417/1283, 1302/1112 and 952/672 cm^{-1}, respectively. In [BMIM][OTF] and its cation, these modes can be assigned to the Raman bands at 1432/1420, 1391/1260, 1226/1197 and 908/699 cm^{-1}. Notice that in this ionic liquid these modes are assigned in approximately the same regions than in [BMIM][NO_3] [13].

5.1.4. SO_3 groups

These groups in [BMIM][OTF] and its [OTF] anion are optimized by B3LYP/6-311++G** calculations with C_{3V} symmetries and, for these reasons, this symmetry was considered in the vibrational analyses of those groups in the two species, as was reported by Johnston and Shriver for trifluoromethanesulfonate anion [40]. Besides, between [BMIM][OTF] and its [OTF] anion a bidentate coordination with two S═O···H bond interactions are observed, as shown in Fig. 1 and, as evidenced by NBO and AIM calculations. Hence, two antisymmetric ($\nu_a SO_3$) and one symmetric stretching ($\nu_s SO_3$) modes are expected for the ionic liquid and its anion. Generally, these stretching modes appear in different regions depending if the group is neutral or anionic and, also in accordance with the medium [34–40]. Thus, in the cyclamate anion in aqueous solution the antisymmetric and symmetric stretching modes are assigned at 1192, 1185 and 993 cm^{-1}, respectively [38] while in the zwitterion acid gas these modes are assigned to 1265, 1251 and 974 cm^{-1}. In this ionic liquid those three modes are predicted at 1206, 1099 and 935 cm^{-1} while in the anion the stretching modes are predicted at 1168 and 938 cm^{-1}. Here, it is very important to analyze the separation between the two antisymmetric modes because for the cyclamate anion in aqueous solution the difference is 7 cm^{-1} while in the zwitterion acid gas is 14 cm^{-1}. On the other hand, in the [OTF] anion the separation between the two antisymmetric modes is null while in the ionic liquid 107 cm^{-1}. Evidently, the presence of [BMIM] cation linked to [OTF] anion generate a very important shifting of one of the two antisymmetric modes of [BMIM][OTF] towards lower wavenumbers due probably to the S═O···H bonds interactions. Hence, the strong IR bands at 1256 and 1162 cm^{-1} are assigned to these two antisymmetric modes with a separation between both modes of 94 cm^{-1}. However, the symmetric stretching ($\nu_s SO_3$) mode from the anion (938 cm^{-1}) to the ionic liquid (935 cm^{-1}) practically is no modified. In similar species the SO_3 antisymmetric and symmetric deformation modes are predicted between 622 and 464 cm^{-1} [34–40]. In this ionic liquid and its anion these modes are assigned between 602 and 451 cm^{-1}. The other rocking and twisting modes are assigned as predicted by calculations between 349/160 and 53/36 cm^{-1}, respectively as was summarized in Table 6. Clearly, these modes were not assigned because the Raman spectrum was recorded up to 70 cm^{-1}.

5.1.5. CF_3 modes

The ionic liquid and its anion were optimized with C_{3V} symmetries, as the SO_3 group of [OTF] and, as a consequence that symmetry was employed to perform the vibrational study, as reported by Johnston and Shriver for trifluoromethanesulfonate anion [40]. Hence, two antisymmetric ($\nu_a CF_3$) and one symmetric stretching ($\nu_s CF_3$) modes are also expected for those two species. These vibration modes in compounds containing similar groups are assigned between 1237 and 1149 cm^{-1} [40–42]. In [BMIM][OTF] and its [OTF] anion, the SQM calculations have predicted the symmetric stretching mode strongly coupled with the symmetric deformation where clearly in both species the higher potential energy contribution was observed for the symmetric deformation mode. Despite of this prediction, the IR bands in the spectrum of ionic liquid at 1222, 1162 and 1030 cm^{-1} were assigned to those stretching modes, as reported by Johnston and Shriver for trifluoromethanesulfonate anion [40] while in the anion they were assigned at 1142, 1074 and 1073 cm^{-1}, as shown in Table 6. The symmetric and antisymmetric deformation modes are predicted in the ionic liquid at 720, 552 and 492 cm^{-1} while in the anion at 710 and 547 cm^{-1}. The rocking and twisting modes in [BMIM][OTF] are predicted at 336/194 and 36 cm^{-1}, respectively while in the anion at 327 and 191 cm^{-1}.

5.1.6. Skeletal modes

The N1=C8 stretching mode in the ionic liquid was predicted in the IR spectrum at 1542 cm^{-1}, and, for this reason, it presents double bond character while the other N2=C8 stretching mode was predicted at 1390 cm^{-1} with partial double bond character. On the other side, the C5–C6 stretching mode was clearly predicted with simple bond character at 1118 cm^{-1} by SQM calculations. The S–C stretching mode in the ionic liquid and its anion was predicted at 279 and 268 cm^{-1}, respectively as was observed in different trifluoromethanesulfonate species [40] and, for these reasons, they were assigned to the Raman band at 288 cm^{-1}. Here, the N–CH_3 stretching mode (N1–C3) in the ionic liquid was predicted at 1299 cm^{-1} while in the anion at 668 cm^{-1}, revealing this way, the strong shifting of this mode as a consequence of change of [OTF] by nitrate anion. The C–C stretching modes belonging to the butyl chain are predicted with simple bond characters, as expected and, for this reason, they are assigned between 1162 and 757 cm^{-1}, as predicted by calculations. For the imidazoline rings, the expected deformations β_{R1} and β_{R2} and torsions τ_{R1} and τ_{R2} rings, were assigned in the approximately the same regions for the ionic liquid and its anion, as reported for [BMIM][NO_3] [13].

6. Force constants

Comparisons of scaled internal force constants for 1-buthyl-3-methyl imidazolium trifluoromethanesulfonate, cation and anion species in gas phase are presented in Table 7 together with those reported for the three conformers most stable of [BMIM][NO_3] [13] in the same medium and by using the B3LYP/6-311++G** method. These constants were calculated with the SQMFF procedure [16] and the Molvib program [17]. In Fig. S6 are represented the scaled internal force constants values for [BMIM][OTF] and the comparisons with those calculated for [BMIM] cation and [OTF] anion. Evaluating first, the force constants values for [BMIM][OTF] and [OTF] anion, it is observed that the *f(νSO$_3$)* force constants for both species have practically the same values while the other *f(νS-C)*, *f(νCF$_3$)* and *f(δSO$_3$)* force constants have higher values in the ionic liquid with exception of the *f(δCF$_3$)* force constant which is higher in the anion. If now the force constants values for [BMIM][OTF] and its [BMIM] cation are compared from Fig. S6, we observed that in general the values are higher for the cation with exception of *f(νC-N)* and *f(δCH$_2$)* force constant. Then, when the force constants for [BMIM][OTF] are compared with the corresponding to the most stable C2 conformer of [BMIM][NO_3] is observed that the *f(δCH$_2$)* force constant is higher in [BMIM][OTF] while the *f(δCH$_3$)* force constant is higher in [BMIM][NO_3] [13]. Here, the bidentate coordination predicted for [BMIM][OTF] with one S–O–-H–C–H bond could probably explain the higher value of the *f(δCH$_2$)* force constant in this ionic liquid.

7. Conformation equilibrium in [BMIM][OTF]

Conformational equilibrium of the [BMIM] cation was investigated monitoring the combination of imidazolium ring deformation and the CH_2 rocking bands [43]. Two Raman bands of different neat ionic liquids were many times investigated and reported as *gauche-trans (gauche)* at lower frequency (602 cm^{-1}) and *trans-trans (trans)* (624 cm^{-1}) conformers. The relative intensity of the band at 601 cm^{-1} to the band at 624 cm^{-1} was proportional to the *gauche/trans* population ratio (I_{gauche}/I_{trans}). In Fig. 8 Raman spectra of pure IL 1-buthyl-3-methyl imidazolium trifluoromethanesulfonate and 1-buthyl-3-methyl imidazolium nitrate in the 540-680 cm^{-1} spectral range are depicted. The positions and intensities of the observed Raman bands well correlated with the relevant parameters of two [BMIM] conformers

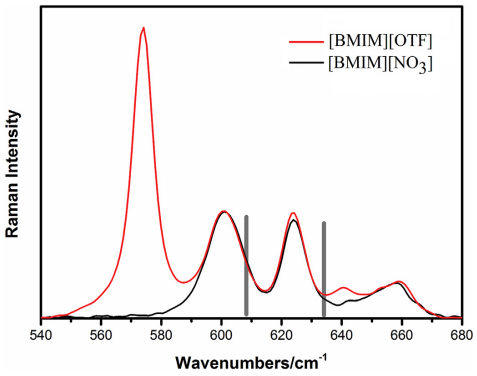

Fig. 8. Raman spectra of neat [BMIM][OTF] (red) and [BMIM][NO_3] (black) ionic liquids in conformations spectral region between 540 and 680 cm^{-1}. Grey bars depict the DFT calculations result for Raman bands assigned to *gauche* and *trans* conformers vibrations. (For interpretation of the references to colour in this figure legend, the reader is referred to the Web version of this article.)

calculated by DFT. Calculated Raman bands depicted by grey bars in Fig. 8 where the at ~609 cm^{-1} and ~634 cm^{-1} indicates the *gauche* and *trans* conformers by the rotations around C12–C15 and C15–C18 bonds (Fig. 2). The presence of both bands indicates that ILs based on [BMIM] cation exist as a mixed state of cation conformers regardless of the anion type. According to the relative band intensities of two bands in Fig. 8, the preference of the *trans* conformation was found in [BMIM][OTF] versus [BMIM][NO_3]. This result could be explained in terms of anion hydrophobicity. Ionic liquids tend to interact with other materials via anion. Previous studies (*Kausteklis, Aleksa, submitted J. Mol.Liq. 2018*) showed that the I_{gauche}/I_{trans} ratio increases when the water was added to neat [BMIM][NO_3] ionic liquid and could help to determine water packing processes in ILs. [BMIM][NO_3] has more hydrophobic anion than [BMIM][OTF] and indicates either more water from the atmosphere or more packed structure of [BMIM][NO_3].

The type of anion influence to the conformational equilibrium was investigated in the set of neat ionic liquids. In Fig. 9 the I_{gauche}/I_{trans} ratio of neat iconic liquids [BMIM][X], X = I, Br, Cl, BF_4, OTF, NO_3 versus anion ionic radius is depicted. The preference of the *trans* conformation was listed in the following order: $I^- > Br^- > Cl^- > OTF^- > NO_3^- > BF_4^-$. The conformation preferences for ILs with halide anions (I^-, Br^-, Cl^-) agreed with the previous report, which proposed the stronger electrostatic field by smaller halide anions imposes the *gauche* conformation [44]. However, no spherical and halide anions did not ordered well together in the distribution of ionic radius versus *gauche*/*trans* conformers ratio. The anion hydrophobicity was used to explain the order of anions determined in our experiments [45]. The I_{gauche}/I_{trans} ratio for the most hydrophilic anion I^- was 0.8 and for the most hydrophobic anion BF_4^- 1.9.

As well as anion hydrophobicity the cation chain length also plays important role in conformational equilibrium. Neat IL's [BMIM][Cl] and [BMIM][Br] I_{gauche}/I_{trans} ratio was compared to long chain ionic liquids 1-decyl-3-methyl-imidazolium chloride and bromine ([DMIM][Cl] and [DMIM][Br]) I_{gauche}/I_{trans} conformers ratio. [DMIM][Cl] showed 1.08 and [DMIM][Br] 0.85 while [BMIM][Cl] showed 1.4 and [BMIM][Br] 1.1, respectively. The preference of the *trans* conformation in IL's with longer cation chain depicts the

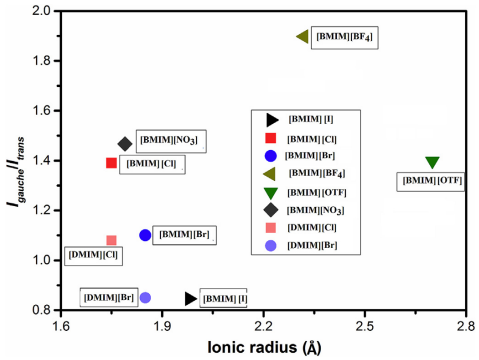

Fig. 9. I_{gauche}/I_{trans} ratio dependence of the [BMIM] cation versus ionic radius of different anions.

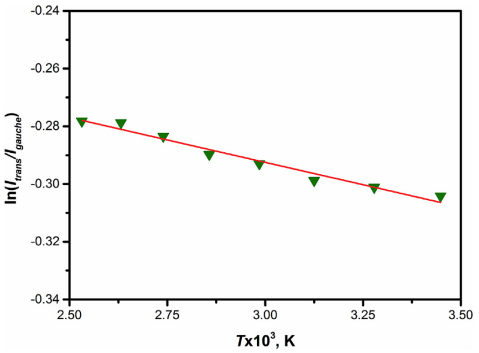

Fig. 11. Temperature dependence of the integrated intensity ratio between the *trans* and *gauche* conformers vibrations in room temperature range for pure [BMIM][OTF].

different lower mobility and more structured behaviour of long chain IL's.

Furthermore the temperature impact was registered for conformational equilibrium (I_{gauche}/I_{trans} ratio) in [BMIM][OTF] and depicted in Fig. 10. Below room temperature the huge increase in I_{gauche}/I_{trans} ratio was noticed. At temperature 305 K we have 1.5 times more ionic liquid cations oriented in *gauche* form than *trans*, while at 200 K this ratio increased to 8.8. The insert in Fig. 10 shows the Raman spectra at described temperatures. The decrease of anion mobility and packaging peculiarities with the decrease of temperature, could explain these results. Moreover, the temperature dependence of conformational equilibrium could be used to investigate the difference in the partial molar enthalpy of the *trans* and *gauche* conformers ($\Delta H_{trans\rightarrow gauche}$). As mentioned before the Raman intensity of the *trans* conformer increases as the temperature was increased for [BMIM][OTF]. Summing up that the ratio of the Raman scattering cross-sections between the *trans (A)* and *gauche (B)* conformers is independent of temperature,

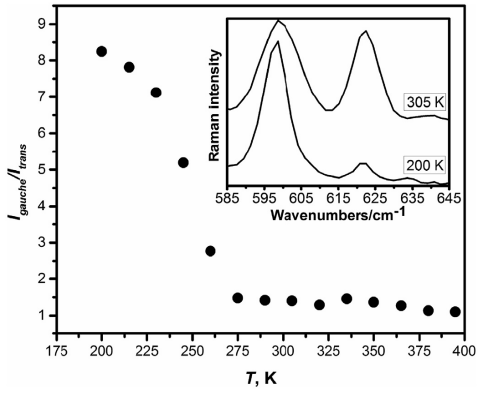

Fig. 10. Temperature dependence of the integrated intensity ratio between the *gauche* and *trans* conformers vibrations in full temperature range for pure [BMIM][OTF].

$\Delta H_{trans\rightarrow gauche}$ is given by (1) [46].

$$\Delta H^{A\rightarrow B} = -R\left\{\frac{\partial \ln(I_B/I_A)}{\partial(1/T)}\right\}_p. \quad (1)$$

In this equation, R, T and p are the gas constant, temperature and pressure, respectively. I_A and I_B indicate the relative Raman intensity of conformers A and B, respectively, and "A" and "B" correspond to the conformers of the [BMIM] cation [46]. From the slope of the line in Fig. 11 $\Delta H_{trans\rightarrow gauche}$ for [BMIM][OTF] is -0.5 ± 0.2 kJ/mol. While the values -1.1 ± 0.2 kJ/mol for [BMIM][NO_3], -1.5 ± 0.4 kJ/mol for [BMIM][SCN], -0.9 ± 0.1 kJ/mol for [BMIM][CH_3COO] and -1.0 ± 0.1 kJ/mol for [BMIM][BF_4], respectively [46], was measured for other RTIL's. Considering the standard error, the value of $\Delta H_{trans\rightarrow gauche}$ in [BMIM][OTF] is close to the value in other RTILs, which approximately are -1.0 kJ/mol and are independent of the anionic species [44,47].

Based on relationship $\Delta G = \Delta H - T\Delta S$, our results agree to the consideration that entropy drives the thermodynamic stability of the conformational equilibrium for [BMIM] anion in [BMIM] based ILs with no spherical anions [46].

8. Conclusions

In this work, the 1-buthyl-3-methyl imidazolium trifluoromethanesulfonate ionic liquid was characterized structural and vibrationally combining the experimental Raman spectrum and the experimental available infrared with DFT calculations based on the B3LYP/6-311++G** method. The theoretical structure of ionic liquid shows that the [OTF] anion is linked to [BMIM] cation by two different S–O–H hydrogen bonds forming a bidentate coordination. One H bond is linked to H atom of ring and the other one to H atom of a CH_2 group. Very good correlations were observed between the predicted infrared and Raman spectra for the proposed structure with the corresponding experimental ones. The high stability of ionic liquid was evidenced by the high dipole moment value and by three intramolecular H bonds and two halogen bonds interactions, as supported by NBO, AIM and bond orders calculations. The *LP(3)O27→ σ*C26–S30* and *LP(3)O28→ σ*C26–S30* transitions predicted in ionic liquid by NBO calculations support the bidentate coordination of anion while the $\Delta ET_{n\rightarrow\sigma^*}$ interactions related to anion show the high stability to ionic liquid. The different values of Mulliken charges observed on the O atoms

that forming the H bonds support the asymmetric bidentate coordination of [OTF] anion with the [BMIM] cation. The [OTF] anion increase the reactivity of [BMIM][OTF], as compared with [BMIM][NO_3] while the [NO_3] anion increases more the reactivity of cation as compared with [OTF]. In addition, the [OTF] anion reduces drastically the electrophilicity and nucleophilicity indexes of cation evidencing the strong influence of anion on the properties of cation. The vibrational analyses for the ionic liquid and its cation and anion have revealed a very important shifting of one of the two antisymmetric modes of [BMIM][OTF] towards lower wavenumbers due probably to the asymmetry of S═O···H bonds interactions which is no observed in the anion. The complete vibrational assignments were performed for ionic liquid, cation and anion and the harmonic scaled force constants were reported at the same level of theory. Finally, the anion hydrophobicity, the cation chain length and the temperature have great impact on the conformation equilibrium in [BMIM][OTF].

Acknowledgements

This work was supported with grants from CIUNT Project Nº 51/D608 (Consejo de Investigaciones, Universidad Nacional de Tucumán). The authors would like to thank Prof. Tom Sundius for his permission to use MOLVIB.

Appendix A. Supplementary data

Supplementary data related to this article can be found at https://doi.org/10.1016/j.molstruc.2018.08.014.

References

[1] H.-C. Chang, W. Teng-Hui, C. Burba, Probing structures of interfacial 1-butyl-3-methylimidazolium trifluoromethanesulfonate ionic liquid on nano-aluminum oxide surfaces using high-pressure infrared spectroscopy, Appl. Sci. 7 (8) (2017) 855.
[2] D.K. Singh, B. Rathke, J. Kiefer, A. Materny, Molecular structure and interactions in the ionic liquid 1-Ethyl-3-methylimidazolium trifluoromethanesulfonate, J. Phys. Chem. A 120 (31) (2016) 6274–6286.
[3] S. Watanabe, M. Nakano, K. Miyake, C. Tadokoro, S. Sasaki, Vibrational Spectroscopic Study on Lubrication and Corrosive Wear Mechanisms of Imidazolium Based Ionic Liquids, Chapter 20, Intech Open, 2015, pp. 545–556.
[4] L.N. Sim, S.R. Majid, A.K. Arof, Effects of 1−butyl−3−methyl imidazolium trifluoromethanesulfonateionic liquid in poly(ethyl methacrylate)/poly(-vinylidenefluoride−co−hexafluoropropylene) blend based polymer electrolyte system, Electrochim. Acta 123 (2014) 190–197.
[5] J.-M. Andanson, A. Baiker, Interactions of 1-Ethyl-3-methylimidazolium trifluoromethanesulfonate ionic liquid with alumina nanoparticles and organic solvents studied by infrared spectroscopy, J. Phys. Chem. C 117 (23) (2013) 12210–12217.
[6] K. Kędra-Krolik, F. Mutelet, J.-C. Moïse, J.-N. Jaubert, Deep fuels desulfurization and denitrogenation using 1-Butyl-3-methylimidazolium trifluoromethanesulfonate, Energy Fuels 25 (4) (2011) 1559–1565.
[7] M. Shamsipur, A.A.M. Beigi, M. Teymouri, S.M. Pourmortazavi, M. Irandoust, Physical and electrochemical properties of ionic liquids 1-ethyl-3-methylimidazolium tetrafluoroborate, 1-butyl-3-methylimidazolium trifluoromethanesulfonate and 1-butyl-1-methylpyrrolidinium bis(trifluoromethyl sulfonyl)imide, J. Mol. Liq. 157 (2010) 43–50.
[8] M.-L. Ge, R.-S. Zhao, Y.-F. Yi, Q. Zhang, L.-S. Wang, Densities and viscosities of 1-Butyl-3-methylimidazolium trifluoromethanesulfonate + H_2O binary Mixtures at T = (303.15 to 343.15) K, J. Chem. Eng. Data 53 (10) (2008) 2408–2411.
[9] K. Ganesan, Y. Alias, S.W. Ng, Imidazolium-based ionic liquid salts: 3,300-dimethyl-1,100-(1,4-phenylenedimethylene) diimidazolium bis(tetrafluoroborate) and 3,300-di-*n*-butyl-1,100-(1,4-phenylenedimethylene)diimidazolium bis(trifluoromethanesulfonate), Acta Crystallogr. C64 (2008) o478–o480.
[10] U. Domanska, A. Marciniak, Measurements for organic solutes and water in the ionic liquid 1-Butyl-3-methylimidazolium trifluoromethanesulfonate, J. Phys. Chem. B 112 (35) (2008) 11100–11105.
[11] M.-L. Ge, L.-S. Wang, M.-Y. Li, J.-S. Wu, Activity coefficients at infinite dilution of alkanes, alkenes, and alkyl benzenes in 1-Butyl-3-methylimidazolium trifluoromethanesulfonate using Gas−Liquid chromatography, J. Chem. Eng. Data 52 (6) (2007) 2257–2260.
[12] A. Arce, O. Rodríguez, A. Soto, *tert*-Amyl ethyl ether separation from its mixtures with ethanol using the 1-Butyl-3-methylimidazolium trifluoromethanesulfonate ionic Liquid: Liquid−Liquid equilibrium, Ind. Eng. Chem. Res. 43 (26) (2004) 8323–8327.
[13] J. Kausteklis, V. Aleksa, M.A. Iramain, S.A. Brandán, Effect of cation-anion interactions on the structural and vibrational properties of 1-buthyl-3-methyl imidazolium nitrate ionic liquid, J. Mol. Struct. 1164 (2018) 1–14.
[14] A.D. Becke, Density functional thermochemistry. III. The role of exact exchange, J. Chem. Phys. 98 (1993) 5648–5652.
[15] C. Lee, W. Yang, R.G. Parr, Development of the Colle-Salvetti correlation-energy formula into a functional of the electron density, Phys. Rev. B 37 (1988) 785–789.
[16] a) G. Rauhut, P. Pulay, J. Phys. Chem. 99 (1995) 3093–3099;
b) *Correction* G. Rauhut, P. Pulay, J. Phys. Chem. 99 (1995) 14572.
[17] T. Sundius, Scaling of ab initio force fields by MOLVIB, Vib. Spectrosc. 29 (2002) 89–95.
[18] E.D. Gledening, J.K. Badenhoop, A.D. Reed, J.E. Carpenter, F.F. Weinhold, NBO 3.1; Theoretical Chemistry Institute, University of Wisconsin, Madison, WI, 1996.
[19] F. Biegler-Köning, J. Schönbohm, D. Bayles, AIM2000; a program to analyze and visualize atoms in molecules, J. Comput. Chem. 22 (2001) 545.
[20] R.G. Parr, R.G. Pearson, Absolute hardness: companion parameter to absolute electronegativity, J. Am. Chem. Soc. 105 (1983) 7512–7516.
[21] J.-L. Brédas, Mind the gap!, Mater. Horiz. 1 (2014) 17–19.
[22] F. Chain, M.A. Iramain, A. Grau, C.A.N. Catalán, S.A. Brandán, Evaluation of the structural, electronic, topological and vibrational properties of *N*-(3,4-dimethoxybenzyl)-hexadecanamide isolated from Maca (*Lepidium meyenii*) using different spectroscopic techniques, J. Mol. Struct. 1119 (2016) 25–38.
[23] D. Romani, S.A. Brandán, M.J. Márquez, M.B. Márquez, Structural, topological and vibrational properties of an isothiazole derivatives series with antiviral activities, J. Mol. Struct. 1100 (2015) 279–289.
[24] D. Romani, S. Tsuchiya, M. Yotsu-Yamashita, S.A. Brandán, Spectroscopic and structural investigation on intermediates species structurally associated to the tricyclic bisguanidine compound and to the toxic agent, saxitoxin, J. Mol. Struct. 1119 (2016) 25–38.
[25] F.E. Chain, M.F. Ladetto, A. Grau, C.A.N. Catalán, S.A. Brandán, Structural, electronic, topological and vibrational properties of a series of N-benzylamides derived from Maca (Lepidium meyenii) combining spectroscopic studies with ONION calculations, J. Mol. Struct. 1105 (2016) 403–414.
[26] M. Minteguiaga, E. Dellacassa, M.A. Iramain, C.A.N. Catalán, S.A. Brandán, Synthesis, Spectroscopic characterization and structural study of carquejiphenol, a 2-Isopropenyl-3-methylphenol derivative with potential medicinal uses, J. Mol. Struct. 1165 (2018) 332–343.
[27] M.A. Iramain, L. Davies, S.A. Brandán, FTIR, FT-Raman and UV-visible spectra of Potassium 3-furoyltrifluoroborate salt, J. Mol. Struct. 1158 (2018) 245–254.
[28] M.A. Iramain, L. Davies, S.A. Brandán, Evaluating structures, properties and vibrational and electronic spectra of the Potassium 2-isonicotinoyltrifluoroborate salt, J. Mol. Struct. (2018). https://doi.org/10.1016/j.molstruc.2018.02.098.
[29] S. Gatfaoui, N. Issaoui, S.A. Brandán, T. Roisnel, H. Marouani, Synthesis and characterization of p-xylylenediaminiumbis(nitrate). Effects of the coordination modes of nitrate groups on their structural and vibrational properties, J. Mol. Struct. 1151 (2018) 152–168.
[30] A.B. Nielsen, A.J. Holder, *GaussView*, User's Reference, GAUSSIAN, Inc, Pittsburgh, PA, USA, 2000-2003.
[31] a) M.J. Frisch, G.W. Trucks, H.B. Schlegel, G.E. Scuseria, M.A. Robb, J.R. Cheeseman, G. Scalmani, V. Barone, B. Mennucci, G.A. Petersson, H. Nakatsuji, M. Caricato, X. Li, H.P. Hratchian, A.F. Izmaylov, J. Bloino, G. Zheng, J.L. Sonnenberg, M. Hada, M. Ehara, K. Toyota, R. Fukuda, J. Hasegawa, M. Ishida, T. Nakajima, Y. Honda, O. Kitao, H. Nakai, T. Vreven, J.A. Montgomery Jr., J.E. Peralta, F. Ogliaro, M. Bearpark, J.J. Heyd, E. Brothers, K.N. Kudin, V.N. Staroverov, R. Kobayashi, J. Normand, K. Raghavachari, A. Rendell, J.C. Burant, S.S. Iyengar, J. Tomasi, M. Cossi, N. Rega, J.M. Millam, M. Klene, J.E. Knox, J.B. Cross, V. Bakken, C. Adamo, J. Jaramillo, R. Gomperts, R.E. Stratmann, O. Yazyev, A.J. Austin, R. Cammi, C. Pomelli, J.W. Ochterski, R.L. Martin, K. Morokuma, V.G. Zakrzewski, G.A. Voth, P. Salvador, J.J. Dannenberg, S. Dapprich, A.D. Daniels, Ö. Farkas, J.B. Foresman, J.V. Ortiz, J. Cioslowski, D.J. Fox, Gaussian 09, Revision A.02, Gaussian, Inc, Wallingford CT, 2009;
b) R.F.W. Bader, Atoms in Molecules, a Quantum Theory, Oxford University Press, Oxford, 1990. ISBN: 0198558651.
[32] G. Keresztury, S. Holly, G. Besenyei, J. Varga, A.Y. Wang, J.R. Durig, Vibrational spectra of monothiocarbamates-II. IR and Raman spectra, vibrational assignment, conformational analysis and ab initio calculations of S-methyl-N,N-dimethylthiocarbamate Spectrochim, Acta 49A (1993) 2007–2026.
[33] D. Michalska, R. Wysokinski, The prediction of Raman spectra of platinum(II) anticancer drugs by density functional theory, Chem. Phys. Lett. 403 (2005) 211–217.
[34] H.A. Höppe, K. Kazmierczak, E. Romano, S.A. Brandán, A structural and vibrational study on the first potassium borosulfate, $K_5[B(SO_4)_4]$ by using the FTIR-Raman and DFT calculations, J. Mol. Struct. 1037 (2013) 294–300.
[35] E. Romano, L. Davies, S.A. Brandán, Structural and vibrational properties of zinc difluoromethanesulfinate. A study combining the FTIR and Raman spectra with ab-initio calculations, J. Mol. Struct. 1044 (2013) 144–151.
[36] A. Ben Altabef, S.A. Brandán, A new vibrational study of chromyl fluorosulfate, $CrO_2(SO_3F)_2$ by DFT calculations, J. Mol. Struct. 981 (2010) 146–152.

[37] S.A. Brandán, Van Godewijckstraat 30, 3311, A Structural and Vibrational Study of the Chromyl Chlorosulfate, Fluorosulfate, and Nitrate Compounds, Editado by Ken Derham, vol. 1, Springer Science, Business Media B.V., GZ Dordrecht, Netherlands, September 2012, p. 82. ISBN: 978-94-007-5762-2.
[38] A.B. Brizuela, A.B. Raschi, M.V. Castillo, L. Davies, E. Romano, S.A. Brandán, Vibrational investigation on species derived from cyclamic acid in aqueous solution by using HATR and Raman spectroscopies and SCRF calculations, J. Mol. Struct. 1074 (2014) 144–156.
[39] D. Romani, I. Salas Tonello, S.A. Brandán, Influence of atomic bonds on the properties of the laxative drug sodium picosulphate, Heliyon 2 (2016), e00190.
[40] D.H. Johnston, D.F. Shriver, Vibrational study of the trifluoromethanesulfonate anion: unambiguous assignment of the asymmetric stretching modes, Inorg. Chem. 32 (1993) 1045–1047.
[41] S.A. Brandán, Structural, topological, electronic and vibrational properties of the antiviral trifluridine agent. Their comparison with thymidine, Paripex, Indian J. Res. 6 (10) (2017) 41–53.
[42] M.A. Iramain, L. Davies, S.A. Brandán, Structural and spectroscopic differences among the Potassium 5-hydroxypentanoyltrifluoroborate salt and the furoyl and isonicotinoyl salts, Submitted, J. Mol. Struct. (2018).
[43] R.W. Berg, M. Deetlefs, K.R. Seddon, I. Shim, J.M. Thompson, Raman and ab initio studies of simple and binary 1-Alkyl-3-methylimidazolium ionic liquids, J. Phys. Chem. B 109 (2005) 19018.
[44] Y. Umebayashi, H. Hamano, S. Tsuzuki, J.N. Canongia Lopes, A.A.H. Pádua, Y. Kameda, S. Kohara, T. Yamaguchi, K. Fujii, S.I. Ishiguro, Dependence of the conformational isomerism in 1-n-Butyl-3-methylimidazolium ionic liquids on the nature of the halide anion, J. Phys. Chem. B 114 (2010) 11715.
[45] Y.-S. Ye, J. Rick, B.-J. Hwang, Ionic liquid polymer electrolytes, J. Mater. Chem. A 1 (2013) 2719.
[46] N. Hatano, T. Takekiyo, H. Abe, Y. Yoshimura, Effect of Counteranions on the conformational equilibrium of 1-Butyl-3-methylimidazolium-Based ionic liquids, Int. J. Spectrosc. 3 (2011) 1.
[47] Y. Jeon, J. Sung, C. Seo, H. Lim, H. Cheong, M. Kang, B. Moon, Y. Ouchi, D. Kim, Structures of ionic liquids with different anions studied by infrared vibration spectroscopy, J. Phys. Chem. B 112 (2008) 4735.

Journal of Molecular Liquids 271 (2018) 747–755

Contents lists available at ScienceDirect

Journal of Molecular Liquids

journal homepage: www.elsevier.com/locate/molliq

Raman spectroscopy study of water confinement in ionic liquid 1-butyl-3-methylimidzolium nitrate

Jonas Kausteklis [a], Martynas Talaikis [b], Valdemaras Aleksa [a,*], Vytautas Balevičius [a]

[a] Institute of Chemical Physics, Vilnius University, Saulėtekio Ave. 3, LT-10257 Vilnius, Lithuania
[b] Institute of Biochemistry, Vilnius University, Saulėtekio Ave. 7, LT-10257 Vilnius, Lithuania

ARTICLE INFO

Article history:
Received 19 April 2018
Received in revised form 30 August 2018
Accepted 10 September 2018
Available online 12 September 2018

Keywords:
Water pockets
Ionic liquids
Hydrogen bonding
Raman spectroscopy

ABSTRACT

Clusterization process of water molecules called "water pockets" in the imidazolium-based room temperature ionic liquid (RTIL) 1 butyl 3 methylimidazolium nitrate ([C_4mim][NO_3]) was investigated using Raman spectroscopy. Changes of Raman spectra were observed in four different spectral regions when the content of heavy water (D_2O) in the RTIL-D_2O system was continuously increased. It was found that different parameters of the Raman bands were sensitive to the added content of D_2O. Discontinuous distribution in the concentration dependencies of those parameters was registered. The extent of "water pockets" formation process was determined from discontinuities in the concentration dependencies of monitored shifts and integral intensities of the Raman bands. The blue shift of symmetric NO_3^- stretching mode at 1041 cm^{-1} and the stretching mode at 2nd carbon position C(2)–H at 3100 cm^{-1} of imidazolium ring was noticed in the spectra even after adding of infinitesimal content of water to the mixture. The identical behavior analyzing the Raman band at 706 cm^{-1} assigned to NO_3^- bending mode was discovered. Moreover, the ratio of integral intensities of two Raman bands at 600 and 625 cm^{-1} assigned to *GT* and *TT* forms of butyl chain was also found to be dependent on the content of D_2O in the mixture. The distribution among relative integral intensities of Raman bands assigned to vibrations of different water clusters was sensitive to the content of D_2O in the mixture too. Overall, the lower boarder of "water pockets" formation process ($X = 0.6$ molar D_2O ratio) in [C_4mim][NO_3] came up with the discontinuous spectral changes observed for NO_3^- stretching mode, and vibrational modes of different water clusters. The upper boarder of "water pockets" formation process ($X = 0.86$ M D_2O ratio) was found out from discontinuities in concentration dependencies of imidazolium ring stretching mode, and vibrational modes of different water clusters. The conformational changes of [C_4mim]$^+$ cation at the same D_2O concentration corresponding to the upper boarder of "water pockets" formation were observed.

1. Introduction

Room temperature ionic liquids (RTILs) – well known molten salts with many attractive physical and chemical properties determined by various interactions between anions and cations [1,2]. Wide liquid range, high ionic conductivity, negligible vapor pressure, high electrochemical and thermal stability and significant ability to solubilize organic, inorganic or polymeric materials are mainly caused by dipolar, electron pair donor-acceptor, columbic interactions and hydrogen bond formation. These properties empower possibilities to use ionic liquids as functionalized materials which engage researchers for theoretical and experimental studies [3–6]. The contaminants changing properties of ionic liquids and the purity of samples are significant to studies of "pure" RTILs. Water is one of impurity which could be found in RTILs when exposed to air [2] and even small amount of it can dramatically change the diffusion coefficients [7], polarity [8], viscosity [9], and surface tension [10] of RTILs. The number of studies was found employing the new strategy emerged of mixing RTILs with compounds which previously used to be impurities depending on the purpose [11,12] i.e. organic compounds [8,9], other RTILs [13] and water [12,14]. However, better perception of RTILs and water interactions as well as the structure of mixtures at different constituent concentrations is needed to devise methods for application of RTILs in combination with water.

With water incorporation into RTILs the increase of ions diffusion coefficient was observed due to decrease in the viscosity of the corresponding ILs arising from suppression of the electrostatic interactions between ions [12]. The variety of different structures of water and RTILs mixtures were reported to be dependent on anion and cation combination and the water concentration too [14–18]. The fascinating water clusterization process called "water pockets" formation in [C_4mim][NO_3] and D_2O mixtures recently was observed applying small-angle X-ray scattering (SAXS), small-angle neutron scattering

* Corresponding author.
E-mail address: valdemaras.aleksa@ff.vu.lt (V. Aleksa).

https://doi.org/10.1016/j.molliq.2018.09.060
0167-7322/

(SANS) and differential scanning calorimetry (DSC) techniques [19–21]. In the $[C_4mim][NO_3]$–water system anomalous freezing occurred discretely for a wide range of water concentrations ($0.7 < X < 0.9$ M D_2O ratio). The molecular dynamics (MD) simulations demonstrated water confinement in imidazolium cation and nitrate anion based RTIL 1-octyl-3-methylimidazolium nitrate ($[C_8mim][NO_3]$) mixtures with water of different concentrations [3]. Confined water existence in the boundary between the polar and non-polar nanodomains was found. Another MD simulation work identified four concentration ranges in hydrophilic RTIL and water systems where four distinct structural regimes were presented: isolated water molecules ($X_{H2O} < 0.5$); chain-like water aggregates ($0.5 < X_{H2O} < 0.8$); bicontinuous system ($0.8 < X_{H2O} < 0.95$); and isolated ions or small ion clusters, respectively ($X_{H2O} > 0.95$) [22]. Previously mentioned aprotic ionic liquids (APILs) together with protic ionic liquids (PILs) are two broad categories used for general classification of ionic liquids. Transport and volumetric properties, heat capacities, viscosity and refractive index together with effect of water on the local structure and phase behavior of PILs mixtures of different molecular solvents were widely investigated in previous studies [23–27]. In the case of PILs differently to APILs the anion does not play crucial role in interactions, while the main attention is focused on interactions near cation and water. Polar —NH groups and hydrophobic anions (e.g. TFSI) make the interaction scheme reversed [26] comparing to aprotic ionic liquids investigated in this study. In particular, water is found to interact with the anions, the cation is less interesting. The applicability of $[C_4mim][NO_3]$ ionic liquid as solvent for proteins [27–29], tool for water removal from the protein surface [30] and advanced lubricant fluid [31] is derived by different capabilities of NO_3^- anion interactions with different materials. Moreover, the evidences for "water pockets" already were studied on short chain cation IL-D_2O systems based on *N*, *N* diethyl *N* methyl *N* 2 methoxyethylammonium tetrafluoroborate and 1 butyl 3 methylimidazolium nitrate [20]. As Raman spectroscopy works well identifying phase changes in long chain ionic liquids and water mixtures [14] for this study a short chain NO_3^- based $[C_4mim][NO_3]$ IL was chosen to broaden the available methods to investigate water structures in short chain cation based ionic liquid mixtures.

2. Experimental

Commercially available high purity ionic liquid 1 butyl 3 methylimidazolium nitrate was received from Merck KGaA Darmstadt and Ionic Liquids Technologies GmbH (≥99%, the structure and atom numbers are shown in Fig. 1 insert). The samples as-received may contain a small amount of water. To remove water and other impurities samples were dried under vacuum at 353 K for 24 h [32]. The decomposition temperature of this IL is 519 K [33]. In our studies the sample temperature was much lower. The water (H_2O) used in experiments was freshly distilled. Heavy water (D_2O) was ordered from Sigma-Aldrich (≥99.9 atom % D). The samples of $[C_4mim][NO_3]$-H_2O and $[C_4mim][NO_3]$-D_2O systems were prepared by weighting (±0.1 mg) the components. Each sample was thoroughly mixed and left to stand for 30 min at 298 K. Prepared mixtures were monitored by Raman spectroscopy, which provides the information on local water and ionic liquid structures. Raman spectra were typically measured at room temperature (298 K) using the Bruker MultiRAM FT-Raman spectrometer with the motorized xyz-sample stage and with the high-sensitivity liquid nitrogen cooled germanium and InGaAs detectors. The 1064 nm wavelength beam of the pulsed Nd:YAG laser (500 mW) and the 785 nm wavelength beam of the Si diode (300 mW) as the excitation sources using the 180° scattering geometry were employed in the experiments, while the resolution of the spectrometer was set to the 2 cm^{-1}. Average of 400 Raman spectra was recorded to get better signal to noise ratio at spectral range 70–4000 cm^{-1}. For sample measurements at low temperatures (293 K–153 K) LinKam temperature control system PE95/T95 with temperature accuracy of 0.05 °C and cooling rate 3 °C/min was used. To avoid the background samples were prepared and measured in silica cells. From measured neat ionic liquids spectra the low background level was found. This let us obtain both qualitative and quantitative information while processing spectra only with normalization and linear baseline subtraction functions. The FT-Raman spectrometer control and experimental data digital processing were performed using the OPUS 7.0 and the Origin 8.0 software program packages.

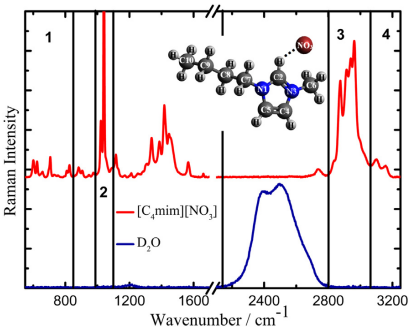

Fig. 1. Raman spectra of neat $[C_4mim][NO_3]$ (upper) and neat D_2O (lower) distributed in four spectral regions sensitive to added D_2O. In the insert the structure of $[C_4mim][NO_3]$.

3. Results and discussion

Raman spectra of the neat $[C_4mim][NO_3]$ and neat D_2O in the whole spectral range between 550 and 3300 cm^{-1} are depicted in Fig. 1. The Raman spectrum was divided to four regions which were found being sensitive to added D_2O content. Assignments of $[C_4mim][NO_3]$ Raman spectral bands were well investigated by previous studies for RTILs which had the similar structure (anion or cation) in comparison to our studied ionic liquid [34–41]. In the spectral Region 1 from 550 to 800 cm^{-1} three Raman bands were analyzed. Two peaks at 600 and 625 cm^{-1} were assigned to vibrational bands of RTIL molecules organized in *gauche-trans* (*GT*) and *trans-trans* (*TT*) conformers which are formed by rotating about the butyl chain C(7)—C(8) bond [42]. One more peak at 706 cm^{-1} was analyzed as anion NO_3^- bending mode. Region 2 represented the Raman spectrum between 1000 and 1100 cm^{-1}. The band at 1041 cm^{-1} was assigned to stretching mode of NO_3^- anion vibrations. Raman vibrational bands in the Region 4 (3100–3200 cm^{-1}) were assigned to imidazolium ring stretching modes at different carbon positions. C(2)–H stretching mode (3100 cm^{-1}) at the 2nd carbon position and C(4,5)–H symmetric and asymmetric stretching modes (3164 and 3152 cm^{-1}) at the 4th and 5th carbon positions. The Raman spectra in Region 3 represented heavy water molecules vibrations, while the 1st, 2nd and 4th regions belong to anion and cation vibrations of ionic liquid. Two main bands in the region between 2100 and 2800 cm^{-1} were assigned to the vibrations of water molecules organized in network with tetrahedral structure (network water (NW) 2420 cm^{-1}) and water molecules that are involved in a distorted network but do not form all four H-bonds with the neighboring water molecules (intermediate water (IW) 2540 cm^{-1}). More Raman bands which will be discussed later were hidden due to overlap with the main water bands shoulders.

3.1. C—H stretching vibrational modes of the imidazolium ring (Region 4)

As mentioned before the most of research of RTIL and water or other solvent systems were focused on imidazolium ring C—H stretching region [13,15,16,42–44]. $[C_4mim][NO_3]$ was not an exception. The Raman spectra of $[C_4mim][NO_3]$-D_2O mixtures at various heavy water

contents in Region 4 and spectra of deconvolution into three components using Voigt functions are shown in Fig. 2A and B. Theoretical and experimental data showed that Raman spectral region above 3100 cm^{-1} is very sensitive to interactions involving imidazolium ring C(n)–H of the of RTILs cation $[C_4mim]^+$ [45–48]. It is worth to mention that the main part of fitted curves was consisted of Gaussian shape. The main peaks were assigned to the C(2)–H, C(4,5)–H asymmetric and C(4,5)–H symmetric stretching vibrational modes on the basis of the previous Raman investigations. In the spectrum of neat $[C_4mim][NO_3]$ ($X_{D2O} = 0$) bands were distributed at 3100 cm^{-1}, 3152 cm^{-1}, 3164 cm^{-1}, which revealed that the H-bond of C(2)–H···NO_3 is stronger than C4–H···NO_3 or C5–H···NO_3. As depicted in Fig. 2C, the positions of these Raman vibrational modes associated with imidazolium ring vibrations close to different carbon positions were slightly blue shifted when water was added to pure $[C_4mim][NO_3]$. Detailed information on such band shifts was reported in previous studies [49], and their results supported our model. This blue shift indicated that added water induced the weakening of interactions between anions and cations involving these hydrogen atoms and their direct environment. The H bonds between the water molecules and anions distracted the H bonds between anions and cations. This result was supported by previous studies which claimed that solvation of organic compounds in aprotic ionic liquids predominantly occurs with the anion [50]. However, the most controversial part is that these blue shifts were not equal and even not homogeneous to the corresponding bands. The C(2)–H band was totally shifted over 13 cm^{-1} (from 3100 to 3113 cm^{-1}, percentage of change 0.419%). The C(4,5)–H asymmetric band totally shifted over 9 cm^{-1} (from 3152 cm^{-1} to 3161 cm^{-1}, percentage of change 0.286%) and C(4,5)–H symmetric band totally shifted over 15 cm^{-1} (from 3164 cm^{-1} to 3179 cm^{-1}, percentage of change 0.474%). The C(2)–H band shift was found to be discontinuous with cross over point at around 0.86 M D_2O fraction, after which the band did not shift any more with added heavy water content. The distribution of other two bands shifts were similar to the previous one and the cross over points were found to be around 0.86 M D_2O fraction too. Differently from the C(2)–H vibrational bands, which showed all blue shift before the crossover point (100% of shift from 0 to 0.86 M D_2O fraction), the C(4,5)–H asymmetric and the C(4,5)–H symmetric bands before the crossover point were shifted only by half (50% of shift from 0 to 0.86 M D_2O fraction) of total shift and other half after the crossover point. Both shifts in the percentage and inverse centimeters of the C(2)–H and C(4,5)–H vibrational bands were comparable and indicated that anions in $[C_4mim][NO_3]$-D_2O mixtures were distracted from all three imidazolium protons equally compared to the whole concentration range of D_2O. The different blue shifts of vibrational modes before the crossover point at 0.86 M D_2O fraction suggested the model that anions located near

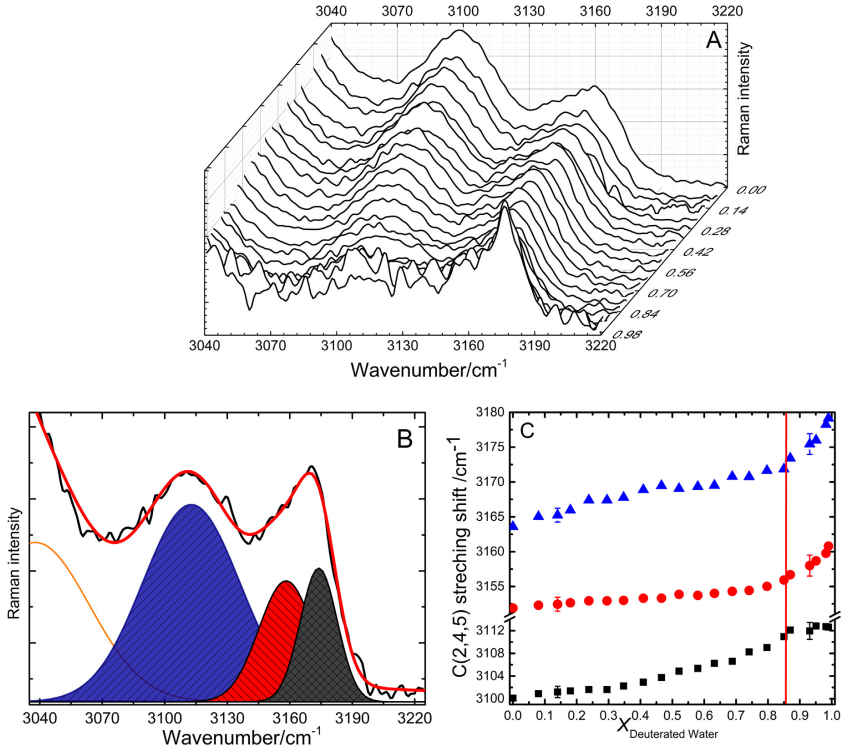

Fig. 2. A: Raman spectra of $[C_4mim][NO_3]/D_2O$ mixtures at different water concentrations in spectral Region 4. B: Raman spectrum (black line) of $[C_4mim][NO_3]/D_2O$ mixture at $X_w = 0.87$, relative fit red line and deconvolution in to three bands. C: C(2)–H (black squares), C(4,5)–H asymmetric (red circles) and C(4,5)–H symmetric (blue triangles) stretching Raman shift plotted as a function of the D_2O molar fraction in the mixtures. Crossover point marked by red line corresponds to the upper boarder of "water pocket" formation. (For interpretation of the references to colour in this figure legend, the reader is referred to the web version of this article.)

more basic 2nd carbon position in imidazolium ring were distracted from cations before anions located near 4th and 5th carbon positions in imidazolium ring. At the crossover point value $X = 0.86$ M D_2O ratio in the mixture we have 9 molecules of water comparing with 1 ionic liquid molecule. ILs are distracted from cation and H bonds water···anion [51], water···water, C(2)–H···water are formed. After crossover point value $X = 0.86$ M D_2O ratio, anions are totally distracted and no more new H bonds C(2)–H···water are formed. However, added water molecules form new H bonds C(4,5)–H···water as it was discussed above.

3.2. NO_3 stretching modes of the RTIL anion (Region 2)

It is well known from the literature that water molecules and anion interacts with each other forming hydrogen bonds in aggregates anion-water-anion [52] at low water content and water-anion-water aggregates at higher water concentrations [22]. The changes of spectral parameters of anion NO_3^- symmetric stretching (at 1041 cm^{-1}) ($\nu_1(NO_3^-)$) and bending (in-plane deformation mode at 706 cm^{-1}) ($\nu_4(NO_3^-)$) vibrational modes are depicted in Fig. 3A and B. The blue shift from 1041.2 cm^{-1} to 1047.7 cm^{-1} totally (by 6.5 cm^{-1}) and band FWHM broadening by 2.5 cm^{-1} was registered to the most intensive Raman spectral band $\nu_1(NO_3^-)$. Larger blue shift from 707 cm^{-1} to 717 cm^{-1} totally (by 10 cm^{-1}) and band FWHM broadening by 11 cm^{-1} was registered to the Raman spectral band $\nu_4(NO_3^-)$ [53].

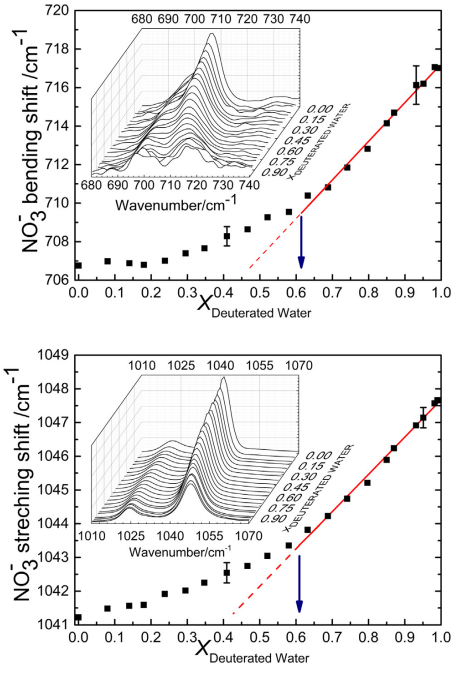

Fig. 3. The Raman shift of NO_3^- symmetric stretching $\nu_1(NO_3^-)$ (lower) and bending $\nu_4(NO_3^-)$ (upper) plotted as a function of the D_2O molar fraction in the mixtures. The crossover points marked as blue arrows in both cases. The Raman spectra of $[C_4mim][NO_3]/D_2O$ mixtures at different water concentrations in spectral Region 2 are depicted in the insets. Crossover points marked by blue arrow correspond to the lower boarder of "water pocket" formation. (For interpretation of the references to colour in this figure legend, the reader is referred to the web version of this article.)

The blue shifts were clearly attributed to the screening and weakening of the interactions between cation $[C_4mim]^+$ and anion NO_3^- but at the same time the band broadening suggested that simultaneously complexes of anion···water and water···anion···water were formed [38,50,53–57]. The crossover point was reached when D_2O molar fraction in RTIL-D_2O mixture reached 0.61. At his point, all possible hydrogen bonds to anions were occupied by water molecules and they started interacting with each other forming distorted solvation shell structures earlier called "water pockets". Discontinuous anion vibrations band shifts remained the same as it was found for C—H stretching mode band shift concentration dependency. The crossover point appeared at the D_2O molar fraction between 0.6 and 0.7. Discontinuities in concentration dependencies of Raman bands blue shift could be associated with so-called "water pockets" formation process boarders. Lower boarder is indicated in spectral Region 2 and upper boarder in spectral Region 4.

3.3. Heavy water OD stretching vibration modes (Region 3)

Multi-structured Raman band shape in Region 3 was clearly distinguished in Fig. 4 [58–60]. The broad distribution of heavy water vibrational frequencies could be related to the different OD structures and their surrounding environment. The higher the red shift of OD stretching band frequency the stronger the intermolecular hydrogen bond. Of course, the accurate assignment of water and heavy water vibrational bands is an actual topic for neat water and its mixtures with different solvents [59]. Raman spectral band assignments were made according to previous works where both Raman and IR spectra were analyzed [61–66].

The first insight to Raman spectra of neat D_2O showed three typical bands centered at around 2400 cm^{-1}, 2525 cm^{-1} and 2643 cm^{-1}. These vibrational bands could be assigned to the different local hydrogen bonding (HB) environments. The band with lowest frequency (ν2400) could be assigned to the OD stretching vibrations of water molecules within the different kinds of tetrahedral H-bonded network, the similar OH stretching band was called network water [NW] [39]. This band was assigned to the high ordered water structure vibrations, because it showed the highest symmetry of all OD stretching vibrational bands in the quenched samples (see Fig. 5). In our experiment it was called (i) strongly hydrogen bonded water band (νSHB) [67]. Another band (ν2525) was assigned to the OD stretching vibrations of water molecules within highly asymmetric single donor (SD) hydrogen bonding configuration or distorted tetrahedral H-bonded network. For OH vibrations this band was called intermediate water [IW], in our experiment it was called (ii) medium hydrogen bonded water band (νMHB) [67]. And finally the highest frequency band (ν2643) was assigned to the vibrations of free OD groups or free water molecules without any hydrogen bonded groups, these molecules are similar to those found in the vapor phase. For OH vibrations this band was called multimer water [MW], in our experiment it was called (iii) weakly hydrogen bonded water band (νWHB) [67]. The similar assignment of OH stretching bands was also obtained by IR spectral analysis of water dynamics upon confinement size in micellar solutions [62]. Very strongly hydrogen bonded water band (VSHB) in quenched mixtures was reported as one more OD stretching band at the low frequency shoulder at 2260 cm^{-1} [67]. To confirm this band assignment the low temperature measurements were performed, the results will be discussed later. The integral intensities of all O–D stretching bands were processed and the changes in relative integral intensities were identified in Fig. 4. It must, however, be noted that all previously mentioned water structures should be found in the system $[C_4mim][NO_3]$-D_2O water rich region (0.7–0.9 mol. D_2O) by the formation of "water pockets" [19,67]. For better water structure understanding of water structure in the "water pockets", two discontinuities on added water content were identified for νMHB band relative integral intensity change. The boarders of "water pockets" formation were set in Fig. 4. The lower boarder at

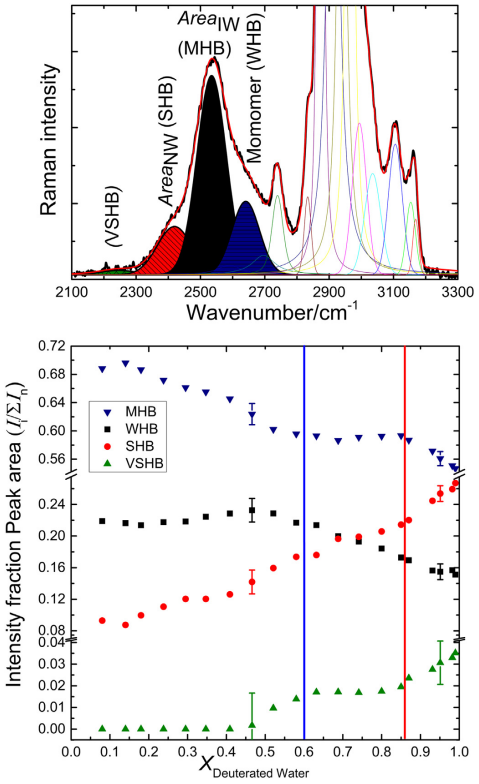

Fig. 4. Upper part Raman spectrum (black line) of $[C_4mim][NO_3]/D_2O$ mixture at X_w 0.87, relative fit red line and deconvolution in to four bands in Region 3. Lower part Intensity fraction of water molecules organized in all types clusters ratio to the total self-aggregated water plotted vs molar water content X_{D2O}. Crossover points marked by blue and red lines correspond to the lower and upper boarders of "water pocket" formation. (For interpretation of the references to colour in this figure legend, the reader is referred to the web version of this article.)

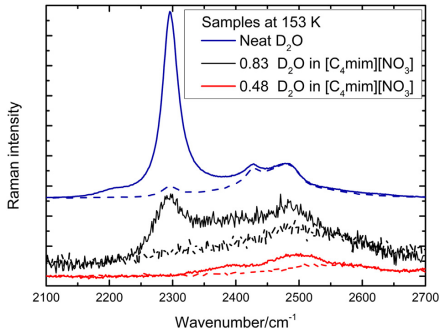

Fig. 5. Raman spectra of $[C_4mim][NO_3]/D_2O$ mixtures at different D_2O molar ratio registered with different polarization at 153 K. Sloid line spectra VV and dash lined spectra VH polarization. From the top to the bottom neat D_2O, 0.83 and 0.43 M D_2O fraction.

0.6 M D_2O ratio was depicted as the blue and upper one at 0.86 M D_2O ratio as the red lines. In this concentration region the constant integral intensity of νMHB band was noticed. The number of water molecules involved in distorted water network with anions remained unchanged and by this result other bands behavior was analyzed as primary process to identify fingerprints of "water pockets" formation. Discontinuities in concentration dependencies of OD stretching bands relative integral intensities indicated the processes which occurred in the water confinement called "water pockets". Together with νMHB, the νVSHB band relative integral intensities did not change in the region where water was confined. Differently clear decrease in integral intensity was registered for the band νWHB while at the concentration region νSHB band integral intensity showed the increase. This outcome was considered as a regroup of sporadic water molecules from the isolated ones to highly ordered water structures and well fitted with MD simulations suggested model [3]. The boarders identified on νMHB band relative integral intensity change could be used as spectral evidences of water confinements in RTIL. It was also noted that all three νSHB, νMHB and νWHB bands had a different concentration dependencies of Raman shift during the $[C_4mim][NO_3]$ dilution with D_2O. The νWHB band Raman shift was constant (2643 ± 3 cm^{-1}) and did not change much in whole concentration range. The different situation with νMHB and νSHB bands was found and depicted in Fig. 6. The νMHB band totally blue shifted by 32 cm^{-1} from 2544 to 2511 cm^{-1} and this shift as well as the relative integral intensity distribution of O–D stretching band was discontinuous. Two discontinuities, at the same concentrations as previously, were identified by monitoring the Raman band assigned to different water clusters shifts. The extent of "water pockets" formation was set in Fig. 6 adding boarders as lines at 0.6 M D_2O ratio (lower, blue line) and at 0.86 M D_2O ratio (upper, red line). The distribution of νSHB band parameters was slightly different from νMHB and νSHB. The band was totally red shifted only by 10 cm^{-1} from 2390 to 2380 cm^{-1}. The distinct crossover point in a band shift at 0.6 M D_2O ratio was registered. At the water concentration range 0–0.6 mol. D_2O the band blue shifted by 42 cm^{-1} from 2390 to 2432 cm^{-1} and at the water concentration range 0.6–1.0 mol. D_2O the red shift from 2432 to 2380 48 cm^{-1} was found (Fig. 6, lower part, left). As a comparison the constant relative integral intensity increase of νSHB was registered in all mixture concentrations. Multiple water molecules interactions with RTIL and other water molecules were indicated at different concentrations in mixtures. The blue shift in mixtures when water concentration was increased from 0 to 0.6 mol. D_2O represented the destruction of highly ordered water structures. Water···water aggregates were changed by the anion···water···anion complexes. Different view was found for the system when water concentration was increased from 0.6 to 0.999 mol. D_2O. The red shift showed the increase of H bond strength. The stronger H bond was associated with closer water··· water interactions in "pockets" when the intermolecular interactions changed from anion···water···anion to water···anion···water. Moreover the same discontinuities in concentration dependencies were registered for the Raman band FWHM parameter (see in Fig. 6, lower part, right). The increase in FWHM from 90 to 115 cm^{-1} with crossover point value 140 cm^{-1} at 0.6 M D_2O fraction was registered and supported our previous results.

One more OD stretching band fit was found when the low temperature Raman experiment with different laser polarizations was performed for various $[C_4mim][NO_3]$-D_2O concentrations and neat D_2O. The low frequency (at around 2250 cm^{-1}) shoulder was reported as VSHB [69]. This band was hardly seen in Raman spectra of $[C_4mim][BF_4]$-D_2O mixtures without formed "water pockets" at room temperature. During the fitting we involved this band to our procedure, but the relative integral intensity of this band was only up to 0.035 counting to all OD stretching bands and deeper analysis of the band was not

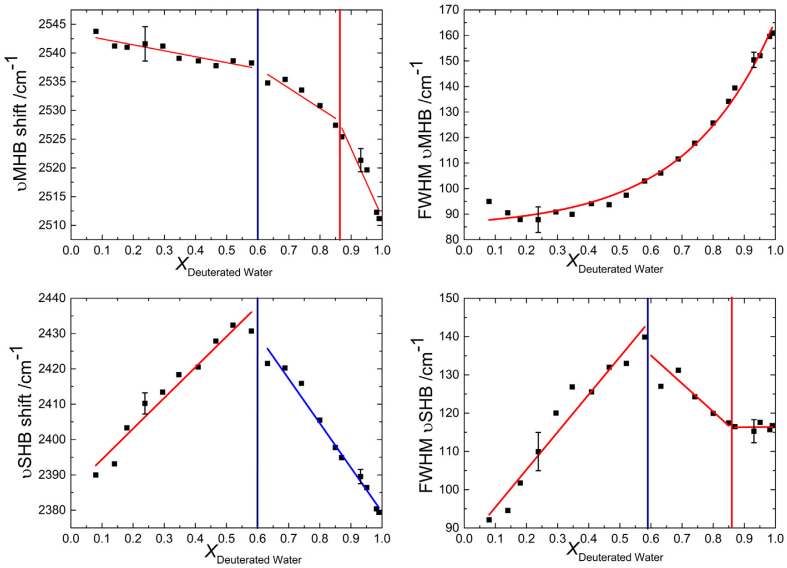

Fig. 6. The Raman shift of υMHB (upper left) and υSHB (lower left) plotted as a function of the D_2O molar fraction in the $[C_4mim][NO_3]/D_2O$ mixtures. The FWHM for Raman bands υMHB (upper right) and υSHB (lower right) plotted as a function of the D_2O molar fraction in the $[C_4mim][NO_3]/D_2O$ mixtures. Crossover points in all cases marked by blue and red lines correspond to the lower and upper boarders of "water pocket" formation. (For interpretation of the references to colour in this figure legend, the reader is referred to the web version of this article.)

performed. Worth to mention, that VSHB band was totally depolarized at low temperature (153 K) measurements, where crystallization of the nano-confined "water pockets" is not induced even if the outer IL crystallizes [70] (see the band at around 2260 cm^{-1} in Fig. 5). Furthermore both VSHB and SHB [68] bands were not found bellow "water pockets" concentration boarder at 0.48 (see in Fig. 5, vibrational bands at 2300 and 2260 cm^{-1}).

3.4. Conformational equilibrium changes (Region 1)

Conformational equilibrium of the $[C_4mim]^+$ cation (see in Fig. 7) was investigated by monitoring the combination of the ring deformation and the CH_2 rocking bands [38]. Two Raman bands in different neat ionic liquids were many times investigated as conformers vibrational modes corresponding to *GT* at lower frequency (601 cm^{-1}) and *TT* (624 cm^{-1}). The intensity ratio of these Raman bands was considered as a number-density ratio of the respective vibrations. The relative intensity of the band at 601 cm^{-1} to the band at 624 cm^{-1} was proportional to the *GT*/*TT* population ratio (I_{GT}/I_{TT}). The discontinuous change in I_{GT}/I_{TT} ratio was reported with addition of heavy water in ionic liquid/water mixture. The similar concentration dependence was also reported for 1 butyl 3 methylimidazolium Tetrafluorborate-D_2O mixtures. The anomalous conformational changes were discussed and deuteration in this mixture was denied [45,70]. In our case no changes in Raman spectra were monitored after the samples were prepared and hold for 60 days. The deuteration was not registered in $[C_4mim][NO_3]$-D_2O mixtures. Moreover, the hypothesis on external base necessity for deuterium exchange to occur in ionic liquids with coordinated and non-basic anion such as tetrafluorborate BF_4 [72] was approved. The ratio of *GT* and *TT* conformers was found being discontinuous upon the increase of water content in aqueous ionic liquid mixtures. The discontinuities in concentration dependency with crossover point were noticed in $[C_4mim][NO_3]$-D_2O mixture at around 0.84 D_2O molar fraction. The same dependency with the same crossover point was found in $[C_4mim][NO_3]$-H_2O mixtures and let us approve the previous experimental results [73] that H/D exchange does not occur in $[C_4mim][NO_3]$ and D_2O mixtures. In previous study [71] it was noticed that H/D effect could take some time to occur. For this case the time dependencies of *GT*/*TT* Raman bands integral intensity ratio (Fig. 8A) and percentage of H/D exchange (Fig. 8B) at different molar D_2O content

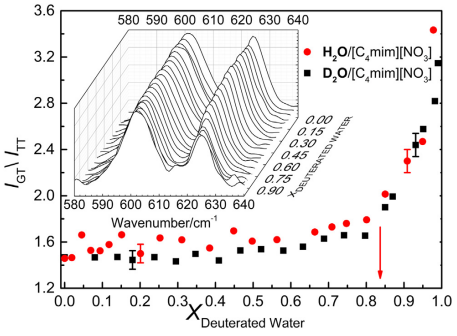

Fig. 7. Area ratio between the *gauche* and *trans* peaks with of $[C_4mim][NO_3]/H_2O$ (red dots) and $[C_4mim][NO_3]/D_2O$ (black squares) plotted as a function of the D_2O molar fraction in the mixtures. In the inset Raman spectra of $[C_4mim][NO_3]/D_2O$ mixtures at different water concentrations in spectral Region 1. Crossover point marked by red arrow corresponds to the upper boarder of "water pocket" formation. (For interpretation of the references to colour in this figure legend, the reader is referred to the web version of this article.)

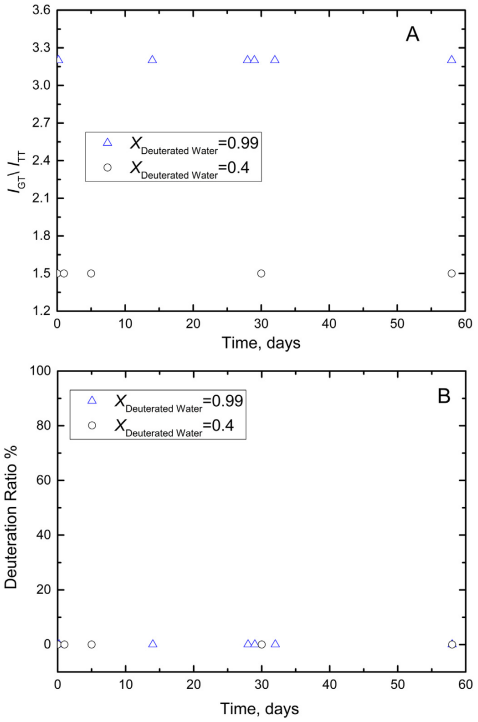

Fig. 8. Time evolution of A: the Raman bands integral intensity ratio (I_{GT}/I_{TT}) between the *GT* and *TT* forms, B: the area ratio {$I_{C(2)-D}/(I_{C(2)-H} + I_{C(2)-D})$}[100 (%)] of two peaks for C (2)–H and C(2)–D in the CH_3 combination band arising from the in-plane ring deformation and CH_3(N) deformation (ν(ring ip + CH_3(N))) vibrations at different molar D_2O content in [C_4mim][NO_3]: 0.99 (triangles), 0.4 (dots).

in [C_4mim][NO_3] 0.99 (triangles), 0.4 (dots) were measured. These results confirm previous studies findings. The constant I_{GT}/I_{TT} ratio at low water concentrations confirmed the hypothesis that water molecules does not interact with cation tail at low water concentrations. The hydrogen bonds were firstly formed with anion and imidazolium ring. At higher water concentrations when the crossover point at approximate 0.84 M D_2O ratio was passed, the increase of I_{GT}/I_{TT} ratio was registered. Ionic liquid molecules lost the molecular packing, because of ionic liquid solvation with the localized "water pockets". The increase in size of "water pockets" determine the merge of them and bulk water formation in whole sample, the same as reported in [3].

4. Concluding remarks

The water clusterization process called "water pockets" in [C_4mim][NO_3]-water system was investigated using Raman spectroscopy. Some of Raman band parameters were changing with added D_2O in ionic liquid and D_2O mixtures and discontinuities in concentration dependences were found. They let us to determine boarders of the "water pockets" process. The extent of "water pockets" was measured to be between 0.60 and 0.86 D_2O molar fraction. This result well correlated to the values found using other (SANS, SAXS and DSC) methods at 0.7–0.9 M D_2O ratio. The boarders of "water pockets" extent determined by our experiment are slightly shifted to lower D_2O concentration region. This difference could be influenced by experimental and fitting errors. One more explanation could be various delays in dynamic response detection of applied SANS, SAXS and Raman techniques. Different wavelengths of excitation source are used for Raman, SANS and SAXS techniques. In SAXS and SANS techniques more precise view of "water pockets" are registered in nanometers scale while Raman technique allows to see more generalized view in hundreds of nanometers scale.

The Raman shifts, relative integral intensities and FWHM of the vibrational bands were found to be sensitive to added D_2O content. Discontinuities in concentration dependences of vibrational band parameters were found for NO_3^- stretching, NO_3^- bending and OD stretching modes of different water clusters. These discontinuities were considered as the lower boarder indication of the "water pockets" formation process. Furthermore, discontinuous concentration dependences of previously mentioned vibrational band parameters were found for imidazolium ring C(2)–H and C(4,5)–H asymmetric and C (4,5)–H symmetric stretching vibration modes as well as different water clusters OD stretching modes. Moreover, the changes of integral intensities ratio of Raman vibrational bands corresponding to *GT* and *TT* conformers was registered in the same concentration region. All these discontinuities in concentration dependences were indicated as the end of "water pockets" formation process (upper boarder).

The changes in Raman spectral parameters which could prove the deuteration process in [C_4mim][NO_3]-D_2O mixtures were not found. Imidazolium ring C(2)–H stretching mode behavior was monitored at different D_2O concentrations in studied mixtures but C(2)–D vibrational band formation was not registered. The time dependence of C(2)–H vibrational band did not show any changes which possibly could be expected from previous work when different IL-D_2O mixtures were studied. Other suggested method to check for the H/D exchange was monitoring the integral intensities ratio of Raman bands corresponding to vibrations of *GT* and *TT* conformers [14,71]. Using this method the same distribution of *GT* and *TT* bands ratio in both [C_4mim][NO_3]-D_2O and [C_4mim][NO_3]-H_2O mixtures was found [73]. Our results proved previously published results that deuteration does not occur in [C_4mim][NO_3]-D_2O mixtures.

Low temperature and polarization measurements of [C_4mim][NO_3]-D_2O Raman spectra at different D_2O content in the mixtures let to ascertain the precise OD stretching band assignment to the very strong, strong, medium and weakly hydrogen bonded water Raman bands [21].

References

[1] T. Welton, Room-temperature ionic liquids. Solvents for synthesis and catalysis, Chem. Rev. 99 (1999) 2071–2084, https://doi.org/10.1021/cr980032t.
[2] J. Dupont, R.F. De Souza, P.A.Z. Suarez, Ionic liquid (molten salt) phase organometallic catalysis, Chem. Rev. 102 (2002) 3667–3692, https://doi.org/10.1021/cr010338r.
[3] W. Jiang, Y. Wang, G.A. Voth, Molecular dynamics simulation of nanostructural organization in ionic liquid/water mixtures, J. Phys. Chem. B 111 (2007) 4812–4818, https://doi.org/10.1021/jp0671421.
[4] K. Dong, S. Zhang, J. Wang, Understanding the hydrogen bonds in ionic liquids and their roles in properties and reactions, Chem. Commun. 52 (2016) 6744–6764, https://doi.org/10.1039/C5CC10120D.
[5] Y. Zhao, S. Gao, J. Wang, J. Tang, Aggregation of ionic liquids [Cnmim]Br (n = 4, 6, 8, 10, 12) in D_2O: a NMR study, J. Phys. Chem. B 112 (2008) 2031–2039, https://doi.org/10.1021/jp076467e.
[6] M.N. Garaga, M. Nayeri, A. Martinelli, Effect of the alkyl chain length in 1 alkyl 3 methylimidazolium ionic liquids on inter-molecular interactions and rotational dynamics, J. Mol. Liq. 210 (2015) 1–9, https://doi.org/10.1016/j.molliq.2015.06.055.
[7] U. Schroder, J.D. Wadhawan, R.G. Compton, F. Marken, P.A.Z. Suarez, C.S. Consorti, F. De Souza, J. Dupont, Water-induced accelerated ion diffusion: voltammetric studies in [BMIM][BF4], R. Soc. Chem. 24 (2000) 1009–1015, https://doi.org/10.1039/b007172m.
[8] K.A. Fletcher, S. Pandey, Solvatochromic probe behavior within ternary room-temperature ionic liquid 1 butyl 3 methylimidazolium hexafluorophosphate + ethanol + water solutions, J. Phys. Chem. B 107 (2003) 13532–13539, https://doi.org/10.1021/jp0276754.
[9] K.R. Seddon, A. Stark, M.-J. Torres, Influence of chloride, water, and organic solvents on the physical properties of ionic liquids, Pure Appl. Chem. 72 (2000) 2275–2287, https://doi.org/10.1351/pac200072122275.
[10] M.G. Freire, P.J. Carvalho, A.M. Fernandes, I.M. Marrucho, A.J. Queimada, J.A.P. Coutinho, Surface tensions of imidazolium based ionic liquids: anion, cation,

temperature and water effect, J. Colloid Interface Sci. 314 (2007) 621–630, https://doi.org/10.1016/j.jcis.2007.06.003.
[11] M. Filice, O. Romero, O. Abian, B. de las Rivas, J.M. Palomo, Low ionic liquid concentration in water: a green and simple approach to improve activity and selectivity of lipases, RSC Adv. 4 (2014) 49115–49122, https://doi.org/10.1039/C4RA07625G.
[12] Y. Kohno, H. Ohno, Ionic liquid/water mixtures: from hostility to conciliation, Chem. Commun. 48 (2012) 7119, https://doi.org/10.1039/c2cc31638b.
[13] S. Cha, D. Kim, Change of hydrogen bonding structure in ionic liquid mixtures by anion type, J. Chem. Phys. 148 (2018) 193827, https://doi.org/10.1063/1.5010067.
[14] J. Kausteklis, V. Balevičius, V. Aleksa, Two-dimensional Raman spectroscopy study of ionogel phase formation in long-chain ionic liquid/water systems, J. Raman Spectrosc. 48 (2017) 126–131, https://doi.org/10.1002/jrs.4983.
[15] V. Klimavicius, Z. Gdaniec, J. Kausteklis, V. Aleksa, K. Aidas, V. Balevicius, NMR and Raman spectroscopy monitoring of proton/deuteron exchange in aqueous solutions of ionic liquids forming hydrogen bond: a role of anions, self-aggregation, and mesophase formation, J. Phys. Chem. B 117 (2013) 10211–10220, https://doi.org/10.1021/jp4021245.
[16] B.A. Marekha, M. Bria, M. Moreau, I. De Waele, F.A. Miannay, Y. Smortsova, T. Takamuku, O.N. Kalugin, M. Kiselev, A. Idrissi, Intermolecular interactions in mixtures of 1 n butyl 3 methylimidazolium acetate and water: insights from IR, Raman, NMR spectroscopy and quantum chemistry calculations, J. Mol. Liq. 210 ((2015) 227–237, https://doi.org/10.1016/j.molliq.2015.05.015.
[17] T. Takamuku, H. Hoke, A. Idrissi, B.A. Marekha, M. Moreau, Y. Honda, T. Umecky, T. Shimomura, Microscopic interactions of the imidazolium-based ionic liquid with molecular liquids depending on their electron-donicity, Phys. Chem. Chem. Phys. 16 (2014) 23627–23638, https://doi.org/10.1039/C4CP03565H.
[18] V. Aleksa, J. Kausteklis, V. Klimavicius, Z. Gdaniec, V. Balevicius, Raman and NMR spectroscopy study of liquid crystalline ionogel phase in ionic liquid/H_2O mixtures: the states of water, J. Mol. Struct. 993 (2011) 91–96, https://doi.org/10.1016/j.molstruc.2010.12.060.
[19] K. Saihara, Y. Yoshimura, S. Ohta, A. Shimizu, Properties of water confined in ionic liquids, Sci. Rep. 5 (2015) 10619, https://doi.org/10.1038/srep10619.
[20] H. Abe, T. Takekiyo, M. Shigemi, Y. Yoshimura, S. Tsuge, T. Hanasaki, K. Ohishi, S. Takata, J. Suzuki, Direct evidence of confined water in room-temperature ionic liquids by complementary use of small-angle X-ray and neutron scattering, J. Phys. Chem. Lett. 5 (2014) 1175–1180, https://doi.org/10.1021/jz500299z.
[21] H. Abe, T. Takekiyo, Y. Yoshimura, K. Saihara, A. Shimizu, Anomalous freezing of nano-confined water in room-temperature ionic liquid 1 butyl 3 methylimidazolium nitrate, ChemPhysChem 17 (2016) 1136–1142, https://doi.org/10.1002/cphc.201501199.
[22] C.E.S. Bernardes, M.E. Minas Da Piedade, J.N. Canongia Lopes, The structure of aqueous solutions of a hydrophilic ionic liquid: the full concentration range of 1 ethyl 3 methylimidazolium ethylsulfate and water, J. Phys. Chem. B 115 (2011) 2067–2074, https://doi.org/10.1021/jp1113202.
[23] M. Anouti, J. Jacquemin, P. Porion, Transport properties investigation of aqueous protic ionic liquid solutions through conductivity, viscosity, and NMR self-diffusion measurements, J. Phys. Chem. B 116 (2012) 4228–4238, https://doi.org/10.1021/jp3010844.
[24] M. Anouti, M. Caillon-Caravanier, Y. Dridi, J. Jacquemin, C. Hardacre, D. Lemordant, Liquid densities, heat capacities, refractive index and excess quantities for {protic ionic liquids + water} binary system, J. Chem. Thermodyn. 41 (2009) 799–808, https://doi.org/10.1016/j.jct.2009.01.011.
[25] M. Anouti, A. Vigeant, J. Jacquemin, C. Brigouleix, D. Lemordant, Volumetric properties, viscosity and refractive index of the protic ionic liquid, pyrrolidinium octanoate, in molecular solvents, J. Chem. Thermodyn. 42 (2010) 834–845, https://doi.org/10.1016/j.jct.2010.01.013.
[26] N. Yaghini, J. Pitawala, A. Matic, A. Martinelli, Effect of water on the local structure and phase behavior of imidazolium-based protic ionic liquids, J. Phys. Chem. B 119 (2015) 1611–1622, https://doi.org/10.1021/jp510691e.
[27] O. Cabeza, L. Segade, M. Domínguez-Pérez, E. Rilo, D. Ausín, A. Martinelli, N. Yaghini, B. Gollas, M. Kriechbaum, O. Russina, A. Triolo, E. López-Lago, L.M. Varela, Mesostructure and physical properties of aqueous mixtures of the ionic liquid 1 ethyl 3 methyl imidazolium octyl sulfate doped with divalent sulfate salts in the liquid and the mesomorphic states, Phys. Chem. Chem. Phys. 20 (2018) 8724–8736, https://doi.org/10.1039/c7cp07999k.
[28] P.R. Burney, J. Pfaendtner, Structural and dynamic features of *Candida rugosa* lipase 1 in water, octane, toluene, and ionic liquids BMIM-PF6 and BMIM-NO3, J. Phys. Chem. B 117 (2013) 2662–2670, https://doi.org/10.1021/jp312299d.
[29] Y. Shu, M. Liu, S. Chen, X. Chen, J. Wang, New insight into molecular interactions of imidazolium ionic liquids with bovine serum albumin, J. Phys. Chem. B 115 (2011) 12306–12314, https://doi.org/10.1021/jp2071925.
[30] N.M. Micaelo, C.M. Soares, Protein structure and dynamics in ionic liquids. Insights from molecular dynamics, J. Phys. Chem. B (2008) 2566–2572, https://doi.org/10.1021/jp0766050.
[31] M.D. Bermúdez, A.E. Jiménez, J. Sanes, F.J. Carrión, Ionic liquids as advanced lubricant fluids, Molecules 14 (2009) 2888–2908, https://doi.org/10.3390/molecules14082888.
[32] M.H. Ghatee, M. Bahrami, N. Khanjari, Measurement and study of density, surface tension, and viscosity of quaternary ammonium-based ionic liquids ([N222(n)]Tf2N), J. Chem. Thermodyn. 65 (2013) 42–52, https://doi.org/10.1016/j.jct.2013.05.031.
[33] Y. Cao, T. Mu, Comprehensive investigation on the thermal stability of 66 ionic liquids by thermogravimetric analysis, Ind. Eng. Chem. Res. 53 (2014) 8651–8664, https://doi.org/10.1021/ie5009597.
[34] E. Bodo, S. Mangialardo, F. Capitani, L. Gontrani, F. Leonelli, P. Postorino, Interaction of a long alkyl chain protic ionic liquid and water, J. Chem. Phys. 140 (2014) 204503, https://doi.org/10.1063/1.4876036.
[35] N.E. Heimer, R.E. Del Sesto, Z. Meng, J.S. Wilkes, W.R. Carper, Vibrational spectra of imidazolium tetrafluoroborate ionic liquids, J. Mol. Liq. 124 (2006) 84–95, https://doi.org/10.1016/j.molliq.2005.08.004.
[36] N. Hatano, T. Takekiyo, H. Abe, Y. Yoshimura, Effect of counteranions on the conformational equilibrium of 1 butyl 3 methylimidazolium-based ionic liquids, Int. J. Spectrosc. 2011 (2011) 1–5, https://doi.org/10.1155/2011/648245.
[37] R.W. Berg, Raman spectroscopy and ab-initio model calculations on ionic liquids, Monatsh. Chem. 138 (2007) 1045–1075, https://doi.org/10.1007/s00706-007-0760-9.
[38] R.W. Berg, M. Deetlefs, K.R. Seddon, I. Shim, J.M. Thompson, Raman and ab initio studies of simple and binary 1 alkyl 3 methylimidazolium ionic liquids, J. Phys. Chem. B 109 (2005) 19018–19025, https://doi.org/10.1021/jp050691r.
[39] B. Fazio, A. Triolo, G. Di Marco, Recent advances in linear and nonlinear Raman spectroscopy I, J. Raman Spectrosc. 39 (2008) 233–237, https://doi.org/10.1002/jrs.
[40] C. Roth, S. Chatzipapadopoulos, D. Kerlé, F. Friedriszik, M. Lütgens, S. Lochbrunner, O. Kühn, R. Ludwig, Hydrogen bonding in ionic liquids probed by linear and nonlinear vibrational spectroscopy, New J. Phys. 14 (2012) 105026, https://doi.org/10.1088/1367-2630/14/10/105026.
[41] J. Kausteklis, V. Aleksa, M.A. Iramain, S.A. Brandan, Effect of cation-anion interactions on the structural and vibrational properties of 1 butyl 3 metylimidazolium nitrate ionic liquid, J. Mol. Struct. 1164 (2018) 1–14, https://doi.org/10.1016/j.molstruc.2018.03.100.
[42] R.O.H. Hamaguchi, Structure of ionic liquids and ionic liquid compounds: are ionic liquids genuine liquids in the conventional sense? Adv. Chem. Ph. 131 (2005) 85–102.
[43] K.-L. Han, G.-J. Zhao, Hydrogen Bonding and Transfer in the Excited State, 2011.
[44] M. Moreno, F. Castiglione, A. Mele, C. Pasqui, G. Raos, Interaction of water with the model ionic liquid [bmim][BF4]: molecular dynamics simulations and comparison with NMR data, J. Phys. Chem. B 112 (2008) 7826–7836, https://doi.org/10.1021/jp800383g.
[45] T. Singh, A. Kumar, Cation-anion-water interactions in aqueous mixtures of imidazolium based ionic liquids, Vib. Spectrosc. 55 (2011) 119–125, https://doi.org/10.1016/j.vibspec.2010.09.009.
[46] S. Cha, M. Ao, W. Sung, B. Moon, B. Ahlström, P. Johansson, Y. Ouchi, D. Kim, Structures of ionic liquid-water mixtures investigated by IR and NMR spectroscopy, Phys. Chem. Chem. Phys. 16 (2014) 9591–9601, https://doi.org/10.1039/c4cp00589a.
[47] Y. Xu, Y. Gao, L. Zhang, J. Yao, C. Wang, H. Li, Microscopic structures of ionic liquids 1 ethyl 3 methylimidazolium tetrafluoroborate in water probed by the relative chemical shift, Sci China Chem 53 (2010) 1561–1565, https://doi.org/10.1007/s11426-010-3198-6.
[48] Y. Chen, Y. Cao, X. Sun, T. Mu, Hydrogen bonding interaction between acetate-based ionic liquid 1 ethyl 3 methylimidazolium acetate and common solvents, J. Mol. Liq. 190 (2014) 151–158, https://doi.org/10.1016/j.molliq.2013.11.010.
[49] J. Joseph, E.D. Jemmis, Red-, blue-, or no-shift in hydrogen bonds: a unified explanation, J. Am. Chem. Soc. 129 (2007) 4620–4632, https://doi.org/10.1021/ja067545z.
[50] C.G. Hanke, N.A. Atamas, R.M. Lynden-Bell, Solvation of small molecules in imidazolium ionic liquids: a simulation study, Green Chem. 4 (2002) 107–111, https://doi.org/10.1039/b109179b.
[51] M.R. Waterland, D. Stockwell, A.M. Kelley, Symmetry breaking effects in NO_3^-: Raman spectra of nitrate salts and ab initio resonance Raman spectra of nitrate-water complexes, J. Chem. Phys. 114 (2001) 6249–6258, https://doi.org/10.1063/1.1355657.
[52] O. Russina, A. Triolo, L. Gontrani, R. Caminiti, D. Xiao, L.G. Hines Jr, R.A. Bartsch, E.L. Quitevis, N. Pleckhova, K.R. Seddon, Morphology and intermolecular dynamics of 1 alkyl 3methylimidazolium bis{(trifluoromethane)sulfonyl}amide ionic liquids: structural and dynamic evidence of nanoscale segregation, J. Phys. Condens. Matter 21 (2009) 424121, https://doi.org/10.1088/0953-8984/21/42/424121.
[53] M.C.C. Ribeiro, High viscosity of imidazolium ionic liquids with the hydrogen sulfate anion: a Raman spectroscopy study, J. Phys. Chem. B 116 (2012) 7281–7290, https://doi.org/10.1021/jp302091d1.
[54] F.W.B. Einstein, D.G. Tuck, A refinement of the crystal structure of $NH_4NO_3{\cdot}2HNO_3$, Acta Cryst B26 (1970) 1117–1120, https://doi.org/10.1107/S0567740869003323.
[55] K. Kaneko, Y. Yoshimura, A. Shimizu, Water concentration dependence of the refractive index of various ionic liquid-water mixtures, J. Mol. Liq. 250 (2018) 283–286, https://doi.org/10.1016/j.molliq.2017.12.009.
[56] S. Mangialardo, L. Baldassarre, E. Bodo, P. Postorino, The Structure of Ionic Liquids, 2014https://doi.org/10.1007/978-3-319-01698-6.
[57] Y. Jeon, J. Sung, D. Kim, C. Seo, H. Cheong, Y. Ouchi, R. Ozawa, H.O. Hamaguchi, Structural change of 1 butyl 3 methylimidazolium tetrafluoroborate + water mixtures studied by infrared vibrational spectroscopy, J. Phys. Chem. B 112 (2008) 923–928, https://doi.org/10.1021/jp0746650.
[58] A. Nilsson, L.G.M. Pettersson, The structural origin of anomalous properties of liquid water, Nat. Commun. 6 (2015) 8998, https://doi.org/10.1038/ncomms9998.
[59] F. Perakis, L. De Marco, A. Shalit, F. Tang, Z.R. Kann, T.D. Kühne, R. Torre, M. Bonn, Y. Nagata, Vibrational spectroscopy and dynamics of water, Chem. Rev. 116 (2016) 7590–7607, https://doi.org/10.1021/acs.chemrev.5b00640.
[60] C. Choe, J. Lademann, M.E. Darvin, Depth profiles of hydrogen bound water molecule types and their relation to lipid and protein interaction in the human stratum corneum in vivo, Analyst 141 (2016) 6329–6337, https://doi.org/10.1039/C6AN01717G.
[61] Q. Hu, H. Zhao, S. Ouyang, Understanding water structure from Raman spectra of isotopic substitution H_2O/D_2O up to 573 K, Phys. Chem. Chem. Phys. 19 (2017) 21540–21547, https://doi.org/10.1039/C7CP02065A.
[62] J.-B. Brubach, A. Mermet, A. Filabozzi, A. Gerschel, D. Lairez, M.P. Krafft, P. Roy, Dependence of water dynamics upon confinement size, J. Phys. Chem. B 105 (2001) 430–435, https://doi.org/10.1021/jp002983s.

[63] C. Boissière, J.B. Brubach, A. Mermet, G. Marzi De, C. Bourgaux, E. Prouzet, P. Roy, Water confined in lamellar structures of AOT surfactants: an infrared investigation, J. Phys. Chem. B 106 (2002) 1032–1035, https://doi.org/10.1021/jp012724i.
[64] A.V. Frontzek, L. Paccou, Y. Guinet, A. Hédoux, Study of the phase transition in lysozyme crystals by Raman spectroscopy, Biochim. Biophys. Acta, Gen. Subj. 1860 (2016) 412–423, https://doi.org/10.1016/j.bbagen.2015.10.020.
[65] A. Lerbret, P. Bordat, F. Affouard, Y. Guinet, A. Hédoux, L. Paccou, D. Prévost, M. Descamps, Influence of homologous disaccharides on the hydrogen-bond network of water: complementary Raman scattering experiments and molecular dynamics simulations, Carbohydr. Res. 340 (2005) 881–887, https://doi.org/10.1016/j.carres.2005.01.036.
[66] K. Kristinaitytė, L. Dagys, J. Kausteklis, V. Klimavicius, I. Doroshenko, V. Pogorelov, N.R. Valevičienė, V. Balevicius, NMR and FTIR studies of clustering of water molecules: from low-temperature matrices to nano-structured materials used in innovative medicine, J. Mol. Liq. 235 (2017)https://doi.org/10.1016/j.molliq.2016.11.076.
[67] T. Takekiyo, K. Yamazaki, E. Yamaguchi, H. Abe, Y. Yoshimura, High ionic liquid concentration-induced structural change of protein in aqueous solution: a case study of lysozyme, J. Phys. Chem. B 116 (2012) 11092–11097, https://doi.org/10.1021/jp3057064.
[68] H. Abe, T. Takekiyo, M. Aono, H. Kishimura, Y. Yoshimura, N. Hamaya, Polymorphs in room-temperature ionic liquids: hierarchical structure, confined water and pressure-induced frustration, J. Mol. Liq. 210 ((2015) 200–214, https://doi.org/10.1016/j.molliq.2015.05.057.
[69] Y. Yoshimura, T. Takekiyo, C. Okamoto, N. Hatano, H. Abe, Switching of hydrogen bonds of water in ionic liquid, 1 butyl 3 methylimidazolium tetrafluoroborate, J. Raman Spectrosc. 44 (2013) 475–480, https://doi.org/10.1002/jrs.4197.
[70] H. Abe, T. Yamada, K. Shibata, Dynamic properties of nano-confined water in an ionic liquid, J. Mol. Liq. 264 (2018) 54–57, https://doi.org/10.1016/j.molliq.2018.05.006.
[71] N. Hatano, M. Watanabe, T. Takekiyo, H. Abe, Y. Yoshimura, Anomalous conformational change in 1 butyl 3 methylimidazolium tetrafluoroborate-D_2O mixtures, J. Phys. Chem. A 116 (2012) 1208–1212, https://doi.org/10.1021/jp2097873.
[72] S. Sowmiah, V. Srinivasadesikan, M.C. Tseng, Y.H. Chu, On the chemical stabilities of ionic liquids, Molecules 14 (2009) 3780–3813, https://doi.org/10.3390/molecules14093780.
[73] Y. Yoshimura, N. Hatano, T. Takekiyo, H. Abe, Direct correlation between the H/D exchange reaction and conformational changes of the cation in imidazolium-based ionic liquid-D_2O mixtures, J. Solut. Chem. (2014) 1509–1518, https://doi.org/10.1007/s10953-014-0181-4.

Journal of Molecular Structure 1164 (2018) 1–14

Contents lists available at ScienceDirect

Journal of Molecular Structure

journal homepage: http://www.elsevier.com/locate/molstruc

Effect of cation-anion interactions on the structural and vibrational properties of 1-buthyl-3-methyl imidazolium nitrate ionic liquid

Jonas Kausteklis [a], Valdemaras Aleksa [a], Maximiliano A. Iramain [b], Silvia Antonia Brandán [b, *]

[a] Vilnius University, Sauletekio al.9-3, LT-10222 Vilnius, Lithuania
[b] Cátedra de Química General, Instituto de Química Inorgánica, Facultad de Bioquímica, Química y Farmacia, Universidad Nacional de Tucumán, Ayacucho 471, 4000 San Miguel de Tucumán, Tucumán, Argentina

ARTICLE INFO

Article history:
Received 3 October 2017
Received in revised form
14 March 2018
Accepted 24 March 2018
Available online 24 March 2018

Keywords:
1-Butyl-3-methylimidazolium nitrate
Vibrational spectra
Molecular structure
Quantum-chemical descriptors
DFT calculations

ABSTRACT

The cation-anion interactions present in the 1-butyl-3-methylimidazolium nitrate ionic liquid [BMIm][NO_3] were studied by using density functional theory (DFT) calculations and the experimental FT-Raman spectrum in liquid phase and its available FT-IR spectrum. For the three most stable conformers found in the potential energy surface and their 1-butyl-3-methylimidazolium [BMIm] cation, the atomic charges, molecular electrostatic potentials, stabilization energies, bond orders and topological properties were computed by using NBO and AIM calculations and the hybrid B3LYP level of theory with the 6-31G* and 6-311++G** basis sets. The force fields, force constants and complete vibrational assignments were also reported for those species by using their internal coordinates and the scaled quantum mechanical force field (SQMFF) approach. The dimeric species of [BMIm][NO_3] were also considered because their presence could probably explain the most intense bands observed at 1344 and 1042 cm^{-1} in both experimental FT-IR and FT-Raman spectra, respectively. The geometrical parameters suggest monodentate cation-anion coordination while the studies by charges, NBO and AIM calculations support bidentate coordinations between those two species. Additionally several quantum chemical descriptors were also calculated in order to interpret various molecular properties such as electronic structure, reactivity of those species and predict their gas phase behaviours.

1. Introduction

The structures of the ionic liquids are based on organic cations, such as the imidazolium, pyridinium, pyrrolidinium, tetraalkylammonium and phosphonium cations [1–17] which are weakly coordinated to inorganic or organic anions, being the most used anions bis(trifluoromethane sulfonyl)amide, trifluoromethanesulfonate, hexafluorophosphate, nitrate, dicyandiamide, tosylate, or n-alkyl sulfates among others [1,2]. The observable properties of these ionic liquids are related directly to the presence of intra- or inter-molecular interactions in their structures and, also to the orientations of cation and anion, as evidenced by using electrochemical studies for 1-butyl-3-methylimidazolium dicyanamide at the platinum-liquid interface by Aliaga and Baldelli [13]. For these reasons, the structural studies of these species are of great interest to explain their behaviour in different media and, especially when these species interact with other [1,3,4,6,9,13,15]. For the same reasons, the vibrational studies of these ionic liquids are of great significance to identify interactions between cation and anion, as reported by Wang et al. [14] for 1-butyl-3-methylimidazolium hexafluorophosphate ionic liquid by using the ^{31}P NMR and FT-IR spectra. So far, the structural and vibrational studies of 1-butyl-3-methylimidazolium nitrate were not reported and, only the infrared spectrum and some bands were identified by Gruzdev et al. [17] while their conductivity, density and viscosity were recently reported by Bennett et al. [3]. The preparation of 1-butyl-3-methylimidazolium salts and their intra-molecular interactions were also studied by Gruzdev et al. [17] while the water effect on physicochemical properties of 1-butyl-3-methylimidazolium were published by Grishina et al. [18]. In this context, the aims of this work are: (i) to know the different types of interactions that present 1-butyl-3-methylimidazolium nitrate, such as ionic interactions (cation-anion) or of hydrogen bonds because for this ionic liquid so far

* Corresponding author.
E-mail addresses: sbrandan@fbqf.unt.edu.ar, brandansa@yahoo.com.ar (S.A. Brandán).

https://doi.org/10.1016/j.molstruc.2018.03.100
0022-2860/

they are not reported NBO and AIM studies [19–21], (ii) to know the structural properties of this ionic liquid because the atomic charges, bond orders, molecular electrostatic potentials, stabilization energies, topological properties were not studied for this ionic liquid and, (iii) to perform the complete vibrational assignments in order to identify this ionic liquid by using the vibrational spectroscopy and to report their force fields and force constants. Here, the theoretical calculations, based on the density functional theory (DFT) by using the hybrid B3LYP method with the 6-31G* and 6-311++G** basis sets are also useful to predict the infrared and Raman spectra which were later compared with the corresponding experimental ones in order to perform the complete assignments. The properties for the 1-butyl-3-methylimidazolium cation were also predicted in order to compare them with those obtained for their ionic liquid. The complete vibrational assignments of ionic liquid and their cation were performed taking into account their internal coordinates and corresponding force fields calculated at the same levels of theory by using the SQMFF methodology and the Molvib program [22,23] and, by using the experimental available infrared spectrum [17]. Here, the experimental Raman spectrum for [BMIm][NO_3] in the liquid state was recorded by us. A 1-butyl-3-methylimidazolium nitrate dimeric species was also considered in order to explain the strong intensities of some bands observed in the vibrational spectra. This work was completed with the calculations of frontier orbitals [24,25] and quantum chemical descriptors for the ionic liquid and their cation [26–28]. After that, all properties were totally evaluated and compared for the cation and their ionic liquid.

2. Experimental section

FT-Raman spectra of 1-butyl-3-methylimidazolium nitrate [BMIm][NO_3] were typically measured at room temperature (298 K) using the Bruker MultiRAM FT-Raman spectrometer with the motorized xyz-sample stage and with the high-sensitivity liquid nitrogen cooled germanium detector. The 1064 nm wavelength beam of the pulsed Nd:YAG laser (500 mW) as the excitation source using the 180° scattering geometry was employed in the experiments, while the resolution of the spectrometer was set to the 2 cm^{-1}. The FT-Raman spectrum was recorded with 400 scans between 4000 and 70 cm^{-1}. To avoid the background, samples were prepared and measured in Silica cells.

3. Computational details

The *GaussView* program [29] was used to model the initial structures of [BMIm][NO_3] and their [BMIm] cation while the hybrid B3LYP method with the 6-31G* and 6-311++G** basis sets were employed together with the Gaussian 09 program Revision A.02 [30] to optimize both structures. It is necessary to explain that the position of the NO_3^- anion confined in the initial structure of [BMIm][NO_3] was taken in accordance to those reported in the literature for other ionic liquids [15,16,31]. The potential energy surfaces (PES) for [BMIm][NO_3] by using both levels of theory were studied for variations of the dihedral N2–C12–C15–C18, C12–C15–C18–C21 and C1–H25–O26–N27 angles. Hence, four structures, named C1, C2, C3 and C4, with energies minima were found on the PES where C2 presents a global minimum by using the B3LYP/6-31G* level of theory while C1 and C3 also present global minima by using the 6-311++G** basis set, as it is observed in Table S1 and Figure S1. On the other hand, from Table S1 we clearly observed that C2 presents practically the same energy than C4 with the greater basis set and, for this reason, their properties are basically the same and, hence, the properties for C4 were not considered in this work. Fig. 1 shows the most stable structures C1, C2, C3 and C4 of [BMIm][NO_3] while in Fig. 2 is presented the electronic

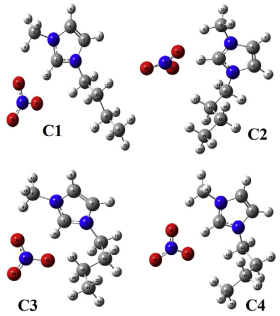

Fig. 1. The B3LYP/6-311++G** optimized molecular structures of all conformers of 1-butyl-3-methylimidazolium nitrate ionic liquid with the atoms numbering.

structure of [BMIm] cation in accordance to that reported for imidazolium cation by Bennett et al. [3]. The atomic natural populations (NPA) and the Mulliken charges were studied for those three structures including the cation while the Merz-Kollman (MK) charges were employed to calculate the corresponding molecular electrostatic potentials (MEP) [32]. The topological properties were calculated employing the AIM2000 program [20] while the, bond orders expressed by Wiberg's indexes and the acceptor-donor interactions energies were obtained from NBO calculations [19]. SQMFF methodology [22] and the Molvib program [23] were used together with the corresponding normal internal coordinates in order to obtain the harmonic force fields for all species. The vibrational assignments were performed from the force fields by using the Potential Energy Distribution (PED) contributions $\geq$ 10% and the experimental available FT-IR spectrum of [BMIm][NO_3] [17] and their experimental FT-Raman spectrum collected for only one sample -1-butyl-3-methylimidazolium nitrate by us. At this point, the dimeric structure of [BMIm][NO3] with the two nitrate anions linked to the C–H bonds belong to the rings [31] was also considered, as shown in Fig. 3. The assignments for the dimeric species were performed with the aid of the *GaussView* program [29]. Now, the predicted infrared and Raman spectra for the dimeric structure are similar to the experimental ones. Here, it is very important to mention that the calculated geometrical parameters and wavenumbers by using both basis sets were compared with the corresponding experimental values by using the root-mean-square

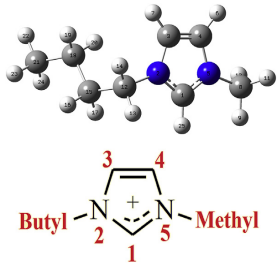

Fig. 2. Molecular theoretical structure of 1-butyl-3-methylimidazolium cation and the atoms numbering by using the B3LYP/6-311++G** method (upper). A scheme of their electronic structure is also presented (bottom).

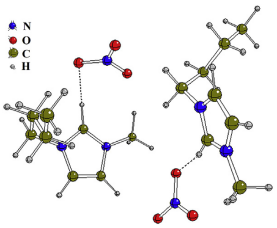

Fig. 3. The geometrical structure of dimer 1-butyl-3-methylimidazolium nitrate ionic liquid calculated by using B3LYP/6-311++G** level. Intramolecular H-bonds are represented with dashed lines.

deviation (RMSD) values in order to find the best results and method in order to perform the corresponding assignments. For all species the volumes in gas phase were computed by using the Moldraw program [33]. The gap values for all species were calculated with the frontier orbitals [24,25] while their reactivities and behaviours were predicted by using global descriptors, as reported in the literature [26–28].

4. Results and discussion

4.1. Structural study in gas phase

In Table 1 the calculated total and relative energies are summarized, together with dipole moments, volume values and populations for the four most stable conformers of [BMIm][NO_3] and, for both cation and dimer. The results by using the B3LYP/6-31G* method show that C2 is the most stable conformer of [BMIm][NO_3] with higher population while C1 and C3 are the most stable species when the 6-311++G** basis set is used. Besides, C1 presents higher relative energy and dipole moment but low population in gas phase by using the B3LYP/6-31G* method. However, when the other basis set is used, their dipole moment and population increases from 12.64 to 13.94 D and from 10.26 to 29%, respectively.

Table 1
Calculated total (E) and relative energies (ΔE), dipolar moment (μ), volume (V) and population values for the most stable conformers of 1-buthyl-3-methyl imidazolium nitrate and their cation in gas phase.

Conformers	E (Hartrees)	ΔE (kJ/mol)	μ (Debye)	V (Å^3)	Population%
B3LYP/6-31G*method/Gas phase					
1-buthyl-3-methyl imidazolium nitrate					
C1	−703.6701	4.20	12.64	222.6	10.23
C2	−703.6717	0.00	11.86	221.1	56.82
C3	−703.6707	2.62	11.67	219.0	19.88
C4	−703.6703	3.67	12.04	223.1	13.07
1-buthyl-3-methyl imidazolium species					
Cation	−423.1781		5.04	188.2	
Dimer	−1407.3829		6.31	454.9	
B3LYP/6-311++G**method/Gas phase					
C1	−703.8838	0.00	13.94	228.3	29
C2	−703.8835	0.79	13.51	226.7	21
C3	−703.8838	0.00	13.84	224.3	29
C4	−703.8835	0.79	13.89	226.5	21
1-buthyl-3-methyl imidazolium cation					
Cation	−423.2869		4.91	191.3	
Dimer	−1407.8013		5.68	458.1	

On the other hand, the pairs of conformers C1 and C3 and, C2 and C4 have the same populations and total and relative energies by using the 6-311++G** basis set. The orientations and directions of the dipole moments vectors corresponding to the four conformers change strongly in relation to the cation, as observed in Fig. 4. Obviously, the presence of two nitrate anions in the dimer evidently modifies the cation structure and, for this reason, also their properties. Hence, when two units of [BMIm][NO_3] are considered by using the 6-31G* basis set the dipole moment value decreases in the dimer to 6.31 D while its volume increases at 454.9 Å^3.

The calculated geometrical parameters for [BMIm][NO_3] by using the 6-31G* level of theory compared with those obtained to the [BMIm] cation by using the RMSD values can be seen in Table 2 while in Table S2 the values for the other basis set are presented In general, the RMSD values for C1 with the 6-31G* basis set are different from those calculated for C2 and C3 where, obviously the better correlations are observed for C2 and C3 but, when the greater basis set is used, C3 clearly presents better correlations for bond lengths and angles (0.008 Å and 1.3°). Carefully evaluating the results, we observed that the N2—C3, C3—C4, C4—N5 and N5—C1 bond lengths practically do not change for one of the two NO_3^- anions of the dimer. However, the values of some parameters for the second nitrate group significantly change, particularly the dihedral angles, as observed in Table 2 and S2. Besides with both basis sets, it is observed that in both monomeric and dimeric species the C1—N2 and N5—C1 bond lengths present practically double bonds characters having in the cation the same values while slightly change in the conformers of ionic liquid. On the other hand, the differences observed in the N2—C12 and N5—C8 bond lengths for the ionic liquid and their cation probably indicate that these two distances are strongly dependent on the length of side chain, thus, when the N atom is linked to the methyl group the value for N5—C8 of C2 is lower by using the 6-31G* basis set (1.467 Å) than N2—C12 whose N atoms are linked to the butyl group (1480 Å), as observed in Table 2 and S2. When the C1—H25 distances are analyzed for all species, we observed that the cation value is lower than those corresponding to the three conformers of [BMIm][NO_3], as it was expected, because the incorporation of the nitrate group to the cation generates H bond interaction between the H25 and O26 atoms and, as a consequence the enlargement of the C1—H25 bonds

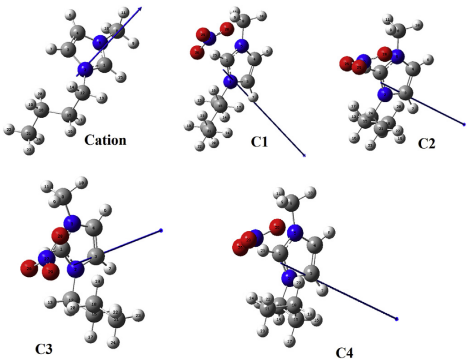

Fig. 4. Magnitudes and orientations of dipole moment vectors corresponding to the most stable conformers of 1-butyl-3-methylimidazolium nitrate and their cation in gas phase at the B3LYP/6-311++G** level of theory.

Table 2
Calculated geometrical parameters for 1-buthyl-3-methyl imidazolium nitrate monomer and dimer compared with those corresponding to the cation.

B3LYP/6-31G* Method[a]					
Parameters	Cation	1-buthyl-3-methyl imidazolium nitrate			
		Monomer			Dimer
		C1	C2	C3	C2
Bond lengths (Å)					
C1–N2	1.338	1.342	1.340	1.339	1.342/1.338
N2–C3	1.382	1.384	1.385	1.386	1.386/1.382
C3–C4	1.363	1.362	1.362	1.362	1.363
C4–N5	1.382	1.384	1.383	1.384	1.382/1.383
N5–C1	1.339	1.339	1.338	1.338	1.338/1.341
N2–C12	1.484	1.478	1.480	1.476	1.480/1484
N5–C8	1.469	1.467	1.467	1.466	1.470/1.466
C1–H25	1.079	1.112	1.107	1.106	1.090/1.098
H25–O26		1.744	1.758	1.751	1.977/1.872
N27–O26		1.287	1.283	1.283	1.267/1.280
N27–O28		1.268	1.269	1.269	1.266/1.254
N27–O29		1.233	1.237	1.236	1.252/1.249
RMSD		**0.012**	**0.010**	**0.010**	
Bond angles (°)					
C1–N2–C3	108.2	109.0	108.9	108.9	108.4/108.7
N2–C3–C4	107.3	106.9	107.0	106.8	107.5/107.1
C3–C4–N5	107.0	106.8	106.8	106.9	106.3/106.9
C4–N5–C1	108.3	109.2	109.1	109.0	109.4/108.7
N5–C1–N2	109.0	107.8	108.0	108.1	108.1/108.4
N5–C1–H25	125.4	126.9	125.2	127.2	126.3/126.5
N2–C1–H25	125.5	125.1	126.6	124.4	125.1/124.9
C4–N5–C8	125.7	126.7	127.3	127.5	125.1/126.7
C1–N5–C8	125.9	123.9	123.3	123.3	125.3/124.5
C1–H25–O26		168.6	167.2	158.3	146.1/162.6
RMSD		**1.1**	**1.2**	**1.4**	
Dihedral angles (°)					
H25–C1–N2–C12	−2.3	1.2	2.1	−0.7	3.7/-3.4
H25–C1–N5–C8	−0.3	−1.3	0.5	−0.6	−6.3/2.7
C1–N2–C3–C4	−0.1	−0.2	−0.1	−0.3	−0.0/0.2
C3–C4–N5–C1	−0.0	−0.0	−0.1	−0.2	0.4/0.0
C12–N2–C3–C4	−178.1	−179.5	−179.1	−175.3	−177.5/-179.4
C8–N5–C4–C3	−179.3	179.4	176.2	176.3	−179.7/-179.5
RMSD		**146.4**	**145.1**	**145.2**	

#Values corresponding to the second nitrate group.
[a] This work.

is observed in the three conformers. In relation to the nitrate groups, we observed that the coordination modes of these groups with the cation is clearly monodentate because the N27–O28 and N27–O29 bond lengths have lower and different values than the N27–O26 bonds by using both basis sets. Hence, partial double bonds characters are observed in those first two bonds, especially by using the 6-311++G** basis set, while the N27–O26 bonds lengths present simple bond characters because these bonds are coordinated to the cations by means of the C1–H25 bonds. Analyzing the bond angles, it is observed that for the cation all the angles by using both basis sets are practically different from those observed in the three conformers of [BMIm][NO_3]. Hence, the three conformers practically show better RMSD values by using the 6-311++G** basis set. Higher differences are observed in the dihedral angles showing better correlations when the 6-311++G** basis set is employed. Such differences can be easily attributed to the different signs and values that present the H25–C1–N2–C12 and C8–N5–C4–C3 dihedral angles. Hence, the length of the side chain has clearly notable influence on the geometrical parameters and, especially on the dihedral angles. Hence, these values also change in the other nitrate group of dimer. Finally, the best approximation to the experimental values was obtained by using the 6-311++G** basis set.

4.2. Charges, molecular electrostatic potentials and bond orders studies

In this section, we have studied the atomic charges, molecular electrostatic potentials and the bond order values for [BMIm][NO_3] and their cation these properties are important due to their ionic nature and to the different interactions expected for these species. Thus, the atomic Merz-Kollman (MK) and Mulliken charges were investigated for all species as a consequence of the nitrate ions present in the ionic liquid. Thus, in Table 3 the calculated MK and Mulliken charges are presented for the most stable conformers of 1-buthyl-3-methyl imidazolium nitrate together with the corresponding to the cation by using the B3LYP/6-31G* level of theory. Table S3 shows those calculated charges by using the 6-311++G** basis set. Note that the MK charges values for the four species by using both basis sets are completely different from the Mulliken ones including for a same atom the values and signs are completely different. For instance, the MK charges on the N2 atoms of the four species by using the 6-31G* basis set have positive signs although the Mulliken ones in these species show negative signs but, by using the 6-311++G** basis set all charges on the N2 atoms have positive signs in all species. On the other side, contrary results can be observed on the C3 and

Table 3
Calculated MK and Mulliken charges for the most stable conformers of 1-buthyl-3-methyl imidazolium nitrate compared with the corresponding to the cation.

B3LYP/6-31G* Method[a]									
MK						Mulliken			
Atoms	Cation	Atoms	C1	C2	C3	Cation	C1	C2	C3
1 C	−0.067	1 C	−0.137	0.000	−0.058	0.302	0.283	0.297	0.292
2 N	0.108	2 N	0.242	0.140	0.083	−0.381	−0.417	−0.413	−0.404
3 C	−0.133	3 C	−0.256	−0.292	−0.198	0.034	0.017	0.018	0.016
4 C	−0.164	4 C	−0.196	−0.165	−0.238	0.031	0.018	0.019	0.020
5 N	0.191	5 N	0.226	0.185	0.271	−0.390	−0.403	−0.400	−0.398
6 H	0.227	6 H	0.202	0.200	0.210	0.234	0.191	0.192	0.191
7 H	0.209	7 H	0.224	0.235	0.219	0.235	0.192	0.192	0.192
8 C	−0.374	8 C	−0.318	−0.359	−0.380	−0.346	−0.359	−0.349	−0.348
9 H	0.175	9 H	0.200	0.202	0.213	0.214	0.271	0.260	0.259
10 H	0.184	10 H	0.140	0.154	0.158	0.230	0.182	0.179	0.182
11 H	0.181	11 H	0.115	0.130	0.126	0.230	0.182	0.186	0.185
12 C	−0.233	12 C	−0.317	−0.147	−0.140	−0.195	−0.155	−0.160	−0.182
13 H	0.136	13 H	0.134	0.095	0.128	0.201	0.192	0.185	0.214
14 H	0.145	14 H	0.103	0.082	0.093	0.205	0.161	0.163	0.166
15 C	0.046	15 C	0.231	0.107	−0.044	−0.263	−0.291	−0.301	−0.262
16 H	0.050	16 H	0.001	0.016	0.018	0.186	0.217	0.147	0.133
17 H	0.020	17 H	−0.023	0.000	0.037	0.156	0.143	0.209	0.152
18 C	0.154	18 C	0.052	0.022	0.266	−0.271	−0.257	−0.260	−0.274
19 H	−0.002	19 H	0.010	−0.004	−0.001	0.150	0.145	0.115	0.157
20 H	−0.019	20 H	−0.009	0.041	−0.015	0.137	0.126	0.161	0.186
21 C	−0.368	21 C	−0.279	−0.302	−0.450	−0.447	−0.447	−0.457	−0.447
22 H	0.115	22 H	0.079	0.085	0.129	0.173	0.146	0.143	0.173
23 H	0.101	23 H	0.084	0.069	0.087	0.166	0.175	0.130	0.130
24 H	0.097	24 H	0.064	0.098	0.101	0.158	0.144	0.200	0.138
25 H	0.220	25 H	0.240	0.183	0.184	0.250	0.322	0.307	0.309
		26 O	−0.576	−0.553	−0.566		−0.520	−0.506	−0.516
		27 N	0.827	0.820	0.848		0.705	0.688	0.693
		28 O	−0.588	−0.566	−0.590		−0.521	−0.507	−0.513
		29 O	−0.473	−0.476	−0.492		−0.442	−0.438	−0.445

C4 atoms with both basis sets. Very important results are obtained regarding the total sum of the MK and Mulliken charges on the C1, N2 and N5 atoms that belong to the imidazole ring, in accordance to the scheme proposed in Fig. 2. We observed that the total sum of the MK charges on those three atoms result in positive values by using both basis sets while the total sum of the Mulliken charges generate negative values for the three conformers of [BMIm][NO_3] with both basis sets, including the cation. Hence, the scheme presented in Fig. 2 where the ring has positive charge is better represented with the MK charges, as compared with the Mulliken ones. The Mulliken charges on the O26 and O28 atoms belong to the nitrate groups and predicted practically the same values by using 6-31G* basis set but slightly different from those observed on the O29 atoms. Hence, this level of theory suggests bidentate coordinations of the nitrate groups in the three conformers. However, a different result is observed from the MK charges, because these charges on the O26 and O28 atoms are unlike between the three O atoms.

In Table 4 the molecular electrostatic potentials (MEP) are summarized for the three conformers of [BMIm][NO_3] and their cation by using the B3LYP/6-31G* level of theory while these values by using the other basis set is presented in Table S4. The mapped surfaces for all species are represented graphically in Fig. 5. The results of Table 4 shows clearly that the MEPs values on all atoms slightly change from cation to the three conformers but the most significant changes are observed on the C1, N2 and N5 atoms located in the rings, in accordance with the corresponding MK charges. Besides, the H25 atoms belong to the C1—H25 bonds also change significantly due to the H bonds formed as a consequence of the coordination of those atoms with the nitrate groups. Here, another very important result is observed in the similar MEP values on the O26, O28 and O29 atoms by using both basis sets indicating probable monodentate coordination for the nitrate groups. If now, we analyzed the different colorations observed from Fig. 5, we observed that the expected blue color that is observed on the cation

Table 4
Calculated molecular electrostatic potentials for 1-buthyl-3-methyl imidazolium nitrate compared with the corresponding to the cation.

B3LYP/6-31G* Method[a]					
Atoms	Cation	Atoms	C1	C2	C3
1 C	−14.474	1 C	−14.642	−14.640	−14.641
2 N	−18.090	2 N	−18.231	−18.232	−18.233
3 C	−14.523	3 C	−14.652	−14.654	−14.655
4 C	−14.523	4 C	−14.654	−14.655	−14.654
5 N	−18.083	5 N	−18.229	−18.231	−18.231
6 H	−0.900	6 H	−1.025	−1.026	−1.026
7 H	−0.902	7 H	−1.024	−1.026	−1.026
8 C	−14.528	8 C	−14.676	−14.674	−14.672
9 H	−0.928	9 H	−1.082	−1.081	−1.078
10 H	−0.934	10 H	−1.073	−1.070	−1.069
11 H	−0.935	11 H	−1.075	−1.074	−1.073
12 C	−14.533	12 C	−14.659	−14.659	−14.663
13 H	−0.946	13 H	−1.076	−1.076	−1.077
14 H	−0.947	14 H	−1.068	−1.070	−1.074
15 C	−14.599	15 C	−14.726	−14.729	−14.719
16 H	−0.986	16 H	−1.117	−1.111	−1.106
17 H	−0.987	17 H	−1.111	−1.120	−1.106
18 C	−14.616	18 C	−14.728	−14.740	−14.747
19 H	−1.009	19 H	−1.122	−1.131	−1.139
20 H	−1.008	20 H	−1.121	−1.135	−1.142
21 C	−14.645	21 C	−14.747	−14.765	−14.756
22 H	−1.027	22 H	−1.127	−1.143	−1.139
23 H	−1.027	23 H	−1.130	−1.143	−1.135
24 H	−1.026	24 H	−1.127	−1.149	−1.136
25 H	−0.870	25 H	−1.039	−1.039	−1.040
		26 O	−22.377	−22.371	−22.374
		27 N	−18.148	−18.143	−18.146
		28 O	−22.379	−22.372	−22.375
		29 O	−22.380	−22.374	−22.377

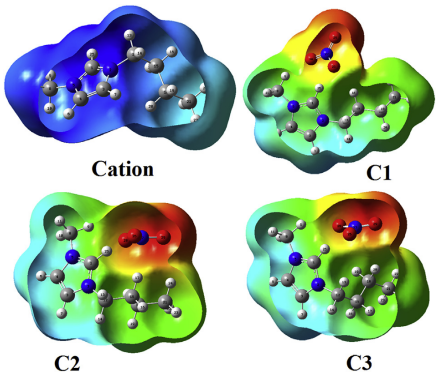

Fig. 5. Molecular electrical potential surfaces of 1-butyl-3-methylimidazolium nitrate and their cation obtained from B3LYP/6-311++G**. Color ranges, in au: from red −0.090 to blue +0.090 and isodensity value of 0.005. (For interpretation of the references to colour in this figure legend, the reader is referred to the Web version of this article.)

clearly represents electrophilic sites while the red and green colours indicate nucleophilic and inert sites, respectively. Here, the red colours observed on the nitrate groups of the three conformers indicate nucleophilic places due to the anionic characteristics of those groups while on the C—H bonds of the rings and, on part of the C—H belong to the CH_3 groups blue colours are observed because these sites are electrophilic places. Finally, on the butyl side chain green colours are observed indicating clearly that these sites are completely inert.

In relation to the bond orders, in Table 5, the bond orders (BO) expressed by Wiberg's indexes for 1-buthyl-3-methyl imidazolium nitrate are given in Table 5 together with the cation while in Table S5 these values are presented by using the other basis set. The bond order values were calculated with the NBO program [19] because they are very useful to indicate the characteristics of the different bonds. In general, the addition of nitrate group to the cation clearly increases the BO of some atoms, as observed by using the 6-31G* basis set. However, when the other basis set is used few atoms decrease their values, as can be seen in Table S5. The BO values for the O26 and O28 atoms belonging to the nitrate groups in the three conformers have approximately the same and low BO values (O—N—O) than those corresponding to the O29 atoms (N═O) which present higher values by using the 6-31G* basis set. But when the other basis set is employed the three O atoms present approximately the same BO values. Evidently, here different coordination modes by using both basis set are predicted for the nitrate groups.

4.3. Energy interactions and topological studies

The above studies by using MK and Mulliken charges, MEPs and bond orders have suggested different coordination modes of the nitrate groups in the three conformers of [BMIm][NO_3] and, for these reasons, the donor-acceptor energy interactions and the topological properties for all species are necessary in order to elucidate the type of interactions that is present in these species. Hence, NBO [19] and AIM calculations were performed to analyze the stabilities of these species by using the topological properties calculated with the AIM2000 program [20] and the Bader' theory

Table 5
Calculated bond orders expressed, as Wiberg indexes by atoms, for the three conformers of 1-buthyl-3-methyl imidazolium nitrate compared with the corresponding to the cation.

B3LYP/6-31G* Method[a]					
Atoms	Cation	Atoms	C1	C2	C3
1 C	2.747	1 C	3.730	3.742	3.738
2 N	2.649	2 N	3.514	3.513	3.514
3 C	2.897	3 C	3.876	3.875	3.876
4 C	2.883	4 C	3.877	3.876	3.877
5 N	2.669	5 N	3.523	3.523	3.517
6 H	0.800	6 H	0.935	0.935	0.935
7 H	0.802	7 H	0.935	0.935	0.935
8 C	2.990	8 C	3.710	3.715	3.718
9 H	0.751	9 H	0.915	0.918	0.917
10 H	0.734	10 H	0.943	0.943	0.943
11 H	0.734	11 H	0.945	0.944	0.944
12 C	3.078	12 C	3.811	3.811	3.801
13 H	0.739	13 H	0.937	0.937	0.929
14 H	0.740	14 H	0.945	0.945	0.942
15 C	3.110	15 C	3.880	3.879	3.902
16 H	0.745	16 H	0.928	0.942	0.951
17 H	0.742	17 H	0.948	0.931	0.942
18 C	3.145	18 C	3.905	3.904	3.889
19 H	0.735	19 H	0.948	0.956	0.947
20 H	0.738	20 H	0.953	0.946	0.938
21 C	3.060	21 C	3.843	3.837	3.848
22 H	0.749	22 H	0.946	0.947	0.939
23 H	0.745	23 H	0.943	0.955	0.955
24 H	0.744	24 H	0.951	0.937	0.953
25 H	0.797	25 H	0.917	0.918	0.917
		26 O	1.852	1.863	1.860
		27 N	4.076	4.077	4.077
		28 O	1.858	1.866	1.861
		29 O	1.989	1.977	1.975

[21]. These donor-acceptor energy interactions for the three conformers of 1-buthyl-3-methyl imidazolium nitrate compared with the corresponding to the cation can be seen in Table 6 while in Table S6 their values are observed with the other basis set. These energy interactions are calculated from the NBO program by using the Second Order Perturbation Theory Analysis of Fock Matrix in NBO Basis, which are expressed as E(2). The deep analysis of these results clearly shows the differences that present the three conformers of [BMIm][NO_3] and their cation. Obviously, the cation is a charged species and, for this reason, it is an unstable species with low donor-acceptor energy interactions, as compared with the neutral species. A total of six interactions are observed for the three conformers but in the cation the $\Delta ET_{LP\rightarrow\ \sigma^*}$ and $\Delta ET_{\pi\rightarrow\ \sigma^*}$ interactions related to the nitrate groups are not observed, as it is expected. Here, the total energy donor-acceptor energy interactions values for C1 and C2 conformers by using both basis sets are higher than those corresponding to C3, being the most stable the C1 conformer by using the 6-31G* basis set but C2 is the most stable species by using the other one. Here, higher stabilities of C1 and C2 are clearly attributed to the π *C1—N2→LPN5* and π*C3-C4→ LPN5* interactions which are not present in C3. Probably, these results could in part be justified by the higher dipole moment values which are observed for both C1 and C2 species and by the higher values of the C1—H25—O26 bond angles observed from Table 2 for those two species (168.6° in C1, 167.2° in C2 and 158.3° in C3). When the greatest basis set is used a new $\Delta ET_{\sigma\rightarrow\ \sigma^*}$ interaction appears which can only be observed in C3. Thus, the total energies support high stabilities for the three species but specifically for C1 by using the 6-31G* basis set and for C2 by using the greatest basis set.

The atom in molecules (AIM) Bader's theory is useful to analyze the intra-molecular and inter-molecular interactions that present different species by using their topological properties [21]. Hence,

Table 6
Main donor-acceptor energy interactions (in kJ/mol) for the three conformers of 1-buthyl-3-methyl imidazolium nitrate compared with the corresponding to the cation.

B3LYP/6-31G*				
Delocalization	Cation	C1	C2	C3
π C1−N2→LPN5	95.60	90.33	89.37	
πC3−C4→ LPN5	0.00	549.00	547.75	
$\Delta ET_{\pi \rightarrow LP}$	**95.60**	**639.33**	**637.12**	
πC1−N2→π^*C3−C4	71.48	77.96	76.91	76.49
πC3-C4→π^* C1−N2	62.41	49.07	48.91	48.24
$\Delta ET_{\pi \rightarrow \pi^*}$	**133.89**	**127.03**	**125.82**	**124.73**
LPN5→ π^*C1−N2	332.10	326.63	328.76	326.33
LPN5 → π^*C3−C4	125.07	136.98	137.40	136.90
LPO26→π^*N27−O29		404.42	304.76	276.97
LPO28→π^*N27−O29		484.09	339.79	306.02
$\Delta ET_{LP \rightarrow \pi^*}$	**457.17**	**1352.10**	**1110.71**	**1046.21**
LPO26→σ^*C1−H25		111.48	87.82	87.11
LPO26→σ^*N27−O29		61.78	67.59	67.17
LPO28→σ^*O26−N27		53.17	53.92	54.38
LPO28→σ^*N27−O29		69.56	68.84	67.84
LPO29→σ^*O26−N27		83.47	80.76	80.47
LPO29→σ^*N27−O28		79.55	78.79	79.50
$\Delta ET_{LP \rightarrow \sigma^*}$		**459.01**	**437.73**	**436.48**
π^*C1−N2→π^*C3−C4	70.98	104.04	102.91	104.67
π^*N27−O29→π^*N27−O29		48.03	45.48	43.68
$\Delta ET_{\pi \rightarrow \pi^*}$	**70.98**	**152.07**	**148.39**	**148.35**
π^*N27−O29→σ^*N27−O29			104.79	141.08
$\Delta ET_{\pi \rightarrow \sigma^*}$			104.79	141.08
ΔE_{Total}	**757.63**	**2729.54**	**2564.55**	**1896.85**

the electron density, $\rho(r)$ and the Laplacian values, $\nabla^2\rho(r)$ were calculated for the three conformers of [BMIm][NO_3] and their cation in the bond critical points (BCPs) by using the AIM 2000 program [20]. The results of those two properties obtained for all species can be seen in Table 7 while in Table S7 the results for the other basis set are summarized. Here, only the interactions for the three conformers were presented because there are not observed

Table 7
Analysis of the topological properties for the three conformers of 1-buthyl-3-methyl imidazolium nitrate compared with the corresponding to the cation.

B3LYP/6-31G*					
C1					
Parameter (a.u.)	H9···O28	H16···O26	H25···O26		
$\rho(r_c)$	0.0202	0.0122	0.0459		
$\nabla^2\rho(r_c)$	0.0644	0.0380	0.1338		
Distances (Å)	2.1030	2.3820	1.7440		
C2					
Parameter (a.u.)	H9···O28	H17···O26	H25···O26	H24···O29	H20···O28
$\rho(r_c)$	0.0173	0.0121	0.0443	0.0075	0.0032
$\nabla^2\rho(r_c)$	0.0542	0.0384	0.1307	0.0260	0.0134
Distances (Å)	2.2030	2.3960	1.7580	2.5800	3.0100
C3					
Parameter (a.u.)	H9···O28		H25···O26	H20···O29	
$\rho(r_c)$	0.0152		0.0451	0.0066	
$\nabla^2\rho(r_c)$	0.0494		0.1357	0.0265	
Distances (Å)	2.2550		1.7510	2.7060	

interactions for the cation. It is necessary to clarify that in $\nabla^2\rho(r) > 0$ and $|\lambda 1|/\lambda 3 < 1$ the interactions are of the H bonds, in accordance with the Bader's theory [21]. Here, the eigenvalues $(\lambda 1, \lambda 2, \lambda 3)$ of the Hessian matrix were no presented. Table 7 and S7 show H bonds formations in the three conformers; having C1 and C3 three H bonds of different characteristics while in C2 the number of H bonds increases to five. Note that by using the 6-31G* basis set the H9···O28 and H25···O26 interactions are present in the three conformers and, that the density observed for the H25···O26 interaction is higher in the C1 conformer probably because the distance between those two atoms is lower. With the other basis set the number of interactions decreases for C1 from 3 to 2 and for C2 from 5 to 3 while for C3 the number of interactions does not change. Those two interactions clearly support the bidentate coordination for the three conformers. Clearly, C2 has the higher number of H bonds and, as a consequence, higher stability is expected for this conformer by using the 6-31G* basis set but, when the other basis set is employed C2 presents the same stability than C3. Obviously, the basis set has notable influence on the H bonds interactions and, hence, on their stabilities.

4.4. Evaluation of gap energies and global descriptors

The energy difference between the HOMO and LUMO frontier orbitals (gap) is important to predict the reactivities of diverse species, in accordance to Parr and Pearson [24] and Brédas [25]. Thus, the HOMO and LUMO orbitals, defined as highest occupied molecular orbital and the lowest unoccupied molecular orbital respectively, are also practical to calculate useful descriptors that are necessary to predict the behaviour of the species in different media [26–28]. Hence, in Table 8 the calculated frontier orbitals, energy band gap, chemical potential (μ), electronegativity (χ), global hardness (η), global softness (S), global electrophilicity index (ω) and global nucleophilicity index (E) for [BMIm][NO_3] and their cation are compared with the values obtained for p-xylylenediaminium bis(nitrate) and their cation [34]. Then, in Table S8 the values by using the 6-311++G** basis set are presented. If first, the gap values for the three conformers and their cation are compared by using the 6-31G* basis set, we observed the same values for C2 and the cation (−4.36 eV) and for C1 and C3 (−4.3764 eV) where the two first have lower values than the second ones, for these reasons, these two C1 and C3 species have slightly low reactivities as compared with those two species. When these gap values are compared by using the B3LYP/6-311++G** method the cation and C2 are the most reactive species but the three conformers of ionic liquid are more reactive than their cation and than the p-xylylenediaminium and their cation [39]. Note that the p-xylylenediaminium cation is less reactive than the [BMIm] one by using the 6-31G* basis set but on the contrary is observed with the other basis set. Analyzing the descriptors, we observed that despite C2 and the [BMIm] cation and C1 and C3 have the same gap values all species, they show different softness values by using both basis sets. In relation to the electrophilicity and nucleophilicity indexes, it is observed that the cations of both nitrate species present higher indexes than the corresponding neutral species but these values are higher for p-xylylenediaminium bis(nitrate) in relation to the ionic liquid probably because this species has two nitrate groups in their structure while the ionic liquid presents only one nitrate group. Both cations are positively charged species and electrophilics and, for these reasons, they have higher electrophilicity indexes. These descriptors are compared in Table 8 and S8 with other reported for species with different properties, such as, the two antimicrobial tautomers of 1,3-benzothiazole, thione and thiol [35], the antiviral thymidine [36] and with the toxic species CN^-, CO and saxitoxin

Table 8
Calculated HOMO and LUMO orbitals, energy band gap, chemical potential (μ), electronegativity (χ), global hardness (η), global softness (S), global electrophilicity index (ω) and global nucleophilicity index (E) for [BMIm][NO_3] and their cation.

B3LYP/6-31G* method[a]					B3LYP/6-311++G**[b]	
Frontier orbitals (eV)	[BMIm]	[BMIm][NO^3]			p-Xylylenediaminium	p-xylylenediaminium bis(nitrate)
	Cation	C1	C2	C3	Cation	neutral
HOMO	−11.6033	−5.0336	−5.1743	−5.0980	−14.4150	−7.5729
LUMO	−4.8613	−0.8388	−0.8143	−0.7216	−8.5800	−1.8621
GAP	−4.3600	−4.3764	−4.3600	−4.3764	−5.8350	−5.7108
Descriptors (eV)						
χ	−3.3710	−2.0974	−2.1800	−2.1882	−2.9175	−2.8554
μ	−8.2323	−2.9362	−2.9943	−2.9098	−11.4975	−4.7175
η	3.3710	2.0974	2.1800	2.1882	2.9175	2.8554
S	0.1483	0.2384	0.2294	0.2285	0.1714	0.1751
ω	10.0520	2.0552	2.0564	1.9347	22.6551	3.8970
E	−27.7511	−6.1584	−6.5276	−6.3672	−33.5440	−13.4703

B3LYP/6-31G*						
Frontier orbitals (eV)	Thionec	Thiol[c]	Thymidine[d]	CN[e]	CO[e]	Saxitoxin[e]
HOMO	−6.4443	−6.8847	−6.9621	−21.0491	−10.1077	−13.656
LUMO	−2.7918	−2.6194	−1.4443	−18.8917	−0.5926	−7.1273
GAP	−3.6525	−4.2653	−5.5178	−2.1574	−9.5151	−6.5287
Descriptors (eV)						
χ	−1.8263	−2.1327	−2.7589	−1.0787	−4.7576	−3.2644
μ	−4.61805	−4.7521	−4.2032	−19.9704	−5.3502	−10.3917
η	1.8263	2.1327	2.7589	1.0787	4.7576	3.2644
S	0.2738	0.2345	0.1812	0.4635	0.1051	0.1532
ω	5.8388	5.2943	3.2018	184.8600	3.0083	16.5403
E	−8.4337	−10.1345	−11.5962	−21.5421	−25.4536	−33.9220

χ = - [E(LUMO) - E(HOMO)]/2; μ = [E(LUMO) + E(HOMO)]/2; η = [E(LUMO) − E(HOMO)]/2.
$S = ½\eta$; $\omega = \mu^2/2\eta$; $E = \mu^*\eta$.
[a] This work.
[b] From Ref [34].
[c] From Ref [35].
[d] From Ref [36].
[e] From Ref [28].

[28]. Here, we observed that the electrophilicity index values for the three conformers of the ionic liquid by using both basis sets are closer to the values observed for CO while their cation also presents nucleophilicity index closer to toxical agent CO [28]. Note that the nucleophilicity indexes for the three conformers with the 6-311++G** basis set are closer to thione [35]. With the greater basis set, C2 is the most reactive conformer including those two compared species while the compared cations have high values of electrophilicity and nucleophilicity indexes. These latter indexes calculated with the 6-311++G** basis set are closer to the value observed for thione [35]. Thus, these results clearly evidence that the basis set has remarkable influence on the reactivities and behaviors of these species in gas phase.

5. Vibrational analysis

In this analysis, the optimized structures in gas phase of the three conformers of [BMIm][NO_3] with monodentate coordination and their cation were considered by using the B3LYP/6-311++G** method, in accordance to their calculated low RMSD values for both geometries and wavenumbers. Hence, all monomeric structures were optimized with C_1 symmetries where the monomers and their cation present 81 and 69 vibration normal modes, respectively and, where all modes present activity in both spectra. The FT-IR spectrum was taken from that reported for [BMIm][NO_3] in liquid phase by Gruzdev et al. [17] while their FT-Raman spectrum was recorded by us. Both spectra are respectively given in Figs. 6 and 7, compared with the corresponding predicted for the most stable monomers C1 and C3 and the dimer. In those two figures we observed good correlations among the experimental and the predicted spectra when the dimeric species are considered. In particular, the Raman spectra shows a very good correlation when the predicted spectrum expressed in activities are corrected to intensities by using equations reported in the literature [37,38]. The band observed in the infrared spectrum at 3490 cm^{-1} can be assigned to the OH stretching modes of water, as reported by Gruzdev et al. [17] because during the preparation of this ionic liquid the reactives are dissolved in water. On the other hand, the band at 2386 cm^{-1} is clearly attributed by Gruzdev et al. [17] to the cation-anion interaction between the imidazole ring and the nitrate groups. Here, the very strong band observed in the IR spectrum at 1344 cm^{-1}, which is assigned to vibrations NO_3^- by Gruzdev et al. [17], is predicted with low intensity in the IR spectra of the monomer while the intensity of this band is increased in the dimer. In the same way, the band at 1362 cm^{-1} predicted in the Raman spectrum with low intensity is clearly increased in the dimer. Besides, the groups of bands located in the higher wavenumbers region in the Raman spectrum of the monomer are visibly predicted with higher intensities than in the dimer. Hence, the presence of the dimer could probably justify the strong intensities of those bands in both spectra. On the other side, the strong Raman band at 1417 cm^{-1} could also justify the presence of the dimer because a

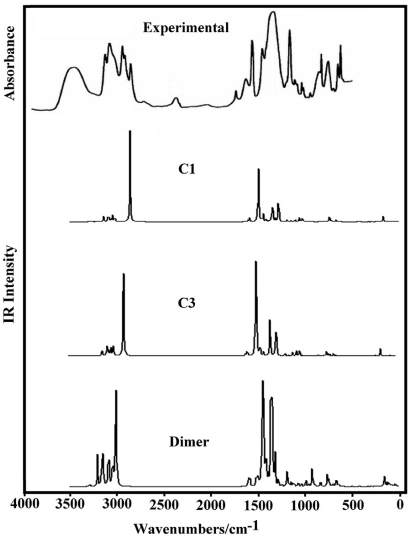

Fig. 6. Comparison of experimental FTIR spectrum [17] with predicted (B3LYP/6-311++G**) gas phase infrared spectra for the most stable monomers C1 and C3 and the dimer of the most stable conformer of 1-butyl-3-methylimidazolium nitrate.

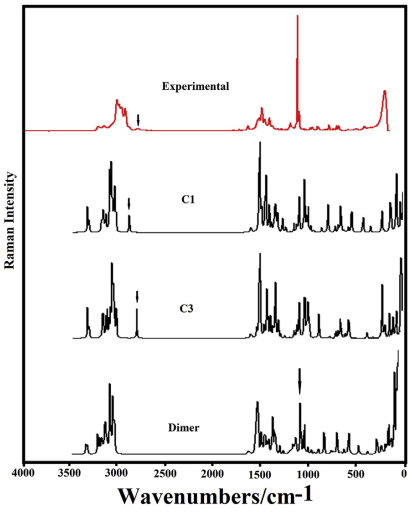

Fig. 7. Experimental Raman spectrum of 1-butyl-3-methylimidazolium nitrate compared with the predicted for the most stable structures of monomer and dimer in the gas phase at B3LYP/6-311++G** level of theory.

symmetric CH_3 deformation mode is predicted in this species at 1416 cm^{-1}. Here, the differences observed between both experimental and predicted spectra can be in part attributed to the calculations because they were performed in gas phase where the packing forces were not considered. The force fields of those monomer and cation species were computed by using the internal coordinates and the SQMFF procedure [22] with the Molvib program [23] and considering harmonic force fields. The scale factors used in the refinement process to obtain the harmonic scaled force fields were those reported in the literature [22]. In Table 9 the observed and calculated wavenumbers are presented together with assignments for the monomers and dimer of 1-buthyl-3-methyl imidazolium nitrate and their cation in gas phase by using the B3LYP/6-311++G** level of theory. Here, the better approximations are obtained with that method because the initial RMSD values for C1, C2, C3 and their cation are respectively 46.70, 45.21, 48.20 and 68.12 cm^{-1} while the final values decrease up to 19.73, 19.01, 18.03 and 24.14 cm^{-1}, respectively. These values are also presented in Table 9. The complete assignments for the three monomers and their cation were performed using the potential energy distribution (PED) contributions $\geq$ 10% and the corresponding experimental spectra while for the dimer the assignments were performed with the *GaussView* program [29]. We have discussed below only the assignments performed for the most important groups of [BMIm][NO_3] and their cation (see Table 9).

5.1. Bands assignments

5.1.1. C–H modes

For the three conformers of [BMIm][NO_3] and their cation are expected the stretching, in-plane and out-of-plane deformation modes due to the C1–H25, C3–H7 and C4–H6 groups that belong to the imidazoline rings. Here, in the three conformers and their cation the C3–H7 and C4–H6 stretching modes are predicted coupled between them by SQM calculations in the 3156-3139 cm^{-1} region while in the dimer these modes are predicted between 3203 and 3007 cm^{-1} and, for these reasons, those modes are assigned between 3170/3163 and 2942/2941 cm^{-1}. As expected, in the four species the symmetrical modes are assigned to the Raman band of medium intensity at 3163 cm^{-1} while the corresponding antisymmetric modes can be assigned to the IR bands at 3147 and 3101 cm^{-1}. Note that in the three conformers of [BMIm][NO_3] the C1–H25 stretching modes are predicted at 2793 and 2717 cm^{-1}, hence, they are easily assigned to the IR and Raman bands at 2743 and 2738 cm^{-1}, respectively. In the cation, the C1–H25 stretching mode is predicted at 3142 cm^{-1} and assigned to the IR band at 3147 cm^{-1}. Obviously, the presences of the nitrate groups shift these modes toward lower wavenumbers in the three conformers. However, the C1–H25 in-plane deformation modes are predicted in all conformers between 1312 and 1307 cm^{-1} while in the cation this mode is predicted at 1134 cm^{-1}. Hence, those modes are assigned in the predicted regions by SQM calculations. The other C3–H7 and C4–H6 in-plane deformation modes are predicted in the cation to higher wavenumbers (1272/1095 cm^{-1}) than the three conformers (1081 and 1078 cm^{-1}). Thus, these modes are assigned between 1272 and 1078 cm^{-1}. In the dimer these modes are predicted between 1319 and 1191 cm^{-1}.

5.1.2. CH_3 modes

In the monomers and cation a total of 18 vibration normal modes are expected because there are two CH_3 groups in their structures. Hence, the antisymmetric modes were predicted between 3033 and 2959 cm^{-1} while the symmetric modes between 2942 and 2893 cm^{-1}. Hence, the Raman bands of the medium intensities at 2941, 2913 and 2874 cm^{-1} are assigned to those symmetrical modes. The deformation modes are predicted in species containing these groups between 1474 and 1366 cm^{-1} [26,36,39],

Table 9
Observed and calculated wavenumbers (cm^{-1}) and assignments for the most stable conformers of 1-buthyl-3-methyl imidazolium nitrate and their cation and dimer in gas phase.

Experimental		Monomer								Dimer[a]	
		Cation[a]		C1[a]		C2[a]		C3[a]			
IR[b]	Ra[a]	SQM[c]	Assignment[a]	SQM[c]	Assignment[a]	SQM[c]	Assignment[a]	SQM[c]	Assignment[a]	Calc[d]	Assignment[a]
3170sh	3163 m									3203	νC−H
3170sh	3163 m	3156	ν_sC−H	3155	ν_sC−H	3156	ν_sC−H	3154	ν_sC−H	3163	$\nu_a CH_3$
3147 m	3147sh	3142	νC1−H25	3137	ν_aC−H	3139	ν_aC−H	3137	ν_aC−H	3151	νC−H
3101s	3101w	3139	ν_aC−H	3011	$\nu_a CH_3$(C8)	3007	$\nu_a CH_3$(C8)	3013	$\nu_a CH_3$(C8)	3144	νC−H
3101s	3101w	3033	$\nu_a CH_3$(C8)	3000	$\nu_a CH_3$(C8)	2998	$\nu_a CH_3$(C8)	3000	$\nu_a CH_3$(C8)	3131	$\nu_a CH_3$
											$\nu_s CH_2$
3057sh	3022sh	3018	$\nu_a CH_3$(C8)							3050	$\nu_s CH_3$
2988sh	2988sh	2995	$\nu_a CH_2$(C12)	2992	$\nu_a CH_2$(C12)	2977	$\nu_a CH_2$(C12)	2993	$\nu_a CH_2$(C12)	3007	νC−H
2962s	2962 m	2979	$\nu_a CH_3$(C21)	2967	$\nu_a CH_3$(C21)	2969	$\nu_a CH_3$(C21)	2967	$\nu_a CH_3$(C21)	3003	$\nu_s CH_2$
2962s	2962 m	2967	$\nu_a CH_3$(C21)	2959	$\nu_a CH_3$(C21)	2960	$\nu_a CH_3$(C21)	2955	$\nu_a CH_3$(C21)	2998	$\nu_s CH_2$
2953sh		2951	$\nu_s CH_2$(C12)								
2942sh	2941 m	2942	$\nu_s CH_3$(C8)	2942	$\nu_s CH_2$(C15)	2943	$\nu_a CH_2$(C15)	2940	$\nu_s CH_2$(C12)		
2942sh	2941 m	2937	$\nu_a CH_2$(C15)	2932	$\nu_s CH_2$(C12)	2929	$\nu_s CH_2$(C12)	2932	$\nu_a CH_2$(C18)		
2924sh	2913 m			2920	$\nu_s CH_3$(C8)	2915	$\nu_s CH_3$(C8)	2921	$\nu_s CH_3$(C8)		
2924sh	2913 m	2909	$\nu_a CH_2$(C18)	2917	$\nu_a CH_2$(C18)	2909	$\nu_a CH_2$(C18)	2918	$\nu_a CH_2$(C15)		
2924sh	2913 m	2907	$\nu_s CH_3$(C21)	2898	$\nu_s CH_3$(C21)	2900	$\nu_s CH_3$(C21)	2897	$\nu_s CH_2$(C18)		
2875s	2874 m	2898	$\nu_s CH_2$(C15)	2891	$\nu_s CH_2$(C15)	2897	$\nu_s CH_2$(C15)	2893	$\nu_s CH_3$(C21)		
2875s	2874 m	2882	$\nu_s CH_2$(C18)	2885	$\nu_s CH_2$(C18)	2872	$\nu_s CH_2$(C18)	2884	$\nu_s CH_2$(C15)		
2743w	2738w			2743	νC1−H25	2717	νC1−H25	2793	νC1−H25		
1646w	1662w									1608	νC=C,νC=N
1579s	1569w	1548	νC3−C4,νN5−C1	1550	νC3−C4	1550	νN5−C1	1550	νC3−C4	1599	νC=C,νC=N
1579s	1569w	1539	νN2−C1	1534	βC1−H25	1539	νC3−C4,νN2−C1	1533	νN2−C1	1582	νC=C,νC=N
1465s	1450 m	1449	$\delta_a CH_3$(C8)	1450	$\delta_a CH_3$(C8)	1450	$\delta_a CH_3$(C8)	1450	$\delta_a CH_3$(C8)	1495	δCH_2
1465s	1450 m	1445	$\delta_a CH_3$(C21)	1448	δCH_2(C18),δCH_2(C15)	1448	$\delta_a CH_3$(C21)	1446	δCH_2(C18)	1488	δCH_2
1465s	1450 m			1443	$\delta_a CH_3$(C8)	1447	$\delta_a CH_3$(C8)	1442	δCH_2(C12)	1469	$\delta_s CH_3$
1465s	1450 m	1438	$\delta_a CH_3$(C21)	1440	$\nu_a NO_2$	1442	δCH_2(C12)	1441	$\delta_a CH_3$(C8)	1450	$\nu_a NO_2$
1465s	1450 m	1434	δCH_2(C12)	1438	$\delta_a CH_3$(C21),δCH_2(C12)	1437	$\nu_a NO_2$	1440	$\nu_a NO_2$	1440	$\nu_a NO_2$
	1417s	1429	δCH_2(C18)	1435	$\delta_a CH_3$(C21)	1436	$\delta_a CH_3$(C21)	1436	$\delta_a CH_3$(C21)		
	1417s			1428	δCH_2(C18)	1432	δCH_2(C15)	1430	$\delta_a CH_3$(C21)	1427	wagCH_2
	1417s	1422	$\delta_a CH_3$(C8)	1423	δCH_2(C15)	1424	δCH_2(C18)				
	1417s	1414	δCH_2(C15)					1417	δCH_2(C15)	1416	$\delta_s CH_3$
1408sh	1387 m	1396	$\delta_s CH_3$(C8)	1400	$\delta_s CH_3$(C8)	1402	$\delta_s CH_3$(C8)	1400	ρCH_2(C12),νN2−C1	1407	wagCH_2
1408sh	1387 m	1391	νN2−C3	1396	νN2−C1,νN2−C3	1396	wagCH_2(C15)	1399	$\delta_s CH_3$(C8)	1400	wagCH_2
	1387 m	1375	wagCH_2(C15)	1385	wagCH_2(C12)	1388	wagCH_2(C12),(C15)	1387	wagCH_2(C18)	1388	wagCH_2
1344vs	1338 m	1363	wagCH_2(C12),(C18)	1368	wagCH_2(C18)			1371	wagCH_2(C12)	1364	νN−C,$\nu_a NO_2$
1344vs	1338 m	1361	$\delta_s CH_3$(C21)			1358	$\delta_s CH_3$(C21)			1360	νN−C,$\nu_a NO_2$
1344vs	1338 m	1354	wagCH_2(C12)	1353	$\delta_s CH_3$(C21)	1352	wagCH_2(C12)	1354	$\delta_s CH_3$(C21)	1357	νN−C,$\nu_a NO_2$
1344vs	1338 m	1316	wagCH_2(C18)	1344	νN5−C1	1340	νN2−C3	1343	νN5−C1	1348	νN−C,$\nu_a NO_2$
	1312sh			1312	βC1−H25,βC4−H6	1327	wagCH_2(C18)	1316	wagCH_2(C15)	1319	βC−H
	1302sh	1300	wagCH_2(C18),(C15)	1302	νN2−C12	1312	βC1−H25	1310	ρCH_2(C18)	1315	βC−H
	1302sh	1300		1302	ρCH_2(C18),ρCH_2(C15)	1301	τC1−H25,νN2−C12	1307	βC1−H25		
1286sh	1283sh	1292	ρCH_2(C18)	1282	wagCH_2(C15)	1289	ρCH_2(C18)	1293	ρCH_2(C18),νN5−C8	1282	ρCH_2
1286sh	1283sh	1272	βC3−H7	1271	ρCH_2(C18),ρCH_2(C12)					1279	ρCH_2
1266sh	1254w	1235	ρCH_2(C15)			1257	νN27−O26,$\nu_s NO_2$	1249	ρCH_2(C12)	1241	ρCH_2
1266sh	1254w			1244	νN27−O26	1250	ρCH_2(C15)	1237	ρCH_2(C15)	1237	ρCH_2
	1212w	1188	ρCH_2(C12)	1192	ρCH_2(C12)	1207	ρCH_2(C12)	1197	ρCH_2(C12)	1191	βC−H
1169s	1168w			1147	νN5−C8	1155	τC1−H25,τO26−H25	1139	βC1−H25,νN2−C12	1168	ρCH_3
	1130sh	1134	βC1−H25	1131	ρ′CH_3(C8)	1132	ρ′CH_3(C8)	1132	ρ′CH_3(C8)	1146	ρCH_3
1119w	1117w	1118	ρ′CH_3(C8)	1105	ρCH_3(C21)					1121	ρCH_3
1099sh	1090w	1095	βC4−H6			1094	ρCH_3(C21)	1092	ρCH_3(C21)	1109	ρCH_3
1087sh		1087	ρCH_3(C21),νC15−C18	1079	βC4−H6,βC3−H7	1081	βC3−H7,βC4−H6	1078	βC4−H6,βC3−H7	1072	$\nu_s NO_2$
1048w	1042vs	1075	ρ′CH_3(C21)	1074	ρ′CH_3(C21),τwCH_2(C15)	1080	ρ′CH_3(C21),ρCH_3(C8)	1071	ρ′CH_3(C21)	1062	νC−C
	1042vs	1069	ρCH_3(C8)	1070	ρCH_3(C8)	1073	ρCH_3(C8)	1067	ρCH_3(C8)	1040	βR_2

	1042vs	1023	βR_2	1024	βR_2	1027	βR_2	1030	$\beta R_2 \nu N2-C3$	1038	βR_2
	1042vs	1013	$\beta R_1 \nu N5-C4$	1021	$\nu_s NO_2$	1025	$\tau C1-H25,\tau O26-H25$	1021	$\nu_s NO_2,\nu N27-O26$	1032	βR_1
1028w	1023 m			1017	$\nu C15-C18,\nu C18-C21$	1017	$\gamma C1-H25$			1031	βR_1
1028w	1023 m	1003	$\nu C18-C21$			1014	$\tau C1-H25,\tau O26-H25$	1011	$\nu C18-C21$		
	988vw			998	$\beta R_1,\nu N5-C4$	999	$\nu N5-C4,\beta R_1$	999	$\beta R_1 \nu N5-C4$	999	$\beta R_1,\nu C-C$
	988vw			992	$\gamma C1-H25$			993	$\gamma C1-H25$	993	$\nu C-C$
982vw	974w			976	$\nu C12-C15$	962	$\nu C12-C15,\nu C18-C21$			989	$\gamma C-H$
952vw	947w	957	$\nu C12-C15$					959	$\nu C12-C15$	957	τwCH_2
897sh	906w	908	$\rho CH_3(C21)$	893	$\tau wCH_2(C12),\rho' CH_3(C21)$	910	$\tau wCH_2(C12)$	911	$\tau wCH_2(C12)$	921	$\gamma C-H$
	883w			888	$\rho CH_3(C21),\nu C15-C18$					891	τwCH_2
862sh	860vw	867	$\gamma_a C-H$							858	$\gamma C-H$
862sh	860vw	842	$\tau wCH_2(C15)$			847	$\tau wCH_2(C15),\rho' CH_3(C21)$	844	$\tau wCH_2(C15)$		
837 m	826w	821	$\gamma C1-H25$	838	$\gamma_a C-H$	840	$\gamma_a C-H$	839	$\gamma_a C-H$	836	γNO_2
825sh	811w			814	γNO_2	817	γNO_2	814	γNO_2	828	γNO_2
761 m		774	$\tau wCH_2(C12),\nu C15-C18$			776	$\tau wCH_2(C12),\nu C15-C18$	778	$\nu C15-C18$	764	τwCH_2
743sh	752w	741	$\gamma_s C-H$	740	$\tau wCH_2(C18)$					760	τwCH_2
731sh	733w			727	$\gamma_s C-H$	729	$\gamma_s C-H$	727	$\gamma_s C-H$	745	$\gamma C-H$
731sh	733w			721	$\nu N2-C12$					720	δNO_2
	711sh	701	$\tau wCH_2(C18)$			712	ρNO_2			717	δNO_2
702w	706w			710	ρNO_2	710	ρNO_2 $\tau wCH_2(C18)$	710	ρNO_2	716	δNO_2
702w	706w			706	δNO_2	707	δNO_2	706	δNO_2	715	δNO_2
	699sh							702	$\tau wCH_2(C18)$	706	$\nu N-C$
672sh		668	$\nu N5-C8$	669	$\tau wCH_2(C15)$	673	$\tau wCH_2(C18),\nu N5-C8$	673	$\nu N5-C8$	672	τR_1
658w	658w			650	$\gamma N2-C12$					663	τR_1
624 m	624w	634	τR_1			636	$\tau C1-H25 \tau R_1$	636	τR_1	641	τR_1
604w	601w	613	τR_2	618	τR_2	615	$\tau R_2 \tau R_1$	615	τR_2	635	τR_2
604w	601w			610	τR_1					600	τR_2
604w	601w	570	$\nu N2-C12$			578	$\nu N2-C12$	581	$\nu N2-C12$	592	τR_2
	500w	481	$\delta_C 12C15C18$	432	$\delta_C 15C18C21,\delta N2C12C15$	501	$\delta_C 15C18C21$	486	$\delta_C 12C15C18$	499	δCCC
	415w	410	$\beta N5-C8,\beta N2-C12$	409	$\beta N2-C12$	413	$\beta N5-C8$	417	$\beta N5-C8,\beta N2-C12$	420	$\beta N-C$
	326w	320	$\delta N2C12C15$	315	$\nu N2-C12$	318	$\delta N2C12C15$	311	$\delta_C 15C18C21,\delta N2C12C15$	331	$\delta CCC,\delta NCC$
	285vw	282	$\delta_C 15C18C21$	281	$\beta N5-C8$	294	$\beta N2-C12,\gamma N2-C12$	299	$\beta N5-C8,\beta N2-C12$	294	$\beta N-C$
	258vw	241	$\gamma N5-C8$	244	$\gamma N5-C8,\delta_C 12C15C18$	251	$\gamma N5-C8$	241	$\gamma N5-C8$	253	$\gamma N-C$
	215sh	221	$\tau wCH_3(C21)$	210	$\tau wCH_3(C21)$	223	$\tau wCH_3(C21)$	219	$\tau wCH_3(C21),\gamma N5-C8$	219	$\gamma N-C$
	198sh	201	$\delta_C 12C15C18,\gamma N5-C8$	195	$\gamma N5-C8,\delta_C 12C15C18$	199	$\delta_C 12C15C18$	204	$\tau wCH_3(C21)$	204	τwCH_3
	198sh					176	$\tau C1-H25,\tau O26-H25$			175	$\tau C-C$
				163	$\nu H25-O26$	164	$\nu H25-O26$	157	$\nu H25-O26$	162	τwCH_3
		141	$\gamma N2-C12$			145	$\tau wCH_3(C8)$	154	$\gamma N2-C12$	149	τwCH_3
				136	$\tau wCH_3(C8)$			134	$\tau wCH_3(C8)$	142	τwCH_3
	110s			105	$\tau C15-C18$	113	$\delta_H 25O26N27,\delta_C 1H25O26$			125	$\delta CHO,\delta HON$
	110s			100	$\delta_H 25O26N27$			95	$\delta_H 25O26N27$	104	δHON
	84sh			82	$\tau C1-H25$	86	$\tau C1-H25,\tau O26-H25$			86	$\tau C-C$
	84sh	75	$\tau C15-C18,\tau C12-C15$					78	$\tau C15-C18,\tau C12-C15$	78	$\tau N-O$
		66	$\gamma N5-C8$	74	$\tau C12-C15$	70	$\tau C12-C15,\tau C15-C18$	70	$\tau C1-H25$	72	$\tau N-O$
						69	$\tau C1-H25$				
		58	$\tau wCH_3(C8)$	56	$\tau N27-O26$			60	$\delta_H 25O26N27,\delta_C 1H25O26$	60	$\tau C-H$
				50	$\delta_H 25O26N27,\tau C1-H25$	45	$\tau C1-H25,\tau O26-H25$	46	$\delta_H 25O26N27,\delta_C 1H25O26$	48	$\tau C-H$
						33	$\tau wC12-N2$	31	$\tau N27-O26,\tau wC12-N2$	37	$\tau wC-N$
				26	$\tau C1-H25,\tau O26-H25$	28	$\tau N27-O26$	23	$\delta_C 1H25O26$	28	$\tau wC-N$
		19	$\tau wC12-N2$	17	$\delta_C 1H25O26$			14	$\tau O26-H25$	20	$\tau O-H$
				11	$\tau O26-H25$	9	$\tau O26-H25$			13	$\tau O-H$
RMSD (cm^{-1})		24.14		19.73		19.01		18.03			

Abbreviations ν, stretching; wag, wagging; τ, torsion; ρ, rocking; τw, twisting; δ, deformation; a, antisymmetric; s, symmetric.

[a] This work.

[b] From Ref [17].

[c] From scaled quantum mechanics force field B3LYP/6-311++G** method.

[d] From B3LYP/6-311++G** method.

Table 10
Comparison of scaled internal force constants for the most stable conformers of 1-buthyl-3-methyl imidazolium nitrate and their cation in gas phase.

B3LYP Method						
Force constants	6-31G*[a]				6-311++G**	6-311++G
	1-buthyl-3-methyl imidazolium	1-buthyl-3-methyl imidazolium nitrate			p-xylylene-diaminium bis(nitrate)[b]	Chromyl nitrate[c]
	Cation	C1	C2	C3		
$f(\nu N{=}O)$		8.50	8.30	8.30	9.74	15.83
$f(\nu N{-}O)$		6.80	6.90	6.90	4.25	3.22
$f(\nu C{-}H)$	5.50	5.16	5.23	5.20		
$f(\nu CH_2)$	4.80	4.78	4.78	4.81		
$f(\nu CH_3)$	4.97	4.88	4.88	4.90		
$f(\nu C{-}N)_R$	6.75	6.75	6.82	6.75		
$f(\nu C{-}N)$	4.25	4.45	4.50	4.50		
$f(\nu C{=}C)$	7.70	7.80	7.80	7.80		
$f(\nu C{-}C)$	4.00	4.03	4.03	4.03		
$f(\delta CH_2)$	0.80	0.80	0.80	0.80		
$f(\delta CH_3)$	0.57	0.60	0.58	0.55		
$f(\delta NO_2)$		1.60	1.60	1.60	1.53	
Force constants	6-311++G**[a]				6-311++G**	6-311++G
	1-buthyl-3-methyl imidazolium	1-buthyl-3-methyl imidazolium nitrate			p-xylylene-diaminium bis(nitrate)[b]	Chromyl nitrate[c]
	Cation	C1	C2	C3		
$f(\nu N{=}O)$		8.00	8.00	7.95	9.74	15.83
$f(\nu N{-}O)$		6.50	6.50	6.50	4.25	3.22
$f(\nu C{-}H)$	5.40	5.10	5.14	5.13		
$f(\nu CH_2)$	4.73	4.73	4.71	4.73		
$f(\nu CH_3)$	4.87	4.82	4.80	4.82		
$f(\nu C{-}N)_R$	6.60	6.57	6.60	6.60		
$f(\nu C{-}N)$	4.15	4.35	4.35	4.35		
$f(\nu C{=}C)$	7.60	7.60	7.60	7.60		
$f(\nu C{-}C)$	3.93	3.93	3.93	3.93		
$f(\delta CH_2)$	0.77	0.8	0.80	0.80		
$f(\delta CH_3)$	0.52	0.52	0.53	0.52		
$f(\delta NO_2)$		1.60	1.60	1.60	1.53	

Units are mdyn $Å^{-1}$ for stretching and mdyn Å rad^{-2} for angle deformations.
[a] This work.
[b] From Ref. [34].
[c] From Ref. [41,42].

in the three conformers they are predicted between 1450 and 1396 cm^{-1} and, for this reason, those modes were clearly assigned in this region, as detailed in Table 9. The symmetric CH_3 deformation mode predicted in the dimer at 1416 cm^{-1} can be easily assigned to the strong Raman band at 1417 cm^{-1}. The rocking modes are predicted in different regions and in some cases coupled with other modes, thus, in the cation they are predicted between 1118 and 908 cm^{-1}, in the three conformers between 1132 and 847 cm^{-1} while in the dimer between 1168 and 1109 cm^{-1}. Hence, the bands observed in those regions are assigned to these vibration modes.

The twisting modes are predicted for all species in approximately the same regions, and in particular, in C3 one of them is predicted coupled with the out-of-plane deformation mode. In the cation, these modes are predicted in 221 and 58 cm^{-1} while in the monomers between 223 and 134 cm^{-1}, as in species with similar groups [26,36,39]. In the dimer these modes are predicted between 204 and 142 cm^{-1}, as indicated in Table 9.

5.1.3. CH_2 modes

The antisymmetric and symmetric stretching modes expected for the three CH_2 groups of cation and the three conformers of [BMIm][NO_3] are predicted between 2993 and 2872 cm^{-1} while in the dimer, they are predicted between 3003 and 2998 cm^{-1}, hence, the IR and Raman bands observed in these regions can be assigned to those vibration modes. Note that the symmetric modes were assigned to the Raman bands of medium intensities at 2962, 2941, 2913 and 2874 cm^{-1}, as observed for other species containing these groups [26,27,36,39]. The deformation, wagging, rocking and twisting modes expected for these species were predicted in the expected regions [26,27,36,39] and for this reason, they were assigned to the IR and Raman bands at 1450/1417, 1417/1283, 1302/1112 and 952/672 cm^{-1}, respectively.

5.1.4. Nitrate groups

Here, the nitrate groups in the three monomers and dimer of [BMIm][NO_3] were considered with monodentate coordinations because the N–O bonds were predicted by SQM calculations with different values (see Table 2) because one of the tree bonds is predicted with lower value (N–O) than the other ones (O=N=O), as observed in similar nitrate species [35,40–43]. For instance, the N=O stretching modes are observed between 1672 and 1460 cm^{-1} [40–42] but, in $NbO(NO_3)_3$ these modes were assigned between 1763 and 1753 cm^{-1} [43]. Considering bidentate coordination in p-xylylenediaminiumbis(nitrate) [34], the NO_2 antisymmetric stretching modes were assigned at 1313 cm^{-1} while the N=O stretching modes were assigned at 1536 cm^{-1}. Here, we expected for the nitrate groups of monomers two NO_2 antisymmetric and symmetric stretching modes and only one N–O stretching mode. The strong IR band at 1465 cm^{-1} is clearly assigned to the NO_2 antisymmetric stretching modes for the three monomers while in the dimer these modes are assigned to the strong IR band at

1344 cm^{-1}. However, the corresponding symmetric modes are predicted in different regions in the three species, thus, these modes in C1 and C3 are assigned to the very strong Raman band at 1042 cm^{-1} while in C2 that symmetric mode is predicted at 1257 cm^{-1} coupled with the N27–O26 stretching mode. In the dimer the symmetric stretching mode is predicted at 1072 cm^{-1} but assigned to the strong Raman band at 1042 cm^{-1}. In p-xylylenediaminiumbis(nitrate) [34] the deformation modes were predicted by calculations at 783 cm^{-1} while the two O═N═O deformation modes in the monomers and dimer species are predicted between 720 and 706 cm^{-1}. Here, these deformation modes were assigned to the Raman bands between 733 and 706 cm^{-1} while the rocking modes were also assigned to the shoulder at 711 cm^{-1} because these modes are predicted in this region. The wagging modes were assigned to the weak Raman bands at 826 and 811 cm^{-1} because they are predicted by calculations at 836/814 cm^{-1}. The torsion modes were assigned as predicted by calculations at 78/28 cm^{-1}, as detailed in Table 9.

5.1.5. Skeletal modes

The N5═C1, N2═C1 and C3═C4 stretching modes were predicted in the three conformers and the cation in different regions, and, for these reasons, these bonds present different double bond characteristics, as observed in Table 9. Thus, in the cation, these modes are predicted at 1548 (N5═C1, C3═C4) and 1539 (N2═C1) cm^{-1} and with double bond characters while in C1 are predicted at 1550 (C3═C4), 1396 (N2═C1) and 1344 (N5═C1) cm^{-1}, where clearly only the two latter have partial double bond character. In C2, the three bonds have double bond characters because they are predicted at 1550 and 1539 cm^{-1} while in C3, the C3═C4 and N2═C1 stretching modes are predicted with double bond characters at 1550 and 1533 cm^{-1} while the N5═C1 stretching mode is predicted with partial double bond character because it is predicted at 1343 cm^{-1}. Evidently, the presence of the anion and the position of the side chain modify in part the nature and characteristics of these bonds. The N5–C8 stretching modes, in species containing the N–CH_3 group, such as tropane species, are predicted at 1128-1031 cm^{-1} [44–46]. Here, the N5–CH_3 stretching modes of the four species are predicted in different regions, hence, in C1 is predicted at 1147 cm^{-1} while in the cation, C2 and C3 are predicted between 673 and 668 cm^{-1}. The other N2–C12 bonds are linked to the buthyl groups, as it is expected due to their longer chain in the lower wavenumbers region. Thus, in the cation that mode is predicted at 570 cm^{-1}, in C1 at 315 cm^{-1}, in C2 at 578 cm^{-1} while in C3 at 581 cm^{-1}. Later, they were assigned in these regions, as can be observed in Table 9. The C–C stretching modes corresponding to the butyl chain are predicted with simple bond characters, as it is expected and, for this reason, they are assigned between 1017 and 778 cm^{-1}, as predicted by calculations. The two expected deformations (β_{R1} and β_{R2}) and torsions (τ_{R1} and τ_{R2}) rings, for the imidazoline rings were assigned as predicted the SQM calculations and, as reported for similar species with five members rings [44–46].

6. Force constants

In Table 10, for the three conformers of [BMIm][NO_3]and their [BMIm] cation, the calculated force constants are presented compared with those reported for p-xylylene-diaminium bis(nitrate) [34] and chromyl nitrate [41,42]. They were computed from their corresponding harmonic force fields calculated at by the using 6-31G* and 6-311++G** basis sets and with the SQMFF methodology [22] and the Molvib program [23]. Analyzing the force constants values for the three conformers at by the using 6-31G* basis set we observed that the *f(νN═O)* and *f(νN-O)* constant values practically do not change in C2 and C3 but in C1 the values are slightly different from C2 and C3. On the other hand, the $f(\nu C{-}N)_R$ and *f(νC–N)* force constants related to the rings and to the side chains are completely different, as it is expected because the bonds related with these constants that belong to the rings present double bonds characters and, for this reason, they have higher values than the other ones. And, for the same reason, the *f(νC═C)* and *f(νC–C)* force constants present different values. When the other basis set is used the values undergo clear diminishing with exception of the $f(\delta CH_2)$ and $f(\delta NO_2)$ force constants probably because their corresponding bond angles do not change when the size of the basis set increases. When the values for the *f(νN═O)* and *f(νN–O)* constants are compared with those reported for p-xylylene-diaminium bis(-nitrate) [34] and for chromyl nitrate [41,42] we observed different values. In the first case, probably the observed differences can be justified by the two nitrate groups present in p-xylylene-diaminium bis(nitrate) [34] while in the second case the presence of strong bidentate coordinations with the Cr atom can explain those differences observed.

7. Conclusions

In the present work, we have studied the cation-anion interactions of the 1-butyl-3-methylimidazolium nitrate ionic liquid in gas phase by using the hybrid B3LYP/6-31G* and B3LYP/6-311++G** calculations and the experimental Raman spectrum. From the four C1, C2, C3 and C4 conformers found in the PES for this ionic liquid, by using both levels of theory, only three of them were studied because C2 and C4 have practically the same energies and properties. The results obtained for C1, C2 and C3 show better correlations in geometries and wavenumbers when the 6-311++G** basis set is employed, as evidenced by their corresponding RMSD values. Here, the atomic charges, molecular electrostatic potentials, stabilization energies, bond orders and topological properties were computed for those three most stable isomers. The MK charges suggest coordination monodentate for the three conformers while the studies by means of the Mulliken charges, MEPs and BO clearly support the coordination bidentate for the nitrate groups of [BMIm][NO_3]. Besides, the total sum of the MK charges on the C1, N2 and N5 atoms evidence positive sign on the imidazole ring, a result different from that obtained for the Mulliken ones. The NBO study shows clear differences among the three conformers being the more stable C1 by using 6-31G* basis set and C2 with the other basis set. Besides, the NBO study evidences high stability of the neutral species as compared with the cation. Evidently, the nitrate groups strongly stabilize the [BMIm] cation in the ionic liquid. The AIM study reveals the high stability of the C2 conformer of [BMIm][NO_3] and clearly supports the bidentate coordination for their three conformers. Both NBO and AIM calculations support the high stability of C2 by using the B3LYP/6-311++G** level of theory. The SQMFF procedure was employed together with the normal internal coordinates and the experimental available FTIR and FTRaman in order to perform the complete vibrational assignments of all species. The force constants were also reported for the monomers and their cation by using both levels of theory. The presence of the dimeric species of ionic liquid supports the strong bands observed in both experimental infrared and Raman spectra at 1344 and 1042 cm^{-1}, respectively. The study by the frontier orbitals reveals that the ionic liquid is slightly less reactive than the cation probably due to the low values of nucleophilicity and electrophilicity indexes of the ionic liquid. Finally, the reactivities and behaviour of these species in gas phase slightly change when the size of the basis set increases.

Acknowledgements

This work was supported with grants from CIUNT Project Nº 26/D207 (Consejo de Investigaciones, Universidad Nacional de Tucumán). The authors would like to thank Prof. Tom Sundius for his permission to use MOLVIB.

Appendix A. Supplementary data

Supplementary data related to this article can be found at https://doi.org/10.1016/j.molstruc.2018.03.100.

References

[1] G. Gonfa, M.A. Bustam, Z. Man, M.I. Abdul Mutalib, Unique structure and solute-solvent interaction in imidazolium based ionic liquids: a review, Asian Trans. Eng. 1 (5) (2011) 24–34 (ATE-20114053).
[2] H. Weingärtner, Understanding ionic liquids at the molecular level: facts, problems, and controversies, Angew. Chem. Int. Ed. 47 (2008) 654–670.
[3] V. Bennett, S.S. Angaye, E.D. Dikio, Conductance of 1-Butyl-3-methylimidazolium nitrate [BMIm][NO3] with N,N-dimethylformamide at T (293.15 – 323.15) K, Int. J. Chem. Chem. Proc. 3 (1) (2017) 23–34.
[4] S. Ivanova, L.F. Bobadilla, A. Penkova, F. Romero Sarria, M.A. Centeno, J.A. Odriozola, Gold functionalized supported ionic liquids catalyst for CO oxidation, Catalysts 1 (2011) 52–68.
[5] K.1 Seethalakshmi, E. Jasmine Vasantha Rani, R.1 Padmavathy, N. Radha, FT-IR spectral analysis of imidazolium chloride, Int. J. Cur. Res. Rev. 4 (19) (2012) 31–36.
[6] L.N. Sim, S.R. Majid, A.K. Arof, Effects of 1-butyl-3-methyl imidazolium trifluoromethanesulfonateionic liquid in poly(ethyl methacrylate)/poly(-vinylidenefluoride–co–hexafluoropropylene) blend based polymer electrolyte system, Electrochim. Acta 123 (2014) 190–197.
[7] Takahiro Takekiyo, Yukihiro Yoshimura, Ionic liquid-induced unique structural transitions of proteins, progress and developments in ionic liquids, Intech, Chapter 5 (2017) 97–116, https://doi.org/10.5772/65886.
[8] Hiranmayee Kandala, Comprehensive Structural, Thermal and Toxicological Characterization of 1-ethyl-3-methylimidazolium Alkylbenzenesulfonate Ionic Liquids, Thesis, South Dakota State University, 2017.
[9] Jingsi Gao, Norman J. Wagner, A new correlation between excess viscosity and excess molar volume for 1-butyl-3-methylimidazolium tetrafluoroborate ([C4mim][BF4]) mixtures with water, Langmuir, J. Mol. Liq. 223 (2016) 678–686.
[10] Alexander Kokorin (Ed.), Ionic liquids: Applications and Perspectives, Intech, 2011.
[11] Mukund Ghavre, Low Toxicity Imidazolium & Pyridinium Ionic Liquids: Synthesis, Antimicrobial Toxicity, Biodegradation Studies and Applications in Tsuji-trost Reactions, Thesis, School of Chemical Sciences Dublin City University, 2012.
[12] M. Keÿler, Nanocatalysis in Ionic Liquids Syntheses, Characterisation and Application of Nanoscale Catalysts, Thesis, Universität zu Köln, 2014.
[13] C. Aliaga, S. Baldelli, Sum frequency generation spectroscopy and double-layer capacitance studies of the 1-butyl-3-methylimidazolium dicyanamide-platinum interface, J. Phys. Chem. B 110 (37) (2006) 18481–18491.
[14] J.-H. Wang, D.-H. Cheng, X.-W. Chen, Z. Du, Z.-L. Fang, Direct extraction of double-stranded DNA into ionic liquid 1-Butyl-3-methylimidazolium hexafluorophosphate and its quantification, Anal. Chem. 79 (2) (2007) 620–625.
[15] M.-A. Neouze, M. Litschauer, Confinement of 1-Butyl-3-methylimidazolium nitrate in metallic silver, J. Phys. Chem. B 112 (51) (2008) 16721–16725.
[16] P.A. Hunt, I.R. Gould, Structural characterization of the 1-Butyl-3-methylimidazolium chloride ion pair using ab initio methods, J. Phys. Chem. 110 (6) (2006) 2269–2282.
[17] M.S. Gruzdev, L.M. Ramenskaya, U.V. Chervonova, R.S. Kumeev, Preparation of 1-butyl-3-methylimidazolium salts and study of their phase behavior and intra-molecular interactions, Russ. J. Gen. Chem. 79 (8) (2009) 1720–1727.
[18] E.P. Grishina, et al., Water effect on physicochemical properties of 1-butyl-3-methylimidazolium based ionic liquids with inorganic anions, J. Mol. Liq. 177 (2013) 267–272.
[19] E.D. Glendening, J.K. Badenhoop, A.D. Reed, J.E. Carpenter, F. Weinhold, NBO 3.1, Theoretical Chemistry Institute, University of Wisconsin, Madison, WI, 1996.
[20] F. Biegler-Köning, J. Schönbohm, D. Bayles, AIM2000; a program to analyze and visualize atoms in molecules, J. Comput. Chem. 22 (2001) 545.
[21] R.F.W. Bader, Atoms in Molecules, a Quantum Theory, Oxford University Press, Oxford, 1990, ISBN 0198558651.
[22] a) G. Rauhut, P. Pulay, J. Phys. Chem. 99 (1995) 3093–3099;
b) Correction G. Rauhut, P. Pulay, J. Phys. Chem. 99 (1995) 14572.
[23] T. Sundius, Scaling of ab initio force fields by MOLVIB, Vib. Spectrosc. 29 (2002) 89–95.
[24] R.G. Parr, R.G. Pearson, Absolute hardness: companion parameter to absolute electronegativity, J. Am. Chem. Soc. 105 (1983) 7512–7516.
[25] J.-L. Brédas, Mind the gap!, Materials Horizons 1 (2014) 17–19.
[26] F. Chain, M.A. Iramain, A. Grau, C.A.N. Catalán, S.A. Brandán, Evaluation of the structural, electronic, topological and vibrational properties of *N*-(3,4-dimethoxybenzyl)-hexadecanamide isolated from Maca (*Lepidium meyenii*) using different spectroscopic techniques, J. Mol. Struct. 1119 (2016) 25–38.
[27] D. Romani, S.A. Brandán, M.J. Márquez, M.B. Márquez, Structural, topological and vibrational properties of an isothiazole derivatives series with antiviral activities, J. Mol. Struct. 1100 (2015) 279–289.
[28] D. Romani, S. Tsuchiya, M. Yotsu-Yamashita, S.A. Brandán, Spectroscopic and structural investigation on intermediates species structurally associated to the tricyclic bisguanidine compound and to the toxic agent, saxitoxin, J. Mol. Struct. 1119 (2016) 25–38.
[29] A.B. Nielsen, A.J. Holder, Gauss View 3.0, User's Reference, GAUSSIAN Inc., Pittsburgh, PA, 2000–2003.
[30] M.J. Frisch, G.W. Trucks, H.B. Schlegel, G.E. Scuseria, M.A. Robb, J.R. Cheeseman, G. Scalmani, V. Barone, B. Mennucci, G.A. Petersson, H. Nakatsuji, M. Caricato, X. Li, H.P. Hratchian, A.F. Izmaylov, J. Bloino, G. Zheng, J.L. Sonnenberg, M. Hada, M. Ehara, K. Toyota, R. Fukuda, J. Hasegawa, M. Ishida, T. Nakajima, Y. Honda, O. Kitao, H. Nakai, T. Vreven, J.A. Montgomery Jr., J.E. Peralta, F. Ogliaro, M. Bearpark, J.J. Heyd, E. Brothers, K.N. Kudin, V.N. Staroverov, R. Kobayashi, J. Normand, K. Raghavachari, A. Rendell, J.C. Burant, S.S. Iyengar, J. Tomasi, M. Cossi, N. Rega, J.M. Millam, M. Klene, J.E. Knox, J.B. Cross, V. Bakken, C. Adamo, J. Jaramillo, R. Gomperts, R.E. Stratmann, O. Yazyev, A.J. Austin, R. Cammi, C. Pomelli, J.W. Ochterski, R.L. Martin, K. Morokuma, V.G. Zakrzewski, G.A. Voth, P. Salvador, J.J. Dannenberg, S. Dapprich, A.D. Daniels, O. Farkas, J.B. Foresman, J.V. Ortiz, J. Cioslowski, D.J. Fox, Gaussian 09, Revision A.02, Gaussian, Inc., Wallingford CT, 2009.
[31] H. Geng, L-h Zhuang, J. Zhang, G-w. Wang, A-l Yuan, 3,3-Dimethyl-1,1-(butane-1,4-diyl)-diimidazolium bis(tetrafluoroborate), Acta Crystallogr. E66 (2010) o1267.
[32] B.H. Besler, K.M. Merz Jr., P.A. Kollman, Atomic charges derived from demi-empirical methods, J. Comp. Chem. 11 (1990) 431–439.
[33] P. Ugliengo, MOLDRAW Program, University of Torino, Dipartimento Chimica IFM, Torino, Italy, 1998.
[34] S. Gatfaoui, N. Issaoui, S.A. Brandán, T. Roisnel, H. Marouani, Synthesis and characterization of p-xylylenediaminiumbis(nitrate). Effects of the coordination modes of nitrate groups on their structural and vibrational properties, J. Mol. Struct. 1135 (2017) 209–221.
[35] D. Romani, S.A. Brandán, Structural, electronic and vibrational studies of two 1,3-benzothiazole tautomers with potential antimicrobial activity in aqueous and organic solvents. Prediction of their reactivities, Computational and Theoretical Chem. 1061 (2015) 89–99.
[36] M.B. Márquez, S.A. Brandán, A structural and vibrational investigation on the antiviral deoxyribonucleoside thymidine agent in gas and aqueous solution phases, Int. J. Quant. Chem. 114 (2014) 209–221.
[37] G. Keresztury, S. Holly, G. Besenyei, J. Varga, A.Y. Wang, J.R. Durig, Vibrational spectra of monothiocarbamates-II. IR and Raman spectra, vibrational assignment, conformational analysis and ab initio calculations of S-methyl-N,N-dimethylthiocarbamate, Spectrochim. Acta 49A (1993) 2007–2026.
[38] D. Michalska, R. Wysokinski, The prediction of Raman spectra of platinum(II) anticancer drugs by density functional theory, Chem. Phys. Lett. 403 (2005) 211–217.
[39] F.E. Chain, M.F. Ladetto, A. Grau, C.A.N. Catalán, S.A. Brandán, Structural, electronic, topological and vibrational properties of a series of N-benzylamides derived from Maca (Lepidium meyenii) combining spectroscopic studies with ONION calculations, J. Mol. Struct. 1105 (2016) 403–414.
[40] ISBN: 978-1-62257-352-3, Edited CollectionS.A. Brandán (Ed.), Nitrate: Occurrence, Characteristics and Health Considerations, Nova Science Publishers, Inc, 2012.
[41] S.A. Brandán, in: Ken Derham (Ed.), A structural and vibrational study of the chromyl chlorosulfate, fluorosulfate, and nitrate compounds, vol. 1, Springer Science, Business Media B.V., Van Godewijckstraat 30, 3311 GZ Dordrecht, Netherlands, 2012. ISBN: 978-94-007-5762-2.
[42] S.A. Brandán (Ed.), Descriptors, Structural and Spectroscopic Properties of Heterocyclic Derivatives of Importance for the Health and the Enviromental, Edited Collection, Nova Science Publishers, Inc, 2015. ISBN: 978-1-63482-708-9.
[43] M.V. Castillo, E. Romano, H.E. Lanús, S.B. Díaz, A.Ben Altabef, S.A. Brandán, Theoretical structural and experimental vibrational study of niobyl nitrate, J. Mol. Struct. 994 (2011) 202–208.
[44] S.A. Brandán, Why morphine is a molecule chemically powerful. Their comparison with cocaine, Indian J. Appl. Res. 7 (7) (2017) 511–528.
[45] R.A. Rudyk, S.A. Brandán, Force field, internal coordinates and vibrational study of alkaloid tropane hydrochloride by using their infrared spectrum and DFT calculations, Paripex Indian J. Res. 6 (8) (2017) 616–623.
[46] D. Romani, S.A. Brandán, Vibrational analyses of alkaloid cocaine as free base, cationic and hydrochloride species based on their internal coordinates and force fields, Paripex Indian J. Res. 6 (9) (2017) 587–602.

Research article

Journal of RAMAN SPECTROSCOPY

Received: 15 January 2016 Revised: 13 May 2016 Accepted: 17 June 2016 Published online in Wiley Online Library

(wileyonlinelibrary.com) DOI 10.1002/jrs.4983

Two-dimensional Raman spectroscopy study of ionogel phase formation in long-chain ionic liquid/water systems

Jonas Kausteklis, Vytautas Balevičius and Valdemaras Aleksa*

The phase behavior of the imidazolium-based room temperature ionic liquids (RTILs) 1-decyl-3-methyl-imidazolium bromide and chloride ([C_{10}mim][Br], [C_{10}mim][Cl]) were studied by 2D Raman correlation spectroscopy and principal component analysis. The hydrogen-bonded network changes and the liquid crystalline ionogel phase formation were observed when water content was continuously increased in the system, and the Raman shift of C–H stretching modes in spectra was monitored. The extent of liquid crystalline ionogel phase was determined from the discontinuities in the concentration dependencies. The focus to the Raman bands originated from the imidazolium ring C–H stretching mode region (3000–3200 cm^{-1}) when water content in the IL was increased allowing to determine the lower border of ionogel phase formation in RTIL/water systems. The upper border of the ionogel phase was determined when main attention was carried out to the Raman bands originated from the O–H stretching vibration region (3200–3800 cm^{-1}). The hypothesis of weaker hydrogen bonds involving the C(4)-H and C(5)-H groups and stronger hydrogen bonds of the C(2)-H groups was supported by Raman results. Copyright © 2016 John Wiley & Sons, Ltd.

Keywords: ionogel; ionic liquids; hydrogen bonding

Introduction

In many fields of application, room temperature ionic liquids (RTILs) are involved as solvents. Important research field persists physical and chemical properties, their assurance of stability, and variation identification. Water significantly changes the properties of IL. Electrical conductivity, solubility, viscosity, and polarity can be changed by impurities, especially water.[1] Therefore the IL/water system behavior must be carefully analyzed in order to broaden the understanding of ionogel phase formation in RTILs/water systems.[2] Raman spectroscopy was used to study RTILs/water systems, while water content was continuously increased from 0 to the 30% mass fraction of water. At this concentration range some of imidazolium-based RTILs with long alkyl chains can form various liquid crystalline (LC) ionogel phases in water solutions.[3–9] Ionogel have attracted considerable attention in the areas of biomaterials, electro-optics, and as templates for the preparation of mesoporous materials and ordered thin films.[10] In certain cases, ionogel can be considered to behave as 'smart' material; it possess an intrinsic ability to sense and definitely to respond to various external stimuli in a predictable way.[5] ILs carry different properties; therefore, structures with water are differently formed; in the case of [C_{12}mim][Br], phases were determined precisely, being lamellar (L_α) and hexagonal (H_1) ones,[5] and for the [C_{10}mim][Br], it was identified as the LC ionogel.[4,9] Various methods were used to study LC phases and heterogeneities of them in neat ILs and ionic RTIL/water mixtures.[11–17] Vibrational spectroscopy, Fourier transform infrared spectroscopy (FTIR) and Raman, can be a particularly powerful method to study the states of imidazolium ring C(2)-H, C(4)-H, and C(5)-H interaction with water in the IL/water mixtures.[18–21] The 2D Raman spectroscopy was employed as a tool of precise determination of LC phase lower border at the [C_{10}mim][Br] and [C_{10}mim][Cl] and explained the role of anion in this process.

Experimental

The 1-decyl-3-methyl-imidazolium bromide and chloride from Merck KGaA Darmstadt and from Ionic Liquids Technologies GmbH (the structure and atom numbers are shown in Fig. 1) were dried under vacuum at 80 °C for 1 day. The water used in experiment was freshly distilled. The samples of [C10mim][Br]/water and [C10mim][Cl]/water systems were prepared by weighting (±0.1 mg) the components. In the cases of extremely viscous gel formed, those RTIL/water mixtures were weighted and mixed homogeneously by standing the samples at 23 °C for half an hour. For the Raman spectra obtainment, the Bruker MultiRAM FT-Raman spectrometer with the motorized xyz-sample stage and with the liquid nitrogen-cooled germanium detector was used. The 1064 nm wavelength beam of the pulsed neodymium-doped yttrium aluminum garnet (Nd:YAG) laser (500 mW) as the excitation source and the 180° scattering geometry was employed in the experiments, while the resolution of the spectrometer was set to the 2 cm^{-1}. Average of the 400 Raman spectra were recorded to get better signal to noise ratio at spectral range 70–4000 cm^{-1} when the temperature at 23 °C was continuously maintained. To avoid background, samples were prepared and measured in silica

* *Correspondence to: Aleksa Valdemaras, Faculty of Physics, Vilnius University, Saulėtekio 9-3, LT-10222 Vilnius, Lithuania.*
E-mail: valdemaras.aleksa@ff.vu.lt

Vilnius University, Faculty of Physics, Saulėtekio 9-3, LT-10222 Vilnius, Lithuania

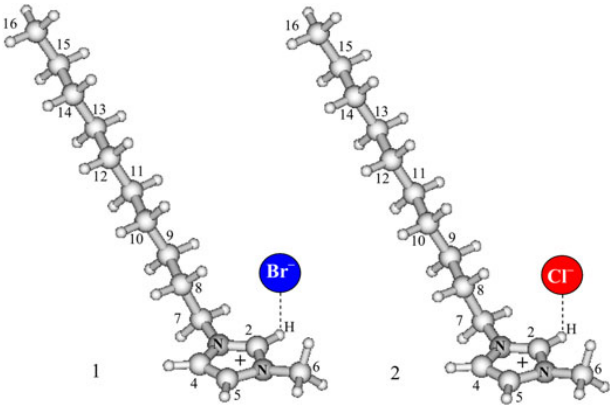

Figure 1. Molecular structure and carbon numbering of [C10mim][X], [X] = Br, Cl.

cells. While neat IL spectra were measured, low background level was found and allowed us to obtain both qualitative and quantitative information only used for spectrum normalization and linear baseline subtraction processing. The FT-Raman spectrometer control and experimental data digital processing were performed using the OPUS 7.0 and the Origin 8.0 software program packages. Principal component analysis (PCA) and 2D Raman correlation analysis was carried out using the MathCAD program written in the Laboratory of Raman Spectroscopy at Vilnius University.

Results and discussion

During the work with ILs/water mixtures, we have encountered various well-known phenomena in phase behavior and aggregation (micellization) process, which were observed in some of imidazolium-based IL [$C_n$mim][X] with long alkyl chains (n = 8–18).[22] When the little water content (0.1% w/w of H_2O) added to [C_{10}mim][Cl] and [C_{10}mim][Br] water molecules tends to interact with anions rather than self-aggregate, complexes anion···H–O–H···anion with symmetrical H bond between anions and water molecules were formed.[20] Such network formation apparently serves to enhance the segregation of the hydrophilic and hydrophobic segments of the [$C_{10}mim^+$], thereby leading to the regions of confined water and, ultimately, to the onset of gel formation.[4] The simultaneous appearance of a smectic LC phase indicates that the formation of H bonds between imidazolium rings, mediated by a channel of water, provides enhanced ordering of the parallel molecular layers.[4] Previous NMR, quantum chemistry calculations, and vibrational spectroscopy studies claim that the most pronounced dependence of chemical shift on amount of water was observed for H-bonded C(2)-H···Br bridge proton, while the weakest effect was detected for the terminal methyl group, C(16)-H_3.[23,24] Further addition of water caused IL/water system conversion from liquid to the gel phase. Gelation is unlikely raised from 2D alkyl chain packing effect.[4] Authors[5,8] discussed various imidazolium-based RTILs with long alkyl chain phase formation models in water and provided the structures of them. For [C_{10}mim][Br], it was identified as LC ionogel,[4] while the coexisting mesophases in [C_{12}mim][Br] were identified as lamellar (LR) and hexagonal (H1).[5,12,25] Moreover, depending on the temperature and sample composition, the regions of various coexisting phases were measured on the phase diagram, and the model suggested that gels are created by noncovalent interactions among the constituent molecules.[5] At the higher content of water (~5% w/w of H_2O) IL/water mixtures, the phase changed from thick liquid into hardened gel. The phase transition could be seen by the eye, but the exact border was measured in our work. The formation of the gel caused the experimental challenge with homogenous sample preparation, which was solved with the usage of mechanical and ultrasound mixing techniques. [C_{10}mim][Br]/H_2O and [C_{10}mim][Cl]/H_2O ionogels were found to be stable over range of ~5–40% w/w of H_2O.[26] In order to check the anion influence for the ionogel phase formation, long-chain ILs, IL/water samples with different water content were prepared and investigated. Main attention was focused to the imidazolium ring Raman vibrational modes at the region 3000–3200 cm^{-1} where the wavenumber changes induced by the addition of water were observed. Raman spectra of [C_{10}mim][Cl] and [C_{10}mim][Br] depicted in Fig. 2 with vibrational wavenumbers of the imidazolium ring

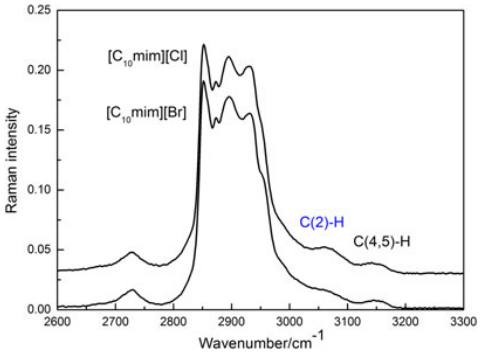

Figure 2. High-frequency range of Raman spectra of neat [C10mim][Cl] (upper) and [C10mim][Br](lower).

Journal of RAMAN SPECTROSCOPY

C(2)-H and C(4,5)-H stretching modes, marked mode 'names' (refer also to Table 1). Raman band structure of ILs, similar to RTILs investigated in our work, was resolved in previous studies.[27,28] The wavenumber correlation was found in experimental data where the assignment was made to the vibrational mode νC(2)-H of the Raman band at around 3080 cm^{-1} and to the vibrational mode νC(4,5)-H of the Raman band at around 3150 cm^{-1} (Table 1). LC phase formation and the strength of the cation–anion interaction through hydrogen bonding were investigated monitoring the wavenumber of Raman spectra bands assigned to the $[C_{10}mim]^+$ cation C–H stretching vibrational modes of imidazolium ring at the carbon positions 2, 4, and 5.[29] According to the literature, the hydrogen bond involving aromatic C–H on the imidazolium ring classified as red shift H bond.[30,31] In Fig. 3, Raman band shift of C(2)-H and C(4,5)-H imidazolium ring stretching modes was depicted with various water mass fractions in

Table 1. Broad vibrational bands in CH region

Ionic liquids	$[C_6mim][Cl]$	$[C_8mim][Cl]$	$[C_{10}mim][Cl]$	$[C_{10}mim][Br]$
Raman shift		Wavenumber/cm^{-1}		
C–H stretching (position 2)	3062	3070	3043	3060
C–H stretching (positions 4 and 5)	3142	3143	3147	3144
Refference	Experiment [27]	Experiment [3]	Our experiment	Our experiment

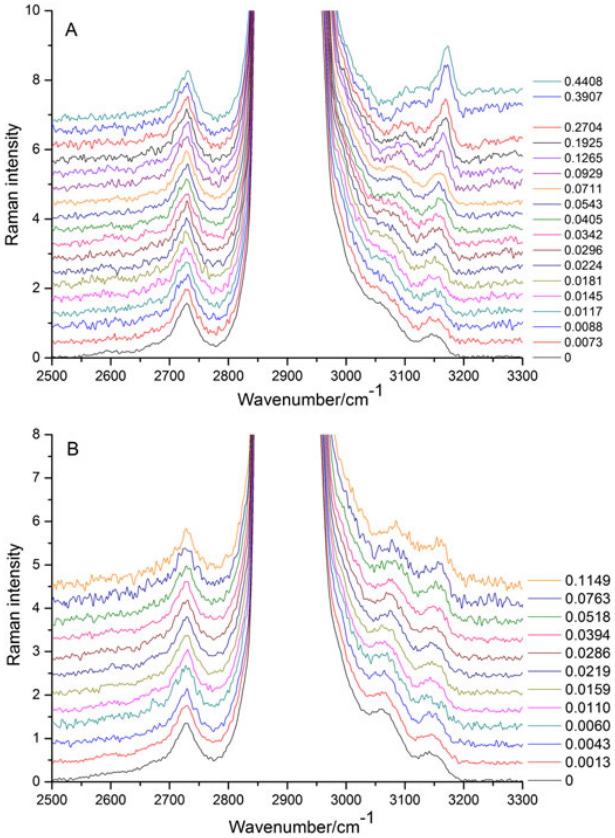

Figure 3. Raman spectra of [C10mim][Cl]/water (upper A) and [C10mim][Br]/water (lower B) mixtures with changing water concentration (w/w). Water concentration values are listed in right side insert.

water–IL mixtures. The observed blue shifts of corresponding bands indicated that water weakens the C–H··· anion hydrogen bonding interactions of [C_{10}mim][X] when the water content was increased from ~0 to 12 % w/w in IL–water mixtures. Regular disorganization of hydrogen bonds was perturbed at 3% w/w for [C_{10}mim][Cl] and at 3% w/w for [C_{10}mim][Br] (Figs. 4 and 5) exactly at the same time when phase from thick liquid into hardened gel was changed. Our results and previous studies' results suggest that gelation arises from diminution of hydrogen bonding between the imidazolium ring and the anion (bromide, chloride) and the concomitant formation of an H-bonded network comprising water, anion, and the imidazolium cation,[4] which was analyzed in our previous studies.[26] The discontinuity at water concentration value ~3% w/w showed the lower border of the LC ionogel phase formation; this value strongly correlates with the LC phase concentration of [C_{10}mim][Br]/H_2O mixtures (~5% w/w) detected by small-angle X-ray scattering (SAXS), differential scanning calorimetry (DSC), and polarized microscopy.[4] The upper border of LC ionogel phase was determined in our previous studies of OH stretching modes of

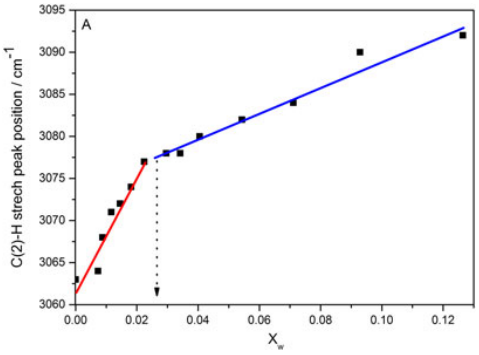

Figure 4. Determinating the lower border of LC ionogel phase in [C10mim][Cl]/H_2O: from the concentration dependence of the Raman bands C(2)-H (A) and C(4,5)-H (B) shifts and from the scores of the first and second PCs (C). More comments in text.

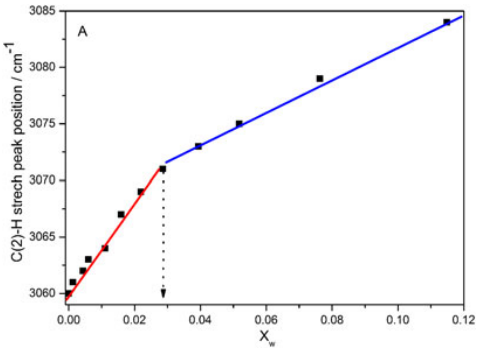

Figure 5. Determinating the lower border of LC ionogel phase in [C10mim][Br]/H_2O: from the concentration dependence of the Raman bands C(2)-H (A) and C(4,5)-H (B) shifts and from the scores of the first and second PCs (C). More comments in text.

water in RTIL/H_2O mixtures.[26] Combining information from two Raman spectral regions, CH stretching modes at 3000–3200 cm^{-1} and OH stretching modes at 3200–3800 cm^{-1}, allows to determine the full extent of LC ionogel phase behavior in RTIL/H_2O systems. The comparable behavior observed for the C(4,5)-H Raman band shifts at both [C_{10}mim][Cl]/H_2O mixtures 13 cm^{-1} from the 3147 cm^{-1} to the 3160 cm^{-1} and [C_{10}mim][Br]/H_2O mixtures, 18 cm^{-1} from the 3144 cm^{-1} to the 3162 cm^{-1}. Nevertheless, the C(2)-H band shifts strongly differ for long-chain ILs with different anions. For the [C_{10}mim][Cl]/H_2O mixtures, the shift of 30 cm^{-1} was observed from the 3062 cm^{-1} to the 3092 cm^{-1} and for the [C_{10}mim][Br]/H_2O mixtures 22 cm^{-1} the shift from 3062 cm^{-1} to the 3084 cm^{-1}. The different Raman shift behavior of the C(4,5)-H and the C(2)-H bands indicated that forming the LC ionogel phase water molecules mediated hydrogen bonds with the ring protons and anions differently. Very large blue shift of the C(2)-H band represented the higher imidazolium ring proton–water interactions as the consequence of ionic dissociation. This can be attributed to the stronger hydrogen bond of the C(2)-H··· anion than that of the C(4,5)-H···anion. Our results correlate with hydrogen bond network strength measurements using Coherent anti-Stokes Raman spectroscopy (CARS).[32] It was found that the degree of heterogeneity for investigated systems 1-decyl-3-methyl-imidazolium bromide/water and chloride/water were not influenced by the anion type. Only temperature and water content could change the heterogeneity of mixture.[5]

The dynamic spectra for the 2D correlation analysis were constructed from the spectral intensity variation upon external perturbation.[33,34] Many reasonable measure of a physical quantity, such as temperature, mechanical deformation, or concentration, could be used as an external stimulus. At the preset work, 'water concentration' (X) was used as the external variable continuous perturbation of the Raman spectra. The Raman spectra (raw spectra, or spectrum vectors) $I(\omega, X_j)$, $j=1,\ldots, m$ of [C_{10}mim][Br] and [C_{10}mim][Cl] in aqueous systems were measured when water content was increased in the system. Total $m=18$ spectra was registered for the [C_{10}mim][Cl] and $m=12$ for the [C_{10}mim][Br]. These data corresponded to various sample compositions listed in the inserts of Fig. 3. The original spectra were baseline corrected and renormalized to the CH_2 Raman band which intensity and wavenumber were constant during measurements. The dynamic spectra $I_d(\omega, X_j)$ were constructed from the spectrum vectors $I(\omega, X_j)$ subtracting the reference spectrum. This selection is somewhat arbitrary. It is usually set to be the averaged spectrum, although other forms may be chosen.[34] However, the results of 2D correlation analysis could be weakly influenced by the choice of the reference. Therefore, in the present work, the zero Raman intensity (after baseline correction) was used as the reference. The experimental data using the 2D Raman correlation spectroscopy (2DCOR) and the PCA were processed and realized in following steps. The data matrix **D** was composed placing the spectra $I_d(\omega, X_j)$ ($I(\omega, X_j)$) in m rows. The corresponding covariance matrix was obtained when multiplied **D** by its transpose $\mathbf{D^T}$:

$$\mathbf{Z} = \mathbf{D^T D}. \quad (1)$$

In this case, i.e. the so-called variable-variable approach,[35] the covariance matrix was coincident with the synchronous correlation spectrum used in the traditional Noda formalism of 2DCOR[34]: $\Phi \sim \mathbf{Z}$, whereas the asynchronous correlation spectrum Ψ was calculated as

$$\Psi \sim \mathbf{D^T H D}, \quad (2)$$

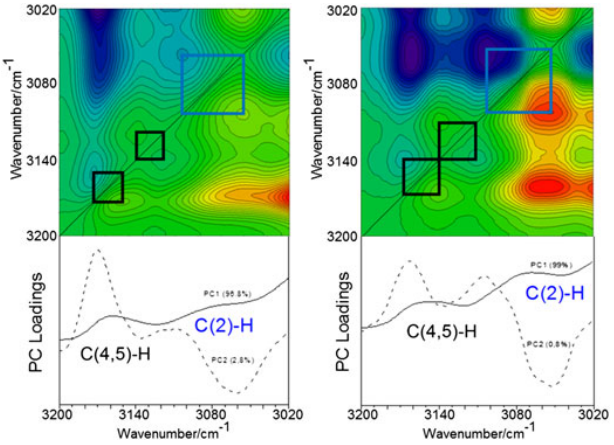

Figure 6. 2D Raman asynchronous correlation spectra in the contour plotting (upper) and loadings on the first and second principal components (lower): in [C10mim][Cl]/H_2O on the left and in [C10mim][Br]/H2O on the right.

where **H** is the Hilbert transform matrix. In the next steps, the load ($\mathbf{p_i}$) vectors were obtained when solved

$$\mathbf{Zp_i} = \lambda_i p_i, \tag{3}$$

where λ_i is the eigenvalue associated with the eigenvector $\boldsymbol{p_i}$.[36] The score vectors ($\boldsymbol{t_i}$) were calculated as

$$t_i = \mathbf{D}p_i. \tag{4}$$

The number of the statistically significant principal components was evaluated using the argument of the physical changes versus nondeterministic variation proposed in.[37]

It was found that first two PCs practically captured the total amount of variation in the Raman spectra in the range of 3000–3200 cm^{-1} upon dilution: for [C_{10}mim][Cl] ~96.8% (PC1) and ~2.8% (PC2), respectively (Fig. 6 lower part left and right) and for [C_{10}mim][Br] ~99% (PC1) and ~0.8% (PC2). For both studied ILs, the scores for the third PC (<0.1%) looked like noise, and therefore, PC3 was further not analyzed. The PC1 and PC2 score concentration dependence (Fig. 4 and 5 C parts) results strongly correlate with obtained blue shift of C(2)-H and C(4,5)-H bands when the water content in the IL/water mixtures was increased. The lower border of LC ionogel formation was indicated at the same point as other studies obtained [4]. The results of 2DCOR analysis of Raman spectra of [C_{10}mim][Cl]/water and [C_{10}mim][Br]/water mixtures are shown in Fig. 6 (upper part). The vibrational C–H bands of IL imidazolium ring was analyzed in the literature solving a broad variety of structuring problems in the systems with H_2O and other solvents as one of the components [4]. It is quite common to decompose broad vibrational bands in CH region into two components, assigning them as listed in Table 1.[38] 2DCOR Raman results correlate with the data obtained using standard Lorenzian band shape approach and the nonlinear curve fitting procedure very well. More fine structures of the bands envelope at the 3000–3200 cm^{-1} can be resolved in the loadings of the principal components as well as in the asynchronous 2D maps (Fig. 6). Namely, the six cross-peaks could be assigned to the three Raman vibrational mode shifts during the increase of water in IL/water mixtures. Two cross-peaks (Fig. 6, square in blue) show the shift of C(2)-H stretching mode at around 3100 cm^{-1}. Other four cross-peaks (squares in black) could be assigned to the symmetric and asymmetric C(4,5)-H stretching vibration mode shifts to 3140 and 3173 cm^{-1} for [C_{10}mim][Cl]/water and to 3139 and 3168 cm^{-1} for [C_{10}mim][Br]/water, respectively. Moreover, the PCA and the 2DCOR analysis allowed getting into more details. The blue shift for C(4,5)-H stretching vibration modes is less for the [C_{10}mim][Cl]/water mixture. The unambiguous result could be obtained only analyzing data with both methods 2DCOR and PCA. PCA provided clearly expressed discontinuous concentration changes, and 2DCOR analysis helped to distinguish the number of Raman band in broad region.

Conclusions

The discontinuous changes in the spectral parameters of imidazolium ring Raman C–H stretching modes in the region 3000–3200 cm^{-1} showed different IL and water structural organization in IL/water mixtures at different water content.

Monitoring of the Raman band shifts of imidazolium ring C2-H, C4-H, and C5-H vibrations, when water content was increased in the mixtures of 1-decyl-3-methyl-imidazolium bromide and chloride with water, provided reliable method to determine the extent of LC ionogel phase formation. Combining the information from two Raman spectral regions, CH stretching modes at 3000–3200 cm^{-1} and OH stretching modes at 3200–3800 cm^{-1}[26] allow to determine the lower and the upper borders of the LC gel phase formation in RTIL/H_2O system. The anion type did not influence the onset of ionogel phase formation for both systems.

Different imidazolium ring Raman shifts for C2-H, C4-H, and C5-H vibrational modes were found, and the result supports hypothesis that long-chain ILs and water molecules form weaker H bonds in positions C4 and C5 than in position C2 with imidazolium ring.

The results allow to ascertain that when water was added to IL, it firstly interacts with anion forming hydrogen-bonded network anion···H–O–H···anion. The advanced mathematical processing of spectral data using 2DCOR and PC analysis allowed looking deeper

into the different intermolecular interactions between IL and water molecules. For the investigated 1-decyl-3-methyl-imidazolium bromide/water and chloride/water systems, the degree of heterogeneity was not influenced by the anion type.

References

[1] S. Cha, M. Ao, W. Sung, B. Moon, B. Ahlström, P. Johansson, Y. Ouchi, D. Kim, *Phys. Chem. Chem. Phys.* **2014**, *16*, 9591–601.
[2] D. R. MacFarlane, N. Tachikawa, M. Forsyth, J. M. Pringle, P. C. Howlett, G. D. Elliott, J. H. Davis, M. Watanabe, P. Simon, C. A. Angell, *Energy Environ. Sci.* **2014**, *7*, 232–250.
[3] T. Singh, A. Kumar, *J. Phys. Chem. B* **2007**, *111*, 7843–7851.
[4] M. A. Firestone, J. A. Dzielawa, P. Zapol, l. A. Curtiss, S. Seifert, M. L. Dietz, *Langmuir* **2002**, *18*, 7258–7260.
[5] T. Inoue, B. Dong, L.-Q. Zheng, *J. Colloid Interface Sci.* **2007**, *307*, 578–81.
[6] B. Dong, X. Zhao, L. Zheng, J. Zhang, N. Li, T. Inoue, *Colloids Surf. A Physicochem. Eng. Asp.* **2008**, *317*, 666–672.
[7] Y. Zhao, X. Yue, X. Wang, X. Chen, *J. Colloid Interface Sci.* **2013**, *389*, 199–205.
[8] M. A. Firestone, P. Thiyagarajan, D. M. Tiede, *Langmuir* **1998**, *14*, 4688–4698.
[9] M. A. Firestone, P. G. Rickert, S. Seifert, M. L. Dietz, *Inorg. Chim. Acta* **2004**, *357*, 3991–3998.
[10] S. A. M. Noor, P. M. Bayley, M. Forsyth, D. R. MacFarlane, *Electrochim. Acta* **2013**, *91*, 219–226.
[11] G. Zhang, X. Chen, Y. Xie, Y. Zhao, H. Qiu, *J. Colloid Interface Sci.* **2007**, *315*, 601–606.
[12] X. W. Li, J. Zhang, B. Dong, L. Q. Zheng, C. H. Tung, *Colloids Surf. A Physicochem. Eng. Asp.* **2009**, *335*, 80–87.
[13] A. M. Moschovi, S. Ntais, V. Dracopoulos, V. Nikolakis, *Vib. Spectrosc.* **2012**, *63*, 350–359.
[14] S. Chen, S. Zhang, X. Liu, J. Wang, J. Wang, K. Dong, J. Sun, B. Xu, *Phys. Chem. Chem. Phys.* **2014**, *16*, 5893–5906.
[15] W. Jiang, Y. Wang, G. A. Voth, *J. Phys. Chem. B* **2007**, *111*, 4812–4818.
[16] H. Weingärtner, C. Cabrele, C. Herrmann, *Phys. Chem. Chem. Phys.* **2012**, *14*, 415–26.
[17] Y. Ji, R. Shi, Y. Wang, G. Saielli, *J. Phys. Chem. B* **2013**, *117*, 1104–9.
[18] W. Kiefer, *J. Raman Spectrosc.* **2007**, *38*, 1538–1553.
[19] Y. Jeon, J. Sung, D. Kim, C. Seo, H. Cheong, Y. Ouchi, R. Ozawa, H. O. Hamaguchi, *J. Phys. Chem. B* **2008**, *112*, 923–928.
[20] L. Cammarata, S. G. Kazarian, P. A. Salter, T. Welton, *Phys. Chem. Chem. Phys.* **2001**, *3*, 5192–5200.
[21] X. Shen, Q. Chen, J. Zhang, P. Fu, *Supramolecular Structures in the Presence of Ionic Liquids, Ionic Liquids: Theory, Properties, New Approaches*, (Eds: A. Kokorin), InTech, **2011**, pp. 427–482.
[22] M. Blesic, A. Lopes, E. Melo, Z. Petrovski, N. V. Plechkova, J. N. Canongia Lopes, K. R. Seddon, L. P. N. Rebelo, *J. Phys. Chem. B* **2008**, *112*, 8645–8650.
[23] V. Balevicius, Z. Gdaniec, K. Aidas, J. Tamuliene, *J. Phys. Chem. A* **2010**, *114*, 5365–71.
[24] B. A. Marekha, M. Bria, M. Moreau, I. De Waele, F.-A. Miannay, Y. Smortsova, T. Takamuku, O. N. Kalugin, M. Kiselev, A. Idrissi, *J. Mol. Liq.* **2015**, *210*, 227–237.
[25] S. Saouane, F. P. A. Fabbiani, *Cryst. Growth Des.* **2015**, *15*, 3875–3884.
[26] V. Aleksa, J. Kausteklis, V. Klimavicius, Z. Gdaniec, V. Balevicius, *J. Mol. Struct.* **2011**, *993*, 91–96.
[27] R. W. Berg, M. Deetlefs, K. R. Seddon, I. Shim, J. M. Thompson, *J. Phys. Chem. B* **2005**, *109*, 19018–19025.
[28] T. Singh, A. Kumar, *Vib. Spectrosc.* **2011**, *55*, 119–125.
[29] N. Yaghini, J. Pitawala, A. Matic, A. Martinelli, *J. Phys. Chem. B* **2015**, *119*, 1611–1622.
[30] J. Joseph, E. D. Jemmis, *J. Am. Chem. Soc.* **2007**, *129*, 4620–4632.
[31] Q. G. Zhang, N. N. Wang, S. L. Wang, Z. W. Yu, *J. Phys. Chem. B* **2011**, *115*, 11127–11136.
[32] C. Roth, S. Chatzipapadopoulos, D. Kerlé, F. Friedriszik, M. Lütgens, S. Lochbrunner, O. Kühn, R. Ludwig, *New J. Phys.* **2012**, *14*, 105026.
[33] Y. O. Isao Noda, Two-dimensional correlation spectroscopy, **2004**.
[34] I. Noda, *Appl. Spectrosc.* **2000**, *54*, 994–999.
[35] V. H. Segtnan, Š. Šašić, T. Isaksson, Y. Ozaki, *Anal. Chem.* **2001**, *73*, 3153–3161.
[36] C. Thibault, P. Huguet, P. Sistat, G. Pourcelly, *Desalination* **2002**, *149*, 429–433.
[37] B. Czarnik-Matusewicz, S. Pilorz, *Vib. Spectrosc.* **2006**, *40*, 235–245.
[38] O. Russina, B. Fazio, G. Di Marco, R. Caminiti, *The Structure of Ionic Liquids*, (Eds: R. Caminiti, L. Gontrani), Springer, **2014**, pp. 39–61.

Journal of Molecular Liquids 235 (2017) 1–6

Contents lists available at ScienceDirect

Journal of Molecular Liquids

journal homepage: www.elsevier.com/locate/molliq

NMR and FTIR studies of clustering of water molecules: From low-temperature matrices to nano-structured materials used in innovative medicine

Kristina Kristinaitytė [a], Laurynas Dagys [a], Jonas Kausteklis [a], Vytautas Klimavicius [a], Iryna Doroshenko [b], Valeriy Pogorelov [b], Nomeda Rima Valevičienė [c], Vytautas Balevicius [a,*]

[a] Faculty of Physics, Vilnius University, Sauletekio 9-3, LT-10222 Vilnius, Lithuania
[b] Faculty of Physics, Taras Shevchenko National University of Kyiv, Volodymyrska Str., 64|13, 01601 Kyiv, Ukraine
[c] Faculty of Medicine, Vilnius University, Santariskiu 2, LT-08661 Vilnius, Lithuania

ARTICLE INFO

Article history:
Received 6 September 2016
Accepted 12 November 2016
Available online 1 December 2016

Keywords:
Water
H-bond clusters
Matrix isolation
Nano-structured calcium hydroxyapatites
NMR spectroscopy
Infrared spectroscopy

ABSTRACT

H-bond clustering of water molecules confined in an argon matrix and in nano-structured calcium hydroxyapatites ($Ca_{10}(PO_4)_6(OH)_2$, CaHA) was studied by means of FTIR and ^{1}H MAS NMR spectroscopy. FTIR spectra of water in matrix were measured from $T = 9$ K to 40 K stepping by 2 K with sequent 2D correlation analysis (2DCOR) carried out in the range of O–H stretching vibrations 3000–3800 cm^{-1}. The peaks of monomer, dimer and the H-bond clusters from trimer to hexamer as well as the surface (dangling) modes were resolved. Some peaks in 2DCOR spectra drop out from the water clustering scheme. They were related to the enhancement of vibration–rotation motion due to increasing temperature and volume of the cavities in argon matrix. Water clusters were revealed in nano-CaHAs in FTIR spectra for the first time. Beside the sharp peak at 3570 cm^{-1} of the stretching vibration of O–H$^-$ ion in the bulk, the bands of water dimer, tetramer, hexamer and several surface O–H and P–O–H modes were resolved at 2900–3900 cm^{-1}. They were assigned comparing with the spectra of water in argon matrix and in hydrophobic solvent (CCl_4). The cluster structure and the size depends on the hydration level. Hexamer- or even higher structures were observed only in the samples containing significant amount of adsorbed water. The amount of adsorbed water in the studied nano-CaHAs was probed using the intensity of the broad ^{1}H signal at ca 5.1 ppm normalized respect to OH$^-$ peak at 0 ppm. Two narrow signals observed in ^{1}H MAS NMR spectra at 0.8 and 1.3 ppm are originated from the surface structured H_2O molecules. The NMR data perfectly correlate with those obtained by FTIR spectroscopy.

1. Introduction

Water is the third most common molecule in the Universe, after H_2 and CO [1]. Moreover, amorphous solid water is the most abundant water ice ubiquitous in the interstellar medium and postulated in the Earth's upper atmosphere [2]. Water vapor in our atmosphere is the dominant absorber of incoming sunlight and the most important greenhouse gas. Water plays an extremely important role in many biological and chemical systems and has long provoked interest due to its role in the formation of molecular key to the origin of life [3 and refs therein]. The exploration of structural and binding properties of small water clusters provides a key for understanding anomalous properties of water in the liquid, from ambient to deeply supercooled, as well as in solid phases [4–6]. At low temperatures these properties deviate particularly strongly from those of a normal liquid. Although the anomalies are extreme in the supercooled regime they are also present even at ambient temperatures, where most of physical, chemical and biological processes occur [4]. Hence, an unabated interest to water properties in each of its phases is easily tracked in the literature revealing more and more tremendous scientific challenges [4–10].

On other hand water can be considered as convenient and at the same time rather complex model to investigate the cooperative interactions and the structural organization of molecular clusters sized over the nano- and mezzo-scales. This can be done by isolating water molecules in low-temperature matrices [11–14], dissolving them in hydrophobic solvents [15], confining in carbon nanotubes [16] or in other mesoporous carbon materials [17,18]. In restricted geometries water molecules can interact with surfaces through hydrophobic and hydrophilic interactions and hydrogen-bond interactions. The competition between the surface–liquid and liquid–liquid interactions can lead to the appearance of interesting new structures and dynamical features of the water that are not observed in bulk water [18].

* Corresponding author.
E-mail address: vytautas.balevicius@ff.vu.lt (V. Balevicius).

http://dx.doi.org/10.1016/j.molliq.2016.11.076
0167-7322/

Hence the nano-structured materials provide a novel possibility for molecular isolation putting molecules in unusual conditions never met before. Moreover, some of those materials, like e.g. calcium hydroxyapatite ($Ca_{10}(PO_4)_6(OH)_2$, further - CaHA), have found many applications in innovative medicine. The knowledge about water states and structures present therein can be useful creating the series of nano-materials as well as correlating the short range order effects with macroscopic properties, like, strength, flexibility, aging effects etc., and maybe even with biocompatibility. Therefore it is challenging to obtain more novel data on the states of water and the clustering phenomena in these materials.

In the present work we have used FTIR and ^{1}H MAS NMR spectroscopy to study the H-bond clustering of water molecules confined in an argon matrix and in nano-CaHAs. In order to determine the correct number of spectral bands and to be sure no fine details were missed we have applied 2DCOR analysis as the novelty to study water in argon matrix. The knowledge about water clustering in inert matrices then were applied recognizing and assigning the water clusters and explaining FTIR and NMR features of water in series of nano-CaHAs (home-made and commercial ones).

2. Experimental

2.1. Samples

The water used was deionized and freshly triple-distilled. The nano-structured CaHAs were derived in Department of Inorganic Chemistry of Vilnius University applying the sol-gel synthesis routes using various complexing agents. The steps and conditions are detailed in Refs. 14, 15. The commercial CaHA was used from Aldrich, synthetic, 99.999%. All materials were characterized by scanning electron microscopy (SEM) and energy-dispersive X-ray analysis (EDX) using a Helios NanoLab 650 scanning electron microscope coupled with energy-dispersive X-ray spectrometry system, etc. [19,20].

The sample preparation for the matrix isolation experiments and the setup was based on the experience of our studies of propanol in argon matrix [21,22]. The samples were prepared mixing the gaseous water obtained by natural evaporation from the liquid with argon (99.995%) in the approximate ratio 1:1000, as measured by standard manometric techniques. The obtained mixture was deposited at 9 K onto a CsI window during 1 h. The deposition rate was 5 mmol of matrix mixture per hour.

The samples containing the water confined in nano-structured CaHAs (each in amount of ca 2 mg) were mixed in the ratio of 1:100 with KBr powder and pressed into a pellet using 10 tons pressing of manually operated hydraulic press Specac.

2.2. FTIR measurements

FTIR measurements in the case of matrix samples were carried out at temperatures from 9 to 50 K using Bruker IFS 113 FTIR spectrometer. A liquid-N_2-cooled mercury cadmium telluride (MCT) detector was used. The stabilization of temperature was provided by a closed-cycle Leybold Heraeus RW2 He cryostat. The temperature was controlled with a Si diode sensor and Lakeshore temperature controller with accuracy 0.1 K. Spectra were recorded with optical resolution 0.5 cm^{-1}. In order to increase the signal-to-noise ratio each spectrum was taken as an average of 512 scans.

FTIR experiments with CaHAs samples were performed at 298 K on Bruker VERTEX 70 spectrometer. FTIR transmission measurements were acquired with 2 cm^{-1} spectral resolution using globar light source and liquid nitrogen cooled MCT detector. Total 128 interferograms were averaged and transformed into spectrum applying the Blackman–Harris 3-Term apodization function and the zero filling factor of 2.

2.3. NMR experiments

NMR experiments were carried out on Bruker AVANCE III HD spectrometer operating at resonance frequencies of 400 and 162 MHz for ^{1}H and ^{31}P, respectively (magnetic field of 9.4 T). All MAS (magic angle spinning) measurements were performed using Bruker 4 mm H/X CP-MAS probe-head, which is capable to spin the sample up to 15 kHz rate. NMR MAS measurements were performed at the spinning rate of 10 kHz for ^{1}H Bloch decay experiments. For all ^{1}H MAS experiments the 90° pulse length was 2.5 μs, 64 scans were accumulated with a repetition delay of 3 s, respectively. NMR spectra were processed using Topsin 3.2 software. Additionally the signal shapes were processed using Microcal Origin 9 and Mathcad 15 packages.

3. Results and discussion

Water in matrix isolation using FTIR spectroscopy have long lasting traditions and the great experience has been accumulated [10–14, 23–26 and Refs cited therein]. It makes the attribution of certain absorption bands to the main water clusters $(H_2O)_n$ more or less sturdy up to $n \leq 6$. In the present work we have applied 2DCOR analysis [21,27] as the novelty to study water in argon matrix. This allows revealing the correct number of overlapping bands being sure no fine details were missed. Namely, FTIR spectra for 2DCOR analysis have been measured using thermal perturbation by heating the sample from $T = 9$ K to

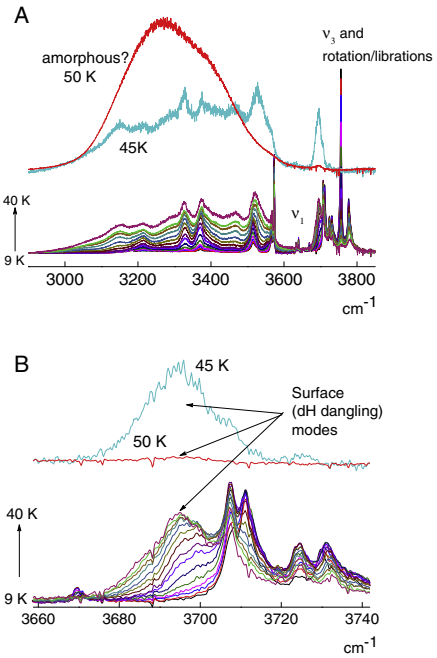

Fig. 1. Part A: measured FTIR spectra of water in argon matrix in O–H stretching region over the temperature range 9–40 K (from bottom to upper, by stepping $\Delta T = 2$ K). The base line was corrected drawing the line through the end points of this range. The spectra at 45 K and 50 K were added to support the assignment of surface (dangling) modes. Part B: the zoomed range 3660–3740 cm^{-1} in order better to display the peculiar thermal evolution of these modes. More comments in text.

40 K stepping by 2 K. The main attention was concentrated to the region of O–H stretching vibrations at 3000–3800 cm^{-1} (Fig. 1).

The mathematical formalism and the further steps of 2D FTIR absorption correlation analysis were the same as in the earlier matrix isolation work on 1-propanol [21]. The synchronous 2D correlation spectrum was obtained by the inner product of two spectrum vectors (1D spectra, Fig. 1), while the asynchronous correlation spectrum (Fig. 2) was calculated by a cross product of the spectrum vector and its Hilbert transformation [21,27].

The band maximum positions determined from the cross peaks positions in 2D asynchronous spectrum (Fig. 2) were used as the initial input parameters of the non-linear curve fitting routine and were refined during the next iterations for each temperature. The fitting result is shown in Fig. 3. The peaks of monomer, dimer and higher clusters up to hexamers have been perfectly resolved and easily identified comparing their positions with those in other works determined experimentally and supported by high-level theoretical calculations [11,13,23–26]. The spectral range 3600–3900 cm^{-1} (Fig. 1) contains the information about the monomer symmetric and antisymmetric stretching (ν_1 and ν_3) as well as about the vibrations of free (terminal) O–H group in some clusters [23,26]. However these data are difficult to process due to the presence of the vibration + rotation/libration peaks [23]. Therefore more detailed attention was paid to the range 3000–3600 cm^{-1}, where the bound O–H…O bands appear.

The bands of water H-bond clusters of various size are indicated in Figs. 2 and 3 by the red bolls. Some peaks (see the blue bolls therein) drop out from the general water clustering scheme. Most probably they are related to the enhancement of vibration–rotation motion due to increasing temperature and the cavities' volume in argon matrix, or can be assigned to be from higher multimers or overtones [26] or noted as the lines, which grow rapidly in annealing/diffusion experiments [13].

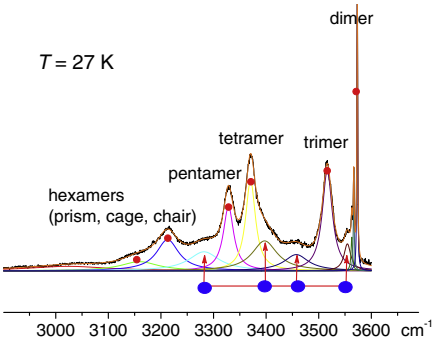

Fig. 3. Non-linear curve fitting of νO–H spectral contour by Lorentz functions ($T = 27$ K, as example) in the spectral range of 3000–3600 cm^{-1}. The maximum positions obtained from the cross-peaks in 2D correlation analysis were used as the zero-order approach for the fitting parameters. The refined values are given in Table 1. The meaning of red and blue bolls is the same as in Fig. 2.

These knowledge about water clustering processes in inert matrices can be very helpful assigning the bands and recognizing the states of

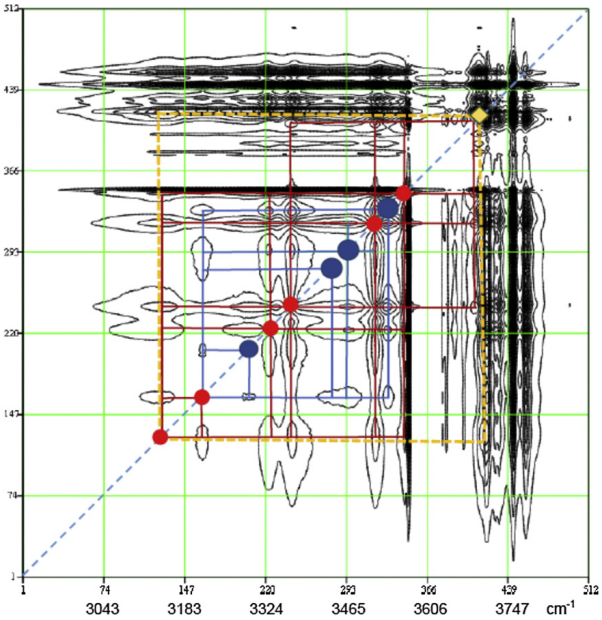

Fig. 2. 2D asynchronous FTIR correlation spectrum of water in argon matrix in νO–H region. Note, the huge number of points (4096) in each 1D spectrum (Fig. 1) was reduced decimating by factor of 8, and thus the correlation matrix 512 × 512 was processed. The correlation squares and the vertices, that correspond to water H-bond clusters of various size, are indicated by red bolls and lines and those, that drop out from the general clustering scheme, are shown by blue bolls and lines. The spectral feature at 3695–3701 cm^{-1} having very peculiar thermal evolution (see Fig. 1) is marked as yellow rhomb.

water in *terra incognita*, i.e. in much less investigated cases - water in nano-structured and other advanced/smart materials. However it has to be noted that the matrix isolation experiments are carried out at very low temperatures, whereas the main interest for many processes and innovative technologies lays in the range around room temperature. It was shown [15] that small water clusters can be detected at room temperature by FTIR spectroscopy dissolving water in hydrophobic solvent CCl_4. Beside the water monomer, a dimer, a cyclic trimer, a cyclic tetramer, and a large hydrogen-bonded structure (supposed - a cage hexamer) were found. These data can be useful moving from very low- to ambient temperature range. However, before doing this, some revision of the assignment of the bands seems to be necessary. First of all it looks that the attribution of the band at 3615–3616 cm^{-1} to ν_1 is rather doubtful and sequent the sizes of clusters $(H_2O)_n$ assigning all other peaks were diminished per 1, i.e. trimer → dimer, tetramer → trimer, etc. The following arguments can be given: i) the intensity of ν_1 is too strong comparing with ν_3; ii) the slope of its maximum vs temperature 1 cm^{-1}/40 K [15] is comparable with that for water dimer in matrix (~0.5 cm^{-1}/30 K, see Table 1); iii) the band assigned as 'dimer' is too broad and its maximum position has too strong dependency on temperature 50 cm^{-1}/40 K, i.e. almost one order higher than for the dimer in matrix; iv) the huge frequency shifts of band maxima in CCl_4 comparing with the gas phase or in liquid helium droplets (~100–200 cm^{-1} for trimer to hexamer) seems to be hardly can be explained by media/temperature effects. For these reasons we have revised this assignment heightening the cluster size: dimer → trimer, trimer → tetramer, etc. After these corrections done the much better coincidence between the matrix and hydrophobic solvent experiments was achieved. The thermal and environmental effects on the cluster band positions are now are <20–30 cm^{-1}, except the cases of dimer and the clusters with $n \geq 6$ (Table 1). Note, the last band is rather weak and very broad and thus the determination of its position may contain significant errors. Besides CCl_4 data, the maxima positions resolved, however not assigned, in FTIR spectrum of water confined in the single wall carbon nanotubes [16] are presented in Table 1 for comparison.

Hydroxyapatites (HA) are widely applied in implantology, orthopedic and periodontal surgery, drug carriers or bone regeneration [28–31]. A special place in these applications occupies calcium hydroxyapatite (CaHA), which shows close similarity to the mineral of hard tissues (bone, enamel, dentin, etc.) and therefore has high biocompatibility with them [30]. Two nano-structured CaHAs derived using various complexing agents as well as commercial one were selected and studied in the present work by means of FTIR and ^{1}H MAS NMR spectroscopy. The results are presented in Figs. 4, 5 and in Table 1.

Some of spectral features in the FTIR and NMR spectra are well-known. Namely, a strong and sharp band in all FTIR spectra at ca 3573 ± 1 cm^{-1} is assigned to the stretching of O–H$^-$ groups inside the columns along the *c*-axis in CaHA crystallites [32,33], i.e. νO–H$^-$ in the bulk (Fig. 4). Its narrowness is indicative of the absence of hydrogen bonding and it is consistent with the long distances between O–H$^-$ groups inside the channels (0.344 nm) [32]. The peak of O–H$^-$ protons in the bulk is easily recognized also in the ^{1}H MAS NMR spectra at ~0 ppm (Fig. 5) [31,34,35].

A special attention has to be paid to the origin of water modes in Ar matrix assigned to the surfaces ones (Fig. 1). Note, the matrix experiments were carried out heating the sample from 9 to 50 K. Thus the matrix undergoes a drastic softening at these conditions and therefore the site effect can be excluded. In the spectrum at 45 K (Fig. 1B) it is clearly seen that the intensity of the band at 3965–3701 cm^{-1} culminates just before sublimation of argon, whereas other vibration-rotation bands of monomers (3707 cm^{-1} and above) and even the dimer peak (3573 cm^{-1}) were already disappeared. After argon has sublimated (50 K) the intensity of the band at 3965 cm^{-1} also drops down very significantly. This could be explained assuming that just before matrix sublimation we observe at 3695–3701 cm^{-1} the O–H modes on the surfaces of many water droplets. In the 'hard' matrix, i.e. at 9–21 K these droplets are not noticeable (Fig. 1B). However, the amount of water molecules in the droplets increases at the further heating. These droplets persist being weakly isolated by the reminders of the matrix up to 50 K. They contain the water clusters of various size in the bulk and a certain amount of water on the surfaces. These droplets combine to form amorphous water when argon is gone. Thus billions of water

Table 1
Water hydrogen bonded clusters and surface (dangling) modes (all in cm^{-1}) in various confinements (argon matrix and in series of nano-structured CaHAs (a, b, c) studied in present work, hydrophobic solvent (CCl_4)) [15].

$(H_2O)_n$	Argon matrix 9–40 K	CCl_4 [15][a] 273–313 K	Nano-structured CaHAs 298 K
Dimer $n = 2$	3573–3573.5 3574 [23] 3574.5 [25]	3615–3616	3526 ± 2 (a) 3591 ± 4 (b) 3598 ± 1 (c)
Trimer $n = 3$	3515–3520 3515 [11] 3516 [23,24] 3517 (?) [25]	3535–3587	–
Tetramer $n = 4$	3369–3374 3372 [11,13] 3372 (?) [25]	3395–3433	3420 ± 2 (a) 3439 ± 2 (b) 3450 ± 2 (c)
Pentamer $n = 5$	3327–3330 3325 (?) [11] 3330 [13]	–	–
Hexamer $n = 6$	3211–3214 3212 [11] 3211 [13] 3327 (chair), 3212 (cage) [26]	3221–3254	3237 ± 2 (a) – (b) 3263 ± 3 (c)
$n \geq 6$	3100–3160 3144 [11] 3140 [13] 3150 (prism) [26]	3043–3074	– (a) – (b) 2940 ± 10 (c)
Surface (dangling) modes	3695–3701 3698 and 3720 [2,3]	Absent or hidden upon monomer + libration modes (non-resolved)	3642, 3737, 3866 (a) 3640, 3737, 3848 (b) ~3651, ~3700 (c)

[a] The revised assignment given in the table is based on the comments in text.

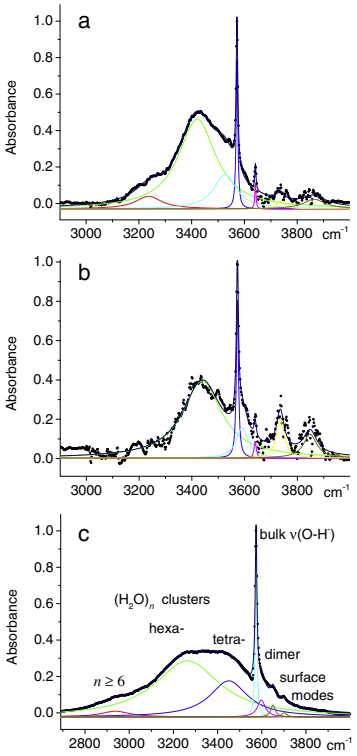

Fig. 4. FTIR spectra of nano-structured CaHAs prepared via the sol-gel synthesis routes using various complexing agents: a - ethylene glycol; b - tartaric acid; c - commercial. The base line was corrected drawing the line through the end points of this range. The intensities were normalized respect to the peak of ν(O–H$^-$)in the bulk at 3573 ± 1 cm^{-1}.

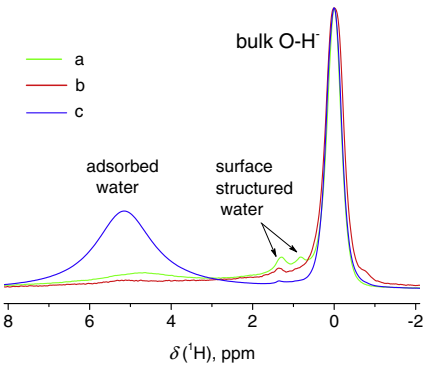

Fig. 5. ^{1}H MAS NMR spectra of CaHAs prepared via the sol-gel synthesis routes using various complexing agents: a - ethylene glycol; b - tartaric acid; c - commercial. The intensities were normalized respect to the peak of O–H$^-$ protons in the bulk at ~0 ppm.

molecules get together forming amorphous phase, however, the total surface area decreases very drastically during this transition. This is manifested on the intensities of the band at 3695 cm^{-1} comparing the spectra at 45 and 50 K (Fig. 1).

The group of the bands of νO–H of H-bonded clusters at 3000–3600 cm^{-1} transforms at 50 K to the broad spectral contour (Fig. 1A). The whole spectrum reminds of the profile observed for amorphous water with the characteristic dangling modes at 3720 and 3698 cm^{-1}, denoted as dH [2,3,6]. Theoretical calculations, supported by experimental studies, suggest that water molecules in the dH mode are bi- or tri-coordinated, presenting one free OH bond dangling at the surface [3]. Due to this similarity the band at 3695–3701 cm^{-1} was ascribed to the surface (dangling) mode.

This mode can be recognized also in the FTIR spectra of water in nano-CaHAs at 3640–3651 cm^{-1}. Another spectral features within 3700–3850 cm^{-1}, which slightly shift depending on the samples (Table 1), can be assigned to the O–H stretching vibration of the P–O–H groups of surface HPO_4^{2-} and/or $H_2PO_4^-$ ions produced by the protonation of PO_4^{3-} ions [32,33]. The presence of protonated ions on the crystallite surfaces in the studied materials was confirmed by ^{1}H–^{31}P CP MAS kinetics experiments [20]. Note, the bands at ≥3800 cm^{-1} that observed in the home-made CaHAs and not seen in the commercial sample, as far we know, were never reported in the literature. Thus, their origin has to be studied in the future works. Several minor peaks in ^{1}H MAS NMR spectra at 0.5–3.0 ppm are often observed in various CaHAs and related materials [35], also in the present case (Fig. 5). Since these peaks do not appear in CP MAS NMR spectra, most probably, they are originated from the highly mobile protons. However, their assignment presented in literature was long time controversial. Only recently in the work [31] it was shown that these peaks were originated to the structured external water molecules stacking in continuity to the columnar O–H channels in CaHAs.

Note, the H-bonded O–H stretching band in FTIR spectra was identified in many works on CaHAs and related systems [32–35]. However this band usually is taken as the unity without getting into its shape and structure. Water clusters were revealed in nano-CaHAs in the present work for the first time. The bands of water dimer, tetramer, hexamer and in the commercial sample maybe even $n \geq 6$ were resolved at 2900–3600 cm^{-1} (Fig. 4). They were assigned comparing with the spectra of water in argon matrix and in hydrophobic solvent (CCl_4). The size of formed cluster depends on the hydration level. Hexamer- or even higher structures were observed only in the samples containing significant amount of adsorbed water (Fig. 4a, c). The amount of adsorbed water in the studied nano-CaHAs was probed using the intensity of the broad ^{1}H signal at ca 5.1 ppm normalized respect to OH$^-$ peak at ~0 ppm (Fig. 5). Thus the NMR data perfectly correlate with those obtained by FTIR spectroscopy.

4. Conclusions

1. FTIR spectra of water in argon matrix have been measured from $T =$ 9 K to 40 K. 2D correlation analysis (2DCOR) has been carried out in the range of O–H stretching vibrations at 3000–3800 cm^{-1}. The peaks of monomer, dimer, as well as the H-bond clusters from trimer to hexamer have been resolved in the spectra. The peaks that drop out from the general water clustering scheme are most probably related to the of vibration–rotation motion enhanced at increasing temperature and the cavities' volume in argon matrix.
2. Water cluster structure was revealed by FTIR spectroscopy in nano-structured CaHAs for the first time. The bands of water dimer, tetramer, hexamer and several surface O–H and P–O–H modes were resolved at 2900–3900 cm^{-1} and assigned comparing with the spectra of water in argon matrix and in CCl_4.
3. The joint application of FTIR and NMR methods allowed to reveal very fine details in the state of water and in the structural organization of OH groups. This could not be achieved applying these

methods separately either because of difficulties assigning the observed spectral features or due to the overflow of information.

Acknowledgments

The work was carried out in the frame of Ukrainian-Lithuanian bilateral agreement supported by Ministries of Education and Science of Ukraine and Lithuania (grants M/49-2016 and TAP-LU-15-017). The authors acknowledge Center of Spectroscopic Characterization of Materials and Electronic/Molecular Processes (Scientific infrastructure "SPECTROVERSUM" www.spectroversum.ff.vu.lt) at Lithuanian National Center for Physical Sciences and Technology for use of spectroscopic equipment. We thank Dr. G. Pitsevich and Dr. J. Ceponkus for fruitful discussions and Prof. A. Kareiva for providing us the nano-structured calcium hydroxyapatites.

References

[1] J. Tennyson, Calculating the vibration–rotation spectrum of water, Phys. Scr. 73 (2006) C53–C56.
[2] J.A. Noble, C. Martin, H.J. Fraser, P. Roubin, S. Coussan, IR selective irradiations of amorphous solid water dangling modes: irradiation vs annealing effects, J. Phys. Chem. C 118 (2014) 20488–20495.
[3] J.A. Noble, C. Martin, H.J. Fraser, P. Roubin, S. Coussan, Unveiling the surface structure of amorphous solid water via selective infrared irradiation of OH stretching modes, J. Phys. Chem. Lett. 5 (2014) 826–829.
[4] L.G.M. Pettersson, A. Nilsson, The structure of water; from ambient to deeply supercooled, J. Non-Cryst. Solids 407 (2015) 399–417.
[5] A. Nilsson, L.G.M. Pettersson, Perspective on the structure of liquid water, Chem. Phys. 389 (2011) 1–34.
[6] S. Coussan, P. Roubin, J.A. Noble, Inhomogeneity of the amorphous solid water dangling bonds, Phys. Chem. Chem. Phys. 17 (2015) 9429–9435.
[7] L.A. Bulavin, T.V. Lokotosh, N.P. Malomuzh, Role of the collective self-diffusion in water and other liquids, J. Mol. Liq. 137 (2008) 1–24.
[8] L.A. Bulavin, A.I. Fisenko, N.P. Malomuzh, Surprising properties of the kinematic shear viscosity of water, Chem. Phys. Lett. 453 (2008) 183–187.
[9] I.I. Adamenko, L.A. Bulavin, V. Ilyin, S.A. Zelinsky, K.O. Moroz, Anomalous behavior of glycerol–water solutions, J. Mol. Liq. 127 (2006) 90–92.
[10] A. Mukhopadhyay, W.T.S. Cole, R.J. Saykally, The water dimer I: experimental characterization, Chem. Phys. Lett. 633 (2015) 13–26.
[11] S. Coussan, P. Roubin, J.P. Perchard, Infrared induced isomerizations of water polymers trapped in nitrogen matrix, Chem. Phys. 324 (2006) 527–540.
[12] I. Doroshenko, G. Pitsevich, V. Sablinskas, J. Ceponkus, V. Pogorelov, V. Balevicius, The initial stages of clustering of water molecules: matrix isolation FTIR/2DCOR study and the concept of combinatorial band broadening, Book of Abstracts of XXIth International Conference Horizons in Hydrogen Bond Research, Wroclaw University, Wroclaw, Poland, P5 September 2015, pp. 13–18.
[13] J. Ceponkus, P. Uvdal, B. Nelander, Water tetramer, pentamer, and hexamer in inert matrices, J. Phys. Chem. A 116 (2012) 4842–4850.
[14] J. Ceponkus, A. Engdahl, P. Uvdal, B. Nelander, Structure and dynamics of small water clusters, trapped in inert matrices, Chem. Phys. Lett. 581 (2013) 1–9.
[15] T. Köddermann, F. Schulte, M. Huelsekopf, R. Ludwig, Formation of water clusters in a hydrophobic solvent, Angew. Chem. Int. Ed. 42 (2003) 4904–4908.
[16] J. Martí, M.C. Gordillo, Effects of confinement on the vibrational spectra of liquid water adsorbed in carbon nanotubes, Phys. Rev. B 63 (2001) 1–5, 165430.
[17] Y. Xu, T. Watermann, H.H. Limbach, T. Gutmann, D. Sebastiani, G. Buntkowsky, Water and small organic molecules as probes for geometric confinement in well-ordered mesoporous carbon materials, Phys. Chem. Chem. Phys. 16 (2014) 9327–9336.
[18] B. Grünberg, T. Emmler, E. Gedat, I. Shenderovich, G.H. Findenegg, H.H. Limbach, G. Buntkowsky, Hydrogen bonding of water confined in mesoporous silica MCM-41 and SBA-15 studied by ^{1}H solid-state NMR, Chem. Eur. J. 10 (2004) 5689–5696.
[19] V. Klimavicius, A. Kareiva, V. Balevicius, Solid-state NMR study of hydroxyapatite containing amorphous phosphate phase and nano-structured hydroxyapatite: cut-off averaging of CP MAS kinetics and size profiles of spin clusters, J. Phys. Chem. C 118 (2014) 28914–28921.
[20] S. Kareiva, V. Klimavicius, A. Momot, J. Kausteklis, A. Prichodko, L. Dagys, F. Ivanauskas, S. Sakirzanovas, V. Balevicius, A. Kareiva, Sol-gel synthesis, phase composition, morphological and structural characterization of $Ca_{10}(PO_4)_6(OH)_2$: XRD, FTIR, SEM, 3D SEM and solid-state NMR studies, J. Mol. Struct. 1119 (2016) 1–11.
[21] V. Balevicius, V. Sablinskas, I. Doroshenko, V. Pogorelov, Propanol clustering in argon matrix: 2D FTIR correlation spectroscopy, Ukr. J. Phys. 56 (2011) 855–860.
[22] I. Doroshenko, V. Balevicius, V. Sablinskas, K. Aidas, G. Pitsevich, V. Pogorelov, FTIR/PCA study of propanol in argon matrix: the initial stage of clustering and conformational transitions, Low Temp. Phys. 40 (2014) 1384–1390.
[23] R.M. Bentwood, A.J. Barnes, W.J. Orville-Thomas, Studies of intermolecular interactions by matrix isolation vibrational spectroscopy. Self-association of water, J. Mol. Spectrosc. 84 (1980) 391–404.
[24] A. Engdahl, B. Nelander, On the structure of the water trimer. A matrix isolation study, J. Chem. Phys. 86 (1987) 4831–4837.
[25] G.P. Ayers, A.D.E. Pullin, The i.r. spectra of matrix isolated water species. I. Assignment of bands to $(H_2O)_2$, $(D_2O)_2$ and HDO dimer species in argon matrices, Spectrochim. Acta 32A (1976) 1629–1639.
[26] K. Ohno, M. Okimura, N. Akai, Y. Katsumoto, The effect of cooperative hydrogen bonding on the OH stretching-band shift for water clusters studied by matrix-isolation infrared spectroscopy and density functional theory, Phys. Chem. Chem. Phys. 7 (2005) 3005–3014.
[27] I. Noda, Advances in two-dimensional correlation spectroscopy, Vib. Spectrosc. 36 (2004) 143–165.
[28] R.Z. Le Geros, J.P. Le Geros, Hydroxyapatite, in: T. Kokubo (Ed.), Bioceramics and their Clinical Applications, Woodhead Publishing, Cambridge 2008, pp. 367–394.
[29] R.Z. Le Geros, Calcium Phosphates in Oral Biology and Medicine, Karger, Basel, 1991.
[30] P.W. Brown, B. Constantz (Eds.), Hydroxyapatite and Related Materials, CRC Press, 1994.
[31] M. Ben Osman, S. Diallo-Garcia, V. Herledan, D. Brouri, T. Yoshioka, J. Kubo, Y. Millot, G. Costentin, Discrimination of surface and bulk structure of crystalline hydroxyapatite nanoparticles by NMR, J. Phys. Chem. C 119 (2015) 23008–23020.
[32] S. Diallo-Garcia, M. Ben Osman, J.M. Krafft, S. Boujday, C. Guylène, Discrimination of infrared fingerprints of bulk and surface POH and OH of hydroxyapatites, Catal. Today 226 (2014) 81–88.
[33] T. Ishikawa, A. Teramachi, H. Tanaka, A. Yasukawa, K. Kandori, Fourier transform infrared spectroscopy study of deuteration of calcium hydroxyapatite particles, Langmuir 16 (2000) 10221–10226.
[34] L. Dagys, V. Klimavicius, J. Kausteklis, A. Chodosovskaja, V. Aleksa, A. Kareiva, V. Balevicius, Solid-state ^{1}H and ^{31}P NMR and FTIR spectroscopy study of static and dynamic structures in sol-gel derived calcium hydroxyapatites, Lith. J. Phys. 55 (2015) 1–9.
[35] J. Kolmas, A. Jaklewicz, A. Zima, M. Bućko, Z. Paszkiewicz, J. Lis, A. Ślosarczyk, W. Kolodziejski, Incorporation of carbonate and magnesium ions into synthetic hydroxyapatite: the effect on physicochemical properties, J. Mol. Struct. 987 (2011) 40–50.

Journal of Molecular Structure 1119 (2016) 1–11

Contents lists available at ScienceDirect

Journal of Molecular Structure

journal homepage: http://www.elsevier.com/locate/molstruc

Sol–gel synthesis, phase composition, morphological and structural characterization of $Ca_{10}(PO_4)_6(OH)_2$: XRD, FTIR, SEM, 3D SEM and solid-state NMR studies

Simonas Kareiva [a], Vytautas Klimavicius [b], Aleksandr Momot [c, 1], Jonas Kausteklis [b], Aleksandra Prichodko [c], Laurynas Dagys [b], Feliksas Ivanauskas [d], Simas Sakirzanovas [a, e], Vytautas Balevicius [b], Aivaras Kareiva [c, *]

[a] Department of Applied Chemistry, Vilnius University, Naugarduko 24, LT-03225, Vilnius, Lithuania
[b] Department of General Physics and Spectroscopy, Vilnius University, Sauletekio 9-3, LT-10222, Vilnius, Lithuania
[c] Department of Inorganic Chemistry, Vilnius University, Naugarduko 24, LT-03225, Vilnius, Lithuania
[d] Department of Computer Science, Vilnius University, Naugarduko 24, LT-03225, Vilnius, Lithuania
[e] Institute of Chemistry, Center for Physical Sciences and Technology, A. Gostauto 9, LT-01108, Vilnius, Lithuania

ARTICLE INFO

Article history:
Received 9 January 2016
Received in revised form
15 April 2016
Accepted 15 April 2016
Available online 20 April 2016

Keywords:
Calcium hydroxyapatite
Sol–gel processing
Morphology
3D reconstruction
Structural features

ABSTRACT

Aqueous sol–gel chemistry route based on ammonium–hydrogen phosphate as the phosphorus precursor, calcium acetate monohydrate as source of calcium ions, and 1,2-ethylendiaminetetraacetic acid (EDTA), or 1,2-diaminocyclohexanetetracetic acid (DCTA), or tartaric acid (TA), or ethylene glycol (EG), or glycerol (GL) as complexing agents have been used to prepare calcium hydroxyapatite ($Ca_{10}(PO_4)_6(OH)_2$, CHAp). The phase transformations, composition, and structural changes in the polycrystalline samples were studied by infrared spectroscopy (FTIR), X-ray powder diffraction analysis (XRD), and scanning electron microscopy (SEM). The local short-range (nano- and mezo-) scale effects in CHAp were studied using solid-state NMR spectroscopy. The spatial 3D data from the SEM images of CHAp samples obtained by TA, EG and GL sol–gel routes were recovered for the first time to our knowledge.

1. Introduction

Development of a morphologically controllable synthesis of different functional materials is urgently important to answer the demand for exploring the potentials of these compounds. For example, well-controlled hierarchical nanostructures of manganese cobaltates or lanthanum manganates revealed that high specific capacitance and magnetic properties of these compounds depend on the morphological features and could be applied as supercapacitor electrode materials [1,2]. The connection between electrical and morphological properties of magnetocaloric nano zinc/nickel ferrites was also recently demonstrated by Hemeda et al. [3]. The importance of surface morphology of nanomaterials to biological responses was revealed in Ref. [4]. The challenges and opportunities of controlling the morphological characteristics of phosphate materials were also put forward [5,6].

Calcium hydroxyapatite, $Ca_{10}(PO_4)_6(OH)_2$, commonly referred to as CHAp, is one of the calcium phosphate based material which makes up the majority of the inorganic components of human bones and teeth. The specific chemical structural and morphological properties of CHAp are highly sensitive to the changes in chemical composition and processing conditions [7–10]. The solid-state synthesis of CHAp from oxide or inorganic salt powders usually requires extensive mechanical mixing and lengthy heat treatments at high temperatures [11,12]. These processing conditions do not allow facile control over micro-structure, grain size and grain size distribution in the resulting powders. Several other techniques such as polymerized complex routes, hydrothermal synthesis, precipitation, microemulsions, spray-, and gel-pyrolysis and sonochemical methods have been used to produce CHAp phases [13–24]. Inhomogeneous CHAp having significant amount

* Corresponding author.
E-mail address: aivaras.kareiva@chf.vu.lt (A. Kareiva).
[1] On leave: Laboratory of Inorganic and Physical Chemistry, Hasselt University, Agoralaan D, B-3590 Diepenbeek, Belgium.

http://dx.doi.org/10.1016/j.molstruc.2016.04.046
0022-2860/

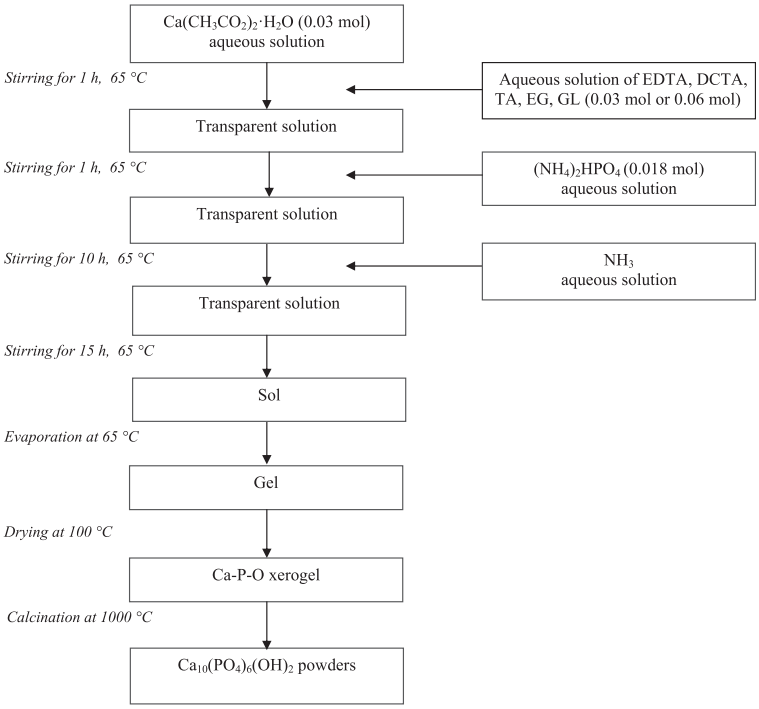

Fig. 1. A schematic diagram of the steps involved in the sol–gel processes used for the preparation of $Ca_{10}(PO_4)_6(OH)_2$ samples.

of impurities was produced using most of these methods.

It has been well demonstrated that the sol–gel process offers considerable advantages of good mixing of the starting materials and excellent chemical homogeneity and stoichiometry of the CHAp. Several sol–gel approaches, starting from nonaqueous solutions of different precursors of calcium and phosphorus, have been used for the preparation of CHAp powders. The major limitation for its applications was found to be very low solubility of the calcium alkoxides in the organic solvents and their low reactivity which caused deviations from the stoichiometry of the final materials. The aqueous synthesis route of sol–gel preparation offers an effective and relatively simple way to produce CHAp [25–28].

Over the last few decades, the sol–gel techniques have been used to prepare a variety of mixed-metal oxides, nanomaterials and nanoscale architectures, nanoporous oxides, organic-inorganic hybrids [29–33]. The aqueous sol–gel synthesis technique for the preparation of $YBa_2Cu_4O_8$ superconductor was studied using two different complexing agents with the same chemical composition, namely L-(+)-tartaric (natural) acid and DL-tartaric (synthetic) acid. The SEM micrographs of the Y–Ba–Cu–O acetate-tartrate gels indicated the formation of monolithic gels with slightly different morphological features [34]. The nature of complexing ligand used in the sol–gel preparation of yttrium aluminium (or gallium) garnets was found to be essential for the morphological properties of sol–gel derived compounds [35,36]. Besides, aqueous sol–gel chemistry routes using different complexing agents have been developed to prepare calcium hydroxyapatite samples with different morphological properties [7,28,37].

NMR and FTIR spectroscopy techniques provide the unique information on the local short-range (nano- and mezo-) scale effects. Therefore these methods are most perspective to study structure and dynamical changes in complex solids, such as calcium hydroxyapatites having different morphological features among them [38–41]. These techniques have been applied in the present work studying very fine structural details, *viz*., the surface effects and the characteristic size profiles of sub-nano $^{31}P-^{1}H_n$ spin clusters. Since the NMR experiments sometimes are long-lasting and thus are hardly applied in technological routes, a hunt around correlations with FTIR data has a definite sense. It would allow to apply FTIR spectroscopy as a very rapid and powerful tool searching for the best complexing agents, controlling and optimizing fine surface and structural features as well as the perfectness (uniformity) of synthesized nano-structures in series of related materials.

These results have initiated the present work on the impact of the nature of the gelation agent used in the sol–gel process on the CHAp formation process and it's morphological features. Five different complexing agents were selected to be used in the sol–gel processing experiments: EDTA, DCTA, tartaric acid, ethylene glycol and glycerol. The aim of this work was to elucidate the impact of the nature of the complexing agent on the calcium hydroxyapatite formation process, phase purity and morphological properties.

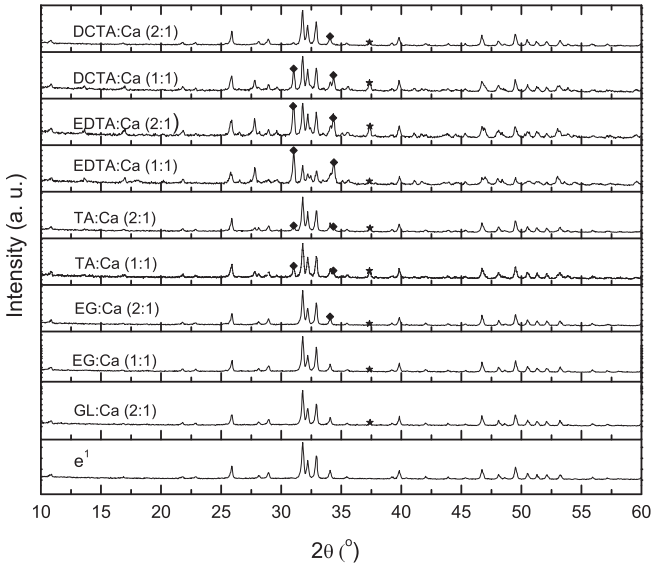

Fig. 2. XRD patterns of CHAp powders obtained after calcination of Ca–P–O precursor gels synthesized using DCTA, EDTA, TA, EG and GL in the sol–gel processing. The molar ratio of complexing agent and Ca was 2 or 1. Impurity phases: $Ca_3(PO_4)_2$ (*) and CaO (◆).

2. Experimental

2.1. Materials and preparation

In the sol–gel process, calcium acetate monohydrate, $Ca(CH_3COO)_2 \cdot H_2O$, and ammonium–hydrogen phosphate, $(NH_4)_2HPO_4$, were selected as Ca and P sources, respectively, in Ca/P molar ratio 1.67. Firstly, calcium acetate monohydrate (0.03 mol) was dissolved in distilled water under continuous stirring at 65 °C. In order to obtain water soluble calcium complexes and thereby avoid undesirable crystallization of calcium phosphates, 1,2-ethylendiaminetetraacetic acid, $C_{10}N_2H_{16}O_8$ (EDTA), or 1,2-diaminecyclohexanetetraacetic acid monohydrate, $C_{14}H_{22}N_2O_8 \cdot H_2O$ (DCTA), or tartaric acid, $C_4H_6O_6$ (TA), or ethylene glycol, $C_2H_6O_2$ (EG), or glycerol, $C_3H_8O_3$ (GL) were dissolved in 100 mL of distilled water, and afterwards added to the initial solution. The amount of complexing agents in the sol–gel processing was used the same as Ca (0.03 mol) or twice as many (0.06 mol). The resulting mixture was stirred for 1 h at the same temperature. Then, $(NH_4)_2HPO_4$ (0.018 mol) dissolved in distilled water was added to the above mentioned solution. The pH of the solution was adjusted to ~9.0 using a solution of 10% NH_3 (aq). Finally, after slow evaporation under continuous stirring at 65 °C, the Ca–P–O sols turned into transparent gels. The oven dried (100 °C) gels powders were ground in an agate mortar, heated up to 1000 °C with heating rate 10 °C min^{-1} and calcined at this temperature for 5 h in air. The flow chart of the sol–gel synthesis of calcium hydroxyapatite is presented in Fig. 1.

2.2. Characterization

The calcination products were characterized by infrared spectroscopy (FTIR), X-ray powder diffraction (XRD) analysis and scanning electron microscopy (SEM). The FTIR spectra were recorded on a PerkinElmer Spectrum 100FT-IR spectrometer in the range of wavenumbers of 4000–400 cm^{-1}. More detailed FTIR measurements were also performed at 298 K on Bruker VERTEX 70 spectrometer. The studied materials (each in amount of ca 2 mg) were mixed in the ratio of 1:100 with KBr powder and pressed into a pellet using 10 tons pressing of manually operated hydraulic press Specac. FTIR transmission measurements were acquired with 2 cm^{-1} spectral resolution using global light source and liquid nitrogen cooled MCT detector. Total 128 interferograms were averaged and transformed into spectrum applying the Blackman–Harris 3-Term anodization function and the zero filling factor of 2. The XRD studies were performed on a Rigaku MiniflexII diffractometer operating with Cu $K_{\alpha 1}$ radiation (step size: 0.04; time per step: 5 s). In order to study the morphology and microstructure of the ceramic samples scanning electron microscope Helios NanoLab 650 was used. The approach by combining two pictures of a specimen from two slightly different angles was used for the reconstruction of 3D SEM images using stereoscopic technique. Combination of two SEM images into an anaglyph was done with freely available software AnaMaker [42]. Extrapolation of spatial data was done from three or more sample images using visual reconstruction software applications. Solid-state NMR experiments were carried out on Bruker AVANCE III HD spectrometer operating at resonance frequencies of 400 and 162 MHz for ^1H and ^{31}P, respectively (magnetic field of 9.4 T). All MAS (magic angle spinning) measurements were performed using Bruker 4 mm H/X CP-MAS probe-head, which is capable to spin the sample up to 15 kHz rate. NMR MAS measurements were performed at the spinning rate of 5 kHz for ^{31}P and 10 kHz for ^1H Bloch decay (BD) experiments. For all $^1H/^{31}P$ MAS experiments the 90° pulse length

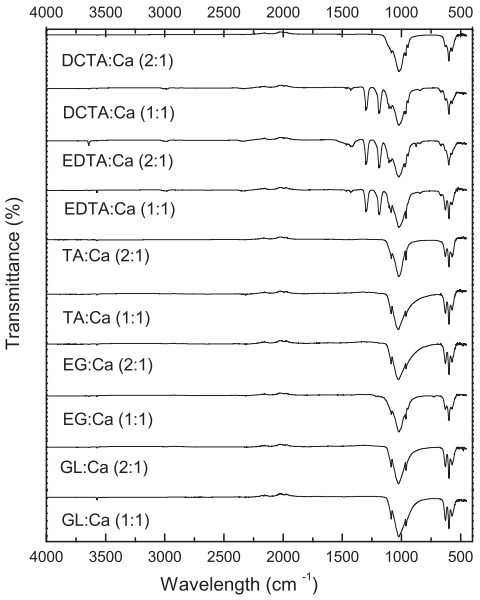

Fig. 3. FTIR spectra of CHAp samples synthesized at 1000 °C using different complexing agents in the sol–gel processing: DCTA, EDTA, TA, EG and GL. The molar ratio of complexing agent and Ca was 2 or 1.

was 2.5/1.8 μs, 64/16 scans were accumulated with a repetition delay of 3/10 s, respectively. NMR spectra were processed using Topsin 3.2 software. Additionally the signal shapes were processed using the Levenberg–Marquardt method implemented in Microcal Origin 9 and Mathcad 15 packages.

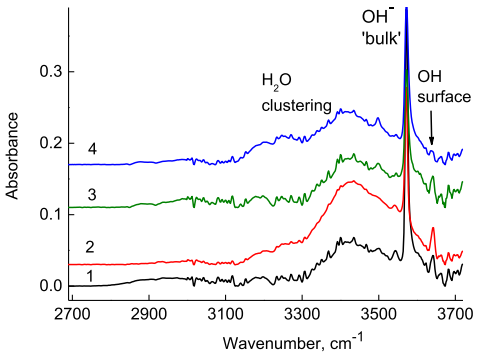

Fig. 4. FTIR spectra of CHAp synthesized using various complexing agents (1 – GL, 2 – EG, 3 – TA and 4 – EDTA) in O–H stretching region. The intensities of the absorption bands are non-normalized; the spectra are shifted along absorbance axis for a more convenient view. For other conditions see Experimental.

3. Results and discussion

3.1. Powder X–ray diffraction analysis

The XRD patterns of samples after calcination of Ca–P–O gels obtained using different complexing agents are shown in Fig. 2. In all cases the main synthesis product obtained after annealing the precursor gels at 1000 °C is CHAp. However, in most of the cases the impurity phases, such as $Ca_3(PO_4)_2$ (PDF [32–176]) and CaO (PDF [28–775]) were formed. Obviously, the amount of impurities was dependent on the concentration of complexing agent used in the sol–gel processing. The higher amount of EDTA, DCTA and TA promotes formation of purer CHAp. Contrary, the phase purity of synthesis products obtained in the glycolate and glycerate sol–gel routes is only slightly dependent on the amount of complexing agent.

XRD analysis results also show that the products obtained after annealing of different Ca–P–O gels at 1000 °C are different. The sample synthesized using DCTA had relatively highest amount of calcium phosphate and calcium oxide side phases. The intensity of diffraction peaks belonging to desirable $Ca_{10}(PO_4)_6(OH)_2$ phase is almost the same in the XRD patterns of samples fabricated using EDTA and TA as complexing agents. Finally, the polycrystalline single-phase $Ca_{10}(PO_4)_6(OH)_2$ was obtained using glycerate sol–gel route when molar ratio of Ca:Gl = 1. These XRD results are in a good agreement with the reference data for $Ca_{10}(PO_4)_6(OH)_2$ (PDF [72–1243]). In addition, there is only minor number of peaks corresponding to $Ca_3(PO_4)_2$ phase in the case of glycolate synthesis. The lattice parameters (a and c) of the synthesized $Ca_{10}(PO_4)_6(OH)_2$ samples were obtained from the diffraction patterns by fitting the peaks of identified reflections. The volume (V) of the hexagonal unit cell of each CHAp formulation was calculated using the relation $V = 2.589a^2c$. The hexagonal lattice parameters and cell volumes determined for the samples were found to be in the ranges $a = 9.45 - 9.32$ Å, $c = 6.89 - 6.84$ Å, and $V = 1593.00 - 1538.23$ Å^3 that correspond to a stoichiometric calcium hydroxyapatite.

3.2. FTIR spectroscopy

FTIR spectroscopy is highly sensitive to the impurities and substitutions in the structure of apatite [43,44]. The FTIR spectra of CHAp samples obtained at 1000 °C in the sol–gel process using different complexing agents and concentrations are shown in Fig. 3. In the spectra of all samples a complex band of the asymmetric stretching vibration of the phosphate group at 1000–1100 cm^{-1} dominates. Fig. 3 also shows well-expressed asymmetric bending ν_4 modes in the region of 660–520 cm^{-1}. Moreover, the specific OH^- vibration mode near 635–630 cm^{-1} is visible in our IR spectra. The peak intensity at 630 cm^{-1} assigned to OH vibration, as well as the band of the stretch vibration of OH group at ~3600 cm^{-1} in hydroxyapatite spectra, remained unchanged for all specimens. At the same time the intensity of the band at 3644 cm^{-1} assigned to $Ca(OH)_2$ decreases. Two additional peaks are expressed at 1300–1225 cm^{-1} in the IR spectra of CHAp samples synthesized using CDTA and EDTA as complexing agents. Unfortunately, these absorption peaks could not be assigned for vibrations in any groups presented in apatite structure.

The representative synthesized materials were analyzed more detailed respect to the presence of the structural manifolds of hydroxyl groups. The structural organization of –OH groups looks to be very similar. Absorption bands could be attributed to adsorbed water and structural hydroxyl groups (OH^-). It can be concluded from FTIR spectra (Fig. 4), that for all materials the amount of structural –OH groups in is significantly higher than from adsorbed water. The sharp strong peak at 3570 cm^{-1} attributed to the

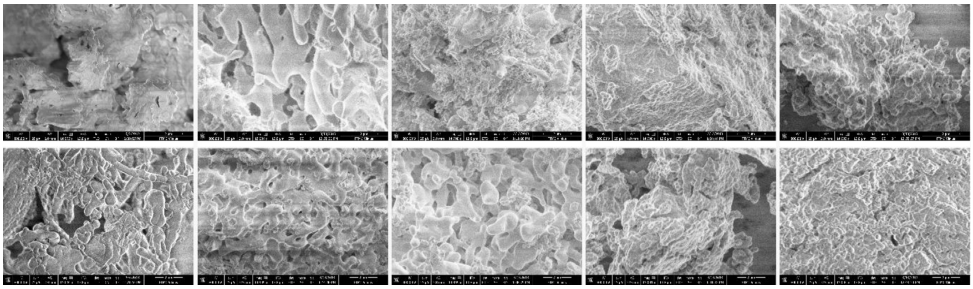

Fig. 5. SEM micrographs of CHAp samples synthesized at 1000 °C from the gels prepared with (from left): DCTA, EDTA, TA, EG and GL. The molar ratio of complexing agent and Ca was 2 (at top) or 1 (at bottom).

stretching vibration of OH^- ions in the crystals [45,46] is clearly seen in all these spectra, whereas the broad contour spread over ~3000–3400 cm^{-1}, that is typical for bulk water [47] and that was dominant in the case of CHAp containing amorphous phosphate phase [41], is practically absent in the present materials. Some bands that are seen over 3100–3600 cm^{-1} range (Fig. 4) can be recognized as those of small water clusters. These will be discussed later.

3.3. Scanning electron microscopy

The CHAp samples were also investigated by scanning electron microscopy. The morphological features of the heated samples of DCTA, EDTA, TA, EG and GL gels are given in Fig. 5. The product of calcination of DCTA gel derived when molar ratio of complexing agent and Ca was 1 is made up of different size and shape particles. The solids are composed of agglomerates of elongated particles 0.5–2.0 μm in size, and some of them are necked to each other. The higher degree of particles agglomeration could be observed when double amount of DCTA was used in the sol–gel processing. Moreover, partially amorphous material was obtained during this synthesis route. Very weak crystalline particles could be observed in the SEM picture of CHAp obtained using EDTA in the synthesis (see Fig. 5). The particles of hardly identified shape are even more aggregated. With increasing amount of EDTA, the particle size obviously increases from 1 μm to 2–3 μm. SEM micrographs of CHAp samples synthesized at 1000 °C from the gel prepared with tartaric acid are also presented in Fig. 5. When the molar ratio of TA and Ca was 1 well-defined elongated particles with width of 0.2–0.5 μm and 1.0–1.5 μm in length have formed. However, these elongated particles are almost fully covered by fine particles with doubtful crystallinity. CHAp nanocrystallites with regular spherically-shaped structure with 20–70 nm in size could be identified when ethylene glycol was used in the sol–gel processing. As seen, the amount of EG has no influence on the surface morphology of CHAp. In both cases, highly agglomerated material of rounded shape crystallites was formed. The monolithic solids of CHAp formed of small particles have been fabricated during the glycerate sol–gel synthesis route. The agglomerates of fine (5–10 nm) and of the bigger rounded particles (20–50 nm) construct nonporous structure of CHAp. It could be concluded from the SEM measurements, that the nature and concentration of complexing agent used in the sol–gel process have an essential influence on the particles shape and size of CHAp. On the other hand, the SEM pictures have not fully reveal the morphological features of the synthesized materials. Obviously, the SEM images are relatively complex and can be interpreted ambiguously. Therefore, for a more detailed interpretation some of the specimens were investigated by solid-state NMR spectroscopy. Moreover, the obtained SEM results were used for the spatial 3D surface reconstruction.

3.4. Spatial 3D surface reconstruction

The technique for recovering spatial data from the SEM pictures is known as spatial reconstruction using structure from sample motion (structure-from-motion). The SEM images of CHAp samples obtained by TA, EG and GL sol–gel routes were taken from different angles and subsequently analyzed for matching points, also the camera position was approximated for each image. The 3D image of CHAp synthesized with tartaric acid (TA:Ca = 1), reconstructed from 12 SEM micrographs using spatial reconstruction is presented in Fig. 6. The reconstruction software produces a cloud of points, which has to be processed externally. Freely available applications, such as MeshLab can be used to join the point cloud to a mesh and, as a second step of reconstruction, apply surface properties to the mesh polygons. Fig. 6 also displays the 3D CHAp surface reconstruction steps, from point cloud, to mesh and surface. As shown in Fig. 6, a dense microstructure that is composed of angular particles was observed in CHAp sample. These images clearly demonstrate that the elongated particles are forming the agglomerates (10–30 μm) having irregular shape. These aggregates are covered by smaller particles and consist of porous microstructure. Fairly similar microstructure could be observed for the CHAp sample synthesized with double amount of tartaric acid (Fig. 7).

However, the CHAp powders prepared using ethylene glycol in the sol–gel processing exhibited different morphological features (Fig. 8, top). After calcination at 1000 °C independent on the amount of ethylene glycol used, the round shaped and smaller particles were obtained. Moreover, the sample could be characterized having a narrow particles size distribution and the abundance of small particles increased in comparison to TA route. Fig. 8 also shows that powders synthesized by EG procedures consist of monoliths with a flat surface. Further statistical analysis could be performed on the image analysis data to determine particle size distribution and particle connectivity. Surprisingly, the spatial 3D surface reconstruction of SEM micrographs of synthesized CHAp samples by sol–gel glycerate route was problematic (see Fig. 8, bottom). These samples showed different morphological features compared with other routes. Thus, unique CHAp surface details (smallest particles, spherical shaped, monolithic surface) make it more difficult to detect matches in several images. Consequently,

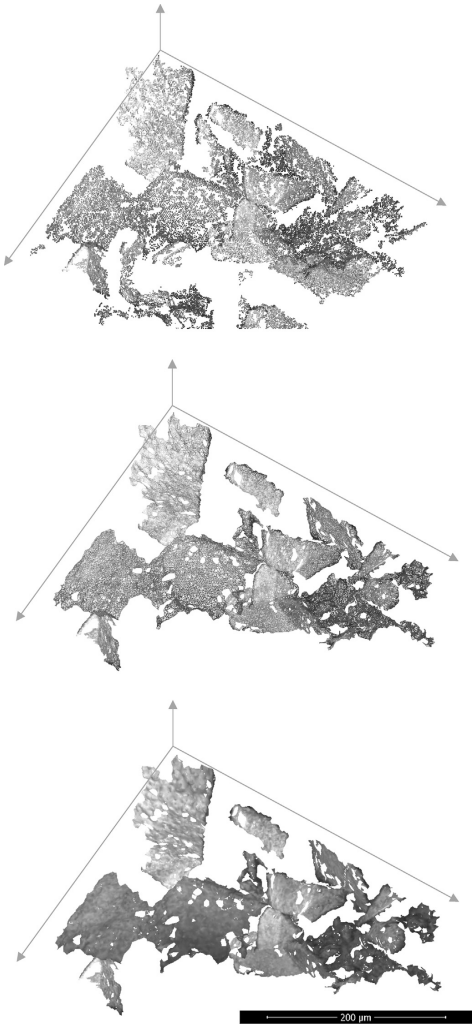

Fig. 6. 3D CHAp synthesized with tartaric acid (TA:Ca = 1) surface reconstruction steps, from point cloud (top), to mesh (middle) and surface (bottom).

during the research these specimens produced worst results among other samples.

3.5. Solid-state NMR spectroscopy

The representative CHAp specimens were analyzed also by means of ^{1}H NMR spectroscopy. In all cases the structural organization of −OH groups looks to be very similar. The ^{1}H NMR spectra consist of broad signal at ~5 ppm and sharp peak at 0.0 ppm that are

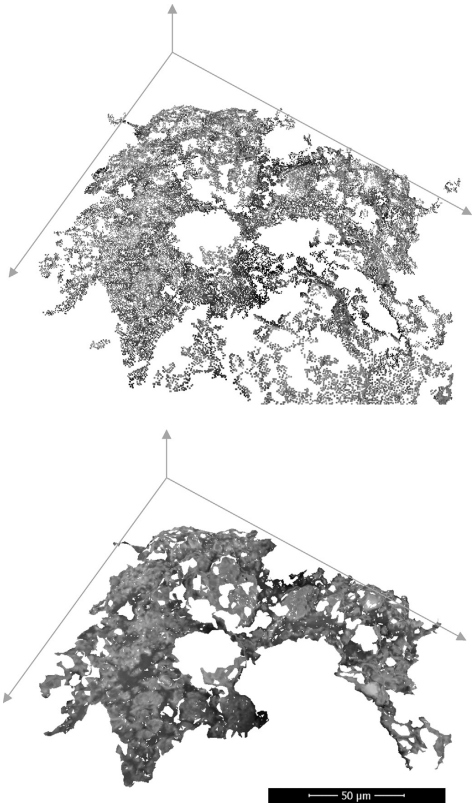

Fig. 7. 3D CHAp synthesized with tartaric acid (TA:Ca = 2) surface reconstruction steps, from mesh (top) to surface (bottom).

attributed to adsorbed water and structural hydroxyl groups (OH^{-}), respectively [40,41,45,48]. The determined ratio of integral intensities of these signals in the range of ca (0.12−0.25)/1.0 for all materials means that the amount of structural −OH groups in is significantly higher than from adsorbed water.

^{31}P NMR signal (Fig. 9) as well as ^{1}H → ^{31}P CP kinetics curves for the sample derived using glycerol as complexing agent drop out from the whole series of data (Fig. 10) exhibiting certain peculiarities. The asymmetry in the ^{31}P NMR signal shape can be caused by the chemical shift anisotropy (CSA) [49]. However the two peak structure survivals upon MAS, where CSA contribution to the signal shape is removed or at least essentially reduced. The ratio of integral intensities of the overlapped peaks is slightly changing getting from the static experiment to MAS (0.6/0.4 to 0.71/0.29, see Fig. 9). This observation is thought-provoking that the present sample is heterogenic. The processing of CP kinetic curves (Figs. 10 and 11) confirms this assumption. Interestingly, the spatial 3D surface reconstruction of SEM micrographs of CHAp samples synthesized by glycerate route was not possible. The unique CHAp surface details of this specimen might be directly connected with sample heterogeneity. Since glycerate derived CHAp samples were

monophasic, the probability of formation of amorphous phosphate phase in the end product is higher.

3.5.1. The models and the processing of CP kinetic data

In the case the I–S heteronuclear dipolar interactions are weak (in the present case I denotes proton and S is ^{31}P), e.g. spins being remote or reduced by molecular motion, while the I–I homonuclear couplings are moderate or strong, the CP kinetics is likely to follow the classical I–S model [38,39]. The kinetic curve, i.e. the dependence of integrated signal intensity on the contact time, is then described by

$$I(t) = I_0\,(1 - T_{CP}/T_{1\rho})^{-1}\,[\exp(-t/T_{1\rho}) - \exp(-t/T_{CP})], \quad (1)$$

where I_0 is the signal amplitude, $T_{1\rho}$ is the spin-lattice relaxation time of protons in the rotating frame and T_{CP} is a CP time constant that depends on the dipolar interactions of ^{31}P spins with protons.

The CP kinetics observed for studied samples exhibit the more or less blurred oscillations of intensity in the short contact time range (Fig. 11). In such cases the CP kinetics can described in the frame of the so-called non-classical I–I*–S (the asterisk denotes protons in close neighbourhood to ^{31}P) kinetics by the following equation [39,40,50]:

$$I(t) = I_0 e^{-t/T_{1\rho}}\left[1 - \lambda e^{-\frac{t}{T_{dif}}} - (1-\lambda)e^{-\frac{3t}{2T_{dif}}}\sum_i P(b_i/2)\cos(2\pi b_i t/2)\right], \quad (2)$$

where T_{dif} is the spin-diffusion time constant, $P\,(b/2)$ is the spin coupling distribution profile, b is the dipolar splitting (in Hz) and λ describes the distribution of polarization in the ^{31}P–(^{1}H)$_n$ spin cluster during the initial stage of CP. This parameter depends on the cluster composition ($\lambda = 1/(n+1)$ for a rigid lattice) as well as molecular motion [39,45]. Thus λ values must be refined for each system during the fitting of the model curve to the experimental data set. For very short contact times or in the case $P\,(b/2)$ can be approached by Gauss-shaped function, Eq. (2) can be simplified as

$$I(t) = I_0 e^{-t/T_{1\rho}}\left[1 - \lambda e^{-\frac{t}{T_{dif}}} - (1-\lambda)e^{-\frac{3t}{2T_{dif}}}e^{-\frac{t^2}{2T_2^2}}\right], \quad (3)$$

where the time constant T_2 characterizes the dipolar ^{31}P–^{1}H coupling. Eq. (3) (further in the present work referred as T2-averaging) is perhaps the most often used for the processing of experimental CP kinetic data in the cases it was deduced that the non-classical I–I*–S model to be more appropriate, compared to the classical one (I–S model), see e.g. Refs. [38–40].

It came out during processing that the CP kinetics in CHAp derived using glycerol as complexing agent cannot be fitted by the

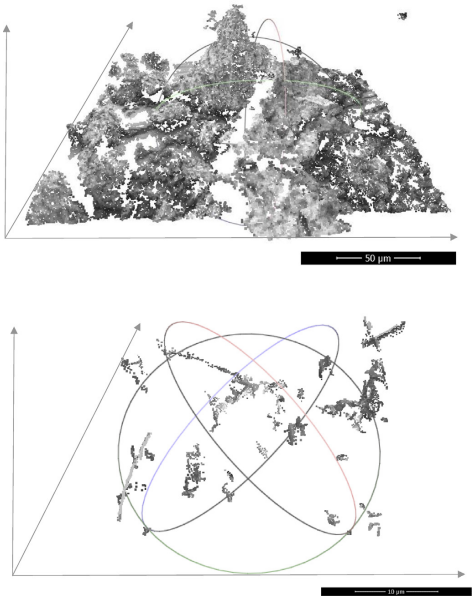

Fig. 8. 3D surface reconstruction of CHAp synthesized with ethylenglycol (EG:Ca = 1) at top and with glycerol (GL:Ca = 2) at bottom.

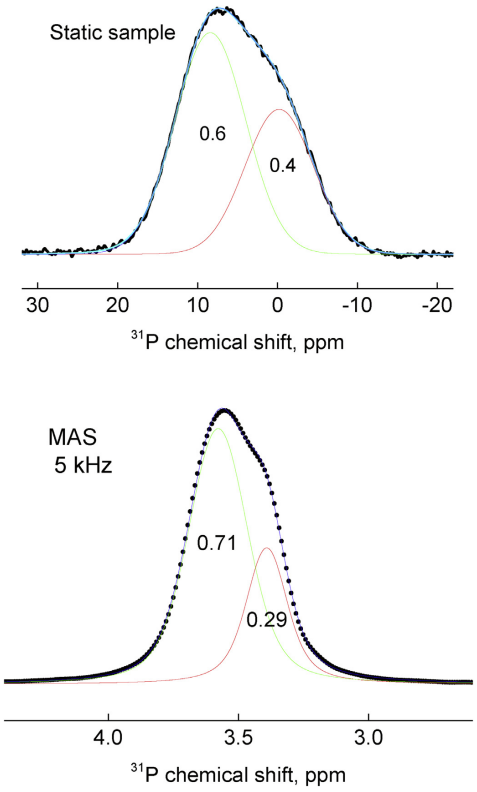

Fig. 9. On the heterogeneity of CHAp derived using complexing agent glycerol: the numbers indicate the relative integral intensities of overlapped ^{31}P NMR signals resolved using Voigt functions. More comments in text.

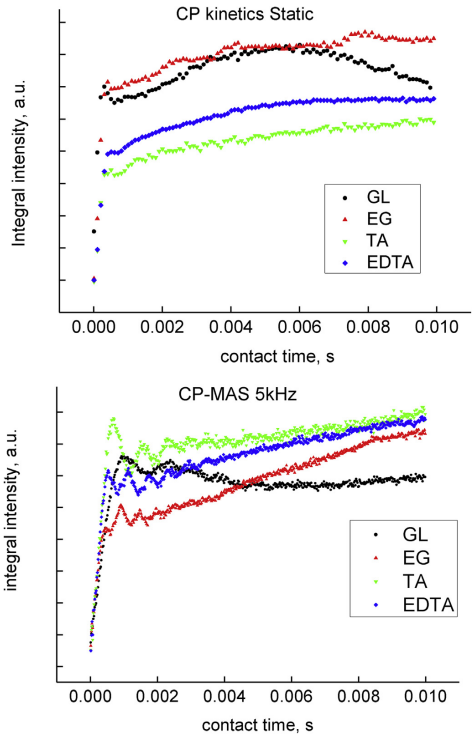

Fig. 10. Comparison of the $^{1}H \rightarrow {}^{31}P$ CP kinetics of synthesized CHAp using different complexing agents in static regime and upon 5 kHz MAS.

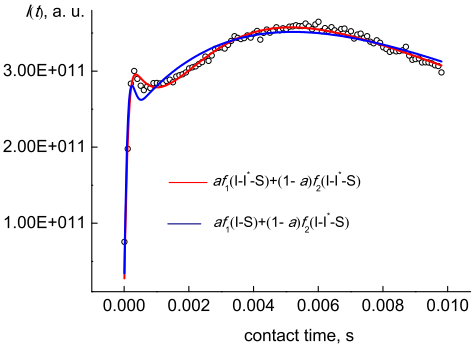

Fig. 11. The processing of CP kinetics in CHAp derived using glycerol as complexing agent. The fitting was carried out using the sum of classical I–S (Eq. (1)) or non-classical I–I*–S (Eq. (3)) models; the values of the weight parameter a was taken 0.6 or 0.4 that correspond to the relative integral intensities of overlapped ^{31}P NMR signals (see Fig. 13).

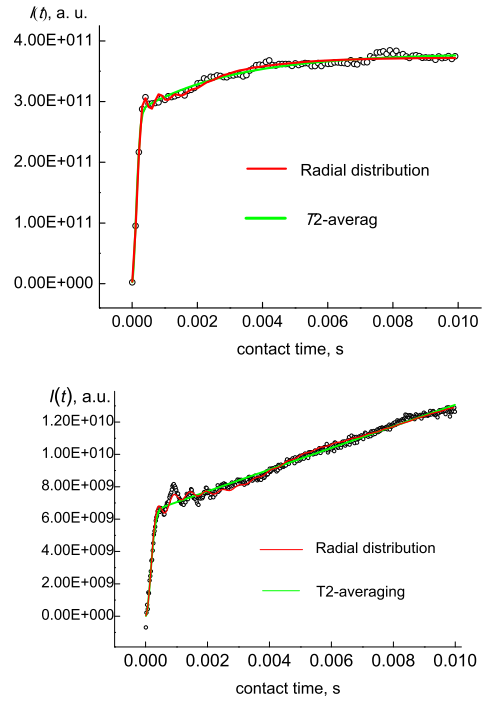

Fig. 12. The processing of CP kinetic curves for CHAp derived using ethylene glycol as complexing agent in static sample (the upper graph) and under 5 kHz MAS (the lower graph).

single kinetic model. The shape of very peculiar kinetic curve was more or less reproduced only by the fitting using the sum of two kinetics, either the classical I–S, or the non-classical I–I*–S (Fig. 11). However, more rigorous decision concerning the validity of the models was not possible because of huge number of the fitting parameters. The standard errors for some parameters were larger than their values. Thus it can be only stated that the using of glycerol led to the formation of heterogeneity. Because of complexity this material was removed from the further consideration.

The CP kinetics curves for other CHAp (Fig. 10) were successfully processed applying the non-classical model. The experimental data were processed using both Eqs. (2) and (3). In the case Eq. (2) was applied, the spin coupling distribution profile $P(b/2)$ was taken to be the radial function approach $P(b/2) \sim b^{-2/3}$ [50]. The fitting results are demonstrated on CHAp derived using ethylene glycol as complexing agent (Fig. 12). The values of fitted parameters for all studied materials are presented in Table 1. Note, T2-averaging is not adequate in the case of MAS was applied because of decimation of dipole–dipole interactions between remote spins [50]. This clearly reflects on the fitting criterions R^2 and χ^2 values (Table 1).

The spatial distributions of protons surround ^{31}P nuclei in the synthesized CHAp have been obtained processing $^{1}H \rightarrow {}^{31}P$ CP kinetic curves and applying the Fourier transform formalism with the

Table 1
CP kinetics fitting parameters for CHAp derived using various complexing agents.

Static regime				
Complexing agent ⇒	GL	EG	TA	EDTA
T2-averaging (Eq. (3))				
I_0, × 10^{11} a. u.	Heterogenic system; More comments in text	3.79 ± 0.02	2.55 ± 0.02	2.862 ± 0.008
λ		0.266 ± 0.007	0.377 ± 0.006	0.384 ± 0.005
T_{dif}, ms		2.9 ± 0.2	4.4 ± 0.3	2.75 ± 0.08
T_2, ms		0.182 ± 0.003	0.190 ± 0.004	0.224 ± 0.003
$T_{1\rho}$, s		∞	∞	∞
R^2		0.995	0.995	0.998
χ^2/I_{max} × 100%		1.49	1.5	0.9
Radial function approach (Eq. (2), with $P(b/2) \sim b^{-2/3}$)				
I_0, × 10^{11} a. u.		3.73 ± 0.02	2.46 ± 0.02	2.836 ± 0.008
λ		0.387	0.415	0.477
T_{dif}, ms		1.8	3.9	2.2
b_{max}, Hz*		4100	4600	3500
b_{SC}, Hz*		700	300	500
$T_{1\rho}$, s		∞	∞	∞
R^2		0.995	0.993	0.999
χ^2/I_{max} × 100%		1.4	1.7	0.8
MAS experiment (5 kHz spinning, Hartmann-Hahn matching $n = -1$)				
Complexing agent ⇒	GL	EG	TA	EDTA
T2-averaging (Eq. (3))				
I_0, × 10^{10} a. u.	Heterogenic system; More comments in text	62.6 ± 0.2	23.3 ± 0.2	2.16 ± 0.01
λ		0.990 ± 0.005	0.952 ± 0.002	0.587 ± 0.001
T_{dif}, ms		0.92 ± 0.02	0.88 ± 0.03	2.2 ± 0.2
T_2, ms		0.16 ± 0.03	0.190 ± 0.004	0.18 ± 0.02
$T_{1\rho}$, s		∞	∞	∞
R^2		0.990	0.940	0.983
χ^2/I_{max} × 100%		2	4.5	3
Radial function approach (Eq. (2), with $P(b/2) \sim b^{-2/3}$)				
I_0, × 10^{10} a. u.		1.98 ± 0.02	1.34 ± 0.02	1.41 ± 0.01
λ		0.725	0.34	0.49
T_{dif}, ms		1.4	2.7	4.7
b_{max}, Hz[a]		3800	2200	3050
b_{SC}, Hz[a]		470	600	520
$T_{1\rho}$, s		∞	∞	∞
R^2		0.995	0.993	0.999
χ^2/I_{max} × 100%		1.4	1.7	0.8

[a] The model parameters in the radial distribution function approach that correspond the 'shortest' $^{31}P-^{1}H$ distances (b_{max}) and the effective extent of spin cluster (b_{SC}) [50].

sequent recalculation of $P(b/2)$ from b-variable to internuclear distances (r) developed in Ref. 40. The results are shown in Fig. 13. The spatial distribution profiles consist of 3 maxima at 0.21–0.22 nm, 0.25–0.32 nm and at ca > 0.5 nm. The differences are seen in their relative heights and in the resolution of the peaks. Particularly interesting is the clear presence of the peaks at 0.21–0.22 nm in nano-CHAp (Fig. 13). They are better resolved upon MAS. The distances of 0.21–0.25 nm are typical for P–O–H structures that are found in some related systems, as calcium phosphate gelatin nano-composites [51], potassium- and ammonium dihydrogen phosphates [52]. In CHAp the protons are not part of the phosphate group, and thus such short P … H contacts should not be met there. In pure crystalline CHAp each P atom has two protons distanced at 0.385 nm, further two at 0.42 nm, while others are 0.6 nm or more away [38]. The P–O–H structural unit with P … H distances of 0.2–0.25 nm are present mainly on the surface layers and therefore extremely hardly seen applying various other experimental techniques because of highly disordered nature of nano-structured CHAp. Some observations using FTIR and NMR techniques confirm the presence of hydrogen phosphate units in the nano-structured samples. It is a hard task because e.g. the FTIR band of HPO_4^{2-} at ca 540 cm^{-1} is strongly overlapped by the intensive modes of PO_4^{3-} [45]. The possible presence $^{31}P-^{1}H$ spin pairs with the closest distance 0.22–0.25 nm in calcium phosphate gelatin nano-composites was deduced only indirectly from the simulation of CP kinetics [51].

The fact that the peaks at 0.21–0.22 nm are well resolved in the spatial distribution profiles of studied CHAp (Fig. 13) can be understood taking into account the presence of large surface areas in nano-structured materials. The spatial distributions correlate with FTIR spectroscopy data (Fig. 4). Namely, beside the sharp peak at 3570 cm^{-1} of the stretching vibration of OH^- ions in the 'bulk' another much weaker peak at ca 3642 cm^{-1} band is noticeable in all cases. These bands can be assigned to the surfaces modes of O–H stretching vibration of P–O–H groups [46] and to some dangling modes of water on the surface [53]. Moreover, despite the amount of adsorbed water in the samples was rather similar, even this difference was enough to form the water clusters different in size and amount. The bands that are seen over 3100–3600 cm^{-1} range (Fig. 4) can be compared and recognized as those of small water clusters (up to hexamers) observed in the low-temperature matrix experiments [54] as well as in FTIR spectra of water in hydrophobic solvents [47]. The presence of various water clusters that are trapped in nano-structured cavities or in surface potholes reflects in the complex spatial distribution of protons surround ^{31}P (Fig. 13).

4. Conclusions

Morphology and crystallinity-controlled an aqueous sol–gel synthesis of calcium hydroxyapatite ($Ca_{10}(PO_4)_6(OH)_2$, CHAp) was developed using different complexing agents, namely 1,2-ethylendiaminetetraacetic acid (EDTA), 1,2-

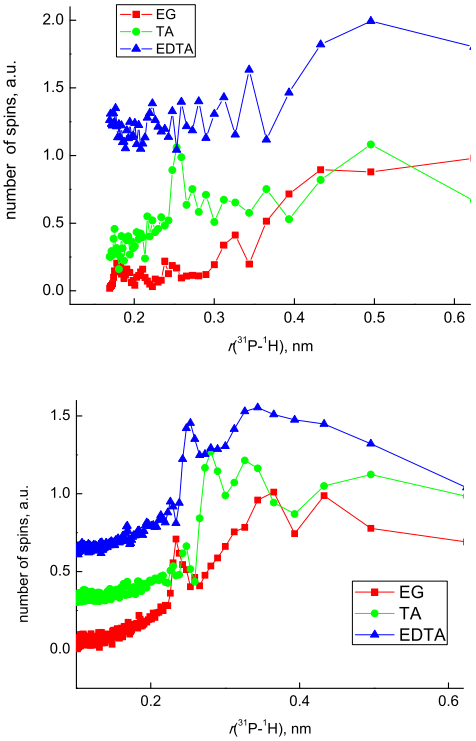

Fig. 13. Spatial distributions of protons surround ^{31}P nuclei in CHAp synthesized using various complexing agents in the static sample (the upper graph) and under 5 kHz MAS (the lower graph).

diaminocyclohexanetetracetic acid (DCTA), tartaric acid (TA), ethylene glycol (EG) and glycerol (GL) in the sol–gel processing. The XRD patterns of the samples after calcination of Ca–P–O gels obtained using different complexing agents in all cases showed formation of CHAp as the main crystalline phase. Obviously, the amount of impurities was dependent on the concentration of complexing agent used in the sol–gel processing. The higher amount of EDTA, DCTA and TA promotes formation of purer CHAp. Contrary, the phase purity of synthesis products obtained in the glycolate and glycerate sol–gel routes only slightly depended on the amount of complexing agent. FTIR spectroscopy results confirmed, that for all materials the amount of structural –OH groups was significantly higher than from adsorbed water. The CHAp solids were composed of agglomerates of elongated particles (DCTA), aggregated of hardly identified shape particles (EDTA), elongated particles (TA), nanocrystalline particles with regular spherically-shaped structure (EG) and monolithic solids of small particles (GL) with 0.5–2.0 μm, 1–3 μm, with width of 0.2–0.5 μm and 1.0–1.5 μm in length, 20–70 nm and 5–10 nm in size, respectively. The spatial 3D data from the SEM images of CHAp samples obtained by TA, EG and GL sol–gel routes were recovered for the first time to our knowledge. Further statistical analysis could be performed on the image analysis data to determine particle size distribution and particle connectivity. The non-classical spin coupling model with the radial distribution function approach perfectly described the CP kinetics in nano-structured CHAp. The P–O–H structural units with P … H distances of 0.21–0.22 nm well resolved in the spatial distribution of protons surround ^{31}P nuclei profiles for the studied CHAp can be understood taking into account the large surface areas in nano-structured materials. The spatial distributions correlated with FTIR spectroscopy data. Despite the structural manifolds of hydroxyl groups in the synthesized materials were deduced to be rather similar, even small differences were enough to form the water clusters different in size and amount. The presence of various water clusters that are trapped in nano-structured cavities or in surface potholes reflected in the complex spatial distribution of protons surround phosphorus atoms. Glycerol was found to be not a proper material as complexing agent. The using of glycerol led to the formation of significant heterogeneity in the sample.

Acknowledgments

This research was funded by a grant KALFOS (No. LJB-2/2015) from the Research Council of Lithuania. The authors acknowledge Center of Spectroscopic Characterization of Materials and Electronic/Molecular Processes (Scientific infrastructure "SPECTROVERSUM") at Lithuanian National Center for Physical Sciences and Technology for use of spectroscopic equipment.

References

[1] F. Li, G. Li, H. Chen, J.Q. Jia, F. Dong, Y.B. Hu, Z.G. Shang, Y.X. Zhang, J. Power Sources 296 (2015) 86–91.
[2] M. Kumaresavanji, C.T. Sousa, A. Apolinario, A.M.L. Lopes, J.P. Araujo, Mater. Sci. Eng. B-Adv. Funct. Solid-State Mater. 200 (2015) 117–123.
[3] O.M. Hemeda, N.Y. Mostafa, O.H. Abd Elkader, D.M. Hemeda, A. Tawfik, M. Mostafa, J. Magn. Magn. Mater. 394 (2015) 96–104.
[4] W. Zhang, T. Huynh, P. Xiu, B. Zhou, C. Ye, B.Q. Luan, R.H. Zhou, Carbon 94 (2015) 895–902.
[5] X.J. Chen, Y.Z. Dai, X.Y. Wang, J. All. Compd. 649 (2015) 910–932.
[6] N.F. Mohammad, R. Othman, F.Y. Yeoh, Ceram. Int. 41 (2015) 10624–10633.
[7] I. Bogdanoviciene, K. Tõnsuaadu, V. Mikli, I. Grigoraviciute-Puroniene, A. Beganskiene, A. Kareiva, Centr. Eur. J. Chem. 8 (2010) 1323–1330.
[8] D. Milovac, G.G. Ferrer, M. Ivankovic, H. Ivankovic, Mater. Sci. Eng. C-Mater. Biol. Appl. 34 (2014) 437–445.
[9] P. Gentile, C.J. Wilcock, C.A. Miller, R. Moorehead, P.V. Hatton, Materials 8 (2015) 2297–2310.
[10] N. Kurgan, V. Karbivskyy, V. Kasyanenko, Nanoscale Res. Lett. 10 (2015) 1–5.
[11] S. Pramanik, A.K. Agarwal, K.N. Rai, A. Garg, Ceram. Int. 33 (2007) 419–426.
[12] K. Teshima, S. Lee, M. Sakurai, Y. Kameno, K. Yubuta, T. Suzuki, T. Shishido, M. Endo, S. Oishi, Cryst. Growth Des. 9 (2009) 2937–2940.
[13] M. Iijima, J. Moradian-Oldak, Biomaterials 26 (2005) 1595–1603.
[14] M. Sadat-Shojai, M. Atai, A. Nodehi, J. Braz. Chem. Soc. 22 (2011) 571–582.
[15] R.N. Panda, M.F. Hsieh, R.J. Chung, T.S. Chin, J. Phys. Chem. Solids 64 (2003) 193–199.
[16] M. Kawata, H. Uchida, K. Itatani, I. Okada, S. Koda, M. Aizawa, J. Mater. Sci. Mater. Med. 15 (2004) 817–823.
[17] P.N. Kumta, C. Sfeir, D.H. Lee, D. Olton, D. Choi, Acta Biomater. 1 (2005) 65–83.
[18] C. Verwilghen, C.M. Chkir, S. Rio, A. Nzihou, P. Sharrock, G. Depelsenaire, Mater. Sci. Eng. C 29 (2009) 771–773.
[19] A.C. Tas, J. Eur. Ceram. Soc. 20 (2000) 2389–2394.
[20] J.S. Cho, Y.C. Kang, J. All. Cmpd 464 (2008) 282–287.
[21] S. Sasikumar, R. Vijayaraghavan, J. Mater. Sci. Technol. 26 (2010) 1114–1118.
[22] K. Itatani, T. Tsugawa, T. Umeda, Y. Musha, I.J. Davies, S. Koda, J. Ceram. Soc. Jpn. 118 (2010) 462–466.
[23] K. Sato, Y. Hotta, T. Nagaoka, M. Yasuoka, K. Watari, J. Mater. Sci. 41 (2006) 5424–5428.
[24] M. Jevtic, M. Mitric, S. Skapin, B. Jancar, N. Ignjatovic, D. Uskokovic, Cryst. Growth Des. 8 (2008) 2217–2222.
[25] H. Zreiqat, R. Roest, S. Valenzuela, A. Milev, B. Ben-Nissan, Key Eng. Mater. 284–286 (2005) 541–544.
[26] I. Bogdanoviciene, A. Beganskiene, K. Tõnsuaadu, J. Glaser, H.-J. Meyer, A. Kareiva, Mater. Res. Bull. 41 (2006) 1754–1762.
[27] M. Malakauskaite-Petruleviciene, Z. Stankeviciute, A. Beganskiene, A. Kareiva, J. Sol-Gel Sci. Technol. 71 (2014) 437–446.
[28] S. Ramesh, A.N. Natasha, C.Y. Tan, L.T. Bang, A. Niakan, J. Purbolaksono,

H. Chandran, C.Y. Ching, S. Ramesh, W.D. Teng, Ceram. Int. 41 (2015) 10434–10441.
[29] O. Opuchovic, A. Beganskiene, A. Kareiva, J. All. Compd. 647 (2015) 189–197.
[30] P. Suresh, S. Srinath, J. All. Compd. 649 (2015) 843–850.
[31] K.I. Choi, W. Lee, S.H. Lee, C. Lim, Mater. Lett. 158 (2015) 36–39.
[32] O. Opuchovic, G. Kreiza, J. Senvaitiene, K. Kazlauskas, A. Beganskiene, A. Kareiva, Dyes Pigm 118 (2015) 176–182.
[33] B. Elgh, A.E.C. Palmqvist, J. Sol-Gel Sci. Technol. 76 (2015) 395–401.
[34] A. Zalga, J. Reklaitis, E. Norkus, A. Beganskiene, A. Kareiva, Chem. Phys. 327 (2006) 220–228.
[35] A. Katelnikovas, J. Barkauskas, F. Ivanauskas, A. Beganskiene, A. Kareiva, J. Sol-Gel Sci. Techn. 41 (2007) 193–201.
[36] S. Mathur, H. Shen, A. Leleckaite, A. Beganskiene, A. Kareiva, Mater. Res. Bull. 40 (2005) 439–446.
[37] J. Trinkunaite-Felsen, A. Prichodko, M. Semasko, R. Skaudzius, A. Beganskiene, A. Kareiva, Adv. Powder Technol. 26 (2015) 1287–1293.
[38] W. Kolodziejski, Top. Curr. Chem. 246 (2004) 235–270.
[39] W. Kolodziejski, J. Klinowski, Chem. Rev. 102 (2002) 613–628.
[40] V. Klimavicius, A. Kareiva, V. Balevicius, J. Phys. Chem. C 118 (2014) 28914–28921.
[41] L. Dagys, V. Klimavicius, J. Kausteklis, A. Chodosovskaja, V. Aleksa, A. Kareiva, V. Balevicius, Lith. J. Phys. 55 (2015) 1–9.
[42] S. Kareiva, A. Selskis, F. Ivanauskas, S. Sakirzanovas, Pure Appl. Chem. 87 (2015) 283–292.
[43] A. Antonakos, E. Liarokapis, T. Leventouri, Biomaterials 28 (2007) 3043–3054.
[44] E. Garskaite, K.A. Gross, S.W. Yang, Thomas C.K. Yang, J.C. Yang, A. Kareiva, Cryst. Eng. Commun. 16 (2014) 3950–3959.
[45] J. Kolmas, A. Jaklewicz, A. Zima, M. Bućko, Z. Paszkiewicz, J. Lis, A. Ślosarczyk, W. Kolodziejski, J. Mol. Struct. 987 (2011) 40–50.
[46] T. Ishikawa, A. Teramachi, H. Tanaka, A. Yasukawa, K. Kandori, Langmuir 16 (2000) 10221–10226.
[47] T. Köddermann, F. Schulte, M. Huelsekopf, R. Ludwig, Angew. Chem. Int. Ed. 42 (2003) 4904–4908.
[48] J. Kolmas, W. Kolodziejski, Chem. Phys. Lett. 554 (2012) 128–132.
[49] E. Davies, M.J. Duer, S.E. Ashbrook, J.M. Griffin, J. Am. Chem. Soc. 134 (2012) 12508–12515.
[50] V. Klimavicius, L. Dagys, V. Balevicius. In press.
[51] A. Vyalikh, P. Simon, T. Kollmann, R. Kniep, U. Scheler, J. Phys. Chem. C 115 (2011) 1513–1519.
[52] D. Xu, D. Xue, J. Cryst. Growth 286 (2006) 108–113.
[53] J.A. Noble, C. Martin, H.J. Fraser, P. Roubin, S. Coussan, J. Phys. Chem. C 118 (2014) 20488–20495.
[54] S. Coussan, P. Roubin, J.P. Perchard, Chem. Phys. 324 (2006) 527–540.

THE JOURNAL OF PHYSICAL CHEMISTRY B

Article

pubs.acs.org/JPCB

NMR and Raman Spectroscopy Monitoring of Proton/Deuteron Exchange in Aqueous Solutions of Ionic Liquids Forming Hydrogen Bond: A Role of Anions, Self-Aggregation, and Mesophase Formation

Vytautas Klimavicius,[†] Zofia Gdaniec,[‡] Jonas Kausteklis,[†] Valdemaras Aleksa,[†] Kestutis Aidas,[†] and Vytautas Balevicius*[,†]

[†]Department of General Physics and Spectroscopy, Vilnius University, Sauletekio 9-3, LT-10222 Vilnius, Lithuania

[‡]Institute of Bioorganic Chemistry, Polish Academy of Sciences, Z. Noskowskiego 12/14, PL-61704 Poznan, Poland

ABSTRACT: The H/D exchange process in the imidazolium-based room temperature ionic liquids (RTILs) 1-decyl-3-methyl-imidazolium bromide- and chloride ([C_{10}mim][Br] and [C_{10}mim][Cl]) in D_2O solutions of various concentrations was studied applying ^1H, ^{13}C NMR, and Raman spectroscopy. The time dependencies of integral intensities in NMR spectra indicate that the H/D exchange in [C_{10}mim][Br] at very high dilution (10^{-4} mole fraction of RTIL) runs only slightly faster than in [C_{10}mim][Cl]. The kinetics of this process drastically changes above critical aggregation concentration (CAC). The time required to reach the apparent reaction saturation regime in the solutions of 0.01 mole fraction of RTIL was less 10 h for [C_{10}mim][Br], whereas no such features were seen for [C_{10}mim][Cl] even tens of days after the sample was prepared. The H/D exchange was not observed in the liquid crystalline gel mesophase. The role of anions, self-aggregation (micellization), and mesophase formation has been discussed. Crucial influence of Br^- and Cl^- anions on the H/D exchange rates above CAC could be related to the short-range ordering and molecular microdynamics, in particular that of water molecules. The concept of the conformational changes coupled with the H/D exchange in imidazolium-based ionic liquids with longer hydrocarbon chains can be rejected in the light of ^{13}C NMR experiment. The revealed changes in ^{13}C NMR spectra are caused by the secondary (^{13}C) isotope effects not being the signal shifts due to the conformational *trans–gauche* transition.

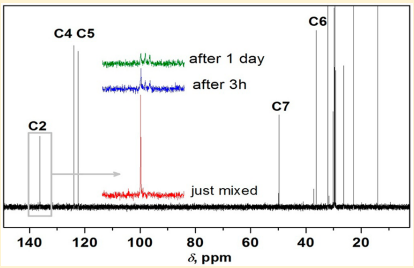

INTRODUCTION

Ionic liquids (ILs)/room temperature ionic liquids (RTILs) can be considered as one of the most successful breakthroughs creating smart materials and multifunctional compositions possessing many appealing features important for the applications in high technologies, including various artificial sensors of new generation, electrochemistry, fuel cells and batteries, (bio-) catalysis, *etc.*[1−4] Nevertheless, the processes taking place in ionic liquids are not completely understood on a molecular level and constitute one of the main challenges in fundamental research. Hydrogen bonding between the anions and cations in certain ILs can play crucial role. Localized and directionally depending H-bonding disorder the Coulomb network, and the system then deviates from the charge symmetry.[5] This intensifies the ionic dynamics and results in a significant decrease of melting points and viscosity. Hence, some important macroscopic properties of ILs can be tuned by adjusting the ratio between Coulomb- and the H-bond contributions, even the latter being energetically less significant.

Ionic liquids are intriguing systems to study in respect of purely H-bonding phenomena. In many of ILs the anions are the conjugate bases of various acids, in certain cases, strong and very strong, as for example, halogenides (Cl^-, Br^-), trifluoroacetate (CF_3COO^-), triflate ($CF_3SO_3^-$), *etc.*[6] Hence, some of ILs can be conceptualized as ionic pair systems $A^-\cdots H^+B$ created by very 'deep' proton transfer from the acid (A) to the defined base (B). These ionic pairs are kind of 'inverted' in respect of the traditional ones that appear in numerous H-bond systems with proton transfer.[7−10] Such ILs structures can be thought as the 'ground state' that can be disturbed by various external stimuli (temperature, media effects, *etc*) reversing the proton migration toward the anion and maybe even culminating with the return of the system to the neutral H-bond A–H···B. If this succeeded, the novel sort of phase transitions could be expected that would create the hybrid state of matter with the properties that occupy an intermediate place between ionic and nonionic liquids. The studies of proton/deuteron (H/D) exchange trying to determine the possible pathways of this reaction and its kinetics would provide extremely valuable information on the picture of H-bond in ILs, including the large amplitude proton motion and thus

Received: March 1, 2013
Revised: August 9, 2013
Published: August 12, 2013

evaluating the chances to provoke the reverse proton migration by proper physically realizable stimuli.

The cation−anion interactions and various aspects of H/D exchange reactions in some imidazolium-based ILs have been studied by means of X-ray photoelectron, NMR, and Raman spectroscopy techniques.[11−16] Several intriguing findings can be listed. For example, charge transfer is not related to H-bonding; however, both H-bonding and charge transfer are seen to be enhanced for small and more strongly coordinating anions;[11] the relation between the slowdown of rotational dynamics and the H/D exchange deactivation has been deduced;[12] complex dependency of the H/D exchange rates on RTIL concentration in water has been observed;[13] anomalous dynamics of ions at very low ionic liquid concentration in D_2O has been revealed;[14] the H/D exchange has induced conformational changes of ILs;[15] the rate of H/D exchange, diffusion coefficients, and spin−lattice relaxation time are affected by critical aggregation of RTILs.[16]

The purposes of present work were (i) to study the anion, self-aggregation, and mesophase effects on the H/D exchange in the 1-decyl-3-methyl-imidazolium bromide- and chloride ($[C_{10}mim][Br]$ and $[C_{10}mim][Cl]$, respectively) in D_2O solution below and above critical aggregation concentration as well as in the liquid crystalline gel mesophase by means of the ^1H, ^{13}C NMR, and Raman spectroscopy and (ii) to check the possibility of conformational changes induced by the H/D exchange in imidazolium-based RTILs with longer alkyl chains.

EXPERIMENTAL SECTION

The 1-decyl-3-methyl-imidazolium bromide and chloride from Merck KGaA Darmstadt and from Ionic Liquids Technologies GmbH (the structure and atom numbering are shown in Figure 1) were dried under vacuum at 80 °C for one day; D_2O (99%, Aldrich) was used without additional treatment. The samples were prepared by weighting (±0.1 mg) the components.

NMR experiments were carried out on Bruker Avance^{II}/400 and Bruker Avance^{III}/500 NMR spectrometers operating at 400/500 and 100/125 MHz for ^1H and ^{13}C, respectively, using 5 mm BBO probe-heads. The temperature of 298 K was controlled with an accuracy of ±0.5 K. The signals of D_2O solution and DMSO in capillary insert were used as the reference and then converted in δ-scale, with respect to TMS, taking their chemical shift values from ref 17. The D_2O and DMSO were also used for locking.

Raman spectra were obtained using Bruker MultiRAM FT-Raman spectrometer with motorized xyz-sample stage and with liquid nitrogen cooled germanium detector. The 1064 nm wavelength beam of the pulsed Nd:YAG laser (500 mW) was used as the excitation source. The 180° scattering geometry was employed. The resolution of the spectrometer was set to 2 cm^{-1}. The Raman spectra were recorded in the 70−4000 cm^{-1} spectral range at 296 K. Some samples were cooled down up to 49 K. FT-Raman spectrometer control and experimental data digital processing were performed using the OPUS 6.5 software program package.

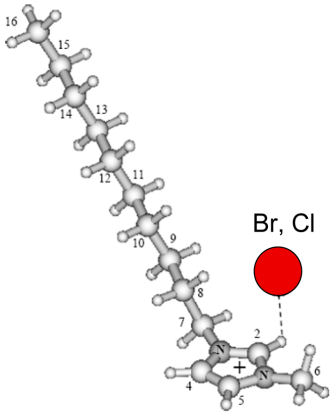

Figure 1. Molecular structure and carbon numbering of $[C_{10}mim][X]$, X = Br, Cl.

COMPUTATIONAL DETAILS

Electronic structure calculations were conducted using Gaussian09 program.[18] Equilibrium geometries and harmonic vibrational frequencies as well as Raman activities of the 1-butyl-3-methyl-imidazolium cation isotopologues are based on the calculations using the B3LYP exchange-correlation functional[19] and the 6-311++G** basis set.[20] Bulk solvent effects are accounted for by using a polarizable continuum model (PCM).[21] Default settings of PCM were utilized apart from parameters *ofac* and *rmim*, which were assigned values of 0.8 and 0.5, respectively. Anharmonic analysis was performed at the B3LYP/6-31G* level *in vacuo* using second order perturbative approach[22] implemented in Gaussian09. ^1H and ^{13}C magnetic shielding tensors were calculated at the level of PBE0/6-311++G(2d,2p)/PCM. More details concerning this choice are given in ref 6.

RESULTS AND DISCUSSION

Phase Behavior and Sample Compositions. It is well-known that some of imidazolium-based RTILs $[C_nmim][X]$ with sufficiently long alkyl chains (n = 6−18) demonstrate a broad variety of phenomena in the phase behavior[23−26] and the aggregation (micellization) processes.[27−33] More details are known regarding the studied compounds. The addition of water to $[C_{10}mim][Br]$ causes its conversion from a viscous liquid to a gel possessing the optical birefringence.[23] The coexisting mesophases for closely related $[C_{12}mim][Br]$ were identified more precisely being as solid, lamellar, and hexagonal ones.[24] At the higher content of water (~15% w/w of H_2O), both $[C_{10}mim][Br]/H_2O$ and $[C_{10}mim][Cl]/H_2O$ solutions convert into hardened gel, which resists flow upon gravity, already at room temperature. Some serious technical problems, such as difficulties to fill the NMR tubes with the hardened substance, the inserting of the lock-capillary, and others, have been met during experiments on gel samples as already reported by us in ref 25. The mesophases disappear at further dilution, and the viscosity of the solutions drops drastically. This highly diluted state (below ~0.05−0.08 mole fraction of RTIL) was called as the aqueous solution.[23] The coexisting solid and liquid phases can appear only below ~290 K.[26]

It is obvious that the rates of H/D exchange process in such RTILs can be crucially influenced by the phase behavior when different molecular sites and peculiar environments in the microscopic or mesoscopic scales appear. For example, the imidazolium groups can get blocked inside of inverted

hexagonal structures, if such formed, or the formation of the regions with confined water (D_2O as deuteron donor) is enhanced due to the interplay between hydrophilic and hydrophobic segments, as well as the formation of the layered structures in the case of the lamellar phase.[24] In order to segregate the pure H-bond-driven contribution to the H/D exchange from possible phase/environmental effects, the composition of the samples should be chosen that makes sure that the systems are in the identical states. The aqueous solution phase (i.e., the one that is by many physical features very close to the 'classical' electrolyte (water + salt) system) would be most suitable. Therefore, two highly diluted samples of $[C_{10}mim][Br]$ and $[C_{10}mim][Cl]$ in D_2O (10^{-4} mole fraction of RTIL) have been first prepared and investigated.

Increasing the concentration in the aqueous solution phase the self-aggregation of some RTILs via micelle formation can take place,[27−33] even the mesophase formation is still excluded. This is important to study, as there are some indications that the rates of H/D exchange, diffusion coefficients, and spin−lattice relaxation time can sufficiently differ for the solutions being below and above of critical aggregation concentration (CAC).[16]

The C(2)−H···X^- bridge proton chemical shift dilution curves can provide useful information when determining the critical aggregation concentration, predicting structures of aggregates, *etc.*, as it was done for some $[C_n mim][X]$ series.[27−29] In those cases, the dilution curves exhibit a typical behavior with two linear dependencies of the chemical shift on concentration whose intersection reminds a break point. The corresponding concentration value is usually accepted as the CAC. In the case of $[C_{10}mim][Br]$ in H_2O, the break point of the chemical shift dilution curve was only roughly evaluated to be less than ~0.01 mole fraction of RTIL.[25] In the present work, the CAC values have been determined more precisely for both studied compounds. The corresponding ^{1}H NMR shift break points are shown in Figure 2. This allowed us to determine the CAC values equal to 6.4×10^{-4} mole fraction and 9.9×10^{-4} mole fraction of $[C_{10}mim][Br]$ and $[C_{10}mim][Cl]$, respectively, which are in a perfect agreement with the available literature data (Table 1). Therefore, the next couple of samples of 0.01 mole fraction of RTIL in D_2O was prepared. Such composition assures that both systems are close to the midpoint between the onsets of aggregation and the gel mesopase formation. Also note that the samples of same composition were used studying the H/D exchange in some other RTIL systems (e.g. $[C_4mim][X]/D_2O$, X = I, BF_4).[34]

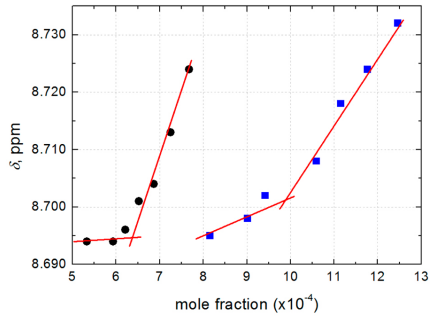

Figure 2. Determination of critical aggregation concentration (CAC) of $[C_{10}mim][X]$, X = Br (black circles), Cl (blue squares) using dependencies of chemical shift of C(2)−H···X^- proton on concentration in H_2O.

Table 1. Literature and Present Work Data on Critical Aggregation Concentration (CAC) of $[C_{10}mim][X]$, X = Br, Cl in H_2O and D_20 at 298 K

$[C_{10}mim][Br]$			$[C_{10}mim][Cl]$		
CAC, M	solvent and method	ref	CAC, M	solvent and method	ref
0.030−0.032	D_2O, NMR	29	0.055	H_2O, interfacial tension	27
0.029	H_2O, surface tension	32	0.045	H_2O, fluorescence	27
0.033	H_2O, conductivity	32	0.055	H_2O, NMR	27
0.04	H_2O, potentiometry	33	0.054	H_2O, surface tension	30
			0.060	H_2O, conductivity	30
CAC values recalculated to mole fraction: (5.3 − 7.2) × 10^{-4}			CAC values recalculated to mole fraction: (8 − 10) × 10^{-4}		
6.4×10^{-4} mole fraction	H_2O, NMR	present work	9.9×10^{-4} mole fraction	H_2O, NMR	present work

$[C_{10}mim][Br]/H_2O$ and $[C_{10}mim][Cl]/H_2O$ solutions convert at higher content of water from a viscous liquid to the anisotropic gel.[23,25] This gel was found to be stable over the range of ~5−40% w/w of water (i.e., 0.08 - 0.53 mole fraction of RTIL). In order to check the influence of this mesophase on the H/D exchange rate another two samples of 0.4 mole fraction of RTIL in D_2O were prepared and investigated.

Monitoring of H/D Exchange Using ^{1}H and ^{13}C NMR. The experimental and calculated ^{1}H and ^{13}C NMR spectra of $[C_{10}mim][Br]$ in the neat RTIL as well as in various solvents and mesophases have been previously reported.[25,26,35] The ^{1}H and ^{13}C NMR spectra of $[C_{10}mim][Br]$ and $[C_{10}mim][Cl]$ (Figures 3 and 4) are very similar, and ^{13}C chemical shifts appear to be less sensitive to the anions used. Similar tendency has been observed for $[C_8mim][X]$ series with X = Br and Cl among those.[11] Instead of narrow symmetric peaks the broad more or less asymmetrically shaped signals are seen in ^{1}H NMR spectra registered in the gel phase (Figure 3). Such signal shapes are common for anisotropic liquids.[26] The greater ordering and more anisotropic character molecular motion in the gel phase is better pronounced in the spectrum of $[C_{10}mim][Cl]$ (Figure 3). The degree of asymmetry of the signal contours indicate that the biaxiality of this phase should be rather close to 1.[26]

The most remarkable changes during the H/D exchange have been observed for NMR signals of the imidazolium ring, as it could be *a priori* expected. This is particularly clearly manifested in ^{13}C NMR spectrum (Figure 4), where the signal corresponding to C(2) carbon atom splits into triplet characterized by $^1J(^{13}C-^2H)$ = 33.6 Hz due to $^{13}C-^2H$ spin coupling. The same value of $^1J(^{13}C-^2H)$ was obtained for both studied RTILs.

The kinetics of the H/D exchange was followed using the relative integral intensity of the ^{1}H NMR signal of C(2)−H proton normalized in respect to the peak of $-C(16)H_3$ group (Figure 5). This choice differs from that applied in ref 13, where the H/D exchange in $[C_4mim][BF_4]/D_2O$ mixtures was

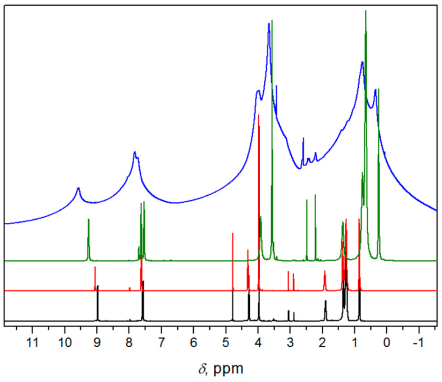

Figure 3. ^{1}H NMR spectra of $[C_{10}mim][X]$ in D_2O solutions: close to the midpoint between the onset of aggregation and the gel formation (0.01 mole fraction of RTIL), X = Cl (black) and X = Br (red); in the gel phase (0.4 mole fraction of RTIL), X = Br (green) and X = Cl (blue); all at T = 298 K. The spectra below CAC are not shown because they inessential differ from those at 0.01 mole fraction of RTIL.

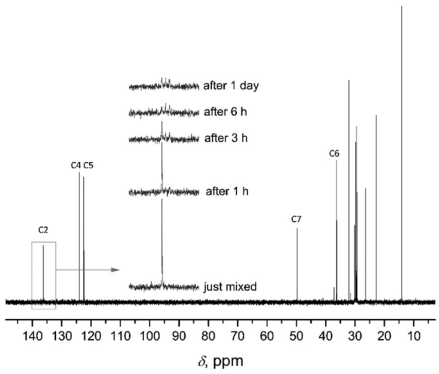

Figure 4. Monitoring of H/D exchange in ^{13}C NMR spectra of $[C_{10}mim][Br]$ in D_2O solution (0.01 mole fraction of RTIL) at T = 298 K.

studied using the relative intensity of C(2)−H signal in respect to HDO. In our opinion, the signal of the terminal $-CH_3$ group is more appropriate because it provides more steady internal reference to normalize the integrals. The intensity of HDO peak can be affected by the H/D exchange between D_2O (i.e., solvent molecules) and traces of H_2O or other R−OH species that may be present in the mixtures as impurities, e.g. adsorbed from the air during the sample preparation when highly hygroscopic RTILs are used.

The H/D exchange rates are very different and depending on the sample composition (Figure 5). The time dependencies of integral intensities in ^{1}H NMR spectra indicate that the H/D exchange in $[C_{10}mim][Br]$ at high dilution (10^{-4} mole fraction of RTIL) runs only slightly faster than in $[C_{10}mim][Cl]$ (Figure 5, top graph). The kinetics of this process drastically changes

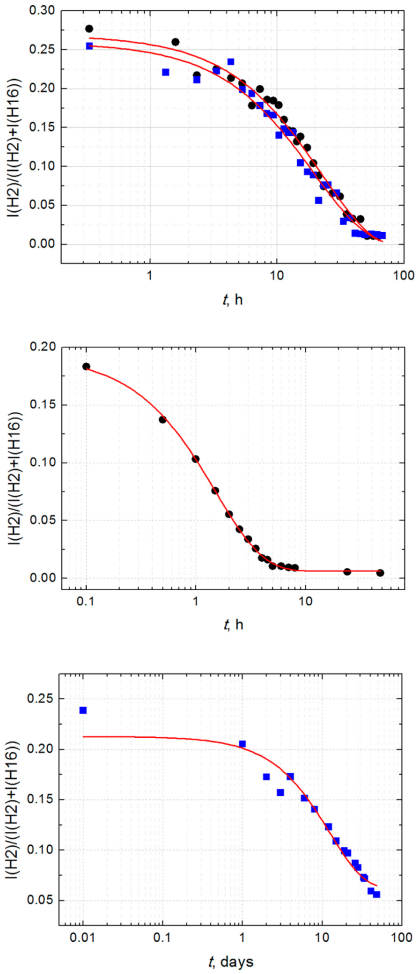

Figure 5. Kinetics of the H/D exchange reaction in $[C_{10}mim][X]$, X = Br (black circles) and Cl (blue squares) in D_2O solutions at high dilution (10^{-4} mole fraction of RTIL, top graph) and above CAC (0.01 mole fraction, middle and bottom graphs) monitored using the relative integral intensity of ^{1}H NMR signal of C(2)−H proton respect to the signal of the terminal $-CH_3$ group.

above CAC. The time required to reach the apparent reaction saturation regime was less 10 h for $[C_{10}mim][Br]$ (Figure 5, middle graph), whereas this reaction runs extremely slowly in $[C_{10}mim][Cl]/D_2O$ solution (Figure 5, bottom graph). Such kinetics is comparable to that observed in $[C_4mim][BF_4]$, where the time necessary to reach the apparent equilibrium state at certain D_2O concentrations was determined to be up to 40 days.[13,15] Note these our observations significantly differ from those in ref 16., where it was deduced that the fast H/D exchange does not occur in the solutions below CAC.

It is interesting to compare the reaction rates in RTILs containing the same anions. According to the data reported in the literature for [C_4mim][Cl], the level of deuteration at C(2) site of 91% was achieved in a 1:20 weight ratio (~ 0.0056 mole fraction, i.e. close to the present work) in D_2O solution in 24 h, however, after rising the sample temperature.[36] A much faster kinetics observed in [C_{10}mim][Br]/D_2O solutions is comparable with the literature data for [C_4mim][I] reported in ref 33. The ^{1}H NMR signal corresponding to the C(2)−H proton disappears completely in 0.01 mole fraction solution in D_2O after 20 h.[34]

No changes in the intensity of ^{1}H NMR signal of C(2)−H proton were noticed for the gel samples (0.4 mole fraction of RTIL) during 48 days of observation from the sample preparation. Thus, we can state that this reaction does not run in the gel phase.

Comparison of other ^{1}H integrals to that of −C(16)H_3 resonance indicates that in imidazolium ring only C(2)−H proton is involved in the H/D exchange under the present experimental conditions. This is important to know because it is quite often assumed that anions can bind to all three imidazolium ring protons[35,36(and refs therein)] and thus they could also undergo the H/D exchange.

Secondary Isotope Effect on ^{13}C Chemical Shifts. The central line of the C(2)−D triplet is shifted in respect to the ^{13}C NMR signal of C(2)−H (Figure 4). This is due to the so-called secondary isotope effect, which has been studied in more detail. The secondary isotope effect, that is, the change of chemical shifts (δ) upon H/D substitution, originates from coupling of the proton and deuteron vibrational wave functions to the rest of the system.[37] In other words, the differences in the geometry of the A−H(D)···B bridge slightly affect the geometry and the local electron density in the rest of molecule and is reflected in the corresponding chemical shift values. The primary isotope effect $\delta_H - \delta_D$, depending on the nuclei involved and H-bond features, can be quite strong, for example, reaching up to ~0.5−0.7 ppm in the case of strong and short H-bonds, such as the intramolecular bonding in quinaldic- or picolinic acid N-oxides, intermolecular complexes of carboxylic acids with pyridine, *etc.*[37,38] The secondary isotope effects are usually much smaller than the primary ones, although in certain cases they can be comparable. For example, $|\delta_H - \delta_D|$ for some ^{13}C resonances in picolinic acid N-oxide reaches 0.47−0.57 ppm (depending on solvent) in comparison to the primary one of 0.48−0.78 ppm.[37] It is quite remarkable that this huge effect was observed for the carbon atom that is distant from the site of deuterium substitution by five chemical bonds, whereas for the carbons closer to the O−H(D)···O moiety the effect was much smaller (0.02−0.23 ppm).

In the present work, the secondary deuterium isotope effect on ^{13}C chemical shifts has been observed for H-bonded ionic liquid systems for the first time. However, the deuterium isotope effects on other nuclei have been already used for the study of H-bond in ionic liquids.[36] In a model system, selectively deuterated [C_4mim][Cl], this effect was found to be very significant for the $^{35/37}$Cl resonances (1.0−1.9 ppm) and practically negligible (0.002−0.004 ppm) for ^{1}H NMR signals. For [C_{10}mim][X], X = Br, Cl used in these studies, it is most pronounced for C(2) being 0.24−0.25 ppm (Table 2). This effect is within 0.02−0.05 ppm for other imidazolium ring and neighboring carbons and negligible for the rest of decyl chain from C(8) to C(16). Hence, the magnitude of the effect differs from that observed in the case of strong and short H-bonded systems.[37,38] Also note that the sign of the secondary (^{13}C) isotope effect is the same ($\delta_H - \delta_D > 0$) for all carbons.

Table 2. Chemical Shifts of Carbon Nuclei and Secondary (^{13}C) Isotope Effects $\delta_H - \delta_D$ (in ppm) in [C_{10}mim][X], X = Br, Cl in D_2O Solution at 298 K

	[C_{10}mim][Cl]			[C_{10}mim][Br]		
carbon no.	H[a]	D[a]	$\delta_H - \delta_D$	H	D	$\delta_H - \delta_D$
C(2)	136.23	135.98	0.25	136.28	136.04	0.24
C(4)	122.34	122.30	0.04	122.46	122.41	0.05
C(5)	124.03	123.98	0.04	124.01	123.97	0.04
C(6)	36.11	36.08	0.03	36.27	36.24	0.03
C(7)	49.72	49.69	0.03	49.78	49.76	0.02

[a]The label 'H' refers to the species with a proton in C(2)−H···X^- bonding, while 'D' refers to that with a deuteron.

These data are very useful when discussing the possibility of conformational changes revealed in other closely related RTILs by Raman spectroscopy[15,34,39,40] and also for the future theoretical treatment of H-bond dynamics in ionic liquids using 2D models with quantum averaging.[37]

Monitoring of H/D Exchange Using Raman Spectra. The sample composition of 0.01 mole fraction of RTIL in D_2O was high enough to carry out the registration of Raman spectra at the same conditions as it was set in NMR studies. The Raman studies are important in trying to reveal the possibility of anomalous conformational changes around the C(7)−C(8) bond (Figure 1) that seem to be coupled with H-bonding and H/D exchange processes.[15,39]

It is reasonable to suppose that the most comprehensive information concerning the H/D exchange should be obtained analyzing the band of C(2)−H stretching vibration (νC(2)−H). However, this band is strongly overlapped with other νC−H bands in the spectral range 2900−3100 cm^{-1}.[34,39] There is also a significant discrepancy between experimental and calculated vibrational frequencies at higher wavenumbers.[39,40] All these factors puzzle the reliable assignment of the modes, as for example, the polemic in refs 41 and 42, and make the processing of the band contours and the determination of their parameters more cumbersome. Therefore, the H/D exchange was monitored using the time evolution of the Raman bands at 1010 and 1024 cm^{-1} (Figure 6), assigned as the combination of the in-plane ring deformation and CH_3(N) deformation.[15,39] These bands have been successfully exploited for the same purpose in Raman studies of [C_4mim][[BF_4]/D_2O mixtures.[15] The time dependency of their integral intensities (Figure 7) indicates that the H/D exchange in [C_{10}mim][Br] is much faster than in [C_{10}mim][Cl]. The time required to reach the apparent reaction saturation regime was ~200 min for [C_{10}mim][Br], whereas no features reaching this were seen for [C_{10}mim][Cl] even at ~1000 min after the sample was prepared (Figure 7). Thus, the Raman spectroscopy results support the NMR ones (Figure 5).

Special attention has been paid in this work to the spectral range around ~600 cm^{-1} (Figure 8). The Raman bands at *ca.* 600 and 620 cm^{-1} are very often used studying the conformational changes in hydrocarbon chains attached to the imidazolium cation.[15,34,39,40] It was deduced that the conformation of the butyl chains depends on the type of anion,[34] the *trans*−*gauche* change can occur at the melting,[40] or it can be coupled with the H/D exchange.[15] The significant relative redistribution in the intensities at 602 and 625 cm^{-1} is clearly seen in the Raman spectra of both studied RTIL/D_2O

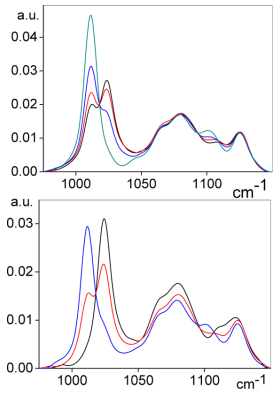

Figure 6. Monitoring of H/D exchange on the Raman bands at 1010 and 1024 cm^{-1} of $[C_{10}mim][X]$, X = Br (top; at 10 (black), 20 (red), 50 (blue), and 900 (green) min after the sample prepared) and Cl (bottom; at 10 (black), 200 (red), and 900 (blue) min) in D_2O solution (0.01 mole fraction of RTIL) at T = 296 K.

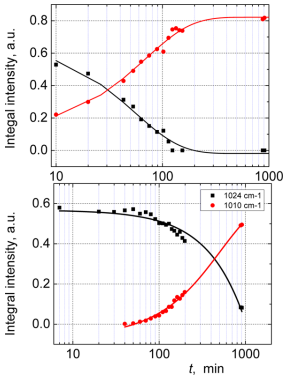

Figure 7. Kinetics of the H/D exchange reaction in $[C_{10}mim][X]$, X = Br (top) and Cl (bottom) in D_2O solution monitored using the integral intensities of Raman bands at 1010 and 1024 cm^{-1} (see Figure 6).

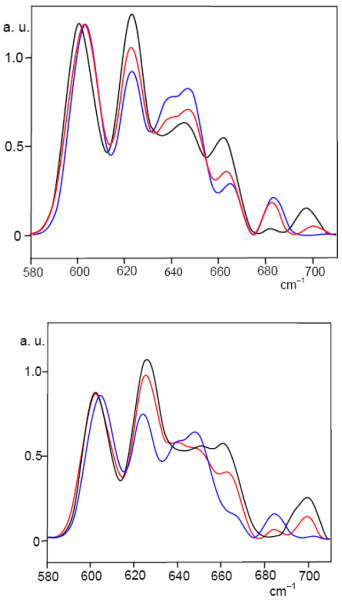

Figure 8. Time dependencies of Raman spectra in the range 600−700 cm^{-1} of $[C_{10}mim][X]$, X = Br (top; at 10 (black), 60 (red), and 150 (blue) min after the sample prepared) and Cl (bottom; at 20 (black), 220 (red), and 900 (blue) min) in D_2O solution (0.01 mole fraction of RTIL) at T = 296 K.

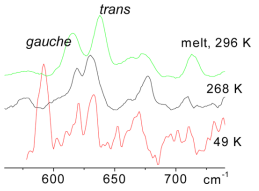

Figure 9. Raman spectra of $[C_{10}mim][Br]$ in the range 600−800 cm^{-1} in the liquid (296 K) and crystalline (268 and 49 K) phases.

systems (Figure 8). However, in the present case of $[C_{10}mim]^+$ (i.e. the cation with 10 carbons in the chain), it is somehow hardly credible to attribute this evolution being a completely conformational effect. Indeed, the Raman experiments carried out varying the temperature in the wide range on the neat $[C_{10}mim][Br]$ have revealed that the conformational composition was hardly changeable even passing through the melting and at further cooling up to 49 K (Figure 9). This behavior completely differs from the case of $[C_4mim][Cl]$ observed at the melting point and thermal equilibration at 72 °C.[40]

We are inclined to think that the complex redistribution of several Raman intensities (Figure 8) is due to the changes in positions of some strongly overlapping bands in this spectral range upon deuteration at C(2) site. To check this idea, vibrational modes in the range 500−700 cm^{-1} have been analyzed using DFT calculations on the *trans* and *gauche* conformers of the $[C_4mim]^+$ cation as a model system. Three different modeling schemes have been adopted. First, harmonic vibrational analysis was performed *in vacuo*. To account for the effects of aqueous environment, we have relied on the PCM as well as supermolecular approach,[43,44] where a hydrogen bonded complex of $[C_4mim]^+$ cation and a water molecule is placed into PCM void. The latter approach is believed to be particularly effective, since it accounts for both short- and long-range interactions simultaneously.[45] The calculated Raman spectra are shown in Figure 10. It is seen that for the *trans*-conformer the one of three bands (labeled as B in Figure 10), contributes the intensity of the neighboring band A. However, the band B shifts upon deuteration of C(2)−H to the lower wavenumbers (dashed arrows, Figure 10). Thus, the observed decrease of Raman intensity in the experimental spectra at 625 cm^{-1} (i.e. the band attributed to *trans*- conformer), (Figure 8) indeed can be explained by the shift of one of the overlapping

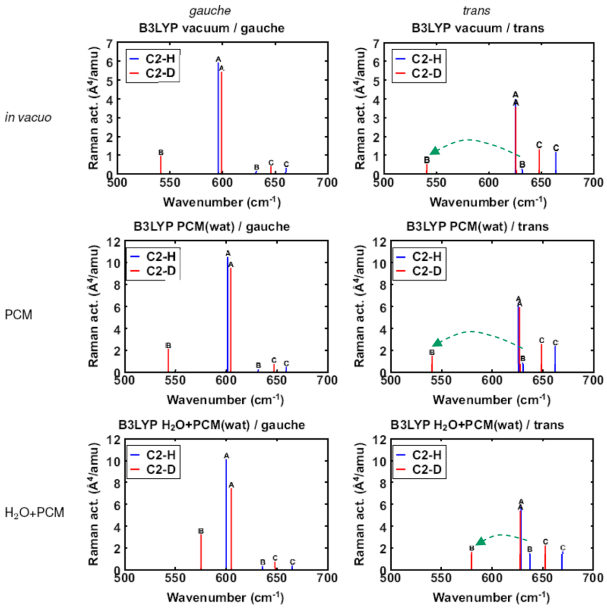

Figure 10. Raman modes of *gauche* and *trans* forms of $[C_4mim]^+$ calculated at the level B3LYP/6-311++G** *in vacuo*, in water as solvent using PCM, as well as for 'supermolecule' $[C_4mim]^+ \cdot H_2O$ in H_2O. More comments in text.

bands. This finding is qualitatively supported by all three modeling schemes used. The performed anharmonic analysis did not lead to the changes in the qualitative picture as well.

Discussion. The obtained results on the H/D exchange reaction rates should be discussed in more details. As it has been noted in ref 11, the interaction between the imidazolium cation and anion is strongly altered by the nature of the anions. On the one hand the smaller and more basic anions (i.e., Cl^- in the studied systems; ionic radii 1.81 Å) strengthen the H-bond as compared to the larger anions (Br^-, ionic radii 1.96 Å). The strengthening of H-bond should stimulate the larger amplitude motion of the proton. In the case of imidazolium-based RTILs, this motion could culminate producing carbene-like motif with a complete proton abstraction.[11,46] Hence, the exchange of proton by deuteron should go easier in the case of Cl^- anions. However, there are some other remarkable features that elucidate to behave the H-bond in the studied systems quite differently from the 'traditional' H-bonds. Such features are, for example, very weak and positive sloped dependence of the chemical shift of the C(2)−H proton on temperature $\Delta\delta/\Delta T \sim +10^{-3}$ ppm/deg, in comparison with $\Delta\delta/\Delta T \sim -10^{-2}$ ppm/deg for water and HDO,[35] the C(2)−H and C(4,5)−H stretching bands in FTIR spectra yielding a blue-shift with increasing dilution in water,[47] *etc.* It means that in this class of ionic liquids we deal with the H-bond systems that are 'inverted' respect to the traditional ones in the sense discussed in the Introduction. On the other hand, the anions in highly diluted aqueous solutions are solvated, and therefore, their role in H-bonding is significantly reduced. Moreover, the H/D exchange is coupled with the rotational dynamics of water molecules.[12] The interaction with anions hinders the rotational motion of D_2O molecules in the solvation shell and is the stronger the smaller the size of the anion. The activation energies for the rotational motion of water molecules in the hydration spheres of Cl^- and Br^- are 3.3 and 2.9 kcal/mol, respectively.[48] The rotational 'freezing' of D_2O molecules can hinder the supply of deuterons to the site of exchange. We assume that these are the main factors that cause only a small difference in the H/D exchange kinetics for both RTILs at high dilution (Figure 5, top graph), where the exchange is taking place between D_2O and the C(2)−H hydrogen of the cation and this process is mediated by the presence of the anion (i.e. Cl^- or Br^-).

The rotational motion of molecules and the diffusion are highly restricted in the liquid crystalline mesophases. Indeed, the H/D exchange was not observed in the gel mesophase, which was identified as liquid crystalline ionogel.[23,24,26] No changes in the spectra have been observed even after 48 days from the sample preparation.

The H/D exchange can be discussed in the terms of the ion pairing.[49,50] The importance of this process for ionic liquids was studied very recently.[50] It was shown that there exists a certain "magic number" of water molecules that is necessary to disrupt the strongly bound ion pairs (contact ion pairs, CIP) initiating their transition to the solvent-separated state (solvent-separated ion pairs, SIPs). For instance, for some protic ionic liquids, it was determined that a minimum of four water molecules were needed to initiate the transition from CIPs to SIPS.[50] It was also noted that this process strongly depends on the anions, and it is expected that for other RTILs such transition may begin at lower water content. Unfortunately, the "magic number" of water molecules is not known for $[C_{10}mim][X]$,

X = Br, Cl solutions in D_2O. Intuitively, it could be supposed that it should be slightly below CAC. Hence, two extreme cases of the present studies, that is, the mixtures at high dilution (10^{-4} mole fraction of RTIL) and in the gel phase (0.4 mole fraction of RTIL), can be considered as the ionic systems being in SIP and CIP states, respectively. The strong anion−cation interaction impedes the H/D exchange process in the gel phase. This factor can be considered as additional contribution to the slowdown of rotational dynamics discussed just above.

The most complex situation appears between these two extreme cases, that is, at the compositions slightly above CAC. The kinetics of H/D exchange drastically changes in the samples of ∼0.01 mole fraction of RTIL (Figure 5). This process, depending on the anions, can be very significantly damped ([C_{10}mim][Cl]) or stimulated ([C_{10}mim][Br]). Unfortunately, it is virtually unknown how certain inherent properties of RTIL influence the self-aggregation and phase behavior of RTIL/water solutions. Theoretical modeling presented in ref 28 has revealed that the micelle sizes and shapes depend on the counterion type and alkyl chain length but also on the number molecules that are involved in the modeling. Water molecules can be trapped in different environments and dictate the shape and size of the aggregates.[28] Various aspects of micelle formation and structure have been explored experimentally by SANS, NMR, fluorescence, surface tension, and conductivity measurements and other techniques.[28,31,32,51−54] It was demonstrated that general features of micellar aggregation of long-chain imidazolium-based RTILs in aqueous solutions are rather similar to those of conventional ionic surfactants having the same hydrocarbon chains.[31,51] Higher inclination for aggregation and thus the lower values of CAC of RTILs can be attributed to the capability of imidazolium groups to form H-bonds with anions.[51] Beside CAC, micelle formation can be characterized by other important parameters such as shape and size, aggregation number, degree of counterion binding, *etc.* Regrettably, not all of these parameters can be collected from the literature for [$C_n$mim][X] with n = 10, X = Br and Cl in aqueous solution which were studied in the present work. Therefore, data for closely related RTILs (e.g. for those with n = 8 − 12 or $X = I^-$, BF_4^-) have to be taken and used for discussion.

Namely, it was deduced that the effect of anions X = Br^- and BF_4^- on the degrees of counterion binding of [$C_n$mim][X] with n = 10 and 12 in water was minor,[32] even though these anions differ in their size and hydrophobicity very significantly. The effect of anions is, however, significant for the size, aggregation number (N_{agg}), and shape of micelles.[52−54] For example, micelles formed in [C_8mim][I] solutions possess over the concentration range for which the structure of aggregates is more or less stable the core radii of 13.2 ± 0.5 Å and $N_{agg} \approx 40$, to be compared to 10.5 ± 0.5 Å and $N_{agg} \approx 20$ for [C_8mim][Br] or 13.4 ± 0.4 Å and $N_{agg} \sim 33 - 45$ for [C_{10}mim][Br] solutions, respectively.[52−54] Also, aggregates in [$C_n$mim][X] systems containing $X = Br^-$ and I^- were found to be nearly spherically shaped. The micelles in [C_{10}mim][Br] solutions become increasingly elongated with increasing RTIL concentration.[54] In contrast to bromine and iodide systems, the [C_8mim][Cl] in aqueous solution appears to form disk-like rather than spherical aggregates.[53,54]

Nevertheless, this data does not provide an answer to the question of why Br^- and Cl^- anions could so crucially influence the H/D exchange reaction rates above CAC. It is likely possible that this is indeed a much finer phenomenon related to the microscopic (short-range) ordering and molecular microdynamics, in particular, that of water molecules. SANS experiments on aqueous solutions of [C_8mim][Cl] suggest the presence of some structures with interdigitated alkyl chains, the ordering of micellar rods, or the formation of sheets of bilayers.[53] Moreover, at moderate concentrations, the long-range order between [C_8mim][Cl] aggregates is more pronounced than in the [C_8mim][I] solutions.[53] The patterns of deuteron quadrupolar splitting in ^{2}H NMR spectra provide extremely valuable information on this. The ^{2}H NMR experiments carried out using deuterated species of [$C_n$mim]-[X], n = 8 and 10, X = Br^- and Cl^- in aqueous solutions have revealed that (i) Cl^- is more strongly solvated than Br^- and thus the D_2O molecules are residing in a more ordered environment in the case of [$C_n$mim][Cl]; (ii) larger anions, viz. Br^-, are less tightly bound to the micelle surface and thus enhanced repulsive interactions can destabilize the mesophase.[54] This conclusion is in fact entirely consistent with our observations, namely greater ordering and much slower dynamics in the gel phase is more clearly pronounced on the ^{1}H NMR signal shapes of [C_{10}mim][Cl] than in the case of [C_{10}mim][Br] gel, as illustrated in Figure 3. It is obvious that these observations first of all highlight the effect of the anions on the differential mesophase properties of studied RTIL/water solutions. However, it is reasonable to expect a certain phase memory, namely, more ordered mesophase can grow from more ordered building units (i.e., micelles).

We would like to conclude that a higher degree of molecular freedom due to the order−disorder effects plays the crucial role in the H/D exchange reaction in the studied systems. The presented experimental results are expected to be useful for the molecular design of ionic liquids and the modeling of micellar structures in aqueous solutions.

The conformational changes that can be coupled with the H/D exchange, as it was observed in ref 15, do not occur in the studied systems. The complex redistribution of several Raman intensities (Figure 8) can be due to the frequency shifts of some strongly overlapped bands upon the H/D exchange. More rigorously, this idea can be rejected in the light of ^{13}C NMR results. For this purpose, the ^{13}C NMR shielding tensors of *trans* and *gauche* forms of $[C_4mim]^+ \cdot H_2O$ 'supermolecule' in H_2O, again as a model system, have been calculated at the level of PBE0/6-311++G(2d,2p)/PCM. We have utilized and checked this theoretical approach in our previous studies, where it was found that the PBE0 functional applied together with the polarizable continuum model (PCM) gives very good agreement between calculated and experimental ^{1}H and ^{13}C chemical shifts and perfectly reproduces many observed tendencies, for H-bonded systems in particular.[6,55,56] The calculated isotropic parts of ^{13}C NMR shielding tensors are given in Table 3. It follows that if *trans−gauche* conformational transition really runs in the studied RTILs it would be easily noticeable in ^{13}C NMR spectra: the spectral distancing between C(4) and C(5) signals should increase ∼1.5 ppm, even more significant shifts should be observed for the carbons in the hydrocarbon chain, for example, − 3.4 ppm for C(8), (Table 3). Nothing like this has been observed in spectra. Thus, the observed changes (Table 2) indeed can be attributed to the secondary (^{13}C) isotope effects, the values of which are comparable with those determined for many other H-bond systems,[37,38] than to suppose that the signal shifts are due to the conformational *trans−gauche* transition.

Table 3. Isotropic Parts of ^{13}C NMR Shielding Tensors (σ) of *trans* and *gauche* Forms of $[C_4mim]^+$ Calculated at the Level of PBE0/6-311++G(2d,2p)/PCM using $[C_4mim]^+ \cdot H_2O$ 'Supermolecule' in H_2O as Solvent and the Predictable Shifts of Corresponding Carbon Signals in NMR Spectra ($\Delta\sigma$) Due to the Conformational Changes (all in ppm)

carbon no.	σ_{trans}	σ_{gauche}	$\Delta\sigma = \sigma_{trans} - \sigma_{gauche}$
C(2)	45.12	44.43	+ 0.69
C(4)	59.07	60.25	− 1.18
C(5)	58.78	58.37	+ 0.41
C(6)	150.52	150.53	− 0.01
C(7)	133.38	133.34	+ 0.04
C(8)	149.44	152.81	− 3.37

CONCLUSIONS

The anions and aggregation effects play crucial role in RTIL aqueous solutions. The anions interact with cations via H-bonds and bind the water molecules in their solvation shells. The overlap and the competition of these processes may cause rather complex dependency of the H/D exchange reaction rate on the sample composition and on other experimental conditions (temperature, degree of purification, *etc.*). The H/D exchange process, depending on the anions, can be very significantly damped or stimulated above critical aggregation (micellization) concentration. This reaction does not run in the liquid crystalline gel phase.

The concept of the conformational changes coupled with the H/D exchange in $[C_{10}mim][X]$, X = Br and Cl, maybe also in others imidazolium-based RTILs with longer hydrocarbon chains, can be rejected by ^{13}C NMR data. The revealed changes in ^{13}C NMR spectra are caused by the secondary isotope effects on chemical shifts not being the signal shifts due to the conformational *trans*−*gauche* transition.

AUTHOR INFORMATION

Corresponding Author

*E-mail: vytautas.balevicius@ff.vu.lt.

Notes

The authors declare no competing financial interest.

ACKNOWLEDGMENTS

The study was funded from the European Community's social foundation under Grant Agreement No. VP1-3.1-ŠMM-08-K-01-004/KS-120000-1756.

REFERENCES

(1) *Ionic Liquids in Synthesis*, 2nd ed.; Wasserscheid, P., Welton, T., Eds.; Wiley-VCH: Weinheim, 2008.
(2) Wishart, J. F.; Castner, E. W. The Physical Chemistry of Ionic Liquids. *J. Phys. Chem. B* **2007**, *111* (18), 4639−4640.
(3) Fukushima, T.; Aida, T. *Chem.—Eur. J.* **2007**, *13*, 5048−5058.
(4) *Electrochemical Aspects of Ionic Liquids*; Ohno, H., Ed.; John Wiley: Hoboken, NJ, 2005.
(5) Fumino, K.; Wulf, A.; Ludwig, R. *Angew. Chem., Int. Ed.* **2008**, *47*, 8731−8734.
(6) Balevicius, V.; Gdaniec, Z.; Aidas, K. *Phys. Chem. Chem. Phys.* **2009**, *11*, 8592−8600.
(7) Balevicius, V.; Bariseviciute, R.; Aidas, K.; Svoboda, I.; Ehrenberg, H.; Fuess, H. *Phys. Chem. Chem. Phys.* **2007**, *9*, 3181−3189.
(8) Szafran, M. *J. Mol. Struct.* **1996**, *381*, 39−64.
(9) Koeppe, B.; Tolstoy, P. M.; Limbach, H. H. *J. Am. Chem. Soc.* **2011**, *133*, 7897−7908.
(10) Balevicius, V.; Aidas, K.; Svoboda, I.; Fuess, H. *J. Phys. Chem. A* **2012**, *116*, 8753−8761.
(11) Cremer, T.; Kolbeck, C.; Lovelock, K. R. J.; Paape, N.; Woelfel, R.; Schulz, P. S.; Wasserscheid, P.; Weber, H.; Thar, J.; Kirchner, B.; Maier, F.; Steinrueck, H. P. *Chem.—Eur. J.* **2010**, *16*, 9018−9033.
(12) Yasaka, Y.; Wakai, C.; Matubayasi, N.; Nakahara, M. *J. Phys. Chem. A* **2007**, *111*, 541−543.
(13) Ohta, S.; Shimizu, A.; Imai, Y.; Abe, H.; Hatano, N.; Yoshimura, Y. *Open J. Phys. Chem.* **2011**, *1*, 70−76.
(14) Nakakoshi, M.; Ishihara, S.; Utsumi, H.; Seki, H.; Koga, Y.; Nishikawa, K. *Chem. Phys. Lett.* **2006**, *427*, 87−90.
(15) Hatano, N.; Watanabe, M.; Takekiyo, T.; Abe, H.; Yoshimura, Y. *J. Phys. Chem. A* **2012**, *116*, 1208−1212.
(16) Dontsov, S.; Shemetova, E. S.; Chernyshev, Y. S. *Abstracts of NMRCM-2012*, 9−13 July, Saint Petersburg, Russia, p 75.
(17) *Almanac*; Bruker-Biospin: Billerica, MA, 2011; p. 22.
(18) Frisch, M. J.; Trucks, G. W.; Schlegel, H. B.; Scuseria, G. E.; Robb, M. A.; Cheeseman, J. R.; Scalmani, G.; Barone, V.; Mennucci, B.; Petersson, G. A. et al. *Gaussian* 09, revision C.01; Gaussian, Inc., Wallingford, CT, 2010.
(19) Becke, A. D. *J. Chem. Phys.* **1993**, *98*, 5648−5652.
(20) Krishnan, R.; Binkley, J. S.; Seeger, R.; Pople, J. A. *J. Chem. Phys.* **1980**, *72*, 650−654.
(21) Tomasi, J.; Mennucci, B.; Cammi, R. *Chem. Rev.* **2005**, *105*, 2999−3093.
(22) Barone, V. *J. Chem. Phys.* **2005**, *122*, 014108(10).
(23) Firestone, M. A.; Dzelawa, J. A.; Zapol, P.; Curtiss, L. A.; Seifert, S.; Dietz, M. L. *Langmuir* **2002**, *18*, 7258−7260.
(24) Inoue, T.; Dong, B.; Zheng, L. Q. *J. Colloid Interface Sci.* **2007**, *307*, 578−581.
(25) Balevicius, V.; Gdaniec, Z.; Aidas, K.; Tamuliene, J. *J. Phys. Chem. A* **2010**, *114*, 5365−5371.
(26) Balevicius, V.; Dziaugys, L.; Kuliesius, F.; Marsalka, A. *Lith. J. Phys.* **2011**, *51*, 212−220.
(27) Blesic, M.; Marques, M. H.; Plechkova, N. V.; Seddon, K. R.; Rebelo, L. P. N.; Lopes, A. *Green Chem.* **2007**, *9*, 481−490.
(28) Singh, T.; Kumar, A. *J. Phys. Chem. B* **2007**, *111*, 7843−7851.
(29) Zhao, Y.; Gao, S.; Wang, J.; Tang, J. *J. Phys. Chem. B* **2008**, *112*, 2031−2039.
(30) Jungnickel, C.; Luczak, J.; Ranke, J.; Fernandez, J. F.; Mueller, A.; Thoeming, J. *Colloids Surf., A* **2008**, *316*, 278−284.
(31) Dong, B.; Zhao, X.; Zheng, L.; Zhang, J.; Li, N.; Inoue, T. *Colloids Surf., A* **2008**, *317*, 666−672.
(32) Dong, B.; Li, N.; Zheng, L.; Inoue, T. *Langmuir* **2007**, *23*, 4178−4182.
(33) Sirieix-Plenet, J.; Gaillon, L.; Letellier, P. *Talanta* **2004**, *63*, 979−986.
(34) Jeon, Y.; Sung, J.; Seo, C.; Lim, H.; Cheong, H.; Kang, M.; Moon, B.; Ouchi, Y.; Kim, D. *J. Phys. Chem. B* **2008**, *112*, 4735−4740.
(35) Balevicius, V.; Gdaniec, Z.; Dziaugys, L.; Kuliesius, F.; Marsalka, A. *Acta Chim. Slov.* **2011**, *58*, 458−464.
(36) Remsing, R. C.; Wildin, J. L.; Rapp, A. L.; Moyna, G. *J. Phys. Chem. B* **2007**, *111*, 11619−11621.
(37) Stare, J.; Jezerska, A.; Ambrozic, G.; Kosir, I.; Kidric, J.; Koll, A.; Mavri, J.; Hadzi, D. *J. Am. Chem. Soc.* **2004**, *126*, 4437−4443.
(38) Dziembowska, T.; Hansen, P. E.; Rozwadowski, Z. *Progr. Magn. Res. Spectrosc.* **2004**, *45*, 1−29.
(39) Berg, R. W.; Deetlefs, M.; Seddon, K. R.; Shim, I.; Thompson, J. M. *J. Phys. Chem. B* **2005**, *109*, 19018−19025.
(40) Berg, W. R. *Monatsh. Chem.* **2007**, *138*, 1045−1075.
(41) Wulf, A.; Fumino, K.; Ludwig, R. *J. Phys. Chem. A* **2010**, *114*, 685−686.
(42) Lassegues, J. C.; Grondin, J.; Cavagnat, D.; Johansson, P. *J. Phys. Chem. A* **2010**, *114*, 687−688.
(43) Noell, J. O.; Morokuma, K. *Chem. Phys. Lett.* **1975**, *36*, 465−469.
(44) Mikkelsen, K. V.; Luo, Y.; Ågren, H.; Jørgensen, P. *J. Chem. Phys.* **1995**, *102*, 9362(7).

(45) Mennucci, B.; Martinez, J. M.; Tomasi, J. *J. Phys. Chem. A* **2001**, *105*, 7287−7296.
(46) Arduengo, A. J., III; Dixon, D. A.; Kumashiro, K. K.; Lee, C.; Power, W. P.; Zilm, K. W. *J. Am. Chem. Soc.* **1994**, *116*, 6361−6367.
(47) Gao, Y.; Zhang, L.; Wang, Y.; Li, H. *J. Phys. Chem. B* **2010**, *114*, 2828−2833.
(48) Endom, L.; Hertz, H. G.; Tuehl, B.; Zeidler, M. D. *Ber. Bunsen-Ges. Phys. Chem.* **1967**, *71*, 1008−1031.
(49) Marcus, Y.; Hefter, G. *Chem. Rev.* **2006**, *106*, 4585−4621.
(50) Stange, P.; Fumino, K.; Ludwig, R. *Angew. Chem., Int. Ed.* **2013**, *52*, 2990−2994.
(51) Inoue, T.; Ebina, H.; Dong, B.; Zheng, L. Q. *J. Colloid Interface Sci.* **2007**, *314*, 236−241.
(52) Wang, J.; Wang, H.; Zhang, S.; Zhang, H.; Zhao, Y. *J. Phys. Chem. B* **2007**, *111*, 6181−6188.
(53) Bowers, J.; Butts, C. P.; Martin, P. J.; Vergara-Gutierrez, M. C.; Heenan, R. K. *Langmuir* **2004**, *20*, 2191−2198.
(54) Goodchild, I.; Collier, L.; Millar, S.; Prokes, I.; Lord, J. C. D.; Butts, C. P.; Bowers, J.; Webster, J. R. P.; Heenan, R. K. *J. Colloid Interface Sci.* **2007**, *307*, 455−468.
(55) Aidas, K.; Marsalka, A.; Gdaniec, Z.; Balevicius, V. *Lith. J. Phys.* **2007**, *47*, 443−449.
(56) Balevicius, V.; Balevicius, V. J.; Aidas, K.; Fuess, H. *J. Phys. Chem. B* **2007**, *111*, 2523−2532.

Journal of Molecular Structure 993 (2011) 91–96

Contents lists available at ScienceDirect

Journal of Molecular Structure

journal homepage: www.elsevier.com/locate/molstruc

Raman and NMR spectroscopy study of liquid crystalline ionogel phase in ionic liquid/H_2O mixtures: The states of water

V. Aleksa [a], J. Kausteklis [a], V. Klimavicius [a], Z. Gdaniec [b], V. Balevicius [a,*]

[a] Vilnius universitety, Faculty of Physics, Sauletekio al. 9-3, LT-10222 Vilnius, Lithuania
[b] Institute of Bioorganic Chemistry, Polish Academy of Sciences, Z. Noskowskiego 12/14, PL-61704 Poznan, Poland

ARTICLE INFO

Article history:
Available online 23 January 2011

Keywords:
Ionogel
Aqueous mixture of ionic liquid
Raman scattering
NMR spectroscopy
PCA
2D correlation analysis

ABSTRACT

The Raman spectra of 1-decyl-3-methyl-imidazolium bromide ([C_{10}mim][Br]) aqueous solutions have been measured while continuously increasing the water content in the system (0–100%). Principal component (PC) and 2D Raman correlation (2DCOR) analysis has been carried out, the main attention concentrating to the region of O–H stretching vibrations at 3100–3800 cm^{-1}. The band structure has been resolved in the loadings on PC1 and PC2 as well as in 2DCOR spectra. It indicates the presence in the studied system of several nonequivalent states of water. Various states of water have been also revealed in the ^{1}H NMR spectra. They have been assigned to non-bonded or weakly H-bonded water molecules, those involved in the fast isotropic reorientational motion as well as in the H-bond exchange processes and finally – water in the LC ionogel structures. The last contributes the ^{1}H NMR line shape typical for anisotropic liquids with zero biaxiality (asymmetry) of magnetic shielding and the chemical shift anisotropy of *ca* 0.6 ppm. The borders of the liquid crystalline (LC) ionogel phase have been determined using the concentration dependence of the integral intensities of Raman bands and the scores on PC1.

1. Introduction

Ionic liquids (ILs, a synonym of molten salts having low melting points) are one of the most successful breakthroughs of the last years creating novel multifunctional materials those posses many appealing features [1,2]. Varying different combinations of anionic and cationic subsystems one can tune their physical and chemical properties. Since the number of such combinations is practically uncountable, the possibility to control various molecular processes in IL media makes these systems very attractive as for fundamental research as well as for technologies.

Ionic liquids and numerous compositions containing IL as one of the component fall into the class of the systems that earlier were called as 'complex fluids' [3]. Their defining feature is the presence of a mesoscopic length scale which plays a key role in determining the most properties of the system. And indeed, numerous recent works on the IL systems revealed the presence of nanoscale organization effects, the appearance of micro-heterogeneous phases, etc. ([4–9] and the references cited therein).

The presence of water in IL systems strongly affects their physical and chemical properties, aggregation and phase behavior, structural changes, etc. [10–15]. The water can be added deliberately by mixing with ILs, or it can present as contaminant, e.g. from air [16]. Some of imidazolium-based room temperature ionic liquids (RTILs) with long alkyl chains can form various liquid crystalline (LC) phases in water solution [10,14,15]. E.g., in the case of [C_{12}mim][Br] the phases were determined more precisely being lamellar (L_α) and hexagonal (H_1) ones [15], and for [C_{10}mim][Br] it was identified as LC ionogel [14]. It exists at room temperature over the wide range of concentration (5–40% mass fraction of water). In these sample conditions a complex-shaped ^{81}Br NMR signal as well as several new ^{1}H peaks has been observed in NMR spectra [8]. These peaks can be originated from the H_2O molecules trapped in inhomogeneous regions of the sample or due to the appearance of non-equivalent water sites in LC ionogel, the exchange between those is highly restricted or even frozen.

The vibrational spectroscopy (FTIR, Raman) can be particularly powerful method studying the states of water in the IL/water compositions [4,12,16,17]. Perhaps the most informative are the modes that are coupled with H-bonding vibrations of water molecules. Unfortunately, in the case of the water νO–H bands the distances between the maxima of the sub-bands are much smaller then their widths. The separation of such strongly overlapped bands cannot be correctly done using the standard treatments, such as the second derivative or Fourier deconvolution [18]. Therefore in the present work the methods of principal components (PCA) and two-dimensional correlation (2DCOR) analysis were used. The PCA [18–20] and 2DCOR [21,22], can give considerable enhancement

* Corresponding author. Tel.: +370 5 2366001; fax: +370 5 2366003.
E-mail address: vytautas.balevicius@ff.vu.lt (V. Balevicius).

0022-2860/$ - see front matter © 2011 Elsevier B.V. All rights reserved.
doi:10.1016/j.molstruc.2010.12.060

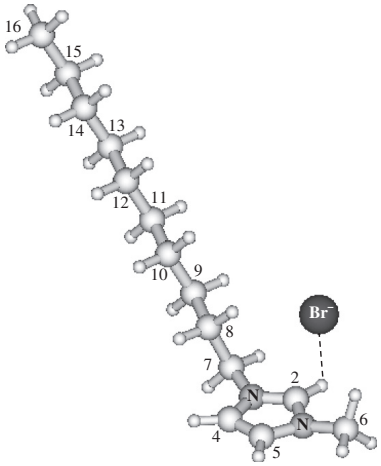

Fig. 1. The structure of [C_{10}mim][Br] (optimized by DFT B3LYP/6-31++G**, *in vacuo* [8]) and the atom numbering.

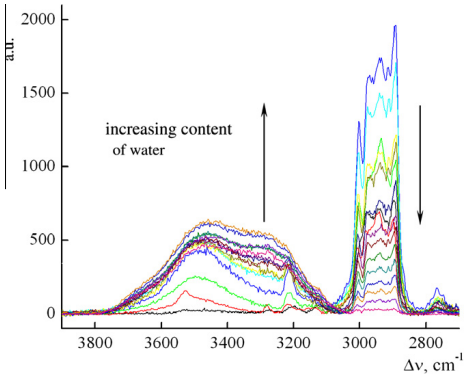

Fig. 2. Raman spectra of [C_{10}mim][Br] aqueous solutions in the O–H and C–H stretching regions (3800–3100 and 3100–2800 cm^{-1}, respectively) with changing concentration: 0.01, 0.12, 0.3, 0.41, 0.47, 0.53, 0.61, 0.65, 0.7, 0.75, 0.78, 0.83, 0.9, 0.93, 0.95 and 0.98 mass fraction of water.

in the resolution, and thus, they can be effective tools solving this problem. It has been already demonstrated on NIR spectra of water [18,19] and on FTIR spectra of IL/water and IL/alcohol systems [23,24]. In the present work these techniques were applied on the Raman spectra.

The purpose of present studies was: (i) to register the Raman spectra of [C_{10}mim][Br] aqueous solutions continuously increasing the water content (0–100%). The whole set of spectral data obtained in this way is then processed them applying PCA and 2DCOR analysis; (ii) to analyze the line shapes in ^{1}H NMR spectra by precise integration of the signals searching for water peaks that can be hidden due to overlap with the signals of [C_{10}mim][Br]. It is expected that the complex exploitation of obtained Raman and NMR data will provide new valuable information on the processes of LC ionogel phase formation, the role and the states of water molecules in this system.

2. Experimental

The room temperature ionic liquid – 1-decyl-3-methyl-imidazolium bromide ([C_{10}mim][Br], from Merck KGaA, Darmstadt, 99% purity) was dried under vacuum at 80 °C for 1 day. Its structure and atom numbering are shown in Fig. 1. The water used was freshly bidistilled. The presence of water was examined by the precise integration of ^{1}H NMR signals of [C_{10}mim][Br] and all those suspected to be originated from the impurities (details below). The water content evaluated in this way was found to be less than 0.05 mol fraction. The samples of [C_{10}mim][Br] in solutions were prepared by weighting (±0.1 mg) the components. In the cases of extremely viscous gel was formed those RTIL/water compositions were weighted and mixed homogeneously by standing the samples at 80 °C for several hours.

Raman spectra were recorded using a DFS-12 double-grating spectrometer with a slit width of 0.08 mm. This value of the slit width was found to be optimal. Namely, a recording of the weakest Raman bands was still possible at this setting, but on the other hand the instrumental broadening of the observed bandwidth could be neglected. The excitation source was an argon-ion laser (Stabilite, *SpectraPhysics*) operating at 488.0 nm (120 mW) or 514.5 nm (120 mW). All measurements were carried out at the 90° scattering geometry. The detection part of the instrument consists of photo-multiplier and a photon-counting system on line with a standard computer. PCA and 2D Raman correlation analysis was carried out using a Mathcad program written in the Laboratory of Raman spectroscopy at Vilnius University.

NMR experiments were carried out on a BRUKER AVANCE^{II}/400 NMR spectrometer operating at 400 for ^{1}H using 5 mm BBO probehead. The temperature in a probe was controlled with an accuracy of ±0.5 K. The signal of DSS in D_2O solution in capillary insert was used as the reference and then converted in δ-scale respect tetramethylsilane (TMS) taking δ(TMS) = 0.015 ppm. The D_2O in the same capillary insert was used for locking.

3. Results and discussion

The dynamic spectra for 2D correlation analysis are constructed using the spectral intensity variation upon external perturbation [21,22]. As an external stimulus can be any reasonable measure of a physical quantity, such as mechanical deformation, temperature, or concentration. The continuous perturbation of the Raman spectra using a 'concentration' (X) as the external variable has been chosen in the present work.

The Raman spectra (raw spectra, or spectrum vectors) $I(\omega, X_j)$, $j = 1, \ldots, m$ of [C_{10}mim][Br] in aqueous solutions have been measured while continuously increasing the water content in the system. Total $m = 16$ spectra have been registered that correspond to various sample compositions listed in the caption of Fig. 2. The original spectra were baseline corrected and renormalized respect to the argon plasma line. Dynamic spectra $I_d(\omega, X_j)$ are constructed from the spectrum vectors $I(\omega, X_j)$ subtracting the reference spectrum. Its selection is somewhat arbitrary. It is usually set to be the averaged spectrum, although other forms may be chosen [22]. However, if one has a series of experiments with stable baseline, or the baseline is well defined, the choice of the reference weakly influents the results of 2D correlation analysis [25]. Therefore in the present work the zero-Raman intensity (after baseline correction) was used as the reference.

The processing of experimental data using PCA and 2DCOR was realized in the following steps. The data matrix **D** was composed

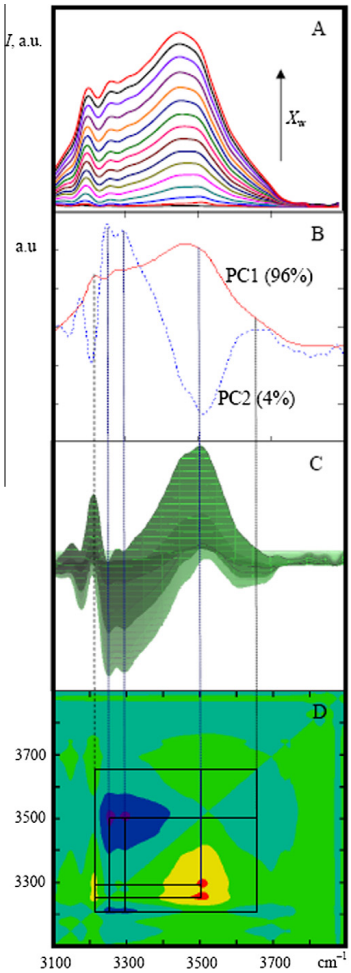

Fig. 3. Raman spectra of [C_{10}mim][Br] aqueous solutions at different water concentrations (X_w = 0 ÷ 0.98 mass fraction) in the range of 3100–3900 cm^{-1} (A); loadings on the first and second principal components (B); 2D Raman asynchronous correlation spectra in the surface (C) and contour plotting (D).

placing the spectra $I_d(\omega, X_j)$ ($I(\omega, X_j)$) in m rows. The corresponding covariance matrix was then obtained multiplying **D** by its transpose $\mathbf{D}^{\mathbf{T}}$:

$$\mathbf{Z} = \mathbf{D}^{\mathbf{T}}\mathbf{D}. \quad (1)$$

In this case, i.e. the so-called variable–variable approach [19], the covariance matrix is coincident with the synchronous correlation spectrum used in the traditional Noda formalism of 2DCOR [22]: $\Phi \sim \mathbf{Z}$, whereas the asynchronous correlation spectrum Ψ can be calculated as

$$\Psi \sim \mathbf{D}^{\mathbf{T}}\mathbf{H}\mathbf{D}, \quad (2)$$

where **H** is the Hilbert transform matrix. In the next steps the loads ($\boldsymbol{p}_i$) vectors were obtained by solving

$$\mathbf{Z}\boldsymbol{p}_i = \lambda_i \boldsymbol{p}_i, \quad (3)$$

where λ_i is the eigenvalue associated with the eigenvector $\boldsymbol{p}_i$ [20]. The scores vectors ($\boldsymbol{t}_i$) were then calculated as

$$\boldsymbol{t}_i = \mathbf{D}\boldsymbol{p}_i. \quad (4)$$

The number of the statistically significant principal components was evaluated using the argument of physical changes *vs.* nondeterministic variation proposed in [18]. It was found that first two PCs capture practically total amount of variation in the Raman spectra in the range of 3100–3900 cm^{-1} upon dilution, viz. ~96% (PC1) and <4% (PC2), respectively (Fig. 3A and B). The scores for the third PC (<1%) looked like a noise and therefore PC3 was further not analyzed. The results of 2DCOR analysis of Raman spectra of [C_{10}mim][Br]/water solution are shown in Fig. 3C and D.

The vibrational νO–H bands of water molecules have been analyzed in the literature solving a broad variety of structuring problems in the systems with H_2O as one of the components [4,12,17,26]. It is quite common to decompose this complex and very broad spectral contour into three components, recognizing them as: 3220–3330 cm^{-1} (H_2O molecules involved in more regular structures of fairly unstrained H-bonds, the 'ice-like' peak, 'network water'); 3400–3560 (water molecules trapped into more

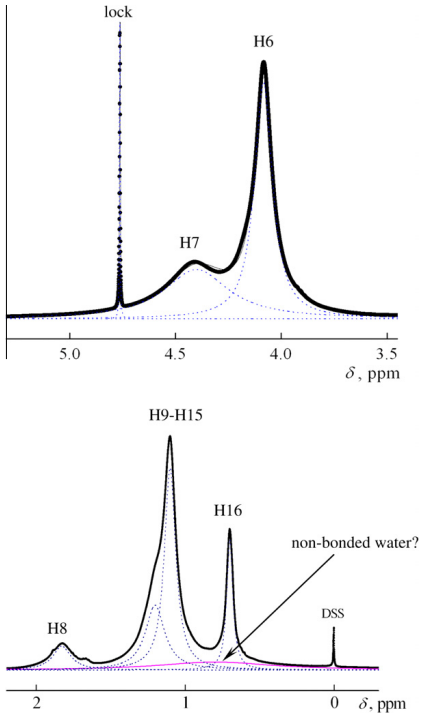

Fig. 4. Searching for contaminant water signal in the neat [C_{10}mim][Br]. For hydrogen numbering see Fig. 1.

irregular structures with energetically unfavorable H-bonds, the 'liquid-like' peak, 'intermediate water') and ~3600 cm^{-1} (H_2O monomers, non-H-bonded or weakly H-bonded OH groups). In brackets are given the terminologies used by different authors. These peaks can be quite easily extracted from the *ν*O–H contours also in the present case of [C_{10}mim][Br]/water solutions (Fig. 2) using standard Gaussian band shape approach and the nonlinear curve fitting procedure. However, the PCA and 2D correlation analysis allowed getting into more details.

The Raman bands below ~3200 cm^{-1} are originated from the imidazolium ring C–H stretching and other *ν*C–H modes of RTIL [12]. More fine structure of the band envelope at 3220–3510 cm^{-1} can be resolved in the loadings of the principal components as well as in the asynchronous 2D maps (Fig. 3). Namely, the cross-peaks at 3220, 3260, 3290 3510 and 3690 cm^{-1} indicate that various non-equivalent states of water are very likely in [C_{10}mim][Br]/H_2O system. These states may appear from several origins. The attribution of the bands at 3690 and 3501 cm^{-1} to non-H-bonded or weakly H-bonded OH groups and, respectively, to water molecules trapped into more irregular structures seems to be most obvious. The last ones can be realized in the different sized/formed cages built up by different conformers of IL and from the H_2O molecules trapped in inhomogeneous regions in LC ionogel phase. The situation can be rather close to that in the reverse microemulsion of [C_4mim][BF_4]/Triton X-100/Cyclohexane [4], where water molecules were found located mainly in the periphery of the polar core of the microemulsion droplets. The broad intensive band at 3290 cm^{-1} can be attributed to the 'ice-like' or 'network water'. Two other peaks at 3220 and 3260 cm^{-1} can be assigned to water molecules very tightly bonded to RTIL. Note two nonequivalent sites (two potential minima on the energy surface) placing water surround Br^- ion in [C_{10}mim][Br] have been found by quantum chemistry calculations [27]. The cross correlation of these peaks in 2D Raman spectrum with that at 3690 cm^{-1}, i.e. H_2O monomers, indicates that the population of these states goes via interacting monomeric water with RTIL species (Fig. 3D). These states should be energetically more favorable than in the regular 'network water'. Moreover, these peaks can be detected in the Raman spectra of [C_{10}mim][Br]/water solutions at very low concentrations of water (~0.01 mass fraction), or sometimes even in the 'neat' RTIL. In such cases water should be considered as a contaminant that cannot be removed from RTIL completely using standard drying methods (see Experimental). Thus the term 'neat ionic liquid' looks then rather provisory and it should be used with a reservation.

Additional information can provide the NMR spectra. More details concerning the H-bonding and the behavior of ^{1}H NMR signals of imidazolium ring protons in [C_{10}mim][Br] are given in Ref. [8]. The main task of the present work was to analyze the line shapes in ^{1}H NMR spectra by precise integration of the signals searching for water peaks that can be hidden due to overlap with the signals of [C_{10}mim][Br].

It is well-known that ^{1}H NMR signal of non-bonded water is expected between *ca* 1–2 ppm, depending on the solvent [28]. The signal that can pretend to be assigned as one of non-H-bonded or weakly H-bonded OH groups was found at ~0.8 ppm only in the neat [C_{10}mim][Br] (Fig. 4). This peak was extracted from the group

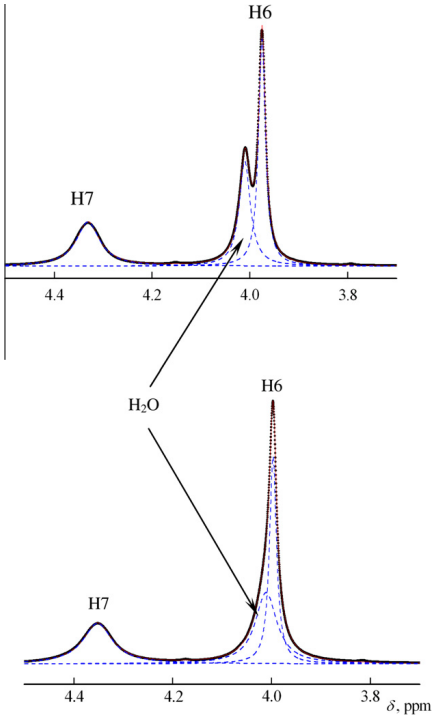

Fig. 5. ^{1}H NMR signals of bounded waterin [C_{10}mim][Br] aqueous solutions at 0.038 and 0.055 mass fraction of H_2O (the lower and the upper spectra, respectively).

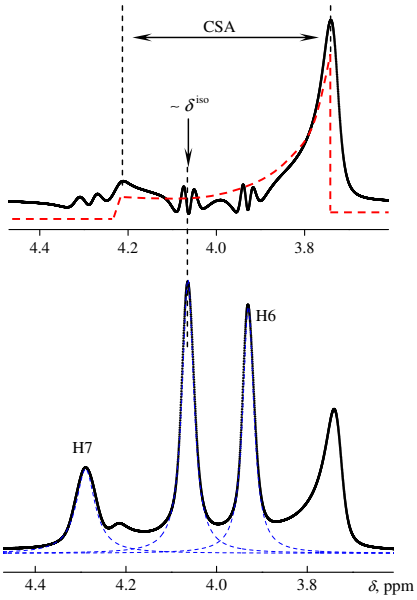

Fig. 6. The line shape of H_2O signal in the LC ionogel phase (0.12 mass fraction of H_2O) obtained from ^{1}H NMR spectrum by the removing of H6 and H7 peaks as well as the signal of water molecules involved in the fast isotropic reorientational motion (δ^{iso}). CSA indicates the approximate magnitude of the chemical shift anisotropy.

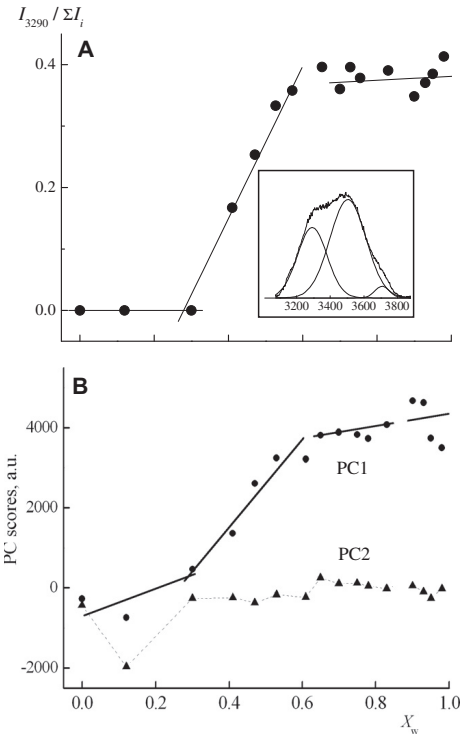

Fig. 7. Determination of the borders of LC ionogel phase in $[C_{10}mim]Br/H_2O$ solution: from the concentration dependence of the integral intensity of overlapped Raman *v*OH bands of water (an insert) by nonlinear curve fitting (A); from the scores of the first and second PCs (B). More comments in text.

of IL signals H8, H9–H15 and H16 (for numbering see Fig. 1) in rather complicated way. Namely, it was added to the curve fitting procedure as an 'extra' peak in order to ensure the correct values of the integral intensities of H8, H9–H15 and H16 signals: 2:14:3. The signal of the bulk water, or water at high concentrations, is shifted to 4.5–5.5 ppm due to H-bonding, depending on solute and temperature (e.g. the peak at 4.7–4.8 ppm of HDO in the capillary insert used for the lock, Fig. 4). The position of bonded- and non-bonded water resonance at the intermediate H_2O concentrations is averaged. No additional water peaks was found at 2–5 ppm range, even hidden under H7 and H6 signals of $[C_{10}mim][Br]$ (Fig. 4). The correct ratio of the integrals of H7 and H6 signals, i.e. 2:3, was achieved by 2 Lorentz functions fitting.

Adding water deliberately, i.e. by mixing with $[C_{10}mim][Br]$, its ^1H NMR signal develops at 4–4.2 ppm (Fig. 5). The water peak is still hidden under the H6 peak, when water concentration in $[C_{10}mim][Br]/H_2O$ is less ca 0.04 mass fractions. Its presence was confirmed by the determination of the excess of the integral intensity of H6 peak from the expected 2:3 ratio of integral intensities of H7 and H6 protons. Above 0.055 mass fractions, i.e. getting into LC ionogel phase, the H_2O peak gradually emerged on the low field side of the H6 contour (Fig. 5).

The most interesting ^1H NMR line shape was observed at the compositions that produce the LC ionogel phase. In these conditions several new ^1H NMR signals appeared in the range of 3.7–4.4 ppm (Fig. 6). The line shape of H_2O signal in the LC ionogel phase was obtained from ^1H NMR spectrum by the removing of H6 and H7 peaks as well as the signal of water molecules involved in the fast isotropic reorientational motion (δ^{iso}). Such ^1H NMR line shape is typical for anisotropic liquids with zero biaxiality (asymmetry) of magnetic shielding [29]. The chemical shift anisotropy (CSA) of *ca* 0.6 ppm can be approximately evaluated from the extent of the anisotropic line shape (Fig. 6).

Some aspects of determination of the borders of LC ionogel phase using spectroscopy data should to be discussed. The most pronounced dependence of chemical shift on amount of water was observed for H-bonded H2. . .Br^- bridge proton and the weakest effect was detected for the terminal methyl group, $-C(16)H_3$ [8]. Unfortunately, only the critical aggregation concentration in the aqueous solution phase at high dilution can be determined using these data [8]. Thus the chemical shifts of $[C_{10}mim][Br]$ are not suitable estimating the borders of the supposed mesophases. The processing of Raman intensities of *v*O–H bands seems to be much powerful tool solving this problem. The scores on the first PC and the concentration dependence of the relative integral intensities of Raman bands of water allow to determine the borders of LC ionogel phase (Fig. 7). These quantities indeed highlight that water is getting drastic ordered in the concentration range 0.2–0.5 mass fraction of H_2O. This range significantly overlaps with those $[C_{10}mim][Br]/H_2O$ compositions (∼0.05–0.4) where liquid crystalline behavior was detected by SAXS, DSC and polarized microscopy [14].

4. Conclusions

1. The Raman spectra of $[C_{10}mim][Br]/H_2O$ solutions have been measured using composition as an external perturbation, *viz.* continuously increasing the water content in the system (0–100%). PCA and 2D Raman correlation analysis has been carried out, the main attention concentrating to the region of O–H stretching vibrations at 3100–3800 cm^{-1}. The band structure has been resolved in the PC loadings and in 2D correlation maps. It indicates the presence of several nonequivalent states of water in the studied system: non-H-bonded (or weakly H-bonded) water molecules, those trapped into irregular structures (different sized/formed cages, inhomogeneous regions in LC ionogel phase, etc.), the ordered ('ice-like') water and H_2O molecules tightly bonded to RTIL.
2. Various states of water have been revealed in the ^1H NMR spectra: non-H-bonded water molecules that can be present in the neat $[C_{10}mim][Br]$ as contaminant (broad NMR signal at ∼0.8 ppm), those involved in the fast isotropic reorientational motion and taking part in the H-bond exchange processes (the averaged signal positioned at ∼4–4.2, depending on concentration), molecules involved in more regular structures, i.e. the 'bulk water' (the signal at 4.8 ppm observed in highly diluted aqueous solution phase), and finally – water in the LC ionogel structures. The last contributes the ^1H NMR line shape typical for anisotropic liquids with zero biaxiality (asymmetry) of magnetic shielding and the chemical shift anisotropy of *ca* 0.6 ppm.
3. The scores on PC1 and the concentration dependence of the integral intensities of overlapped Raman *v*OH bands of water highlight the borders of LC ionogel phase.

Acknowledgments

We are grateful to Profs. Wolffram Schröer (Bremen University), Hermann Weingärtner (Bochum University), Miroslaw Czarnecki

(Wroclaw University) and Dr. Joze Grdadolnik (National Institute of Chemistry, Ljubljana) for stimulating discussions and comments. The work was supported by the Research Council of Lithuania.

References

[1] R. Ludwig, Chem. Phys. Chem. 7 (2006) 1415.
[2] M. Koel, W. Linert, P. Gaertner, Monatsh. Chem. 138 (2007) V–VI.
[3] W.M. Gelbart, A. Ben-Saul, J. Phys. Chem. 100 (1996) 13169.
[4] Y. Gao, L. Hilfer, A. Voigt, K. Sundmacher, J. Phys. Chem. B 112 (2008) 3711.
[5] A. Triolo, O. Russina, H.J. Bleif, E. Di Cola, J. Phys. Chem. B 111 (2007) 4641.
[6] A. Triolo, O. Russina, B. Fazio, G.B. Appetecchi, M. Carewska, S. Passerini, J. Chem. Phys. 130 (2009). 164521/1-6.
[7] M. Blesic, A. Lopes, E. Melo, Z. Petrovski, N.V. Plechkova, J.N. Canongia Lopes, K.R. Seddon, L.P.N. Rebelo, J. Phys. Chem. B 112 (2008) 8645.
[8] V. Balevicius, Z. Gdaniec, K. Aidas, J. Tamuliene, J. Phys. Chem. A 114 (2010) 5365.
[9] C. Jungnickel, J. Luczak, J. Ranke, J.F. Fernandez, A. Mueller, J. Thoerming, J. Thoerming, Colloids and Surfaces A: Physicochem. Eng. Aspect. 316 (2008) 278.
[10] T. Singh, A. Kumar, J. Phys. Chem. B 111 (2007) 7843.
[11] T. Takamuku, Y. Kyoshoin, T. Shimomura, S. Kittaka, T. Yamaguchi, J. Phys. Chem. B 113 (2009) 10817.
[12] B. Fazio, A. Triolo, G. Di Marco, J. Raman Spectrosc. 39 (2008) 233.
[13] B. Dong, X. Zhao, L. Zheng, J. Zhang, N. Li, T. Inoue, Colloids and Surfaces A: Physicochem. Eng. Aspect. 317 (2008) 666.
[14] M.A. Firestone, J.A. Dzelawa, P. Zapol, L.A. Curtiss, S. Seifert, M.L. Dietz, Langmuir 18 (2002) 7258.
[15] T. Inoue, B. Dong, L.Q. Zheng, J. Coll. Int. Sc. 307 (2007) 578.
[16] L. Cammarata, S.G. Kazarian, P.A. Salter, T. Welton, Phys. Chem. Chem. Phys. 3 (2001) 5192.
[17] Y. Jeon, J. Sung, D. Kim, C. Seo, H. Cheong, Y. Ouchi, R. Ozawa, H. Hamaguchi, J. Phys. Chem. B 112 (2008) 923.
[18] B. Czarnik-Matusewitz, S. Pilorz, Vib. Spectrosc. 40 (2006) 235.
[19] V.H. Segtnan, Š. Šašic, T. Isaksson, Y. Ozaki, Anal. Chem. 73 (2001) 3153.
[20] C. Thibault, P. Huguet, P. Sistat, G. Pourcelly, Desalination 149 (2002) 429.
[21] I. Noda, Y. Ozaki, Two-Dimensional Correlation Spectroscopy: Applications in Vibrational and Optical Spectroscopy, Wiley, Chichester, 2004.
[22] I. Noda, Appl. Spectrosc. 54 (2000) 994.
[23] L. Zhang, Z. Xu, Y. Wang, H. Li, J. Phys. Chem. B 112 (2008) 6411.
[24] M. Lopez-Pastor, M.J. Ayora-Canada, M. Valcarcel, B. Lendl, J. Phys. Chem. B 110 (2006) 10896.
[25] J. Grdadolnik, Private Communication.
[26] M. Freda, G. Onori, A. Santucci, J. Phys. Chem. B 105 (2001) 12714.
[27] A. Gruodis, V. Aleksa, V. Pogorelov, I. Doroshenko, V. Balevicius, Abstracts of International Conference Physics of Liquid Matter: Modern Problems, Kyiv, Ukraine, May 21–24, 2010, p. 164.
[28] M. Nakahara, C. Wakai, Chem. Lett. (1992) 809.
[29] M.H. Levitt, Spin Dynamics: Basics of Nuclear Magnetic Resonance, Wiley, Chichester, 2008. p. 205.

NOTES

Vilniaus universiteto leidykla
Universiteto g. 1, LT-01513 Vilnius
El. p. info@leidykla.vu.lt,
www.leidykla.vu.lt
Tiražas 15 egz.